Simulating Correlations with Computers

Eva Pavarini and Erik Koch (Eds.)

JÜLICH
Forschungszentrum

Forschungszentrum Jülich GmbH
Institute for Advanced Simulation

**Lecture Notes of the Autumn School on
Correlated Electrons 2021**

Eva Pavarini and Erik Koch (Eds.)

Simulating Correlations with Computers

Autumn School organized by
the Institute for Advanced Simulation
at Forschungszentrum Jülich
20 – 24 September 2021

Contents

Preface

Index

Preface

The combinatorial growth of the Hilbert space makes the many-electron problem one of the grand challenges of theoretical physics. Progress relies on the development of non-perturbative methods, based on either wavefunctions or self energies. This made, in recent years, calculations for strongly correlated materials a reality. These simulations draw their power from three sources: theoretical advances, algorithmic developments, and the raw power of massively parallel supercomputers. Turning to quantum hardware could give quantum materials science the ultimate boost. Before quantum parallelism can be exploited, however, many questions, algorithmic and engineering, need to be addressed.

This year's school will provide students with an overview of the state-of-the-art of many-body simulations and the promises of quantum computers. After introducing the basic modeling techniques and the concept of entanglement in correlated states, lectures will turn to methods that do not rely on wavefunctions, comparing density-functional theory, the GW method and dynamical mean-field approaches. Advanced lectures will broaden the discussion, addressing topics from the Luttinger-Ward functional to non-equilibrium Green functions. As a glimpse of future possibilities, the basics of quantum computing and its possible uses in materials simulations will be outlined.

Eva Pavarini and Erik Koch

August 2021

1 Second Quantization and Jordan-Wigner Representations

Erik Koch

Jülich Supercomputer Centre

Forschungszentrum Jülich

Contents

1 Many-electron states

One of the great mysteries of quantum mechanics is the existence of indistinguishable objects. Classically this is not possible: objects can always be distinguished, at least by their position in space, meaning that indistinguishable objects must be identical. This is Leibniz' Principle of the Identity of Indiscernibles [1]. For quantum objects, however, the uncertainty principle makes the distinction of particles by their position impossible. This allows for the existence of elementary particles. They form the basic units of all matter. So, quite remarkably, all the different objects we know are made of indistinguishable building blocks.

In the formalism of quantum mechanics, indistinguishability means that no observable lets us distinguish one of these particles from the other. Consequently, every observable for, e.g., electrons, must treat each electron in the same way. Thus, in principle, observables must act on all the electrons in the universe. In practice we can, of course, distinguish electrons localized on the moon from those in our lab to an excellent approximation. Thus, for all practical purposes, we can restrict ourselves to the electrons in the system under consideration, assuming that the differential overlap with all other electrons vanishes. Any observable $M(x_1, \ldots, x_N)$ for the N electrons in our system must then be symmetric under permutations of the coordinates x_i.

The consequences are straightforward: An observable $M(x)$ acting on a single-particle degree of freedom x must act on all indistinguishable particles in the same way, i.e., $\sum_i M(x_i)$. Likewise, a two-body observable $M(x, x')$ must act on all pairs in the same way, $\sum_{i,j} M(x_i, x_j)$ with $M(x, x') = M(x', x)$. We can thus write any observable in the form

$$M(\mathbf{x}) = M^{(0)} + \sum_i M^{(1)}(x_i) + \frac{1}{2!} \sum_{i \neq j} M^{(2)}(x_i, x_j) + \frac{1}{3!} \sum_{i \neq j \neq k} M^{(3)}(x_i, x_j, x_k) + \cdots \quad (1)$$

$$= M^{(0)} + \sum_i M^{(1)}(x_i) + \sum_{i < j} M^{(2)}(x_i, x_j) + \sum_{i < j < k} M^{(3)}(x_i, x_j, x_k) + \cdots, \quad (2)$$

where the summations can be restricted since the operators must be symmetric in their arguments, while for two or more identical coordinates the operator is really one of lower order: $M^{(2)}(x_i, x_i)$, e.g., only acts on a single coordinate and should be included in $M^{(1)}$.

For the many-body wave functions $\Psi(x_1, x_2, \cdots)$ the situation is slightly more complex. Since the probability density $|\Psi(x_1, x_2, \cdots)|^2$ is an observable, the wave function should transform as one-dimensional (irreducible) representations of the permutation group. Which irreducible representation applies to a given type of elementary particle is determined by the spin-statistics theorem [2, 3]: The wave functions of particles with integer spin are symmetric, those of particles with half-integer spin change sign when two arguments are exchanged. From an arbitrary N-particle wave function we thus obtain a many-electron wavefunction by antisymmetrizing

$$\mathcal{A}\Psi(x_1, \ldots, x_N) := \frac{1}{N!} \sum_P (-1)^P \Psi\left(x_{p(1)}, \ldots, x_{p(N)}\right), \quad (3)$$

where $(-1)^P$ is the parity of the permutation P that maps $n \to p(n)$. Since there are $N!$ different permutations, this can easily become an extremely costly operation. Remarkably, a product of

N single-electron states φ_α can be antisymmetrized much more efficiently (in $\mathcal{O}(N^3)$ steps) by writing it in the form of a determinant

$$\Phi_{\alpha_1,\dots,\alpha_N}(x_1,\dots,x_N) := \frac{1}{\sqrt{N!}} \begin{vmatrix} \varphi_{\alpha_1}(x_1) & \varphi_{\alpha_2}(x_1) & \cdots & \varphi_{\alpha_N}(x_1) \\ \varphi_{\alpha_1}(x_2) & \varphi_{\alpha_2}(x_2) & \cdots & \varphi_{\alpha_N}(x_2) \\ \vdots & \vdots & \ddots & \vdots \\ \varphi_{\alpha_1}(x_N) & \varphi_{\alpha_2}(x_N) & \cdots & \varphi_{\alpha_N}(x_N) \end{vmatrix} = \sqrt{N!}\,\mathcal{A}\,\varphi_{\alpha_1}(x_1)\cdots\varphi_{\alpha_N}(x_N)$$

$$(4)$$

For $N=1$ the Slater determinant is simply the one-electron orbital $\Phi_\alpha(x) = \varphi_\alpha(x)$ while for $N=2$ we get the familiar expression $\Phi_{\alpha,\alpha'}(x,x') = \big(\varphi_\alpha(x)\varphi_{\alpha'}(x') - \varphi_{\alpha'}(x)\varphi_\alpha(x')\big)/\sqrt{2}$ for the two-electron Slater determinant.

Slater determinants are important because they can be used to build a basis of the many-electron Hilbert space. To see how, we consider a complete set of orthonormal single-electron states

$$\sum_n \overline{\varphi_{\alpha_n}(x)}\,\varphi_{\alpha_n}(x') = \delta(x-x') \text{ (complete)} \quad \int dx\,\overline{\varphi_{\alpha_n}(x)}\,\varphi_{\alpha_m}(x) = \delta_{n,m} \text{ (orthonormal)}.$$

$$(5)$$

To expand an arbitrary N-particle function $a(x_1,\dots,x_N)$, we start by considering it as a function of x_1 with the $x_2,\dots,x_N$ kept fixed. We can then expand it in the complete set $\{\varphi_{\alpha_n}\}$ as

$$a(x_1,\dots,x_N) = \sum_{\alpha_1} a_{\alpha_1}(x_2,\dots,x_N)\,\varphi_{\alpha_1}(x_1)$$

with expansion coefficients that depend on the remaining coordinates

$$a_{\alpha_1}(x_2,\dots,x_N) = \int dx_1\,\overline{\varphi_{\alpha_1}(x_1)}\,a(x_1,x_2,\dots,x_N).$$

These, in turn, can be expanded as a functions of x_2

$$a_{\alpha_1}(x_2,\dots,x_N) = \sum_{\alpha_2} a_{\alpha_1,\alpha_2}(x_3,\dots,x_N)\,\varphi_{\alpha_2}(x_2).$$

Repeating this, we obtain the expansion of a in product states

$$a(x_1,\dots,x_N) = \sum_{\alpha_1,\dots,\alpha_N} a_{\alpha_1,\dots,\alpha_N}\,\varphi_{\alpha_1}(x_1)\cdots\varphi_{\alpha_N}(x_N).$$

When the N-particle function is antisymmetric, the expansion coefficients must be antisymmetric under permutation of the indices: $a_{\alpha_{p(1)},\dots,\alpha_{p(N)}} = (-1)^P a_{\alpha_1,\dots,\alpha_N}$. Fixing some particular order of the indices, e.g., $\alpha_1 < \alpha_2 < \dots < \alpha_N$, we thus get an expansion in Slater determinants

$$\Psi(x_1,\dots,x_N) = \sum_{\alpha_1<\dots<\alpha_N} a_{\alpha_1,\dots,\alpha_N} \underbrace{\sum_P (-1)^P \varphi_{\alpha_{p(1)}}(x_1)\cdots\varphi_{\alpha_{p(N)}}(x_N)}_{=\sqrt{N!}\,\Phi_{\alpha_1,\dots,\alpha_N}(x_1,\dots,x_N)}.$$

Since we can write any antisymmetric function as such a configuration-interaction expansion, the set of Slater determinants

$$\left\{ \Phi_{\alpha_1,\dots,\alpha_N}(x_1,\dots,x_N)\,\middle|\,\alpha_1 < \alpha_2 < \cdots < \alpha_N \right\} \tag{6}$$

forms a basis of the N-electron Hilbert space. Since the overlap of two Slater determinants

$$\int d\boldsymbol{x}\, \overline{\Phi_{\alpha_1,\ldots,\alpha_N}(\boldsymbol{x})}\, \Phi_{\beta_1,\ldots,\beta_N}(\boldsymbol{x}) = \frac{1}{N!}\sum_{P,P'}(-1)^{P+P'}\prod_n \int dx_n\, \overline{\varphi_{\alpha_{p(n)}}(x_n)}\, \varphi_{\alpha_{p'(n)}}(x_n)$$

$$= \begin{vmatrix} \langle\varphi_{\alpha_1}|\varphi_{\beta_1}\rangle & \cdots & \langle\varphi_{\alpha_1}|\varphi_{\beta_N}\rangle \\ \vdots & \ddots & \vdots \\ \langle\varphi_{\alpha_N}|\varphi_{\beta_1}\rangle & \cdots & \langle\varphi_{\alpha_N}|\varphi_{\beta_N}\rangle \end{vmatrix} \quad (7)$$

is the determinant of the overlap of the constituent orbitals, the Slater determinants (6) form a complete orthonormal basis of the N-electron Hilbert space when the orbitals $\varphi_n(x)$ are a complete orthonormal basis of the one-electron Hilbert space.

While we use a set of N one-electron orbitals $\varphi_n(x)$ to define an N-electron Slater determinant $\Phi_{\alpha_1,\ldots,\alpha_N}(\boldsymbol{x})$, this representation is not unique: Any unitary transformation among the N occupied orbitals will not change the determinant (up to a phase). It is thus sufficient to give the N-dimensional subspace spanned by the orbitals $\varphi_1, \ldots, \varphi_N$ in the single-electron Hilbert space. The projector to this space is the one-body density matrix

$$\Gamma^{(1)}(x,x') = N\int dx_2\cdots dx_N\, \overline{\Phi(x,x_2,\ldots,x_N)}\, \Phi(x',x_2,\ldots,x_N)\,. \quad (8)$$

To see this, we expand the Slater determinant along its first row

$$\Phi_{\alpha_1\cdots\alpha_N}(x_1,\ldots,x_N) = \frac{1}{\sqrt{N}}\sum_{n=1}^{N}(-1)^{1+n}\varphi_{\alpha_n}(x_1)\,\Phi_{\alpha_{i\neq n}}(x_2,\ldots,x_N)\,, \quad (9)$$

where $\Phi_{\alpha_{i\neq n}}(x_2,\ldots,x_N)$ is the determinant with the first row and the n-th column removed, which can be written as $N-1$-electron Slater determinants with orbital α_n removed. Inserting this into (8) we find

$$\Gamma_\Phi^{(1)}(x,x') = \sum_{n=1}^{N}\overline{\varphi_{\alpha_n}(x)}\,\varphi_{\alpha_n}(x')\,, \quad (10)$$

which is the expansion of the one-body density matrix in eigenfunctions (natural orbitals), with eigenvalues (natural occupation numbers) either one or zero. Due to the degeneracy of the natural occupation numbers the natural orbitals are not unique. Any many-electron wave function $\Psi(\boldsymbol{x})$ with the same one-body density matrix $\Gamma_\Phi^{(1)}$ equals the Slater determinant $\Phi(\boldsymbol{x})$ up to a phase, i.e., $|\langle\Psi|\Phi\rangle| = 1$. We can generalize this procedure and calculate higher order density matrices by introducing the generalized Laplace expansion

$$\Phi_{\alpha_1\cdots\alpha_N}(\mathbf{x}) = \frac{1}{\sqrt{\binom{N}{p}}}\sum_{n_1<\cdots<n_p}(-1)^{1+\sum_i n_i}\,\Phi_{\alpha_{n_1}\cdots\alpha_{n_p}}(x_1,\ldots,x_p)\Phi_{\alpha_{i\notin\{n_1,\ldots,n_p\}}}(x_{p+1},\ldots,x_N),$$

which is obtained by writing the permutation of all N indices as a permutation of $N-p$ indices and the remaining p indices separately summing over all distinct sets of p indices. This allows us to evaluate arbitrary matrix elements and higher order density matrices [4,5]. But as can be seen from the above expansion, the expressions very quickly get quite cumbersome. Fortunately there is a representation that is much better suited to handling antisymmetric wave functions. It is called second quantization.

2   Second quantization

The idea behind the second quantized approach to writing many-body wave functions is remarkably simple: When writing Slater determinants in the form (4) we are working in a real-space basis. It is, however, often simpler to consider abstract states: Instead of a wave function $\varphi_\alpha(x)$, we write a Dirac state $|\alpha\rangle$. Second quantization allows us to do the same for Slater determinants. Let us consider a Slater determinant for two electrons, one in state $\varphi_\alpha(x)$, the other in state $\varphi_\beta(x)$. It is simply the antisymmetrized product of the two states

$$\Phi_{\alpha\beta}(x_1, x_2) = \frac{1}{\sqrt{2}} \left(\varphi_\alpha(x_1)\varphi_\beta(x_2) - \varphi_\beta(x_1)\varphi_\alpha(x_2) \right). \tag{11}$$

This expression is quite cumbersome because we explicitly specify the coordinates. We can try to get rid of the coordinates by defining a two-particle Dirac state

$$|\alpha, \beta\rangle := \frac{1}{\sqrt{2}} \left(|\alpha\rangle|\beta\rangle - |\beta\rangle|\alpha\rangle \right).$$

While the expression is already simpler, we still have to keep track of the order of the particles by specifying the position of the kets. The idea of second quantization is to specify the states using operators

$$|\alpha, \beta\rangle = c_\beta^\dagger c_\alpha^\dagger |0\rangle. \tag{12}$$

Now the order of the particles is specified by the order of the operators. To ensure the antisymmetry of the wave function the operators have to change sign when they are reordered

$$|\alpha, \beta\rangle = c_\beta^\dagger c_\alpha^\dagger |0\rangle = -c_\alpha^\dagger c_\beta^\dagger |0\rangle = -|\beta, \alpha\rangle. \tag{13}$$

2.1   Creation and annihilation operators

To arrive at the formalism of second quantization we postulate a set of operators that have certain reasonable properties. We then verify that we can use these operators to represent Slater determinants. But first we consider a few simple states to motivate what properties the new operators ought to have.

To be able to construct many-electron states, we start from the simplest such state: $|0\rangle$ the *vacuum state* with no electron, which we assume to be normalized $\langle 0|0\rangle = 1$. Next we introduce for each single-electron state $|\alpha\rangle$ an operator $c_\alpha^\dagger$ such that $c_\alpha^\dagger|0\rangle = |\alpha\rangle$. We call them *creation operators* since they add an electron (in state α) to the state that they act on: in $c_\alpha^\dagger|0\rangle$ the creation operator adds an electron to the vacuum state ($N{=}0$), resulting in a single-electron state ($N{=}1$). Applying another creation operator produces a two-electron state $c_\beta^\dagger c_\alpha^\dagger|0\rangle$, ($N{=}2$). To ensure the antisymmetry of the two electron state, the product of creation operators has to change sign when they are reordered: $c_\alpha^\dagger c_\beta^\dagger = -c_\beta^\dagger c_\alpha^\dagger$. This is more conveniently written as $\{c_\alpha^\dagger, c_\beta^\dagger\} = 0$ by introducing the *anti-commutator*

$$\{A, B\} := A\,B + B\,A. \tag{14}$$

As we have seen, the simplest state we can produce with the creation operators is the single-electron state $|\alpha\rangle = c_\alpha^\dagger|0\rangle$. When we want to calculate its norm, we have to consider the adjoint of $c_\alpha^\dagger|0\rangle$, formally obtaining $\langle\alpha|\alpha\rangle = \langle 0|c_\alpha c_\alpha^\dagger|0\rangle$, or, more generally, $\langle\alpha|\beta\rangle = \langle 0|c_\alpha c_\beta^\dagger|0\rangle$. This implies that c_α, the adjoint of a creation operator, must remove an electron from the state, otherwise the overlap of $c_\alpha c_\beta^\dagger|0\rangle$ with the vacuum state $\langle 0|$ would vanish. We therefore call the adjoint of the creation operator an *annihilation operator*. We certainly cannot take an electron out of the vacuum state, so $c_\alpha|0\rangle = 0$. To obtain the overlap of one-electron states we postulate the anticommutation relation $\{c_\alpha, c_\beta^\dagger\} = \langle\alpha|\beta\rangle$, giving $\langle 0|c_\alpha c_\beta^\dagger|0\rangle = \langle 0|\{c_\alpha, c_\beta^\dagger\} - c_\beta^\dagger c_\alpha|0\rangle = \langle\alpha|\beta\rangle$. For completeness, taking the adjoint of the anticommutation relation for the creation operators, we obtain the corresponding anticommutator of the annihilators: $\{c_\alpha, c_\beta\} = 0$.

Thus, we are led to define the vacuum state $|0\rangle$ and the set of operators c_α related to single-electron states $|\alpha\rangle$ with the properties

$$\boxed{\begin{array}{ll} c_\alpha|0\rangle = 0 & \{c_\alpha, c_\beta\} = 0 = \{c_\alpha^\dagger, c_\beta^\dagger\} \\[2mm] \langle 0|0\rangle = 1 & \{c_\alpha, c_\beta^\dagger\} = \langle\alpha|\beta\rangle \end{array}} \tag{15}$$

As a direct consequence we obtain the Pauli principle in the form $c_\alpha c_\alpha = 0 = c_\alpha^\dagger c_\alpha^\dagger$.

We note that the creators transform in the same way as the single-electron states they represent

$$|\tilde{\alpha}_i\rangle = \sum_\mu |\alpha_\mu\rangle\, U_{\mu i} \qquad \rightsquigarrow \qquad \tilde{c}_{\tilde{\alpha}_i}^\dagger|0\rangle = \sum_\mu c_{\alpha_\mu}^\dagger|0\rangle\, U_{\mu i} = \left(\sum_\mu c_{\alpha_\mu}^\dagger U_{\mu i}\right)|0\rangle. \tag{16}$$

The creators and annihilators are clearly not operators in a Hilbert space, but transfer states from an N-electron to a $N\pm 1$-electron Hilbert space, i.e., they are operators defined on *Fock space*. It is also remarkable that the mixed anti-commutator is the only place where the orbitals that distinguish different operators enter.

To make contact with the notation of first quantization, we introduce the *field operators* $\hat{\Psi}^\dagger(x)$, with $x = (r, \sigma)$, that create an electron of spin σ at position r, i.e., in state $|x\rangle = |r, \sigma\rangle$. Given a complete, orthonormal set of orbitals $\{\varphi_n\}$, we can expand $|x\rangle$

$$\hat{\Psi}^\dagger(x)|0\rangle = |x\rangle = \sum_n |\varphi_n\rangle\langle\varphi_n|x\rangle = \sum_n c_{\varphi_n}^\dagger|0\rangle\langle\varphi_n|x\rangle \tag{17}$$

from which we obtain

$$\hat{\Psi}^\dagger(x) = \sum_n \overline{\langle x|\varphi_n\rangle}\, c_{\varphi_n}^\dagger = \sum_n \overline{\varphi_n(x)}\, c_{\varphi_n}^\dagger. \tag{18}$$

The anticommutators then follow from (15) for an orthonormal and complete set, e.g.,

$$\{\hat{\Psi}(x), \hat{\Psi}^\dagger(x')\} = \sum_{n,m}\langle x|\varphi_n\rangle\, \underbrace{\{c_{\varphi_n}, c_{\varphi_m}^\dagger\}}_{=\delta_{n,m}}\, \langle\varphi_m|x'\rangle = \sum_n \langle x|\varphi_n\rangle\langle\varphi_n|x'\rangle = \langle x|x'\rangle = \delta(x - x'),$$

resulting in the anticommutation relations for the field operators

$$\{\hat{\Psi}(x), \hat{\Psi}(x')\} = 0 = \{\hat{\Psi}^\dagger(x), \hat{\Psi}^\dagger(x')\} \quad \text{and} \quad \{\hat{\Psi}(x), \hat{\Psi}^\dagger(x')\} = \langle x|x'\rangle. \tag{19}$$

We can, of course, expand the field operators also in a non-orthogonal set of orbitals $\{|\chi_i\rangle\}$, as long as it is complete, $\sum_{i,j} |\chi_i\rangle (S^{-1})_{ij} \langle\chi_j| = \mathbb{1}$, where $S_{ij} = \langle\chi_i|\chi_j\rangle$ is the overlap matrix

$$\hat{\Psi}^\dagger(x) = \sum_{i,j} c_i^\dagger \, (S^{-1})_{ij} \, \langle\chi_j|x\rangle. \tag{20}$$

Conversely, given any single-electron wave functions in real space $\varphi(x)$, we can express the corresponding creation operator in terms of the field operators

$$c_\varphi^\dagger = \int dx \, \varphi(x) \, \hat{\Psi}^\dagger(x). \tag{21}$$

Its anticommutator with the field annihilator just gives back the single-electron wave function

$$\{\hat{\Psi}(x),\, c_\varphi^\dagger\} = \int dx' \, \varphi(x') \, \{\hat{\Psi}(x),\, \hat{\Psi}^\dagger(x')\} = \varphi(x)\,. \tag{22}$$

2.2   Representation of Slater determinants

We have now all the tools in place to write the Slater determinant (4) in second quantization, using the creation operators to specify the occupied orbitals and the field operators to give the coordinates for the real-space representation:

$$\Phi_{\alpha_1\alpha_2\ldots\alpha_N}(x_1, x_2, \ldots, x_N) = \frac{1}{\sqrt{N!}} \, \langle 0| \, \hat{\Psi}(x_1)\hat{\Psi}(x_2)\ldots\hat{\Psi}(x_N) \ \ c_{\alpha_N}^\dagger \ldots c_{\alpha_2}^\dagger c_{\alpha_1}^\dagger |0\rangle. \tag{23}$$

Note how writing the Slater determinant as an expectation value of annihilation and creation operators nicely separates the coordinates on the left from the orbitals on the right. This is just the desired generalization of the Dirac notation $\varphi(x) = \langle x|\varphi\rangle$.

Not surprisingly, the proof of (23) is by induction. As a warm-up we consider the case of a single-electron wave function ($N=1$). Using the anticommutation relation (22), we see that

$$\langle 0| \, \hat{\Psi}(x_1) \, c_{\alpha_1}^\dagger |0\rangle = \langle 0| \, \varphi_{\alpha_1}(x_1) - c_{\alpha_1}^\dagger \hat{\Psi}(x_1)|0\rangle = \varphi_{\alpha_1}(x_1)\,. \tag{24}$$

For the two-electron state $N = 2$, we anticommute $\hat{\Psi}(x_2)$ in two steps to the right

$$\begin{aligned}
\langle 0| \, \hat{\Psi}(x_1)\hat{\Psi}(x_2) \, c_{\alpha_2}^\dagger c_{\alpha_1}^\dagger |0\rangle &= \langle 0| \, \hat{\Psi}(x_1)\big(\varphi_{\alpha_2}(x_2) - c_{\alpha_2}^\dagger \hat{\Psi}(x_2)\big) c_{\alpha_1}^\dagger |0\rangle \\
&= \langle 0| \, \hat{\Psi}(x_1)c_{\alpha_1}^\dagger |0\rangle \, \varphi_{\alpha_2}(x_2) - \langle 0| \, \hat{\Psi}(x_1)c_{\alpha_2}^\dagger \hat{\Psi}(x_2)c_{\alpha_1}^\dagger |0\rangle \\
&= \varphi_{\alpha_1}(x_1)\varphi_{\alpha_2}(x_2) - \varphi_{\alpha_2}(x_1)\varphi_{\alpha_1}(x_2)\,. \tag{25}
\end{aligned}$$

We see how anticommuting automatically produces the appropriate signs for the antisymmetric wave function. Dividing by $\sqrt{2}$, we obtain the desired two-electron Slater determinant.

The general case of an N-electron state works just the same. Anti-commuting $\hat{\Psi}(x_N)$ all the way to the right produces N terms with alternating sign

$$\langle 0| \, \hat{\Psi}(x_1)\cdots\hat{\Psi}(x_{N-1})\hat{\Psi}(x_N) \, c_{\alpha_N}^\dagger c_{\alpha_{N-1}}^\dagger \cdots c_{\alpha_1}^\dagger |0\rangle =$$

$$\begin{aligned}
&+ & \langle 0| \, \hat{\Psi}(x_1)\cdots\hat{\Psi}(x_{N-1}) \, c_{\alpha_{N-1}}^\dagger \cdots c_{\alpha_1}^\dagger |0\rangle \ \ &\varphi_{\alpha_N}(x_N) \\
&- & \langle 0| \, \hat{\Psi}(x_1)\cdots\hat{\Psi}(x_{N-1}) \, \textstyle\prod_{n\neq N-1} c_{\alpha_n}^\dagger |0\rangle \ \ &\varphi_{\alpha_{N-1}}(x_N) \\
&\vdots & & \\
(-1)^{N-1} & & \langle 0| \, \hat{\Psi}(x_1)\cdots\hat{\Psi}(x_{N-1}) \, c_{\alpha_N}^\dagger \ \ \cdots \ \ c_{\alpha_2}^\dagger |0\rangle \ \ &\varphi_{\alpha_1}(x_N)\,.
\end{aligned}$$

Using (23) for the $N-1$-electron states, this is nothing but the Laplace expansion of

$$
D = \begin{vmatrix}
\varphi_{\alpha_1}(x_1) & \varphi_{\alpha_2}(x_1) & \cdots & \varphi_{\alpha_N}(x_1) \\
\varphi_{\alpha_1}(x_2) & \varphi_{\alpha_2}(x_2) & \cdots & \varphi_{\alpha_N}(x_2) \\
\vdots & \vdots & \ddots & \vdots \\
\varphi_{\alpha_1}(x_N) & \varphi_{\alpha_2}(x_N) & \cdots & \varphi_{\alpha_N}(x_N)
\end{vmatrix}
$$

along the Nth row. Dividing by $\sqrt{N!}$ we see that we have shown (23) for N-electron states, completing the proof by induction.

Given this representation of Slater determinants it is easy to eliminate the coordinates so we can work with N-electron states rather than N-electron wave functions—just as in Dirac notation. In particular we can rewrite the basis of Slater determinants (6) into a basis of product states

$$
\left\{ c^\dagger_{\alpha_N} \cdots c^\dagger_{\alpha_1} |0\rangle \ \big| \ \alpha_1 < \cdots < \alpha_N \right\}, \tag{26}
$$

which allows us to express any N-electron state as

$$
|\Psi\rangle = \sum_{\alpha_1 < \cdots < \alpha_N} a_{\alpha_1, \ldots, \alpha_N} \, c^\dagger_{\alpha_N} \cdots c^\dagger_{\alpha_1} |0\rangle. \tag{27}
$$

2.3   Representation of n-body operators

To work with N-electron states rather than Slater determinants, we also have to rewrite the N-electron operators $M(\boldsymbol{x})$ appropriately. This is easily done by incorporating the coordinates that we have separated from the Slater determinants into the operators such that the expectation values remain unchanged. This is, again, analogous to the Dirac formalism:

$$
\int dx \, \overline{\varphi_n(x)} \, M(x) \, \varphi_m(x) = \langle \varphi_n | \underbrace{\int dx \, |x\rangle M(x)\langle x|}_{=:\hat{M}} \varphi_m \rangle = \langle \varphi_n | \hat{M} | \varphi_m \rangle. \tag{28}
$$

For N-electron Slater determinants this becomes

$$
\int dx_1 \cdots dx_N \, \overline{\Phi_{\beta_1 \cdots \beta_N}(x_1, \cdots, x_N)} \, M(x_1, \ldots, x_N) \, \Phi_{\alpha_1 \cdots \alpha_N}(x_1, \cdots, x_N)
$$

$$
= \int dx_1 \cdots dx_N \langle 0|c_{\beta_1} \cdots c_{\beta_N} \hat{\Psi}^\dagger(x_N) \cdots \hat{\Psi}^\dagger(x_1)|0\rangle M(x_1, \ldots, x_N) \langle 0|\hat{\Psi}(x_1) \cdots \hat{\Psi}(x_N) c^\dagger_{\alpha_N} \cdots c^\dagger_{\alpha_1}|0\rangle
$$

$$
= \big\langle 0 \big| \, c_{\beta_1} \cdots c_{\beta_N} \, \hat{M} \, c^\dagger_{\alpha_N} \cdots c^\dagger_{\alpha_1} \big| 0 \big\rangle
$$

with the representation of the n-body operator in terms of field operators

$$
\hat{M} = \frac{1}{N!} \int dx_1 \cdots x_N \, \hat{\Psi}^\dagger(x_N) \cdots \hat{\Psi}^\dagger(x_1) \, M(x_1, \cdots, x_N) \, \hat{\Psi}(x_1) \cdots \hat{\Psi}(x_N). \tag{29}
$$

Note that this particular form of the operator is only valid when applied to N-electron states, since we have used that the N annihilation operators bring us to the zero-electron space, where $|0\rangle\langle 0| = \mathbb{1}_0$. Keeping this in mind, we can work entirely in terms of our algebra (15).

To see what (29) means we look, in turn, at the different n-body parts of $M(\boldsymbol{x})$, (2):

$$M(\mathbf{x}) = M^{(0)} + \sum_i M^{(1)}(x_i) + \sum_{i<j} M^{(2)}(x_i, x_j) + \sum_{i<j<k} M^{(3)}(x_i, x_j, x_k) + \cdots \quad (30)$$

We start with the simplest case, the zero-body operator, which, up to a trivial prefactor, is $M^{(0)}(x_1, \cdots, x_N) = 1$. Operating on an N-electron state, it gives

$$\begin{aligned}
\hat{M}^{(0)} &= \frac{1}{N!} \int dx_1 dx_2 \cdots x_N \, \hat{\Psi}^\dagger(x_N) \cdots \hat{\Psi}^\dagger(x_2) \hat{\Psi}^\dagger(x_1) \, \hat{\Psi}(x_1) \hat{\Psi}(x_2) \cdots \hat{\Psi}(x_N) \\
&= \frac{1}{N!} \int \quad dx_2 \cdots x_N \, \hat{\Psi}^\dagger(x_N) \cdots \hat{\Psi}^\dagger(x_2) \qquad \hat{N} \qquad \hat{\Psi}(x_2) \cdots \hat{\Psi}(x_N) \\
&= \frac{1}{N!} \int \quad dx_2 \cdots x_N \, \hat{\Psi}^\dagger(x_N) \cdots \hat{\Psi}^\dagger(x_2) \qquad 1 \qquad \hat{\Psi}(x_2) \cdots \hat{\Psi}(x_N) \\
&\vdots \\
&= \frac{1}{N!} \, 1 \cdot 2 \, \cdots \, N = 1 \,,
\end{aligned} \qquad (31)$$

where we have used that the operator

$$\int dx \, \hat{\Psi}^\dagger(x) \hat{\Psi}(x) = \hat{N}$$

counts the number of electrons: Applied to the vacuum state it gives $\hat{N} |0\rangle = 0$, while each creation operator increases the count by one: $\hat{N} c_n^\dagger = c_n^\dagger(\hat{N}+1)$, which follows from

$$[\hat{N}, c_n^\dagger] = \int dx \, [\hat{\Psi}^\dagger(x)\hat{\Psi}(x), c_n^\dagger] = \int dx \, \hat{\Psi}^\dagger(x) \, \{\hat{\Psi}(x), c_n^\dagger\} = \int dx \, \hat{\Psi}^\dagger(x) \, \varphi_n(x) = c_n^\dagger, \quad (32)$$

where we have used the simple relation $[AB, C] = A\{B, C\} - \{A, C\}B$. Adjoining this relation gives a minus sign, i.e., annihilators reduce the count by one: $\hat{N} c_n = c_n(\hat{N}-1)$. Thus, commuting $\hat{N}$ through a general product state, we obtain for each creation operator that we encounter a copy of the state, while for each annihilator we obtain minus that state, giving in total the original state times the difference in the number of creation and annihilation operators. Remarkably, while we started from an operator acting on N-electron states, the resulting operator in second quantized form is independent of the number of electrons. We will see that this is an important general feature of operators in second quantization which makes working in Fock spaces amazingly simple.

We note that (31) just means that the overlap of two Slater determinants (7) is equal to that of the corresponding product states

$$\int d\boldsymbol{x} \, \overline{\Phi_{\alpha_1,\ldots,\alpha_N}(\boldsymbol{x})} \, \Phi_{\beta_1,\ldots,\beta_N}(\boldsymbol{x}) = \langle 0 | \, c_{\alpha_1} \cdots c_{\alpha_N} \, c_{\beta_N}^\dagger \cdots c_{\beta_1}^\dagger \, |0\rangle. \qquad (33)$$

2.3.1   One-body operators

Next we consider one-body operators $\sum_j M^{(1)}(x_j)$

$$
\begin{aligned}
\hat{M}^{(1)} &= \frac{1}{N!} \int dx_1 \cdots dx_N \, \hat{\Psi}^\dagger(x_N) \cdots \hat{\Psi}^\dagger(x_1) \sum_j M^{(1)}(x_j) \, \hat{\Psi}(x_1) \cdots \hat{\Psi}(x_N) \\
&= \frac{1}{N!} \sum_j \int dx_j \, \hat{\Psi}^\dagger(x_j) \, M^{(1)}(x_j) \, (N-1)! \, \hat{\Psi}(x_j) \\
&= \frac{1}{N} \sum_j \int dx_j \, \hat{\Psi}^\dagger(x_j) \, M^{(1)}(x_j) \, \hat{\Psi}(x_j) \\
&= \int dx \quad \hat{\Psi}^\dagger(x) \, M^{(1)}(x) \, \hat{\Psi}(x)
\end{aligned}
\tag{34}
$$

Here we have first anticommuted $\hat{\Psi}^\dagger(x_j)$ all the way to the left and $\hat{\Psi}(x_j)$ to the right. Since these take the same numbers of anticommutations, there is no sign involved. In between these field operators we are left with a zero-body operator for $N-1$ electrons, producing, when $\hat{M}^{(1)}$ acts on an N-electron state, a factor of $(N-1)!$. Again we notice that we obtain an operator that no longer depends on the number of electrons, i.e., that is valid in the entire Fock space. Expanding the field-operators in a complete orthonormal set $\hat{\Psi}(x) = \sum_n \varphi_n(x)\, c_n$ gives

$$
\hat{M}^{(1)} = \sum_{n,m} \int dx \, \overline{\varphi_n(x)} \, M(x) \, \varphi_m(x) \, c_n^\dagger c_m = \sum_{n,m} \langle \varphi_n | M^{(1)} | \varphi_m \rangle \, c_n^\dagger c_m = \sum_{n,m} c_n^\dagger \, M_{nm}^{(1)} \, c_m. \tag{35}
$$

The matrix elements $M_{nm}^{(1)} = \langle \varphi_n | M^{(1)} | \varphi_m \rangle$ transform like a single-electron matrix $\boldsymbol{M}^{(1)}$: From (16) and writing the annihilation operators as a column vector $\boldsymbol{c}$ we see that

$$
\hat{M}^{(1)} = \boldsymbol{c}^\dagger \, \boldsymbol{M}^{(1)} \, \boldsymbol{c} \; = \boldsymbol{c}^\dagger \boldsymbol{U}^\dagger \, \boldsymbol{U} \boldsymbol{M}^{(1)} \boldsymbol{U}^\dagger \, \boldsymbol{U} \boldsymbol{c} = \tilde{\boldsymbol{c}}^\dagger \, \tilde{\boldsymbol{M}}^{(1)} \, \tilde{\boldsymbol{c}}. \tag{36}
$$

Once we have arrived at the representation in terms of orbitals, we can restrict the orbital basis to a non-complete set. This simply gives the operator in the variational (Fock) subspace spanned by the orbitals.

We note that the expression (35) not only works for local operators but also for differential operators like the momentum or kinetic energy: we have taken care not to exchange the order of $M^{(1)}$ and one of its field operators. We can write truly non-local operators in a similar way. As an example, the one-body density operator is given by

$$
\hat{\Gamma}^{(1)}(x; x') = \hat{\Psi}^\dagger(x) \hat{\Psi}(x') \tag{37}
$$

so that one coordinate is not integrated over, rather setting it to x in the bra and x' in the ket. In an orthonormal basis it becomes

$$
\hat{\Gamma}^{(1)}(x; x') = \sum_{n,m} \overline{\varphi_n(x)} \, \varphi_m(x') \, c_n^\dagger c_m \,. \tag{38}
$$

2.3.2   Two-body operators

For the two-body operators $\sum_{i<j} M^{(2)}(x_i, x_j)$ we proceed in the familiar way, anti-commuting first the operators with the coordinates involved in $M^{(2)}$ all the way to the left and right, respectively. This time we are left with a zero-body operator for $N-2$ electrons:

$$
\begin{aligned}
\hat{M}^{(2)} &= \frac{1}{N!} \int dx_1 \cdots dx_N \, \hat{\Psi}^\dagger(x_N) \cdots \hat{\Psi}^\dagger(x_1) \sum_{i<j} M^{(2)}(x_i, x_j) \, \hat{\Psi}(x_1) \cdots \hat{\Psi}(x_N) \\
&= \frac{1}{N!} \sum_{i<j} \int dx_i dx_j \, \hat{\Psi}^\dagger(x_j) \hat{\Psi}^\dagger(x_i) \, M^{(2)}(x_i, x_j) \, (N-2)! \, \hat{\Psi}(x_i) \hat{\Psi}(x_j) \\
&= \frac{1}{N(N-1)} \sum_{i<j} \int dx_i dx_j \, \hat{\Psi}^\dagger(x_j) \hat{\Psi}^\dagger(x_i) \, M^{(2)}(x_i, x_j) \, \hat{\Psi}(x_i) \hat{\Psi}(x_j) \\
&= \qquad \frac{1}{2} \int dx \, dx' \, \hat{\Psi}^\dagger(x') \, \hat{\Psi}^\dagger(x) \, M^{(2)}(x, x') \, \hat{\Psi}(x) \, \hat{\Psi}(x')
\end{aligned}
$$

Expanding in an orthonormal basis, we get

$$
\begin{aligned}
\hat{M}^{(2)} &= \frac{1}{2} \sum_{n,n',m,m'} \int dx dx' \, \overline{\varphi_{n'}(x')} \, \overline{\varphi_n(x)} \, M^{(2)}(x, x') \, \varphi_m(x) \varphi_{m'}(x') \quad c_{n'}^\dagger c_n^\dagger c_m c_{m'} \\
&= \frac{1}{2} \sum_{n,n',m,m'} \langle \varphi_n \varphi_{n'} | M^{(2)} | \varphi_m \varphi_{m'} \rangle \qquad\qquad c_{n'}^\dagger c_n^\dagger c_m c_{m'} \qquad (39)
\end{aligned}
$$

where the exchange of the indices in the second line is a consequence of the way the Dirac state for two electrons is usually written: first index for the first coordinate, second index for the second. A more natural choice would be to exchange the order in the bra, reflecting that taking the adjoint of the operators changes their order. Either way, $M_{nn', mm'} = \langle \varphi_n \varphi_{n'} | M^{(2)} | \varphi_m \varphi_{m'} \rangle$ transforms like a fourth-order tensor: Transforming to a different basis (16) gives

$$
\tilde{M}^{(2)}_{\nu\nu', \mu\mu'} = \sum_{n,n',m,m'} U_{\nu n}^\dagger U_{\nu' n'}^\dagger M_{nn', mm'} U_{m\mu} U_{m'\mu'} \,. \qquad (40)
$$

Form the symmetry of the two-body operator $M^{(2)}(x, x') = M^{(2)}(x', x)$ follows $M_{nn', mm'} = M_{n'n, m'm}$. Moreover, $M_{nn, mm'}$ will not contribute to $\hat{M}^{(2)}$ since $c_n^\dagger c_n^\dagger = \{c_n^\dagger, c_n^\dagger\}/2 = 0$, and likewise for $M_{nn', mm}$.

Note that the representation (39) is not quite as efficient as it could be: The terms with n and n' and/or m and m' exchanged connect the same basis states. Collecting these terms by introducing an ordering of the operators and using the symmetry of the matrix elements we obtain

$$
\hat{M}^{(2)} = \sum_{n'>n, \, m'>m} c_{n'}^\dagger c_n^\dagger \underbrace{\left(M^{(2)}_{nn', mm'} - M^{(2)}_{n'n, mm'} \right)}_{=: \breve{M}^{(2)}_{nn', mm'}} c_m c_{m'} \,. \qquad (41)
$$

Since the states $\{ c_{n'}^\dagger c_n^\dagger | 0 \rangle \mid n' > n \}$ form a basis of the two-electron Hilbert space, considering nn' as the index of a basis state, the $\breve{M}^{(2)}_{nn', mm'}$ form a two-electron matrix $\breve{\boldsymbol{M}}^{(2)}$.

The procedure of rewriting operators in second quantization obviously generalizes to observables acting on more than two electrons in the natural way.

We note that, while we started from a form of the operators (30) that was explicitly formulated in an N-electron Hilbert space, the results (31), (35), and (39) are of the same form no matter what value N takes. Thus these operators are valid not just on some N-electron Hilbert space, but on the entire Fock space. This is a particular strength of the second-quantized formalism.

2.4   Transforming the orbital basis

We noted in (16) that the creators transform in the same way as the orbitals they represent

$$|\beta_i\rangle = U|\alpha_i\rangle = \sum_j |\beta_j\rangle\langle\alpha_j|\alpha_i\rangle = \sum_\mu |\alpha_\mu\rangle \underbrace{\langle\alpha_\mu|U|\alpha_i\rangle}_{=:U_{\mu i}} \quad \rightsquigarrow \quad c^\dagger_{\beta_i} = \sum_\mu c^\dagger_{\alpha_\mu} U_{\mu i}\,, \qquad (42)$$

so the "operators" really transform like states. Writing the transformation matrix as $\boldsymbol{U} = e^{\boldsymbol{M}}$, where $\boldsymbol{M}$ is anti-Hermitian, $\boldsymbol{M}^\dagger = -\boldsymbol{M}$, when $\boldsymbol{U}$ is unitary, but can be any matrix when $\boldsymbol{U}$ is merely invertible, we can write the basis transformation in a form appropriate for operators:

$$c^\dagger_{\beta_i} = e^{\boldsymbol{c}^\dagger \boldsymbol{M} \boldsymbol{c}} c^\dagger_{\alpha_\mu} e^{-\boldsymbol{c}^\dagger \boldsymbol{M} \boldsymbol{c}}\,. \qquad (43)$$

To see this, we use the Baker-Campbell-Hausdorff formula in the form

$$e^{\lambda A} B\, e^{-\lambda A} = B + \lambda\, [A,\, B] + \frac{\lambda^2}{2!}\big[A,\, [A,\, B]\big] + \frac{\lambda^3}{3!}\Big[A,\, \big[A,\, [A,\, B]\big]\Big] + \cdots\,, \qquad (44)$$

where the expansion coefficients follow by taking the derivatives of the left hand side at $\lambda = 0$, together with the commutator $[c^\dagger_{\alpha_\mu} c_{\alpha_\nu},\, c^\dagger_{\alpha_\kappa}] = c^\dagger_{\alpha_\mu}\, \delta_{\nu,\kappa}$, from which we obtain for the repeated commutators

$$\Big[\sum_{\mu,\nu} M_{\mu\nu} c^\dagger_{\alpha_\mu} c_{\alpha_\nu},\, \sum_\kappa c^\dagger_{\alpha_\kappa} \big(M^n\big)_{\kappa i}\Big] = \sum_{\mu\nu\kappa} c^\dagger_{\alpha_\mu} M_{\mu\nu}\, \delta_{\nu,\kappa} \big(M^n\big)_{\kappa i} = \sum_\mu c^\dagger_{\alpha_\mu} \big(M^{n+1}\big)_{\mu i}\,. \qquad (45)$$

To keep the derivation simple, we have chosen to transform an operator from the orthonormal basis that we also used to write the exponential operator. Being linear, the transform works, of course, the same for an arbitrary operator.

Using this form of the basis transformation and noticing that $e^{-\boldsymbol{c}^\dagger \boldsymbol{M} \boldsymbol{c}}|0\rangle = |0\rangle$, we immediately see that acting with the exponential of a one-body operator on a product state results in another product state

$$e^{\boldsymbol{c}^\dagger \boldsymbol{M} \boldsymbol{c}} \prod c^\dagger_{\alpha_n}|0\rangle = \prod e^{\boldsymbol{c}^\dagger \boldsymbol{M} \boldsymbol{c}} c^\dagger_{\alpha_n} e^{-\boldsymbol{c}^\dagger \boldsymbol{M} \boldsymbol{c}}|0\rangle = \prod c^\dagger_{\beta_n}|0\rangle\,. \qquad (46)$$

This is, e.g., used when working in the interaction picture. Anticommutators with transformed operators, (42), are simply $\big\{c_{\alpha_j},\, e^{-\boldsymbol{c}^\dagger \boldsymbol{M} \boldsymbol{c}} c^\dagger_{\alpha_i} e^{-\boldsymbol{c}^\dagger \boldsymbol{M} \boldsymbol{c}}\big\} = \langle\alpha_j|e^M|\alpha_i\rangle$.

Annihilation operators, being the adjoint of the creators, transform in just the expected way

$$c_{\beta_i} = e^{-\boldsymbol{c}^\dagger \boldsymbol{M}^\dagger \boldsymbol{c}} c_{\alpha_\mu} e^{\boldsymbol{c}^\dagger \boldsymbol{M}^\dagger \boldsymbol{c}}\,, \qquad (47)$$

which means that for unitary transformations, where $\boldsymbol{M}$ is anti-Hermitian, creators and annihilators transform in the same way. Note that in the imaginary-time formalism the annihilators are, via analytic continuation, chosen to transform in the same way as the creators, making them different from the adjoint of the creators.

3 Exact diagonalization

We have worked, so far, with complete, i.e., infinite bases. This is, of course, not possible in actual computer simulations, where we have to confine ourselves to finite basis sets. Such calculations on subspaces are based on the variational principle.

3.1 Variational principles

The variational principle and the Schrödinger equation are equivalent. Consider the energy expectation value as a wave-function functional

$$E[\Psi] = \frac{\langle \Psi | H | \Psi \rangle}{\langle \Psi | \Psi \rangle} \ . \tag{48}$$

Its variation is

$$E[\Psi + \delta\Psi] = E[\Psi] + \frac{\langle \delta\Psi | H | \Psi \rangle + \langle \Psi | H | \delta\Psi \rangle}{\langle \Psi | \Psi \rangle} - \langle \Psi | H | \Psi \rangle \frac{\langle \delta\Psi | \Psi \rangle + \langle \Psi | \delta\Psi \rangle}{\langle \Psi | \Psi \rangle^2} + \mathcal{O}^2. \tag{49}$$

The first-order term vanishes for $H|\Psi\rangle = E[\Psi]\,|\Psi\rangle$, which is the Schrödinger equation. Since the eigenfunctions

$$H|\Psi_n\rangle = E_n|\Psi\rangle \, , \tag{50}$$

can be chosen to form an orthonormal basis, we can expand any wavefunction as

$$|\Psi\rangle = \sum_n |\Psi_n\rangle \, \langle \Psi_n | \Psi \rangle \tag{51}$$

and determine, as long as $\langle \Psi | \Psi \rangle \neq 0$, its energy expectation value

$$\frac{\langle \Psi | H | \Psi \rangle}{\langle \Psi | \Psi \rangle} = \frac{\sum_{m,n} \langle \Psi | \Psi_m \rangle \langle \Psi_m | H | \Psi_n \rangle \langle \Psi_n | \Psi \rangle}{\sum_{m,n} \langle \Psi | \Psi_m \rangle \langle \Psi_m | \Psi_n \rangle \langle \Psi_n | \Psi \rangle} = \frac{\sum_n E_n \left| \langle \Psi_n | \Psi \rangle \right|^2}{\sum_n \left| \langle \Psi_n | \Psi \rangle \right|^2} \ . \tag{52}$$

Since by definition no eigenenergy can be lower than the ground state energy E_0, we immediately see that the energy expectation value can never drop below the ground state energy

$$\frac{\langle \Psi | H | \Psi \rangle}{\langle \Psi | \Psi \rangle} = \frac{\sum_n E_n \left| \langle \Psi_n | \Psi \rangle \right|^2}{\sum_n \left| \langle \Psi_n | \Psi \rangle \right|^2} \geq \frac{\sum_n E_0 \left| \langle \Psi_n | \Psi \rangle \right|^2}{\sum_n \left| \langle \Psi_n | \Psi \rangle \right|^2} = E_0 \ . \tag{53}$$

We can use the same argument to generalize this variational principle: Assume we have arranged the eigenenergies in ascending order, $E_0 \leq E_1 \leq \cdots$, then the energy expectation value for a wavefunction that is orthogonal to the n lowest eigenstates, can not drop below E_n

$$\frac{\langle \Psi_{\perp_n} | H | \Psi_{\perp_n} \rangle}{\langle \Psi_{\perp_n} | \Psi_{\perp_n} \rangle} \geq E_n \quad \text{if } \langle \Psi_i | \Psi_{\perp_n} \rangle = 0 \text{ for } i = 0, \ldots, n{-}1. \tag{54}$$

This generalized variational principle is, of course, only of practical use if we know something about the eigenstates, e.g., when we can use symmetries to ensure orthogonality.

For an ab-initio Hamiltonian of N electrons in the field of nuclei of charge Z_α at position $\boldsymbol{R}_\alpha$,

$$H = -\frac{1}{2} \sum_i \Delta_i - \sum_{i,\alpha} \frac{Z_\alpha}{|\boldsymbol{r}_i - \boldsymbol{R}_\alpha|} + \sum_{i<j} \frac{1}{|\boldsymbol{r}_i - \boldsymbol{r}_j|} + \sum_{\alpha<\beta} \frac{Z_\alpha Z_\beta}{|\boldsymbol{R}_\alpha - \boldsymbol{R}_\beta|} , \tag{55}$$

the Schrödinger equation is a partial differential equation. In second quantization it becomes a linear-algebra problem: We introduce an orbital basis set $\{\varphi_k \,|\, k\}$, which for simplicity we assume here to be orthonormal, from which we construct an orthonormal basis of N-electron product states, $\{\Phi_{k_1,\dots,k_N} \,|\, k_1 < \cdots < k_N\}$. To simplify the notation we sort the basis states, e.g., lexicographically in the orbital indices $\boldsymbol{k} = (k_1, \dots, k_N)$ and define the row vector of basis states $|\boldsymbol{\Phi}\rangle := (|\Phi_1\rangle, |\Phi_2\rangle, \dots)$. The expansion of a state $|\Psi\rangle$ in this basis can then be written as

$$|\Psi\rangle = \sum_{k_1<\cdots<k_N} a_{k_1,\dots,k_N} |\Phi_{k_1,\dots,k_N}\rangle = \sum_i a_i |\Phi_i\rangle = |\boldsymbol{\Phi}\rangle \, \boldsymbol{a} , \tag{56}$$

where $\boldsymbol{a}$ is the vector of expansion coefficients. Likewise we can write the Schrödinger equation as a matrix eigenvalue problem

$$\boldsymbol{H}\boldsymbol{a} = \langle\boldsymbol{\Phi}|\hat{H}|\boldsymbol{\Phi}\rangle\boldsymbol{a} = \begin{pmatrix} \langle\Phi_1|\hat{H}|\Phi_1\rangle & \langle\Phi_1|\hat{H}|\Phi_2\rangle & \cdots \\ \langle\Phi_2|\hat{H}|\Phi_1\rangle & \langle\Phi_2|\hat{H}|\Phi_2\rangle & \cdots \\ \vdots & \vdots & \ddots \end{pmatrix} \begin{pmatrix} a_1 \\ a_2 \\ \vdots \end{pmatrix} = E \begin{pmatrix} a_1 \\ a_2 \\ \vdots \end{pmatrix} = E\boldsymbol{a} . \tag{57}$$

From the eigenvectors of the matrix $\boldsymbol{H}$ we easily recover the eigenstates of the Hamiltonian

$$\boldsymbol{H}\boldsymbol{a}_n = E_n\boldsymbol{a}_n \quad \rightsquigarrow \quad \hat{H}|\Psi_n\rangle = E_n|\Psi_n\rangle \quad \text{with } |\Psi_n\rangle = |\boldsymbol{\Phi}\rangle \, \boldsymbol{a}_n . \tag{58}$$

Unfortunately, for an ab-initio Hamiltonian like (55) we need an infinite orbital basis set, so that the Hamiltonian matrix $\boldsymbol{H}$ is infinite dimensional. A pragmatic approach to allow for computer simulations is to simply restrict the calculation to a finite basis $|\tilde{\boldsymbol{\Phi}}\rangle := (|\tilde{\Phi}_1\rangle, \dots, |\tilde{\Phi}_{\tilde{L}}\rangle)$, i.e., work with a finite matrix $\tilde{\boldsymbol{H}} := \langle\tilde{\boldsymbol{\Phi}}|\hat{H}|\tilde{\boldsymbol{\Phi}}\rangle$ of dimension $\tilde{L}$. The crucial question is then how the eigenvectors

$$\tilde{\boldsymbol{H}}\tilde{\boldsymbol{a}}_n = \tilde{E}_n\tilde{\boldsymbol{a}}_n \quad \rightsquigarrow \quad |\tilde{\Psi}_n\rangle := |\tilde{\boldsymbol{\Phi}}\rangle \, \tilde{\boldsymbol{a}}_n \tag{59}$$

are related to those of H. The answer is surprisingly simple [6]: The eigenvalues of $\tilde{\boldsymbol{H}}$, ordered as $\tilde{E}_0 \leq \tilde{E}_1 \leq \cdots \leq \tilde{E}_{\tilde{L}-1}$, are variational with respect to those of H:

$$E_n \leq \tilde{E}_n \quad \text{for } n \in \{0, \dots, \tilde{L}-1\} . \tag{60}$$

To show this, we construct a state in $\mathrm{span}\left(|\tilde{\Psi}_0\rangle, \dots, |\tilde{\Psi}_n\rangle\right)$, which by construction has an energy expectation value $\leq \tilde{E}_n$, that is orthogonal to the exact eigenstates $|\Psi_0\rangle, \dots, |\Psi_{n-1}\rangle$, so that by the generalized variational principle its expectation value is $\geq E_n$. Being the non-zero solution of $n-1$ linear equations with n variables, such a state certainly exists, hence $E_n \leq \tilde{E}_n$.

To get reliable results, we simply have to systematically increase the basis until the change in the desired eigenvalues becomes smaller than the accuracy required by the physical problem. The art is, of course to devise clever basis sets such that this is achieved already for bases of low dimensions.

The convergence of the matrix eigenvalues with increasing basis size is surprisingly regular. Let us extend our original basis of $\tilde{L}$ states by an additional $L - \tilde{L}$ states. Then, repeating the above argument with the L-dimensional problem taking the role of $\hat{H}$, we obtain (60) with E_n being the eigenvalues of the L-dimensional Hamiltonian matrix $\boldsymbol{H}$. Being finite, we can use the same argument for $-\boldsymbol{H}$, obtaining

$$- E_{L-i} \leq -\tilde{E}_{\tilde{L}-i} \quad \text{for } i \in \{1, \ldots, \tilde{L}\}. \tag{61}$$

Taking the two inequalities together we obtain

$$E_n \leq \tilde{E}_n \leq E_{n+(L-\tilde{L})} \quad \text{for } n \in \{0, \ldots, \tilde{L}-1\}. \tag{62}$$

For the special case $L = \tilde{L}+1$ of adding a single basis state, this is the Hylleraas-Undheim/Mac-Donald nesting property for eigenvalues in successive approximations

$$E_1 \leq \tilde{E}_1 \leq E_2 \leq \tilde{E}_2 \leq \cdots \leq \tilde{E}_L \leq E_{L+1}. \tag{63}$$

3.2   Matrix eigenvalue problem

For practical calculations we have to set up the Hamiltonian matrix $\tilde{\boldsymbol{H}} = \langle \tilde{\boldsymbol{\Phi}} | \hat{H} | \tilde{\boldsymbol{\Phi}} \rangle$ and the state vectors $\tilde{\boldsymbol{a}}$ for the chosen basis. This is particularly easy for a basis of Slater determinants constructed from a basis set of K orbitals $\{\varphi_k \,|\, k = 0, \ldots, K-1\}$. The basis states are then the N-electron product states of $|\Phi_{k_1,\ldots,k_N}\rangle = c_{k_N}^\dagger \cdots c_{k_1}^\dagger |0\rangle$ with $k_1 < \cdots k_N$. We can write this more computer friendly as

$$|n_{K-1}, \ldots, n_0\rangle = \prod_{k=0}^{K-1} \left(c_k^\dagger\right)^{n_k} |0\rangle \tag{64}$$

which is the occupation number representation with $n_k \in \{0, 1\}$ and $\sum n_k = N$. It is natural to interpret the vector of occupation numbers as the binary representation of the integer $\sum_k 2^{n_k}$. This implies a natural ordering of the basis functions $|\Phi_l\rangle$. For the simple case of $K=4$ orbitals and $N=2$ electrons we obtain

i	(n_3, n_2, n_1, n_0)	state	l
0	0000		
1	0001		
2	0010		
3	0011	$c_1^\dagger c_0^\dagger |0\rangle = |\Phi_1\rangle$	1
4	0100		
5	0101	$c_2^\dagger c_0^\dagger |0\rangle = |\Phi_2\rangle$	2
6	0110	$c_2^\dagger c_1^\dagger |0\rangle = |\Phi_3\rangle$	3
7	0111		
8	1000		
9	1001	$c_3^\dagger c_0^\dagger |0\rangle = |\Phi_4\rangle$	4
10	1010	$c_3^\dagger c_1^\dagger |0\rangle = |\Phi_5\rangle$	5
11	1011		
12	1100	$c_3^\dagger c_2^\dagger |0\rangle = |\Phi_6\rangle$	6
13	1101		
14	1110		
15	1111		

The bit representation of the basis states also simplifies setting up the Hamiltonian matrix. Given the Hamiltonian in second quantization

$$\hat{H} = \sum_{n,m} T_{nm}\, c_n^\dagger c_m + \sum_{n'>n,\, m'>m} \underbrace{\left(U_{nn',mm'} - U_{n'n,mm'}\right)}_{=\breve{U}_{nn',mm'}} c_{n'}^\dagger c_n^\dagger c_m c_{m'} \tag{65}$$

the matrix element $\langle \Phi_l|\hat{H}|\Phi_{l'}'\rangle$, with $|\Phi_{l'}\rangle = c_{k_N'}^\dagger \cdots c_{l_1'}^\dagger|0\rangle$, is given by

$$\sum_{n,m} T_{nm}\langle 0|c_{l_1}\cdots c_{l_N}\, c_n^\dagger c_m\, c_{l_N'}^\dagger \cdots c_{l_1'}^\dagger|0\rangle + \sum_{\substack{n'>n \\ m'>m}} \breve{U}_{nn',mm'}\langle 0|c_{l_1}\cdots c_{l_N}\, c_{n'}^\dagger c_n^\dagger c_m c_{m'}\, c_{l_N'}^\dagger \cdots c_{l_1'}^\dagger|0\rangle.$$

Anticommuting the operators coming from the operators, the matrix elements become overlaps of $N+1$ and $N+2$-electron product states, which, by (33) and (7), are just the determinants of the overlap matrices of the corresponding orbitals. When $\hat{H}$ is written in the same orbitals as the $|\Phi_l\rangle$, the overlap matrices simplify to permutation matrices with determinant ± 1. In the occupation number representation, calculating this Fermi sign reduces to counting set bits. As an example we consider a simple hopping of an electron:

$$\begin{aligned}
c_6^\dagger c_2|\Phi_{l(181)}\rangle &= c_6^\dagger c_2\, c_7^\dagger c_5^\dagger c_4^\dagger c_2^\dagger c_0^\dagger|0\rangle \\
&= (-1)^3 c_6^\dagger c_7^\dagger c_5^\dagger c_4^\dagger c_2 c_2^\dagger c_0^\dagger|0\rangle \\
&= (-1)^3 c_6^\dagger c_7^\dagger c_5^\dagger c_4^\dagger \left(1 - c_2^\dagger c_2\right) c_0^\dagger|0\rangle \\
&= (-1)^3 c_6^\dagger c_7^\dagger c_5^\dagger c_4^\dagger \cdot c_0^\dagger|0\rangle \\
= +|\Phi_{l(241)}\rangle &= (-1)^2 c_7^\dagger c_6^\dagger c_5^\dagger c_4^\dagger \cdot c_0^\dagger|0\rangle
\end{aligned}$$

In the occupation number representation this becomes

$$\texttt{1 0 1 1 0 1 0 1} \quad = \quad (-1)^c\ \texttt{1 1 1 1 0 0 0 1} \tag{66}$$

where c is the count of set bits between the positions the electron hop. Note that a dedicated machine instruction, `popcnt`, for counting set bits is part of the x86 SSE4 instruction set, see also [7]

3.3 Dimension of the Hilbert space and sparseness

Setting up basis states and Hamiltonian matrix in this way, we can easily solve the many-body problem on our variational space by using any linear algebra library. This is the exact diagonalization approach. As discussed above, it gives us variational estimates of the ground and excited states. But there is a serious practical problem: the dimension of the many-body Hilbert space. For an N-electron problem with a basis set of K orbitals there are $K(K-1)(K-2)\cdots(K-(N-1))$ ways of picking N indices out of K. Since we only use one specific ordering of these indices, we have to divide by $N!$ to obtain the number of such determinants:

$$\dim \mathcal{H}_K^{(N)} = \frac{K!}{N!(K-N)!} = \binom{K}{N}. \tag{67}$$

Using Stirling's formula we see that for an N-electron problem this increases faster than exponentially with the size K of the basis set. This is the problem we face when converging the basis set for a finite system, e.g., a molecule. For solids we usually keep the number of orbitals per lattice site fixed, but scale to the thermodynamic limit, increasing the system size M while keeping the electron density N/M fixed. Also here the Hilbert space increases faster than exponentially. To give an impression of the problem we note that for $N = 25$ electrons and $K = 100$ orbitals the dimension already exceeds 10^{23}.

For exact diagonalization the problem gets even worse. Assuming we have a machine with 1 TeraBytes $= 2^{40}$ Bytes of RAM available. Using single precision (4 bytes) for the matrix elements, storing a matrix of dimension $(2^{40}/4)^{1/2} = 524\,288$ would already use up all memory. The dimension problem can be somewhat mitigated by exploiting symmetries: When the Hamiltonian commutes with the projection of the total spin, the number of up- and down-spin electrons is conserved separately. The N-electron Hamiltonian is then block diagonal in the sectors with fixed $N_\uparrow$ and $N_\downarrow$. The dimension of these blocks is significantly smaller than that of the full N-electron Hilbert space. Using the same orbital basis for each spin

$$\dim \mathcal{H}_{2K}^{(N_\uparrow, N_\downarrow)} = \binom{K}{N_\uparrow} \times \binom{K}{N_\downarrow}. \tag{68}$$

The S_z symmetry can be very easily implemented using the same ideas as introduced for the general case: just carry bit representations for the up- and down-spin electrons separately. In fact, when the total spin projection is conserved, we can distinguish electrons of different spin! Still, the Hilbert space of the single-band, half-filled Hubbard model with just 12 sites has dimension $853\,776$. Using further symmetries, if they exist, we could bring down the dimension somewhat further, however at the expense of considerable and problem-specific effort.

The key to going to larger systems is the realization that the vast majority of the elements of the Hamiltonian matrix is zero. This is quite easy to see. For the ab-initio Hamiltonian (55) with electron-electron repulsion, matrix elements between configurations that differ in more than two electron occupations vanish. Thus, for each configuration there may only be the diagonal element, $N \times (K-1)$ hopping terms, and $N(N-1)/2 \times (K-N)(K-N-1)/2$ pair-hopping terms. Thus the fraction of non-zero matrix elements of $\tilde{H}$ to the total number is

$$\left(1 + N\left(1 + \frac{N-1}{2}\frac{(K-N-1)}{2}\right)(K-N)\right) \bigg/ \binom{K}{N} \tag{69}$$

which, with increasing problem size, rapidly approaches zero. For the example of $N = 25$ electrons in $K = 100$ orbitals only $834\,376$ of the (over 10^{23}) matrix elements per row can be non-zero. This is the worst case. The sparsity of many-body Hamiltonians is even more pronounced when working in a tight-binding basis with short-ranged hopping and local electron-electron repulsion. Thus, many-body Hamiltonians are exceedingly sparse and the more so the larger the problem. They are therefore ideally suited for approaches like the Lanczos method, that are based on matrix-vector products, which for the sparse matrices scale close to linearly in the matrix dimension.

3.4   Non-interacting electrons

Even when considering a system of N non-interacting electrons we have to solve the large matrix eigenvalue problem (57). Writing the non-interacting Hamiltonian in the basis used for the CI expansion (56) we obtain

$$\hat{H} = \sum_{n,m} H_{nm}\, c_n^\dagger c_m \,,$$

which, in general, has non-vanishing matrix elements between Slater determinants that differ in at most one operator. But we can simplify things drastically by realizing that we can choose any basis for the CI expansion. If we choose the eigenstates of the single-electron matrix H_{nm} as basis, the second-quantized Hamiltonian is

$$\hat{H} = \sum_{n,m} \varepsilon_n \delta_{n,m}\, c_n^\dagger c_m = \sum_n \varepsilon_n\, c_n^\dagger c_n \,.$$

In this basis all off-diagonal matrix elements vanish and the CI Hamiltonian (57) is diagonal. Thus all $\binom{K}{N}$ eigenstates are Slater determinants

$$|\Phi_{\boldsymbol{n}}\rangle = c_{n_N}^\dagger \cdots c_{n_1}^\dagger |0\rangle \qquad \text{with eigenenergy} \quad E_{\boldsymbol{n}} = \sum_i \varepsilon_{n_i} \,. \tag{70}$$

This shows that choosing an appropriate basis for a CI expansion is crucial. A good general strategy should thus be to solve the matrix problem (57) and at the same time look for the basis set (of given size) that minimizes the variational energy. The simplest example, where the many-body basis consists of a single Slater determinant, is the Hartree-Fock method.

4   Jordan-Wigner representation

The breakthrough in the development of quantum mechanics was Heisenberg's insight that position and momentum of a particle must be represented by non-commuting matrices [8]. The canonical commutation relations $[\hat{r}_i,\, \hat{p}_j] = \mathrm{i}\hbar\delta_{ij}$ are the essence of quantization. In order to develop a quantum theory of radiation, Dirac quantized a plane wave $\vec{E}_{\vec{k}}(\vec{r},t) = \vec{E}_{\vec{k}}\, \mathrm{e}^{\mathrm{i}(\vec{k}\cdot\vec{r}-\omega t)}$ using the same idea, describing the wave by its energy E and phase $\theta = -\omega t$, postulating matrices with canonical commutation relation $[E, t] = \mathrm{i}\hbar$. In analogy to Heisenberg's first quantization, this step is called *second* quantization. It is quite plausible, considering the time-dependent Schrödinger equation: $\mathrm{i}\hbar\frac{d}{dt} = E$. It follows from the commutation relation $[E,\, \mathrm{e}^{-\mathrm{i}\omega t}] = \hbar\omega\, \mathrm{e}^{-\mathrm{i}\omega t}$ that the operator $\mathrm{e}^{\mathrm{i}\theta}$ adds a photon to the radiation field: $E\mathrm{e}^{\mathrm{i}\theta} = \mathrm{e}^{\mathrm{i}\theta}(E+\hbar\omega)$.

Instead of working with these operators directly, Dirac relates them to the expansion coefficient b_k of a many-photon wave function in the basis of plane waves and requires that $|b_k|^2 = b_k^\dagger b_k$ gives the occupation $N_k = E/\hbar\omega_k$ of mode k. This means that, in second quantization, the expansion coefficients become operators, e.g.,

$$b_k = \mathrm{e}^{-\mathrm{i}\theta_k} N_k^{1/2} \quad \text{and} \quad b_k^\dagger = N_k^{1/2} \mathrm{e}^{\mathrm{i}\theta_k} \tag{71}$$

with $b_k^\dagger b_k = N_k$ and commutation relation

$$\left[b_k,\, b_k^\dagger\right] = e^{-i\theta_k} N_k e^{i\theta_k} - N_k = e^{-i\theta_k} e^{i\theta_k}(N_k+1) - N_k = 1\,. \tag{72}$$

Pascual Jordan realized [10] that the central part of Dirac's argument is the commutation relation $[N_k,\, e^{i\theta_k}] = e^{i\theta_k}$, showing that $e^{i\theta}$ acts as a ladder operator. To derive a similar description for electrons, he implemented the Pauli principle by restricting occupations to the values 0 and 1. In its eigenbasis, N_k can then be written as a $2{\times}2$ matrix

$$N = \begin{pmatrix} 1 & 0 \\ 0 & 0 \end{pmatrix} = \frac{1}{2}(\sigma_z+1) \tag{73}$$

so that the ladder operators, fulfilling $\left[N,\, e^{\pm i\theta}\right] = \pm e^{\pm i\theta}$, take the form

$$e^{i\theta} = \begin{pmatrix} 0 & 1 \\ 0 & 0 \end{pmatrix} = \frac{1}{2}(\sigma_x+i\sigma_y) \quad\text{and}\quad e^{-i\theta} = \begin{pmatrix} 0 & 0 \\ 1 & 0 \end{pmatrix} = \frac{1}{2}(\sigma_x-i\sigma_y) \tag{74}$$

and, using $N^2 = N \rightsquigarrow N^{1/2} = N$, the creators and annihilators (71) become

$$d^\dagger = N^{1/2}\, e^{i\theta} = \begin{pmatrix} 1 & 0 \\ 0 & 0 \end{pmatrix}\begin{pmatrix} 0 & 1 \\ 0 & 0 \end{pmatrix} = \begin{pmatrix} 0 & 1 \\ 0 & 0 \end{pmatrix} = \frac{1}{2}(\sigma_x+i\sigma_y) \tag{75}$$

$$d = e^{-i\theta} N^{1/2} = \begin{pmatrix} 0 & 0 \\ 1 & 0 \end{pmatrix}\begin{pmatrix} 1 & 0 \\ 0 & 0 \end{pmatrix} = \begin{pmatrix} 0 & 0 \\ 1 & 0 \end{pmatrix} = \frac{1}{2}(\sigma_x-i\sigma_y). \tag{76}$$

The resulting Paulions do not fulfill a canonical *commutation* relation ($[d^\dagger,\, d] = \sigma_z$), instead their *anti*-commutator is analogous to (72)

$$d\, d^\dagger + d^\dagger d = \left\{d,\, d^\dagger\right\} = 1\,. \tag{77}$$

Using $S^\pm = S^x \pm iS^y = (\sigma_x \pm i\sigma_y)/2$ and $S^z = \sigma_z/2$, we see from the simple mapping

$$\begin{array}{c|ccccc} \text{paulion} & |0\rangle & |1\rangle & d^\dagger & d & N \\ \hline \text{spin-½} & |{\downarrow}\rangle & |{\uparrow}\rangle & S^+ & S^- & S^z+\frac{1}{2} \end{array} \tag{78}$$

that a paulions behaves just like a spin-½. Extending the analogy to more modes/spins, we obtain the algebra of hard-core bosons [12], where operators involving different spins commute: $[d_i,\, d_j] = 0 = [d_i^\dagger,\, d_j^\dagger]$, and $[d_i,\, d_j^\dagger] = 0$ for $i{\neq}j$, while on the same site they fulfill the canonical anticommutation relations

$$\left\{d_i,\, d_i^\dagger\right\} = 1 \quad\text{and}\quad \left\{d_i,\, d_i\right\} = 0 = \left\{d_i^\dagger,\, d_i^\dagger\right\}. \tag{79}$$

While hard-core bosons always fulfill the Pauli principle: $\left(d_i^\dagger\right)^2 = 0$, they change character under basis transformations. This is most easily seen in the case of two sites: Transforming from d_1 and d_2 to $d_\pm = (d_1 \pm d_2)/\sqrt{2}$, we see that in the new basis the operators on different modes need no longer commute

$$\left[d_+,\, d_-^\dagger\right] = \frac{1}{2}\Big(\left[d_1, d_1^\dagger\right] - \left[d_2, d_2^\dagger\right]\Big) = N_2 - N_1\,,$$

where we have used $[A, B] = \{A, B\} - 2BA$. The problem arises from the on-site anticommutators mixing into the off-site commutators.

This can be fixed by requiring fermionic anticommutation relations for all operators

$$\{c_i, c_j^\dagger\} = \delta_{ij} \quad \text{and} \quad \{c_i, c_j\} = 0 = \{c_i^\dagger, c_j^\dagger\} \tag{80}$$

which, just like the bosonic commutators, remain unchanged under (unitary) basis transformations $c_{\beta_i}^\dagger = \sum_\mu c_{\alpha_\mu}^\dagger U_{\mu i}$:

$$[c_{\beta_i}, c_{\beta_j}^\dagger]_\pm = \sum_{\mu,\nu} \overline{U_{\mu i}} \, U_{\nu j} \underbrace{[c_{\alpha_\mu}, c_{\alpha_\nu}^\dagger]_\pm}_{=\delta_{\mu,\nu}} = \sum_\mu (U^\dagger)_{i\mu} U_{\mu j} = 1 \,. \tag{81}$$

This was realized by Jordan and Wigner [11]. To make operators on different sites anticommute, they introduced operators to keep track of the Fermi sign encountered, e.g., when calculating hopping terms in the occupation number representation as in (66). The Fermi string operator $\prod_{k=1}^{i-1}(-\sigma_z^k)$ collects a factor -1 for every occupied mode (i.e., spin up) below the mode the ladder operator acts on

$$c_i^\dagger = S_i^+ \otimes (-2S_{i-1}^z) \otimes \cdots \otimes (-2S_1^z) \quad \text{and} \quad c_i = S_i^- \otimes (-2S_{i-1}^z) \otimes \cdots \otimes (-2S_1^z) \tag{82}$$

Since $(\sigma_z)^2 = 1$ this does not change the anticommutation relations between operators on the same sites, e.g.,

$$\{c_i, c_i^\dagger\} = \{S_i^-, S_i^+\} \otimes (-\sigma_z^{i-1})^2 \otimes \cdots \otimes (-\sigma_z^1)^2 = 1 \tag{83}$$

while the operators on different sites now anticommute as desired, e.g., for $i > j$

$$\{c_i, c_j^\dagger\} = S_i^- \otimes (-\sigma_z^{i-1}) \otimes \cdots \otimes (-\sigma_z^{j+1}) \otimes \underbrace{\{S_j^+, -\sigma_z^i\}}_{=0} \otimes (-\sigma_z^{j-1})^2 \otimes \cdots (-\sigma_z^1)^2 = 0 \,. \tag{84}$$

Thus the operators c_i and $c_j^\dagger$ fulfill canonical anticommutation relations, the form of which remains unchanged under basis transformations, cf. (81). It follows from (83) that also for paulions the hard-core constraint $N_i^2 = N_i$ is invariant under basis transformations.

We note in passing that the Pauli principle has interesting consequences for the classical description of electrons first noticed by Rudolf Peierls [6]: Given the particle-wave duality in quantum mechanics one may wonder why, in the classical limit, electrons behave not like radiation but as particles. This may be seen as a consequence of the uncertainty relation between particle number and phase following from $[N, \theta] = -i$, which formed the basis of second quantization. A classical wave has a well defined phase, which can only be obtained when the uncertainty in N is large. This condition can be fulfilled for bosons in the limit of large average number of photons. For fermions, however, the uncertainty in N is severely limited by the Pauli principle, making it impossible to get a classical wave with well defined phase.

Such arguments based on a phase operator, as well as the derivation of second quantization sketched above have, however, to be taken with caution, as working with phase and angle operators is not straightforward [13]. We can see that there is something not quite right with the phase operator θ already from (74), which shows that $e^{i\theta}$ is *not* unitary, i.e., that θ is not hermitian. The same is true for the corresponding ladder operators in the bosonic case. The reason is that the number of particles is bounded from below, which means that there is a lowest state that is annihilated by $e^{-i\theta}$, so that this operator cannot have an inverse.

This problem no longer appears in relativistic quantum mechanics: the second-quantization commutation relation $[E, t] = i\hbar$ is related to the first-quantization $[r_i, p_i] = i\hbar\delta_{ij}$ by Lorentz invariance. Correspondingly, the relativistic energy spectrum is not bounded from below, but has hole states of negative energy.

Non-relativistic second quantization, on the other hand, does not need these commutation relations, since it is nothing but an extremely economical way of representing states. The bosonic commutation relations are just those for the ladder operators $a = \left(x/x_0 + ix_0 p_x/\hbar\right)/\sqrt{2}$ of a harmonic oscillator with $x_0 = \sqrt{\hbar/m\omega}$, for which they are, in fact, just a consequence of the position-momentum commutator

$$i\hbar = [x, p_x] = \left[\frac{x_0}{\sqrt{2}}\left(a+a^\dagger\right), -\frac{i\hbar}{\sqrt{2}x_0}\left(a-a^\dagger\right)\right] = -\frac{i\hbar}{2}\left[a+a^\dagger, a-a^\dagger\right] = +i\hbar\left[a, a^\dagger\right].$$

For fermions there is a simple relation between an N-electron wave function $\Psi(x_1, \ldots, x_N)$ and the corresponding N-electron state $|\Psi\rangle$:

$$|\Psi\rangle = \frac{1}{\sqrt{N!}}\int dx_1 \cdots dx_N\, \Psi(x_1, \ldots, x_N)\, \hat{\Psi}^\dagger(x_N)\cdots\hat{\Psi}^\dagger(x_1)|0\rangle \tag{85}$$

$$\Psi(x_1, \ldots, x_N) = \frac{1}{\sqrt{N!}}\langle 0|\hat{\Psi}(x_1)\cdots\hat{\Psi}(x_N)|\Psi\rangle \tag{86}$$

with unitarity relations

$$\frac{1}{N!}\int dx_1 \cdots dx_N\, \hat{\Psi}^\dagger(x_N)\cdots\hat{\Psi}^\dagger(x_1)|0\rangle\langle 0|\hat{\Psi}(x_1)\cdots\hat{\Psi}(x_N) = \mathbb{1}_N \tag{87}$$

and

$$\langle 0|\hat{\Psi}(x_1)\cdots\hat{\Psi}(x_N)\,\hat{\Psi}^\dagger(x_N')\cdots\hat{\Psi}^\dagger(x_1')|0\rangle = \begin{vmatrix} \delta(x_1-x_1') & \cdots & \delta(x_1-x_N') \\ \vdots & & \vdots \\ \delta(x_N-x_1') & \cdots & \delta(x_N-x_N') \end{vmatrix} \tag{88}$$

so that normalizations are kept

$$\int dx_1 \cdots dx_N\, \left|\Psi(x_1, \ldots, x_N)\right|^2 = 1 \quad\Leftrightarrow\quad \langle\Psi|\Psi\rangle = 1\,. \tag{89}$$

Note that first-quantized wave functions involve factors $1/\sqrt{N!}$, since the normalization integral is over all permutations of the coordinates, while integration over a single domain $x_1 < \cdots < x_n$ (assuming a suitable ordering of the coordinates) already contains all relevant information.

4.1 Spins, hard-core bosons, and fermions

The equivalence between spin operators and hard-core bosons makes it possible to rewrite spin-½ Heisenberg models like

$$J \sum_{\langle ij \rangle} \vec{S}_i \cdot \vec{S}_j \tag{90}$$

using $S^x = (S^+ + S^-)/2$, $S^y = (S^+ - S^-)/2i$, and (78) as dictionary, into

$$J \sum_{\langle ij \rangle} \frac{1}{2} \left(d_i^\dagger d_j + d_i d_j^\dagger \right) + \left(d_i^\dagger d_i - \tfrac{1}{2} \right) \left(d_j^\dagger d_j - \tfrac{1}{2} \right), \tag{91}$$

where an (anti)ferromagnetic coupling of the spins corresponds to a (repulsive) attractive interaction between the hard-core bosons, while the transverse components of the spin interaction corresponds to a hopping of paulions. Thus, e.g., the XY-model

$$\sum_{\langle ij \rangle} J_x S_i^x S_j^x + J_y S_i^y S_j^y \tag{92}$$

maps to the non-interacting hard-core boson model

$$\sum_{\langle ij \rangle} \frac{J_x + J_y}{4} \left(d_i^\dagger d_j + d_i d_j^\dagger \right) + \frac{J_x - J_y}{4} \left(d_i^\dagger d_j^\dagger + d_i d_j \right). \tag{93}$$

For the XX-model, $J_x = J_y$, there are just hopping terms, for the general XY-model there are also pairing terms. The opposite limit, $J_x = 0 = J_y$, the Ising model, here with transverse field

$$J \sum_{\langle ij \rangle} S_i^z S_j^z + H \sum_i S_i^x \tag{94}$$

seems at first to necessarily lead to a model of interacting hard-core bosons. We can, however, easily rotate the spin-direction so that the external field points in z direction, to obtain a hard-core boson model with only one-body terms

$$\frac{J}{4} \sum_{\langle ij \rangle} \left(d_i^\dagger + d_i \right) \left(d_j^\dagger + d_j \right) + H \sum_i \left(d_i^\dagger d_i - \tfrac{1}{2} \right). \tag{95}$$

where the first term is just (93) with $J_y = 0$.

It is tempting to try to solve these non-interacting hard-core boson Hamiltonians by diagonalizing the one-body matrix and using a Bogoliubov transformation. As we have seen, however, the commutation relations between paulions are not invariant under basis changes, so that the eigenstates are not simple product states as in (70). This only works for fermions, i.e., when we multiply the Pauli operators with Fermi strings to obtain fermions $c_i^\dagger = d_i^\dagger \prod_{k=1}^{i-1} (-1)^{n_k}$ with $n_k = d_k^\dagger d_k$ or, equivalently, $d_i^\dagger = c_i^\dagger \prod_{k=1}^{i-1} (-1)^{n_k}$ with $n_k = c_k^\dagger c_k$. Since the sign operators act on different modes than the creator/annihilator, they commute with the Fermi strings. Rewriting the paulion models we thus get terms like

$$d_i^\dagger d_j = c_i^\dagger \prod_{k=1}^{i-1} (-1)^{n_k} \prod_{k=1}^{j-1} (-1)^{n_k} c_j = c_i^\dagger \prod_{k=\min(i,j)}^{\max(i,j)-1} (-1)^{n_k} c_j. \tag{96}$$

so that the simple hopping or pairing terms are complicated by the product of spin operators. Things remain simple, however, for terms involving the same site

$$d_i^\dagger d_i = c_i^\dagger \sum_{k=i}^{i-1} (-1)^{n_k} c_i = c_i^\dagger c_i \tag{97}$$

or adjacent sites (just consider the cases $n_i=0$ or 1 separately)

$$d_{i+1}^\dagger d_i = c_{i+1}^\dagger (-1)^{n_i} c_i = c_{i+1}^\dagger c_i \quad \text{and} \quad d_{i+1}^\dagger d_i^\dagger = c_{i+1}^\dagger (-1)^{n_i} c_i^\dagger = -c_{i+1}^\dagger c_i^\dagger \tag{98}$$

and, taking the adjoint

$$d_i^\dagger d_{i+1} = \left(d_{i+1}^\dagger d_i\right)^\dagger = c_i^\dagger c_{i+1} \quad \text{and} \quad d_i d_{i+1} = \left(d_{i+1}^\dagger d_i^\dagger\right)^\dagger = -c_i c_{i+1} \, . \tag{99}$$

For a one-dimensional spin chain, the XY-model or the Ising model with transverse field can thus be written as a model of non-interacting fermions, e.g., (93) becomes

$$\sum_j \frac{J_x + J_y}{4} \left(c_{j+1}^\dagger c_j + c_j^\dagger c_{j+1}\right) + \frac{J_x - J_y}{4} \left(-c_{j+1}^\dagger c_j^\dagger - c_j c_{j+1}\right) \tag{100}$$

and, since now we are dealing with non-interacting fermions, solved in the usual way [14].

A Appendix

A.1 Atomic units

Practical electronic structure calculations are usually done in atomic units, a.u. for short. While the idea behind the atomic units is remarkably simple, in practice there is often some confusion when trying to convert to SI units. We therefore give a brief explanation.

The motivation for introducing atomic units is to simplify the equations. For example, in SI units the Hamiltonian of a hydrogen atom is

$$H = -\frac{\hbar^2}{2m_e}\nabla^2 - \frac{e^2}{4\pi\epsilon_0\, r} \ . \tag{101}$$

When we implement such an equation in a computer program, we need to enter the numerical values of all the fundamental constants. We can avoid this by using a system of units in which the *numerical values* of the electron mass m_e, the elementary charge e, the Planck-constant $\hbar$, and the dielectric constant $4\pi\epsilon_0$ are all equal to one. In these units the above equation can be programmed as

$$H = -\frac{1}{2}\nabla^2 - \frac{1}{r} \ . \tag{102}$$

This immediately tells us: 1 a.u. mass $= m_e$ and 1 a.u. charge $= e$. To complete the set of basis units we still need the atomic unit of length, which we call a_0, and of time, t_0. To find the values of a_0 and t_0 we write $\hbar$ and $4\pi\epsilon_0$ (using simple dimensional analysis) in atomic units: $\hbar = 1\, m_e a_0^2/t_0$ and $4\pi\epsilon_0 = 1\, t_0^2 e^2/(m_e a_0^3)$. Solving this system of equations, we find

$$
\begin{array}{lllll}
1 \text{ a.u. length} & = a_0 & = & 4\pi\epsilon_0\hbar^2/m_e e^2 & \approx 5.2918 \cdot 10^{-11} & \text{m} \\
1 \text{ a.u. mass} & = m_e & = & & \approx 9.1095 \cdot 10^{-31} & \text{kg} \\
1 \text{ a.u. time} & = t_0 & = & (4\pi\epsilon_0)^2\hbar^3/m_e e^4 & \approx 2.4189 \cdot 10^{-17} & \text{s} \\
1 \text{ a.u. charge} & = e & = & & \approx 1.6022 \cdot 10^{-19} & \text{C}
\end{array}
$$

The atomic unit of length, a_0, is the Bohr radius. As the dimension of energy is mass times length squared divided by time squared, its atomic unit is $m_e a_0^2/t_0^2 = m_e e^4/(4\pi\epsilon_0)^2\hbar^2$. Because of its importance the atomic unit of energy has a name, the Hartree. One Hartree is minus twice the ground-state energy of the hydrogen atom, $1\,\text{Ha} \approx 27.211\,\text{eV}$.

It would be tempting to try to set the numerical value of all fundamental constants to unity. But this must obviously fail, as the system of equations to solve becomes overdetermined when we try to prescribe the numerical values of constants that are not linearly independent in the space of basis units. Thus, we cannot, e.g., choose also the speed of light to have value one, as would be practical for relativistic calculations. Instead, in atomic units it is given by $c\,t_0/a_0 = 4\pi\varepsilon_0\hbar c/e^2 = 1/\alpha$, where α is the fine structure constant. Thus $c = \alpha^{-1}$ a.u. ≈ 137 a.u. The Bohr magneton is $\mu_B = 1/2$ a.u. The Boltzmann constant k_B, on the other hand, is independent of the previous constants. Setting its value to one fixes the unit of temperature to 1 a.u. temperature $= m_e e^4/(4\pi\epsilon_0)^2\hbar^2 k_B = \text{Ha}/k_B \approx 3.158 \cdot 10^5\,\text{K}$.

A.2 Non-orthonormal basis

A general one-electron basis of functions $|\chi_n\rangle$ will have an overlap matrix $S_{nm} = \langle\chi_n|\chi_m\rangle$ that is positive definite (and hence invertible) and hermitian. The completeness relation is

$$\mathbb{1} = \sum_{k,l}|\chi_k\rangle(S^{-1})_{kl}\langle\chi_l| \, . \tag{103}$$

With it we can easily write the Schrödinger equation $\hat{H}|v\rangle = \varepsilon|v\rangle$ in matrix form

$$\sum_k \underbrace{\langle\chi_i|H|\chi_k\rangle}_{=:H_{ik}} \underbrace{\sum_l (S^{-1})_{kl}\langle\chi_l|v\rangle}_{=:v_k}\langle\chi_i|\hat{H}|v\rangle = \varepsilon\langle\chi_i|v\rangle = \varepsilon\sum_k \underbrace{\langle\chi_i|\chi_k\rangle}_{=S_{ik}}\underbrace{\sum_l(S^{-1})_{kl}\langle\chi_l|v\rangle}_{=v_k} \, . \tag{104}$$

Collecting all components, this becomes the generalized eigenvalue problem $\boldsymbol{H}\boldsymbol{v} = \varepsilon\boldsymbol{S}\boldsymbol{v}$. From the solution $\boldsymbol{v}$ we can easily construct $|v\rangle = \sum v_k|\chi_k\rangle$. It is, however, often more convenient to have an orthonormal basis, so that we do not have to deal with the overlap matrices in the definition of the second quantized operators or the generalized eigenvalue problem.

To orthonormalize the basis $\{|\chi_n\rangle\}$, we need to find a basis transformation $\boldsymbol{T}$ such that

$$|\varphi_n\rangle := \sum_m|\chi_m\rangle\,T_{mn} \qquad \text{with} \quad \langle\varphi_n|\varphi_m\rangle = \delta_{mn} \, . \tag{105}$$

This implies that $\boldsymbol{T}^\dagger\boldsymbol{S}\boldsymbol{T} = \mathbb{1}$, or equivalently $\boldsymbol{S}^{-1} = \boldsymbol{T}\boldsymbol{T}^\dagger$. This condition does not uniquely determine $\boldsymbol{T}$. In fact there are many orthonormalization techniques, e.g., Gram-Schmidt orthonormalization or Cholesky decomposition.

Usually we will have chosen the basis functions $|\chi_n\rangle$ for a physical reason, e.g., atomic orbitals, so that we would like the orthonormal basis functions to be as close to the original basis as possible, i.e, we ask for the basis transformation $\boldsymbol{T}$ that minimizes

$$\sum_n \big\||\varphi_n\rangle - |\chi_n\rangle\big\|^2 = \sum_n \Big\|\sum_m|\chi_m\rangle(T_{mn}-\delta_{mn})\Big\|^2$$
$$= \operatorname{Tr}(\boldsymbol{T}^\dagger-\mathbb{1})\,\boldsymbol{S}\,(\boldsymbol{T}-\mathbb{1}) = \operatorname{Tr}(\underbrace{\boldsymbol{T}^\dagger\boldsymbol{S}\boldsymbol{T}}_{=\mathbb{1}}-\boldsymbol{T}^\dagger\boldsymbol{S} - \boldsymbol{S}\boldsymbol{T} + \boldsymbol{S}) \, . \tag{106}$$

Given an orthonormalization $\boldsymbol{T}$, we can obtain any other orthonormalization $\tilde{\boldsymbol{T}}$ by performing a unitary transformation, i.e., $\tilde{\boldsymbol{T}} = \boldsymbol{T}\boldsymbol{U}$. Writing $\boldsymbol{U} = \exp(i\lambda\boldsymbol{M})$ with $\boldsymbol{M}$ a Hermitian matrix, we obtain the variational condition

$$0 \overset{!}{=} \operatorname{Tr}(+i\boldsymbol{M}\boldsymbol{T}^\dagger\boldsymbol{S} - i\boldsymbol{S}\boldsymbol{T}\boldsymbol{M}) = i\operatorname{Tr}(\boldsymbol{T}^\dagger\boldsymbol{S} - \boldsymbol{S}\boldsymbol{T})\boldsymbol{M}, \tag{107}$$

which is fulfilled for $\boldsymbol{S}\boldsymbol{T} = \boldsymbol{T}^\dagger\boldsymbol{S}$, i.e., $\boldsymbol{S}\boldsymbol{T}^2 = \boldsymbol{T}^\dagger\boldsymbol{S}\boldsymbol{T} = \mathbb{1}$. The second variation at $\boldsymbol{T} = \boldsymbol{S}^{-1/2}$

$$\frac{1}{2}\operatorname{Tr}(\boldsymbol{M}^2\boldsymbol{S}^{1/2} + \boldsymbol{S}^{1/2}\boldsymbol{M}^2) > 0 \tag{108}$$

is positive, since $\boldsymbol{S}$ and the square of the hermitian matrix $\boldsymbol{M}$ are both positive definite. Hence the Löwdin symmetric orthogonalization [15]

$$\boldsymbol{T}_{\text{Löwdin}} = \boldsymbol{S}^{-1/2} \tag{109}$$

minimizes the modification of the basis vectors due to orthogonalization.

A.3 Pauli matrices

The spin matrices were defined by Pauli [16] as

$$\sigma_x = \begin{pmatrix} 0 & 1 \\ 1 & 0 \end{pmatrix} \quad \sigma_y = \begin{pmatrix} 0 & -i \\ i & 0 \end{pmatrix} \quad \sigma_z = \begin{pmatrix} 1 & 0 \\ 0 & -1 \end{pmatrix}$$

They are hermitian and unitary, so that $\sigma_j^2 = \sigma_j \sigma_j^\dagger = \mathbb{1}$. Moreover, $\det \sigma_j = -1$ and $\operatorname{Tr} \sigma_j = 0$. By explicit multiplication we find $\sigma_x \sigma_y = i\sigma_z$, from which we get the more symmetric equation $\sigma_x \sigma_y \sigma_z = i$. These relations are cyclic, which is easily seen by repeatedly using $\sigma_j^2 = \mathbb{1}$

$$\sigma_x \sigma_y = i\sigma_z \overset{\cdot \sigma_z}{\rightsquigarrow} \sigma_x \sigma_y \sigma_z = i \overset{\sigma_x \cdot}{\rightsquigarrow} \sigma_y \sigma_z = i\sigma_x \overset{\cdot \sigma_x}{\rightsquigarrow} \sigma_y \sigma_z \sigma_x = i \overset{\sigma_y \cdot}{\rightsquigarrow} \sigma_z \sigma_x = i\sigma_y \overset{\cdot \sigma_y}{\rightsquigarrow} \sigma_z \sigma_x \sigma_y = i \,.$$

Exchanging two adjacent indices changes the sign, e.g., multiplying $\sigma_x \sigma_y \sigma_z = i$ from the left with $\sigma_y \sigma_x$ gives $\sigma_y \sigma_x = -i\sigma_z$, which is again cyclic in the indices. We note that the multiplication table of the matrices $-i\sigma_j$ is the same as the that of the basic quaternions. We can summarize the products of the Pauli matrices in the form

$$\left(\vec{a} \cdot \vec{\sigma}\right)\left(\vec{b} \cdot \vec{\sigma}\right) = \sum a_j b_k \, \sigma_j \sigma_k = \left(\vec{a} \cdot \vec{b}\right)\mathbb{1} + i\left(\vec{a} \times \vec{b}\right) \cdot \vec{\sigma} \,. \tag{110}$$

From the products follow the familiar commutation relations $[\sigma_x, \sigma_y] = 2i\sigma_z$ (cyclic), while the anticommutators are $\{\sigma_j, \sigma_k\} = 2\delta_{j,k}\,\mathbb{1}$.

Together with the unit matrix, the Pauli matrices form a basis of the four-dimensional algebra of complex 2×2 matrices and we can write

$$\begin{pmatrix} m_{11} & m_{12} \\ m_{21} & m_{22} \end{pmatrix} = M = m_0\mathbb{1} + \vec{m} \cdot \vec{\sigma} = \begin{pmatrix} m_0 + m_z & m_x - im_y \\ m_x + im_y & m_0 - m_z \end{pmatrix} \tag{111}$$

with $2m_0 = m_{11} + m_{22}$, $2m_z = m_{11} - m_{22}$, $2m_x = m_{12} + m_{21}$, and $2m_x = i(m_{12} - m_{21})$, which can be written as $2m_j = \operatorname{Tr} M\sigma_j$, with $\sigma_0 := \mathbb{1}$. When the m_0 and $\vec{m}$ are real, M is hermitian. Matrix products are easily evaluated using (110). As a simple example we find

$$(m_0\mathbb{1} + \vec{m} \cdot \vec{\sigma})(m_0\mathbb{1} - \vec{m} \cdot \vec{\sigma}) = m_0^2 - m_x^2 - m_y^2 - m_z^2 = \det M$$

(remember $\det \alpha \mathbb{1}_N = \alpha^N$). Thus, when $\det M \neq 0$, the inverse of M is

$$M = m_0\mathbb{1} + \vec{m} \cdot \vec{\sigma} \quad \rightsquigarrow \quad M^{-1} = (m_0\mathbb{1} - \vec{m} \cdot \vec{\sigma})/\det M \,. \tag{112}$$

For a unitary matrix $U = u_0 + \vec{u} \cdot \vec{\sigma}$ with $\det U = 1$ we then see from $U^\dagger = u_0^* + \vec{u}^* \cdot \vec{\sigma} \overset{!}{=} u_0 - \vec{u} \cdot \vec{\sigma}$ that u_0 must be real and $\vec{u} = i\vec{n}$ imaginary, so that $1 = \det U = u_0^2 + \|\vec{n}\|^2$, which allows us to write $u_0 = \cos \alpha$ and $\vec{n} = \sin \alpha \, \hat{n}$ with unit vector $\hat{n} := \vec{n}/\|\vec{n}\|$ and $\alpha \in [0, 2\pi)$. Thus any special unitary 2×2 matrix $U \in \mathrm{SU}(2)$ can be written, using $(\hat{n} \cdot \vec{\sigma})^2 = \mathbb{1}$ from (110) in the power series,

$$U_{\hat{n},\alpha} = \cos \alpha \, \mathbb{1} + i \sin \alpha \, (\hat{n} \cdot \vec{\sigma}) = \exp\left(i\alpha \, \hat{n} \cdot \vec{\sigma}\right). \tag{113}$$

General unitary matrices with $\det U = e^{i\alpha_0}$ have the form $U = e^{i\alpha_0/2} U_{\hat{n},\alpha}$.

The U are related to rotations of vectors $\vec{a} \in \mathbb{R}^3$ via $U(\vec{a} \cdot \vec{\sigma})U^\dagger$. To see this we remember that $\vec{a} \cdot \vec{\sigma}$ is a hermitian 2×2 matrix with zero trace. By the cyclic property of the trace $\mathrm{Tr}\, U(\vec{a} \cdot \vec{\sigma})U^\dagger = \mathrm{Tr}\, \vec{a} \cdot \vec{\sigma}$, so that there exists a unique $\vec{a}_U$ with $U(\vec{a} \cdot \vec{\sigma})U^\dagger = \vec{a}_U \cdot \vec{\sigma}$. This mapping $\vec{a} \to \vec{a}_U$ is linear, $U\big((c\vec{a} + \vec{b}) \cdot \vec{\sigma}\big)U^\dagger = cU(\vec{a} \cdot \vec{\sigma})U^\dagger + U(\vec{b} \cdot \vec{\sigma})U^\dagger$, and preserves the inner product

$$\vec{a} \cdot \vec{b} = \tfrac{1}{2}\,\mathrm{Tr}(\vec{a} \cdot \vec{\sigma})(\vec{b} \cdot \vec{\sigma}) = \tfrac{1}{2}\,\mathrm{Tr}\, U(\vec{a} \cdot \vec{\sigma})U^\dagger U(\vec{b} \cdot \vec{\sigma})U^\dagger = \tfrac{1}{2}\,\mathrm{Tr}(\vec{a}_U \cdot \vec{\sigma})(\vec{b}_U \cdot \vec{\sigma}) = \vec{a}_U \cdot \vec{b}_U$$

so that it must be a proper rotation, $\vec{a}_U = R_U\,\vec{a}$ with $R_U \in \mathrm{SO}(3)$. To identify which rotation, we consider the special case $\vec{a}_\parallel = c_a \hat{n}$ for which, by (110), $\vec{a}_\parallel \cdot \vec{\sigma}$ commutes with $\hat{n} \cdot \vec{\sigma}$ so that $U(\vec{a}_\parallel \cdot \vec{\sigma})U^\dagger = \vec{a}_\parallel \cdot \vec{\sigma}$, i.e., $\hat{n}$ is the axis of rotation. To find the rotation angle ϑ, we consider a unit vector $\hat{a}_\perp$ perpendicular to $\hat{n}$, for which, using $(\hat{a}_\perp \cdot \vec{\sigma})(\hat{n} \cdot \vec{\sigma}) = \mathrm{i}(\hat{a}_\perp \times \hat{n}) \cdot \vec{\sigma}$ and $\mathrm{Tr}\, \vec{v} \cdot \vec{\sigma} = 0$,

$$\begin{aligned}
\cos\vartheta = \hat{a}_\perp \cdot R_U \hat{a}_\perp &= \tfrac{1}{2}\,\mathrm{Tr}(\hat{a}_\perp \cdot \vec{\sigma})U(\hat{a}_\perp \cdot \vec{\sigma})U^\dagger \\
&= \tfrac{1}{2}\,\mathrm{Tr}(\hat{a}_\perp \cdot \vec{\sigma})(\cos\alpha + \mathrm{i}\sin\alpha\,(\hat{n} \cdot \vec{\sigma}))\ (\hat{a}_\perp \cdot \vec{\sigma})(\cos\alpha - \mathrm{i}\sin\alpha\,(\hat{n} \cdot \vec{\sigma})) \\
&= \tfrac{1}{2}\,\mathrm{Tr}\big(\cos\alpha\,\hat{a}_\perp - \sin\alpha\,(\hat{a}_\perp \times \hat{n})\big) \cdot \vec{\sigma}\ \ \big(\cos\alpha\,\hat{a}_\perp + \sin\alpha\,(\hat{a}_\perp \times \hat{n})\big) \cdot \vec{\sigma} \\
&= \big(\cos\alpha\,\hat{a}_\perp - \sin\alpha\,(\hat{a}_\perp \times \hat{n})\big) \cdot \big(\cos\alpha\,\hat{a}_\perp + \sin\alpha\,(\hat{a}_\perp \times \hat{n})\big) = (\cos\alpha)^2 - (\sin\alpha)^2 = \cos 2\alpha
\end{aligned}$$

Hence, $U_{\hat{n},\alpha} \in \mathrm{SU}(2)$ induces a rotation $R_U \in \mathrm{SO}(3)$ about the axis $\hat{n}$ through the angle $\vartheta = 2\alpha$. Therefore, matrices in $\mathrm{SU}(2)$ are commonly written using the angle of rotation $\vartheta \in [0, 4\pi)$ instead of $\alpha \in [0, 2\pi)$ as $U(\hat{n}, \vartheta) = \exp(\mathrm{i}\tfrac{\vartheta}{2}\,\hat{n} \cdot \vec{\sigma})$. We see, in particular, that the two matrices $U(\hat{n}, \vartheta)$ and $U(\hat{n}, \vartheta + 2\pi) = -U(\hat{n}, \vartheta)$ in $\mathrm{SU}(2)$ induce the same rotation $R_{-U} = R_U \in \mathrm{SO}(3)$.

Diagonalizing a hermitian 2×2 matrix $M = m_0 \mathbb{1} + \vec{m} \cdot \vec{\sigma}$ is now simple: just rotate $\hat{m} \to \hat{z}$

$$U\big(m_0 \mathbb{1} + \|\vec{m}\|\,(\hat{m} \cdot \vec{\sigma})\big)U^\dagger = m_0 \mathbb{1} + \|\vec{m}\|\,\sigma_z$$

from which we easily read off the eigenvalues

$$\varepsilon_\pm = m_0 \pm \|\vec{m}\| = \frac{m_{11} + m_{22}}{2} \pm \sqrt{\frac{(m_{11} - m_{22})^2}{4} + |m_{12}|^2} = \tfrac{1}{2}\,\mathrm{Tr}\, M \pm \sqrt{\big(\tfrac{1}{2}\,\mathrm{Tr}\, M\big)^2 - \det M},$$

while the eigenvalues are the columns vectors of $U^\dagger = (\boldsymbol{v}_+,\ \boldsymbol{v}_-)$

$$m_0 \mathbb{1} + \vec{m} \cdot \vec{\sigma} = U^\dagger\big(m_0 \mathbb{1} + \|\vec{m}\|\,\sigma_z\big)U = m_0 \mathbb{1} + \|\vec{m}\|\,(\boldsymbol{v}_+, \boldsymbol{v}_-)\,\sigma_z \begin{pmatrix} \boldsymbol{v}_+^\dagger \\ \boldsymbol{v}_-^\dagger \end{pmatrix}$$

We still need to determine a U that rotates $\hat{m} \to \hat{z}$. The rotation axis should be orthogonal to both vectors, i.e., $\hat{n} = \hat{z} \times \hat{m} / \|\hat{z} \times \hat{m}\| = (m_x \hat{y} - m_y \hat{x}) / \sqrt{m_x^2 + m_y^2}$, so that the rotation angle $\vartheta \in [0, \pi]$ is determined by $\cos\vartheta = \hat{m} \cdot \hat{z} = m_z / \|\vec{m}\|$. Using also the other spherical coordinates $m_x = \|\vec{m}\| \sin\vartheta \cos\varphi$ and $m_y = \|\vec{m}\| \sin\vartheta \sin\varphi$, we get $\hat{n} = \cos\varphi\,\hat{y} - \sin\varphi\,\hat{x}$ so that

$$U(\hat{n}, \vartheta) = \begin{pmatrix} \cos\tfrac{\vartheta}{2} + \mathrm{i}n_z \sin\tfrac{\vartheta}{2} & (n_y + \mathrm{i}n_x)\sin\tfrac{\vartheta}{2} \\ -(n_y - \mathrm{i}n_x)\sin\tfrac{\vartheta}{2} & \cos\tfrac{\vartheta}{2} - \mathrm{i}n_z \sin\tfrac{\vartheta}{2} \end{pmatrix} = \begin{pmatrix} \cos\tfrac{\vartheta}{2} & +\mathrm{e}^{-\mathrm{i}\varphi}\sin\tfrac{\vartheta}{2} \\ -\mathrm{e}^{+\mathrm{i}\varphi}\sin\tfrac{\vartheta}{2} & \cos\tfrac{\vartheta}{2} \end{pmatrix}$$

from which we read off the eigenvectors as the columns of $U^\dagger$ (which you may want to check for simple cases like $M = \sigma_z$, σ_x or σ_y)

$$\boldsymbol{v}_+ = \begin{pmatrix} \cos\tfrac{\vartheta}{2} \\ +\mathrm{e}^{+\mathrm{i}\varphi}\sin\tfrac{\vartheta}{2} \end{pmatrix} \text{ and } \boldsymbol{v}_- = \begin{pmatrix} -\mathrm{e}^{-\mathrm{i}\varphi}\sin\tfrac{\vartheta}{2} \\ \cos\tfrac{\vartheta}{2} \end{pmatrix} \text{ with } \begin{array}{l} \varphi = \arg(m_{21}) = -\arg(m_{12}) \\ \vartheta = \arccos\dfrac{m_{11} - m_{22}}{\varepsilon_+ - \varepsilon_-} \end{array} . \tag{114}$$

A more symmetric form of the eigenvectors may be obtained by writing $\mathrm{e}^{\mp \mathrm{i}\varphi/2}\boldsymbol{v}_\pm$.

A.4   Some useful commutation relations

Commuting an operator through a product of operators is straightforward

$$
\begin{aligned}
AB_1 \cdots B_N &= [A,\, B_1]\, B_2 \cdots B_N + B_1 A B_2 \cdots B_N \\
&= [A,\, B_1]\, B_2 \cdots B_N + B_1 [A,\, B_2] \cdots B_N + B_1 B_2 A \cdots B_N \\
&\;\;\vdots \\
&= \sum_{n=1}^{N} \prod_{i=1}^{n-1} B_i\ [A,\, B_n] \prod_{i=n+1}^{N} B_i + B_1 \cdots B_N A
\end{aligned}
$$

while, working analogously, anticommuting introduces alternating signs

$$
\begin{aligned}
AB_1 \cdots B_N &= \{A,\, B_1\}\, B_2 \cdots B_N - B_1 A B_2 \cdots B_N \\
&= \{A,\, B_1\}\, B_2 \cdots B_N - B_1 \{A,\, B_2\} \cdots B_N - B_1 B_2 A \cdots B_N \\
&\;\;\vdots \\
&= \sum_{n=1}^{N} (-1)^{n-1} \prod_{i=1}^{n-1} B_i\ \{A,\, B_n\} \prod_{i=n+1}^{N} B_i + (-1)^N B_1 \cdots B_N A
\end{aligned}
$$

The following special cases are particularly useful

$$
\begin{aligned}
[A,\, BC] &= [A,\, B]\, C + B\,[A,\, C] \\
&= \{A,\, B\}C - B\{A,\, C\}
\end{aligned}
$$

$$
\begin{aligned}
[AB,\, C] &= A\,[B,\, C] + [A,\, C]\, B \\
&= A\{B,\, C\} - \{A,\, C\}B
\end{aligned}
$$

$$
\begin{aligned}
[AB,\, CD] &= A\,[B,\, C]\, D + AC\,[B,\, D] + [A, C]\, DB + C\,[A,\, D]\, B \\
&= A\{B,\, C\}D - AC\{B,\, D\} + \{A, C\}DB - C\{A,\, D\}B
\end{aligned}
$$

Important examples are $\left[c_i^\dagger c_j,\, c_\gamma^\dagger \right] = \langle j|\gamma\rangle\, c_i^\dagger$ and $\left[c_i^\dagger c_j,\, c_\gamma \right] = -\langle i\,|\gamma\rangle\, c_j$.

For the commutator of products of creation and annihilation operators appearing in one- and two-body operators we find

$$
\left[c_i^\dagger c_j,\, c_\alpha^\dagger c_\beta \right] = \left[c_i^\dagger c_j,\, c_\alpha^\dagger \right] c_\beta + c_\alpha^\dagger \left[c_i^\dagger c_j,\, c_\beta \right] = \langle j|\alpha\rangle\, c_i^\dagger c_\beta - \langle \beta|i\rangle\, c_\alpha^\dagger c_j
$$

and

$$
\left[c_i^\dagger c_j^\dagger c_k c_l,\, c_\alpha^\dagger c_\beta \right] = \langle l|\alpha\rangle\, c_i^\dagger c_j^\dagger c_k c_\beta + \langle k|\alpha\rangle\, c_i^\dagger c_j^\dagger c_\beta c_l - \langle \beta|j\rangle\, c_i^\dagger c_\alpha^\dagger c_k c_l - \langle \beta|i\rangle\, c_\alpha^\dagger c_j^\dagger c_k c_l \,.
$$

References

[1] P. Forrest: *The Identity of Indiscernibles*, in The Stanford Encyclopedia of Philosophy
     http://plato.stanford.edu/entries/identity-indiscernible/

[2] W. Pauli: *The connection between spin and statistics,* Phys. Rev. **58**, 716 (1940)

[3] R.F. Streater and A.S. Wightman: *PCT, Spin and Statistics, and All That*
     (Benjamin, New York, 1964)

[4] P.-O. Löwdin: *Quantum Theory of Many-Particle Systems I,* Phys. Rev. **97**, 1474 (1955)

[5] E. Koch: *Many-Electron States*, in [17]

[6] R. Peierls: *Surprises in Theoretical Physics* (Princeton University Press, 1979)

[7] H.S. Warren: *Hacker's Delight*, 2nd ed. (Addison-Wesley, 2013)

[8] W. Heisenberg: *Über quantentheoretische Umdeutung kinematischer und mechanischer
     Beziehungen,* Z. Phys. **33**, 879 (1925)

[9] P.M.A. Dirac: *The Quantum Theory of the Emission and Absorption of Radiation,*
     Proc. Roy. Soc. Lond. A **114**, 243 (1927)

[10] P. Jordan: *Zur Quantenmechanik der Gasentartung,* Z. Phys. **44**, 473 (1927)

[11] P. Jordan and E. Wigner: *Über das Paulische Äquivalenzverbot,* Z. Phys. **47**, 631 (1928)

[12] T. Matsubara and H. Matsuda: *A Lattice Model of Liquid Helium, I,*
     Prog. Theor. Phys. **16**, 569 (1956)

[13] P. Carruthers and M.M. Nieto: *Phase and Angle Variables in Quantum Mechanics,*
     Rev. Mod. Phys. **40**, 411 (1968)

[14] E. Lieb, T. Schulz, and D. Mattis: *Two Soluble Models of an Antiferromagnetic Chain,*
     Ann. Phys. **16**, 407 (1961)

[15] P.-O. Löwdin: *On the Non-Orthogonality Problem Connected with the Use of Atomic
     Wave Functions in the Theory of Molecules and Crystals,* J. Chem. Phys. **18**, 365 (1950)

[16] W. Pauli jr.: *Zur Quantenmechanik des magnetischen Elektrons*, Z. Phys. **43**, 601 (1927)

[17] E. Pavarini, E. Koch, and U. Schollwöck (eds.):
     Emergent Phenomena in Correlated Matter,
     Modeling and Simulation, Vol. 3 (Forschungszentrum Jülich, 2013)
     http://www.cond-mat.de/events/correl13

2 Fundamentals of Quantum Chemistry

Klaus Doll
Molpro Quantum Chemistry Software
Institute of Theoretical Chemistry
University of Stuttgart

Contents

1 Introduction

When the Schrödinger equation and quantum mechanics were invented, the hydrogen atom was the first system targeted. The field of quantum chemistry may be considered to start also at this point, or alternatively when the first molecule, H_2, was addressed.

The research in this field involves enormous calculations, and thus a major advance came with electronic computers. Programming languages and compilers facilitate code development, and since a few decades, computer codes for electronic structure calculations have been developed and continuously grow.

This chapter will deal with quantum chemical methods. They usually start from a Hartree-Fock calculation, and are followed by a correlation (post-Hartree-Fock) calculation. This way of including electron correlation is wave function based. As a numerical tool, basis sets (usually Gaussian basis sets) are introduced. The notion *ab initio* calculations is used in this context, with the denotation that there are no parameters fitted to experiment.

Density functional theory is at the border of quantum chemistry, and will be treated in other chapters of this book. A short section on density functional theory has been included also in this chapter, to establish the connection between Hartree-Fock and density functional theory.

This chapter aims at introducing basic notions of the field. For further reading, a couple of textbooks can be recommended, e.g. [1–6].

2 Setting up the Hamiltonian

For the electronic structure problem, we will consider a total energy expression which initially consists of kinetic energy contributions (electrons, nuclei) and the Coulomb interaction.

In a simple example, we consider two atoms (figure 1).
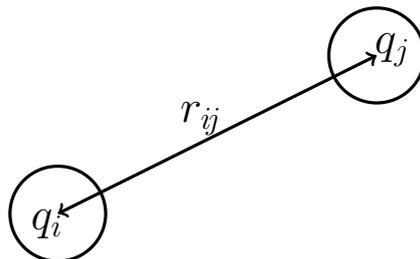
Fig. 1: *A simple example with two atoms, separated by a distance r_{ij}.*

The Coulomb interaction of the nuclei can be expressed as

$$V(r_{ij}) = \frac{q_i q_j}{4\pi\epsilon_0 r_{ij}} =: \frac{q_i q_j}{r_{ij}} \,, \tag{1}$$

where atomic units ($\hbar = m_{el} = e = 4\pi\epsilon_0 = 1$) have been used in the last step.

The kinetic energy consists of contributions due to the nuclei and N electrons

$$E_{\text{kinetic}} = \frac{1}{2} M_i \vec{v}_i{}^2 + \frac{1}{2} M_j \vec{v}_j{}^2 + \sum_{k=1}^{N} \frac{1}{2} m_{el} \vec{v}_k{}^2 \,. \tag{2}$$

In general, we obtain

$$E = E_{\text{kinetic}} + E_{\text{Coulomb}} \left(+ E_{\text{external fields}} + E_{\text{relativistic corrections}} \right). \tag{3}$$

In the following, external fields (e.g. electric or magnetic fields) will not be considered, also relativistic effects are neglected. The classical energy then becomes, for a system of n nuclei of charges Z_j, and N electrons

$$E = \frac{1}{2} \sum_{j=1}^{n} \frac{\vec{p}_j^2}{M_j} + \frac{1}{2} \sum_{i=1}^{N} \frac{\vec{p}_{el,i}^2}{m_{el}} + \sum_{j=1}^{n} \sum_{j'=j+1}^{n} \frac{Z_j Z_{j'}}{|\vec{R}_j - \vec{R}_{j'}|} + \sum_{i=1}^{N} \sum_{i'=i+1}^{N} \frac{1}{|\vec{r}_i - \vec{r}_{i'}|} - \sum_{i=1}^{N} \sum_{j=1}^{n} \frac{Z_j}{|\vec{r}_i - \vec{R}_j|} \tag{4}$$

As the masses of the nuclei M_j are much larger than the masses of the electrons m_{el}, the kinetic energy of the nuclei is neglected: the Born-Oppenheimer approximation is made.

After replacing the momentum $\vec{p}$ with the corresponding quantum mechanical operator $-i\hbar\nabla$, we obtain the quantum mechanical Hamiltonian, in atomic units,

$$H = -\frac{1}{2} \sum_{i=1}^{N} \nabla_i^2 + \sum_{\substack{j,j'=1 \\ j'>j}}^{n} \frac{Z_j Z_{j'}}{|\vec{R}_j - \vec{R}_{j'}|} + \sum_{\substack{i,i'=1 \\ i'>i}}^{N} \frac{1}{|\vec{r}_i - \vec{r}_{i'}|} - \sum_{i=1}^{N} \sum_{j=1}^{n} \frac{Z_j}{|\vec{r}_i - \vec{R}_j|} . \tag{5}$$

Finally, the Schrödinger equation is obtained

$$H\Psi(\vec{x}_1, \vec{x}_2, ..., \vec{x}_N) = E\Psi(\vec{x}_1, \vec{x}_2, ..., \vec{x}_N) \tag{6}$$

with the many-body wave function $\Psi(\vec{x}_1, \vec{x}_2, ..., \vec{x}_N)$ where $\vec{x}$ represents the spatial coordinate $\vec{r}$ and the spin s.

An analytical solution is possible only in few exceptional cases, such as the hydrogen atom. Remember that even the classical 3-body problem can, in general, not be solved exactly. Consequently, from the time quantum mechanics was introduced, also methods to tackle the many-body problem have been developed.

3   Quantum chemical approach

The target is the description of real materials, without employing parameters from the experiment. Quantum chemistry started with the description of atoms and molecules, and meanwhile has been extended to systems with periodicity such as 3D (bulk), 2D (surfaces), or 1D (e.g. nanotubes).

Originally, the notion quantum chemistry was restricted to wave function based methods. The first step is the description of a system with a single Slater determinant, the Hartree-Fock approach. In the next step, based on the Hartree-Fock wave function, more than one Slater determinant is considered, by post-Hartree-Fock methods (correlation methods). There has been an enormous development in this area, and is still ongoing, to perform high-level calculations for demanding systems. The strength is that these calculations are mathematically well defined, and can be systematically improved.

Hartree-Fock   improved correlation   full CI
                      treatment: CI(SD), ...

minimal
basis set

improved   typical
basis set   calculation

complete   Hartree-Fock   exact
basis set   limit   solution
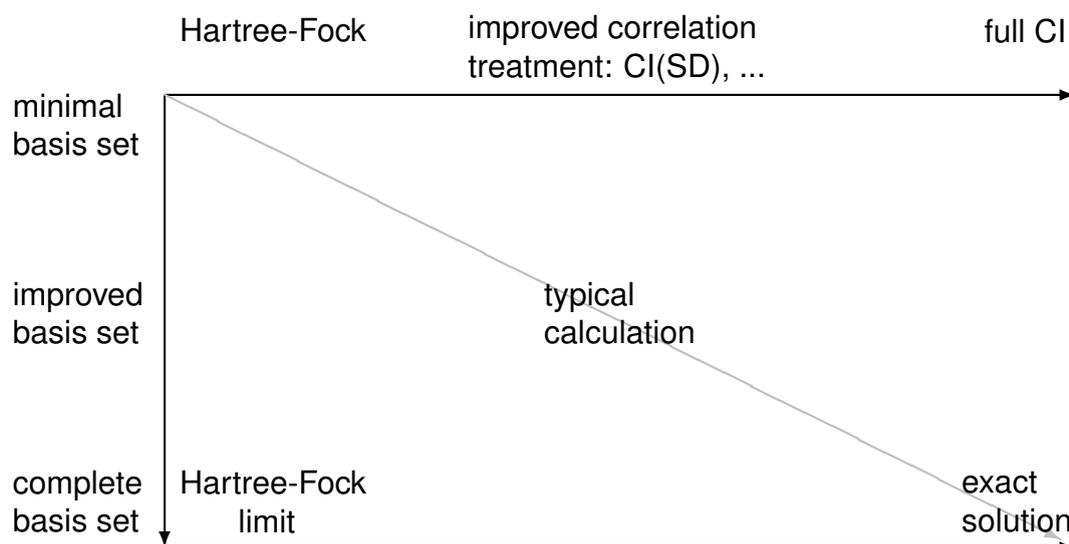
Fig. 2: *Hierarchies of methods and computational parameters (basis set).*

Closely related is density functional theory, which has become the main tool for electronic struc-
ture calculations. It is based on the Hohenberg-Kohn theorem [7] that an (unknown) functional
should describe a system in its ground state. In this book chapter, this method will however be
only marginally described, as there are other contributions in the present autumn school, or also
in last year's edition [8]. Nevertheless, there are close connections also concerning implemen-
tation issues (Hartree-Fock versus density functional theory in the Kohn-Sham formulation), so
that density functional theory will be addressed in this chapter.

Finally, there are further methods which will not be discussed here, such as quantum Monte
Carlo. Also, semiempirical methods, methods based on force fields, or combinations of quan-
tum mechanical methods with molecular mechanics (QM/MM) will not be included.

A hierarchy of methods can be constructed with increasing accuracy, but usually also increasing
computational demand. Besides the approximation due to the method employed, it is also usu-
ally necessary to make an approximation concerning the computational parameters. In quantum
chemistry, the main parameter set are the basis functions which are used to express the wave
function and the orbitals. This leads to a second hierarchy concerning the choice of the basis
set. The situation is visualized in figure 2: The basic method is Hartree-Fock, followed by
methods such as configuration interaction (CI) with singles and doubles substitution, CI(SD),
up to full configuration interaction as the maximum for a given basis set. On the basis set side,
the smallest possible basis set has one basis function per orbital (minimal basis set), up to high-
level basis sets which have multiple basis functions at least for the valence orbitals, and also
span a large range of angular momenta.

Besides, there are further parameters such as the way integrals are computed, approximated, or
possibly even discarded if they are below a certain threshold. If a numerical integration is done,
then the grid size plays an important role. In calculations for periodic systems, there are further
parameters such as the number of points in the reciprocal lattice.

4   Hartree-Fock

In the following, we assume, for simplicity, that the Hamiltonian is spin-independent. A single electron is described by a spin orbital $\chi(\vec{x}) = \psi(\vec{r})\alpha(s)$, with a spatial part ψ and a spin part α. The spatial orbitals are assumed to be orthonormal, as well as the spin parts. The integration is performed over $d\vec{x}$ which consists of an integral over space d^3r and over spin. The latter gives 1 if both spins are the same (both up, both down), and 0 if the spins are different (one up, the other down). The wave function is then expressed as a Slater determinant

$$\Psi_{HF}(\vec{x}_1, ..., \vec{x}_N) = \frac{1}{\sqrt{N!}}
\begin{vmatrix}
\chi_1(\vec{x}_1) & \chi_2(\vec{x}_1) & \cdots & \chi_N(\vec{x}_1) \\
\chi_1(\vec{x}_2) & \chi_2(\vec{x}_2) & \cdots & \chi_N(\vec{x}_2) \\
\vdots & \vdots & \ddots & \vdots \\
\chi_1(\vec{x}_N) & \chi_2(\vec{x}_N) & \cdots & \chi_N(\vec{x}_N)
\end{vmatrix} \tag{7}$$

This is evaluated as a determinant with the corresponding rules for the sign. Note that electrons are fermions, and thus the wave function is supposed to change sign when two electrons are exchanged. This way, the Pauli principle is included: if there were two electrons in the same spin orbital (e.g. $\chi_1 = \chi_2$), then there would be two identical columns and the wave function would be identical to zero.

The total energy, on the Hartree-Fock level, is then obtained as the expectation value of the Hamiltonian

$$E_{total,\ HF} = \langle \Psi_{HF} | H | \Psi_{HF} \rangle . \tag{8}$$

As Ψ_{HF} is normalized, this expectation value is an upper bound of the total energy, as guaranteed by the variational principle.

4.1   Hartree-Fock equations

The Hartree-Fock energy has to be minimized by varying the spin orbitals χ_i, under the condition that they must remain orthonormal

$$\langle \chi_i | \chi_j \rangle = \delta_{ij} . \tag{9}$$

This is important to guarantee the normalization of the Slater determinant. We may take this condition into account with the help of Lagrange multipliers, ε_{ba}, so that we obtain

$$L = E_{total,\ HF} - \sum_{a,b=1}^{N} \varepsilon_{ba} \Big(\langle \chi_a | \chi_b \rangle - \delta_{ab} \Big). \tag{10}$$

We will in the following assume the simplest case of closed-shell restricted Hartree-Fock. Restricted means that spatial orbitals for up- and down-spin are the same, reflecting the symmetry of the spin-independent Hamiltonian. Closed-shell means that each spatial orbital is either occupied with two electrons of opposing spin, or is empty.

The Hartree-Fock energy is obtained in terms of the spin orbitals as [1]

$$
\begin{aligned}
E_{total,\,HF} = E_{NN} &+ \sum_{a=1}^{N} \int \chi_a^*(\vec{x})\big(H_{\text{kin}}+H_{\text{el-nuc}}\big)\chi_a(\vec{x})\,d\vec{x} \\
&+ \frac{1}{2}\sum_{a,b=1}^{N} \iint \frac{\chi_a{}^*(\vec{x}_1)\chi_a(\vec{x}_1)\chi_b^*(\vec{x}_2)\chi_b(\vec{x}_2)}{|\vec{r}_1-\vec{r}_2|}\,d\vec{x}_1 d\vec{x}_2 \\
&- \frac{1}{2}\sum_{a,b=1}^{N} \iint \frac{\chi_a{}^*(\vec{x}_1)\chi_b(\vec{x}_1)\chi_b^*(\vec{x}_2)\chi_a(\vec{x}_2)}{|\vec{r}_1-\vec{r}_2|}\,d\vec{x}_1 d\vec{x}_2\,.
\end{aligned}
\tag{11}
$$

Besides the nuclear-nuclear repulsion, kinetic energy and electron-nuclear attraction, we have the Coulomb repulsion between the electrons. The last term is due to the antisymmetry of the wave function, and is called the exchange term. The Coulomb term is similar to the Coulomb interaction in classical electrodynamics. There is however no classical analogue for the exchange term, and it is thus a quantum mechanical effect.

Equation (11) is the energy expression for a single Slater determinant. A better, but also more demanding approach would be to include more than one Slater determinant, see section 7. They include effects beyond Hartree-Fock, i.e, correlation effects. These correlations reflect the fact that the electrons are not independent, but instead the probability to find an electron at a certain position depends on the positions of the other electrons.

The variation δL of (10) is obtained by varying the spin orbitals

$$
\chi \to \chi + \delta\chi\,.
\tag{12}
$$

This results for $\delta E_{total,\,HF}$ in

$$
\big(H_{\text{kin}}+H_{\text{el-nuc}}\big)\chi_a(\vec{x}_1) + \sum_{b\neq a}^{N} \int \frac{\chi_b^*(\vec{x}_2)\chi_b(\vec{x}_2)}{|\vec{r}_1-\vec{r}_2|}\,d\vec{x}_2\,\chi_a(\vec{x}_1) - \sum_{b\neq a}^{N} \int \frac{\chi_b^*(\vec{x}_2)\chi_a(\vec{x}_2)}{|\vec{r}_1-\vec{r}_2|}\,d\vec{x}_2\,\chi_b(\vec{x}_1).
\tag{13}
$$

With the local (i.e. defined at a point $\vec{r}_1$) Coulomb potential

$$
J_b(\vec{x}_1) = \int \frac{\chi_b^*(\vec{x}_2)\chi_b(\vec{x}_2)}{|\vec{r}_1-\vec{r}_2|}d\vec{x}_2
\tag{14}
$$

and the non-local exchange potential (non-local meaning that it cannot be written as a potential at some local point $\vec{r}_1$)

$$
K_b(\vec{x}_1)\chi_a(\vec{x}_1) = \int \frac{\chi_b^*(\vec{x}_2)\chi_a(\vec{x}_2)}{|\vec{r}_1-\vec{r}_2|}\,d\vec{x}_2\,\chi_b(\vec{x}_1)
\tag{15}
$$

we finally obtain the Hartree-Fock equations

$$
\big(H_{\text{kin}}+H_{\text{el-nuc}}\big)\chi_a(x_1) + \sum_{b\neq a}^{N} J_b(\vec{x}_1)\chi_a(\vec{x}_1) - \sum_{b\neq a}^{N} K_b(\vec{x}_1)\chi_a(\vec{x}_1) = \varepsilon_a\chi_a(\vec{x}_1).
\tag{16}
$$

Note that ε_{ab} does not appear, but only ε_a. This is due to a unitary transformation of the orbitals in such a way that ε_{ab} becomes diagonal and is replaced by ε_a. These orbitals are called canonical orbitals. They may be transformed to other orbital sets with the same Hartree-Fock energy. In fact, any unitary transformation among the occupied orbitals leaves the Slater determinant unchanged. Such a different choice may be more convenient, for example localized orbitals for correlation calculations.

A shorthand notation of the Hartree-Fock equations is

$$f(\vec{x}_1)\chi_a(\vec{x}_1) = \varepsilon_a(\vec{x}_1)\chi_a(\vec{x}_1). \tag{17}$$

Here we have introduced the Fock operator f. It acts on a spin orbital, but also depends on the other spin orbitals. This equation is thus not simply an eigenvalue equation, but an integro-differential equation. The Hartree-Fock equations can normally only be solved numerically.

4.2   Finite basis set: Hartree-Fock-Roothaan

The Hartree-Fock equations are usually solved by employing a finite basis set. The spatial orbitals are expressed with the help of a set of K basis functions $\phi_\nu(\vec{r})$

$$\psi_i(\vec{r}) = \sum_{\nu=1}^{K} c_{\nu i}\, \phi_\nu(\vec{r}). \tag{18}$$

After integrating with $\int d^3r\, \phi_\mu^*(\vec{r})$, we obtain the Fock matrix

$$F_{\mu\nu} = \int \phi_\mu^*(\vec{r})f(\vec{r})\phi_\nu(\vec{r})\, d^3r \tag{19}$$

and the overlap matrix

$$S_{\mu\nu} = \int \phi_\mu^*(\vec{r})\phi_\nu(\vec{r})\, d^3r\,. \tag{20}$$

The Hartree-Fock equations (17) with a finite basis set thus may be written in matrix form

$$\sum_{\nu=1}^{K} F_{\mu\nu}c_{\nu i} = \varepsilon_i \sum_{\nu=1}^{K} S_{\mu\nu}c_{\nu i} \tag{21}$$

The coefficients $c_{\nu i}$ and the eigenvalues ε_i have to be determined by solving this generalized eigenvalue problem. An analogous procedure may be performed for periodic systems. The equation then additionally depends on the reciprocal lattice vectors $\vec{k}$

$$\sum_{\nu=1}^{K} F_{\mu\nu}(\vec{k})c_{\nu i}(\vec{k}) = \varepsilon_i(\vec{k}) \sum_{\nu=1}^{K} S_{\mu\nu}(\vec{k})c_{\nu i}(\vec{k}) \tag{22}$$

and the eigenvalues $\varepsilon_i(\vec{k})$ are interpreted as the band structure.

Specify molecule / periodic system => Schrödinger equation

Initial guess for $c_{\mu\nu} \Rightarrow \Psi_{guess}(\vec{x}_1, \vec{x}_2, \vec{x}_3, ..., \vec{x}_N)$

set up Hartree-Fock-Roothaan equations: $\sum_{\nu=1}^{K} F_{\mu\nu} c_{\nu i} = \epsilon_i \sum_{\nu=1}^{K} S_{\mu\nu} c_{\nu i}$

solve equations, obtain new $c_{\mu\nu}$, compute total energy

Insert new $c_{\mu\nu}$ as guess in Hartree-Fock-Roothaan equations: new $\Psi_{guess}(\vec{x}_1, \vec{x}_2, \vec{x}_3, ..., \vec{x}_N)$

Repeat until $\psi_{new\,guess} = \psi_{previous\,guess}$ or energy difference between iterations below threshold

Converged: self consistent field solution

Fig. 3: *The self-consistent field procedure.*

4.3   Solution of the Hartree-Fock equations

Even after introducing a finite basis set, the Hartree-Fock equations (21) and (22) cannot be solved analytically. Instead, an iterative procedure is performed as displayed in figure 3.

After specifying the geometry and setting up the Schrödinger equation, the computational parameters are defined (basis set and other parameters). It may be advantageous to compute integrals (matrix elements of the various one and two-electron operators) beforehand and store them on disk. After this, an initial guess for the unknown coefficients $c_{\mu\nu}$ is made. The Fock matrix is constructed based on the initial guess (remember that the Fock matrix $F_{\mu\nu}$ depends on the $c_{\mu\nu}$). The Hartree-Fock-Roothaan equations are solved, and new coefficients $c_{\mu\nu}$ are obtained, together with the orbital eigenvalues ε_i. The new solution is used to set up the Fock operator once again, and the procedure is repeated. This is iteratively done until the energy difference between two iterations is below a threshold, or the change of the coefficients $c_{\mu\nu}$ is below a threshold (self-consistency).

The procedure works reasonably well for molecules with large gaps between highest occupied (HOMO) and lowest unoccupied molecular orbital (LUMO). Near-degeneracies, on the other hand, usually cause convergence problems. These convergence problems may be addressed by mixing the previous guess with a certain weight (Fock matrix mixing), or more sophisticated methods such as the direct inversion in the iterative subspace (DIIS) [9]. Also, level shifting is often used, e.g., in the case of transition metals. Here, the orbital eigenvalues of the unoccupied orbitals are shifted by a certain value to help finding the right occupancy; in spin-polarized systems, a different level shift is chosen for up and down spins.

5 Density functional theory

Density functional theory was initially mainly applied in solid state physics, but has meanwhile gained more and more importance in molecular electronic structure theory.

It is based on the Hohenberg-Kohn theorem [7], which shows that the energy can be written as a functional of the electron density $\rho(\vec{r})$

$$E_{total} = E[\rho] = E_{nn} + E_{kin}[\rho] + E_{ee}[\rho] + E_{ne}[\rho] \tag{23}$$

with contributions from the nuclear-nuclear repulsion E_{nn}, the kinetic energy of the electrons E_{kin}, the electron-electron repulsion E_{ee} and the attraction of the electrons by the nuclei, E_{ne}, as an external potential.

The important finding was that two external potentials which differ by more than a constant will result in different ground-state densities [7]. There is thus a one-to-one correspondence between the external potential and the electron density of the corresponding ground state. The variational principle states that the exact density minimizes E_{total}. However, the exact functional is unknown.

Kohn and Sham [10] then suggested to express the exact density as that of non-interacting electrons

$$\rho(\vec{r}) = \sum_{i=1}^{N} |\chi_i(\vec{r})|^2. \tag{24}$$

This corresponds to the density obtained from a reference system described by a single Slater determinant constructed from the N orbitals χ_i. We assume again, for simplicity, the case without explicit spin-dependence (i.e. closed-shell, restricted DFT), and use the notation $\chi(\vec{r})$ for the spin orbitals.

The kinetic energy is then obtained as

$$E_{kin} = -\frac{1}{2} \sum_{i=1}^{N} \int \chi_i(\vec{r}) \Delta \chi_i(\vec{r}) \, d^3r. \tag{25}$$

This is the expression for a non-interacting system, and would not be the correct one for an interacting system which, in general, has to be described by more than one Slater determinant. However, we have the correct density. As there is a one-to-one correspondence between the density and the potential, we still have the correct potential, though the kinetic energy expression alone is incorrect. The error is fixed by adding the difference between the correct kinetic energy and that of the non-interacting system into the term which describes the electron-electron interaction.

The nuclear-electron attraction is obtained simply as

$$E_{ne}[\rho] = -\sum_{j=1}^{n} \int \frac{Z_j \, \rho(\vec{r})}{|\vec{r} - \vec{R}_j|} \, d^3r \tag{26}$$

while the electron-electron interaction is finally expressed as

$$E_{ee}[\rho] = E_H[\rho] + E_{XC}[\rho] \tag{27}$$

with the electron-electron Coulomb interaction (Hartree energy)

$$E_H = \frac{1}{2} \iint \frac{\rho(\vec{r})\rho(\vec{r}\,')}{|\vec{r}-\vec{r}\,'|}\, d^3r d^3r'. \tag{28}$$

The unknown term for the exchange and correlation energy (which, as mentioned above, also includes the correction for the kinetic energy) is thus $E_{XC}[\rho]$.

As the exact density minimizes the energy, the density is obtained by a variation. Because the density is expressed with the help of the spin orbitals $\chi(\vec{r})$, the procedure is similar to Hartree-Fock theory. In the end, the Kohn-Sham equations are obtained

$$\left(-\frac{1}{2}\Delta + V_{eff}(\vec{r})\right)\chi_i(\vec{r}) = \varepsilon_i\,\chi_i(\vec{r}) \tag{29}$$

with the effective potential

$$V_{eff}(\vec{r}) = -\sum_{j=1}^{n} \frac{Z_j}{|\vec{r}-\vec{R}_j|} + \int \frac{\rho(\vec{r}\,')}{|\vec{r}-\vec{r}\,'|}\, d^3r' + \frac{\delta E_{XC}[\rho]}{\delta\rho}\,. \tag{30}$$

The unknown part is thus the exchange-correlation functional E_{XC}. Numerous functionals have been suggested, and the number of functionals is still growing enormously.

Note the similarity between the Kohn-Sham equations in equation (29) and the Hartree-Fock equations in equation (17). This has also practical implications: a code which solves the Hartree-Fock equations can usually be modified to perform also density functional calculations. The reverse, i.e., going from a density functional code to a Hartree-Fock code, is significantly more difficult, as the exact Fock exchange (15), which is non-local, has to be implemented.

Nowadays, most calculations are performed on the density functional level, and pure Hartree-Fock is rarely used. Due to the unknown exchange-correlation functional, an error is introduced. The order of magnitude of this error may be estimated by comparing different functionals and thus obtaining a band width of results. Particularly sensitive properties are band gaps or excitation energies which are difficult to describe in density functional theory. Functionals such as the local density approximation or gradient corrected functionals tend to underestimate gaps, whereas Hartree-Fock tends to overestimate. Though there are hybrid functionals with an admixture of Fock exchange and which often give surprisingly good values for band gaps, one still has to keep in mind that these functionals have to be calibrated and are not as systematic as wave function based correlation.

The major importance of Hartree-Fock theory is nowadays that it serves as a starting point for correlation calculations which will be discussed in Sec. 7.

6   Basis sets

As the Hartree-Fock (or Kohn-Sham) equations can, in general, not be solved analytically, the molecular (or crystalline) orbitals are instead expanded in basis functions. For a recent

overview, see [11]. In molecular quantum chemistry, local basis sets are preferably used. They can be applied to periodic systems as well – one just has to construct Bloch functions. Alternatively, plane waves are often used as basis functions in solid state applications. Here, the crystalline orbitals are expressed as

$$\Phi(\vec{r}, \vec{k}) = \sum_{\vec{K}} c_{\vec{k}, \vec{K}} \, \exp\left(-\mathrm{i}(\vec{k}+\vec{K})\vec{r}\right) \tag{31}$$

where the sum over reciprocal lattice vectors $\vec{K}$ is truncated according to the condition

$$\frac{\hbar^2}{2m_{el}}(\vec{k}+\vec{K})^2 \leq E_{\text{cutoff}} \tag{32}$$

with a cutoff energy E_{cutoff}.

In the following, the focus will be on local basis sets. An obvious starting point would be to use properties of the functions which are solutions of the hydrogen atom. Thus, basis functions of the following form have been suggested

$$\phi(\vec{r}-\vec{A}) = N(x-A_x)^a(y-A_y)^b(z-A_z)^c \exp\left(-\zeta|\vec{r}-\vec{A}|\right), \tag{33}$$

where $\vec{A}$ is the position of the nucleus, and a, b, c are integers. Exponents are traditionally labeled with ζ. These functions are called Slater functions or Slater type orbitals. The factor $\exp(-\zeta|\vec{r}-\vec{A}|)$ has the shape of the exact solution of the hydrogen atom. Most importantly, when approaching the positions of the nuclei, Slater functions may satisfy the cusp conditions (see below) which is a major advantage. However, they suffer from the drawback that integrals are difficult to evaluate.

Gaussian basis functions

Instead, Gaussian basis functions have become very popular, as integrals are easier to be evaluated. Their structure is

$$\phi_{\text{primitive}}(\vec{r}-\vec{A}) = N(x-A_x)^a(y-A_y)^b(z-A_z)^c \exp\left(-\zeta(\vec{r}-\vec{A})^2\right) \tag{34}$$

They have various shortcomings such as that their derivative exists at the position nucleus, whereas this is in general not the case for the exact solution: Instead, a cusp condition should be fulfilled at the nucleus [2]

$$\lim_{r \to 0} \left(\frac{\partial \Psi}{\partial r}\right)_{\text{ave}} = -Z\,\Psi(r{=}0) \tag{35}$$

where ave means the spherical average, and this holds if $\Psi(r=0) \neq 0$. Similarly, the electronic cusp condition

$$\lim_{r_{12} \to 0} \left(\frac{\partial \Psi}{\partial r_{12}}\right)_{\text{ave}} = \frac{1}{2}\,\Psi(r_{12}{=}0) \tag{36}$$

with $r_{12} = |\vec{r}_1-\vec{r}_2|$ is not fulfilled.

Gaussian basis functions
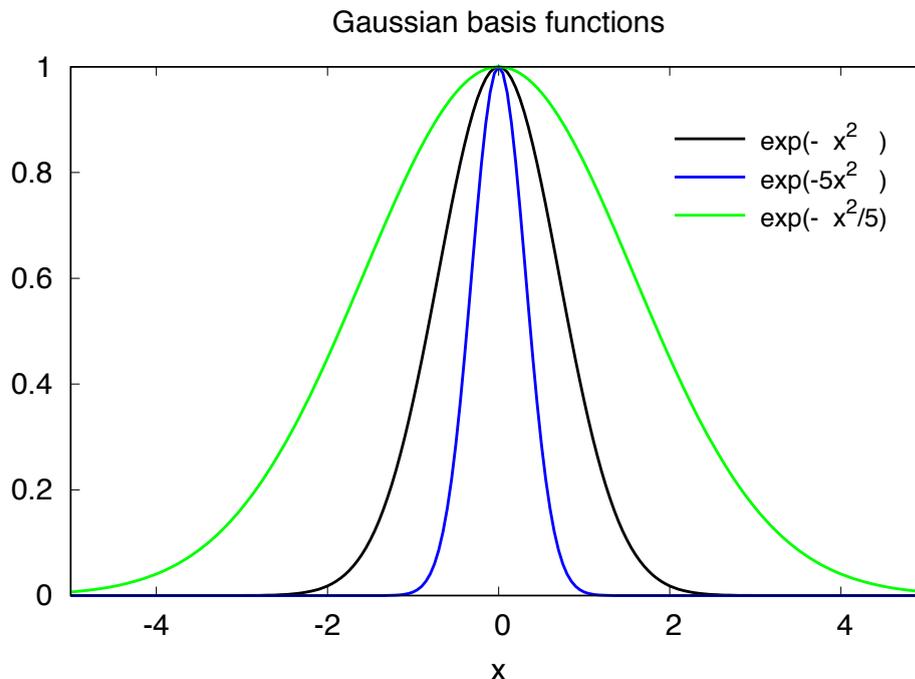
Fig. 4: *Visualization of Gaussians: tight (blue, mainly relevant for the core region); diffuse (green, important for the region of the chemical bond).*

Despite these formal disadvantages of Gaussians, they have become dominant in the field of molecular quantum chemistry.

The value of the exponent ζ determines whether the Gaussian function is called tight (roughly those with $\zeta \gg 1$) or diffuse (roughly: $\zeta \ll 1$ in atomic units). Tight functions are more relevant to describe the core region, whereas diffuse functions are more relevant for the chemical bond (see figure 4).

For efficiency reasons, several primitive Gaussians may be combined into a contracted Gaussian with fixed contraction coefficients d_i

$$\phi(\vec{r}-\vec{A}) = N\,(x-A_x)^a(y-A_y)^b(z-A_z)^c \sum_{i=1}^{L} d_i \, \exp\left(-\zeta_i(\vec{r}-\vec{A})^2\right) \tag{37}$$

This is usually done for tight exponents: if the contraction coefficients d_i were allowed to be optimized, then they would not change very much from system to system, as the tight functions mainly describe the core region close to the cusp at the nuclear position. It is thus more efficient to optimize the contraction coefficients d_i once for a given atom, and then keep them fixed. The molecular orbitals are then expanded as shown in equation (18).

In a similar way, crystalline orbitals for periodic systems may be obtained. First, basis functions are constructed which satisfy the Bloch condition for electrons in a periodic potential

$$\Phi_\mu(\vec{r},\vec{k}) = \sum_{\vec{g}} \phi_\mu(\vec{r}-\vec{A}_\mu-\vec{g}) \exp(\mathrm{i}\vec{k}\vec{g}) \tag{38}$$

where the summation is over the direct lattice vectors $\vec{g}$, and the basis functions now depend on the reciprocal lattice vector $\vec{k}$. Analogous to molecular orbitals, equation (18), crystalline

orbitals are expressed as

$$\Psi_i(\vec{r}, \vec{k}) = \sum_\nu c_{\nu i}(\vec{k})\, \Phi_\nu(\vec{r}, \vec{k}). \tag{39}$$

Angular part

The angular part is obtained by multiplying a spherical harmonic $Y_{lm}(\vartheta, \varphi)$ with a factor the r^l which leads to the solid harmonics

$$r^l\, Y_{lm}(\vartheta, \varphi) \tag{40}$$

which are the solutions of the Laplace equation $\nabla^2 \phi(\vec{r}) = 0$ that are regular at the origin, being (orthogonal) polynomials in the coordinates x, y, and z of degree l..

The solid harmonics are in general complex. However, only in the case of atoms and linear molecules, L_z is a good quantum number. Therefore, real solid harmonics are usually used [2] by taking the real or imaginary part of the complex solid harmonics, mixing quantum numbers m and $-m$, as this reduces the computational effort.

Examples are (normalization is ignored):

$$
\begin{aligned}
l = 0: \qquad & Y_{00} && \Rightarrow\ \sim 1 \\[1em]
l = 1: \quad & r(Y_{11}-Y_{1-1}) && \Rightarrow\ \sim x \\
& r(Y_{11}+Y_{1-1}) && \Rightarrow\ \sim y \\
& rY_{10} && \Rightarrow\ \sim z \\[1em]
l = 2: \qquad & r^2 Y_{20} && \Rightarrow\ \sim 3z^2-r^2 = 2z^2-x^2-y^2 \\
& r^2(Y_{21}-Y_{2-1}) && \Rightarrow\ \sim xz \\
& r^2(Y_{21}+Y_{2-1}) && \Rightarrow\ \sim yz \\
& r^2(Y_{22}+Y_{2-2}) && \Rightarrow\ \sim x^2-y^2 \\
& r^2(Y_{22}-Y_{2-2}) && \Rightarrow\ \sim xy
\end{aligned}
\tag{41}
$$

Some codes work with the five d functions as listed in equation (41), whereas others work with six Cartesian d functions $(x^2, y^2, z^2, xy, xz, yz)$. The latter choice seems at first glance in contradiction to quantum mechanics as there are only five d functions. This can however be explained as there is a combination $x^2+y^2+z^2$ which is s-like and corresponds to a function $r^2 \exp(-\zeta r^2)$. The choice of six d functions thus leads to a larger basis set and usually a lower energy compared to the case of five d function. Some codes offer the option to switch between five and six d functions (and correspondingly seven or ten f functions).

The order in which the functions are implemented depends on the code. It is important to know this order for population analyses or projected densities of states; or to understand occupancies of orbitals, e.g., in the presence of crystal field splitting.

Choice of basis sets

Even tempered basis sets

A simple yet good choice for the basis set is to use even tempered exponents [12]. A set of exponents ζ is obtained according to the formula

$$\zeta_k = \alpha\beta^k \tag{42}$$

with the parameters α and β to be optimized, $k = 1, ..., M$. This has been done in [12] for the atoms in the first three periods. It turned out that β should be in he range from $2...4$.

Databases

For molecular calculations, large databases exist, especially (web addresses last accessed on June 7, 2021):

- the basis set database of the Environmental Molecular Sciences Laboratory (EMSL) employing the basis set exchange software [13, 14] at
  `www.basissetexchange.org`

- the basis set library of the Molpro [15] code at
  `www.molpro.net/info/basis.php?portal=user&choice=Basis+library`

- for periodic systems, the basis set library of the CRYSTAL [16] code at
  `www.crystal.unito.it/basis-sets.php`

Some notions: double zeta and similar, polarization functions

The smallest possible choice would be a minimal basis set (see section 3) which is, however, a poor choice. It lacks flexibility when, e.g., a chemical bond is formed. Such basis sets are rarely chosen. An exception may be embedding, when some atoms far away from the interesting region need to be described in a very efficient way.

A better choice would be to have two basis functions per orbitals, which is called a double-zeta basis set. This may be further extended to triple-, quadruple-, ... zeta basis sets.

As the inner orbitals change less when a molecular bond is formed so that they can be well described by a contracted Gaussian, a standard choice is to use more basis functions which mainly describe the valence shell. Normally, at least two basis functions for the valence shells should be used, which corresponds to a valence double zeta basis set.

When a free atom gets exposed to an electric field, or when a second atom is introduced and a chemical bond is formed, then the electronic charge distribution will not be radially symmetric any more. To be able to describe this, polarization functions are necessary. For example, for a hydrogen atom in its ground state, s-functions would be sufficient. To describe polarization, at least p-functions are required. This is visualized in figure 5.

A valence double-zeta plus polarization function basis may already be a good starting point for Hartree-Fock or DFT calculations. For wave function based correlation, it is important
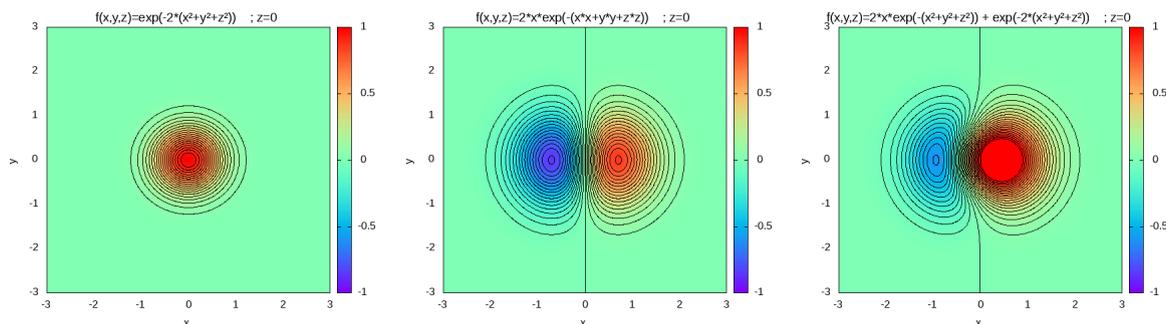
Fig. 5: *An s function, which is always spherically symmetric (left); a p function in order to polarize the charge distribution (middle); and the two function added together, e.g. in response to an electric field (right).*

that excitations to unoccupied orbitals can be described. This requires in general much larger basis sets, with higher angular momenta and extra diffuse functions. A hierarchy of correlation-consistent basis sets has been developed and is continuously extended [17].

Recommendations

Various issues have to be considered when choosing the basis set:

- The basis set depends on the charge state of the atom. Negative ions have a larger radius than positive ions and thus require diffuse exponents (e.g. oxygen usually needs extra diffuse functions).

- Wave function based correlation calculations need (significantly) larger basis sets compared to Hartree-Fock of DFT calculations.

- Polarisation functions should usually be included.

- Different properties may require enlarged basis sets, e.g., higher angular momenta when polarizabilities are computed, or extra tight functions for properties near or at the nucleus.

- Diffuse exponents are important for the describing chemical bonds.

- Effective core potentials may be advantageous from the first row of transition metals on.

To test a basis set, one may compare selected properties (total energy, band structure, equilibrium geometry) with an enhanced basis set. The Mulliken population is computationally practically without cost, and may thus always be computed; it gives the occupancies of the individual basis functions and thus a possibility to judge the importance of the various functions.

An enormous variety of basis sets has been generated, and the names are not systematic. A way of characterizing the basis set is to count the number of uncontracted and contracted basis functions, and then label the basis with a name such as

$$(10s4p)/[3s2p] \tag{43}$$

While this is not unambiguous, it gives an idea of the size and quality of the basis set.

7 Beyond Hartree-Fock: electron correlation

Up to now, the wave function based methods were restricted to using a single Slater determinant, i.e., the Hartree-Fock level. This however lacks electron correlation [18]: on the Hartree-Fock level, only the averaged position of the other electrons is considered; whereas the electrons interact with each other according to the actual position of the other electrons.

To describe this, more than one Slater determinant is required. Due to the variational principle, this will lower the energy: compared to the energy at the Hartree-Fock level, an additional contribution is obtained, the correlation energy. The correlation energy is only a small fraction of the total energy, and the computed energy thus changes by only a small amount. Nevertheless, the correlation energy is important to obtain correct values for energy differences, which affects, e.g., the binding energy, electron affinities, ionization potentials. In solids, the band gap depends strongly on electron correlation: band gaps on the Hartree-Fock level are usually largely overestimated, because, e.g., screening is not properly taken into account. As the correlation energy depends on the geometry, it will thus influence the equilibrium geometry.

Another fundamental problem of Hartree-Fock theory is that it gives a vanishing density of states for metals [19].

Despite these problems of the Hartree-Fock approach, it is nevertheless of enormous importance, for several reasons: it is a mathematically clear theory, without unknown parameters. Moreover, it can be systematically improved. Systematic and controlled approaches usually start from the Hartree-Fock level, and with these post-Hartree-Fock methods, high accuracy is achieved.

7.1 Second Quantization

To describe excitations from a Slater determinant, it is more convenient to use second quantization. Here, excitations are described with creation and annihilation operators. Instead of a Slater determinant

$$\Psi_{HF}(\vec{x}_1,...,\vec{x}_N) = \frac{1}{\sqrt{N!}} \begin{vmatrix} \chi_1(\vec{x}_1) & \cdots & \chi_i(\vec{x}_1) & \cdots & \chi_N(\vec{x}_1) \\ \chi_1(\vec{x}_2) & \cdots & \chi_i(\vec{x}_2) & \cdots & \chi_N(\vec{x}_2) \\ \vdots & & \vdots & & \vdots \\ \chi_1(\vec{x}_N) & \cdots & \chi_i(\vec{x}_N) & \cdots & \chi_N(\vec{x}_N) \end{vmatrix} \tag{44}$$

we write

$$|\Psi_{HF}\rangle = a_1^\dagger \cdots a_i^\dagger \cdots a_N^\dagger |0\rangle.$$

$a_i^\dagger$ and a_i are creation and annihilation operators for an electron in a molecular orbital i, with the anti-commutation relations

$$\{a_i^\dagger, a_j\} = a_i^\dagger a_j + a_j a_i^\dagger = \delta_{ij} \quad \text{and} \qquad \{a_i^\dagger, a_j^\dagger\} = \{a_i, a_j\} = 0$$

A determinant of an excited state, with electron excited from orbital i into orbital a

$$\Psi_i^a(\vec{x}_1, ..., \vec{x}_N) = \frac{1}{\sqrt{N!}} \begin{vmatrix} \chi_1(\vec{x}_1) & \cdots & \chi_a(\vec{x}_1) & \cdots & \chi_N(\vec{x}_1) \\ \chi_1(\vec{x}_2) & \cdots & \chi_a(\vec{x}_2) & \cdots & \chi_N(\vec{x}_2) \\ \vdots & & \vdots & & \vdots \\ \chi_1(\vec{x}_N) & \cdots & \chi_a(\vec{x}_N) & \cdots & \chi_N(\vec{x}_N) \end{vmatrix} \tag{45}$$

can then be conveniently written in second quantization as

$$|\Psi_i^a\rangle = a_a^\dagger a_i |\Psi_{HF}\rangle.$$

Similarly, a two-fold excited state

$$\Psi_{ij}^{ab}(\vec{x}_1, ..., \vec{x}_N) = \frac{1}{\sqrt{N!}} \begin{vmatrix} \chi_1(\vec{x}_1) & \cdots & \chi_a(\vec{x}_1) & \cdots & \chi_b(\vec{x}_1) & \cdots & \chi_N(\vec{x}_1) \\ \chi_1(\vec{x}_2) & \cdots & \chi_a(\vec{x}_2) & \cdots & \chi_b(\vec{x}_2) & \cdots & \chi_N(\vec{x}_2) \\ \vdots & & \vdots & & \vdots & & \vdots \\ \chi_1(\vec{x}_N) & \cdots & \chi_a(\vec{x}_N) & \cdots & \chi_b(\vec{x}_N) & \cdots & \chi_N(\vec{x}_N) \end{vmatrix} \tag{46}$$

becomes

$$|\Psi_{ij}^{ab}\rangle = a_b^\dagger a_a^\dagger a_i a_j |\Psi_{HF}\rangle.$$

Operators must have the same matrix elements in first and second quantization. This leads (see, e.g. [2]) to the mappings

$$H = H_1 + H_2 + H_{nn}$$

with the one-electron part of the Hamiltonian in second quantization being given by

$$H_1 = \sum_{pq} \langle \chi_p | h | \chi_q \rangle \, a_p^\dagger a_q$$

and the corresponding expression for the two-electron part

$$H_2 = \frac{1}{2} \sum_{pqrs} \left\langle \chi_p \chi_q \middle| \frac{1}{r_{12}} \middle| \chi_r \chi_s \right\rangle a_p^\dagger a_q^\dagger a_s a_r$$

where the sums over p, q, r, s run over all spin orbitals, while the nuclear-nuclear repulsion H_{nn} is, of course, just a number, determined by the positions of the nuclei and their charges.

7.2 Wave function based correlation

Full configuration interaction

A wave function based approach to include correlation can now be expressed by adding all possible excited determinants, which corresponds to full configuration interaction (full CI),

$$\Psi_{\text{full CI}} = \left(1 + \sum_{\substack{a \\ i}} t_a^i \, a_a^\dagger a_i + \sum_{\substack{a<b \\ i<j}} t_{ab}^{ij} \, a_b^\dagger a_a^\dagger a_i a_j + \sum_{\substack{a<b<c \\ i<j<k}} t_{abc}^{ijk} \, a_c^\dagger a_b^\dagger a_a^\dagger a_i a_j a_k + ... \right) |\Psi_{HF}\rangle = \sum_I c_I |\Psi_I\rangle.$$

The energy is obtained as

$$E_{\text{full CI}} = \frac{\langle \Psi_{\text{full CI}}|H|\Psi_{\text{full CI}}\rangle}{\langle \Psi_{\text{full CI}}|\Psi_{\text{full CI}}\rangle}.$$

This is normalized, variational, and size-consistent (see below). However, the computational effort is enormous, as a huge matrix has to be diagonalized in the end: From

$$H|\Psi_{\text{full CI}}\rangle = E|\Psi_{\text{full CI}}\rangle$$

it follows that for all Ψ_I, it must hold

$$\langle \Psi_I|H - E_{\text{full CI}}|\Psi_{\text{full CI}}\rangle = 0$$

This is an eigenvalue problem. The lowest eigenvalue corresponds to the ground state energy, and the higher eigenvalues correspond to energies of excited states. Due to the finite basis set, the energies are upper bounds of the exact eigen-energies of the corresponding Hamiltonian: $E_n^{\text{exact}} \leq E_n^{\text{full CI}}$.

A general strategy in a CI calculation is to keep the low lying orbitals, the core orbitals, doubly occupied. This reduces the number of determinants without a great loss in accuracy.

Configuration interaction with single and double substitutions: CI(SD)

As full configuration interaction is usually too demanding, a restriction to wave functions with single and double substitutions is made instead

$$|\Psi_{\text{CI(SD)}}\rangle = \left(1 + \sum_{\substack{a \\ i}} t_a^i\, a_a^\dagger a_i + \sum_{\substack{a<b \\ i<j}} t_{ab}^{ij}\, a_b^\dagger a_a^\dagger a_i a_j \right)|\Psi_{HF}\rangle$$

and the energy is obtained as the expectation value

$$E_{\text{CI(SD)}} = \frac{\langle \Psi_{\text{CI(SD)}}|H|\Psi_{\text{CI(SD)}}\rangle}{\langle \Psi_{\text{CI(SD)}}|\Psi_{\text{CI(SD)}}\rangle}.$$

This is again normalized and variational, but it is not size-consistent, as illustrated in figure 6: When the energy of two helium atoms at a very large distance is computed, then it should be the sum of the energy of the individual atoms. In two separate CI(SD) calculations for the atoms, all excitations are considered. In a single CI(SD) calculation for the supersystem of both atoms, not all excitations are considered: states where 3 or 4 electrons are excited are not considered. The sum of the energy of two separate CI(SD) calculations will thus be lower than the energy of a single CI(SD) calculation for the whole system. Thus, CI(SD) suffers from the size-consistency problem. The argument obviously holds for any truncated CI method, which only includes a finite number of excitations.

Besides, there are pathological cases such as H_2 described by a restricted closed shell wave function. When the hydrogen atoms are pulled apart, this wave function does not allow the molecule to properly dissociate. In this case, Hartree-Fock is not size-consistent. We will, however, in the following, exclude these cases when discussing size-consistency.
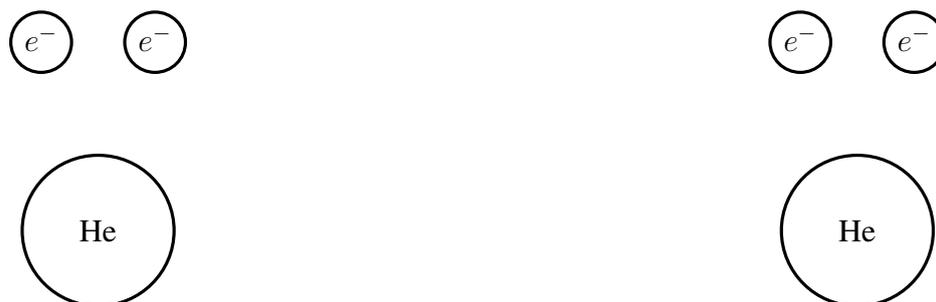
Fig. 6: *Two helium atoms at a large distance, to illustrate the size-consistency problem.*

Coupled cluster

Because of the size-consistency problem, CI(SD) is not a popular method. Instead, coupled cluster methods based on an exponential ansatz are nowadays preferred

$$|\Psi_{CCSD}\rangle = \exp\left(\sum_{\substack{a \\ i}} t_a^i\, a_a^\dagger a_i + \sum_{\substack{a<b \\ i<j}} t_{ab}^{ij}\, a_b^\dagger a_a^\dagger a_i a_j \right)|\Psi_{HF}\rangle = \exp(T)|\Psi_{HF}\rangle$$

The above ansatz is labeled CCSD, coupled cluster with single and double substitutions. Since the exponential ensures that arbitrary powers of single and double substitutions are included, the approach is size consistent.

In coupled cluster methods, intermediate normalization is used: $\langle \Psi_{HF}|\Psi_{CCSD}\rangle = 1$. From $H|\Psi_{CCSD}\rangle = E|\Psi_{CCSD}\rangle$, the energy and the coefficients (amplitudes) t_a^i, t_{ab}^{ij} are obtained

$$\langle \Psi_{HF}|H{-}E|\Psi_{CCSD}\rangle = 0$$
$$\langle \Psi_i^a\ |H{-}E|\Psi_{CCSD}\rangle = 0$$
$$\langle \Psi_{ij}^{ab}\ |H{-}E|\Psi_{CCSD}\rangle = 0\,.$$

The obtained coupled cluster energy is, however, not variational.

Møller-Plesset Perturbation theory, 2nd order: MP2

Perturbation theory is one of the methods frequently used to approximately solve the Schrödinger equation. It decomposes the full Hamiltonian H into an unperturbed part H_0 and the remaining part H_1. Subsequently, the wave function and eigenvalues are expanded in a power series of a coupling parameter λ.

In MP2, the unperturbed Hamiltonian is chosen to be the Fock operator

$$H = H_0 + H_1 = \sum_{i=1}^{N} f(i) = \sum_{i=1}^{N} \big(h(i){+}v_{HF}(i)\big)$$

where $h(i)$ is the one-electron part, i.e., kinetic energy and nuclear attraction. The 0th order wave function is thus the Hartree-Fock Slater determinant, equation (7). The 0th order energy

is just the sum of the eigenvalues

$$E_0 = \sum_{i=1}^{N} \varepsilon_i.$$

The first order energy is obtained as the expectation value of the perturbation H_1

$$E_1 = \langle \Psi_0 | H_1 | \Psi_0 \rangle = \langle \Psi_0 | H - H_0 | \Psi_0 \rangle = E_{HF} - E_0 \,.$$

The sum of zeroth and first order energies is thus just the Hartree-Fock energy

$$E_0 + E_1 = E_{HF} \,.$$

The perturbation can be written as

$$H_1 = \sum_{\substack{i,j=1 \\ i<j}}^{N} \frac{1}{r_{ij}} - \sum_{i=1}^{N} v_{HF}(i)$$

The second order correction is obtained as

$$E_{MP2} = -\sum_{a<b}\sum_{k<l} \frac{\iint d^3 r_1 d^3 r_2 \left(\frac{\chi_a^*(\vec{r}_1)\chi_k(\vec{r}_1)\chi_b^*(\vec{r}_2)\chi_l(\vec{r}_2) - \chi_a^*(\vec{r}_1)\chi_l(\vec{r}_1)\chi_b^*(\vec{r}_2)\chi_k(\vec{r}_2)}{|\vec{r}_1 - \vec{r}_2|} \right)^2}{\varepsilon_a + \varepsilon_b - \varepsilon_k - \varepsilon_l}$$

where a and b refer to unoccupied orbitals, k and l to occupied ones.
MP2 is size-consistent, but not variational. Compared to CI(SD) or CCSD, MP2 is computationally cheap.

7.2.1 Multi-configuration SCF (MCSCF)

In the case of (near-)degeneracies or low-lying excited states (usually occurring in strongly correlated systems), multi-configuration self-consistent field calculations may be a remedy. Here, a set of Slater determinants is used instead of just one

$$|\Psi_{MCSCF}\rangle = \sum_I C_I |\Psi_I\rangle.$$

The Slater determinants are from an active space

$$|\Psi_I\rangle \in \left\{ c_0 |\Psi_{HF}\rangle \,,\; c_a^k |\Psi_k^a\rangle \,,\; c_{ab}^{kl} |\Psi_{kl}^{ab}\rangle \,,\; c_{abc}^{klm} |\Psi_{klm}^{abc}\rangle, ... \right\} \,.$$

The coefficients c and some of the orbitals are optimized.
The active space and which orbitals are optimized is left to the user of the code, but determine the computational effort. MCSCF is good to treat static correlation effects, where static correlation means correlation due to (near-)degeneracies.
Electron correlation due to the Coulomb repulsion is in contrast called dynamical correlation. To describe dynamical correlation, excitations to many virtual orbitals are necessary, which is better done with configuration interaction.

Besides systems with low-lying excited states, MCSCF can also be used in the aforementioned case of the dissociation of H_2. With an MCSCF ansatz, two hydrogen atoms at large distance can be well described, and size-consistency achieved. Another example is the proper description of oxygen in its ground state: the p-occupancy is $2p^4$. A single Slater determinant with, e.g., an occupancy of $p_x^2 \, p_y \, p_z$ would break the spherical symmetry. Such a wave function is not an eigenstate of L^2. To restore symmetry, a state-averaged calculation with 3 determinants $(p_x^2 \, p_y \, p_z, \, p_x \, p_y^2 \, p_z, \, p_x \, p_y \, p_z^2)$ is performed in MCSCF.

MCSCF alone does usually not recover a large fraction of the correlation energy, as this would require an enormous active space. It is, however, able to provide better starting orbitals for a subsequent CI calculation.

Multi-reference configuration interaction (MRCI)

A powerful tool in these situations is to follow a multi-configuration self-consistent field calculation with a configuration interaction calculation, which is multi-reference CI

$$|\Psi_{MRCI(SD)}\rangle = \left(1 + \sum_{ai} t_a^i \, a_a^\dagger a_i + \sum_{abij} t_{ab}^{ij} \, a_b^\dagger a_a^\dagger a_i a_j \right) |\Psi_{MCSCF}\rangle$$

where the coefficients t are optimized.

Explicit correlation: F12

To take the electronic cusp condition (equation (36)) into account, explicit correlation has been introduced by multiplying the wave function with a factor such as

$$\left(1 - \frac{1}{\gamma} \exp\left(-\gamma|\vec{r}_1 - \vec{r}_2|\right)\right)$$

This makes accurate calculations possible which would otherwise require very large basis sets. This is similar to Jastrow factors in quantum Monte Carlo. Explicit correlation was pioneered by Hylleraas [20] in his treatment of the He atom, where he introduced an ansatz for the wavefunction depending on the distance $|\vec{r}_1 - \vec{r}_2|$.

Local correlation schemes

Local correlation methods have become popular, to reduce the computational effort, and make schemes such as coupled cluster available for extended systems. One variant is based on pair natural orbitals [21]. Also, the treatment of correlation in periodic systems has been targeted with local methods, e.g., the incremental scheme [22, 23].

8   Properties

After computing the total energy, calculating other properties is particularly interesting, as usually a comparison with the experiment can be made. The global minimum of the total energy as

a function of geometrical parameters gives the equilibrium geometry. Here, the first derivative of the energy with respect to nuclear positions is of great use. At the global minimum, second derivatives with respect to nuclear positions give the vibrational spectrum. Further derivatives are extremely useful, e.g., infrared intensities may be expressed as second derivatives, one derivative with respect to nuclear positions and one with respect to an external electric field, or Raman intensities as third derivatives, one derivative with respect to nuclear positions and two with respect to an external electric field.

As a whole, measurable properties may be expressed as derivatives with respect to electric field $\vec{F}$, magnetic field $\vec{B}$, nuclear magnetic moment $\vec{I}$, electron magnetic moment $\vec{s}$, or nuclear position $\vec{R}$, in such a way (see also the overview given in [3])

$$\frac{\partial^{n_F+n_B+n_I+n_s+n_R} E}{\partial \vec{F}^{n_F} \partial \vec{B}^{n_B} \partial \vec{I}^{n_I} \partial \vec{s}^{n_s} \partial \vec{R}^{n_R}} \, .$$

These derivatives may be obtained analytically or numerically. Analytical gradients are often difficult to implement; however, once they are available, they are advantageous, as they are faster and have less numerical noise.

9   Examples

Oxygen electron affinity

A challenging example is the calculation of the electron affinity of oxygen shown in table 1. High-level correlation calculations with extended basis sets are required to achieve good agreement with the experiment. Including triples perturbatively (marked with (T)) is important to get close to the experimental value.

Note that on the Hartree-Fock level, even the sign is wrong. Importantly, the orbital eigenvalues of the occupied orbitals are negative which makes the calculation meaningful. This is in general not the case for density functional calculations: many functionals suffer from the drawback that the eigenvalues of occupied orbitals may be positive when an atom is negatively charged [24, 25]. Negative ions would be instable in such a case of positive orbital eigenvalues.

A similar comparison (various properties such as geometries, atomization energies, reaction enthalpies) for a set of molecules can be found in [2].

Table 1: *Computed (with Molpro [15] and MCHF [26]) electron affinity of oxygen (in eV). The experimental value is 1.461 eV.*

| basis set	method					
	HF	CI(SD)	CCSD	CCSD(T)	CCSD-F12	CCSD(T)-F12
aug-cc-pvdz	–0.493	0.941	1.086	1.188	1.294	1.394
aug-cc-pvtz	–0.525	1.016	1.185	1.335	1.299	1.445
aug-cc-pvqz-f12	–0.534	1.068	1.245	1.410	1.303	1.465
aug-cc-pv5z-f12	–0.535	1.084	1.264	1.431	1.298	1.464
numerical (MCHF)	–0.535					
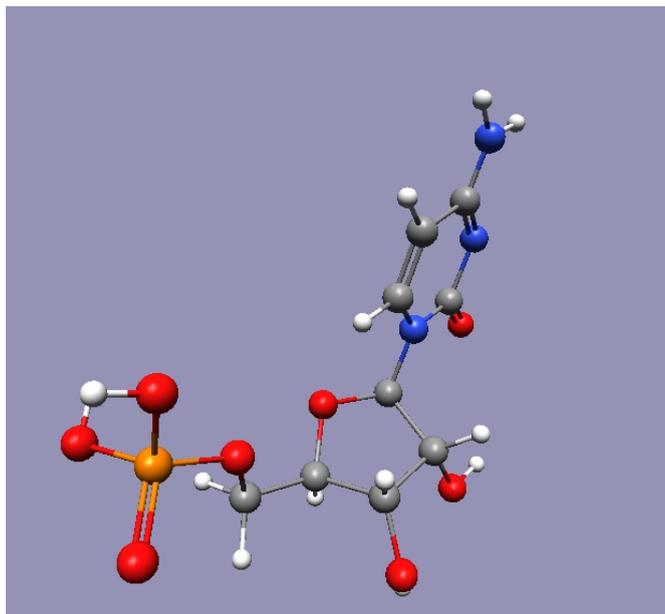
Fig. 7: *The molecule cytidine monophosphate; 35 atoms, 835 basis functions, PNO-LCCSD(T).*

Local correlation calculation

An example of today's state of the art is shown in figure 7. The molecule cytidine monophosphate (35 atoms, 168 electrons in total, 118 electrons correlated) is calculated at the level of PNO-LCCSD(T), with a cc-pV(T+d)Z basis set (835 contractions). PNO-LCCSD(T) means that pair natural orbitals are used for the correlation calculation, which is local coupled cluster (singles, doubles are fully, and triples perturbatively taken into account). The energy calculation with Molpro [15] takes about 174 minutes on 12 cores. For comparison, a traditional CCSD calculation would not be feasible, or require enormous CPU time.

Superexchange calculation

In the field of strong correlation, the *ab initio* calculation of magnetic coupling parameters is a challenging task. NiO is a prototype example. Here, two next-nearest neighboring Ni atoms couple antiferromagnetically via an oxygen atom (figure 8).
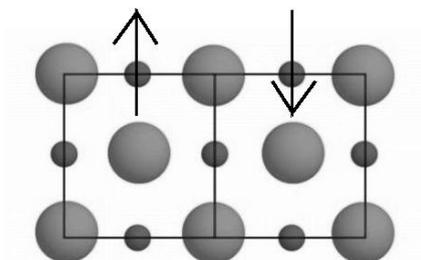
Fig. 8: *NiO: two nickel spins are marked with arrows. They couple antiferromagnetically via the oxygen atom in between.*
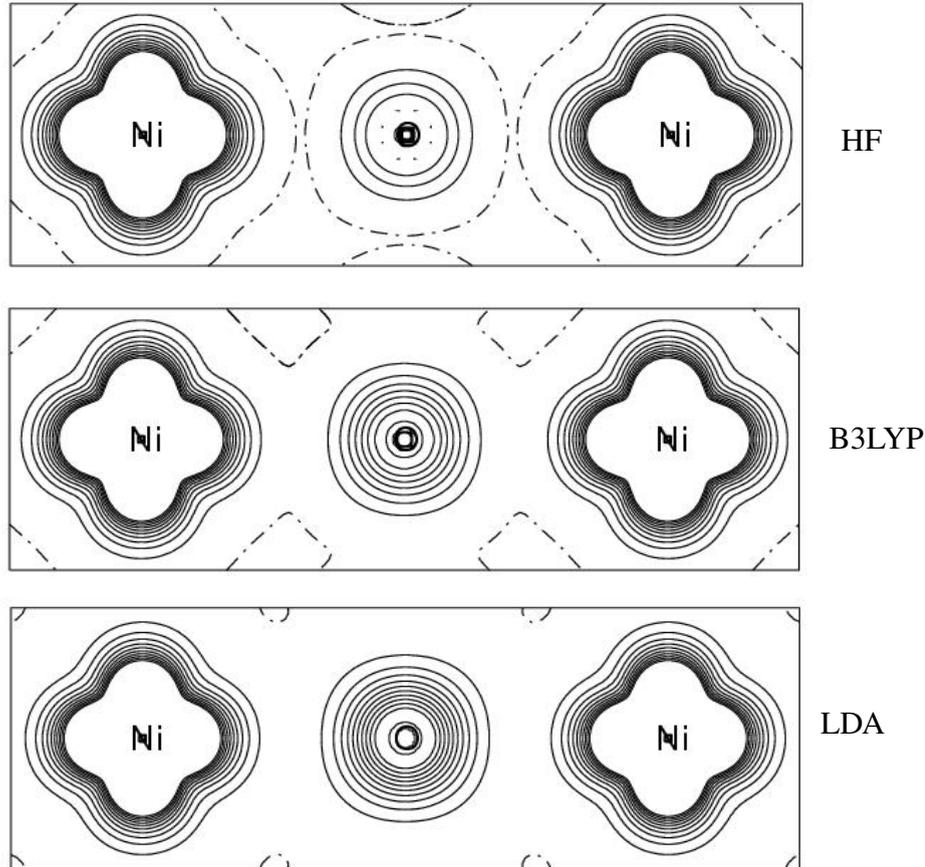
Fig. 9: *NiO: spin densities in the ferromagnetic state, at the level of Hartree-Fock (top), B3LYP (middle), LDA (bottom). The same values of the contour lines are used in the three plots.*

Exchange couplings may be computed by calculating the energies of the ferromagnetic state and the antiferromagnetic state, and then fitting to a model Hamiltonian such as the Ising or Heisenberg model. The energy difference ΔE will then be proportional to the number of neighbors z (i.e. the number of couplings), the spins on the two sites (S_1, S_2), and the exchange coupling J, here $\Delta E \sim zJS^2$ for the Ising model. This can be compared with experimental values for the Néel temperature.

Spin densities at the level of Hartree-Fock, the local density approximation (LDA), and the hybrid functional B3LYP are shown in figure 9. To emphasize the differences, the spin densities are shown for the ferromagnetic state.

Hartree-Fock theory leads to a rather localized spin density which is shown at the top of figure 9. The computed Ni magnetic moment is about $1.9\,\mu_{\rm B}$. LDA shows a much more delocalized spin density, with a Ni magnetic moment of $1.6\,\mu_{\rm B}$. The hybrid functional B3LYP which has admixtures of Hartree-Fock and LDA is somewhere in between, with $1.8\,\mu_{\rm B}$.

Due to the more delocalized spin density in B3LYP, and even more so in LDA, exchange couplings are much larger in magnitude. The computed superexchange value ranges from –5.4 meV (Hartree-Fock) and –29 meV (B3LYP) to –94 meV (LDA). This is thus an example where Hartree-Fock severely deviates due to the lack of correlation, and density functional theory produces results varying over a very wide range.
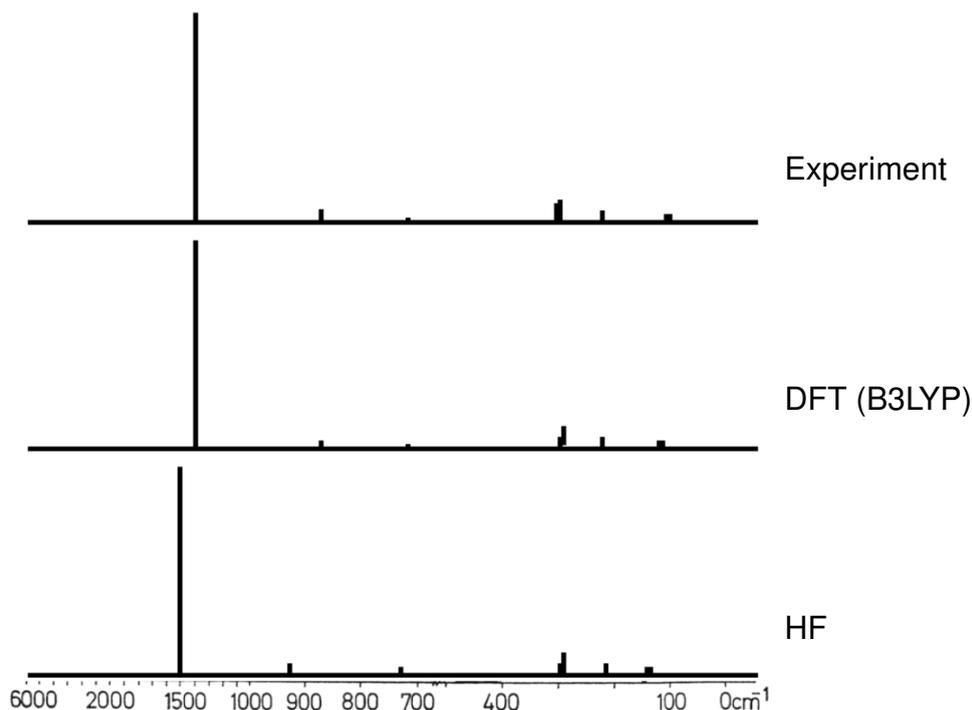
Fig. 10: *The infrared spectrum of calcite: experimental (top), DFT with B3LYP (middle), Hartree-Fock (bottom).*

A controlled approach is possible by using a cluster and embedding it, to model the bulk. This way, calculations with molecular codes become feasible, and wave function based methods such as CASPT2 may be used. This gives better agreement with experiment (–20 meV), with CASPT2 values in the range of about from –14 to –17 meV [27, 28].

Vibrational spectroscopy

We finish with another example from the solid state, is displayed in figure 10, computed with CRYSTAL [16]. The infrared spectrum of calcite ($CaCO_3$) [29] matches the experiment [30] excellent at the DFT level, with the hybrid functional B3LYP. At the Hartree-Fock level, the agreement is less good, but still reasonable.

In general, geometries usually agree well with experiment in DFT. Vibrational frequencies deviate a bit more, but are still in good agreement with experiment. Also, IR and Raman intensities usually agree well. As wave function based correlation is not available for IR or Raman spectra of solids, it is state of the art to employ DFT. It is recommended to compare various functionals to have a band width of results. E.g., here and for many other materials, B3LYP works excellent, but there are exceptions such as the narrow band gap insulator FeSi where B3LYP strongly deviates from experiment, and even a simple LDA calculation performs much better. Calculated vibrational spectra have become a powerful tool, and computed IR and Raman spectra are now often used to complement experimental results.

10 Conclusion

Quantum chemical methods have gained enormously in importance in recent years, and their use has become more widespread. This is, on the one hand, due to the growth in computational resources. On the other hand, even traditional methods such as Hartree-Fock have been made significantly more efficient due to approximations in the integral calculation with density fitting. Also, new highly efficient methods to treat wave function based correlation have been introduced.

Programs have become user-friendly so that they may be handled by a broad community. Numerous properties may be computed, which has attracted great interest from experimentalists also, e.g., for infrared, Raman, and NMR spectroscopy. The codes have also grown enormously in size and complexity. Still, wave function based correlation, especially for periodic systems, remains one of the key challenges.

References

[1] A. Szabo and N.S. Ostlund: *Modern Quantum Chemistry* (McGraw-Hill, New York, 1989)

[2] T. Helgaker, P. Jørgensen, J. Olsen: *Molecular Electronic-Structure Theory*
    (Wiley, Chichester, 2000)

[3] F. Jensen: *Introduction to Computational Chemistry* (Wiley, Chichester, 2017)

[4] Christopher J. Cramer: *Essentials of Computational Chemistry: Theories and Models*
    (Wiley, Chichester, 2004)

[5] W.J. Hehre, L. Radom, P.v.R. Schleyer, and J.A. Pople: *Ab initio molecular orbital theory*
    (Wiley, New York, 1986)

[6] W. Kutzelnigg: *Einführung in die Theoretische Chemie* (Wiley-VCH, Weinheim, 2001)

[7] P. Hohenberg, W. Kohn, Phys. Rev. **136**, B 864 (1964)

[8] R. Jones, in: E. Pavarini and E. Koch (Eds.): *Topology, Entanglement, and Strong
    Correlations*, Reihe Modeling and Simulation, Vol. 10 (Forschungszentrum Jülich, 2020)
    http://www.cond-mat.de/events/correl20

[9] P. Pulay, Chem. Phys. Lett. **73**, 393 (1980)

[10] W. Kohn, L.J. Sham, Phys. Rev. **140**, A 1133 (1965)

[11] E. Perlt (Ed.): *Basis Sets in Computational Chemistry*,
     Lecture Notes in Chemistry Vol. 107 (Springer, 2021)

[12] M.W. Schmidt and K. Ruedenberg, J. Chem. Phys. **71**, 3951 (1979)

[13] D. Feller, J. Comp. Chem., **17**, 1571 (1996)

[14] K.L. Schuchardt, B.T. Didier, T. Elsethagen, L. Sun, V. Gurumoorthi, J. Chase, J. Li, and
     T.L. Windus, J. Chem. Inf. Model. **47**, 1045, (2007)

[15] H.-J. Werner, P.J. Knowles, F.R. Manby, J.A. Black, K. Doll, A. Heßelmann, D. Kats,
     A. Köhn, T. Korona, D.A. Kreplin, Q. Ma, T.F. Miller III, A. Mitrushchenkov,
     K.A. Peterson, I. Polyak, G. Rauhut, and M. Sibaev, J. Chem. Phys. **152**, 144107 (2020)

[16] R. Dovesi, V.R. Saunders, C. Roetti, R. Orlando, C.M. Zicovich-Wilson, F. Pascale,
     B. Civalleri, K. Doll, N.M. Harrison, I.J. Bush, Ph. D'Arco, M. Llunell, M. Causà,
     Y. Noël, L. Maschio, A. Erba, M. Rérat, S. Casassa
     CRYSTAL 2017 User's Manual, University of Torino, Torino (2017)

[17] T.H. Dunning, Jr., K.A. Peterson, and D.E. Woon, in: P.v.R. Schleyer (Ed.): *Encyclopedia of Computational Chemistry: Correlation consistent basis sets for molecular calculations* (Wiley, Chichester, 1998)

[18] P. Fulde: *Electron Correlations in Molecules and Solids* (Springer, Berlin, 1993)

[19] N.W. Ashcroft, N.D. Mermin: *Solid State Physics* (Saunders College, Philadelphia, 1976)

[20] E.A. Hylleraas, Z. Phys. **54**, 347 (1929)

[21] H.-J. Werner, C. Köppl, Q. Ma, and M. Schwilk, in: Mark S. Gordon (Ed.): *Fragmentation: Towards Accurate Calculations on Complex Molecular Systems* (Wiley, Chichester, 2017)

[22] H. Stoll, Chem. Phys. Lett. **191**, 548 (1992)

[23] K. Doll, H. Stoll, Phys. Rev. B **56**, 10121 (1997)

[24] H.B. Shore, J.H. Rose, E. Zaremba, Phys. Rev. B **15**, 2858 (1977)

[25] T. Grabo, E.K.U. Gross, Chem. Phys. Lett. **240**, 141 (1995)

[26] C. Froese Fischer, Comput. Phys. Commun. **64**, 369 (1991)

[27] C. de Graaf, R. Broer, and W.C. Nieuwpoort, Chem. Phys. Lett. **271**, 372 (1997)

[28] I. de P.R. Moreira, F. Illas, R.L. Martin, Phys. Rev. B **65**, 155102 (2002)

[29] L. Valenzano, F.J. Torres, K. Doll, F. Pascale, C.M. Zicovich-Wilson and R. Dovesi, Z. Phys. Chem. **220**, 893 (2006)

[30] K.H. Hellwege, W. Lesch, M. Plihal, and G. Schaack, Z. Phys. **232**, 61 (1970)

3 Lies My Teacher Told Me About Density Functional Theory: Seeing Through Them with the Hubbard Dimer

Kieron Burke and John Kozlowski
University of California, Irvine
Irvine, CA, USA

Contents

1   Introduction

Density functional theory (DFT) is an extremely sophisticated approach to many-body problems [1, 2]. It must be among the most used and least understood of all successful theories in physics. Currently, about 50,000 papers each year report results of Kohn-Sham (KS) DFT calculations [3], including room temperature superconductors under high pressure [4], heterogeneous catalysis at metal surfaces and for nanoparticles [5], understanding the interior of Jupiter and exoplanets [6], studying how ocean acidification affects the seabream population [7], and even which water to use when making coffee [8].

But much of modern condensed matter physics involves using model Hamiltonians to study strongly correlated systems, where understanding new phenomena is considered far more important than generating accurate materials-specific properties [9, 10]. In fact, our standard diagrammatic approach (expansions in the strength of the electron-electron coupling) is hard-wired into all our descriptions of such many-body phenomena, be it the fractional quantum Hall effect [11] or the Kondo effect (even when perturbation theory fails, we still think of resummed diagrams) [12].

Because DFT is *logically* subtle, without requiring much mathematical gymnastics (although they are available for those that enjoy them [13]) or skill with summing Feynman diagrams, and because DFT is entirely different from the standard approach, most of what you may have learned is hopelessly confused or simply downright untrue. Hence the title of this article, taken from a popular book on history [14]. For example, any conflation of the KS scheme with traditional mean-field theory is a dire mistake, and should be avoided at all costs.

This chapter is primarily designed to explain essential concepts of DFT to theorists more familiar with standard many-body theory and perhaps more experienced in dealing with strongly correlated systems. It should also prove useful for anyone performing DFT calculations on weakly correlated systems, who might be wondering where things go wrong as correlations grow stronger. Additionally, the Hubbard dimer is a wonderful teaching tool for basic concepts, as so many of its exact results can be derived analytically.

The first use of this material came in a conversation between KB and Duncan Haldane at a meeting sponsored by the US Department of Energy. Duncan asked KB to explain this DFT business, and he suggested the dimer as the minimal relevant model. After 45 minutes of tough argument, Haldane said "That's the first time I've ever really understood this Kohn-Sham scheme. Thanks." Within 2 years, he was awarded a share in a Nobel Prize in physics [15]. While correlation is not causation, Haldane did not win his share until *after* he understood KS-DFT with the aid of this simple model!

However, it is important to note that the benefits of this type of analysis are not solely limited to those working in theoretical physics. In the fields of theoretical chemistry and material science, for instance, where ground-state electronic energies are often required to be extremely accurate [16–18], there has been growing technological interest in the study of both chemically complex and strongly correlated materials [19, 20]. This chapter was partly designed with these fields in mind, serving as a resource for any computational scientist who wishes to better comprehend

the limitations of their computational methods. Throughout this text, there will be various highlighted sections dedicated to examples, exercises, and key concepts to aid the reader in applying what is learned in this study to their own endeavors.

There are now a huge number of diverse introductions to DFT, with many different perspectives. These include a simple tutorial for anyone with knowledge of quantum mechanics [21], a very long online textbook with lots of nasty problems [22], a many-body introduction [23], and even video lectures [24]. But this chapter is specifically aimed at explaining the most essential concepts, and why strongly correlated systems are more challenging in DFT. All the Hubbard material appears in two long review articles, one on the ground state theory [25] and a second on linear-response TDDFT [26]. The Hubbard dimer has been recently used to explore effects in other aspects of DFT, such as magnetic DFT [27], ensemble DFT [28], and thermal DFT [29].

> **Takeaway:** DFT appears deceptively simple to understand. It is much trickier than people realize. This chapter provides a unique explanation of basic ideas using a simple model.

1.1 Background

We work in the non-relativistic non-magnetic Born-Oppenheimer approximation, using Hartree atomic units ($e^2 = \hbar = m_e = 1$). The Hamiltonian for the electrons is simple and known exactly

$$\hat{H} = \hat{T} + \hat{V}_{\text{ee}} + \hat{V}, \tag{1}$$

where $\hat{T}$ is their kinetic energy, $\hat{V}_{\text{ee}}$ is the electron-electron Coulomb repulsion, and $\hat{V}$ is the one-body potential, equal to a sum of Coulomb attractions to the ions in an isolated molecule or solid. We let N be the number of electrons.

A first-principles approach to this problem is to feed a computer a list of nuclear types and positions and, following a recipe, it spits out various properties of the electronic system. In quantum chemistry [30], the recipe is called a model chemistry [31, 32] if both the method (e.g. Hartree-Fock) and the basis set are specified.

We contrast this with traditional approaches in condensed matter [33]. Often a model Hamiltonian is written down, hoping that it describes the dominant physical effects. For most interesting problems, standard approaches to solving this Hamiltonian will fail, i.e., be hopelessly inadequate or require near-infinite computer resources. An inspired approximation may be found that works well enough, and so the underlying physics can be explained. Well enough will usually mean that with good estimates of the model parameters, qualitative and even semi-quantitative agreement is found with key properties of interest.

Each of these are excellent approaches, especially for the purposes they were designed for. Modern DFT calculations of weakly correlated materials (and molecules) are of the first-principles type, and often yield atomic positions within 1-2 hundredths of an Ångstrom and phonon frequencies within 10%, without any materials-specific input, an impossibility with a simple model Hamiltonian. On the other hand, with standard approximations, DFT calculations always

fail whenever a bond such as H_2 is stretched, and correlations become strong [34]. Even simple Mott-Hubbard physics is beyond such methods (and we shall see why in this chapter), or Kondo physics (but see Reference [35]).

But more and more of modern materials research requires the intelligent application of both approaches, and many methods, such as DFT+U [36] or dynamical mean field theory (DMFT) [37–40] are being developed to bridge the gap. Many of the materials of greatest practical interest to energy research (such as for batteries [19] or photovoltaics [20]) include a moderate level of correlation that require a pure DFT approach to be enhanced, by adding vital missing ingredients of the physics.

The US and Britain are friends 'separated by a common language' [41]. This is essentially true of the mass of confusion between traditional many-body theory and DFT. In DFT, we use the same words as in MBT, but giving them different meanings, simply because we enjoy confusing folks.

Finally, we mention an intermediate Hamiltonian between the dazzling complexity of the real physical and chemical world and the beautiful simplicity of the Hubbard model. A great challenge to studying the effects of strong correlation has been the difficulty in producing highly accurate benchmark data. Molecular electronic structure calculations are much simpler than materials calculations, and quantum chemistry has long been able to provide highly accurate answers for many small molecules at or near equilibrium [32], as well as the complete binding energy curves of others [42]. But this is much harder to do for materials. Recent illustrations of this difficulty are the careful bench-marking of model Hamiltonians (such as an 8×8 Hubbard lattice) using highly accurate many-body solvers [43], the amount of computation needed to find an accurate cohesive energy of the benzene crystal [44], and the celebration of merely being able to agree on approximate DFT results with a variety of solid-state codes [45].

To overcome this difficulty, about 10 years ago, a mimic of realistic electronic structure calculations was established [46]. This mimic uses potentials that are defined continuously in space (i.e., not a lattice model) but are one-dimensional. In fact, ultimately, a single exponential was chosen [47], whose details mimic those of the popular soft Coulomb potential. With about 20 grid points per 'atom', standard density-matrix renormalization (DMRG) methods [48, 49] could then rapidly produce extremely accurate ground-state energies and densities for chains of up to about 100 atoms [46]. By living in 1D, not only is DMRG very efficient, but the thermodynamic limit (of the number of atoms going to infinity with fixed interatomic spacing) is also reached much more quickly than in 3D. Moreover, the parameters were chosen so that standard density functional approximations, such as the local density approximation [50], succeeded and failed in ways that were qualitatively similar to those in the real world [51]. We will refer to this 1D laboratory for further demonstration of some of the simple results shown in this chapter.

> **Takeaway:** DFT is ideally suited to produce useful accuracy for ground-state energetics of realistic Hamiltonians. Many-body theory is more often used to produce approximate answers to model Hamiltonians, and often focuses on response properties. Both are useful in their own fields and, increasingly, interesting problems require input from both.
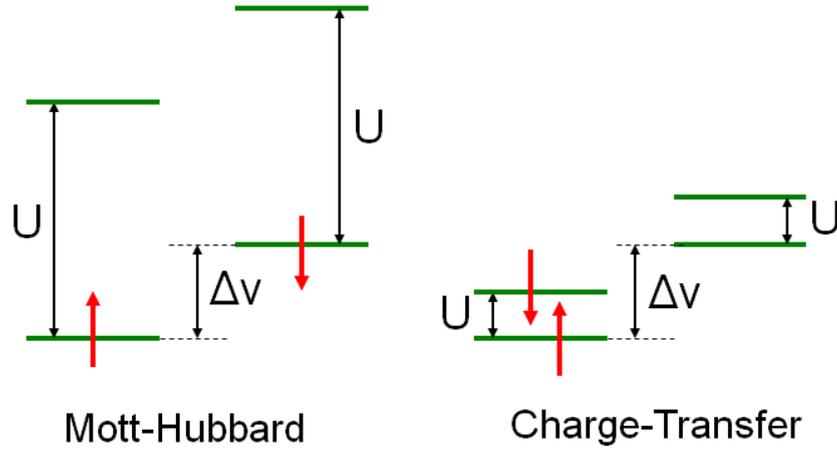
Fig. 1: *Two distinct regimes of the asymmetric Hubbard dimer. On the left, the charging energy is much greater than the difference in on-site potentials, and the left- and right-occupation numbers are similar. On the right, the situation is reversed, and the occupation on the left is much greater than that of the right.*

1.2   Hubbard dimer

The Hubbard model (in 1, 2 or 3D) [52] is the standard model for studying the effects of strong correlation on electrons. By default, it implies an infinite periodic array of sites. For our demonstration, we simply need two sites. We have $N = 2$ and the ground-state is always a singlet. The Hamiltonian (in 2nd quantization) is

$$\hat{H} = -t \sum_{\sigma} \left(\hat{c}_{1\sigma}^{\dagger} \hat{c}_{2\sigma} + h.c. \right) + U \sum_{i} \hat{n}_{i\uparrow} \hat{n}_{i\downarrow} + \sum_{i} v_i \hat{n}_i \,. \tag{2}$$

The kinetic term is just hopping between the sites, and is the discretization of the kinetic operator on the lattice, with the diagonal elements set to 0. The electron-electron repulsion is just an onsite U, while the one-body operator is just an on-site potential, v_1 and v_2.

In this chapter, we imagine a world in which Eq. (1) is replaced by Eq. (2), i.e., as if the many-body problem to be solved is simply that of Eq. (2). So, for us, the Hubbard dimer is *not* an approximation to anything. We will choose the values of U, t, and v_i as we wish, to explore various regimes in the model. Any question concerning the origins of these values in terms of realistic orbitals and matrix elements is irrelevant to our work here.

Since a constant in the potential is just a shift in the energy, we set $v_2 = -v_1$ and use the parameter $\Delta v = v_2 - v_1$ as the sole determinant of the potential of our system. Similarly, with $N = 2$, $n_2 = N - n_1$, and we use $\Delta n = n_2 - n_1$ as the single parameter characterizing the ground-state density. Thus ground-state DFT in this model is simply site-occupation function theory (SOFT) and density functionals are replaced by simple functions of a single variable, Δn. Finally, we choose $t = 1/2$ and report all variables in units of $2t$, as one can scale all energies by a constant. Different physics appears depending on the ratio of U to Δv, i.e., on-site repulsion versus inhomogeneity, see Fig. 1. When $U \gg \Delta v$, the system is strongly correlated, with both site occupations close to 1, despite any inhomogeneity. For $\Delta v \gg U$, the system is weakly correlated, and the on-site U is insufficient to stop one occupation becoming much greater than the other.
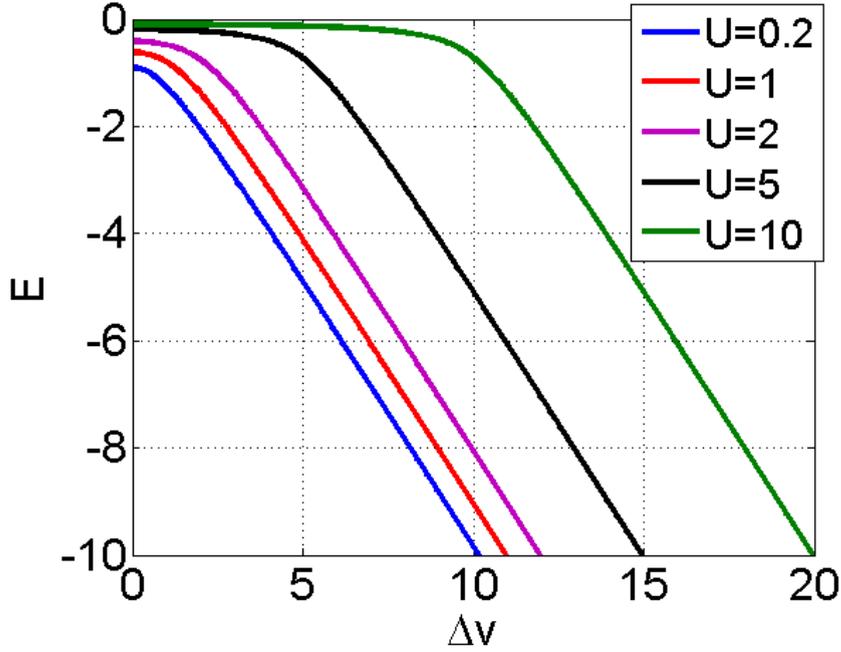
Fig. 2: *Exact ground-state energy of the Hubbard dimer as a function of Δv for several values of U. The qualitative behavior changes as Δv passes through U.*

For those with a chemical inclination, this is a minimal basis model for a diatomic with 2 electrons (with some matrix elements and orbital overlap ignored). For H_2, $\Delta v = 0$, but t decreases as the separation between the nuclei is increased, so that U (in units of $2t$) grows exponentially. The ground-state is close to a single Slater determinant near equilibrium ($U \ll 1$), so that Hartree-Fock (HF) is a reasonable approximation. But $U \gg 1$ when very stretched, so that the ground-state is now a Heitler-London wavefunction, and (restricted) HF is very poor. The highly unsymmetric case corresponds to HeH^+, where both electrons reside on the He side, as long as Δv remains larger than U as the bond is stretched.

There are well-known analytic solutions for all states of the 2-site Hubbard model and the behavior of the ground-state energy [25] is shown in Fig. 2. Simple limits include the symmetric case

$$E = -\sqrt{1 + (U/2)^2} + U/2, \quad \Delta n = 0 \qquad \text{SYM} \qquad (3)$$

An expansion of the square root in the symmetric case in powers of U has a radius of convergence of 2, while the opposite expansion in $1/U$ has a radius of 1/2. Thus there is a well-defined critical point at $U = 2$, below which perturbation in the electron-electron coupling strength converges, i.e., the system is weakly correlated, and above which it is strongly correlated. Another simple limit is the non-interacting (tight-binding) case ($U = 0$)

$$E = -\sqrt{1 + \Delta v^2}, \quad \Delta n = -2\frac{\Delta v}{\sqrt{1 + \Delta v^2}} \qquad (U=0) \qquad (4)$$

which is given by the blue curve in the figure. We see from the figure that, on a broad scale, $E \approx -(\Delta v - U)\,\Theta(\Delta v - U)$. Explicit formulas exist for all the excited-state energies, wavefunctions, and densities also. Approximations in many different limits are given in the many appendices of Reference [25].
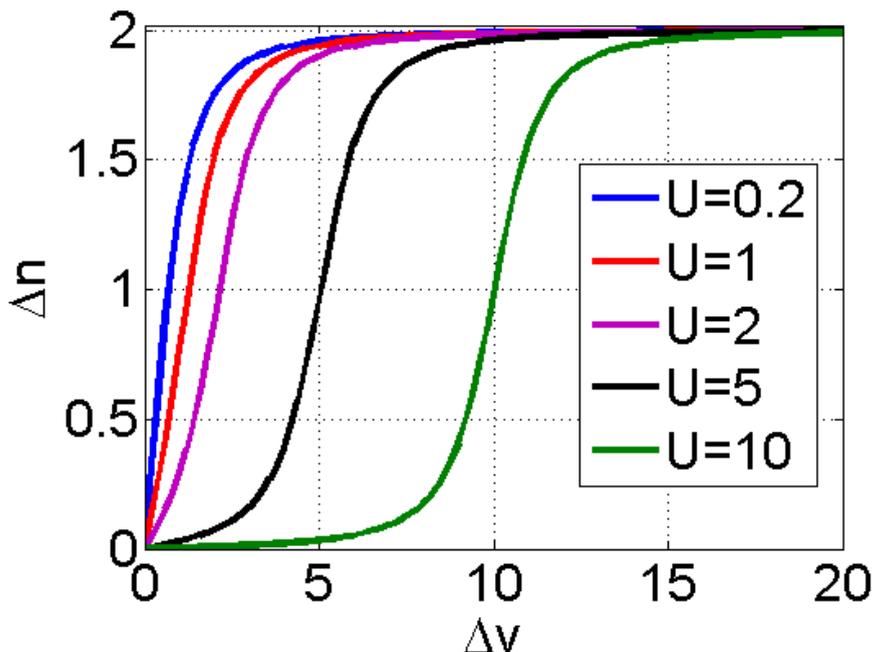
Fig. 3: *Ground-state occupation of the Hubbard dimer as function of Δv for several values of U.*

We can also extract any other property we wish from the analytic solution, such as the one-electron density (here the occupations). Fig. 3 shows the ground-state density as a function of Δv for several values of U. For any U, $n_2 = n_1$ when $\Delta v = 0$. The blue line is essentially the tight-binding solution. In that case, as Δv increases, the occupation difference rapidly increases towards 2. Then, as we turn on U, this increase becomes less and less rapid. By the time U reaches 10, the occupations remain close to balanced until Δv becomes close to 10, when (on the scale of Δv), it rapidly flips to close to 2.

> **Takeaway:** We take the 2-site Hubbard model as our Hamiltonian, and apply DFT concepts directly to it. Here, it is not a simple model for a more realistic Hamiltonian. Analytic solutions are trivial, and we can plot any properties we wish.

2   Density functional theory

We have now defined the machinery required to understand the central theorems of DFT through the lens of the Hubbard dimer. The theorems discussed in this section, like their real-space counterparts, are exact and apply directly to ground-state calculations (we will cover time-dependent DFT later). Most DFT calculations are used to determine the ground-state electronic energy of a system, or more specifically, determine the energy of a system as a function of nuclear coordinates. In this section, we will discuss the underlying principles of these calculations by examining their role at the most fundamental level, in their simplest form.
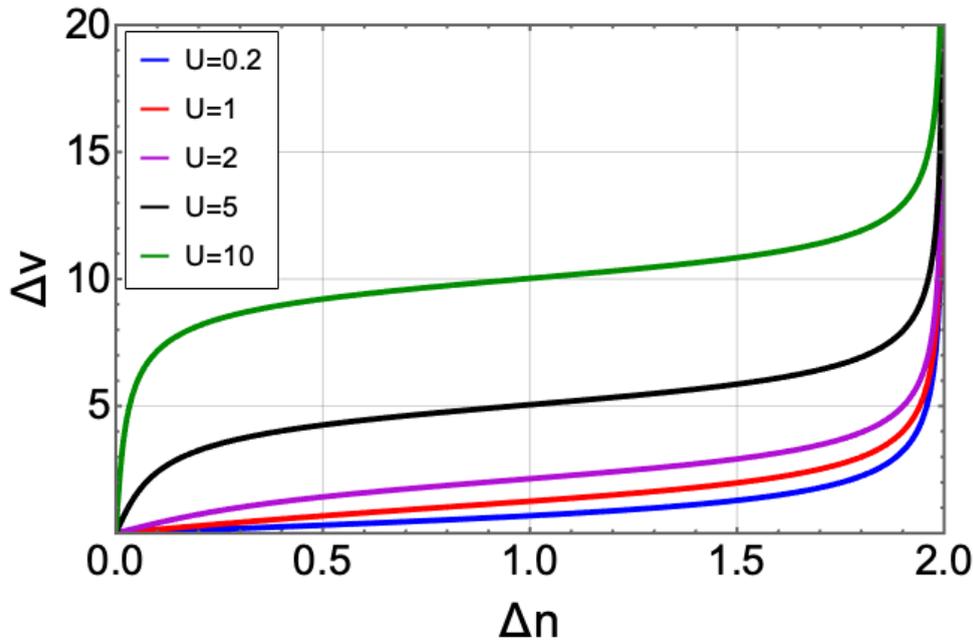
Fig. 4: *Ground-state potential difference as a function of Δn for several values of U.*

The Hohenberg-Kohn theorem [53] is actually three theorems in sequence. These were proved in a simple proof-by-contradiction argument based on the Rayleigh-Ritz variational principle for the wavefunction. Later, the more direct and more general constrained search approach was given by Levy [54] and Lieb [13].

2.1 Hohenberg-Kohn I

HKI proves that the (usual) map of $\Delta v \to \Delta n$ is invertible, i.e., Δn is a single-valued function of Δv for a given U. This is obvious from Fig. 3 (and its inversion, Fig. 4), and in the TB case

$$\Delta v = \frac{\Delta n}{\sqrt{4 - \Delta n^2}} \qquad\qquad (U = 0). \qquad\qquad (5)$$

Fig. 4 is simply Fig. 3 drawn sideways, i.e., with x and y axes reversed. Clearly, for any given value of U, there is a unique Δv.

A much-stated (but often out of context) corollary of this is that *all* properties of the system are (implicitly) functionals of n_1. While this is true, almost all research in DFT focuses on the ground-state energy functional, because it is so useful, and we have few useful approximations for others (e.g., for the first excited-state energy, but see discussion in TDDFT section). Recently, machine learning methods have been trained to find some of these other functionals [55, 56].
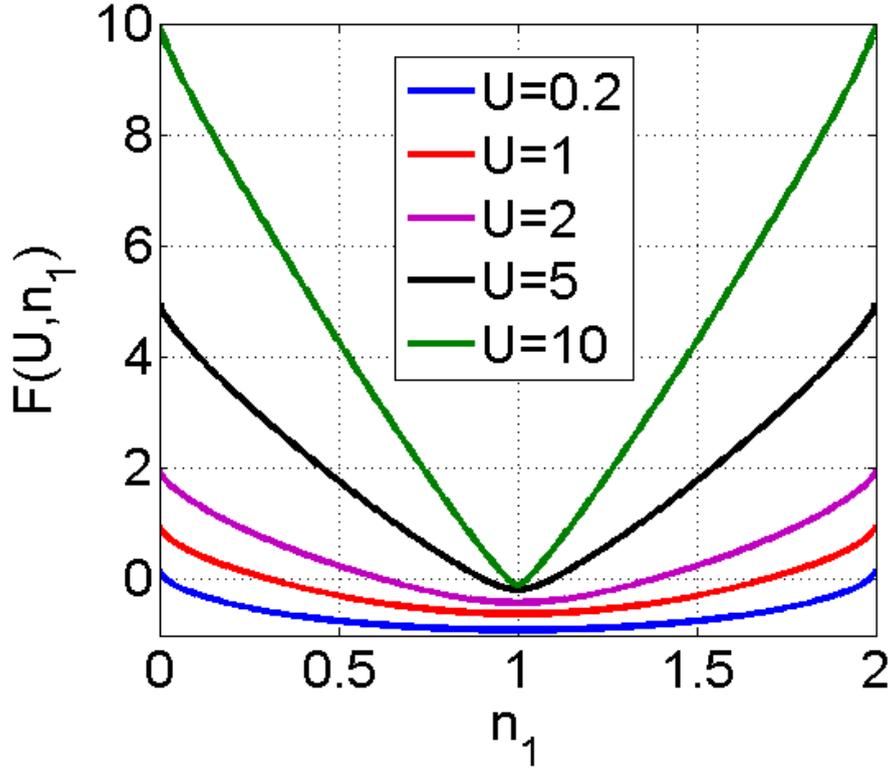
Fig. 5: *Universal part of the energy function(al) of a Hubbard dimer as a function of n_1 for several values of U. As U increases, F tends to $U|1-n_1|$.*

2.2 Hohenberg-Kohn II

HKII states that the function below exists and is independent of Δv:

$$F_{\text{U}}(n_1) = \min_{\Psi \to n_1} \langle \Psi | \hat{T} + \hat{V}_{\text{ee}} | \Psi \rangle = \max_{\Delta v} \left\{ E(\Delta v) - \Delta v \Delta n / 2 \right\}. \tag{6}$$

where the minimum is over all antisymmetrized normalized 2-electron wavefunctions whose occupation of site 1 is n_1. The middle expression is the constrained search definition due to Levy [57]. The rightmost form is due to Lieb [13]. Either definition works here. This F_{U} functional was termed universal by HK, by which they simply meant that it does not depend on the Δv of your given system, i.e., it is a pure density functional. The phrase, often appearing in the literature, that F is a universal functional, is not meaningful.

Although one can write analytic formulas for the ground-state energy for the dimer, there is no explicit analytic formula for F. It is trivial to calculate F numerically and F is shown in the Fig. 5. In the special case of $U = 0$, it is easy,

$$F_{U=0}(n_1) = T_{\text{s}}(n_1) = -\sqrt{n_1(2 - n_1)}. \tag{7}$$

Here we have attached the subscript S to remind us that $U = 0$, so this is the kinetic energy function for a single Slater determinant, and is indistinguishable from the blue line of Fig. 5.

2.3 Hohenberg-Kohn III

HKIII states that there is a variational principle for the ground-state energy directly in terms of the density alone:

$$E(\Delta v) = \min_{n_1} \left\{ F_{\mathrm{U}}(n_1) + \Delta v \Delta n / 2 \right\}. \tag{8}$$

This bypasses all the difficulties of approximating the wavefunction (but of course buries them in the definition of F_{U}). Usually, the minimum can be found from the Euler equation

$$\frac{dF_{\mathrm{U}}(n_1)}{dn_1} - \frac{\Delta v}{2} = 0, \tag{9}$$

and the unique $n_1(\Delta v)$ is the one that satisfies this equation.

This allows us to find a solution to the many-body problem, without ever calculating the wavefunction. Given an expression for $F_{\mathrm{U}}(n_1)$, either exact or approximate, for any value of Δv, one can solve Eq. (9) above to find the corresponding Δv (exact or approximate) and insert into Eq. (8) to find the energy. Any approximation to $F(n_1)$ provides approximate solutions to all many body problems (every value of Δv).

> **Takeaway:** The HK theorems prove the existence of an exact variational principle for the ground-state energy based on the density, not the wavefunction, but give no information on how to approximate it. This is an (almost) useless statement in practice. But to any unbeliever in DFT, one can always tell them (to go look at) F_{U}.

3 Kohn-Sham DFT

The original DFT, called Thomas-Fermi theory [58, 59], tried to approximate $F_{\mathrm{U}}(n_1)$ directly, but such direct approximations have never been accurate enough for most electronic structure calculations. A tremendous step forward occurred when Kohn and Sham considered a fictitious system of non-interacting fermions with the same ground-state density as the true many-body one [60]. In our case, this is just the TB problem, for which we already have explicit solutions. They wrote the F function in terms of quantities that could easily be calculated in such a system:

$$F_{\mathrm{U}}(n_1) = T_{\mathrm{S}}(n_1) + U_{\mathrm{H}}(n_1) + E_{\mathrm{XC}}(n_1). \tag{10}$$

Here, T_{S} is just the TB hopping energy of Eq. (4), and the Hartree energy is just the mean-field electron-electron repulsion

$$U_{\mathrm{H}} = \frac{U}{2} \left(n_1^2 + n_2^2 \right), \tag{11}$$

which is an explicit function of the occupations. Then E_{XC}, the exchange-correlation (XC) energy (about which, much more, later) is simply everything else, i.e., E_{XC} is defined by Eq. (10). It is then trivial to show, from the Euler equation, that the TB potentials that will reproduce the exact occupations are

$$v_{\mathrm{S,i}} = v_i + U n_i + \frac{\partial E_{\mathrm{XC}}}{\partial n_i}. \tag{12}$$
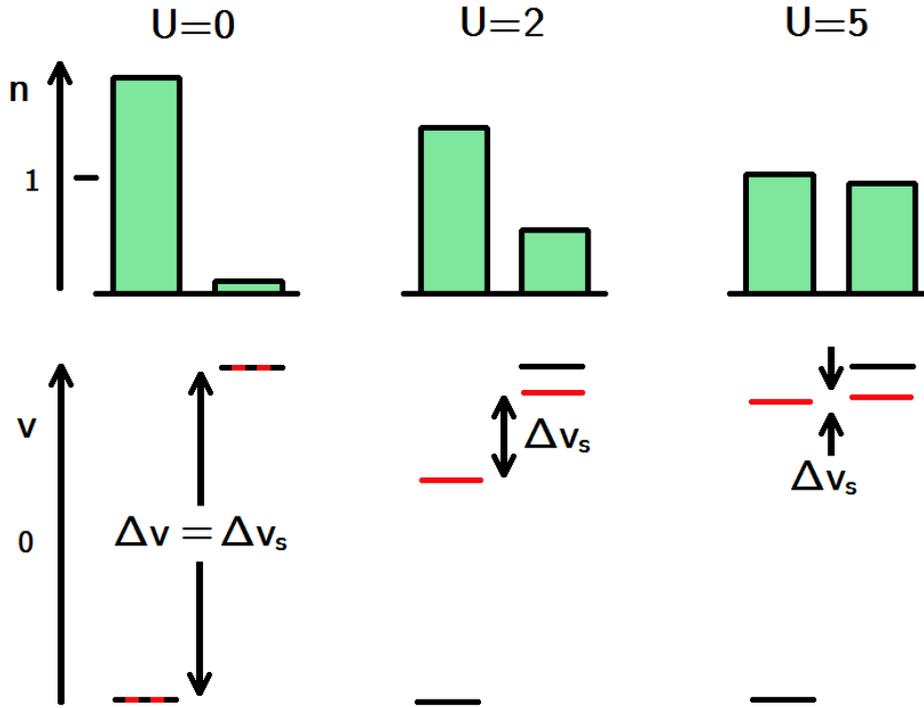
Fig. 6: *KS DFT view of an asymmetric half-filled Hubbard dimer as a function of U. The on-site potential difference Δv is shown in black and the KS on-site potential difference Δv_{s} is in red.*

The first correction to v_i is the Hartree potential, while the second is the XC potential. These KS TB equations must be solved self-consistently, as the potentials depend on the occupations. Once converged, the final densities can be used to extract the total energy of the MB system, via

$$E = T_{\mathrm{s}} + U_{\mathrm{H}} + E_{\mathrm{XC}} + V = \varepsilon - U_{\mathrm{H}} + E_{\mathrm{XC}} - \Delta v_{\mathrm{XC}} \Delta n/2\,, \tag{13}$$

where ε is the eigenvalue in the TB KS calculation. Again, just like in the HK case, once $E_{\mathrm{XC}}(n_1)$ is given (either approximate or exact), the KS equations can be solved for any electronic system and a ground-state energy and occupation extracted.

The wondrous improvement due to the KS scheme is that only a small fraction of the total energy (the XC part) need be approximated. Many of the most important quantum effects, such as screening, shell structure, binding energies, etc. are mostly accounted for by the quantum effects of the one-body system. Finally, a very simple, intuitive approximation suggested by KS themselves (the local density approximation (LDA) [61, 50]) produced far better results than they expected (but with binding energy errors too large for quantum chemistry taste).

Fig. 6 gives us some sense of how this works, for $\Delta v = 1$. Then, if $U = 0$, most occupation is on the left. For $U = 2$, the repulsion makes the occupations more equal. The KS potential is simply that TB potential that produces those (many-body) occupations. So it must be a smaller potential difference than the real potential. One can see that the Hartree potential will typically overestimate repulsion, while XC corrects that to give the exact answer. Finally, when U is ramped up to 5, the occupations become very close to equal, and the KS potential difference becomes very small.

Traditionally, E_{XC} is separated into an exchange and a correlation contribution. The exchange contribution is then defined as

$$E_{\mathrm{X}} = \langle \Phi_{\mathrm{S}} | \hat{V}_{\mathrm{ee}} | \Phi_{\mathrm{S}} \rangle - U_{\mathrm{H}}, \tag{14}$$

where Φ_{S} is the KS wavefunction, and E_{X} is always negative. Then one can show correlation is just

$$E_{\mathrm{C}} = \langle \Psi | \hat{H} | \Psi \rangle - \langle \Phi_{\mathrm{S}} | \hat{H} | \Phi_{\mathrm{S}} \rangle \tag{15}$$

and, by the variational principle, is also never positive. These definitions (almost) match those of quantum chemistry [62], except that in KS-DFT, all orbitals come from a single potential, while in HF orbitals are freely chosen to minimize the HF energy. But there are some surprises relative to the traditional many-body expansion. For example, because of the definitions, E_{X} includes some 'self-exchange', i.e., it is non-zero even for a single electron (where E_{X} is $-U_{\mathrm{H}}$ and $E_{\mathrm{C}} = 0$). DFT approximations which do not satisfy these conditions for all one-electron densities are said to have self-interaction errors [63]. Moreover, 'higher-order exchange effects' are all lumped into the correlation energy. In any event, for our 2-electron problem, in a spin singlet, $E_{\mathrm{X}} = -U_{\mathrm{H}}/2$, but no simple relation exists for larger N.

The traditional Hartree-Fock approximation comes from expanding the electron-electron interaction to first order, which means neglecting E_{C}, and then minimizing the energy. In full DFT terms, for our 2-electron system,

$$F^{\mathrm{HF}} = T_{\mathrm{S}} + \frac{1}{2} U_{\mathrm{H}}, \tag{16}$$

or in KS-DFT terms

$$E_{\mathrm{XC}}^{\mathrm{HF}} = -U_{\mathrm{H}}/2\,. \tag{17}$$

Thus, solving the TB equation self-consistently with Eq. (17) produces the minimum for the total energy using F^{HF} of Eq. (16).

In Fig. 7, we show the contributions to the KS potential for a sequence of different U values, as a function of the occupation. The effect of repulsion is to always oppose the potential difference, making the KS potential difference smaller. In the first, U is small, and correlation is of order U^2 (see Reference [25]). Thus the correlation contribution is negligible (red and green overlap) and HF is an excellent approximation. In the middle, $U = 1$ is moderate, and now we begin to see the difference correlation makes in the potential. Moreover, its effect is to make Δv_{HXC} deviate from a straight line. Finally, for strong correlation, the HXC potential (almost) exactly is equal and opposite to the one-body potential. Again, the HX contribution has much curvature, but now correlation wipes that out (almost) entirely. Clearly, the HF approximation will be terrible for the potential in this case, and yield entirely incorrect densities. In fact, a lower-energy solution appears if one allows spin symmetry breaking [64].

It is now relatively routine to calculate accurate KS potentials from highly accurate densities found, e.g., via quantum chemical methods [65]. In an insanely demanding calculation, it is even possible to solve the KS equations using the exact XC functional [66]. Convergence becomes more difficult as correlations grow stronger, but remains possible [67].
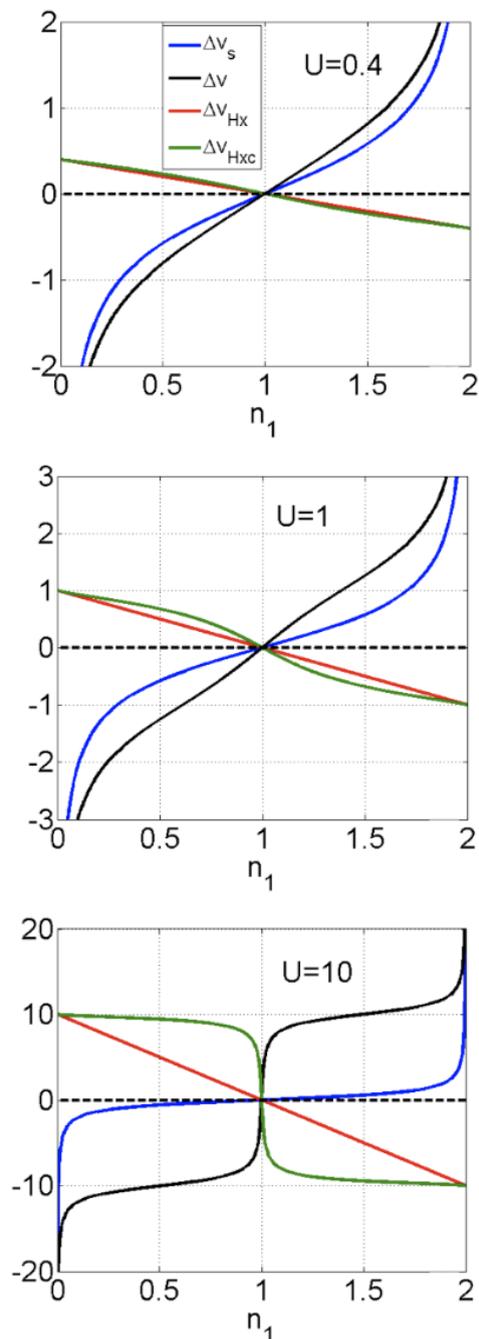
Fig. 7: *Plots of Δv_s (blue) and its components, the one-body potential Δv (black), the Hartree plus exchange potentials, $U\Delta n/2$ (red), and the same with correlation added, $U\Delta n/2 + \Delta v_\mathrm{C}$ (green) plotted against n_1 for various values of U.*

Takeaway: The KS scheme is exact meaning that, if we only knew the exact exchange-correlation functional, we could determine the ground-state energy exactly, of every electronic problem. There are many existing calculations of the exact XC potential. In practice, we must approximate XC, but because XC is a small fraction of the total energy, standard KS calculations are usefully accurate for ground-state energies and densities.

3.1   KS spectral function

There is a *pernicious superstition* [68] that the KS spectrum is related to the physical response properties of the real system. This false belief has arisen because, for weakly correlated systems, this is approximately true, apart from the fundamental gap of a semiconductor. From a practical viewpoint, the KS bands are marvelously useful as a starting point for Green function calculations of real spectral functions. Moreover, long ago, when the local density approximation ruled supreme, there was no way to know if differences between the KS and exact response properties was due to the crudeness of this approximation [69, 70]. These days, there are simple exact answers to such speculations, if we only have the patience to read them.

3.2   The ionization potential theorem

As a simple example of the mysterious workings of the exact functional, we state an important exact result

$$I(N) = E(N{-}1) - E(N) = -\varepsilon^{\mathrm{HO}}(N). \tag{18}$$

Here $E(N)$ is the ground-state of the N-electron system, and $\varepsilon^{\mathrm{HO}}$ is the energy of the highest-occupied KS orbital. (For those with some chemistry leaning, Koopmans' theorem is an approximate version of this for HF calculations [71]). This illustrates some of the power of KS-DFT. You might think that, with the exact functional, all one can extract is the ground-state energy and density of our system. But the above result shows that the HO of the KS scheme also tells you the ionization energy. One can also extract all static response functions exactly by turning on weak external perturbations, and applying the exact functional to the perturbed systems. In practice, standard DFT approximations tend to violate this exact condition very badly [69, 70, 72]. Nonetheless, they often still yield usefully accurate ground-state energies, thus performing their primary function. (On the other hand, returning to the discussion of HKI, knowing the exact XC does *not*, in general, give you access to, say, the first excited state energy. It is a functional of n_1 alone, but we cannot deduce that functional from $E_{\mathrm{XC}}(n_1)$.)

Increasing N by 1 in Eq. (18) yields

$$A(N) = E(N) - E(N{+}1) = -\varepsilon^{\mathrm{HO}}(N{+}1) \neq \varepsilon^{\mathrm{LU}}(N), \tag{19}$$

where A is called the electron affinity of the system in chemistry. The difference between the KS HO of the $N{+}1$ electron system and the lowest unoccupied (LU) level of the N-electron system is called Δ_{XC}, where the Δ indicates its origin from the infamous derivative discontinuity of DFT [69]. This simply means, that at zero temperature, the energy of the system consists of straight line segments between integer values, as shown below in Fig. 8. The energy itself is continuous, but its derivative, the chemical potential, is not. For a neutral system, the chemical potential is $-I$ below the integer and $-A$ above. This discontinuous jump in μ shifts the KS HO eigenvalue by the same amount, producing the difference with the KS LU of the neutral. (Realistic electronic systems do not have an upward pointing portion of the curve in Fig. 8. This occurs for the dimer because electrons cannot escape to outside the system.)
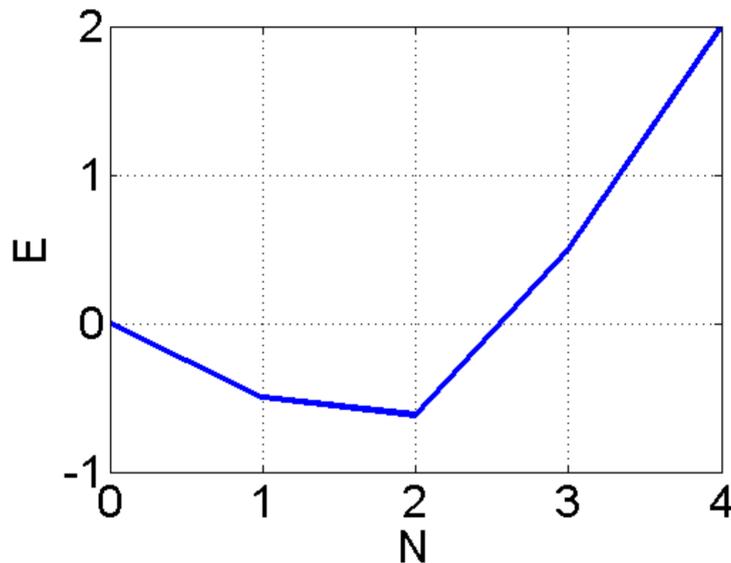
Fig. 8: *Plot of $E(N)$ for $U = 1$ and $\Delta v = 0$.*

3.3   Mind the gap

We are now ready to see the relevance of this to solids. Even for a finite system, we define the charge (or fundamental) gap as

$$E_g = I - A. \tag{20}$$

As the size of the system grows toward a bulk material, this quantity tends to the fundamental charge (or transport) gap of the system (at least for ordered systems [73]). But, because of Eqs. (18) and (19) above, we find

$$E_g = E_{s,g} + \Delta_{\mathrm{XC}}, \tag{21}$$

where $E_{s,g}$ is the KS gap (i.e., the difference between the LU and HO level, or the gap between the KS valence and conduction bands in a solid). Thus, with the *exact* XC functional of ground-state DFT, we do not get the true gap by looking at its KS value for the neutral system.

Fig. 9 shows the spectral function (projected onto the left-hand site) in a weakly correlated case [26], the symmetric dimer with $U = 1$. We can see the sense in which the KS spectral function (red) resembles the blue exact one: the significant KS peaks are of about the same height and position as their blue counterparts, and the blue peaks without KS counterparts are relatively small. The KS gap is smaller than the true gap, but not by much. Because both the KS and the exact spectral functions satisfy the same sum rule (even with an approximate XC), if the dominant peaks are reproduced (even with the wrong gap), only small peaks are missed in the KS spectrum.

On the other hand, Fig. 10 shows the same system with a larger U value. Now the strong KS peaks are not in the right place and are noticeably too large. Moreover, the blue peaks with no KS analogs are a substantial contribution. Finally, in the inhomogeneous case, the potential asymmetry overcomes the effects of the Hubbard U. In Fig. 11, we see that for $\Delta v = 2$ and $U = 1$, the KS spectral function is almost identical to the true one.
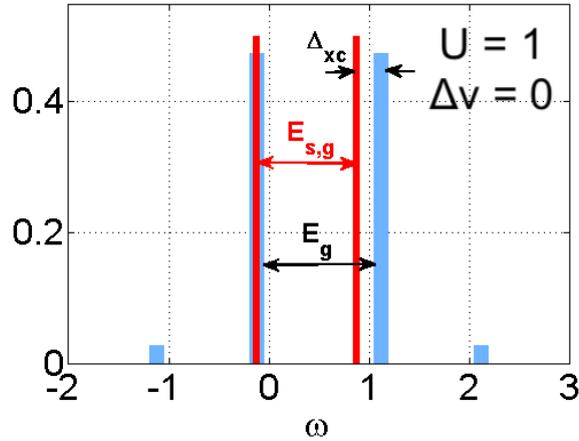
Fig. 9: *Spectral function of the symmetric dimer for $U = 1$ and $\Delta v = 0$. The physical MB peaks are plotted in blue, the KS in red. Here $I = 0.1$, $A = -1.1$, and $\varepsilon^{LU} = 0.9$.*
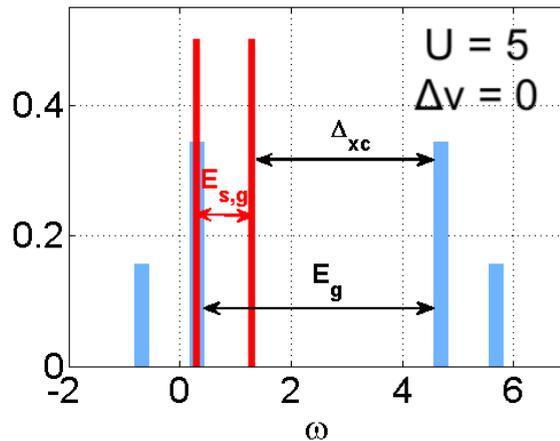

Fig. 10: *Same as Fig. 9, but now $U = 5$. Here $I = -0.3$, $A = -4.7$, and $\varepsilon^{LU} = 1.3$. Note that the KS gap remains unchanged by the alteration of U because $\Delta n = 0$ in both cases.*

Lastly, we finish this section illustrating the relevance of this discussion to the thermodynamic limit. The canonical example of the Mott-Hubbard transition is a chain (or lattice) of H atoms. Each atom has one electron, so the bands of the KS potential are always half-filled, with no gap at the Fermi energy. Thus the gap is always zero and the KS band structure suggests it's a metal. This may be true at moderate separations of the atoms, but as the separation is increased, the electrons must localize on atoms, and it must become a Mott insulator.

Fig. 12 shows the gap, calculated for chains of well-separated 1D H atoms of increasing length [46]. By performing the calculation with finite systems, i.e., without periodic boundary conditions, we calculate the gap for each N by adding and removing electrons, as in Eq. (20), and then take the limit as $N \to \infty$. On the other hand, we extract the exact ground-state density from our DMRG calculation at each N, and find the corresponding exact KS potential for each N. We could then as easily extrapolate the KS gap, from the HO and LU, showing that indeed the KS gap vanishes in the thermodynamic limit – exactly the same as if we had calculated the KS band structure, in which the Fermi energy would be right in the middle of the band. This provides a dramatic illustration of the KS underestimate of the true gap, even when using the exact XC functional.
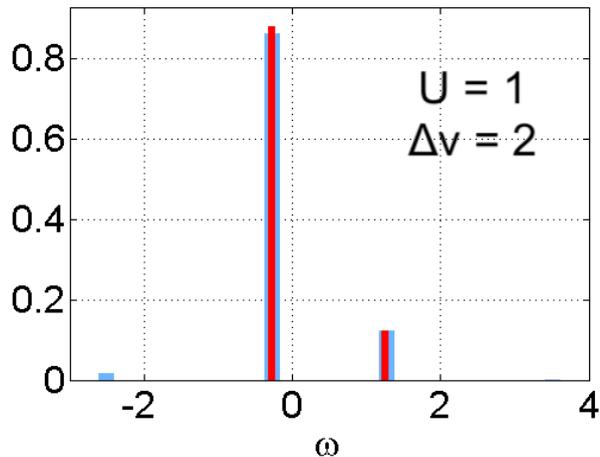
Fig. 11: *Same as Fig. 9, but now $U = 1$, $\Delta v = 2$. Here $I = 0.27$, $A = -1.27$, and $\varepsilon^{\mathrm{LU}} = 1.25$.*
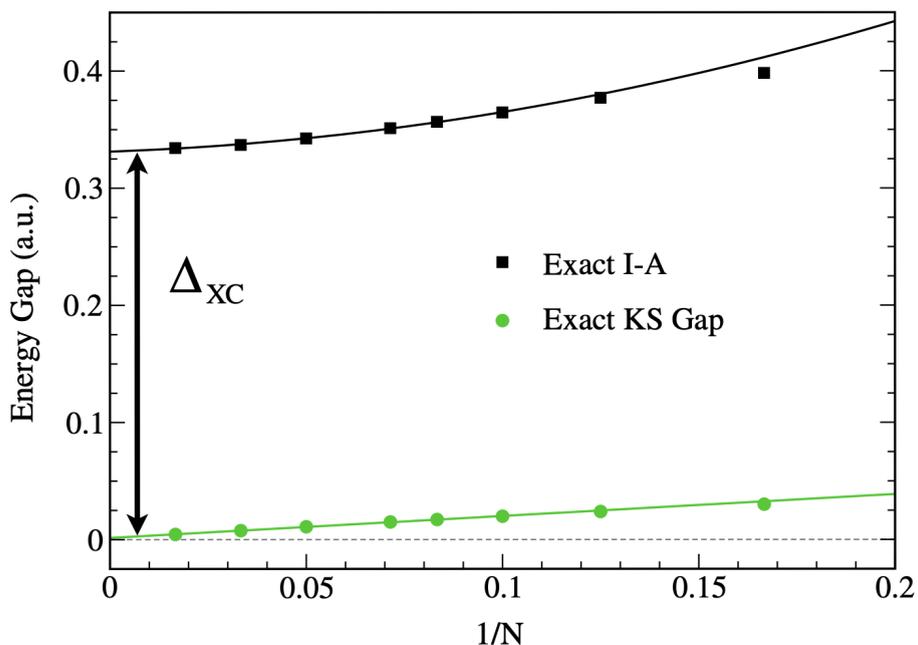
Fig. 12: *Exact gaps for chains of N soft hydrogen atoms with atomic separation $b = 4$ (error bars are less than symbol sizes). The upper curve is a quadratic fit of exact gaps of the largest six systems and extrapolates to a finite value $E_g \approx 0.33$. The exact Kohn-Sham gaps, in contrast, extrapolate to zero showing that for $N \to \infty$ the true KS system is metallic (lower curve is a linear fit of exact KS gaps of the largest six systems). Taken from Reference [46].*

> **Takeaway:** The KS Green function does not match the true Green function. If correlation is weak, it may be a good approximation to it, with its main deficiency being an underestimate of the gap. For stronger correlations, there can be huge differences, and there are always more features in the real Green function. In the thermodynamic limit, the exact KS gap can vanish for a simple Mott insulator.

3.4   Talking about ground-state DFT

First, we review our crucial formal points.

1. In general, the KS scheme with the exact functional yields ground-state energy and density, and any other quantities that can be teased from them, such as static response properties and ionization potentials.

2. There is no formal meaning for most KS eigenvalues in ground-state DFT, despite the fact that many practitioners treat them as if there were. Of course, they do provide tremendous physical and intuitive insight, especially for weakly correlated systems, where they are good approximations to the excitations (either quasi-particle or optical). But when correlations are strong, explicit methods are needed to correct them [74].

3. The strongest manifestation of point 2 above is that the exact KS gap is typically smaller than the true gap, and can vanish in cases where the true gap is finite (Mott insulator).

4. Moreover, there is an exact formula relating the total energy to the sum of the KS eigenvalues, which contains finite corrections for double counting. There is no ambiguity about these corrections, they are derived from the formal theory, and yield the exact many-body energy. But when correlated methods are used for a *subset* of the orbitals, ambiguities can arise that affect occupancies [75].

5. Although in principle, all properties are functionals of the ground-state density, knowledge of the exact ground-state energy functional (via E_{xc}) does not provide a way to calculate these other functionals. As we see later, TDDFT is a way to do precisely this.

Next, we discuss how these points show up in practical DFT calculations of solids, where XC approximations must be made.

1. The steady progress within quantum chemistry and materials in functional development is almost entirely focused on improvements in accuracy and reliability of the total energy for weakly correlated systems [76, 77]. This is by far the most important use of DFT in modern electronic structure. Such improvements are often not particularly relevant to the response properties of greatest interest in strongly correlated materials. For example, the KS eigenvalues are often not improved significantly by functionals yielding better energies [78, 79]. Although the KS eigenvalues cannot be directly interpreted in general, they are uniquely defined (up to a constant). Thus the exact KS Hamiltonian is a well-defined starting point for many-body methods.

2. The KS scheme is not a mean-field scheme in the traditional sense of the word, and it can be extremely difficult to relate its features to those of traditional many-body theory. The KS wavefunction is typically a single Slater determinant, but yields the exact many-body energy via its density.

3. Standard approximations, such as LDA and generalized gradient approximations (GGA), by construction produce total energies that are smooth and continuous at integer N, unlike the exact $E(N)$. Thus their corresponding Δ_{xc} is zero [69]. According to Sec. 3.3, the KS band gap in such approximations *is* their prediction for the fundamental gap. In fact, it has been found that their KS gaps are likely a good approximation to the exact KS gap [80], but their lack of discontinuous behavior means they miss the correction to turn it into the true gap.

4. On the other hand, the range-separated hybrid functional HSE06 is well-known to produce reasonable gaps for moderate gap semiconductors. This is because, instead of performing a true pure KS calculation, most codes (like VASP) perform a *generalized* KS calculation [81] when a functional is orbital-dependent [82, 83]. They treat the orbital-dependent part of the potential as if it were a many-body potential, just as is done in HF. (A similar but smaller effect occurs in meta-GGA's that depend on the kinetic energy density, such as SCAN [84]). And in fact clever tricks may be used to extract the true gap, even from a periodic code [85].

> **Takeaway:** Even with the exact functional, the KS band gap does not equal the true transport gap of the system. Likely, semilocal functionals yield accurate KS gaps but, because they lack a discontinuous behavior at integer particle numbers, cannot yield accurate transport gaps. Modern hybrid functionals that depend explicitly on KS orbitals yield band gaps closer to fundamental gaps, but only when treated with generalized KS theory.

4 Time-dependent DFT (TDDFT)

Our last main section is about time-dependent density functional theory (TDDFT) [86–89]. While this uses many of the forms and conventions of ground-state DFT, it is in fact based on a very different theorem from the HK theorems. When applied to the linear response of a system to a dynamic electric field, it yields the optical transitions (and oscillator strengths) of that system. It has become the standard method for extracting low-level excitations in molecules, where traditional quantum chemical calculations are even more demanding than those for the ground state.

The Runge-Gross theorem [90] states that, for a given initial wavefunction, statistics, and interaction, the *time-dependent* density uniquely determines the one-body potential. In principle, this can be used for any many-electron time-dependent problem, including those in strong laser fields [86]. In practice, such calculations are limited by the accuracy of the approximations and whether the observable of interest can be extracted directly from the one-electron density. One constructs TD KS equations, defined to yield the exact time-dependent one-electron density.

Because TDDFT applies to the time-dependent Schrödinger equation, the XC functional differs from that of ground-state DFT in general, and has a time-dependence.

Our interest will be only in the linear-response regime. In that case, one can derive a crucial result, which we give in operator form, called the Gross-Kohn equation [91]

$$\chi(\omega) = \chi_{\mathrm{S}}(\omega) + \chi_{\mathrm{S}}(\omega) * (f_{\mathrm{H}} + f_{\mathrm{XC}}(\omega)) * \chi(\omega), \tag{22}$$

where $\chi(\omega)$ is the dynamic density-density response function of the system, and χ_{S} is its KS counterpart. The kernel, f, is the functional derivative of the time-dependent potential. Thus, f_{H} is the Hartree contribution, while $f_{\mathrm{XC}}(\omega)$ is the XC correction.

Eq. (22) is a Dyson-like equation for the polarization. If we set $f_{\mathrm{XC}} = 0$, it is the standard random-phase approximation, the Coulomb interaction simply dressing the bare interaction, and producing all the bubble diagrams. But things get a little weird when we assert that inclusion of $f_{\mathrm{XC}}(\omega)$ produces the *exact* response of the system, for all frequencies. From a many-body viewpoint, this is suspicious, as these are a closed set of equations without coupling to 4-point functions. But the logic is sound and exactly analogous to the ground-state: there exists such a function that could be considered as defined by Eq. (22).

The excitations of a system are given by poles of its response function. Simple analysis (exactly that of RPA) yields a matrix equation that corrects KS transition frequencies to the true transition frequencies, where the matrix elements involve $f_{\mathrm{H}} + f_{\mathrm{XC}}$. With standard ground-state approximations, folks have merrily calculated mostly low-lying valence transitions from the ground-state of many molecules [92], finding accuracies a little lower than those of ground-state DFT [93], and computational costs that are comparable. This has been invaluable for larger molecules, where many excitations of the same symmetry may overlap, and so TDDFT yields a semiquantitative signature that can be easily matched with experiment [94].

However, not all is well in paradise. Almost immediately, it was noticed that the use of a ground-state approximation is simply the static limit of the corresponding kernel, and can be easily shown to produce only single excitations. While useful workarounds were created for some cases, it was also found that going to higher-order response does not solve the problem. And many of the most exciting transitions in biochemistry are double excitations.

> **Takeaway:** Time-dependent DFT applies DFT methods to time-dependent problems. Within linear response, this yields exact expressions for the dynamic polarization, but at the cost of introducing a new functional, the frequency-dependent XC kernel. Ignoring its frequency dependence yields useful accuracy for low-lying molecular excitations with standard functionals. TDDFT is now standard for calculating optical response of molecules and materials.

4.1 Hubbard dimer

Happily we care only about Hubbard dimers, where everything is much simpler. First, we note our Hubbard dimer, in the singlet space, has just three states: the ground-state, the first excited
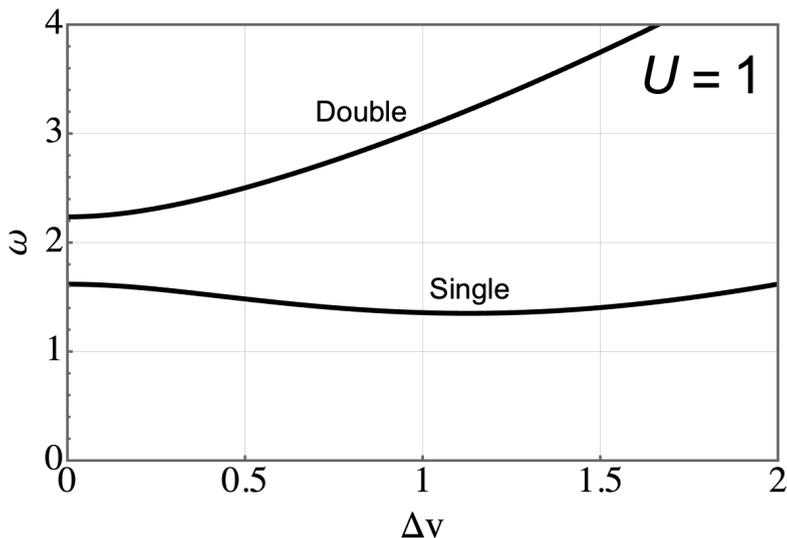
Fig. 13: *Transition frequencies of the first and second excitations as a function of Δv for $U = 1$.*

state, which has a single excitation, and the second excited state, which is a double excitation out of the ground-state. Since there are no spatial degrees of freedom, our $\chi(\omega)$ is the Fourier transform of $\Delta n(t)/\Delta v(0)$, which is just a scalar, with ω-dependence

$$\chi_n(\omega) = \frac{a_1}{\omega^2 - \omega_1^2} + \frac{a_2}{\omega^2 - \omega_2^2}, \tag{23}$$

where ω_i denotes the transition frequency and a_i is related to its oscillator strength [26]. Thus χ has poles at each of the transition frequencies. Fig. 13 shows the value of each of these transitions as a function of Δv for $U = 1$. The double excitation is a little above the single for the symmetric case, but grows linearly with Δv. The single remains about the same, and even dips, until $\Delta v = U$, and then begins to grow itself. Here we can use our model system to examine one of the key mysteries of practical TDDFT: Where did all the higher excitations go? First we do an exact ground-state KS calculation, as in the previous sections. Thus the exact KS system is a tight-binding problem with effective potential, Δv_s, defined to yield the exact ground state Δn. This yields two eigenvalues, the lower symmetric combination and the higher asymmetric combination. The KS ground-state has the lower one doubly occupied. There do exist KS analogs of the many-body states. The single excitation has one electron excited to the higher level, the double has both. Fig. 14 adds the KS transitions to Fig. 13, showing that they loosely follow the accurate transitions, but are significantly different.

In the KS response function, χ_S, the matrix elements of the density operator between ground and double excitation are zero, since both KS orbitals are different, so the Slater determinants are not coupled by a single density operator. Hence, such states have no numerator, eliminating any poles that might have arisen in the denominator, i.e.,

$$\chi_S(\omega) = \frac{a_s}{\omega^2 - \omega_s^2}. \tag{24}$$

Thus the second KS transition, the double, does not appear at all in the response function! It's position is correctly marked in Fig. 14, but cannot be seen in χ_S.
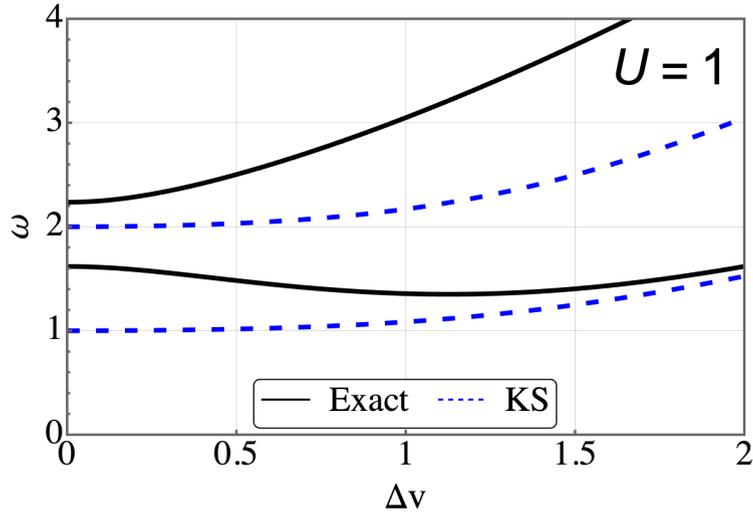
Fig. 14: *Same as Fig. 13, but with KS transitions (depicted in blue). For $\Delta v > U$, the KS transition is a very good approximation to the true transition.*
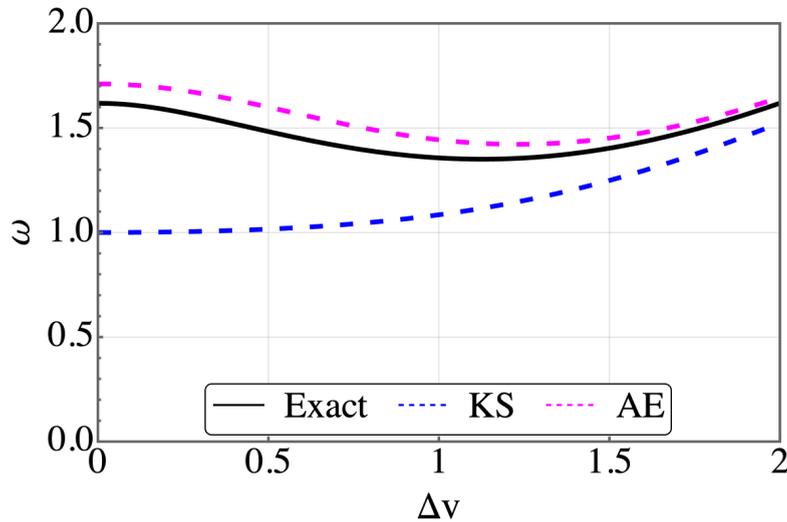

Fig. 15: *Same as Fig. 13, but with the adiabatically exact approximation (AE, pink dashes).*

By requiring the poles occur at the right places, one finds (in general) a matrix equation in the space of single excitations for the true transitions, whose elements are determined by the kernel. Here, this is one dimensional, yielding

$$\omega^2 = \omega_{\text{s}}^2 + 2\omega_{\text{s}}\, f_{\text{HXC}}(\omega)\, \frac{2}{1 + \Delta v_{\text{s}}^2}\,. \tag{25}$$

The adiabatically exact approximation (AE) is to use the exact ground-state functional here to calculate f_{HXC}. This corrects the single KS transition and is shown in Fig. 15. This works extremely well to capture almost all the difference with the KS transition, yielding very accurate excitations. This becomes even better for Δv greater than U, where the corrections virtually vanish (just as in Fig. 11 for the spectral function).

But Eq. (25) just has one solution if the ω-dependence in the kernel is neglected. On the other hand, if there is strong frequency dependence in the kernel, new transitions, not in the KS system, may appear. In fact, we know that is precisely what happens, as the physical system
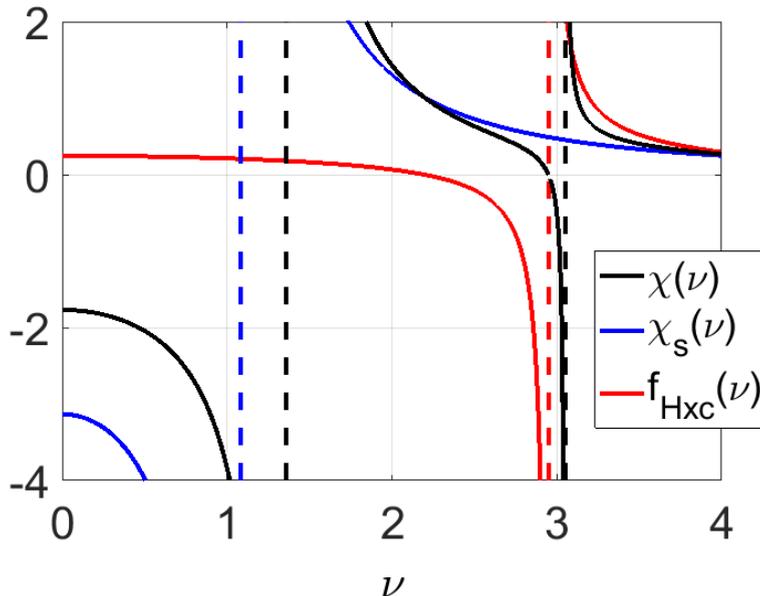
Fig. 16: *Frequency dependence of exact (black) and Kohn-Sham susceptibilities (blue) and exchange-correlation kernel (red) for $U = \Delta v = 1$. Poles marked by dashed vertical lines, as a function of frequency ν. The red line shows the exchange-correlation kernel.*

does have a double excitation. To understand how standard TDDFT fails, we note that we can calculate the exact kernel by finding $\chi(\omega)$ from many-body calculations, $\chi_{\rm s}(\omega)$ by the techniques of the earlier section, inverting and subtracting

$$f_{\rm HXC}(\omega) = \chi_{\rm s}^{-1}(\omega) - \chi^{-1}(\omega). \tag{26}$$

Fig. 16 shows the singular frequency-dependence of the kernel from Eq. (26), which allows Eq. (25) to have an additional solution.

However, while all this provides insight into how the exact functional performs its magic, it does not tell us directly how to create a general purpose model, which would build this frequency-dependence into an explicit density functional sufficiently accurately to capture double excitations [89].

> **Takeaway:** The Hubbard dimer demonstrates the accuracy of the adiabatic approximation in TDDFT for single excitations, and also the missing frequency dependence needed to generate the double excitations missing in adiabatic TDDFT.

4.2   Talking about TDDFT

We saw in the earlier sections how the KS eigenvalues did not have a formal meaning in pure ground-state KS-DFT. We have seen here that, with the advent of TDDFT, they form the starting point of a scheme which produces the *optical* excitations. These are not the quasi-particle excitations associated with the Green function, which involve a change in particle number.

While the primary function of approximate ground-state DFT is to find energies, it usually also produces reasonably accurate densities, but rather erroneous XC potentials. In fact, this feat is

achieved by having all the occupied orbitals shifted (higher) than their exact KS counterparts. A constant shift has no effect on the density. But if the unoccupied levels (at least, the low-lying valence excitations) suffer the same shift, then KS transition frequencies are unaffected, and the adiabatic approximation (usually applied to the same XC approximation as the ground-state calculation) is reasonably accurate for many weakly correlated molecules.

Linear-response TDDFT has been less used in solids, because in the case of insulators, it became clear early on [95] that there is a long-range contribution to the XC kernel (as long-ranged as the Hartree contribution is) that is missed when using a semilocal ground-state approximation adiabatically. There are now many ways around this difficulty [96], some based on modelling the kernel using many-body techniques.

There have been many other approaches suggested for extracting optical excitations from DFT. An old simple one is called Δ-SCF [97], which involves simply using excited-state occupation numbers in a KS calculation, and finding the energy the usual way. Another, which has seen considerable recent interest [98, 99], is to use ensemble DFT [100].

> **Takeaway:** TDDFT can be considered an algorithm for finding the functional (of the ground-state density) for optical excitations.

5   Summary

This short review is aimed at broadening understanding of the basic differences between a density functional viewpoint and that of traditional many-body theory. The emphasis here has been on the exact theory, which we have illustrated on the 2-site Hubbard model. We have shown it is confusing to consider KS theory as any kind of traditional mean-field theory, and how the addition of TDDFT allows one to consider the KS eigenvalues as zero-order approximations to the optical excitations, not the quasiparticle excitations.

However, the only reason that anyone cares about the exact theory of DFT is because, in practice, it is extremely useful with relatively unsophisticated approximations. These begin with the famous local density approximation, in which the XC energy per electron at each point in a system is approximated by that of a uniform gas matching the density at this point. This was introduced already in the KS paper (where the statement of exactness appears as a mere footnote), thereby totally muddying the waters between exact and approximate statements. Walter Kohn told KB that he simply noticed the exact nature of the KS scheme after submitting the paper. From about 1990 onwards, many users began using more sophisticated functionals, whose primary effect was to improve total energies and energy differences.

This article has said little or nothing about how to understand such approximations. This is because local (and semilocal) approximations capture a universal limit of all electronic systems, by yielding relatively exact XC energies in this limit [101–104]. Traditional many-body theory generally considers a power series expansion in the electron-electron interaction. The alternative limit simultaneously increases the number of particles, in a way that the total electron-

electron repulsion remains a finite fraction of the total energy even as interactions become weaker. The simplest example of this is that the LDA for exchange, whose formula can be derived by hand, has a percentage error that vanishes for atoms as $Z = N \to \infty$ [102].

This limit is hard-wired into the last term of the real-space Hamiltonian of Eq. (1), which is the integral of the density times the one-body potential. This is why the density is the basic variable in DFT. Even if formal theorems can be proven using other variables, this is why density functional theory has been so successful. It is also the case that the one-body potentials to which we apply DFT are diagonal in coordinate space, which is related to why the LDA is a universal limit.

Thus, key aspects of DFT approximations that are crucial to its success are missing from lattice models like the Hubbard model. There is no corresponding universal limit in which LDA becomes exact, even if one uses an approximation based on the uniform case [105, 106]. Again, this is why we created our 1D real-space mimic of 3D reality, instead of just solving lattice models.

> **Takeaway:** This chapter has illustrated a variety of key conceptual points about DFT on a simple model system. Anyone who can answer the exercises will have absorbed 90% of the material, and should be well-qualified to understand exactly what a DFT calculation does, and does not, tell you. In the twenty-first century, with so many DFT calculations being performed in so many different fields, the phrase "Oh, that's just mean-field theory" should no longer have any place in scientific discussions about DFT results.

Acknowledgments

A   Exercises

If you have followed the logic throughout this tutorial, you will enjoy sorting out these little questions. If you want solutions, please email either of the authors, with a brief note about your current status and interests.

1. State which aspect of Fig. 4 illustrates the HKI theorem.

2. What geometrical construction gives you the corresponding ground-state potential for a given n_1 in Fig. 5?

3. Study the extreme edges ($n_1 = 0$ and 2) of Fig. 5. What interesting qualitative feature is barely visible, and why must it be there?

4. What feature must always be present in Fig. 5 near $n_1 = 1$? Explain.

5. How can you be sure that, no matter how large U becomes, $F_U(n_1)$ is never quite $U|1-n_1|$?

6. Assuming the blue line is essentially that of $U = 0$, use geometry on Fig. 3 to find Δv_S for $U = 5$.

7. What is the relation, if any, between each of the blue plots in the three panels of Fig. 7? Explain.

8. What is the relation, if any, between each of the red plots in the three panels of Fig. 7? Explain.

9. Why is the green line almost the mirror image of the black line in the $U = 10$ panel of Fig. 7? Could it be the exact mirror image? Explain.

10. From Fig. 8, using $E(N)$ about $N = 2$, determine the locations of the largest peaks of Fig. 9 and compute the gap between them.

11. Sketch how Fig. 8 must look if $U = 10$ and $\Delta v = 0$.

12. What is the relation between the two blue lines in Fig. 14? Explain.

13. Give a rule relating the numbers of vertical lines of different color in Fig. 16. Explain its significance.

14. Recall the definition of the kernel from section 4. Using this, derive f_H and f_X, and draw them on Fig. 16. Explain where double excitations must come from for 2 electrons.

15. Using formulas and figures from both sections, deduce the results of Fig. 15 in the absence of correlation (Hint: You will need to solve the Hartree-Fock self-consistent equations), and comment on the relative errors. This is a little more work than the other exercises.

References

[1] G.D. Mahan: *Many-Particle Physics* (Springer, 3rd edition, New York, 2000)

[2] P. Blöchl: *Theory and Practice of Density-Functional Theory*, in [107]

[3] A. Pribram-Jones, D.A. Gross, and K. Burke, Annu. Rev. Phys. Chem. **66**, 283 (2015)

[4] C.J. Pickard, I. Errea, and M.I. Eremets, Annu. Rev. Condens. Matter Phys. **11**, 57 (2020)

[5] J.K. Nørskov, F. Abild-Pedersen, F. Studt, and T. Bligaard,
Proc. Natl. Acad. Sci. U.S.A. **108**, 937 (2011)

[6] L. Zeng, S.B. Jacobsen, D.D. Sasselov, M.I. Petaev, A. Vanderburg, M. Lopez-Morales,
J. Perez-Mercader, T.R. Mattsson, G. Li, M.Z. Heising, A.S. Bonomo, M. Damasso,
T.A. Berger, H. Cao, A. Levi, and R.D. Wordsworth,
Proc. Natl. Acad. Sci. U.S.A. **116**, 9723 (2019)

[7] Z. Velez, C.C. Roggatz, D.M. Benoit, J.D. Hardege, and P.C. Hubbard,
Front. Physiol. **10**, 731 (2019)

[8] C.H. Hendon, L. Colonna-Dashwood, and M. Colonna-Dashwood,
J. Agric. Food Chem. **62**, 4947 (2014)

[9] F. Lechermann: *Model Hamiltonians and Basic Techniques*, in [107]

[10] I.V. Solovyev, J. Phys.: Condens. Matter **20**, 293201 (2008)

[11] D.C. Tsui, H.L. Stormer, and A.C. Gossard, Phys. Rev. Lett. **48**, 1559 (1982)

[12] J. Kondo, Prog. Theor. Phys. **32**, 37 (1964)

[13] E.H. Lieb, Int. J. Quantum Chem. **24**, 243 (1983)

[14] J. Loewen: *Lies My Teacher Told Me: Everything Your American History Textbook
Got Wrong* (New Press, 2008)

[15] F.D.M. Haldane, Rev. Mod. Phys. **89**, 040502 (2017)

[16] T.J. Lee and G.E. Scuseria: *Achieving Chemical Accuracy with Coupled-Cluster Theory*
(Springer Netherlands, Dordrecht, 1995), pp. 47–108

[17] D. Feller and K.A. Peterson, J. Chem. Phys. **126**, 114105 (2007)

[18] S. Vuckovic, S. Song, J. Kozlowski, E. Sim, and K. Burke,
J. Chem. Theory Comput. **15**, 6636 (2019)

[19] J. Hafner, C. Wolverton, and G. Ceder, MRS Bull. **31**, 659 (2011)

[20] B. O'Regan and M. Grätzel, Nature **353**, 737 (1991)

[21] K. Burke and L.O. Wagner, Int. J. Quantum Chem. **113**, 96 (2013)

[22] K. Burke: *The ABC of DFT* (2007) `http://dft.uci.edu/learnDFT.php`

[23] R. Dreizler and E. Gross: *Density Functional Theory:*
     An Approach to the Quantum Many-Body Problem (Springer Berlin Heidelberg, 1989)

[24] CECAM: *Teaching the Theory in Density Functional Theory*
     `http://www.youtube.com/channel/UCfLssAro7SMxgaeKTNFFeeA/featured`

[25] D.J. Carrascal, J. Ferrer, J.C. Smith, and K. Burke,
     J. Phys.: Condens. Matter **27**, 393001 (2015)

[26] D.J. Carrascal, J. Ferrer, N. Maitra, and K. Burke, Eur. Phys. J. B **91**, 142 (2018)

[27] C.A. Ullrich, Phys. Rev. B **98**, 035140 (2018)

[28] F. Sagredo and K. Burke, J. Chem. Phys. **149**, 134103 (2018)

[29] F. Sagredo and K. Burke, J. Chem. Theory Comput. **16**, 7225 (2020)

[30] A. Szabo and N.S. Ostlund: *Modern Quantum Chemistry* (Dover Publishing, 1996)

[31] J.W. Ochterski, G.A. Petersson, and K.B. Wiberg, J. Am. Chem. Soc. **117**, 11299 (1995)

[32] R.J. Bartlett and M. Musial, Rev. Mod. Phys. **79**, 291 (2007)

[33] S. Girvin and K. Yang: *Modern Condensed Matter Physics*
     (Cambridge University Press, 2019)

[34] A.J. Cohen, P. Mori-Sánchez, and W. Yang, Science **321**, 792 (2008)

[35] D. Jacob, G. Stefanucci, and S. Kurth, Phys. Rev. Lett. **125**, 216401 (2020)

[36] B. Himmetoglu, A. Floris, S. de Gironcoli, and M. Cococcioni,
     Int. J. Quantum Chem. **114**, 14 (2014)

[37] V.I. Anisimov, A.I. Poteryaev, M.A. Korotin, A.O. Anokhin, and G. Kotliar,
     J. Phys.: Condens. Matter **9**, 7359 (1997)

[38] G. Kotliar, S.Y. Savrasov, K. Haule, V.S. Oudovenko, O. Parcollet, and C.A. Marianetti,
     Rev. Mod. Phys. **78**, 865 (2006)

[39] D. Vollhardt: *Dynamical Mean-Field Approach for Strongly Correlated Materials*, in [107]

[40] E. Pavarini: *The LDA+DMFT Approach*, in [107]

[41] O. Wilde: *The Canterville Ghost* (1887)

[42] J.E. Harriman, Phys. Rev. A **34**, 29 (1986)

[43] G. Knizia and G.K.L. Chan, Phys. Rev. Lett. **109**, 186404 (2012)

[44] J. Yang, W. Hu, D. Usvyat, D. Matthews, M. Schütz, and G.K.L. Chan,
Science **345**, 640 (2014)

[45] K. Lejaeghere *et al.*, Science **351** (2016)

[46] E.M. Stoudenmire, L.O. Wagner, S.R. White, and K. Burke,
Phys. Rev. Lett. **109**, 056402 (2012)

[47] T.E. Baker, E.M. Stoudenmire, L.O. Wagner, K. Burke, and S.R. White,
Phys. Rev. B **91**, 235141 (2015)

[48] S.R. White, Phys. Rev. Lett. **69**, 2863 (1992)

[49] S.R. White, Phys. Rev. B **48**, 10345 (1993)

[50] W. Kohn and L.J. Sham, Phys. Rev. **140**, A1133 (1965)

[51] L.O. Wagner, E.M. Stoudenmire, K. Burke, and S.R. White,
Phys. Chem. Chem. Phys. **14**, 8581 (2012)

[52] J. Hubbard, Proc. Roy. Soc. London. Ser. A. **276**, 238 (1963)

[53] P. Hohenberg and W. Kohn, Phys. Rev. **136**, B864 (1964)

[54] M. Levy, Phys. Rev. A **26**, 1200 (1982)

[55] J.R. Moreno, G. Carleo, and A. Georges, Phys. Rev. Lett. **125**, 076402 (2020)

[56] J.R. Moreno, J. Flick, and A. Georges: *Machine learning band gaps from the
electron density* (2021)

[57] M. Levy, Proc. Natl. Acad. Sci. U.S.A. **76**, 6062 (1979)

[58] L.H. Thomas, Math. Proc. Camb. Phil. Soc. **23**, 542 (1927)

[59] E. Fermi, Z. Phys. **48**, 73 (1928)

[60] K. Burke, J. Chem. Phys. **136**, 150901 (2012)

[61] P.A.M. Dirac, Math. Proc. Camb. Phil. Soc. **26**, 376 (1930)

[62] C.J. Umrigar and X. Gonze, Phys. Rev. A **50**, 3827 (1994)

[63] J.P. Perdew and A. Zunger, Phys. Rev. B **23**, 5048 (1981)

[64] J.P. Perdew, A. Savin, and K. Burke, Phys. Rev. A **51**, 4531 (1995)

[65] A.P. Gaiduk, D.S. Firaha, and V.N. Staroverov, Phys. Rev. Lett. **108**, 253005 (2012)

[66] L.O. Wagner, T.E. Baker, M. Stoudenmire, K. Burke, and S.R. White,
     Phys. Rev. B **90**, 045109 (2014)

[67] L.O. Wagner, E.M. Stoudenmire, K. Burke, and S.R. White,
     Phys. Rev. Lett. **111**, 093003 (2013)

[68] P.C. Tacitus: *Annales* XV.44 (109)

[69] J.P. Perdew, R.G. Parr, M. Levy, and J.L. Balduz, Phys. Rev. Lett. **49**, 1691 (1982)

[70] L.J. Sham and M. Schlüter, Phys. Rev. Lett. **51**, 1888 (1983)

[71] R.G. Parr and W. Yang: *Density Functional Theory of Atoms and Molecules*
     (Oxford University Press, 1989)

[72] J.P. Perdew and M. Levy, Phys. Rev. Lett. **51**, 1884 (1983)

[73] W. Kohn, Phys. Rev. **133**, A171 (1964)

[74] G. Zhang and E. Pavarini, Phys. Rev. B **99**, 125102 (2019)

[75] X. Wang, M.J. Han, L. de'Medici, H. Park, C.A. Marianetti, and A.J. Millis,
     Phys. Rev. B **86**, 195136 (2012)

[76] W. Kohn, A. Becke, and R.G. Parr, J. Phys. Chem. **100**, 12974 (1996)

[77] N. Mardirossian and M. Head-Gordon, Mol. Phys. **19**, 2315 (2017)

[78] R. Stowasser and R. Hoffmann, J. Am. Chem. Soc. **121**, 3414 (1999)

[79] D.J. Tozer and N.C. Handy, J. Chem. Phys. **109**, 10180 (1998)

[80] M. Grüning, A. Marini, and A. Rubio, J. Chem. Phys. **124**, 154108 (2006)

[81] A. Seidl, A. Görling, P. Vogl, J.A. Majewski, and M. Levy, Phys. Rev. B **53**, 3764 (1996)

[82] J. Hafner, J. Comput. Chem. **29**, 2044 (2008)

[83] J.P. Perdew, W. Yang, K. Burke, Z. Yang, E.K.U. Gross, M. Scheffler, G.E. Scuseria,
     T.M. Henderson, I.Y. Zhang, A. Ruzsinszky, H. Peng, J. Sun, E. Trushin, and A. Görling,
     Proc. Natl. Acad. Sci. U.S.A. **114**, 2801 (2017)

[84] J. Sun, R.C. Remsing, Y. Zhang, Z. Sun, A. Ruzsinszky, H. Peng, Z. Yang, A. Paul,
     U. Waghmare, X. Wu, M.L. Klein, and J.P. Perdew, Nat. Chem. **8**, 831 (2016)

[85] A. Görling, Phys. Rev. B **91**, 245120 (2015)

[86] K. Burke, J. Werschnik, and E.K.U. Gross, J. Chem. Phys. **123**, 062206 (2005)

[87] M.A.L. Marques, N.T. Maitra, F.M.S. Nogueira, E.K.U. Gross, and A. Rubio (eds.):
     Fundamentals of Time-Dependent Density Functional Theory
     Lecture Notes in Physics 837 (Springer, Heidelberg, 2012)

[88] C.A. Ullrich: *Time-Dependent Density-Functional Theory*
     (Oxford University Press, 2012)

[89] N.T. Maitra, J. Chem. Phys. **144**, 220901 (2016)

[90] E. Runge and E.K.U. Gross, Phys. Rev. Lett. **52**, 997 (1984)

[91] E. Gross and W. Kohn, Phys. Rev. Lett. **55**, 2850 (1985)

[92] C. Adamo and D. Jacquemin, Chem. Soc. Rev. **42**, 845 (2013)

[93] D. Jacquemin, V. Wathelet, E.A. Perpète, and C. Adamo,
     J. Chem. Theory Comput. **5**, 2420 (2009)

[94] R. Bauernschmitt, R. Ahlrichs, F.H. Hennrich, and M.M. Kappes,
     J. Am. Chem. Soc. **120**, 5052 (1998)

[95] G. Onida, L. Reining, and A. Rubio, Rev. Mod. Phys. **74**, 601 (2002)

[96] S. Sharma, J.K. Dewhurst, A. Sanna, and E.K.U. Gross,
     Phys. Rev. Lett. **107**, 186401 (2011)

[97] T. Ziegler, A. Rauk, and E.J. Baerends, Theor. Chim. Acta **43**, 261 (1977)

[98] T. Gould and S. Pittalis, Phys. Rev. Lett. **123**, 016401 (2019)

[99] Z.h. Yang, A. Pribram-Jones, K. Burke, and C.A. Ullrich,
     Phys. Rev. Lett. **119**, 033003 (2017)

[100] E. Gross, L. Oliveira, and W. Kohn, Phys. Rev. A **37**, 2809 (1988)

[101] E. Lieb and B. Simon, Phys. Rev. Lett. **31**, 681 (1973)

[102] P. Elliott and K. Burke, Can. J. Chem. Ecol. **87**, 1485 (2009)

[103] A. Cancio, G.P. Chen, B.T. Krull, and K. Burke, J. Chem. Phys. **149**, 084116 (2018)

[104] P. Okun and K. Burke: *Semiclassics: The hidden theory behind the success of DFT*,
      arXiv:2105.04384

[105] N.A. Lima, L.N. Oliveira, and K. Capelle, Europhys. Lett. (EPL) **60**, 601 (2002)

[106] V.V. Franca, D. Vieira, and K. Capelle, arXiv:1102.5018v1

[107] E. Pavarini, E. Koch, D. Vollhardt, and A. Lichtenstein (eds.):
The LDA+DMFT approach to strongly correlated materials,
Modeling and Simulation Vol. 1 (Forschungszentrum Jülich, 2011)
`http://www.cond-mat.de/events/correl11`

4   Hubbard Dimer in GW and Beyond

Pina Romaniello

Laboratoire de Physique Théorique

Université de Toulouse

18 Route de Narbonne

31062 Toulouse Cedex 4, France

Contents

1   Introduction

Exactly solvable models are of paramount importance to test the quality of approximations used in various theoretical methods. Having at hand the exact solution of a given problem can allow one to observe possible problems of a given approximation, to get insights into the origin of them, and, ideally, to suggest possible solutions. Several models can be used for this purpose. Here we will concentrate on the Hubbard model. This model is widely used to deal with the physics of strongly correlated materials. Since the model can be solved exactly for small cluster sizes, it is very useful for theoretical investigations. Of course care must be taken when extrapolating conclusions to realistic systems. In this chapter we will use it to scrutinize approximations used in many-body perturbation theory based on Green functions. We will concentrate on the one-body Green function (1-GF) at zero temperature and at equilibrium, which corresponds to the electronic Hamiltonian $\hat{H} = \hat{T} + \hat{V} + \hat{W}$, with $\hat{T}$, $\hat{V}$, and $\hat{W}$ the kinetic-energy operator, the operator corresponding to an external time-independent potential (for example the external potential of the nuclei), and the electron-electron interaction operator, respectively. The 1-GF is a powerful quantity since it contains a wealth of information about a physical system, such as the expectation value of any single-particle operator over the ground state, the ground-state total energy and the spectral function (which is related to photoemission spectra). It can be obtained by solving a Dyson equation of the form $G = G_0 + G_0 \Sigma G$, where G_0 is the non-interacting one-body Green function and the self-energy Σ is an effective potential which contains all the many-body effects of the system under study. In practice Σ needs to be approximated and a well-known approximation is the so called GW approximation (GWA) in which the self-energy reads $\Sigma = v_H + iGW$, where v_H is the classical Hartree potential, and W the dynamically screened Coulomb potential. The GWA works well for many systems, but it also suffers from some shortcomings, such as self-screening (i.e. the fact that an electron screens itself, which is unphysical) and wrong atomic limit (i.e. the fact that the GWA does not capture the so-called strong correlation). These errors of the GWA and possible solutions will be illustrated using the Hubbard dimer.

Notation

We will use combined space-spin-time coordinates of the type $(1) \equiv (\mathbf{x}_1, t_1) \equiv (\mathbf{r}_1, s_1, t_1)$ and $(1^+) = (\mathbf{x}_1, t_1^+)$ with $t_1^+ = t_1 + \delta$ ($\delta \to 0^+$). Moreover, to keep a light notation, integration over indices not present on the left-hand side of an equation is implied.

2   Theoretical background: the GW approximation & beyond

Much of the success of many-body perturbation theory based on Green functions [1] is due to the simplicity to access photoemission spectra through the one-body Green function. As illustrated in Fig. 1 photoemission is about absorption and emission of single electrons and it is a unique source of information about electronic structure and excitations in materials. We will focus precisely on this observable in the rest of the chapter.
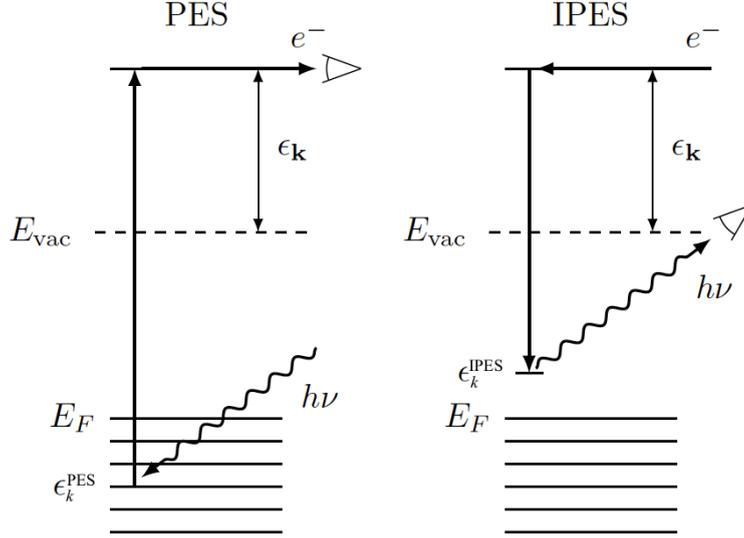
Fig. 1: *Schematic picture of direct (PES) and inverse photoemission spectroscopies (IPSE). In PES (IPES) one samples the occupied (unoccupied) energy levels $\varepsilon_k^{PES} = E_0^N - E_k^{N-1}$ ($\varepsilon_k^{IPES} = E_k^{N+1} - E_0^N$) of the system.*

Let us consider the following many-body Hamiltonian in second quantization

$$\hat{H} = \int d\mathbf{x}\, \hat{\psi}^\dagger(\mathbf{x}) h(\mathbf{r}) \hat{\psi}(\mathbf{x}) + \frac{1}{2} \iint d\mathbf{x} d\mathbf{x}'\, \hat{\psi}^\dagger(\mathbf{x}) \hat{\psi}^\dagger(\mathbf{x}') \hat{\psi}(\mathbf{x}') \hat{\psi}(\mathbf{x}) v_c(\mathbf{x}, \mathbf{x}'), \qquad (1)$$

where $\hat{\psi}$ and $\hat{\psi}^\dagger$ are field operators, v_c is the Coulomb potential, and $h(x) = -\nabla_\mathbf{r}^2/2 + v_{ext}(\mathbf{r})$ is the one-body part of the Hamiltonian, which comprises the kinetic term and a local external potential. At zero temperature the time-ordered equilibrium 1-GF can be written in terms of its Lehmann representation in frequency space as

$$G(\mathbf{x}, \mathbf{x}'; \omega) = \lim_{\eta \to 0^+} \left(\sum_m \frac{B_m^A(\mathbf{x}, \mathbf{x}')}{\omega - (E_m^{N+1} - E_0^N) + i\eta} + \sum_n \frac{B_n^R(\mathbf{x}, \mathbf{x}')}{\omega - (E_0^N - E_n^{N-1}) - i\eta} \right), \qquad (2)$$

where $B_m^A(\mathbf{x}, \mathbf{x}') = \langle \Psi_0^N | \hat{\psi}(\mathbf{x}) | \Psi_m^{N+1} \rangle \langle \Psi_m^{N+1} | \hat{\psi}^\dagger(\mathbf{x}') | \Psi_0^N \rangle$ and $B_n^R(\mathbf{x}, \mathbf{x}') = \langle \Psi_0^N | \hat{\psi}^\dagger(\mathbf{x}') | \Psi_n^{N-1} \rangle \langle \Psi_n^{N-1} | \hat{\psi}(\mathbf{x}) | \Psi_0^N \rangle$, $|\Psi_0^N\rangle$ and E_0 are the many-body ground-state wavefunction and energy of the N-electron system, respectively, and $|\Psi_m^{N\pm1}\rangle$ and $E_m^{N\pm1}$ are the many-body wavefunctions and corresponding energies of the $(N \pm 1)$-electron system. This definition of the 1-GF makes clear its connection to the charged excitations of the system, which are measured in photoemission experiments. It is indeed convenient to define the spectral function in terms of the imaginary part of the 1-GF according to

$$A(\mathbf{x}, \mathbf{x}'; \omega) = \frac{1}{\pi} \text{sign}(\mu - \omega) \, \text{Im}\, G(\mathbf{x}, \mathbf{x}'; \omega)$$

$$= \sum_m B_m^A(\mathbf{x}, \mathbf{x}') \delta\big(\omega - (E_m^{N+1} - E_0^N)\big) + \sum_n B_m^R(\mathbf{x}, \mathbf{x}') \delta\big(\omega - (E_0^N - E_n^{N-1})\big), \quad (3)$$

where μ is the chemical potential. Of course the definition (2) is not very useful for determining the 1-GF, since it relies on the knowledge of many-body wavefunctions, which is precisely what

one wants to avoid when using theories based on simpler physical quantities, such as the 1-GF. Therefore the development of approximate methods to calculate the 1-GF has been an active research topic in many-body physics since the sixties, and many routes have been explored in order to find increasingly accurate GFs. A very popular class of methods is based on the solution of an integral equation for the 1-GF, namely,

$$G(1,2) = G_0(1,2) + G_0(1,3)\Sigma(3,4)G(4,2),\qquad(4)$$

where G_0 is the noninteracting 1-GF and Σ the self-energy. A good starting point to make approximations to the self-energy is to use Hedin's equations, which are often solved within the so-called GW approximation (GWA) to the self-energy [2], where G is the one-particle Green function and W the dynamically screened Coulomb potential. Within this approximation one neglects so-called vertex corrections, which take into account the fermionic nature of the system, and one treats the system and its response classically (besides exchange). This becomes clear by starting from the following exact expression for the self-energy [3,4]

$$\Sigma(11') = v_H(1)\delta(11') + \Sigma_x(11') + iv_c(1^+2)G(13)\Xi(35;1'4)L(42;52^+),\qquad(5)$$

with $v_H(1) = -i \int d2\, v_c(12)G(22^+)$ the Hartree potential, $\Sigma_x(11') = iv_c(1^+1')G(11')$ the exchange contribution to the self-energy, $\Xi(35;1'4) = \frac{\delta\Sigma(31')}{\delta G(45)}$ the effective interaction, and $L(42;52) = \frac{\delta G(45)}{\delta U_{ext}(2)}\Big|_{U_{ext}=0}$ the time-ordered "response" of the system to an external perturbation U_{ext}. This way to write the self-energy directly displays the physics behind it, i.e., the description of a particle interacting with the system: the particle can scatter against the density of the system (Hartree term), it can exchange with another particle of the system (exchange term), it can do something to the system (last term), i.e., it can have an effective interaction with the system (Ξ), the system responds (L), and the particle feels this response through the Coulomb interaction (v_c). There are two crucial ingredients in Eq. (5), namely the response of the system L and the effective interaction Ξ. Combining approximations to these two quantities, various approximations to the self-energy can be created. In situations where the screening is important one can treat L accurately and use a rough approximation to the induced potential Ξ, whereas in situations where the quantum nature of the interaction is important[1] one would concentrate on Ξ, although L and Ξ are of course in principle linked through the Bethe-Salpeter equation [5] and one might wish to keep them approximately consistent.

2.1 GW

Neglecting the variation of $\Sigma_{xc} = \Sigma - v_H$ in Ξ, i.e., keeping only the classical interaction v_c, one obtains $\Sigma_{xc}(11') = \Sigma_x(11') + iv_c(12)G(11')v_c(1'4)\chi(42)$, with $\chi(42) = -iL(42;42)$ the time-ordered response function. Hence one gets a screening contribution with respect to Σ_x: this is the GW form, with $W = v_c + v_c\chi v_c$, which can also be written as $W = v_c + v_c PW$

---

[1]The atomic limit of the Hubbard molecule is an example where the correlation part of the interaction is crucial; see later.
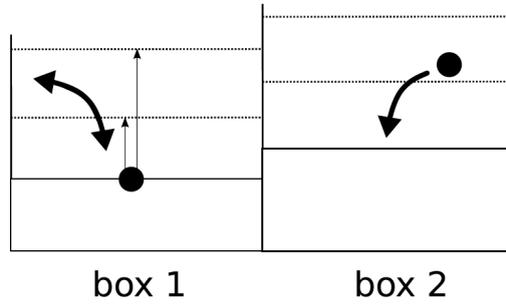
Fig. 2: *Model system for removal and addition energies from Ref. [10]: first an electron is added to/removed from box 1 occupied by zero/one electron; in a second step an electron is added to box 2 in presence of the electron in box 1 (see text).*

with the polarizability $P = \chi(1 + v_c\chi)^{-1}$. At this stage it has not been specified yet how to calculate the screening: different approximations to the screening will give the various GW flavors, e.g. GW^{RPA}, in which $P = -iGG$, and beyond.[2] If one keeps an approximate Σ_{xc} in Ξ, one goes beyond GW and includes so-called vertex corrections. The GW approximation works well for systems where the screening is important; instead in systems which show atomic-like physics, such as transition-metal oxides, the GWA shows difficulties or even failures [3, 7–15]. More accurate approximations are then needed. One way to go beyond the standard methods is to try to correct some basic shortcomings that plague them. Here we will focus on the following two errors GW suffers from:

- **Self-screening error**
  This error [16, 10, 17] can be illustrated by considering an empty box with a potential V_0, as depicted in Fig. 2. The problem of adding a particle to the empty box can be solved exactly by the independent-particle Schrödinger equation

$$\left(-\frac{\nabla^2}{2} + V_0(x_1)\right)\phi_1(x_1) = \varepsilon_1\phi_1(x_1). \tag{6}$$

  The total energy difference between the system with $N = 0$ and $N+1 = 1$ particles is given by the eigenvalue ε_1. This situation is described exactly by the GWA (the same holds for any other commonly used approach, like DFT or Hartree-Fock, since the density of the system is zero). Problems arise when looking at the reverse problem, namely to extract the particle from the box, since now there is a non-vanishing charge density in the box. Again, Eq. (6) correctly describes the total energy difference between $N = 1$ and $N-1 = 0$ particles. Also Hartree-Fock (HF) is exact, as one can easily verify, since there is the exact cancellation between the Hartree and the Fock terms because the density is built with just the state ϕ_1 one is looking at. It then becomes clear that GW does not give the exact result, since the exchange term that in HF cancelled the Hartree self-interaction is now screened, and the cancellation is no longer perfect. If we

---

[2]In this case the nature of the screening is always test-charge-test-charge [6].

had $W = v_c$ (no screening) we would be back to the exact HF result. However, the screening is in general non-zero, since it depends on the density of the system, which is non-zero for a particle in a box. Therefore, it becomes clear that GW *suffers from a self-screening problem*: the particle that is extracted from the system screens itself, which makes the approach non-symmetric with respect to the case where the particle is added to the empty box. In other words, when the quasiparticle eigenvalue is used to represent a total energy difference, the energy of the system has changed after one has first added and then extracted one electron.

- **Atomic limit**:

  Another very important diagnostic tool is the study of the atomic limit. This limit corresponds to pulling apart the atoms of a system, so that the overlap between wavefunctions on different atoms is negligible. In particular H_2^+ and H_2 dissociations have been extensively studied in order to trace errors in the approximations used in DFT and MBPT. The study of the H_2 dissociation within GW shows that this approximation is not size-consistent, i.e., the total energy in the atomic limit is not equal to the sum of the total energies of the two isolated atoms [8, 9]. Also the description of the spectrum can be expected to be problematic, and this can be understood as follows: the GW approximation takes into account only the Hartree, exchange, and induced Hartree potentials to describe an interacting system and its response to an additional electron or hole, i.e., besides exchange it gives a classical description of the system and of its response. This means for the example H_2^+ that an additional electron sees half an electron on each atom at any distance between the two atoms; this results in only one type of addition energy, as we will later show using the Hubbard dimer at 1/4 filling. In reality, instead, one has the same probability of finding the whole electron on one or the other atom, resulting in two types of addition energies depending if the additional electron is added to an empty or to an occupied atom.

2.2 Vertex corrections

We can now formulate vertex corrections with the aim to correct the problems of self-screening and wrong atomic limit that GW suffers from. If one keeps an approximate Σ_{xc} in Ξ of Eq. (5) one goes beyond GW and includes vertex corrections. The question is which approximate Σ_{xc} to consider.

2.2.1 Vertex corrections from DFT

By approximating Σ_{xc} by the exchange-correlation potential of DFT, v_{xc}, one gets the expression $\Sigma_{xc}(1, 1') = \Sigma_x(1, 1') + iv_c(1, 2)G(1, 1')\left[v_c(1', 4) + f_{xc}(1', 4)\right]\chi(4, 2)$, where $f_{xc} = \frac{\delta v_{xc}}{\delta\rho}$; this leads to $\Sigma_{xc} = iG\tilde{W}$, with a modified screened Coulomb interaction $\tilde{W} = v_c + (v_c + f_{xc})\chi v_c$ [6]. This is a test-charge test-electron screened Coulomb interaction (TC-TE) instead of a test-charge test-charge W, and it expresses the fact that an additional particle in the system can-

not be described as a classical charge. This approximate xc self-energy can be rewritten as $\Sigma_{xc} = iGW\Gamma$ with $\Gamma = 1 + f_{xc}P$ a two-point vertex and P the irreducible polarizability.[3] The f_{xc} that appears makes the one-electron case exact, since for this case $f_{xc} = -v_c$ from which $\Sigma_{xc} = iGv_c$, which exactly cancels the Hartree term for one electron. In the simple case of one electron, hence, this simple vertex correction removes the self-screening and yields the exact result for the highest occupied state. It seems reasonable to generalize these intuitive findings to the case of more bands. In fact, we know that the KS potential yields often a quite good description for all valence bands, not only the highest occupied one. In these cases one should expect that the test-charge test-electron approximation for the self-energy derived above is the method of choice to describe valence bands. Of course, the exact KS potential and kernel are not known, but one might use LDA as a first approximation. For conduction states that are spatially distinct from valence states or with different spin, which are modelled by a second electron added to a second separate box in Fig. 2, one can argue that one should rather use GW [10]. The effectiveness of this approach has yet to be investigated and it is an interesting outlook. Preliminary results on silicon indicate that this kind of vertex corrections appear to affect just the quasiparticle energies [18].

### 2.2.2 Vertex corrections from the T-matrix approximation

As we will show using the Hubbard dimer, the vertex corrections which cure the self-screening problem are not sufficient to improve the description of the atomic limit, precisely because the two problems have a different nature; therefore, a more complex vertex is needed to fix both. For the spectral function in the atomic limit what matters is that the electron in the system and the electron added to the system "see" each other. In other words it is the quantum nature of the electron interaction that is important. Starting from the exact expression for the self-energy, Eq. (5), one could use the rough approximation $L(4, 2; 5, 2) \simeq L_0(4, 2; 5, 2)$ for the response of the system but concentrate on a clever approximation for Ξ. To this end one can introduce an effective 4-point interaction T such that, similar to GW, $\Sigma(1, 1') = iG(4', 2')\, T(1, 2'; 1', 4')$. T is linked to Ξ through the functional derivative of the self-energy as $\Xi(3, 5; 1', 4) = iT(3, 5; 1', 4) + iG(4, 2)\frac{\delta T(3, 2; 1', 4)}{\delta G(4, 5)}$. Neglecting $\frac{\delta T(3, 2; 1', 4)}{\delta G(4, 5)}$, in analogy with what one usually does in the framework of Bethe-Salpeter calculations based on GW [19–21], Eq. (5) becomes an integral equation for GT

$$\Sigma(1, 1') = iG(4', 2')\, T(1, 2'; 1', 4')$$
$$= v_H(1)\, \delta(11') + \Sigma_x(11') - v_c(12)\, G(1, 3)\, G(42)\, G(25)\, T(3, 5; 1', 4). \tag{7}$$

Since $G(4', 2')\, T(1, 2'; 1', 4')$ cannot be inverted to find T, several choices of T make the correct Σ. A possible solution is

$$T^{pp}(1, 2; 1', 4) = - v_c(1, 2)\, \delta(1, 1')\, \delta(4, 2) + v_c(1, 2)\, \delta(2, 1')\, \delta(4, 1)$$
$$+ iv_c(1, 2\, G(1, 3)\, G(2, 5)\, T^{pp}(3, 5; 1', 4), \tag{8}$$

---

[3]This can be obtained by considering that $W = v_c + v_c\chi v_c$ and $\chi v_c = PW$.
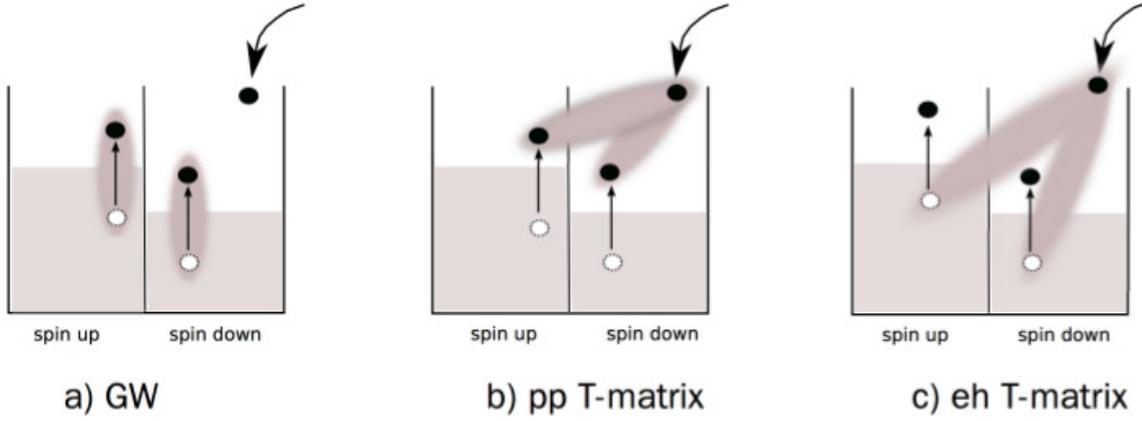
Fig. 3: *Schematic representation of the physical contents of GW (a), pp T-matrix (b), and eh T-matrix for particles with collinear spins from Ref. [3].*

which defines the particle-particle (because the kernel $G(1,3) G(2,5)$ in the correlation part describe two propagating electrons or holes) T-matrix [22, 23]. One can, moreover, decompose T^{pp} into a direct term (Hartree-like contribution) $T_1^{pp} = -v_c + iv_c G G T_1^{pp}$ and an exchange term (exchange-like contribution) $T_2^{pp} = v_c + iv_c G G T_2^{pp}$. Another possible solution of Eq. (7) is the electron-hole T-matrix, defined as

$$T^{eh}(1, 5; 1', 2) = - v_c(1', 2)\, \delta(1, 1')\, \delta(5, 2) + v_c(1', 2)\, \delta(1, 2)\, \delta(1', 5)$$
$$+ iv_c(1, 2)\, G(1, 3)\, G(4, 2)\, T^{eh}(3, 5; 1', 4), \tag{9}$$

where now the kernel $G(1,3) G(4,2)$ in the correlation part describes an electron and a hole. The structure of the T-matrix self-energy is hence very close to the structure of GW: one has a "particle-particle-screened" interaction T (or an "electron-hole-screened" interaction T in case of the electron-hole T-matrix, but where the electron-hole excitations involved are different by those involved in GW (see Fig. 3)). Based on (5), we can now directly compare the different approximations. Both GW and T-matrix allow one to describe physical processes involving three particles: the particle which is added to the system and the electron-hole pair that it creates. Ideally, one would propagate the three particles together, which can be numerically heavy. Therefore one chooses to propagate a pair and to treat the third particle in a kind of mean-field of the other two. This is illustrated in Fig. (3): in GW one propagates together the electron-hole pair created by the additional particle, whereas in the T-matrix one propagates together the additional electron (additional hole) and the excited electron (hole left behind) (pp T-matrix) or the additional electron (additional hole) and the hole left behind in the electron excitation (excited electron) (eh T-matrix).

As shown in Fig. 3 the additional particle with a given spin couples with a second, excited, particle (electron or hole) that can have spin up or down. In the GWA, electron and hole have necessarily the same spin. The T-matrix approximation contains instead also spin-flips.

In general none of the three possibilities (GWA, particle-particle or electron-hole T-matrix) will give an exhaustive description. This reflects the dilemma of how to decide which two-particle
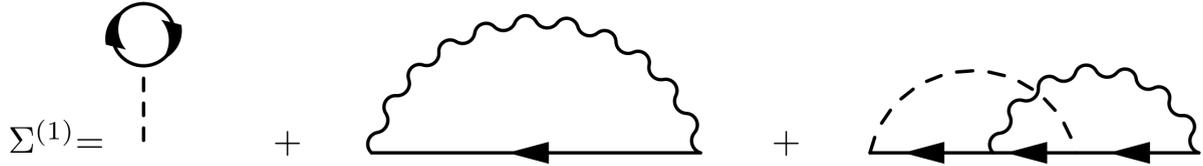
Fig. 4: *Diagrams corresponding to the self-energy obtained with the first iteration of the screened T-matrix. The diagrams, from left to right, represent the Hartree, GW, and second-order screened exchange (SOSEX) terms, respectively.*

correlation to privilege in the description of a (at least) three-particle problem. It suggests to work with combinations.

The success of the GWA is due to the screening of the Coulomb interaction with respect to Hartree-Fock. In the T-matrix one uses a rough approximation for the screening, i.e. $L \approx L_0$. One can go beyond this approximation and include the Hartree potential or even a local part of the xc self-energy, $\Sigma_{xc}^{loc}(1)\,\delta(1,1)$, in the variation $\delta G^{-1}/\delta U_{ext}$ contained in $L = \delta G/\delta U_{ext} = -G\left(\delta G^{-1}/\delta U_{ext}\right)G$. This yields $L(4,2;5,2) \simeq G(4,7)\,\varepsilon^{-1}(7,2)\,G(7,5)$ where ε^{-1} is a test-charge test-charge screening function $\varepsilon^{-1} = 1 + v_c\chi$ if only the Hartree part is included, otherwise at least a partially test-charge test-electron screening $\varepsilon^{-1} = 1 + \left(v_c + \frac{\delta\Sigma_{xc}^{loc}}{\delta\rho}\right)\chi$ [6]. This makes the expression much more, though not fully, consistent: now ε^{-1} contains a large part of the derivative of the self-energy, that is also considered in the effective interaction, and L contains the screening of the formerly independent propagators GG, that is itself based on the two-particle correlation function. One arrives then at a screened version of the T-matrix (referred to as T_s in the following), where the bare Coulomb potential in the correlation part of the (unscreened) T-matrix is replaced by the screened one. The pp screened T-matrix reads

$$
\begin{aligned}
T_s(1,2;1',4) = &- v_c(1,2)\,\delta(1,1')\,\delta(4,2) + v_c(1,2)\,\delta(2,1')\,\delta(4,1) \\
&+ iW(1,2)\,G(1,3)\,G(2,5)\,T_s(3,5;1',4).
\end{aligned}
\tag{10}
$$

One can write a similar equation also for the eh screened T-matrix. The first iteration of the pp and eh screened T-matrix equations produces the same self-energy, which contains the Hartree and GW contributions, and a term corresponding to the second-order screened exchange (SOSEX) (see Fig. 4). We hence can conclude that GW is contained in this screened T-matrix approach, which moreover contains higher-order terms, which can be identified as vertex corrections. For short-range interactions, where screening is not important, the screened T-matrix reduces to the T-matrix, which is suitable for treating short-range correlation. For long-range interaction, where, instead, screening is important, we find that the screened T-matrix behaves more like GW (in its first iteration, indeed, it gives GW and SOSEX, which is actually already used to improve GW), which is capable of taking into account long-range correlation. Therefore the screened T-matrix should be able to capture the physics of systems with effective short-range interactions as well as of systems with effective long-range interactions.

3 The Hubbard dimer

The Hubbard Hamiltonian can be obtained from the many-body Hamiltonian in (1) in which the field operators are expressed in the atomic basis (we will consider only one basis function per atom). Retaining only the diagonal elements of the Coulomb interaction (indicated as U) and indicating as $-t$ and ε_0 the off-diagonal and diagonal elements, respectively, of the kinetic energy operator, one arrives at

$$\hat{H} = -t \sum_{\langle i,j \rangle} \sum_{\sigma} \hat{c}_{i\sigma}^{\dagger} \hat{c}_{j\sigma} + U \sum_{i} \hat{c}_{i\uparrow}^{\dagger} \hat{c}_{i\uparrow} \hat{c}_{i\downarrow}^{\dagger} \hat{c}_{i\downarrow} + \varepsilon_0 \sum_{i} \sum_{\sigma} \hat{c}_{i\sigma}^{\dagger} \hat{c}_{i\sigma} + \hat{V}_0 \,. \tag{11}$$

Here $c_{i\sigma}^{\dagger}$ and $c_{i\sigma}$ are the creation and annihilation operators for an electron at site (atomic position) i with spin σ, while U is the on-site (spin-independent) interaction, $-t$ is the hopping energy, and ε_0 the orbital energy. The summation $\sum_{\langle i,j \rangle}$ is restricted to the nearest-neighbor sites. The Hamiltonian further contains a potential V_0 that can be chosen to fix the zero-energy scale. The model does not contain a long-range interaction, hence everything linked to non-locality is not treated, but we can suppose that these kind of issues are well treated by Hartree-Fock, GW, etc. Moreover, to keep the discussion simple, we will consider only sites that have the same energy, thus neglecting any inhomogeneity which can mimic the role of the crystal potential in a solid [24]. The physics of the Hubbard model arises from the competition between the hopping term, which prefers to delocalize electrons, and the on-site interaction, which favors localization. The ratio U/t is a measure for the relative contribution of both terms and is the intrinsic, dimensionless coupling constant of the Hubbard model. Depending on this ratio the system is a metal or an insulator.

This model can be solved exactly for small clusters. In the following we will consider a "molecule" made up of two equivalent sites, each with one orbital. We will look at the one- and two-electron cases (quarter and half filling, respectively) in order to cover a wide physics.

3.1 Exact solution

In order to calculate the exact 1-GF for the Hubbard dimer we start from its Lehmann representation (2) and we project it onto the (orthonormal) one-electron site basis $\{\varphi_i(x)\}$, such that[4] $G(x_1, x_2; \omega) = \sum_{ij} G_{ij}(\omega) \varphi_i(x_1) \varphi_j^*(x_2)$ and

$$G_{ij\sigma}(\omega) = \lim_{\eta \to 0^+} \left(\sum_m \frac{\langle \Psi_0^N | \hat{c}_i | \Psi_m^{N+1} \rangle \langle \Psi_m^{N+1} | \hat{c}_j^{\dagger} | \Psi_0^N \rangle}{\omega - (E_m^{N+1} - E_0^N) + i\eta} + \sum_n \frac{\langle \Psi_0^N | \hat{c}_j^{\dagger} | \Psi_n^{N-1} \rangle \langle \Psi_n^{N-1} | \hat{c}_i | \Psi_0^N \rangle}{\omega - (E_0^N - E_n^{N-1}) - i\eta} \right), \tag{12}$$

with the indices i, j running over the sites. The ground-state wavefunction and energy $|\Psi_0^N\rangle$ and E_0^N of the N-electron system as well as the wavefunctions and energies $|\Psi_m^{N\pm1}\rangle$ and $E_m^{N\pm1}$ of

---

[4]This expression for the 1-GF comes naturally by using the following basis transformation for the field operators: $\hat{\psi}(\mathbf{x}) = \sum_i \hat{c}_i \varphi_i(\mathbf{x})$ and $\hat{\psi}^{\dagger}(\mathbf{x}) = \sum_i \hat{c}_i^{\dagger} \varphi_i^*(\mathbf{x})$, where $\hat{c}_i$ and $\hat{c}_i^{\dagger}$ are annihilation and creation operators, respectively.

the $(N\pm 1)$-electron system can be obtained by diagonalizing the Hamiltonian for $N-1$, N, and $N+1$ electrons, separately (as shown in Appendix A).

3.1.1 $N = 1$

- **One site**

  In the limit $t \to 0$ the two-site Hubbard model should represent two isolated atoms [25, 26]. In order to compare this limiting case with the solution of an isolated atom, we calculate the exact 1-GF for the case of a one-site Hubbard model with one electron. We choose as ground state the spin-up configuration $|\uparrow\rangle$ which has energy ε_0 (equivalently, the spin-down configuration could be chosen). There is only one state with $N-1 = 0$ electrons, i.e., the vacuum $|\ \rangle$ with energy 0, and only one state with $N+1 = 2$ electrons, i.e., $|\uparrow\downarrow\rangle$ with energy $\varepsilon_0 + U$. Moreover, note that, since we consider a spin-independent Hamiltonian, the 1-GF in (12) is diagonal in spin. Therefore the exact one-particle Green function reads

$$G^\uparrow = \frac{1}{\omega - \varepsilon_0 - i\eta}, \qquad G^\downarrow = \frac{1}{\omega - U - \varepsilon_0 + i\eta}. \tag{13}$$

  There is only a removal energy, $\omega = \varepsilon_0$, and an addition energy, $\omega = \varepsilon_0 + U$, for this system. Note that by taking $U = 0$ in (13) one gets the non-interacting G_0.

  The exact self-energy can be obtained from the Dyson equation $\Sigma(\omega)=G_0^{-1}(\omega)-G^{-1}(\omega)$

$$\Sigma(\omega) = \begin{pmatrix} 0 & 0 \\ 0 & U \end{pmatrix}, \tag{14}$$

  which reflects the fact that the electron in the ground-state can interact only with an additional spin-down electron.

- **Two sites**

  Using the information in Tables 1-2 of the Appendix A we can build the 1-GF at quarter filling. The 1-GF has the following structure

$$G(\omega) = \begin{pmatrix} G^\uparrow_{11} & G^\uparrow_{12} & 0 & 0 \\ G^\uparrow_{21\uparrow} & G^\uparrow_{22} & 0 & 0 \\ 0 & 0 & G^\downarrow_{11} & G^\downarrow_{12} \\ 0 & 0 & G^\downarrow_{21} & G^\downarrow_{22} \end{pmatrix}. \tag{15}$$

  with

$$G^\uparrow_{ij}(\omega) = \frac{(-1)^{i-j}}{2}\left(\frac{1}{\omega - (\varepsilon_0 + t) + i\eta} + \frac{(-1)^{i-j}}{\omega - (\varepsilon_0 - t) - i\eta} \right), \tag{16}$$

  and
$$G^\downarrow_{ij}(\omega) = \frac{(-1)^{i-j}}{4}\left(\frac{1}{\omega - (\varepsilon_0 + t) + i\eta} + \frac{1}{\omega - (\varepsilon_0 + t + U) + i\eta} \right)$$
$$+ \frac{1}{2}\left(\frac{\frac{1}{a^2}\left(1 + \frac{4t}{(c-U)}\right)^2}{\omega - \left(\varepsilon_0 + t - \frac{c-U}{2}\right) + i\eta} + \frac{\frac{1}{b^2}\left(1 - \frac{4t}{(c+U)}\right)^2}{\omega - \left(\varepsilon_0 + t + \frac{c+U}{2}\right) + i\eta} \right), \tag{17}$$

where $c = \sqrt{16t^2 + U^2}$, $a = \sqrt{2\left(\frac{16t^2}{(c-U)^2} + 1\right)}$, and $b = \sqrt{2\left(\frac{16t^2}{(c+U)^2} + 1\right)}$. The one-particle Green function is spin-diagonal; the spin-down block has only the electron part, whereas the spin-up block has both electron and hole parts. This is consistent with the fact that with a spin-up electron in the ground state one can have only spin-up holes. Note also that $G_{11\uparrow} = G_{11\uparrow}^{U=0}$ and $G_{12\uparrow} = G_{12\uparrow}^{U=0}$, whereas

$$G_{ij\downarrow}^{U=0}(\omega) = \frac{(-1)^{i-j}}{2}\left(\frac{1}{\omega - (\varepsilon_0 + t) + i\eta} + \frac{(-1)^{i-j}}{\omega - (\varepsilon_0 - t) + i\eta}\right). \qquad (18)$$

One can interpret the poles of the Green function using a simple molecular picture with the energies of the bonding and antibonding orbitals at $\varepsilon_0 - t$ and $\varepsilon_0 + t$, respectively, and with the spin-up electron in the bonding orbital. If $U = 0$ one can remove (add) a spin-up (spin-down) electron from (to) the bonding orbital ($\omega = \varepsilon_0 - t$), and one can add a spin-up/spin-down electron to the antibonding orbital ($\omega = \varepsilon_0 + t$). When the on-site electron-electron interaction U is switched on, the energy for the addition of a spin-down electron to the bonding state evolves to $\omega = \varepsilon_0 + t + (U - c)/2$, and the addition energy to the antibonding state is split into $\omega = \varepsilon_0 + t$ and $\omega = \varepsilon_0 + t + U$. The addition of a spin-down electron, furthermore, can excite the system, giving rise to the satellite $\omega = \varepsilon_0 + t + (U + c)/2$.

We now discuss two limiting cases, which are directly related to the importance of correlation: the noninteracting limit and the atomic limit.

– **noninteracting limit: $U \to 0$**

Of course in this limit one retrieves the noninteracting Green function. The spectral weight of the pole $\omega = \varepsilon_0 + t + (c + U)/2$, which becomes $\omega = \varepsilon_0 + 3t$, is suppressed. Note that $\omega = \varepsilon_0 + 3t$ deviates from the antibonding peak by an energy $\Delta = 2t$, which is a pole of the polarizability P (as shown later in Eq. (22)): this pole of the Green function involves hence an excitation of the system, which justifies the identification of the related peak as a satellite.

– **atomic limit: $t \to 0$**

We first notice that for $t = 0$ the ground state energy goes to $E_0 = \varepsilon_0$ so that it approaches degeneracy with the other doublet state in the $N = 1$ spin-up subspace (see Table 1 in Appendix A). However for any small but finite t this degeneracy is lifted. In this limit the poles of the Green function reduce to the addition and removal energies of two isolated atoms, one with one electron and the other one empty [25, 26]. Indeed the spin-up poles retain the same equal weight ($\pm 1/2$) and go towards $\omega = \varepsilon_0$, which can be interpreted as the removal energy of an atom with a spin-up electron and the addition energy of an empty atom, respectively. The spin-down poles $\omega = \varepsilon_0 + t$ and $\omega = \varepsilon_0 + t - (c - U)/2$, and $\omega = \varepsilon_0 + t + U$ and $\omega = \varepsilon_0 + t + (c + U)/2$ (satellite) merge at $\omega = \varepsilon_0$ and $\omega = \varepsilon_0 + U$, respectively, all with equal weight ($\pm 1/4$) (see Appendix A). These two energies can be interpreted

as the energy for the addition of a spin-down electron to an empty atom and to an atom with a spin-up electron, respectively.

The self-energy $\Sigma(\omega) = G_0^{-1}(\omega) - G^{-1}(\omega)$, has the following structure

$$
\Sigma(\omega) = \begin{pmatrix} 0 & 0 & 0 & 0 \\ 0 & 0 & 0 & 0 \\ 0 & 0 & \Sigma_{11}^{\downarrow} & \Sigma_{12}^{\downarrow} \\ 0 & 0 & \Sigma_{12}^{\downarrow} & \Sigma_{11}^{\downarrow} \end{pmatrix}. \tag{19}
$$

The self-energy has only a spin-down part, i.e., the electron in the system interacts only with spin-down electrons. This is in line with the fact that our system consists of one electron with spin up. When we add a second electron to the system, it can have spin up or spin down. If the second electron has spin up, the two electrons are locked in a configuration where two different sites are occupied, and therefore there is no interaction. If the second electron has spin down, the two electrons can interact.

3.1.2 $N = 2$

Using the information in Tables 1-3 of the Appendix A we can build the 1-GF at half filling. It has the structure given in Eq. (15), with the components gives by

$$
G_{ij}^{\sigma}(\omega) = \frac{(-1)^{i-j}}{2a^2} \left(\frac{\left(1 + 4t/(c-U)\right)^2}{\omega - \left(\varepsilon_0 - t + (c+U)/2\right) + i\eta} + \frac{(-1)^{i-j}\left(1 - 4t/(c-U)\right)^2}{\omega - \left(\varepsilon_0 + t + (c+U)/2\right) + i\eta} \right)
$$
$$
+ \frac{1}{2a^2} \left(\frac{\left(1 + 4t/(c-U)\right)^2}{\omega - \left(\varepsilon_0 + t - (c-U)/2\right) - i\eta} + \frac{(-1)^{i-j}\left(1 - 4t/(c-U)\right)^2}{\omega - \left(\varepsilon_0 - t - (c-U)/2\right) - i\eta} \right), \tag{20}
$$

which enjoys a nice spin symmetry $G_{ij}^{\uparrow} = G_{ij}^{\downarrow}$. We can now study the limits $U \to 0$ and $t \to 0$.

- **noninteracting limit: $U \to 0$**

  In this limit the ground state becomes $|\Psi_0\rangle = \frac{1}{2}\big(|\uparrow, \downarrow\rangle - |\downarrow, \uparrow\rangle + |\uparrow\downarrow, \cdot\rangle + |\cdot, \uparrow\downarrow\rangle\big)$ (where $|1, 2\rangle$, with occupations of the sites 1, 2 given by $\cdot, \uparrow, \downarrow, \uparrow\downarrow$ indicate Slater determinants) with energy $E_0 = 2(\varepsilon_0 - t)$, and the one-particle Green function reduces to the noninteracting one

  $$
  G_{ij\sigma}^{U=0}(\omega) = \frac{(-1)^{i-j}}{2} \left(\frac{1}{\omega - (\varepsilon_0 + t) + i\eta} + \frac{(-1)^{i-j}}{\omega - (\varepsilon_0 - t) - i\eta} \right). \tag{21}
  $$

  Note that this is the same as the one for the spin-up block of the one-electron case.

- **atomic limit: $t \to 0$**

  In the atomic limit there are no double occupancies (Heitler-London limit), therefore the two electrons, one with spin up and the other with spin down, are localized one on one site and the other on the other site with equal probability, i.e. the ground state is the singlet $|\Psi_0\rangle = \frac{1}{\sqrt{2}}\big(|\uparrow, \downarrow\rangle - |\downarrow, \uparrow\rangle\big)$. The spectral function thus shows, for each spin, two peaks

with the same spectral weight (1/2), one for the removal of an electron (peak at ε_0), and one for the addition of a second electron (peak at $\varepsilon_0 + U$), which represents the removal and addition energies, respectively, of an isolate atom with one electron.

As far as the self-energy is concerned, unlike for the case at half filling, it has a spin-up and spin-down block, with the two blocks being the same. This again reflects the fact that the system is symmetric with respect to spin.

3.2   GW

The GW equations, as well as all the other approximations to the self-energy, should, in principle, be solved self-consistently, since the self-energy is a functional of the one-body Green function. In this chapter, however, we will not use self-consistency. In particular for GW we will use G_0 to build W and Σ: $\Sigma = v_H + iG_0W_0$, with $v_H = -iv_cG_0$ and $W_0 = [1 + iv_cG_0G_0]^{-1}v_c$. This approach is called G_0W_0 or one-shot GW, and it is often used in practice (although one uses a G_0 that already contains part of the interaction through a suitable single-particle Hamiltonian, like KS, HF, or quasiparticle self-consistent GW), since a fully self-consistent procedure is computationally demanding, especially for large systems. Besides this, it is important to stress that the failures of GW we discuss in this chapter are not solved by self-consistency since they are rooted in the fundamental structure of the GW approximation.

3.2.1 $N = 1$

- **One site**
  The RPA polarizability $P(\omega) = -i \int \frac{d\omega'}{2\pi} G(\omega + \omega') G(\omega')$ is zero, consistent with the fact that the system has only one state (the site orbital) in which it could be excited, which would however require a spin-flip, which is not allowed. Therefore there is no response of the system, and thus the screened potential equals the bare Coulomb potential, $W = U$. The GW self-energy, therefore, is equal to the exact one, and, consequently, also the Green function. Therefore, together with the fact that GW is also exact for the empty atom, for two separate one-site Hubbard models the GWA yields the exact solution, contrary to the $t \to 0$ limit of the two sites, as we will show in the following. This shows again the relation of the GWA to the classical description of the system charge: for the one-site Hubbard model, where the electron is well confined, the classical description of the system works well (i.e. one knows where the electron is). For the two-site Hubbard model, where, instead, the electron shows its quantum nature, this classical picture fails. This is in line with the size-consistency problem GW suffers from [8, 9] and it is analogous to what is observed in DFT [27].

- **Two sites**
  The RPA polarizability $P = -iGG$ is given by

$$P_{ij}^{\uparrow}(\omega) = \frac{(-1)^{i-j}}{4} \left(\frac{1}{\omega - 2t + i\eta} - \frac{1}{\omega + 2t - i\eta} \right). \tag{22}$$

Note that, since we have only one electron with spin up in the ground state the polarizability is not zero only for the spin-up block. Moreover the same result is obtained whether the noninteracting or exact G is used, since they are equal for the spin-up block. The RPA screened interaction $W(\omega) = \left(1 - U P(\omega)\right)^{-1} U$ becomes

$$W_{ij}(\omega) = U\delta_{ij} + (-1)^{i-j}\frac{U^2 t}{\omega^2 - h^2}\,, \tag{23}$$

with $h^2 = 4t^2 + 2Ut$. The self-energy $\Sigma(\omega) = v_H + \frac{i}{2\pi}\int d\omega' G(\omega+\omega')\,W(\omega')e^{i\omega'\eta}$, has the following structure,

$$\Sigma(\omega) = \begin{pmatrix} \Sigma_{11\uparrow} & \Sigma_{12\uparrow} & 0 & 0 \\ \Sigma_{12\uparrow} & \Sigma_{11\uparrow} & 0 & 0 \\ 0 & 0 & \Sigma_{11\downarrow} & \Sigma_{12\downarrow} \\ 0 & 0 & \Sigma_{12\downarrow} & \Sigma_{22\downarrow} \end{pmatrix}. \tag{24}$$

A striking difference with respect to the exact self-energy in Eq. (19) is the nonzero elements of the spin-up block. Moreover, since $G_\uparrow = G_{0\uparrow}$, G_0W_0, G_0W, GW_0, and GW (with G the exact Green function) give the same expression for the spin-up self-energy. As we will discuss in the following this is a direct consequence of the self-screening error in the GWA.

The 1-GF can be obtained from

$$G^{GW}(\omega) = \left(G_0^{-1}(\omega) - \Sigma(\omega)\right)^{-1}. \tag{25}$$

It reads

$$G_{ij\uparrow}^{GW}(\omega) = (-1)^{i-j}\left(\frac{\frac{1}{4}+\frac{2t+h}{4A}}{\omega-\omega_1^+ +i\eta} + \frac{\frac{1}{4}-\frac{2t+h}{4A}}{\omega-\omega_1^- -i\eta}\right) + \frac{\frac{1}{4}-\frac{2t+h}{4A}}{\omega-\omega_2^+ +i\eta} + \frac{\frac{1}{4}+\frac{2t+h}{4A}}{\omega-\omega_2^- -i\eta}\,, \tag{26}$$

$$G_{ij\downarrow}^{GW}(\omega) = (-1)^{i-j}\left(\frac{\frac{1}{4}+\frac{2t-h+U/2}{4B}}{\omega-\omega_3^+ +i\eta} + \frac{\frac{1}{4}-\frac{2t-h+U/2}{4B}}{\omega-\omega_3^- +i\eta}\right) + \frac{\frac{1}{4}-\frac{2t+h-U/2}{4C}}{\omega-\omega_4^+ +i\eta} + \frac{\frac{1}{4}+\frac{2t+h-U/2}{4C}}{\omega-\omega_4^- +i\eta}\,, \tag{27}$$

where

$$A = \sqrt{\left(h+2t\right)^2+\frac{2U^2t}{h}}\,, \quad B = \sqrt{\left(h-2t-\frac{U}{2}\right)^2+\frac{2U^2t}{h}}\,, \quad C = \sqrt{\left(h+2t-\frac{U}{2}\right)^2+\frac{2U^2t}{h}}$$

and the poles are at

$$\omega_1^{+/-} = \left(2\varepsilon_0 - h \pm A\right)/2\,, \qquad\qquad \omega_2^{+/-} = \left(2\varepsilon_0 + h \pm A\right)/2\,,$$
$$\omega_3^{+/-} = \left(2\varepsilon_0 + h + U/2 \pm B/2\right)\,, \qquad \omega_4^{+/-} = \left(2\varepsilon_0 + h + U/2 \pm C\right)/2\,.$$

We can now study the noninteracting limit and the atomic limit.
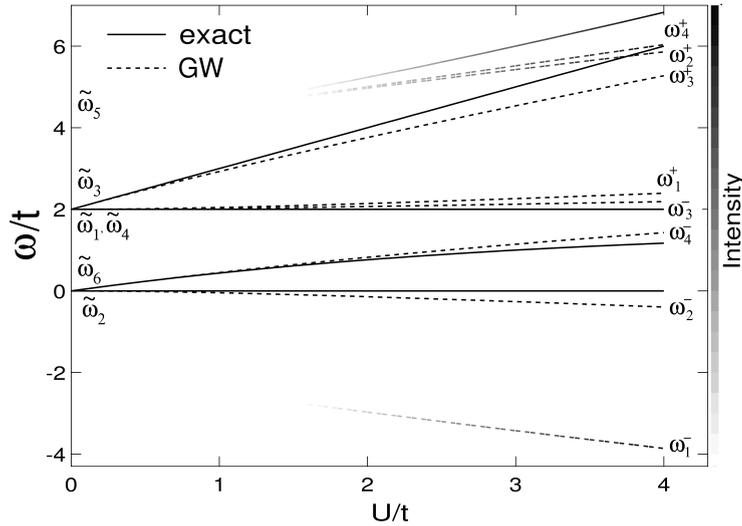
Fig. 5: *Two-site Hubbard model at quarter filling from Ref. [10]: comparison between exact (solid lines) and GW (dashed lines) renormalized excitation energies ω/t as function of U/t, with $\varepsilon_0 = t = 1$ eV. The thin lines represent weak satellites, which appear with increasing interaction U. The labels on the left of the figure refer to the exact energies, with $\tilde{\omega}_1 = \tilde{\omega}_4 = \varepsilon_0 + t$, $\tilde{\omega}_2 = \varepsilon_0 - t$, $\tilde{\omega}_3 = \varepsilon_0 + t + U$, $\tilde{\omega}_5 = \varepsilon_0 + t + U/2 + c/2$, and $\tilde{\omega}_6 = \varepsilon_0 + t + U/2 - c/2$, whereas the labels on the right refer to the GW energies.*

- **noninteracting limit: $U \to 0$**

  In this limit the interacting GW Green function reduces of course to the noninteracting one, with the poles ω_1^+, ω_2^-, ω_3^+, ω_3^-, and ω_4^- collapsing to the bonding and antibonding energies $\omega = \varepsilon_0 - t$ and $\omega = \varepsilon_0 + t$, respectively. The poles ω_1^-, ω_2^+, and ω_4^+, instead, collapse to $\omega = \varepsilon_0 - 3t$ and $\omega = \varepsilon_0 + 3t$ with zero intensity. Note also that the energies $\omega = \varepsilon_0 - 3t$ and $\omega = \varepsilon_0 + 3t$ deviate from the bonding and antibonding peaks, respectively, by $\pm 2t$, which are the poles of the RPA polarizability P. This means that these energies arise from excitations of the system. The poles ω_1^-, ω_2^+, and ω_4^+ can be, therefore, identified as satellites.

- **atomic limit: $t \to 0$**

  In this limit all the spin-up poles acquire an equal weight ($\pm 1/4$) and go towards $\omega = \varepsilon_0$, in agreement with the exact solution. The unphysical poles, and hence the self-screening problem, cannot be detected in the atomic limit because the excitation energy $2t \to 0$. The spin-down poles ω_3^+ and ω_4^+ (satellite) go towards $\omega = \varepsilon_0 + \frac{U}{2}$, each with weight ($\pm 1/2$), whereas ω_3^- and ω_4^- merge at $\omega = \varepsilon_0$ with zero weight. This is in contrast with the exact solution where the four poles go towards $\omega = \varepsilon_0$ and $\omega = \varepsilon_0 + U$ with equal weight ($\pm 1/4$). The error stems from the fact that the GW self-energy is static in this limit (it consists of the Hartree potential $U/2$ only for the spin-down block). The exact atomic-limit self-energy, instead, has an extra term that is frequency-dependent, namely

  $$\Sigma_{ij}^{\downarrow}(\omega) = \delta_{ij} \frac{U}{2} \left(1 + \frac{U}{2(\omega - \varepsilon_0) - U + i\eta} \right).$$
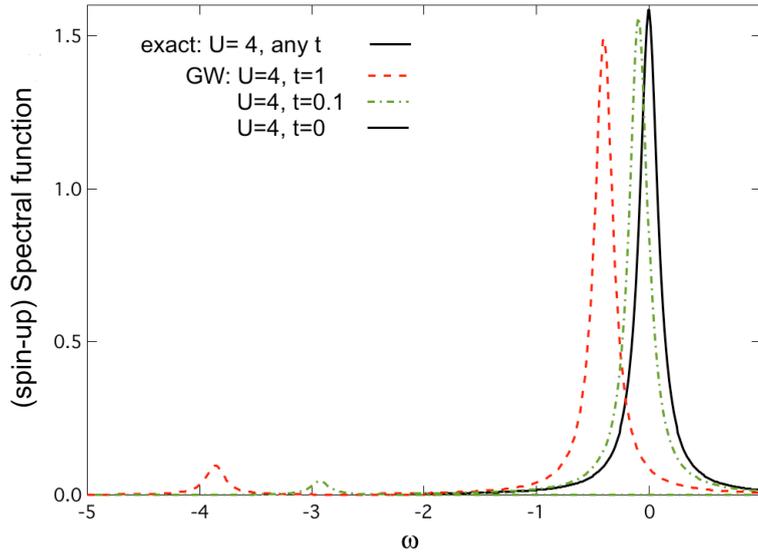
Fig. 6: *Two-site Hubbard model at quarter filling: comparison between exact (black continuous line) and GW (red dashed, green dash-dotted, and black continuous lines for $t = 1$, 0.1, and 0, respectively) spectral function (removal part) at $U = 4$ and $\varepsilon_0 = t$.*

This self-energy shows, in addition to the Hartree potential, a frequency-dependent term that creates the extra pole $\omega = \varepsilon_0 + U$ besides the only pole $\omega = \varepsilon_0$ of the noninteracting Green function (for $t \to 0$). The appearance of the peak $\omega = \varepsilon_0 + U$ is an effect of "strong correlation". One can understand that the problems of GW in the atomic limit arise from the interpretation of the charge density: in GW, it is treated as a classical charge distribution, namely half an electron on each atom in the limit $t \to 0$, that responds to the additional electron or hole. Instead, it should rather express the probability for an electron to be on one or the other atom, so that the additional electron can meet an empty or occupied atom with equal probability, which leads to the peak splitting.

In Fig. 5 we compare the GW and exact addition/removal energies. The GW approximation yields two satellites more than the exact solution, namely, ω_1^- and ω_2^+. These satellites come from the poles of the spin-up Green function and are produced by the frequency-dependent spin-up self-energy. This is a consequence of the self-screening problem the GWA suffers from. The direct consequences of the self-screening error on photoemission spectra are illustrated in Fig. 6, where we reported the spectral function $A(\omega)$ for the spin-up channel. We see that the exact result shows only one peak, which corresponds to the site energy ε_0, whereas the GW approximation gives in general spurious peaks at any value of the hopping, except at $t = 0$. This is due to the fact that one and the same electron can be used twice; for example, once to be removed, and at the same time to screen this perturbation. At $t = 0$, instead, the electron does not hop between the two sites, therefore there is no screening in the system, $W = v_c$ and we retrieve the HF exact result. The spectral function for the spin-down channel at quarter filling is reported
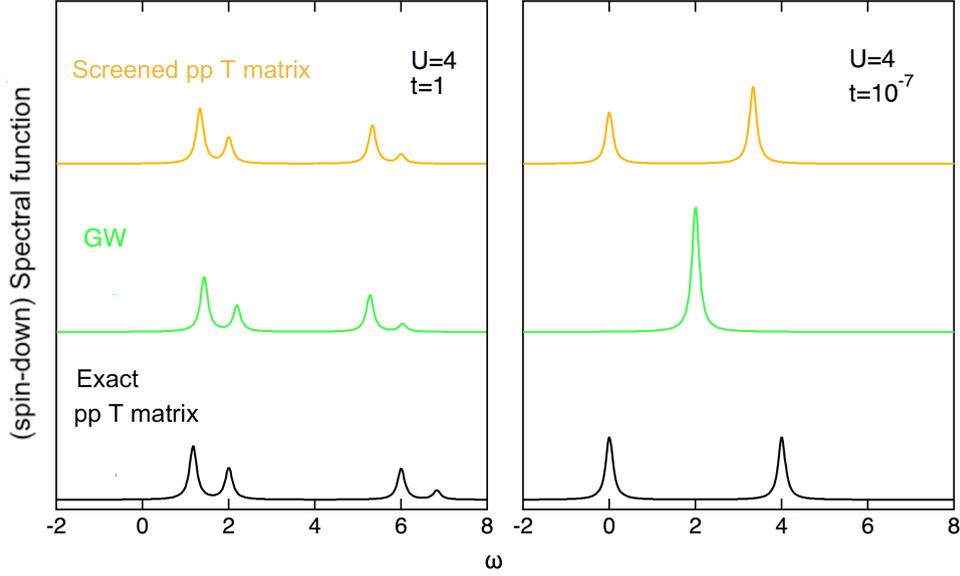
Fig. 7: *Spectral function at quarter filling: exact (lower panel) vs. GW (middle panel), pp T-matrix, and screened pp T-matrix (upper panel).*

in Fig. 7. The GWA produces a spectral function profile in good agreement with the exact one at moderately strong interaction U/t (middle left panel). In the atomic limit (middle right panel), instead, GW produces only one peak.

The inclusion of an explicit vertex in the self-energy, namely a two-point $\Gamma = \delta + f_{xc}P$ for valence bands and, e.g., $\Gamma = \delta$ for the well separated conduction bands, removes by construction the self-screening error for the one-electron case. Indeed, using this vertex it is clear that the self-energy remains unchanged for the spin-down block, whereas for the spin-up block $\Sigma_{xc} = -v_H$. Therefore, we arrive at

$$\Sigma(\omega) = \begin{pmatrix} 0 & 0 & 0 & 0 \\ 0 & 0 & 0 & 0 \\ 0 & 0 & \Sigma_{11}^{\downarrow} & \Sigma_{12}^{\downarrow} \\ 0 & 0 & \Sigma_{12}^{\downarrow} & \Sigma_{22}^{\downarrow} \end{pmatrix}, \tag{28}$$

with $\Sigma_{11\downarrow}$ and $\Sigma_{12\downarrow}$ within the GW approximation. We now get a self-energy with the same structure as the correct one. It is clear that now the spin-up block of the one-particle Green function equals the noninteracting Green function, like the exact one. For the spin-down block we get four poles as in the exact case, although they still differ from the exact values by the GW error.

We point out that it is essential to use a three-point vertex in order to get the correct number of poles. Indeed, by using the two-point vertex $\Gamma = \delta + f_{xc}P$ both for valence and conduction bands, one would get a zero self-energy for the spin-down block. Therefore the spin-down Green function would equal the noninteracting one, which has only two poles instead of four as the exact interacting Green function: there would be no satellites since there would be no screening.

One can readily understand that these vertex corrections will not correct the wrong atomic limit of GW, since the two problems have a different nature; therefore a more complex vertex, able to introduce an additional frequency-dependence in Σ, is needed to fix both.

3.2.2 $N = 2$

In order to calculate the one-body Green function within the GWA (G_0W_0), we need the following ingredients,

$$P_{ij}^{\sigma}(\omega) = \frac{(-1)^{i-j}}{4} \left(\frac{1}{\omega - 2t + i\eta} - \frac{1}{\omega + 2t - i\eta} \right) , \tag{29}$$

$$W_{ij}(\omega) = U\delta_{ij} + (-1)^{i-j} \frac{2U^2 t}{\omega^2 - h'^2} , \tag{30}$$

$$\Sigma_{ij}^{\sigma}(\omega) = \frac{U}{2}\delta_{ij} + \frac{U^2 t}{2h'} \left(\frac{1}{\omega - (\varepsilon_0 + t + h') + i\eta} + \frac{(-1)^{i-j}}{\omega - (\varepsilon_0 - t - h') - i\eta} \right), \tag{31}$$

with $h'^2 = 4t^2 + 4tU$. The one-body Green function hence reads

$$G_{ij\sigma}^{GW} = (-1)^{i-j} \left(\frac{\frac{1}{4} + \frac{h' + 2t + \frac{U}{2}}{4A'}}{\omega - \omega_1^+ + i\eta} + \frac{\frac{1}{4} - \frac{h' + 2t + \frac{U}{2}}{4A'}}{\omega - \omega_1^- - i\eta} \right) + \frac{\frac{1}{4} + \frac{-h' - 2t + \frac{U}{2}}{4B'}}{\omega - \omega_2^+ + i\eta} + \frac{\frac{1}{4} - \frac{-h' - 2t + \frac{U}{2}}{4B'}}{\omega - \omega_2^- - i\eta} \tag{32}$$

with

$$A' = \sqrt{\left(2t + h' + \frac{U}{2}\right)^2 + \frac{4U^2 t}{h'}} , \quad B' = \sqrt{\left(2t + h' - \frac{U}{2}\right)^2 + \frac{4U^2 t}{h'}} ,$$

and

$$\omega_1^{+/-} = \frac{1}{2}\left(2\varepsilon_0 - h' + \frac{U}{2} \pm A'\right) , \quad \omega_2^{+/-} = \frac{1}{2}\left(2\varepsilon_0 + h' + \frac{U}{2} \pm B'\right) .$$

We can now study the two limits $U \to 0$ and $t \to 0$.

- **noninteracting limit: $U \to 0$**
  In this limit $h' \approx 2t$, therefore the poles ω_1^+ and ω_2^- collapse to the poles of G_0, $\omega = \varepsilon_0 + 2t$ and $\omega = \varepsilon_0 - 2t$, whereas ω_1^- and ω_2^+ collapse to $\omega = \varepsilon_0 - 3t$ and $\omega = \varepsilon_0 + 3t$. These last two poles have zero intensity at $U = 0$ and deviate from the bonding/antibonding energies by $\pm 2t$ (poles of P), which justify their identification as satellites.

- **atomic limit: $t \to 0$**
  In the limit $t \to 0$ we have $h' \approx 0$, from where it follows that the poles ω_1^+ and ω_2^+ merge at $\omega = \varepsilon_0 + \frac{U}{2}$, whereas the poles ω_1^- and ω_2^- go towards $\omega = \varepsilon_0$. This is in contrast with the exact solution where the poles go towards the poles of the isolated atom ($\omega = \varepsilon_0$ and $\omega = \varepsilon_0 + U$). This can again be understood considering that GW treats the charge/spin density as a classical charge distribution, namely an half electron with half spin up and half an electron with half spin down on each atom that respond to the additional electron or hole in the atomic limit.
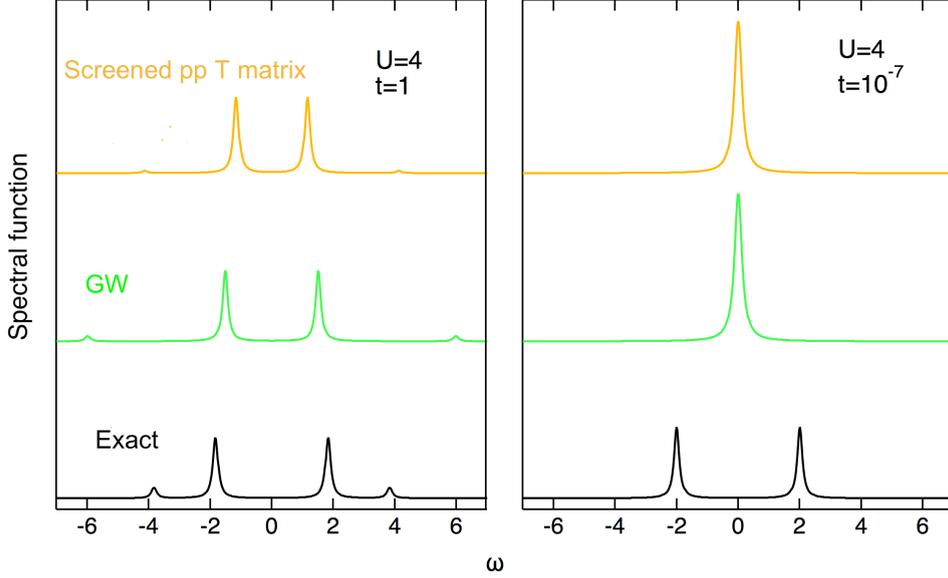
Fig. 8: *Spectral function at half filling: exact (lower panel) vs. GW (middle panel) and screened pp T-matrix (upper panel).*

The spectral function at half filling is reported in Fig. 8: for moderately strong interaction (middle left panel), GW performs quite well (although the position of the satellites is overestimated), whereas at strong correlation (middle right panel), no gap is observed.[5]

Finally, we compare the LUMO at quarter filling with the HOMO at half filling. The LUMO in the N-electron system should be equal to the HOMO in the $N+1$-electron system. This occurs for the exact case, and it is the pole at $\omega = \varepsilon_0 + t - (c - U)/2$. Within the GW approximation the two energies, namely ω_4^- at quarter filling and ω_2^- at half filling, are different. The difference stems from the different polarizability P, which is used to build the screening for the N and $N+1$ cases. This simply shows again that the problem arises from the use of a TC-TC screening, which depends only on the charge density of the system but not on the charge that is to be screened. Indeed, the removal of an electron from the $N+1$-electron system should be screened by N electrons only—which can be expressed through vertex corrections. The source of this error comes from the fact that direct and exchange interactions are not treated on equal footing in GW.

3.3   T-matrix

Also for the T-matrix approximation we adopt the same protocol adopted for the GWA, namely we use G_0 to build T and Σ. Projected in the (orthonormal) site-basis of the Hubbard model the

---

[5]We note that the Hubbard dimer at half filling enjoys an interesting symmetry (particle-hole symmetry) [28] by setting $\varepsilon_0 = -U/2$ and $V_0 = U$ in the Hubbard Hamiltonian. With this choice the exact 1-GF has the same expression as in (20) but with $\varepsilon_0 = -U/2$. For the GW and T-matrix 1-GF one has to set $\varepsilon_0 = 0$. For $U \neq 0$ the particle-hole symmetry is lost in the GW and T-matrix approximations due to the use of G_0. We enforce this symmetry by dropping the terms U/2 in the poles and corresponding weights of the GW and T-matrix 1-GF.

(unscreened) T-matrix becomes

$$T^{\sigma\sigma'}_{ilkj}(\omega) = -\mathrm{i}\delta_{il}\delta_{jk}\left(\bar{T}^{\sigma\sigma'}_{1,ij}(\omega) - \delta_{\sigma\sigma'}\bar{T}^{\sigma\sigma}_{1,ij}(\omega)\right), \tag{33}$$

with $\bar{T}^{\sigma\sigma'}_1(\omega) = \left(1 + UL^{\sigma\sigma'}_0(\omega)\right)^{-1}U$, from which

$$\Sigma^\sigma_{ij}(\omega) = -\mathrm{i}\int\frac{d\nu}{2\pi}\,G^{\bar\sigma}_{ji}(\nu)\,\bar{T}^{\sigma\bar\sigma}_{ij}(\omega{\pm}\nu). \tag{34}$$

Here $\bar\sigma$ indicates a spin opposite to σ, the sign '+' refers to the particle-particle contribution for which $L^{\sigma\sigma',pp}_{0,ij}(\omega) = -\mathrm{i}\int\frac{d\omega'}{2\pi}\,G^\sigma_{ij}(\omega')\,G^{\sigma'}_{ij}(\omega-\omega')e^{-\mathrm{i}\omega'\eta}$, and the sign '−' refers to the electron-hole contribution for which $L^{\sigma\sigma',eh}_{0,ij}(\omega) = -\mathrm{i}\int\frac{d\omega'}{2\pi}\,G^\sigma_{ij}(\omega')G^{\sigma'}_{ij}(\omega'-\omega)e^{\mathrm{i}\omega'\eta}$. More details on the spin and time structure of the T-matrix can be found in Refs. [3,4].

The screened T-matrix approximation is more difficult to handle, because the screened interaction is frequency dependent. However, in the atomic limit $t \to 0$ there is no screening in the system and the screened T-matrix reduces to the unscreened one. For $t > 0$ we assume that for the model used here the major contribution to the T-matrix arises from the on-site screened interaction. This is dominated by the bare interaction U, which justifies to take the screened interaction in its static ($\omega = 0$) limit. In this case the structure of the screened T-matrix is the same as for the unscreened T-matrix with the onsite screened Coulomb interaction $W = U - (1+\delta_{N,2})U^2t/h^2$, with $h^2 = 4t^2 + 2Ut(1+\delta_{N,2})$ and N the total number of electrons in the system, replacing U. We notice that with this approximation, in particular assuming a static W, the screened T-matrix will not reduce anymore to the unscreened T-matrix in the atomic limit.

3.3.1 $N = 1$

- **One site**
  In this case the particle-particle correlator $L^{\sigma\sigma',pp}_0(\omega) = -\mathrm{i}\int\frac{d\omega'}{2\pi}\,G^\sigma(\omega')\,G^{\sigma'}(\omega-\omega')e^{-\mathrm{i}\omega'\eta}$ is zero and $T = U$. The self-energy, therefore, is equal to the exact one, and, consequently, also the Green function

- **Two sites**
  In order to calculate the one-body Green function within the pp T-matrix approximation ($G_0T^{pp}_0$), we need the following ingredients,

$$L^{\sigma\bar\sigma,pp}_{ij}(\omega) = -\frac{1}{4}\left(\frac{1}{\omega - 2(\varepsilon_0{+}t) + \mathrm{i}\eta} + \frac{(-1)^{i-j}}{\omega - 2\varepsilon_0 + \mathrm{i}\eta}\right), \tag{35}$$

$$\bar{T}^{\sigma\bar\sigma,pp}_{ij}(\omega) = U\delta_{ij} + \frac{U^2}{4}\left(\frac{1}{\omega - 2\varepsilon_0 - \frac{U}{2} - 2t + \mathrm{i}\eta} + \frac{1}{\omega - 2\varepsilon_0 - \frac{U}{2} + \mathrm{i}\eta}\right), \tag{36}$$

from which the self-energy reads

$$\Sigma^\uparrow_{ij} = 0, \tag{37}$$

$$\Sigma^\downarrow_{ij} = \frac{U}{2}\delta_{ij} + \frac{U^2}{8}\left(\frac{1}{\omega - \varepsilon_0 - \frac{U}{2} - 3t + \mathrm{i}\eta} + \frac{(-1)^{i-j}}{\omega - \varepsilon_0 - \frac{U}{2} - t + \mathrm{i}\eta}\right), \tag{38}$$
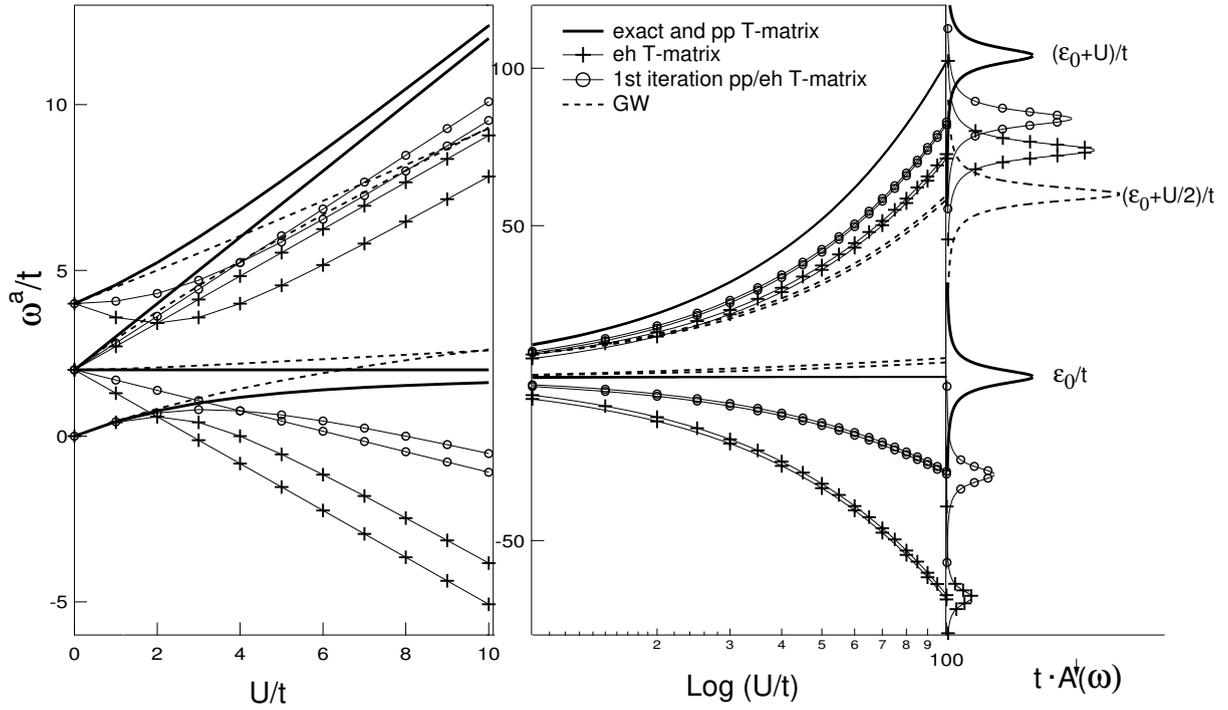
Fig. 9: *Two-site Hubbard model at quarter filling from Ref. [3]: comparison between the exact spin-down renormalized addition energies ω^a/t (solid lines) as function of U/t (left panel) and Log(U/t) (right panel) and the results obtained from GW (dashes), particle-particle (solid lines, equal to the exact result), electron-hole (crosses), and 1st iteration unscreened T-matrix (circles). In the atomic limit the spectral function, i.e., the peak positions and weights, is illustrated on the right-hand side, upon multiplying by t and taking the $t \to 0$ limit.*

which equals the exact self-energy. Of course this self-energy produces the exact 1-GF. Note that the unscreened T-matrix approximation does not suffer from the self-screening problem of GW, as one can expect since no screening is involved.

The eh T-matrix gives a self-energy with the same structure as the pp T-matrix (hence no self-screening), but with poles that are shifted by U from the exact ones, so that one cannot retrieve the exact result.

Moreover, since the pp T-matrix gives the exact results, it becomes clear that its screened version worsens the results, except in the atomic limit, where $W \to v_c$ and one has to get back the unscreened T-matrix results. As already discussed, this is not the case within the static approximation to W we are considering here. However, even with an approximate W the pp screened T-matrix is better than GW as shown in Fig. 9, where the renormalized addition energies ω^a/t for the spin-down channel are reported vs. U/t. Particularly interesting is the spectral function at $U/t \to \infty$: unlike the GWA, the T-matrix approximation "sees" where the electron is, although only the pp T-matrix "sees" well. Indeed, the eh T-matrix yields two peaks with the correct spectral weight, but at the wrong position, namely $\varepsilon_0 + U/\sqrt{2}$ and $\varepsilon_0 - U/\sqrt{2}$. Therefore, it is clear that in the case

of the Hubbard dimer with one electron, the particle-particle contribution to the T-matrix describes the essential physics.

Also note from Fig. 9 that the eh T-matrix and the pp T-matrix give the same results at the first iteration, since $\Sigma^{eh,(1)} = \Sigma^{pp,(1)}$. In particular, in the atomic limit their first iteration shows two peaks in the spin-down spectral function, although they are not correctly located and they do not have the same spectral weight. It hence contains the right physics, although the results are still poor. Finally the spectral function calculated using the pp screened T-matrix is shown in Fig. 7: although introducing screening in the pp T-matrix corrupts the exact result, the spectral function profile is in good agreement with the exact one and of similar quality as the GWA at moderately strong interaction U/t (upper left panel). In the atomic limit (middle right panel), instead, the screened pp T-matrix is superior to GW.

3.3.2 $N = 2$

In this case neither the pp nor the eh unscreened T-matrix reproduce the exact result. In particular, in the case of the pp T-matrix approximation we get

$$L_{ij}^{\sigma\bar{\sigma},pp} = -\frac{1}{4}\left(\frac{1}{\omega - 2(\varepsilon_0+t) + i\eta} - \frac{1}{\omega - 2(\varepsilon_0-t) - i\eta}\right), \tag{39}$$

$$T_{ij}^{\sigma\bar{\sigma},pp}(\omega) = U\delta_{ij} + \frac{U^2 t}{2\bar{h}}\left(\frac{1}{\omega - 2\varepsilon_0 - \bar{h} + i\eta} - \frac{1}{\omega - 2\varepsilon_0 + \bar{h} - i\eta}\right), \tag{40}$$

$$\Sigma_{ij}^{\sigma}(\omega) = \frac{U}{2}\delta_{ij} + \frac{U^2 t}{4\bar{h}}\left(\frac{1}{\omega - \varepsilon_0 - t - \bar{h} + i\eta} + \frac{(-1)^{i-j}}{\omega - \varepsilon_0 + t + \bar{h} - i\eta}\right), \tag{41}$$

with $\bar{h}^2 = 4t^2 + 2tU$. The one-body Green function hence reads

$$G_{ij\sigma}^{T^{pp}} = (-1)^{i-j}\left(\frac{\frac{1}{4} + \frac{\bar{h}+2t+\frac{U}{2}}{4A''}}{\omega - \omega_1^+ + i\eta} + \frac{\frac{1}{4} - \frac{\bar{h}+2t+\frac{U}{2}}{4A''}}{\omega - \omega_1^- - i\eta}\right) + \frac{\frac{1}{4} + \frac{-\bar{h}-2t+\frac{U}{2}}{4B''}}{\omega - \omega_2^+ + i\eta} + \frac{\frac{1}{4} - \frac{-\bar{h}-2t+\frac{U}{2}}{4B''}}{\omega - \omega_2^- - i\eta} \tag{42}$$

with

$$A'' = \sqrt{\left(2t + \bar{h} + \frac{U}{2}\right)^2 + \frac{2U^2 t}{\bar{h}}}, \quad B'' = \sqrt{\left(2t + \bar{h} - \frac{U}{2}\right)^2 + \frac{2U^2 t}{h'}},$$

and

$$\omega_1^{+/-} = \frac{1}{2}\left(2\varepsilon_0 - \bar{h} + \frac{U}{2} \pm A''\right), \quad \omega_2^{+/-} = \frac{1}{2}\left(2\varepsilon_0 + \bar{h} + \frac{U}{2} \pm B''\right).$$

Similar equations hold for the eh T-matrix approximation and the pp and eh (statically) screened T-matrix approximation. The pp T-matrix performs rather well over a wide U/t range as one can see in Fig. 10. In particular the satellite energies are better described than in GW. The energies calculated using the electron-hole unscreened T-matrix (not shown in the figure), instead, show divergencies. Finally, the screened pp T-matrix is overall superior to the GW and unscreened T-matrix in the selected U/t range in the left panel of Fig. 10. In the $U/t \to \infty$ limit, all approximations studied are rather poor. Interestingly if one looks at the first iteration, both
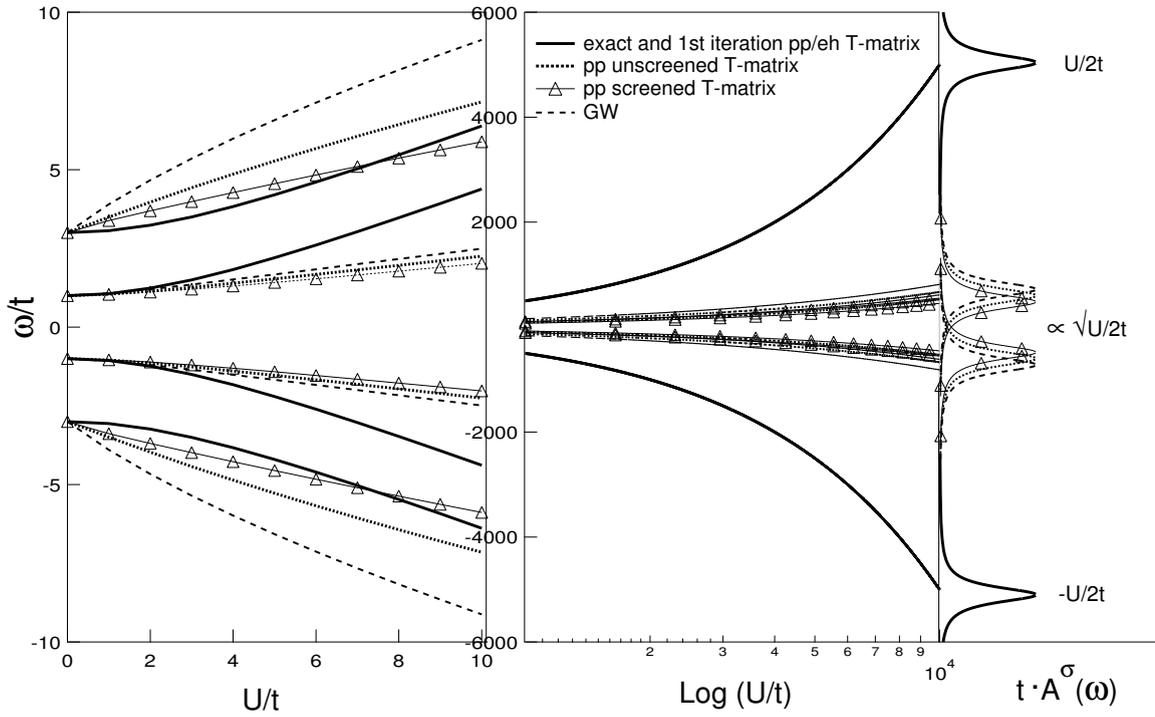
Fig. 10: *Two-site Hubbard model at half filling from Ref. [3]: comparison between the exact renormalized addition/removal energies ω/t (solid lines) as function of U/t (left panel) and Log(U/t) (right panel) and the results obtained from GW (dashes) and particle-particle (dots) and screened T-matrix (triangles). In the atomic limit the spectral function, i.e., the peak positions and weights, is illustrated on the right-hand side, upon multiplying by t and taking the $t \to 0$ limit.*

the particle-particle and electron-hole contributions to the T-matrix give the exact results for all t. Finally the spectral function calculated using the pp screened T-matrix is shown in Fig. 8 where one can better appreciate the superiority of the pp screened T-matrix approximation (at least for the description of satellite energies) with respect to the GWA at moderately strong interaction U/t (upper left panel). In the atomic limit (middle right panel), instead, the screened pp T-matrix fails just as GW.

Why is the pp T-matrix approximation exact for one electron in the atomic limit, and not for two electrons? To derive the unscreened T-matrix we used the approximation $\frac{\delta G}{\delta U_{ext}} \approx GG$. In the case of one electron this is not an approximation, but it is the exact time-ordered response, and therefore the (pp) unscreened T-matrix yields the exact result for one electron. This is not the case for two electrons for which $\frac{\delta G}{\delta U_{ext}} \approx GG$ is a rough approximation, and one needs to include some screening. The screened matrix indeed improves over the unscreened T-matrix for two electrons even with an approximate RPA screening; such approximate screening is instead dramatic for one electron and a more accurate screening is needed (as pointed out above the exact screening would yield the unscreened T-matrix and hence an exact result for one electron). *One should hence use a screened T-matrix with a screened interaction adapted to the system.*

4   Conclusions and outlook

In this chapter we discussed the importance of vertex corrections in relation to two major short-comings of the GW approximation to the self-energy: the self-screening error and the incorrect atomic limit. Because of the self-screening, the GWA produces extra unphysical removal and addition energies in the spectrum of the Hubbard dimer with one electron. We showed that this error can be corrected by a two-point vertex $\Gamma = \delta + f_{xc} P$, derived from time-dependent density functional theory, but it should be used only for the valence state, for which it produces exact results. For the conduction state, instead, this two-point vertex produces fewer poles than the exact solution. In fact, it seems to be more reasonable to stick to the TC-TC description of the screening for the conduction state, with $\Gamma = \delta$, which yields the correct number of energies, although the values are still different from the exact ones. One could extrapolate these findings for the case of more bands in the situation where the valence bands are similar and the conduction bands are localized elsewhere or with different spin. The comparison with the exact solution for the two-site Hubbard model sheds light on another feature of the GW approximation: in the atomic limit ($t \rightarrow 0$) the GW solution for the two-site model does not reduce to the solution for two isolated sites; this is caused by the description of the electrons as an average charge distribution, instead of a probability. The approximate three-point vertex, which cures the self-screening problem and yields the correct number of poles in the one-particle Green function, is not sufficient to correct the atomic limit. To correct the atomic limit we have derived a vertex function from a screened version of the T-matrix approximation. The screened T-matrix, in which Hartree and exchange terms are treated on an equal footing, reduces to the T-matrix in the atomic limit when a dynamically screened interaction is used, which gives the exact result for the Hubbard dimer at quarter-filling; even with an approximate W it is better than GW at quarter filling, whereas at half filling it is overall superior to both the pp T-matrix and GW over a wide U/t range. This means that the vertex corrections derived from this version of the pp screened T-matrix can improve over GW. In the atomic limit at half-filling, however, the screened T-matrix performs as badly as GW. It remains hence to understand "*Why, in the atomic limit, is the pp screened T-matrix exact for one electron but not for two electrons? Which approximations we use in the derivation of the T-matrix self-energy is harmless for the one-electron case, but dramatic for the two-electron case? And why? Will realistic systems be more forgiving than the Hubbard dimer when the screened pp T-matrix approximation is used?*"

Acknowledgements

A   Solutions for 2±1 electrons

To treat the case at 1/4 and 1/2 filling we need to diagonalize the two-site Hamiltonian for one, two, and three electrons. Since the Hamiltonian conserves particle number we can diagonalize it separately for the various N sectors. The eigenstates of the system will be linear combinations of Slater determinants, which are denoted by the kets $|1\,,\,2\rangle$, with occupations of the sites 1 and 2 given by $\cdot, \uparrow, \downarrow, \uparrow\downarrow$. We choose $V_0 = 0$, so that the vacuum state $\zeta^{N=0}\rangle = |\,\cdot\,,\,\cdot\,\rangle$ has zero energy for the dimer. Moreover, the following convention as to fermionic ordering is used

$$| \uparrow\downarrow\,,\,\uparrow\downarrow\,\rangle = c_{2\downarrow}^{\dagger}c_{2\uparrow}^{\dagger}c_{1\downarrow}^{\dagger}c_{1\uparrow}^{\dagger}|0_1\,0_2\rangle. \tag{43}$$

A.1   One electron

In the case of one electron, the basis vectors are $|\uparrow,\cdot\rangle, |\downarrow,\cdot\rangle, |\cdot,\uparrow\rangle$, and $|\cdot,\downarrow\rangle$. In this basis the Hamiltonian matrix reads

$$H = \begin{pmatrix} \varepsilon_0 & 0 & -t & 0 \\ 0 & \varepsilon_0 & 0 & -t \\ -t & 0 & \varepsilon_0 & 0 \\ 0 & -t & 0 & \varepsilon_0 \end{pmatrix}, \tag{44}$$

and we get the eigenvalues E_i and corresponding eigenvectors in Table 1.

E_i	$|\uparrow,\cdot\rangle$	$|\downarrow,\cdot\rangle$	$|\cdot,\uparrow\rangle$	$|\cdot,\downarrow\rangle$
$\varepsilon_0 - t$	0	$1/\sqrt{2}$	0	$1/\sqrt{2}$
$\varepsilon_0 - t$	$1/\sqrt{2}$	0	$1/\sqrt{2}$	0
$\varepsilon_0 + t$	0	$1/\sqrt{2}$	0	$-1/\sqrt{2}$
$\varepsilon_0 + t$	$1/\sqrt{2}$	0	$-1/\sqrt{2}$	0

Table 1: *Eigenvalues and corresponding eigenvectors for the one-electron sector.*

A.2   Two electrons

In the case of two electrons, the basis vectors are $|\uparrow,\downarrow\rangle, |\downarrow,\uparrow\rangle, |\uparrow,\uparrow\rangle, |\downarrow,\downarrow\rangle, |\uparrow\downarrow,\cdot\rangle$, and $|\cdot,\uparrow\downarrow\rangle$. In this basis the Hamiltonian matrix reads

$$H = \begin{pmatrix} 2\varepsilon_0 & 0 & 0 & 0 & -t & -t \\ 0 & 2\varepsilon_0 & 0 & 0 & t & t \\ 0 & 0 & 2\varepsilon_0 & 0 & 0 & 0 \\ 0 & 0 & 0 & 2\varepsilon_0 & 0 & 0 \\ -t & t & 0 & 0 & 2\varepsilon_0+U & 0 \\ -t & t & 0 & 0 & 0 & 2\varepsilon_0+U \end{pmatrix}, \tag{45}$$

which yields the eigenvalues E_i and corresponding eigenvectors in Table 2, where

$$c = \sqrt{16t^2+U^2} \quad a = \frac{\sqrt{2}}{(c-U)}\sqrt{16t^2 + (c-U)^2}, \quad b = \frac{\sqrt{2}}{(c+U)}\sqrt{16t^2 + (c+U)^2}\,.$$

E_i	$\lvert\uparrow,\downarrow\rangle$	$\lvert\downarrow,\uparrow\rangle$	$\lvert\uparrow,\uparrow\rangle$	$\lvert\downarrow,\downarrow\rangle$	$\lvert\uparrow\downarrow,\cdot\rangle$	$\lvert\cdot,\uparrow\downarrow\rangle$
$2\varepsilon_0 + (U-c)/2$	$\frac{4t}{a(c-U)}$	$-\frac{4t}{a(c-U)}$	0	0	$1/a$	$1/a$
$2\varepsilon_0 + (U+c)/2$	$-\frac{4t}{b(c+U)}$	$\frac{4t}{b(c+U)}$	0	0	$1/b$	$1/b$
$2\varepsilon_0 + U$	0	0	0	0	$-1/\sqrt{2}$	$1/\sqrt{2}$
$2\varepsilon_0$	0	0	0	1	0	0
$2\varepsilon_0$	0	0	1	0	0	0
$2\varepsilon_0$	$1/\sqrt{2}$	$1/\sqrt{2}$	0	0	0	0

Table 2: *Eigenvalues and corresponding eigenvectors for the two-electron sector.*

The first three solutions are singlets, the last three triplets. The first singlet is the ground state. It is interesting to consider the limits $U \to 0$ and $U \to \infty$ or $t \to 0$. The expansion of the coefficients for these limits are:

$U \to 0$:

$$c \approx 4t \left(1 + \frac{U^2}{32t^2}\right) \tag{46}$$

so $\frac{1}{c-U} \approx \frac{1}{4t(1+U^2/32t^2 - U/4t)} \approx \frac{1}{4t}\left(1 + \frac{U}{4t} - \frac{U^2}{32t^2} + \frac{U^2}{16t^2}\right) \approx \frac{1}{4t}\left(1 + \frac{U}{4t} + \frac{U^2}{32t^2}\right)$ and

$$
\begin{aligned}
a &= \sqrt{2}\sqrt{16t^2/(c-U)^2 + 1} \approx \sqrt{2}\sqrt{(1 + \frac{U}{4t} + \frac{U^2}{32t^2})^2 + 1} \approx 2\sqrt{1 + U/4t + U^2/16t^2} \\
&\approx 2\left(1 + U/8t + U^2/32t^2 - U^2/128t^2\right)
\end{aligned}
\tag{47}
$$

$$
\begin{aligned}
b &= \sqrt{2}\sqrt{16t^2/(c+U)^2 + 1} \approx \sqrt{2}\sqrt{(1 - \frac{U}{4t} + \frac{U^2}{32t^2})^2 + 1} \\
&\approx 2\sqrt{1 - U/4t + U^2/16t^2} \approx 2\left(1 - U/8t + 3U^2/128t^2\right)
\end{aligned}
\tag{48}
$$

In the non-interacting ($U = 0$) case, we have hence a weight of $1/2$ for double occupation. For $U \to \infty$

$$c \approx U \left(1 + \frac{8t^2}{U^2}\right) \tag{49}$$

$$a \approx \sqrt{2}\sqrt{U^2/4t^2 + 1} \approx \frac{U}{\sqrt{2}t}\left(1 + 2t^2/U^2\right) \tag{50}$$

$$b \approx -a \tag{51}$$

In particular we get $a(c-U) \approx \frac{U}{\sqrt{2}t}(1 + 2t^2/U^2)\, 8t^2/U = \frac{8t}{\sqrt{2}}(1+2t^2/U^2)$ so that the coefficients on the single occupations are $\pm 1/\sqrt{2}$, whereas double occupancies are impossible (Heitler-London limit).

For $t \to 0$ we have the same expansion as for $U \to \infty$ since the ratio t/U is what matters; the only peculiarity is the fact that the ground state energy goes to zero, so that it approaches degeneracy with the threefold degenerate triplet states (case $t = 0$). (However for any small but finite t the ground state is the singlet $S = 0$).

A.3 Three electrons

The basis vectors for three electrons are $|\uparrow, \uparrow\downarrow\rangle$, $|\downarrow, \uparrow\downarrow\rangle$, $|\uparrow\downarrow, \uparrow\rangle$, and $|\uparrow\downarrow, \downarrow\rangle$, and the Hamiltonian matrix, the same as for one electron but with negative (hole) hopping

$$H = \begin{pmatrix} 3\varepsilon_0+U & 0 & t & 0 \\ 0 & \varepsilon_0+U & 0 & t \\ t & 0 & \varepsilon_0+U & 0 \\ 0 & t & 0 & \varepsilon_0+U \end{pmatrix}. \tag{52}$$

This yields eigenvalues E_i and corresponding eigenvectors in Table 3.

E_i	$\|\uparrow, \uparrow\downarrow\rangle$	$\|\downarrow, \uparrow\downarrow\rangle$	$\|\uparrow\downarrow, \uparrow\rangle$	$\|\uparrow\downarrow, \downarrow\rangle$
$3\varepsilon_0-t+U$	0	$-1/\sqrt{2}$	0	$1/\sqrt{2}$
$3\varepsilon_0-t+U$	$-1/\sqrt{2}$	0	$1/\sqrt{2}$	0
$3\varepsilon_0+t+U$	0	$1/\sqrt{2}$	0	$1/\sqrt{2}$
$3\varepsilon_0+t+U$	$1/\sqrt{2}$	0	$1/\sqrt{2}$	0

Table 3: *Eigenvalues and corresponding eigenvectors for the three-electron sector.*

References

[1] A.L. Fetter and J.D. Walecka: *Quantum Theory of Many-Particle Systems*
     (Benjamin, New York, 1964)

[2] L. Hedin, Phys. Rev. **139**, A796 (1965)

[3] P. Romaniello, F. Bechstedt, and L. Reining, Phys. Rev. B **85**, 155131 (2012)

[4] R.M. Martin, L. Reining, and D.M. Ceperley:
     Interacting Electrons: Theory and Computational Approaches
     (Cambridge University Press, 2016)

[5] G. Strinati, Riv. Nuovo Cimento **11**, 1 (1988)

[6] F. Bruneval, F. Sottile, V. Olevano, R. Del Sole, and L. Reining,
     Phys. Rev. Lett. **94**, 186402 (2005)

[7] M. Springer, F. Aryasetiawan, and K. Karlsson, Phys. Rev. Lett. **80**, 2389 (1998)

[8] N.E. Dahlen, R. van Leeuwen, and U. von Barth, Phys. Rev. A **73**, 012511 (2006)

[9] A. Stan, N.E. Dahlen, and R. van Leeuwen, Europhys. Lett. **76**, 298 (2006)

[10] P. Romaniello, S. Guyot, and L. Reining, J. Chem. Phys. **131**, 154111 (2009)

[11] M. Puig von Friesen, C. Verdozzi, and C.-O. Almbladh,
     Phys. Rev. Lett. **103**, 176404 (2009)

[12] M. Puig von Friesen, C. Verdozzi, and C.-O. Almbladh, Phys. Rev. B **82** 155108 (2010)

[13] S. Di Sabatino, J. A. Berger, L. Reining, and P. Romaniello,
     J. Chem. Phys. **143**, 024108 (2015)

[14] S. Di Sabatino, J. A. Berger, L. Reining, and P. Romaniello,
     Phys. Rev. B **94**, 155141 (2016)

[15] S. Di Sabatino, J. Koskelo, J. A. Berger, and P. Romaniello,
     Phys. Rev. Research **3**, 013172 (2021)

[16] W. Nelson, P. Bokes, P. Rinke, and R.W. Godby, Phys. Rev. A **75**, 032505 (2007)

[17] F. Aryasetiawan, R. Sakuma, and K. Karlsson, Phys. Rev. B **85**, 035106 (2012)

[18] M. Guzzo, PhD thesis, École Polytechnique (2013)

[19] W. Hanke and L.J. Sham, Phys. Rev. B **21**, 4656 (1980)

[20] G. Strinati, Phys. Rev. B **29**, 5718 (1984)

[21] G. Strinati, Phys. Rev. Lett. **49**, 1519 (1982)

[22] V.M. Galitskii, Zh. Eksp. Teor. Fiz. **34**, 251 (1958) [Sov. Phys. JETP **7**, 104 (1958)]

[23] L.P. Kadanoff and G. Baym: *Quantum Statistical Mechanics*
      (W.A. Benjamin, New York, 1964)

[24] M. Vanzini, L. Reining, and M. Gatti, Eur. Phys. J. B **91**, 192 (2018)

[25] J. Hubbard, Proc. R. Soc. London, Ser. **A 276**, 238 (1963)

[26] J. Hubbard, Proc. R. Soc. London, Ser. **A 277**, 237 (1964)

[27] A.J. Cohen, P. Mori-Sanchez, and W.T. Yang, Science **321**, 792 (2008)

[28] G. Stefanucci and R. van Leeuwen:
      Nonequilibrium Many-Body Theory of Quantum Systems: A Modern Introduction
      (Cambridge University Press, 2013)

5 Dynamical Mean-Field Theory for Materials

Eva Pavarini
Institute for Advanced Simulation
Forschungszentrum Jülich

Contents

1 Introduction

In 1965, when the two founding papers [1] of density-functional theory (DFT) had just been published in the Physical Review, very few could recognize the revolution in the making. Efficient techniques for materials science applications were missing and computers were not that powerful. And yet in 50 years, thanks to remarkable ideas, novel algorithms and steady advance in computational power, brilliant minds brought DFT to its present splendor, making it the *standard model* of condensed matter physics. In 1998, in his Nobel lecture [2], Walter Kohn, described the most important contributions of DFT to science with these words

> *The first is in the area of fundamental <u>understanding</u>. Theoretical chemists and physicists, following the path of the Schrödinger equation, have become accustomed to think in a truncated Hilbert space of single particle orbitals. The spectacular advances achieved in this way attest to the fruitfulness of this perspective. However, when very high accuracy is required, so many Slater determinants are required (in some calculations up to $\sim 10^9$!) that <u>comprehension</u> becomes difficult.*

DFT changed the focus from the N-electron ground-state wavefunction $\Psi(\boldsymbol{r}_1, \ldots, \boldsymbol{r}_N)$ to a three-dimensional variable, the electronic ground-state density $n(\boldsymbol{r})$, or other directly measurable quantities, such as response functions. These, within a given approximation of the DFT exchange-correlation functional, could be calculated *from first principles*, i.e., using as input the type of atoms involved and, at most, their positions. In practice, $n(\boldsymbol{r})$ is obtained by mapping the actual many-body problem onto an auxiliary single-electron Hamiltonian with the same ground-state electron density, the Kohn-Sham Hamiltonian. The associated Kohn-Sham eigenvalues are thus in principle merely Lagrange multipliers. Remarkably, however, the big success of DFT came, in part, from bold applications of the theory beyond its actual realm of validity. To general surprise, the Kohn-Sham eigenvalues turned out to be in many cases excellent approximations to the actual elementary excitations of a given material. Early on it became clear, however, that this Ansatz fails qualitatively for a whole category of systems, those in which <u>local</u> Coulomb repulsion effects are large, also known as *strongly-correlated materials*. Paradoxically, in describing strong-correlation phenomena, simple models describing generic features of the microscopic mechanism are much more effective than DFT-based materials-specific calculations. This happens, e.g., for the Kondo effect, heavy-fermion behavior, or the metal-insulator transition. Thus criticisms arose. Particularly outspoken in this contest was another Nobel laureate, P.W. Anderson, who emphasized the emergent nature of a true many-body phenomenon [3]. Emergent states typically elude a simple mapping to an effective non-interacting system. For a while, two apparently incompatible philosophies thus coexisted. The first-principles school identified in the materials dependence the essential ingredient for understanding the real world, and tried to correct the failures of the practical implementations of DFT by corrections, often ad hoc, of the exchange-correlation potential. Instead, the many-body models school identified canonical models which explain specific emergent phenomena, dismissing the materials dependence as non-relevant, non-generic detail. Only in recent years these two world-views started to merge, and it became apparent that both sides were right and wrong at the same time. While the <u>local</u>

Coulomb repulsion is indeed key, materials aspects turn out to be essential for understanding real correlated materials. In hindsight, we can now put this debate in a different perspective. The electronic many-body problem, in the non-relativistic limit and in the Born-Oppenheimer approximation, is described by the Hamiltonian

$$\hat{H}_e = -\frac{1}{2}\sum_i \nabla_i^2 - \sum_i \sum_\alpha \frac{Z_\alpha}{|\boldsymbol{r}_i - \boldsymbol{R}_\alpha|} + \sum_{i>j}\frac{1}{|\boldsymbol{r}_i - \boldsymbol{r}_j|} + \sum_{\alpha > \alpha'} \frac{Z_\alpha Z_{\alpha'}}{|\boldsymbol{R}_\alpha - \boldsymbol{R}_{\alpha'}|}, \tag{1}$$

where $\{\boldsymbol{r}_i\}$ are electron coordinates, $\{\boldsymbol{R}_\alpha\}$ nuclear coordinates and Z_α the nuclear charges. Using a complete one-electron basis, for example the basis $\{\varphi_a(\boldsymbol{r})\}$, where $\{a\}$ are the quantum numbers, we can write this Hamiltonian in second quantization as

$$\hat{H}_e = \underbrace{-\sum_{ab} t_{ab} c_a^\dagger c_b}_{\hat{H}_0} + \underbrace{\frac{1}{2}\sum_{aa'bb'} U_{aa'bb'}\, c_a^\dagger c_{a'}^\dagger c_{b'} c_b}_{\hat{H}_U}. \tag{2}$$

Here the hopping integrals are given by

$$t_{ab} = -\int d\mathbf{r}\, \overline{\varphi_a}(\boldsymbol{r}) \left(-\frac{1}{2}\nabla^2 \underbrace{- \sum_\alpha \frac{Z_\alpha}{|\boldsymbol{r} - \boldsymbol{R}_\alpha|}}_{v_{\mathrm{en}}(\boldsymbol{r})}\right)\varphi_b(\boldsymbol{r}), \tag{3}$$

while the elements of the Coulomb tensor are

$$U_{aa'bb'} = \int d\mathbf{r}_2 \int d\mathbf{r}_2\, \overline{\varphi_a}(\boldsymbol{r}_1)\,\overline{\varphi_{a'}}(\boldsymbol{r}_2)\,\frac{1}{|\boldsymbol{r}_1 - \boldsymbol{r}_2|}\,\varphi_{b'}(\boldsymbol{r}_2)\,\varphi_b(\boldsymbol{r}_1). \tag{4}$$

In principle, all complete one-electron bases are equivalent. In practice, since, in the general case, we cannot solve the N-electron problem exactly, some bases are better than others. One possible choice for the basis are the Kohn-Sham orbitals, $\{\varphi_a^{\mathrm{KS}}(\boldsymbol{r})\}$, obtained, e.g., in the local density approximation (LDA) or its simple extensions.[1] In this case, it is useful to replace the electron-nuclei interaction $v_{\mathrm{en}}(\boldsymbol{r})$ with the DFT potential $v_R(\boldsymbol{r})$, which includes in addition the Hartree term $v_{\mathrm{H}}(\boldsymbol{r})$ and the (approximate) exchange-correlation potential $v_{\mathrm{xc}}(\boldsymbol{r})$

$$v_{\mathrm{R}}(\boldsymbol{r}) = v_{\mathrm{en}}(\boldsymbol{r}) + \underbrace{\int d\mathbf{r}'\, \frac{n(\boldsymbol{r}')}{|\boldsymbol{r} - \boldsymbol{r}'|}}_{v_{\mathrm{H}}(\boldsymbol{r})} + v_{\mathrm{xc}}(\boldsymbol{r}) \tag{5}$$

so that

$$\tilde{t}_{ab} = -\int d\mathbf{r}\, \overline{\varphi_a^{\mathrm{KS}}}(\boldsymbol{r})\left(-\frac{1}{2}\nabla^2 + v_{\mathrm{R}}(\boldsymbol{r})\right)\varphi_b^{\mathrm{KS}}(\boldsymbol{r}). \tag{6}$$

To avoid double counting (DC), we have, however, to subtract from $\hat{H}_U$ the term $\hat{H}_{\mathrm{DC}}$, which describes the Coulomb terms already included in the hopping integrals

$$\hat{H}_e = \underbrace{-\sum_{ab}\tilde{t}_{ab}\, c_a^\dagger c_b}_{\hat{H}_0 = \hat{H}_e^{\mathrm{LDA}}} + \underbrace{\frac{1}{2}\sum_{aba'b'}\tilde{U}_{aa'bb'}\, c_a^\dagger c_{a'}^\dagger c_{b'} c_b - \hat{H}_{\mathrm{DC}}}_{\Delta \hat{H}_U}. \tag{7}$$

---

[1]For the purpose of many-body calculations the differences between LDA, GGA or their simple extensions are in practice negligible; for simplicity, in the rest of the lecture, we thus adopt LDA as representative functional.

For weakly-correlated systems, in the Kohn-Sham basis, the effects included in $\Delta \hat{H}_U$ can, in first approximation, either be neglected or treated as a perturbation. This implies that $\hat{H}_e^{\text{LDA}} \sim \hat{H}_{\text{eff}}$, where $\hat{H}_{\text{eff}}$ is the effective model which provides a good description of the system (at least) at low energy, and which describes emergent effective "elementary particles" and their interactions. Hypothetically, one could imagine that $\hat{H}_{\text{eff}}$ is obtained via a canonical transformation, so that $\hat{H}_{\text{eff}} \sim \hat{S}^{-1} \hat{H}_e \hat{S}$, although the exact form of the operator $\hat{S}$ is unknown.

A defining feature of strong-correlation effects is that they cannot be described via a single-electron Hamiltonian, however. A model of form $\hat{H}_e^{\text{LDA}}$ does not describe correctly the Mott metal-insulator transition, no matter what the specific values of the parameters $\tilde{t}_{ab}$ are.[2] Thus for strongly-correlated systems the low-energy effective model must have a different form. For Mott systems a canonical Hamiltonian is the Hubbard model

$$\hat{H} = -\sum_{\sigma} \sum_{ii'} t^{i,i'} c_{i\sigma}^{\dagger} c_{i'\sigma} + U \sum_{i} \hat{n}_{i\uparrow} \hat{n}_{i\downarrow}, \tag{8}$$

which includes, in addition to a single-electron term, the on-site Coulomb repulsion. This Hamiltonian captures the essence of the Mott transition. At half filling, for $U = 0$ it describes a paramagnetic metal, and for $t^{i,i'}(1 - \delta_{i,i'}) = 0$ an insulating set of paramagnetic atoms. Unfortunately, differently from Hamiltonians of type $\hat{H}_e^{\text{LDA}}$, Hubbard-like models cannot be solved exactly in the general case. Remarkably, till 30 years ago, no method for describing the complete phase diagram of (8) in one coherent framework, including the paramagnetic insulating phase, was actually known. This changed between 1989 and 1992, when the dynamical mean-field theory (DMFT) was developed [4–7]. The key idea of DMFT consists in mapping the Hubbard model onto a self-consistent *auxiliary quantum-impurity problem*, which can be solved exactly. The mapping is based on the *local dynamical self-energy approximation*, very good for realistic three-dimensional lattices—and becoming exact in the infinite coordination limit [4, 5].

DMFT was initially applied to simple cases, due to limitations in model building, computational power, and numerical methods for solving the auxiliary impurity problem (the quantum impurity solvers). In the last twenty years remarkable progress lifted many of these limitations. First, reliable schemes to build realistic low-energy materials-specific Hubbard-like models have been devised, in particular using Kohn-Sham localized Wannier functions. This is remarkable, given that we do not know the exact operator $\hat{S}$ which gives the effective low-energy Hamiltonian, and thus a truly systematic derivation is not possible. Second, key advances in quantum impurity solvers and increasingly more powerful supercomputers made it possible to study always more complex many-body Hamiltonians. The approach which emerged, consisting in solving within DMFT materials-specific many-body Hamiltonian constructed via LDA, is known as the LDA+DMFT method [8–10]. This technique (and its extensions) is now the state-of-the-art for describing strongly-correlated materials. In this lecture I will outline the basic ideas on which the method is based, its successes and its limitations.

---

[2]One can obtain an insulator by reducing the symmetry, e.g, by increasing the size of the primitive cell. This Slater-type insulator has however different properties than a Mott-type insulator.

2   From DMFT to LDA+DMFT

In this section we introduce the basics of dynamical mean-field theory. We start from a case for which we can perform analytic calculations, the two-site Hubbard Hamiltonian. This is a toy model, useful to illustrate how the method works, but for which, as we will see, DMFT is not a good approximation. Indeed, the Hubbard dimer is the worst case for DMFT, since the coordination number is the lowest possible. Next we extend the formalism to the one-band and then to the multi-orbital Hubbard Hamiltonian. For three-dimensional lattices the coordination number is typically large and thus DMFT is an excellent approximation. In Sec. 3 we describe modern schemes to construct materials-specific many-body models. They are based on Kohn-Sham Wannier orbitals, calculated, e.g, using the LDA functional. The solution of such models via DMFT defines the LDA+DMFT method.

2.1   DMFT for a toy model: The Hubbard dimer

The two-site Hubbard model is given by

$$\hat{H} = \varepsilon_d \sum_{i\sigma} \hat{n}_{i\sigma} - t \sum_{\sigma} \left(c_{1\sigma}^{\dagger} c_{2\sigma} + c_{2\sigma}^{\dagger} c_{1\sigma} \right) + U \sum_i \hat{n}_{i\uparrow} \hat{n}_{i\downarrow}, \tag{9}$$

with $i = 1, 2$. The ground state for $N = 2$ electrons (half filling) is the singlet[3]

$$|G\rangle_H = \frac{a_2(t,U)}{\sqrt{2}} \left(c_{1\uparrow}^{\dagger} c_{2\downarrow}^{\dagger} - c_{1\downarrow}^{\dagger} c_{2\uparrow}^{\dagger} \right) |0\rangle + \frac{a_1(t,U)}{\sqrt{2}} \left(c_{1\uparrow}^{\dagger} c_{1\downarrow}^{\dagger} + c_{2\uparrow}^{\dagger} c_{2\downarrow}^{\dagger} \right) |0\rangle \tag{10}$$

with

$$a_1^2(t,U) = \frac{1}{\Delta(t,U)} \frac{\Delta(t,U) - U}{2}, \qquad a_2^2(t,U) = \frac{4t^2}{\Delta(t,U)} \frac{2}{\Delta(t,U) - U}, \tag{11}$$

and

$$\Delta(t,U) = \sqrt{U^2 + 16t^2}. \tag{12}$$

The energy of this state is

$$E_0(2) = 2\varepsilon_d + \frac{1}{2} \big(U - \Delta(t,U) \big). \tag{13}$$

In the $T \to 0$ limit, using the Lehmann representation (see Appendix B), one can show that the local Matsubara Green function for spin σ takes then the form

$$G_{i,i}^{\sigma}(i\nu_n) = \frac{1}{4} \Bigg(\frac{1 + w(t,U)}{i\nu_n - \big(\underbrace{E_0(2) - \varepsilon_d + t - \mu}_{E_0(2) - E_-(1) - \mu} \big)} + \frac{1 - w(t,U)}{i\nu_n - \big(\underbrace{-E_0(2) + U + 3\varepsilon_d + t - \mu}_{E_+(3) - E_0(2) - \mu} \big)}$$

$$+ \frac{1 - w(t,U)}{i\nu_n - \big(\underbrace{E_0(2) - \varepsilon_d - t - \mu}_{E_0(2) - E_+(1) - \mu} \big)} + \frac{1 + w(t,U)}{i\nu_n - \big(\underbrace{-E_0(2) + U + 3\varepsilon_d - t - \mu}_{E_-(3) - E_0(2) - \mu} \big)} \Bigg), \tag{14}$$

---

[3]Eigenstates and eigenvalues of the Hubbard dimer for arbitrary filling can be found in Appendix A.1.

where $\nu_n = \pi(2n+1)/\beta$ are fermionic Matsubara frequencies and $\mu = \varepsilon_d + U/2$ is the chemical potential. The weights are

$$w_\pm(t, U) = \frac{1}{4}\big(1 \pm w(t, U)\big), \tag{15}$$

$$w(t, U) = 2a_1(t, U)a_2(t, U) = \frac{4t}{\Delta(t, U)}. \tag{16}$$

The local Green function can be rewritten as the average of the Green function for the bonding ($k = 0$) and the anti-bonding state ($k = \pi$), i.e.,

$$G_{i,i}^\sigma(i\nu_n) = \frac{1}{2}\left(\underbrace{\frac{1}{i\nu_n + \mu - \varepsilon_d + t - \Sigma^\sigma(0; i\nu_n)}}_{G^\sigma(0; i\nu_n)} + \underbrace{\frac{1}{i\nu_n + \mu - \varepsilon_d - t - \Sigma^\sigma(\pi; i\nu_n)}}_{G^\sigma(\pi; i\nu_n)}\right). \tag{17}$$

The self-energy is given by

$$\Sigma^\sigma(k; i\nu_n) = \frac{U}{2} + \frac{U^2}{4}\frac{1}{i\nu_n + \mu - \varepsilon_d - \frac{U}{2} - e^{ik}\,3t}. \tag{18}$$

The self-energies $\Sigma^\sigma(0; i\nu_n)$ and $\Sigma^\sigma(\pi; i\nu_n)$ differ due to the phase $e^{ik} = \pm 1$ in their denominators. The local self-energy is, by definition, the average of the two

$$\Sigma_l^\sigma(i\nu_n) = \frac{1}{2}\left(\Sigma^\sigma(\pi; i\nu_n) + \Sigma^\sigma(0; i\nu_n)\right) = \frac{U}{2} + \frac{U^2}{4}\frac{i\nu_n + \mu - \varepsilon_d - \frac{U}{2}}{(i\nu_n + \mu - \varepsilon_d - \frac{U}{2})^2 - (3t)^2}$$

$$= \frac{U}{2} + \frac{U^2}{4}\frac{i\nu_n}{(i\nu_n)^2 - (3t)^2} \tag{19}$$

The difference

$$\Delta\Sigma_l^\sigma(i\nu_n) = \frac{1}{2}\left(\Sigma^\sigma(\pi; i\nu_n) - \Sigma^\sigma(0; i\nu_n)\right) = \frac{U^2}{4}\frac{3t}{(i\nu_n + \mu - \varepsilon_d - \frac{U}{2})^2 - (3t)^2}$$

$$= \frac{U^2}{4}\frac{3t}{(i\nu_n)^2 - (3t)^2}, \tag{20}$$

thus measures the importance of non-local effects; it would be zero if the self-energy was independent of k. Next we define the hybridization function

$$F^\sigma(i\nu_n) = \frac{\big(t + \Delta\Sigma_l^\sigma(i\nu_n)\big)^2}{i\nu_n + \mu - \varepsilon_d - \Sigma_l^\sigma(i\nu_n)} \tag{21}$$

which for $U = 0$ becomes

$$F_0^\sigma(i\nu_n) = \frac{t^2}{i\nu_n}. \tag{22}$$

By using these definitions, we can rewrite the local Green function as

$$G_{i,i}^\sigma(i\nu_n) = \frac{1}{i\nu_n + \mu - \varepsilon_d - F^\sigma(i\nu_n) - \Sigma_l^\sigma(i\nu_n)}. \tag{23}$$
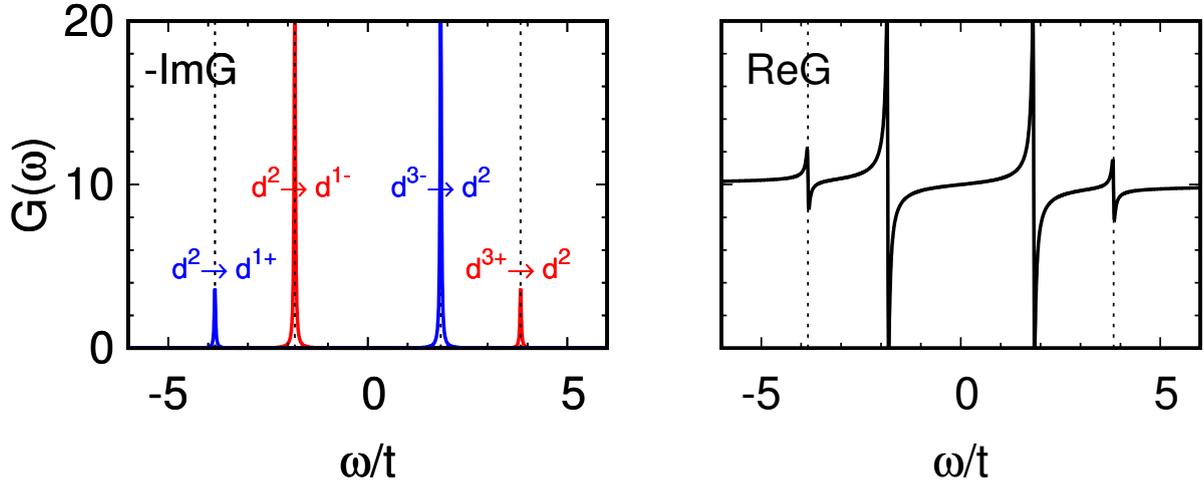
Fig. 1: *Hubbard dimer: Imaginary (left) and real (right) part of the retarded Green function, obtained setting $i\nu_n \to \omega + i\delta$ (analytic continuation) in Eq. (14). Red lines: $k = 0$ contribution. Blue lines: $k = \pi$ contribution. Dashed lines: Poles of the retarded Green function. Parameters: $t = 1, U = 4$. The weight of the poles yielding the smaller peaks, $w_-(t, U)$, defined in Eq. (15), goes to zero for $U \to 0$. In the atomic limit, instead, all four poles have the same weight; the energies of the two positive (negative) poles become identical, however.*

The associated retarded Green function, obtained via analytic continuation ($i\nu_n \to \omega + i\delta$), is shown in Fig. 1. It is important to point out that, as one may see from the formulas just discussed, the local Green function and the local self-energy satisfy the *local Dyson equation*

$$\Sigma_l^\sigma(i\nu_n) = \frac{1}{\mathfrak{G}_{i,i}^\sigma(i\nu_n)} - \frac{1}{G_{i,i}^\sigma(i\nu_n)}, \tag{24}$$

where $\mathfrak{G}_{i,i}^\sigma(i\nu_n)$ is given by

$$\mathfrak{G}_{i,i}^\sigma(i\nu_n) = \frac{1}{i\nu_n + \mu - \varepsilon_d - F^\sigma(i\nu_n)}. \tag{25}$$

Thus, one could think of mapping the Hubbard dimer into an auxiliary quantum-impurity model, chosen such that, within certain approximations, the impurity Green function is as close as possible to the local Green function of the original problem. How can we do this? Let us adopt as auxiliary model the Anderson molecule

$$\hat{H}^A = \varepsilon_s \sum_\sigma \hat{n}_{s\sigma} - t \sum_\sigma \left(c_{d\sigma}^\dagger c_{s\sigma} + c_{s\sigma}^\dagger c_{d\sigma} \right) + \varepsilon_d \sum_\sigma \hat{n}_{d\sigma} + U\hat{n}_{d\uparrow}\hat{n}_{d\downarrow}, \tag{26}$$

where s labels the uncorrelated bath site and d the correlated quantum-impurity site. The first constraint would be that Hamiltonian (26) has a ground state with the same occupations of the 2-site Hubbard model, i.e., at half filling, $n_d = n_s = 1$. Such a *self-consistency condition* is satisfied if $\varepsilon_s = \mu = \varepsilon_d + U/2$. This can be understood by comparing the Hamiltonian matrices of the two models in the Hilbert space with $N = 2$ electrons. To this end, we first order the

two-electron states of the Hubbard dimer as

$$|1\rangle = c_{1\uparrow}^\dagger c_{2\uparrow}^\dagger|0\rangle, \qquad\qquad |4\rangle = \tfrac{1}{\sqrt{2}}(c_{1\uparrow}^\dagger c_{2\downarrow}^\dagger - c_{1\downarrow}^\dagger c_{2\uparrow}^\dagger)|0\rangle,$$

$$|2\rangle = c_{1\downarrow}^\dagger c_{2\downarrow}^\dagger|0\rangle, \qquad\qquad |5\rangle = c_{1\uparrow}^\dagger c_{1\downarrow}^\dagger|0\rangle, \qquad\qquad (27)$$

$$|3\rangle = \tfrac{1}{\sqrt{2}}(c_{1\uparrow}^\dagger c_{2\downarrow}^\dagger + c_{1\downarrow}^\dagger c_{2\uparrow}^\dagger)|0\rangle, \qquad\qquad |6\rangle = c_{2\uparrow}^\dagger c_{2\downarrow}^\dagger|0\rangle.$$

In this basis the Hamiltonian of the Hubbard dimer has the matrix form

$$\hat{H}_2(\varepsilon_d, U, t) = \begin{pmatrix} 2\varepsilon_d & 0 & 0 & 0 & 0 & 0 \\ 0 & 2\varepsilon_d & 0 & 0 & 0 & 0 \\ 0 & 0 & 2\varepsilon_d & 0 & 0 & 0 \\ 0 & 0 & 0 & 2\varepsilon_d & -\sqrt{2}t & -\sqrt{2}t \\ 0 & 0 & 0 & -\sqrt{2}t & 2\varepsilon_d+U & 0 \\ 0 & 0 & 0 & -\sqrt{2}t & 0 & 2\varepsilon_d+U \end{pmatrix}. \qquad (28)$$

The ground state, the singlet given in Eq. (10), can be obtained by diagonalizing the lower 3×3 block. For the Anderson molecule, ordering the basis in the same way ($1 \to d, 2 \to s$), this Hamiltonian becomes

$$\hat{H}_2^A(\varepsilon_d, U, t; \varepsilon_s) = \begin{pmatrix} \varepsilon_d+\varepsilon_s & 0 & 0 & 0 & 0 & 0 \\ 0 & \varepsilon_d+\varepsilon_s & 0 & 0 & 0 & 0 \\ 0 & 0 & \varepsilon_d+\varepsilon_s & 0 & 0 & 0 \\ 0 & 0 & 0 & \varepsilon_d+\varepsilon_s & -\sqrt{2}t & -\sqrt{2}t \\ 0 & 0 & 0 & -\sqrt{2}t & 2\varepsilon_d+U & 0 \\ 0 & 0 & 0 & -\sqrt{2}t & 0 & 2\varepsilon_s \end{pmatrix}. \qquad (29)$$

Comparing the lower 3×3 block of $\hat{H}_2^A(\varepsilon_d, U, t; \varepsilon_s)$ with the corresponding block of $\hat{H}_2(\varepsilon_d, U, t)$ we can see that, unless $\varepsilon_s = \mu = \varepsilon_d + U/2$, the two doubly occupied states $|5\rangle$ and $|6\rangle$ have different energies and thus the two sites $i = 1, 2$ are differently occupied in the ground state. By setting $\varepsilon_s = \mu$ we find that

$$\hat{H}_2^A(\varepsilon_d, U, t; \mu) = \hat{H}_2(\varepsilon_d+\tfrac{U}{4}, \tfrac{U}{2}, t). \qquad (30)$$

The $N = 2$ ground state of $\hat{H}_2^A(\varepsilon_d, U, t; \mu)$ has thus the form of the ground-state for the Hubbard dimer

$$|G\rangle_A = \frac{a_2(t, U/2)}{\sqrt{2}} \left(c_{d\uparrow}^\dagger c_{s\downarrow}^\dagger - c_{d\downarrow}^\dagger c_{s\uparrow}^\dagger \right) |0\rangle + \frac{a_1(t, U/2)}{\sqrt{2}} \left(c_{d\uparrow}^\dagger c_{d\downarrow}^\dagger + c_{s\uparrow}^\dagger c_{s\downarrow}^\dagger \right) |0\rangle, \qquad (31)$$

and the condition $n_s = n_d = 1$ is satisfied. Since $\varepsilon_s \neq \varepsilon_d$, however, the eigenstates of $\hat{H}^A$ for one electron ($N = 1$) or one hole ($N = 3$) are not the bonding and antibonding states of the

Hubbard dimer.[4] The impurity Green function is then given by

$$G_{d,d}^{\sigma}(i\nu_n) = \frac{1}{4}\Bigg(\frac{1 + w'(t,U)}{i\nu_n - (E_0(2) - E_-(1) - \mu)} + \frac{1 - w'(t,U)}{i\nu_n - (E_+(3) - E_0(2) - \mu)}$$

$$\frac{1 - w'(t,U)}{i\nu_n - (E_0(2) - E_+(1) - \mu)} + \frac{1 + w'(t,U)}{i\nu_n - (E_-(3) - E_0(2) - \mu)}\Bigg), \qquad (32)$$

where

$$E_0(2) - E_{\pm}(1) - \mu = -\Big(E_{\pm}(3) - E_0(2) - \mu\Big) = -\frac{1}{4}\Big(2\Delta(t,U/2) \pm \Delta(t,U)\Big) \qquad (33)$$

and

$$w'(t,U) = \frac{1}{2}\frac{32t^2 - U^2}{\Delta(t,U)\Delta(t,U/2)} . \qquad (34)$$

After some rearrangement we obtain a much simpler expression

$$G_{d,d}^{\sigma}(i\nu_n) = \frac{1}{i\nu_n + \mu - \varepsilon_d - \mathcal{F}_0^{\sigma}(i\nu_n) - \Sigma_A^{\sigma}(i\nu_n)} . \qquad (35)$$

The impurity self-energy equals the local self-energy of the Hubbard dimer

$$\Sigma_A^{\sigma}(i\nu_n) = \frac{U}{2} + \frac{U^2}{4}\frac{i\nu_n}{(i\nu_n)^2 - (3t)^2} , \qquad (36)$$

as one may see comparing it to equation (19). The hybridization function is given by

$$\mathcal{F}_0^{\sigma}(i\nu_n) = \frac{t^2}{i\nu_n} , \qquad (37)$$

as for the non-interacting Hubbard dimer, Eq. (22). For $U = 0$, $G_{d,d}^{\sigma}(i\nu_n)$ equals the non-interacting impurity Green function

$$G_{d,d}^{0\sigma}(i\nu_n) = \frac{1}{i\nu_n + \mu - \varepsilon_d - \mathcal{F}_0^{\sigma}(i\nu_n)} . \qquad (38)$$

The impurity Green function thus satisfies the *impurity Dyson equation*

$$\Sigma_A^{\sigma}(i\nu_n) = \frac{1}{G_{d,d}^{0\sigma}(i\nu_n)} - \frac{1}{G_{d,d}^{\sigma}(i\nu_n)} . \qquad (39)$$

In Fig. 2 we show the retarded impurity Green function of the Anderson molecule (orange, right panels) and the retarded local Green function of the 2-site Hubbard model, both in the local self-energy approximation (blue, right panels) and exact (blue, left panels). Comparing left and right panels we can see that setting $\Delta\Sigma_l^{\sigma}(\omega) = 0$ yields large errors. The right panels demonstrate, however, that the spectral function of the Anderson molecule is quite similar to the one of the Hubbard dimer with $\Delta\Sigma_l^{\sigma}(\omega) = 0$. The small remaining deviations come from the

---

[4]The complete list of eigenvalues and eigenvectors of the Anderson molecule for $\varepsilon_s = \varepsilon_d + U/2$ and arbitrary electron number N can be found in Appendix A.2.
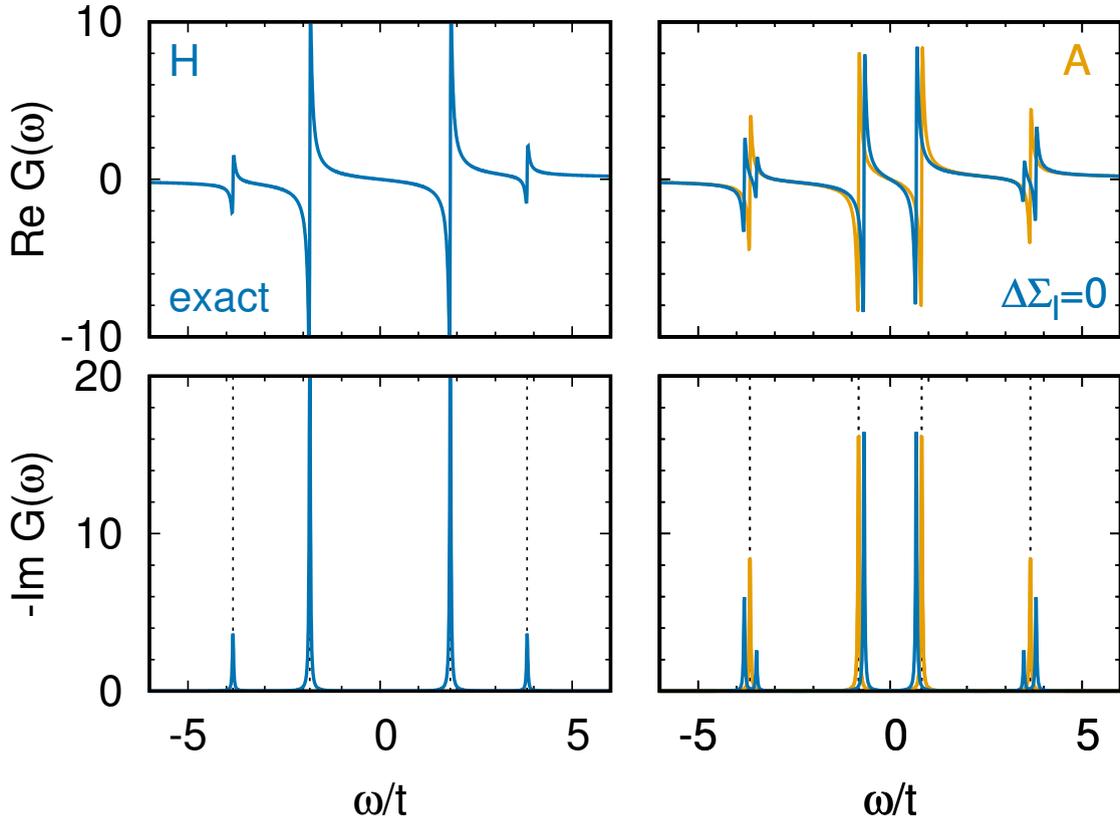
Fig. 2: *Retarded Green function of the Hubbard dimer ($t = 1, U = 4$) and of the Anderson molecule ($\varepsilon_s = \varepsilon_d + U/2$) in the zero temperature limit. Left panels: Hubbard dimer, exact Green function. Right panels, blue: Hubbard dimer in the local self-energy approximation, i.e., with $\Delta\Sigma_l^\sigma(\omega) = 0$. Right panels, orange: Anderson molecule. Dashed lines: Poles for the Hubbard dimer (left) or the Anderson molecule (right).*

fact that, for the Hubbard dimer, in the impurity Dyson equation, the non-interacting impurity Green function is replaced by $\mathfrak{G}_{i,i}^\sigma(i\nu_n)$ in the local self-energy approximation, i.e., by the *bath* Green function

$$\mathcal{G}_{i,i}^\sigma(i\nu_n) = \frac{1}{i\nu_n + \mu - \varepsilon_d - \mathcal{F}_l^\sigma(i\nu_n)} \,, \tag{40}$$

where

$$\mathcal{F}_l^\sigma(i\nu_n) = \frac{t^2}{i\nu_n + \mu - \varepsilon_d - \Sigma_A^\sigma(i\nu_n)} \,. \tag{41}$$

We are now in the position of explaining how DMFT works for the Hamiltonian of the Hubbard dimer, choosing the Anderson molecule Hamiltonian (26) as the auxiliary quantum-impurity model. The procedure can be split in the following steps

1. Build the initial quantum impurity model with $G_{d,d}^{0\sigma}(i\nu_n) = G_{i,i}^{0\sigma}(i\nu_n)$. The initial bath is thus defined by energy $\varepsilon_s = \varepsilon_d$ and hopping t.

2. Calculate the local Green function $G_{d,d}^\sigma(i\nu_n)$ for the auxiliary model.

3. Use the local Dyson equation to calculate the impurity self-energy

$$\Sigma_A^\sigma(i\nu_n) = \frac{1}{G_{d,d}^{0\sigma}(i\nu_n)} - \frac{1}{G_{d,d}^\sigma(i\nu_n)}.$$

4. Calculate the local Green function of the Hubbard dimer setting the self-energy equal to the one of the quantum-impurity model

$$G_{i,i}^\sigma(i\nu_n) \sim \frac{1}{2}\left(\frac{1}{i\nu_n + \mu - \varepsilon_d + t - \Sigma_A^\sigma(i\nu_n)} + \frac{1}{i\nu_n + \mu - \varepsilon_d - t - \Sigma_A^\sigma(i\nu_n)} \right).$$

5. Calculate a new bath Green function $\mathcal{G}_{i,i}^\sigma(i\nu_n)$ from the local Dyson equation

$$\mathcal{G}_{i,i}^\sigma(i\nu_n) = \frac{1}{\Sigma_A^\sigma(i\nu_n) + 1/G_{i,i}^\sigma(i\nu_n)}.$$

6. Build a new $G_{d,d}^{0\sigma}(i\nu_n)$ from $\mathcal{G}_{i,i}^\sigma(i\nu_n)$.

7. Restart from the second step.

8. Iterate till self-consistency, i.e., here till $n_d^\sigma = n_i^\sigma$ and $\Sigma_A^\sigma(i\nu_n)$ does not change any more.

The Anderson molecule satisfies the self-consistency requirements for $\varepsilon_s = \mu$. The remaining difference between $G_{d,d}^\sigma(i\nu_n)$, the impurity Green function, and $G_{i,i}^\sigma(i\nu_n)$, the local Green function of the Hubbard dimer in the local self-energy approximation, arises from the difference in the associated hybridization functions

$$\Delta\mathcal{F}_l(i\nu_n) = \mathcal{F}_l^\sigma(i\nu_n) - \mathcal{F}_0^\sigma(i\nu_n) = t^2 p^2 \left(-\frac{2}{i\nu_n} + \frac{1}{i\nu_n - \varepsilon_a} + \frac{1}{i\nu_n + \varepsilon_a} \right) \qquad (42)$$

where $p^2 = U^2/8\varepsilon_a^2$ and $\varepsilon_a = \sqrt{9t^2 + U^2/4}$. The error made is small, however, as shown in the right panels of Fig. 2. To further improve we would have to modify the auxiliary model adding more bath sites. Staying with the Anderson molecule, in Fig. 3 we compare in more detail its spectral function with the exact spectral function of the Hubbard dimer. The figure emphasizes several important conclusions. The top right panel reminds us that DMFT is not a good approximation for molecular complexes with two (or few) correlated sites. This is because in such systems the coordination number is the lowest possible, the worst case for dynamical mean-field theory. In three-dimensional crystals, instead, the coordination number is typically large enough to make dynamical mean-field theory an excellent approximation. The bottom left panel of Fig. 3 shows that, in the local-self-energy approximation, the agreement between Anderson and Hubbard Green functions remains very good for any U value. This indicates that when the local-self-energy approximation works well, as in the case of three-dimensional crystals, it can be successfully used to study the behavior of a given system as a function of U. Leaving for a moment DMFT aside, the two bottom panels of Fig. 3 show that the evolution with U is different for the impurity Green function of the Anderson molecule and the exact local Green function of the Hubbard dimer. Anticipating the discussion of later sections, if we compare to
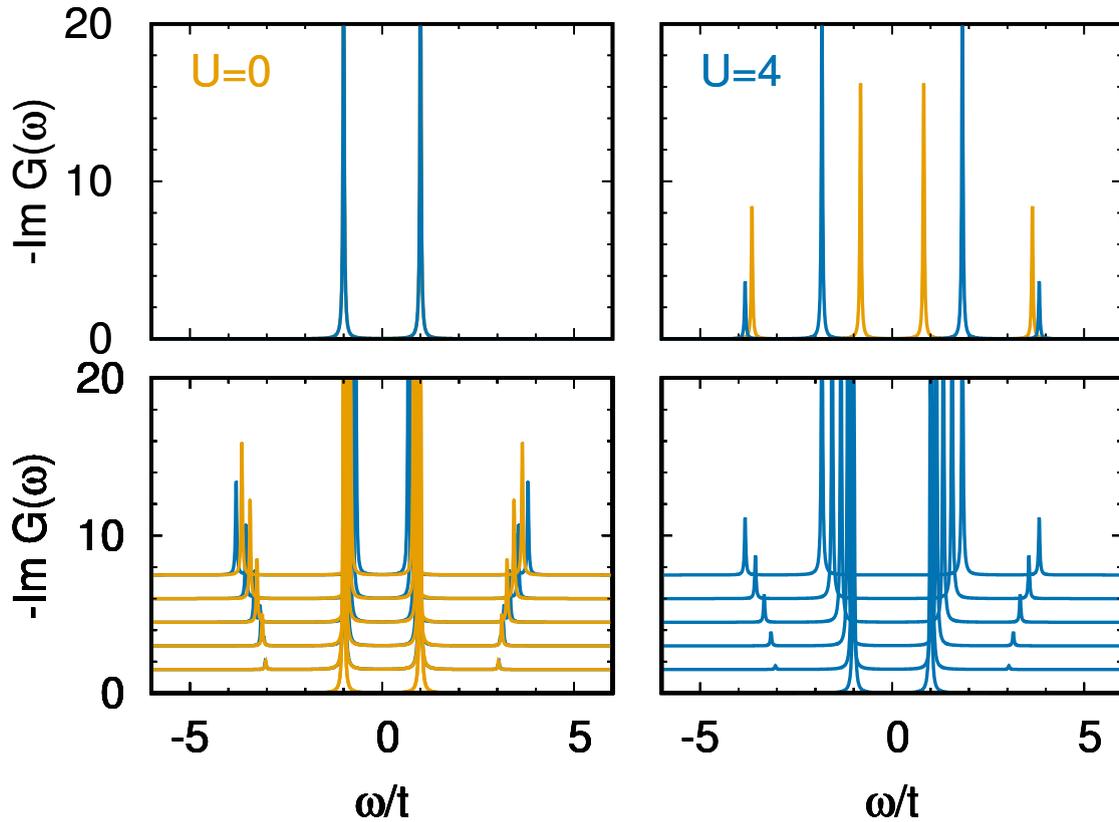
Fig. 3: *Imaginary part of the retarded Green function of the Anderson molecule (orange) and Hubbard dimer (blue) in the zero temperature limit. In the bottom left panel the local self-energy approximation is adopted for the Hubbard dimer; in all other cases the exact Green function of the Hubbard dimer is shown. Parameters: $t = 1$, $\varepsilon_s = \mu$. Top: $U = 0$ (left) and $U = 4t$ (right). Bottom: Evolution with increasing U from 0 to $4t$ in equal steps.*

the spectral function of the actual *lattice* Hubbard model, we could say that the Hubbard dimer captures well the evolution of the Hubbard bands and the gap in the large-U limit. On the other hand, the Anderson molecule partially captures the behavior of the central "quasi-particle" or "Kondo" peak, although the Kondo effect itself is unrealistically described; as a matter of fact, the Kondo energy gain (the "Kondo temperature") is perturbative ($\propto t^2/U$) in the case of the Anderson molecule, while it is exponentially small for a Kondo impurity in a metallic bath. Going back to DMFT, this also points to the possible shortcomings of calculations in which the quantum-impurity model for the lattice Hubbard model is solved via exact diagonalization, however using a single bath site or very few; this might perhaps be sufficient in the limit of large gap,[5] but is bound to eventually fail approaching the metallic regime. Indeed, this failure is one of the reasons why the solution of the Kondo problem required the development of—at the time new—non-perturbative techniques such as the numerical renormalization group.

---

[5]For a discussion of bath parametrization in exact diagonalization and the actual convergence with the number of bath sites for the lattice Hubbard model see Ref. [11].

2.2 Non-local Coulomb interaction

In Sec. 2.1 we have seen that the local Coulomb interaction gives rise, *alone*, to non-local self-energy terms, which can be very important. What is, instead, the effect of the non-local part of the Coulomb interaction? For a Hubbard dimer, extending the Coulomb interaction to first neighbors leads to the Hamiltonian

$$
\hat{H} = \varepsilon_d \sum_{i\sigma} \hat{n}_{i\sigma} - t \sum_\sigma \left(c_{1\sigma}^\dagger c_{2\sigma} + c_{2\sigma}^\dagger c_{1\sigma} \right) + U \sum_{i=1,2} \hat{n}_{i\uparrow} \hat{n}_{i\downarrow}
$$

$$
+ \sum_{\sigma\sigma'} (V - 2J_V - J_V \, \delta_{\sigma\sigma'}) \hat{n}_{1\sigma} \hat{n}_{2\sigma'} - J_V \sum_{i \neq i'} \left(c_{i\uparrow}^\dagger c_{i\downarrow} c_{i'\downarrow}^\dagger c_{i'\uparrow} + c_{i'\uparrow}^\dagger c_{i'\downarrow}^\dagger c_{i\uparrow} c_{i\downarrow} \right), \qquad (43)
$$

where the parameters in the last two terms are the intersite direct (V) and exchange (J_V) Coulomb interaction. For two electrons the Hamiltonian, in a matrix form, becomes

$$
\hat{H}_2^{\mathrm{NL}} = \begin{pmatrix}
2\varepsilon_d + V - 3J_V & 0 & 0 & 0 & 0 & 0 \\
0 & 2\varepsilon_d + V - 3J_V & 0 & 0 & 0 & 0 \\
0 & 0 & 2\varepsilon_d + V - 3J_V & 0 & 0 & 0 \\
0 & 0 & 0 & 2\varepsilon_d + V - J_V & -\sqrt{2}t & -\sqrt{2}t \\
0 & 0 & 0 & -\sqrt{2}t & 2\varepsilon_d + U & -J_V \\
0 & 0 & 0 & -\sqrt{2}t & -J_V & 2\varepsilon_d + U
\end{pmatrix},
$$

where the basis is defined in Eq. (27). In the atomic ($t = 0$) limit, the triplet states, $|1\rangle$, $|2\rangle$ and $|3\rangle$, have lower energy than the singlet states, $|4\rangle$, $|5\rangle$ and $|6\rangle$, as one can see by comparing the diagonal elements of the upper and lower 3×3 block of the matrix $\hat{H}_2^{\mathrm{NL}}$ here above. This is due to the fact that J_V is positive (ferromagnetic) and $V < U$. The triplet can remain the ground multiplet even for finite t. If, however, J_V is sufficiently small, the ground state is a singlet, as in the case $V = J_V = 0$. Setting for simplicity $J_V = 0$, we notice that $\hat{H}_2^{\mathrm{NL}} = \hat{H}_2(\varepsilon_d', U', t)$, where the right-hand-side term is the $N = 2$-electron Hamiltonian of the $J_V = V = 0$ Hubbard dimer, Eq. (28), with parameters $\varepsilon_d' = \varepsilon_d + V/2$ and $U' = U - V$. The $N = 2$ ground state is thus still given by Eq. (10), provided that we replace U with U' in the coefficients. Eventually, in the limiting case $U = V$, $\hat{H}_2^{\mathrm{NL}}$ equals the corresponding Hamiltonian of an effective non-correlated dimer, $\hat{H}_2(\varepsilon_d', 0, t)$. What happens away from half filling? For $N = 1$ electrons, eigenvectors and eigenvalues are the same as in the $V = 0$ case; for $N = 3$ electrons all energies are shifted by $2V$. Summarizing, we can obtain the Green function for $V \neq 0$ from Eq. (14) setting

$$
E_\pm(N=1, U; V) = E_\pm(N=1, U; 0) \qquad\qquad = \varepsilon_d \pm t
$$

$$
E_\pm(N=3, U; V) = E_\pm(N=3, U; 0) + 2V \qquad\qquad = 3\varepsilon_d \pm t + U + 2V
$$

$$
E_0(N=2, U; V) = E_0(N=2, U-V; 0) + V \qquad\qquad = E_0(2, U-V) + V
$$

$$
\mu(U; V) = \mu(U) + V \qquad\qquad = \mu + V
$$

$$
w_\pm(t, U; V) = w_\pm(t, U-V; 0).
$$
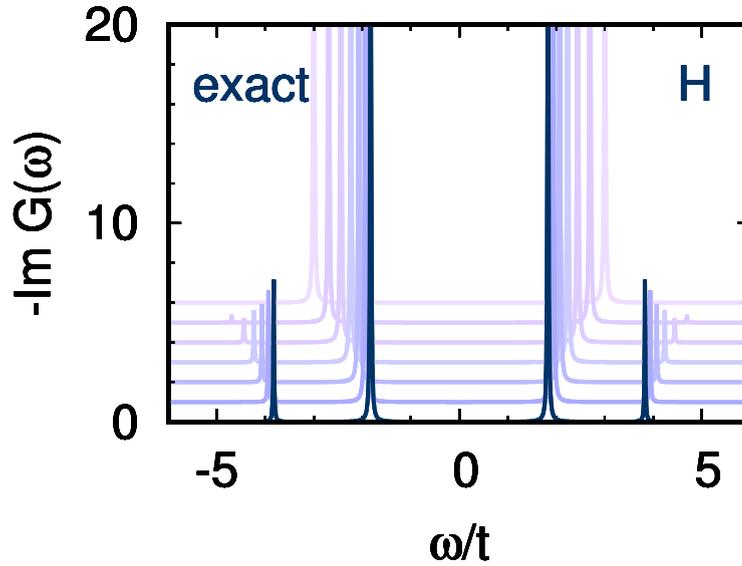
Fig. 4: *Imaginary part of the retarded Green function of the Hubbard dimer in the zero temperature limit ($U = 4$, $t = 1$), increasing the intersite Coulomb repulsion V from 0 to $V = U = 4$ in equal steps; we have set $J_V = 0$. The dark blue line corresponds to $V = 0$.*

Thus we have, recalling that $U' = U - V$,

$$
\begin{aligned}
G_{i,i}^{\sigma}(i\nu_n) = & \frac{w_+(t, U')}{i\nu_n - \left(E_0'(2) - \frac{1}{2}V - \varepsilon_d + t - \mu'\right)} + \frac{w_-(t, U')}{i\nu_n - \left(-E_0'(2) + U' + \frac{1}{2}V + 3\varepsilon_d + t - \mu'\right)} \\
& + \frac{w_-(t, U')}{i\nu_n - \left(E_0'(2) - \frac{1}{2}V - \varepsilon_d - t - \mu'\right)} + \frac{w_+(t, U')}{i\nu_n - \left(-E_0'(2) + U' + \frac{1}{2}V + 3\varepsilon_d - t - \mu'\right)},
\end{aligned} \tag{44}
$$

where we set $\mu' = \mu - V/2 = 2\varepsilon_d + U'/2$ and $E_0'(2) = E_0(2, U')$. The associated spectral function is shown in Fig. 4. The figure illustrates that increasing V from 0 to U makes the spectra progressively closer to the one of a non-correlated system. Eventually, for $U = V$, only two poles contribute, since $w_-(t, U') = 0$. In this limit, the spectral function is identical to the one of the non-interacting Hubbard dimer, however with an enhanced effective hopping, $t \longrightarrow t + V/2$. We can thus say that, in first approximation, the (positive) intersite coupling V effectively reduces the strength of correlations in the Hubbard dimer. In conclusion, the case of the Hubbard dimer explains why *strong-correlation* effects typically appear when the *local term of the electron-electron repulsion dominates*, i.e., when it is much larger than long-range terms. A hypothetical system in which the Coulomb interaction strength is independent on the distance between sites (for the dimer, $U = V$) is likely to be already well described via an *effective weakly correlated model*. Of course, in real materials, the effects of long-range Coulomb repulsion can be much more complicated than in the two-site model just discussed, but the general considerations made here remain true even in realistic cases.

2.3   Quantum-impurity solvers: Continuous-time quantum Monte Carlo

For the case of the Anderson molecule exact diagonalization is the simplest quantum-impurity solver and the one that provides most insights. Methods based on quantum Monte Carlo (QMC) sampling are often, however, the only option for realistic multi-orbital and/or multi-site models. Thus, here we explain how to obtain the impurity Green function of the Anderson molecule via hybridization-expansion continuous-time QMC [12], a very successful QMC-based quantum-impurity solver. In this approach, the first step consists in splitting the Hamiltonian into bath $(\hat{H}_{\text{bath}})$, hybridization $(\hat{H}_{\text{hyb}})$, and local $(\hat{H}_{\text{loc}})$ terms

$$\hat{H}^{\text{A}} = \underbrace{\varepsilon_s \sum_\sigma \hat{n}_{s\sigma}}_{\hat{H}_{\text{bath}}} \underbrace{-t \sum_\sigma \left(c_{d\sigma}^\dagger c_{s\sigma} + c_{s\sigma}^\dagger c_{d\sigma} \right)}_{\hat{H}_{\text{hyb}}} + \underbrace{\varepsilon_d \sum_\sigma \hat{n}_{d\sigma} + U \hat{n}_{d\uparrow} \hat{n}_{d\downarrow}}_{\hat{H}_{\text{loc}}} . \tag{45}$$

Next, we write the partition function Z as a perturbation series in the hybridization. To this end, we define $\hat{H}_0 = \hat{H}_{\text{bath}} + \hat{H}_{\text{loc}}$ and rewrite the partition function as

$$Z = \text{Tr} \left(e^{-\beta(\hat{H}_0 - \mu\hat{N})} \hat{V}(\beta) \right) \tag{46}$$

where the operator $\hat{V}(\beta)$ is given by

$$\hat{V}(\beta) = e^{\beta(\hat{H}_0 - \mu\hat{N})} \, e^{-\beta(\hat{H}_0 + \hat{H}_{\text{hyb}} - \mu\hat{N})} = \sum_m \underbrace{\int_0^\beta d\tau_1 \cdots \int_{\tau_{m-1}}^\beta d\tau_m}_{\int d\boldsymbol{\tau}^m} \underbrace{(-1)^m \prod_{l=m}^1 \hat{H}_{\text{hyb}}(\tau_l)}_{\hat{O}^m(\boldsymbol{\tau})}, \tag{47}$$

and

$$\hat{H}_{\text{hyb}}(\tau_l) = e^{\tau_l(\hat{H}_0 - \mu\hat{N})} \, \hat{H}_{\text{hyb}} \, e^{-\tau_l(\hat{H}_0 - \mu\hat{N})} = -t \sum_\sigma \left(c_{d\sigma_l}^\dagger(\tau_l) c_{s\sigma_l}(\tau_l) + c_{s\sigma_l}^\dagger(\tau_l) c_{d\sigma_l}(\tau_l) \right). \tag{48}$$

In this expansion, the only terms that contribute to the trace are even order ones $(m = 2k)$ and they are products of impurity (d) and bath (s) creator-annihilator pairs. We can thus rewrite

$$\int d\boldsymbol{\tau}^{2k} \longrightarrow \int d\boldsymbol{\tau}^k \int d\bar{\boldsymbol{\tau}}^k \quad \text{and} \quad \hat{O}^{2k}(\boldsymbol{\tau}) \longrightarrow \sum_{\boldsymbol{\sigma}, \bar{\boldsymbol{\sigma}}} \hat{O}_{\boldsymbol{\sigma}, \bar{\boldsymbol{\sigma}}}^{2k}(\boldsymbol{\tau}, \bar{\boldsymbol{\tau}}) \tag{49}$$

where

$$\hat{O}_{\boldsymbol{\sigma}, \bar{\boldsymbol{\sigma}}}^{2k}(\boldsymbol{\tau}, \bar{\boldsymbol{\tau}}) = (t)^{2k} \prod_{i=1}^k \left(c_{d\bar{\sigma}_i}^\dagger(\bar{\tau}_i) c_{s\bar{\sigma}_i}(\bar{\tau}_i) c_{s\sigma_i}^\dagger(\tau_i) c_{d\sigma_i}(\tau_i) \right). \tag{50}$$

The vector $\boldsymbol{\sigma} = (\sigma_1, \sigma_2, ..., \sigma_k)$ gives the spins $\{\sigma_i\}$ associated with the k impurity annihilators at imaginary times $\{\tau_i\}$, while $\bar{\boldsymbol{\sigma}} = (\bar{\sigma}_1, \bar{\sigma}_2, ..., \bar{\sigma}_k)$ gives the spins $\{\bar{\sigma}_i\}$ associated with the k impurity creators at imaginary times $\{\bar{\tau}_i\}$. It follows that the local and bath traces can be

decoupled and the partition function can be rewritten as

$$\frac{Z}{Z_{\text{bath}}} = \sum_k \int d\boldsymbol{\tau}^k \int d\bar{\boldsymbol{\tau}}^k \sum_{\boldsymbol{\sigma},\bar{\boldsymbol{\sigma}}} d^k_{\bar{\boldsymbol{\sigma}},\boldsymbol{\sigma}}(\boldsymbol{\tau},\bar{\boldsymbol{\tau}})\, t^k_{\boldsymbol{\sigma},\bar{\boldsymbol{\sigma}}}(\boldsymbol{\tau},\bar{\boldsymbol{\tau}}) \tag{51}$$

$$d^k_{\bar{\boldsymbol{\sigma}},\boldsymbol{\sigma}}(\boldsymbol{\tau},\bar{\boldsymbol{\tau}}) = \frac{t^{2k}}{Z_{\text{bath}}}\,\text{Tr}_{\text{bath}}\left(e^{-\beta(\hat{H}_{\text{bath}}-\mu\hat{N}_s)}\mathcal{T}\prod_{i=k}^{1} c^{\dagger}_{s\sigma_i}(\tau_i)c_{s\bar{\sigma}_i}(\bar{\tau}_i)\right) \tag{52}$$

$$t^k_{\boldsymbol{\sigma},\bar{\boldsymbol{\sigma}}}(\boldsymbol{\tau},\bar{\boldsymbol{\tau}}) = \text{Tr}_{\text{loc}}\left(e^{-\beta(\hat{H}_{\text{loc}}-\mu\hat{N}_d)}\mathcal{T}\prod_{i=k}^{1} c_{d\sigma_i}(\tau_i)c^{\dagger}_{d\bar{\sigma}_i}(\bar{\tau}_i)\right), \tag{53}$$

where $Z_{\text{bath}} = 1 + 2e^{-\beta(\varepsilon_s-\mu)} + e^{-2\beta(\varepsilon_s-\mu)}$ and

$$c_{d\sigma}(\tau) = e^{\tau(\hat{H}_{\text{loc}}-\mu\hat{N}_d)}c_{d\sigma}e^{-\tau(\hat{H}_{\text{loc}}-\mu\hat{N}_d)}, \qquad c_{s\sigma}(\tau) = e^{\tau(\hat{H}_{\text{bath}}-\mu\hat{N}_s)}c_{s\sigma}e^{-\tau(\hat{H}_{\text{bath}}-\mu\hat{N}_s)}.$$

The trace involving only bath operators is simple to calculate, since $\hat{H}_{\text{bath}}$ describes an independent-electron problem for which Wick's theorem holds. It is given by the determinant

$$d^k_{\bar{\boldsymbol{\sigma}},\boldsymbol{\sigma}}(\boldsymbol{\tau},\bar{\boldsymbol{\tau}}) = \det\left(\mathcal{F}^k_{\bar{\boldsymbol{\sigma}},\boldsymbol{\sigma}}(\boldsymbol{\tau},\bar{\boldsymbol{\tau}})\right) \tag{54}$$

of the $k\times k$ non-interacting hybridization-function matrix, with elements

$$\left(\mathcal{F}^k_{\bar{\boldsymbol{\sigma}},\boldsymbol{\sigma}}(\boldsymbol{\tau},\bar{\boldsymbol{\tau}})\right)_{i',i} = \mathcal{F}^0_{\bar{\sigma}_{i'},\sigma_i}(\bar{\tau}_{i'}-\tau_i) \tag{55}$$

where

$$\mathcal{F}^0_{\bar{\sigma},\sigma}(\tau) = \delta_{\bar{\sigma},\sigma}\frac{t^2}{1+e^{-\beta(\varepsilon_s-\mu)}} \times \begin{cases} -e^{-\tau(\varepsilon_s-\mu)} & \tau > 0, \\ +e^{-(\beta+\tau)(\varepsilon_s-\mu)} & \tau < 0. \end{cases} \tag{56}$$

This is the imaginary time Fourier transform of the hybridization function introduced previously

$$\mathcal{F}^0_{\bar{\sigma},\sigma}(i\nu_n) = \frac{t^2}{i\nu_n - (\varepsilon_s-\mu)}\,\delta_{\bar{\sigma},\sigma}. \tag{57}$$

The calculation of the local trace is in general more complicated. In the case discussed here, the Hamiltonian does not flip spins. Thus only terms with an equal number of creation and annihilation operators *per spin* contribute to the local trace, and we can express the partition function in expansion orders per spin, k_σ. This yields [13]

$$\frac{Z}{Z_{\text{bath}}} = \left(\prod_\sigma \sum_{k_\sigma=0}^{\infty} \int d\boldsymbol{\tau}_\sigma^{k_\sigma} \int d\bar{\boldsymbol{\tau}}_\sigma^{k_\sigma}\right) d^k_{\bar{\boldsymbol{\sigma}},\boldsymbol{\sigma}}(\boldsymbol{\tau},\bar{\boldsymbol{\tau}})t^k_{\boldsymbol{\sigma},\bar{\boldsymbol{\sigma}}}(\boldsymbol{\tau},\bar{\boldsymbol{\tau}}) \tag{58}$$

where the vectors $\boldsymbol{\sigma} = (\boldsymbol{\sigma}_\uparrow, \boldsymbol{\sigma}_\downarrow)$ and $\bar{\boldsymbol{\sigma}} = (\bar{\boldsymbol{\sigma}}_\uparrow, \bar{\boldsymbol{\sigma}}_\downarrow)$ have $(k_\uparrow, k_\downarrow)$ components, and for each k_σ component $\sigma_i = \bar{\sigma}_i = \sigma$. Thus

$$t^k_{\boldsymbol{\sigma},\bar{\boldsymbol{\sigma}}}(\boldsymbol{\tau},\bar{\boldsymbol{\tau}}) = \text{Tr}_{\text{loc}}\left(e^{-\beta(\hat{H}_{\text{loc}}-\mu\hat{N}_d)}\mathcal{T}\prod_\sigma\prod_{i=k_\sigma}^{1} c_{d\sigma}(\tau_{\sigma_i})c^{\dagger}_{d\sigma}(\bar{\tau}_{\bar{\sigma}_i})\right). \tag{59}$$

The latter can be calculated analytically. To do this, first we parametrize all configurations for a given spin via a timeline $[0,\beta)$ plus a number of creator/annihilator pairs which define segments
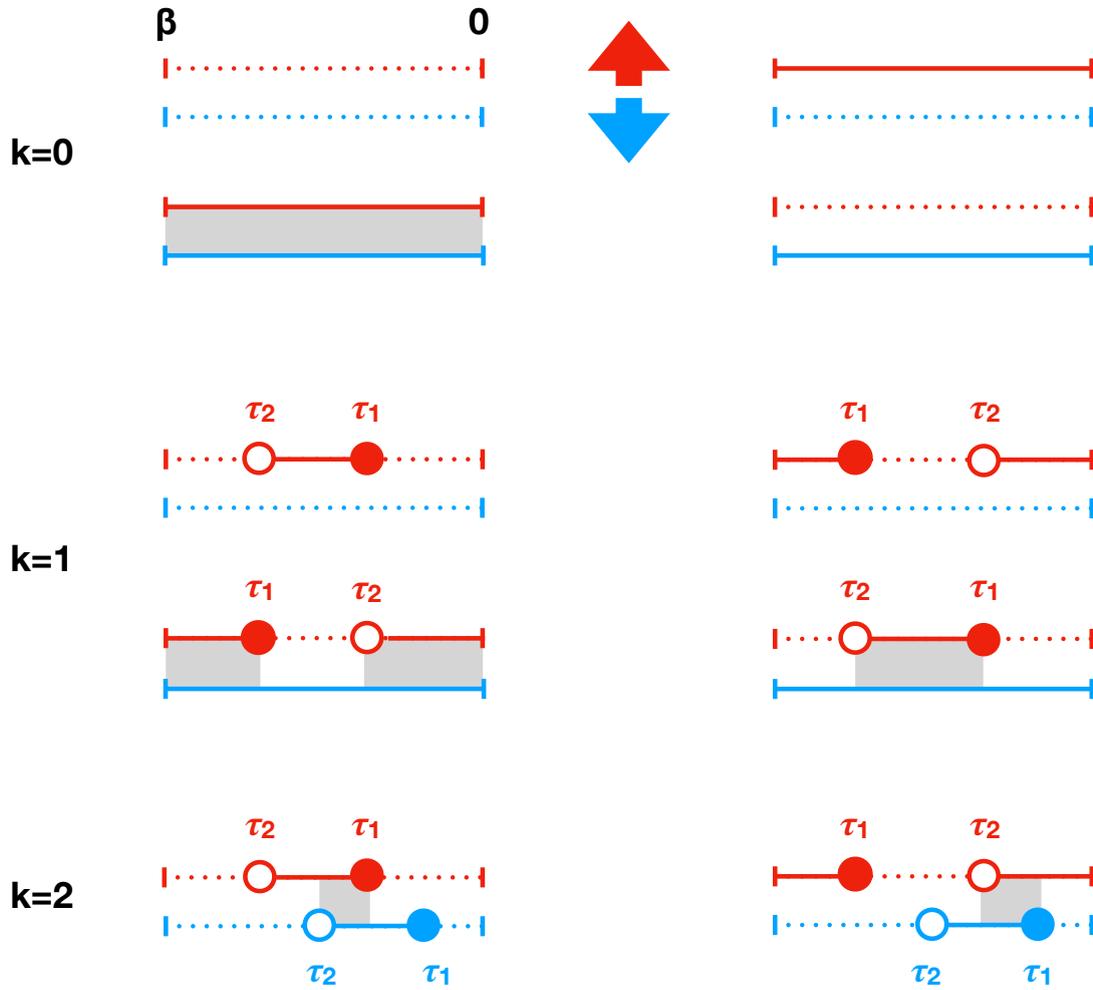
Fig. 5: *Representative configurations contributing to the local trace at zeroth, first and second order. The timelines for spin up are red and those for spin down are blue. The filled circles correspond to the insertion of a creator (time τ_1), and the empty circles to the insertion of an annihilator (time τ_2). Dotted lines represent the vacuum state for a given spin, full lines the occupied state. The grey boxes indicate the regions in which $l_{\uparrow,\downarrow} \neq 0$.*

on the timeline. At zeroth order two possible configurations exist per spin, an empty timeline, which corresponds to the vacuum state $|0\rangle$, and a full timeline, which corresponds to the state $c^\dagger_{d\sigma}|0\rangle$. A given configuration yields, at order $k = k_\uparrow + k_\downarrow$

$$t^k_{\sigma,\bar{\sigma}}(\boldsymbol{\tau}, \bar{\boldsymbol{\tau}}) = \left(\prod_\sigma s^{k_\sigma}_\sigma\right) e^{-\sum_{\sigma\sigma'}((\varepsilon_d - \mu)\delta_{\sigma\sigma'} + \frac{U}{2}(1-\delta_{\sigma,\sigma'}))l_{\sigma,\sigma'}} \qquad (60)$$

where $l_{\sigma,\sigma'}$ is the length of the overlap of the τ segments for spins σ and σ', respectively, while $s_\sigma = \text{sign}(\tau_{\sigma_1} - \bar{\tau}_{\sigma_1})$ is the fermionic sign. Possible configurations at order $k = 0, 1, 2$ are shown in Fig. 5. At order $k = 0$, summing up the contribution of the four configurations shown in Fig. 5 yields the local partition function $Z_{\text{loc}} = 1 + 2e^{-\beta(\varepsilon_d - \mu)} + e^{-\beta(2(\varepsilon_d - \mu) + U)}$. Order $k = 1$ is already more complicated. Setting $\varepsilon_s = \mu$ as in the self-consistent solution, the contribution

to the bath trace in this case is

$$d_{\bar{\sigma}\sigma}^1(\tau_1, \tau_2) = \mathcal{F}_{\bar{\sigma}\sigma}^0(\tau_1, \tau_2) = -\frac{t^2}{2}\delta_{\sigma,\bar{\sigma}} \operatorname{sign}(\tau_1-\tau_2). \tag{61}$$

The local trace at the same order is instead given by

$$t_{\sigma\bar{\sigma}}^1(\tau_2, \tau_1) = \operatorname{Tr}_{\mathrm{loc}}\left(e^{-\beta(\hat{H}_{\mathrm{loc}}-\mu\hat{N}_d)}\mathcal{T}c_{d\sigma}(\tau_2)c_{d\sigma}^\dagger(\tau_1)\right). \tag{62}$$

We can now calculate the contribution at half filling of the four $k = 1$ configurations shown in Fig. 5. In the case $k_\uparrow = 1$ and $k_\downarrow = 0$ we have, going from left to right in each row

$$t_{\uparrow\uparrow}^1(\tau_2, \tau_1) = \begin{cases} +e^{-(\tau_2-\tau_1)(\varepsilon_d-\mu)} & = +e^{+\tau_{21}U/2} \\ -e^{-(\beta-(\tau_1-\tau_2))(\varepsilon_d-\mu)} & = -e^{(\beta+\tau_{21})U/2} \\ -e^{-\beta(2(\varepsilon_d-\mu)+U)+(\tau_1-\tau_2)(\varepsilon_d-\mu+U)} & = -e^{-\tau_{21}U/2} \\ +e^{-(\tau_2-\tau_1)(\varepsilon_d-\mu+U)-\beta(\varepsilon_d-\mu)} & = +e^{(\beta-\tau_{21})U/2} \end{cases} \tag{63}$$

where $\tau_{21} = \tau_2 - \tau_1$ and $\mu = \varepsilon_d + U/2$. Similar results can be obtained for $k_\uparrow = 0$ and $k_\downarrow = 1$. Summing up all terms up to order one we find

$$\frac{Z}{Z_{\mathrm{bath}}} \sim Z_{\mathrm{loc}} + \sum_\sigma \int_0^\beta d\tau_2 \int_0^\beta d\tau_1 \, d_{\sigma\sigma}^1(\tau_1, \tau_2) \, t_{\sigma\sigma}^1(\tau_2, \tau_1)$$

$$\sim Z_{\mathrm{loc}}\left(1 - \beta\frac{1-e^{\frac{\beta U}{2}}}{1+e^{\frac{\beta U}{2}}}\frac{2t^2}{U}\right). \tag{64}$$

The exact formula of the partition function can be obtained from the eigenvalues and eigenvectors in Appendix A.2

$$\frac{Z}{Z_{\mathrm{bath}}} = Z_{\mathrm{loc}}\frac{3(1+e^{\frac{\beta U}{2}}) + e^{\frac{\beta U}{4}}\left(4e^{-\frac{\beta\Delta(t,U)}{4}} + 4e^{+\frac{\beta\Delta(t,U)}{4}} + e^{+\frac{\beta\Delta(t,U/2)}{2}} + e^{-\frac{\beta\Delta(t,U/2)}{2}}\right)}{8(1+e^{\frac{\beta U}{2}})}. \tag{65}$$

Its Taylor expansion in powers of t/U yields, at second order, the expression above. Going back to Eq. (62), one can observe that, for $k = 1$, the local trace is proportional to the local Green function, $G_{d,d}^\sigma(\tau)$. Indeed, $G_{d,d}^\sigma(\tau)$ can be calculated using the configurations just described—provided that we start from $k = 1$ and we divide by the hybridization function. More specifically, for $k = 1$ and $\tau > 0$ we have

$$G_{d,d}^\sigma(\tau) \sim -\frac{1}{\beta}\int_0^\beta\int_0^\beta \underbrace{d\tau_2 d\tau_1 \, d_{\sigma\sigma}^1(\tau_1, \tau_2)t_{\sigma\sigma}^1(\tau_2, \tau_1)}_{w^1} \delta\big(\tau - (\tau_2-\tau_1)\big) \frac{1}{\mathcal{F}_{\sigma\sigma}^0(\tau_1-\tau_2)}. \tag{66}$$

We are now ready to generalize to arbitrary order. Taking all k values into account, the partition function can be expressed as the sum over all configurations $\{c\}$, i.e., in short

$$Z = \sum_c w_c = \sum_c |w_c| \operatorname{sign} w_c. \tag{67}$$

In a compact form, we can write $w_c = d\boldsymbol{\tau}_c \, d_c \, t_c$ where $d\boldsymbol{\tau}_c = \prod_\sigma \prod_i^{k_\sigma} d\tau_{\sigma_i} d\bar{\tau}_{\bar{\sigma}_i}$, and d_c and t_c are the bath and local traces for the configuration c. This expression of the partition function shows that we can interpret $|w_c|$ as the sampling weight of configuration c. A generic observable $\hat{O}$ can then be obtained as the Monte Carlo average on a finite number of configurations N_c

$$\langle \hat{O} \rangle = \frac{\sum_c \langle \hat{O} \rangle_c |w_c| \, \mathrm{sign} \, w_c}{\sum_c |w_c| \, \mathrm{sign} \, w_c} = \frac{\sum_c \mathrm{sign} \, w_c \langle \hat{O} \rangle_c \, |w_c| / \sum_c |w_c|}{\sum_c \mathrm{sign} \, w_c \, |w_c| / \sum_c |w_c|} \approx \frac{\frac{1}{N_c} \sum_c^{N_c} \langle \hat{O} \rangle_c \, \mathrm{sign} \, w_c}{\frac{1}{N_c} \sum_c \mathrm{sign} \, w_c}. \tag{68}$$

The term $\frac{1}{N_c} \sum_c \mathrm{sign} \, w_c$ in the denominator is the average fermionic sign. When this is small, much longer runs are required to obtain data of the same quality; eventually the computational time can become so long that the calculation is unfeasible—in these cases we have a sign problem. In practice, the QMC simulation starts from a random configuration c. Next we propose an update $c \to c'$. Within the Metropolis algorithm, the acceptance ratio is

$$R_{c \to c'} = \min\left(1, \frac{p_{c' \to c}}{p_{c \to c'}} \frac{|w_{c'}|}{|w_c|}\right) \tag{69}$$

where $p_{c \to c'}$ is the proposal probability for the update $c \to c'$. In the approach described here, known as *segment solver*, the basic updates are addition and removal of segments, antisegments (segments winding over the borders of the timeline, see Fig. 5), or complete lines. As example, let us consider the insertion of a segment for spin σ. A segment is made by a creator and an annihilator. The creator is inserted at time τ_{in}; the move is rejected if τ_{in} is in a region where a segment exists. If created, the segment can have at most length l_{max}, given by the distance between τ_{in} and the time at which the next creator is, hence

$$p_{c \to c'} = \frac{d\bar{\tau}}{\beta} \frac{d\tau}{l_{\mathrm{max}}}. \tag{70}$$

The proposal probability of the reverse move (removing a segment) is instead given by the inverse of the number of existing segments

$$p_{c' \to c} = \frac{1}{k_\sigma + 1}. \tag{71}$$

The acceptance ratio for the insertion of a segment becomes then

$$R_{c \to c'} = \min\left(1, \frac{\beta l_{max}}{k_\sigma + 1} \left|\frac{d_{c'}}{d_c} \frac{t_{c'}}{t_c}\right|\right). \tag{72}$$

For the impurity Green function, here the most important observable, the direct average yields

$$\langle \hat{O} \rangle_c = \langle G_{d,d}^\sigma \rangle_c = \sum_{\sigma'} \sum_{i=1}^{k_\sigma} \sum_{j=1}^{k_\sigma} \Delta(\tau, \tau_{\sigma'j} - \bar{\tau}_{\sigma'j}) \left(M^{k'_\sigma}\right)_{\sigma'j, \sigma'i} \delta_{\sigma, \sigma_{\sigma'j}} \delta_{\sigma, \bar{\sigma}_{\sigma'i}} \tag{73}$$

where $M^k = \left(\mathcal{F}^k\right)^{-1}$ is the inverse of the hybridization matrix and

$$\Delta(\tau, \tau') = -\frac{1}{\beta} \begin{cases} \delta(\tau - \tau') & \tau' > 0 \\ -\delta(\tau - (\tau' + \beta)) & \tau' < 0 \end{cases}. \tag{74}$$

One can verify that at order $k = 1$ this indeed returns Eq. (66).

2.4   Hartree-Fock versus DMFT approximation

Let us now compare the exact solution of the Hubbard dimer with the result of the Hartree-Fock (HF) approximation, which consists in replacing

$$\hat{H}_U = U \sum_i \hat{n}_{i\uparrow}\hat{n}_{i\downarrow} \rightarrow \hat{H}_U^{\text{HF}} = U \sum_i \left(\hat{n}_{i\uparrow}\bar{n}_{i\downarrow} + \hat{n}_{i\downarrow}\bar{n}_{i\uparrow} - \bar{n}_{i\uparrow}\bar{n}_{i\downarrow} \right), \tag{75}$$

where $\bar{n}_{i\sigma}$ is the HF expectation value of the operator $\hat{n}_{i\sigma}$. It is convenient to define

$$n_i = \quad \bar{n}_{i\uparrow} + \bar{n}_{i\downarrow} \qquad\qquad n = \frac{1}{2}\left(n_1 + n_2\right) \qquad\qquad \delta n = \frac{1}{2}\left(n_1 - n_2\right)$$

$$m_i = \frac{1}{2}\left(\bar{n}_{i\uparrow} - \bar{n}_{i\downarrow}\right) \qquad\qquad m_+ = \frac{1}{2}\left(m_1 + m_2\right) \qquad\qquad m_- = \frac{1}{2}\left(m_1 - m_2\right)$$

Inverting these relations, in the absence of charge disproportionation ($\delta n = 0$), we find

$$\bar{n}_{i\uparrow} = \left(m_+ + (-1)^{i-1}m_- \right) + n/2 \qquad\qquad \bar{n}_{i\downarrow} = - \left(m_+ + (-1)^{i-1}m_- \right) + n/2 \,.$$

The Hartree-Fock version of the Hubbard dimer Hamiltonian equals the non-interacting Hamiltonian plus a shift of the on-site level. This shift depends on the site and the spin

$$\hat{H}_{\text{HF}} = \sum_{i\sigma} \left(\varepsilon_d + \Delta_{i\sigma} \right)\hat{n}_{i\sigma} - t \sum_\sigma \left(c_{1\sigma}^\dagger c_{2\sigma} + c_{2\sigma}^\dagger c_{1\sigma} \right) - \Delta_0 \tag{76}$$

$$\Delta_0 = 2U \left(\frac{n^2}{4} - m_+^2 - m_-^2 \right) \tag{77}$$

$$\Delta_{i\sigma} = U \left(\frac{1}{2}n - \sigma \left(m_+ + (-1)^{i-1}m_- \right) \right), \tag{78}$$

where $\sigma = +1$ for spin up and $\sigma = -1$ for spin down. Thus we can write immediately the local Green function matrix for site i. It is convenient to use the site basis, hence, to calculate the matrix $G_{i,i'}^\sigma(i\nu_n)$. Then we have

$$G_{i,i}^\sigma(i\nu_n) = \begin{pmatrix} i\nu_n - \left(\varepsilon_d - \mu + \Sigma_{1,1}^\sigma(i\nu_n) \right) & t \\ t & i\nu_n - \left(\varepsilon_d - \mu + \Sigma_{2,2}^\sigma(i\nu_n) \right) \end{pmatrix}_{i,i}^{-1} \tag{79}$$

where we introduced the diagonal self-energy matrix $\Sigma_{i,i'}^\sigma(i\nu_n) = \Delta_{i\sigma}\,\delta_{i,i'}$. This shows that the Hartree-Fock self-energy is not dependent on the frequency, i.e., Hartree-Fock is a *static* mean-field approach. The value of the parameters m_+ and m_- have to be found solving the *self-consistent equations*

$$\bar{n}_{i\sigma} = \langle \hat{n}_{i\sigma} \rangle = \frac{1}{\beta} \sum_n e^{-i\nu_n 0^-} G_{i,i}^\sigma(i\nu_n) = G_{i,i}^\sigma(0^-). \tag{80}$$

Since the exact ground state of the Hubbard dimer is a singlet, let us consider first the anti-ferromagnetic Hartree-Fock solution ($m_+=0$ and $m_-\neq0$). In this case, the Hartree-Fock self-energy depends on the site and the interaction couples states with different k. This becomes

clear rewriting the Green-function matrix in the basis of the bonding $(k = 0)$ and anti-bonding $(k = \pi)$ creation/annihilation operators

$$G^\sigma(i\nu_n) = \frac{1}{2} \begin{pmatrix} i\nu_n - \left(\varepsilon_d - t - \mu + \frac{1}{2}\sum_i \Sigma_{i\sigma}(i\nu_n)\right) & \frac{1}{2}\sum_i (-1)^{i-1}\Sigma_{i\sigma}(i\nu_n) \\ \frac{1}{2}\sum_i (-1)^{i-1}\Sigma_{i\sigma}(i\nu_n) & i\nu_n - \left(\varepsilon_d + t - \mu + \frac{1}{2}\sum_i \Sigma_{i\sigma}(i\nu_n)\right) \end{pmatrix}^{-1}. \quad (81)$$

The diagonal terms of the matrix $\Sigma^\sigma_{k,k'}(i\nu_n)$ are thus identical

$$\Sigma^\sigma_{0,0}(i\nu_n) = \Sigma^\sigma_{\pi,\pi}(i\nu_n) = \frac{1}{2}\left(\Sigma^\sigma_{1,1}(i\nu_n) + \Sigma^\sigma_{2,2}(i\nu_n)\right). \quad (82)$$

The off-diagonal terms $\Sigma^\sigma_{0,\pi}(i\nu_n)$ and $\Sigma^\sigma_{\pi,0}(i\nu_n)$ are not zero, however. This tells us that, by introducing the antiferromagnetic HF correction, we lower the symmetry of the system. Let us now calculate explicitly the eigenstates for different fillings. It is sufficient to diagonalize $\hat{H}_1$, the Hamiltonian in the 1-electron sector; the many-electron states can be obtained by filling the one-electron states respecting the Pauli principle. The Hamiltonian $\hat{H}_1$ can be written as $\hat{H}_1 = \hat{H}'_1 + \varepsilon_d \hat{N} - \Delta_0$, and, in the antiferromagnetic case we then have

$$\hat{H}'_1 = \begin{pmatrix} U\left(\frac{1}{2}n - m_-\right) & -t & 0 & 0 \\ -t & U\left(\frac{1}{2}n + m_-\right) & 0 & 0 \\ 0 & 0 & U\left(\frac{1}{2}n + m_-\right) & -t \\ 0 & 0 & -t & U\left(\frac{1}{2}n - m_-\right) \end{pmatrix}. \quad (83)$$

This leads to the (normalized) states

$\lvert 1\rangle_l$	$E_l(1)$
$\lvert 1\rangle_3 = a_2\lvert 1, 1/2, \uparrow\rangle_1 - a_1\lvert 1, 1/2, \uparrow\rangle_2$	$\varepsilon_0(1) + \Delta_1(t, U)$
$\lvert 1\rangle_2 = a_1\lvert 1, 1/2, \downarrow\rangle_1 - a_2\lvert 1, 1/2, \downarrow\rangle_2$	$\varepsilon_0(1) + \Delta_1(t, U)$
$\lvert 1\rangle_1 = a_1\lvert 1, 1/2, \uparrow\rangle_1 + a_2\lvert 1, 1/2, \uparrow\rangle_2$	$\varepsilon_0(1) - \Delta_1(t, U)$
$\lvert 1\rangle_0 = a_2\lvert 1, 1/2, \downarrow\rangle_1 + a_1\lvert 1, 1/2, \downarrow\rangle_2$	$\varepsilon_0(1) - \Delta_1(t, U)$

where $\varepsilon_0(1) = \varepsilon_d + U\left(1/2 + 2m_-^2 - n^2/2\right)$ and $a_1^2 = \frac{1}{2}\left(1 + \frac{Um_-}{\Delta_1(t,U)}\right)$, while $\Delta_1(t, U) = \sqrt{(m_-U)^2 + t^2}$. At half filling, if we assume that only the ground doublet is occupied, solving the self-consistent equations (80) yields

$$m_- = 0 \quad \text{or} \quad m_- = \frac{1}{2}\sqrt{1 - \frac{4t^2}{U^2}}. \quad (84)$$

As a result, for the non-trivial solution $(m_- \neq 0)$, the gap at half filling is $E_g^{\text{HF}} = 2\Delta_1(t, U) = U$. In Fig. 6, Hartree-Fock and exact spectral function are compared for a specific parameter choice. Looking at the size of the gap only, one could naively infer that, for the case shown, Hartree-Fock is an excellent approximation, better than DMFT (see Fig. 3, top-right panel). This would
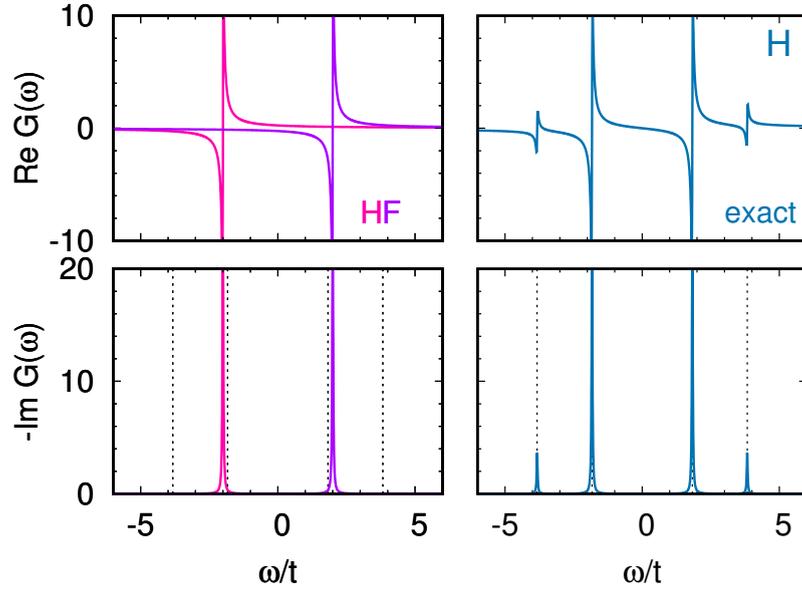
Fig. 6: *Local retarded Green function $G^\sigma(\omega)$ of the Hubbard dimer ($t = 1, U = 4$) at half filling and in the zero temperature limit. Left: Antiferromagnetic Hartree-Fock (HF) approximation; green and violet distinguish $G^\uparrow(\omega)$ and $G^\downarrow(\omega)$ at a given site. Right: Exact local Green function, for which $G^\uparrow(\omega) = G^\downarrow(\omega)$. Dashed lines: Poles of the exact local Green function.*

be, however, the wrong conclusion. Although, due to the small coordination number, in this specific case, DMFT indeed sizably underestimates the gap, it nevertheless captures the essential nature of the ground state. Instead, while HF, in this specific case,[6] gives an almost exact gap, it does it via a qualitatively incorrect description (antiferromagnetic instead of singlet ground state). Increasing the coordination number, DMFT approaches the exact solution both in the paramagnetic and magnetic phase, while HF does not. Let us analyze in more detail the differences between the HF approximation and the exact solution of the Hubbard dimer. The HF Hamiltonian for two electrons is given by $\hat{H}_2 = \hat{H}_2' + \varepsilon_d \hat{N} - \Delta_0$, and

$$
\hat{H}_2' = \begin{pmatrix}
U & 0 & 0 & -2Um_- & 0 & 0 \\
0 & U(1-2m_+) & 0 & 0 & 0 & 0 \\
0 & 0 & U(1+2m_+) & 0 & 0 & 0 \\
-2Um_- & 0 & 0 & U & -\sqrt{2}t & -\sqrt{2}t \\
0 & 0 & 0 & -\sqrt{2}t & U & 0 \\
0 & 0 & 0 & -\sqrt{2}t & 0 & U
\end{pmatrix} . \tag{85}
$$

---

[6]The Hartree-Fock approximation often overestimates the size of the gap, however.

For $m_+=0$ and $m_- \neq 0$ (antiferromagnetic solution) the eigenvalues and eigenvectors are

$|2\rangle_l$	$E_l(2)$
$|2\rangle_5 = \frac{1}{\sqrt{2}}\left(|2,0,0\rangle_0 + a_2|2,1,0\rangle - \frac{a_1}{\sqrt{2}}\left(|2,0,0\rangle_1 + |2,0,0\rangle_2\right)\right)$	$\varepsilon_0(2) + 2\Delta_1(t,U)$
$|2\rangle_4 = \frac{1}{\sqrt{2}}\left(|2,0,0\rangle_1 - |2,0,0\rangle_2\right)$	$\varepsilon_0(2)$
$|2\rangle_3 = |2,1,1\rangle$	$\varepsilon_0(2)$
$|2\rangle_2 = |2,1,-1\rangle$	$\varepsilon_0(2)$
$|2\rangle_1 = a_1|2,1,0\rangle + a_2\frac{1}{\sqrt{2}}\left(|2,0,0\rangle_1 + |2,0,0\rangle_2\right)$	$\varepsilon_0(2)$
$|2\rangle_0 = \frac{1}{\sqrt{2}}\left(|2,0,0\rangle_0 - a_2|2,1,0\rangle + \frac{a_1}{\sqrt{2}}\left(|2,0,0\rangle_1 + |2,0,0\rangle_2\right)\right)$	$\varepsilon_0(2) - 2\Delta_1(t,U)$

where $\varepsilon_0(2) = 2\varepsilon_d + U\left(1 + 2m_-^2 - n^2/2\right)$, and $a_1^2 = t^2/\Delta_1^2(t,U)$. The antiferromagnetic Hartree-Fock ground state has an overlap with the correct ground state, however incorrectly mixes triplet and singlet states, thus breaking the rotational symmetry of the model. For this reason, its energy, in the large U limit, is $2\varepsilon_d - 2t^2/U$ and not $2\varepsilon_d - 4t^2/U$ as in the exact case. For the ferromagnetic solution of the Hartree-Fock equations ($m_-=0$ and $m_+ \neq 0$) the eigenvalues and eigenvectors are instead

$|2\rangle_l$	$E_l(2)$
$|2\rangle_5 = |2,1,-1\rangle$	$\varepsilon_0^+(2) + 2Um_+$
$|2\rangle_4 = \frac{1}{\sqrt{2}}\left(|2,0,0\rangle_0 - \frac{1}{\sqrt{2}}\left(|2,0,0\rangle_1 + |2,0,0\rangle_2\right)\right)$	$\varepsilon_0^+(2) + 2t$
$|2\rangle_3 = \frac{1}{\sqrt{2}}\left(|2,0,0\rangle_1 - |2,0,0\rangle_2\right)$	$\varepsilon_0^+(2)$
$|2\rangle_2 = |2,1,\ \ 0\rangle$	$\varepsilon_0^+(2)$
$|2\rangle_1 = \frac{1}{\sqrt{2}}\left(|2,0,0\rangle_0 + \frac{1}{\sqrt{2}}\left(|2,0,0\rangle_1 + |2,0,0\rangle_2\right)\right)$	$\varepsilon_0^+(2) - 2t$
$|2\rangle_0 = |2,1,\ \ 1\rangle$	$\varepsilon_0^+(2) - 2Um_+$

where $\varepsilon_0^+(2) = 2\varepsilon_d + U(1 + 2m_+^2 - n^2/2)$. The ferromagnetic Hartree-Fock correction thus yields an incorrect sequence of levels; the ground state for large U/t, indicated as $|2\rangle_0$ in the table, has no overlap with the exact ground state of the Hubbard dimer. It is, instead, one of the states of the first excited triplet. An important observation is that, despite the errors, the energy difference between ferro- and antiferro-magnetic ground state is

$$E_\text{F} - E_\text{AF} \sim \frac{2t^2}{U}, \tag{86}$$

which is indeed the correct value in the small t/U limit. It does not correspond, however, to the actual singlet-triplet excitation energy, $\Gamma \sim 4t^2/U$.

We can now directly compare the Hartree-Fock and the dynamical mean-field approximation for the two-site Hubbard model. Both approaches are based on the solution of self-consistent mean-field-type equations, and therefore they are both mean-field methods. In Hartree-Fock the self-energy is frequency-independent (static), while in DMFT depends on the frequency (dynamical). In Hartree-Fock the self-energy can be site-dependent, as we have seen in the antiferromagnetic case. In DMFT, allowing for a site-dependent self-energy leads to cluster or cluster-like extensions of the method. If the same unit cell is used in DMFT and Hartree-Fock, we can identify another relation between the two methods. In the infinite-frequency limit, the DMFT self-energy equals the Hartree-Fock self-energy. This can be shown analytically in a simple way. For the case of the two-site Hubbard model, the expansion of the local lattice Green function at high frequency in the local-self-energy approximation is

$$G_{i,i}^{\sigma}(i\nu_n) = \frac{1}{i\nu_n} - \frac{\left(\mu - \varepsilon_d - \Sigma_l^{\sigma}(\infty)\right)}{(i\nu_n)^2} + \mathcal{O}\left(\frac{1}{(i\nu_n)^3}\right). \tag{87}$$

Instead, the expansion of the impurity Green-function can be written as

$$
\begin{aligned}
G_{d,d}^{\sigma}(i\nu_n) &= \int_0^\beta d\tau\, e^{i\nu_n\tau} G_{d,d}^{\sigma}(\tau) \\
&= \frac{1}{i\nu_n}\int_0^\beta d\tau \frac{de^{i\nu_n\tau}}{d\tau} G_{d,d}^{\sigma}(\tau) = \frac{1}{i\nu_n}\left(-G_{d,d}^{\sigma}(\beta^-) - G_{d,d}^{\sigma}(0^+) - \int_0^\beta d\tau\, e^{i\nu_n\tau}\frac{dG_{d,d}^{\sigma}(\tau)}{d\tau}\right) \\
&= \frac{1}{i\nu_n} + \frac{1}{(i\nu_n)^2}\left(\left.\frac{dG_{d,d}^{\sigma}(\tau)}{d\tau}\right|_{\beta^-} + \left.\frac{dG_{d,d}^{\sigma}(\tau)}{d\tau}\right|_{0^+} + \int_0^\beta d\tau\, e^{i\nu_n\tau}\frac{d^2 G_{d,d}^{\sigma}(\tau)}{d\tau^2}\right) \\
&= \frac{1}{i\nu_n} + \frac{\left.\frac{dG_{d,d}^{\sigma}(\tau)}{d\tau}\right|_{\beta^-} + \left.\frac{dG_{d,d}^{\sigma}(\tau)}{d\tau}\right|_{0^+}}{(i\nu_n)^2} + \mathcal{O}\left(\frac{1}{(i\nu_n)^3}\right)
\end{aligned} \tag{88}
$$

where

$$\left.\frac{dG_{d,d}^{\sigma}(\tau)}{d\tau}\right|_{\beta^-} + \left.\frac{dG_{d,d}^{\sigma}(\tau)}{d\tau}\right|_{0^+} = -\left\langle\left\{\left[\hat{H}_A - \mu\hat{N},\, c_{d\sigma}\right],\, c_{d\sigma}^\dagger\right\}\right\rangle = -\mu + \varepsilon_d + U\langle\hat{n}_{-\sigma}\rangle. \tag{89}$$

From this result we can conclude that, assuming self-consistency has been reached,

$$\Sigma_l^{\sigma}(\infty) = U\langle\hat{n}_{-\sigma}\rangle. \tag{90}$$

This is exactly the Hartree-Fock expression of the self-energy that we found earlier, and indeed equals the infinite-frequency limit of the DMFT self-energy we previously calculated; however, the occupations $\langle\hat{n}_{-\sigma}\rangle$ in DMFT and Hartree-Fock calculations are typically not the same. In the case of the dimer, DMFT yields $\langle\hat{n}_{-\sigma}\rangle = 1/2$; this would correspond in Hartree-Fock to a trivial solution, in which the self-energy merely shifts all the energy levels by the same amount, and has therefore no relevant effects.

2.5 DMFT for the one-band Hubbard model

The Hubbard Hamiltonian (8) is in principle the simplest model for the description of the Mott metal-insulator transition. In the tight-binding approximation it becomes

$$\hat{H} = \varepsilon_d \sum_{\sigma i} \hat{n}_{i\sigma} - t \sum_{\sigma \langle ii' \rangle} c_{i\sigma}^\dagger c_{i'\sigma} + U \sum_i \hat{n}_{i\uparrow}\hat{n}_{i\downarrow}, \tag{91}$$

where $\langle ii' \rangle$ is a sum over first neighbors. As discussed in the introduction, for $U = 0$, at half-filling, this Hamiltonian describes a metallic band. For $t = 0$ it describes an insulating collection of disconnected atoms. Somewhere in between, at a critical value of t/U, a metal to insulator transition must occur. In this section we will discuss the DMFT solution of (91) and the picture of the metal-insulator transition emerging from it. The first step consists in mapping the original many-body Hamiltonian into an effective quantum-impurity model, such as the Anderson Hamiltonian

$$\hat{H}^A = \underbrace{\sum_{\boldsymbol{k}\sigma} \varepsilon_{\boldsymbol{k}}^s \hat{n}_{\boldsymbol{k}\sigma}}_{\hat{H}_{\mathrm{bath}}} + \underbrace{\sum_{\boldsymbol{k}\sigma} \left(V_{\boldsymbol{k}}^s c_{\boldsymbol{k}\sigma}^\dagger c_{d\sigma} + \mathrm{h.c.} \right)}_{\hat{H}_{\mathrm{hyb}}} + \underbrace{\varepsilon_d \sum_\sigma \hat{n}_{d\sigma} + U\hat{n}_{d\uparrow}\hat{n}_{d\downarrow}}_{\hat{H}_{\mathrm{imp}}}. \tag{92}$$

In this model the on-site Coulomb repulsion U appears only in the impurity Hamiltonian, $\hat{H}_{\mathrm{imp}}$, while the terms $\hat{H}_{\mathrm{bath}}$ and $\hat{H}_{\mathrm{hyb}}$, describe, respectively, the bath and the bath-impurity hybridization. In the next step, the quantum-impurity model is solved. Differently from the case of the Anderson molecule, this cannot be done analytically. It requires non-perturbative numerical methods, such as exact diagonalization, the numerical renormalization group, density-matrix renormalization group or QMC. Here we describe the DMFT self-consistency loop for a QMC quantum-impurity solver. Solving the quantum-impurity model yields the impurity Green function $G_{d,d}^\sigma(i\nu_n)$. From the impurity Dyson equation we can calculate the impurity self-energy

$$\Sigma_A^\sigma(i\nu_n) = \left(G_{d,d}^{0\sigma}(i\nu_n) \right)^{-1} - \left(G_{d,d}^\sigma(i\nu_n) \right)^{-1}. \tag{93}$$

Next, we adopt the local self-energy approximation, i.e., we assume that the self-energy of the Hubbard model equals the impurity self-energy. Then, the local Green function is given by

$$G_{i_c,i_c}^\sigma(i\nu_n) = \frac{1}{N_{\boldsymbol{k}}} \sum_{\boldsymbol{k}} \frac{1}{i\nu_n + \mu - \varepsilon_{\boldsymbol{k}} - \Sigma_A^\sigma(i\nu_n)}, \tag{94}$$

where $N_{\boldsymbol{k}}$ is the number of $\boldsymbol{k}$ points. The local Dyson equation is used once more, this time to calculate the bath Green function $\mathcal{G}^\sigma(i\nu_n)$, which in turn defines a new quantum-impurity model. This procedure is repeated until self-consistency is reached, i.e., the number of electrons is correct and the self-energy does not change anymore (within a given numerical accuracy). In this situation we have

$$G_{i_c,i_c}^\sigma(i\nu_n) \sim G_{d,d}^\sigma(i\nu_n). \tag{95}$$
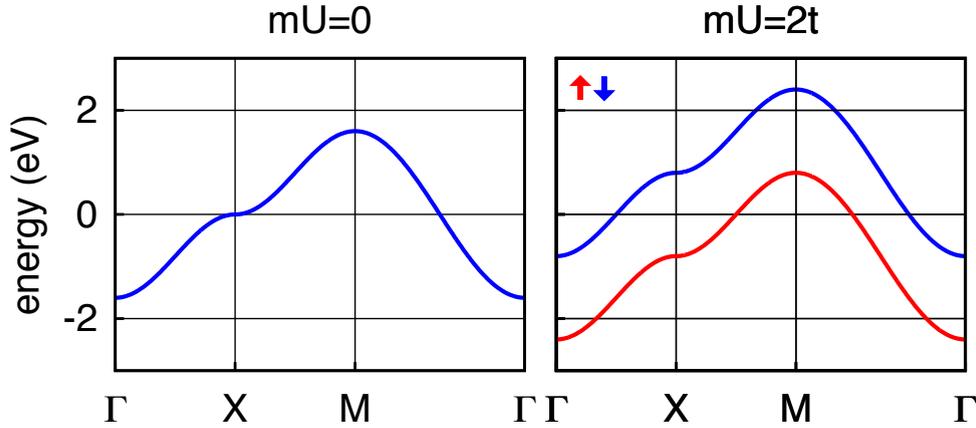
Fig. 7: *The metal-insulator transition in ferromagnetic Hartree-Fock. The calculation is for a square lattice tight-binding model with dispersion $\varepsilon_{\boldsymbol{k}} = -2t(\cos k_x + \cos k_y)$.*

It is important to underline that self-consistency is key to the success of DMFT in describing the metal-to-insulator transition. This can, perhaps, be best understood looking once more at the effects of self-consistency in a simpler approach, the static mean-field Hartree-Fock method.[7] If we chose the same primitive cell as in DMFT, the Hartree-Fock self-energy matrix is

$$\Sigma_{i,i'}^{\sigma}(i\nu_n) = U\left(\frac{n}{2} - \sigma m\right)\delta_{i,i'}, \tag{96}$$

where $\sigma = +1$ for spin up and $\sigma = -1$ for spin down and $m = m_+ = (n_\uparrow - n_\downarrow)/2$, with $n_\sigma = n_{i\sigma}$. The approximation is then identical to replacing the Hubbard Hamiltonian with

$$\hat{H}_{\text{HF}} = \sum_{\boldsymbol{k}\sigma}\left[\varepsilon_{\boldsymbol{k}} + U\left(\frac{1}{2} - \sigma m\right)\right]\hat{n}_{\boldsymbol{k}\sigma}. \tag{97}$$

This shows that $h_{\text{eff}} = 2Um$ plays the role of an effective magnetic field (Weiss field). The self-consistency criterion is

$$\bar{n}_\sigma = \bar{n}_{i\sigma} = \langle\hat{n}_{i\sigma}\rangle_{\text{HF}}, \tag{98}$$

where the expectation value $\langle\hat{n}_{i\sigma}\rangle_{\text{HF}}$ is calculated using the Hamiltonian $\hat{H}_{\text{HF}}$, which in turn depends on $\bar{n}_\sigma$ via m. This gives the self-consistency equation

$$m = \frac{1}{2}\frac{1}{N_{\boldsymbol{k}}}\sum_{\boldsymbol{k}\sigma}\frac{\sigma e^{-\beta(\varepsilon_{\boldsymbol{k}} + U(\frac{1}{2} - \sigma m) - \mu)}}{1 + e^{-\beta(\varepsilon_{\boldsymbol{k}} + U(\frac{1}{2} - \sigma m) - \mu)}}. \tag{99}$$

If we set $m = 0$ the equation is satisfied; for such a trivial solution the static mean-field correction in Eq. (97) merely redefines the chemical potential and has therefore no effect. For sufficiently large U, however, a non-trivial solution ($m \neq 0$) can be found. If $m \neq 0$ the spin up and spin down bands split, and eventually a gap can open. This is shown in Fig. 7. The static mean-field correction in Eq. (97) equals the contribution of the Hartree diagram to the self-energy, $\Sigma_{\text{H}}^{\sigma}(i\nu_n) = U\bar{n}_{-\sigma}$. In many-body perturbation theory, however, $\bar{n}_\sigma = 1/2$, i.e., $m = 0$.

---

[7]Keeping in mind that many self-consistent solutions obtained with the Hartree-Fock method are spurious.
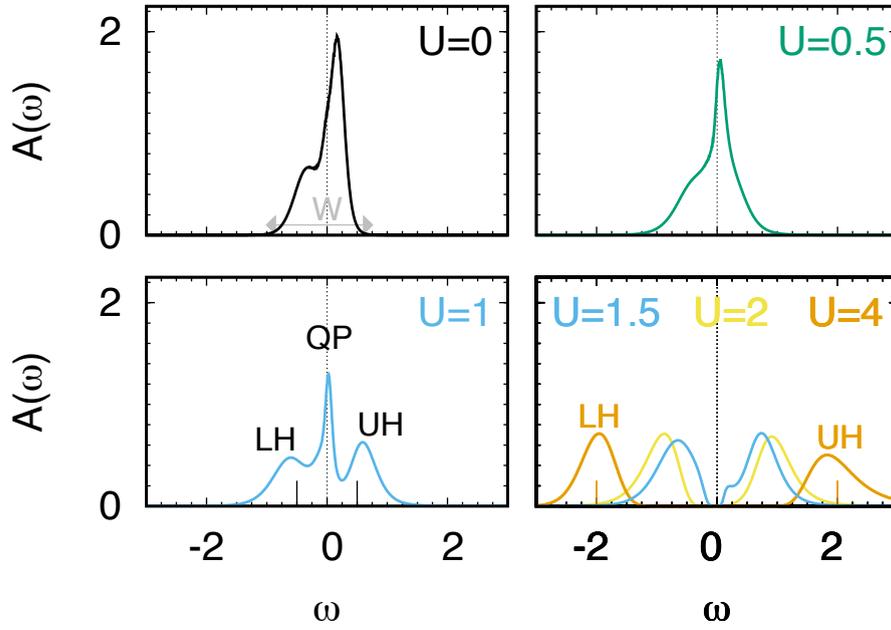
Fig. 8: *VOMoO$_4$: LDA+DMFT spectral function at finite temperature for $0 \leq U \leq 4$. Energies are in eV and spectral functions in states/spin/eV. The calculations have been done using a continuous-time hybridization-expansion QMC solver [13]. A detailed LDA+DMFT study of the electronic and magnetic properties VOMoO$_4$ can be found in Ref. [14].*

In the self-consistent static mean-field approximation, instead, m can differ from zero, and a phenomenon not described by the mere Hartree diagram can be captured, ferromagnetism in a correlated metal. If mU is larger than the bandwidth, the system can even become an insulator. In DMFT the role of the Weiss mean field is played by the bath Green function $\mathcal{G}_{i,i}^{\sigma}(i\nu_n)$. The emerging picture of the Mott transition is described in Fig. 8 for a representative single-band material. In the $U = 0$ limit, the spectral function $A_0(\omega)$ is metallic at half filling (top left panel). For finite U, if we set $\Sigma_A^{\sigma}(\omega) = 0$ as initial guess, the DMFT self-consistency loop starts with $A(\omega) = A_0(\omega)$. For small U/t, the *converged* spectral function $A(\omega)$ is still similar to $A_0(\omega)$. This can be seen comparing the $U = 0.5$ and $U = 0$ panels in Fig. 8. Further increasing U/t, sizable spectral weight is transferred from the zero-energy quasi-particle peak to the lower (LH) and upper (UH) Hubbard bands, centered at $\omega \sim \pm U/2$. This can be observed in the $U = 1$ panel of Fig. 8. The system is still metallic, but with strongly renormalized masses and short lifetimes, reflected in the narrow quasi-particle (QP) peak. Finally, for U larger than a critical value ($U \geq 1.5$ in the figure) a gap opens and the system becomes a Mott insulator. When this happens the self-energy diverges at low frequency, where

$$\Sigma_A^{\sigma}(\omega + i0^+) \sim \frac{U}{2} + \frac{U^2}{4} \frac{a(t, U)}{\omega + i0^+}. \tag{100}$$

In the large U/t limit the gap increases linearly with the Coulomb repulsion, i.e., $E_g(1) \sim U - W$, where W is the bandwidth.

2.6 DMFT for multi-orbital models

The multi-orbital Hubbard-like Hamiltonian has the form

$$\hat{H} = \hat{H}_0 + \hat{H}_U \tag{101}$$

$$\hat{H}_0 = -\sum_{ii'}\sum_{\sigma\sigma'}\sum_{mm'} t^{i,i'}_{m\sigma,m'\sigma'}\, c^{\dagger}_{im\sigma}c_{i'm'\sigma'} \tag{102}$$

$$\hat{H}_U = \frac{1}{2}\sum_{i}\sum_{\sigma\sigma'}\sum_{mm'}\sum_{pp'} U_{mpm'p'}\, c^{\dagger}_{im\sigma}c^{\dagger}_{ip\sigma'}c_{ip'\sigma'}c_{im'\sigma}, \tag{103}$$

where m, m' and p, p' are different orbitals and the Coulomb tensor is local. The DMFT approach can be extended to solve models of this form, mapping them to multi-orbital quantum-impurity models. The main changes with respect to the formalism introduced in the previous section are then the following

$$\varepsilon_{\bm{k}} \to (H_{\bm{k}})_{m\sigma,m'\sigma'} \qquad\qquad (i\nu_n+\mu) \to (i\nu_n+\mu)\,\hat{1}_{m\sigma,m'\sigma'}$$

$$t^{i,i'} \to t^{i,i'}_{m\sigma,m'\sigma'} \qquad\qquad \varepsilon_d \to \varepsilon^{i,i'}_{m\sigma,m'\sigma'} = -t^{i,i}_{m\sigma,m'\sigma'}$$

where $\hat{1}$ is the identity matrix. As a consequence, the local Green function, the bath Green function, the hybridization function, and the self-energy also become matrices

$$\mathcal{G}^{\sigma}(i\nu_n) \to \mathcal{G}^{\sigma,\sigma'}_{m,m'}(i\nu_n) \qquad\quad G^{\sigma}(i\nu_n) \to G^{\sigma,\sigma'}_{m,m'}(i\nu_n) \qquad\quad \Sigma^{\sigma}(i\nu_n) \to \Sigma^{\sigma,\sigma'}_{m,m'}(i\nu_n).$$

The corresponding generalization of the self-consistency loop is shown schematically in Fig. 9. Although the extension of DMFT to Hubbard models with many orbitals might appear straight-forward, in practice it is not. The bottleneck is the solution of the generalized multi-orbital quantum-impurity problem. The most flexible solvers available so far are all based on QMC. Despite being flexible, QMC-based approaches have limitations. These can be classified in two types. First, with increasing the number of degrees of freedom, calculations become very quickly computationally too expensive—how quickly depends on the specific QMC algorithm used and the actual implementation. Thus, going beyond a rather small number of orbitals and reaching the zero-temperature limit is unfeasible in practice. The second type of limitation is more severe. Increasing the number of degrees of freedom leads, eventually, to the infamous sign problem; when this happens, QMC calculations cannot be performed at all. In order to deal with limitations of the first type, it is crucial to restrict QMC calculations to the essential degrees of freedom; furthermore, we should exploit symmetries, develop fast algorithms and use the power of massively parallel supercomputers to reduce the actual computational time. For the second type of problems not a lot can be done; nevertheless, it has been shown that a severe sign problem might appear earlier with some basis choices than with others [13]. Although eventually we cannot escape it, this suggests that the model set up can be used as a tool to expand the moderate sign-problem zone. For what concerns symmetries, in the paramagnetic case and in absence of spin-orbit interaction or external fields, an obvious symmetry to exploit
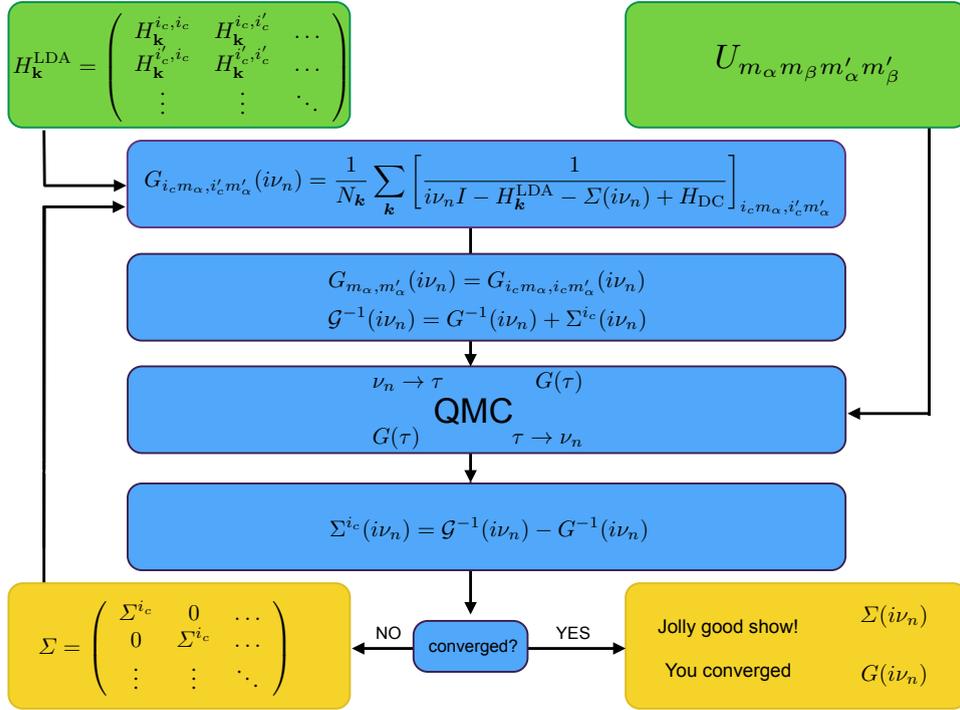
Fig. 9: *LDA+DMFT self-consistency loop. The one-electron Hamiltonian is built in the basis of Bloch states obtained from localized Wannier functions, for example in the local-density approximation (LDA); this gives $H_{\mathbf{k}}^{\mathrm{LDA}}$. The set $\{i_c\}$ labels the equivalent correlated sites inside the unit cell. The local Green-function matrix is at first calculated using an initial guess for the self-energy matrix. The bath Green-function matrix is then obtained via the Dyson equation and used to construct an effective quantum-impurity model. The latter is solved via a quantum-impurity solver, here quantum Monte Carlo (QMC). This yields the impurity Green-function matrix. Through the Dyson equation the self-energy is then obtained, and the procedure is repeated until self-consistency is reached.*

is the rotational invariance of spins, from which follows

$$A_{m,m'}^{\sigma,\sigma'}(i\nu_n) = \delta_{\sigma,\sigma'}\, A_{m,m'}(i\nu_n), \tag{104}$$

where $A = \mathcal{G}, G, \Sigma$. In addition, if we use a basis of real functions, the local Green-function matrices are real and symmetric in imaginary time τ, hence

$$A_{m,m'}^{\sigma,\sigma'}(i\nu_n) = \delta_{\sigma,\sigma'}\, A_{m,m'}(i\nu_n) = \delta_{\sigma,\sigma'}\, A_{m',m}(i\nu_n). \tag{105}$$

Finally, often the unit cell contains several equivalent correlated sites, indicated as $\{i_c\}$ in Fig. 9. In order to avoid expensive cluster calculations, we can use space-group symmetries to construct the matrices $\mathcal{G}, G, \Sigma$ at a given site i_c' from the corresponding matrices at an equivalent site, e.g., $i_c = 1$. Space-group symmetries also tell us if some matrix elements are zero. For example, for a model with only t_{2g} (or only e_g) states, in cubic symmetry, in the paramagnetic case and in absence of spin-orbit interaction or external fields, we have

$$A_{m,m'}^{\sigma,\sigma'}(i\nu_n) = \delta_{\sigma,\sigma'}\, A_{m,m}(i\nu_n)\, \delta_{m,m'}. \tag{106}$$

3 Building materials-specific many-body models

3.1 Model construction

How do we build realistic Hubbard-like models for correlated materials? The state-of-the art approach relies on constructing, for a given system, *materials-specific* Kohn-Sham Wannier functions $\varphi_{im\sigma}^{\mathrm{KS}}(\boldsymbol{r})$. These can be obtained via electronic structure calculations based on density-functional theory [8–10], e.g., in the LDA approximation.[8] After we constructed the complete one-electron basis, the first steps in model-building are those described in the introduction. We recall here the essential points and then discuss the next stage. The many-body Hamiltonian can be expressed as $\hat{H} = \hat{H}_0 + \hat{H}_U - \hat{H}_{\mathrm{DC}}$, with $\hat{H}_0 = \hat{H}^{\mathrm{LDA}}$ and

$$\hat{H}_0 = -\sum_{ii'} \sum_{\sigma\sigma'} \sum_{mm'} t_{m\sigma,m'\sigma'}^{i,i'} c_{im\sigma}^{\dagger} c_{i'm'\sigma'}, \tag{107}$$

$$\hat{H}_U = \frac{1}{2} \sum_{ii'jj'} \sum_{\sigma\sigma'} \sum_{mm'pp'} U_{mp\,m'p'}^{iji'j'} c_{im\sigma}^{\dagger} c_{jp\sigma'}^{\dagger} c_{j'p'\sigma'} c_{i'm'\sigma}. \tag{108}$$

The hopping integrals in $\hat{H}_0$ are calculated replacing the electron-nuclei interaction, $v_{\mathrm{en}}(\boldsymbol{r})$, with the self-consistent DFT reference potential, $v_{\mathrm{R}}(\boldsymbol{r}) = v_{\mathrm{en}}(\boldsymbol{r}) + v_{\mathrm{H}}(\boldsymbol{r}) + v_{\mathrm{xc}}(\boldsymbol{r})$, defined in Eq. (5). The latter includes the long-range Hartree term, $v_{\mathrm{H}}(\boldsymbol{r})$, and the exchange-correlation contribution, $v_{\mathrm{xc}}(\boldsymbol{r})$; to avoid including the *effects* of these terms twice, we thus introduce the double-counting correction, $\hat{H}_{\mathrm{DC}}$, so that

$$\hat{H}_U \rightarrow \Delta\hat{H}_U = \hat{H}_U - \hat{H}_{\mathrm{DC}}.$$

Unfortunately we do not know which important correlation effects are included in $\hat{H}_0$ via $v_{\mathrm{R}}(\boldsymbol{r})$, and therefore the exact expression of $\Delta\hat{H}_U$ is also unknown. The remarkable successes of the LDA suggest, however, that in many materials the LDA is overall a good approximation, and therefore, in those systems at least, the term $\Delta\hat{H}_U$ can be completely neglected. What about strongly-correlated materials? Even in correlated systems, most likely, the LDA works rather well for the delocalized electrons or in describing the average or the long-range Coulomb effects. Thus one can think of separating the electrons into *uncorrelated* and *correlated*; only for the latter we do take the correction $\Delta\hat{H}_U$ into account explicitly, assuming furthermore that $\Delta\hat{H}_U$ is local or almost local [8], since we know that it is the local term which is responsible for most non-trivial many-body effects. Typically, correlated electrons are those that partially retain their atomic character, e.g., those that originate from localized d and f shells; for convenience, here we assume that in a given system they stem from a single atomic shell l (e.g., d for transition-metal oxides or f for heavy-fermion systems) and label their states with the atomic quantum numbers l and $m = -l, \ldots, l$ of that shell. Thus

$$U_{mp\,m'p'}^{iji'j'} \sim \begin{cases} U_{mp\,m'p'}^{l} & iji'j' = iiii \;\; \wedge \;\; mp, m'p' \in l \\ 0 & iji'j' \neq iiii \;\; \vee \;\; mp, m'p' \notin l. \end{cases}$$

---

[8]Using GGA or similar functionals in place of LDA yields minor differences in the many-body Hamiltonian; on the other hand, using LDA+U or similar approximations yields Hartree-Fock-like effects that would have to be subtracted via the double-counting correction.

Within this approximation $\Delta \hat{H}_U$ is replaced by $\Delta \hat{H}_U^l = \hat{H}_U^l - \hat{H}_{DC}^l$, where $\hat{H}_{DC}^l$ is, e.g., given by the static mean-field contribution of $\hat{H}_U^l$. There is a drawback in this procedure, however. By splitting electrons into correlated and uncorrelated we implicitly assume that the main effect of the latter is the renormalization or *screening* of parameters for the former, in particular of the Coulomb interaction. The computation of screening effects remains, unfortunately, a challenge. The calculation of exact screening would require the solution of the original many-body problem, taking all degrees of freedom into account, an impossible task. Commonly-used approximate schemes are the constrained LDA approximation (cLDA) and the constrained random-phase approximation (RPA) [8–10]. Both methods give reasonable estimates of screened Coulomb parameters for DMFT calculations. Typically cRPA calculations include more screening channels and are performed for less localized bases than cLDA calculations; thus cRPA parameters turn out to be often smaller than cLDA ones. To some extent, the difference can be taken as an estimate of the error bar.

After we have selected the electrons for which we think is necessary to include explicitly the Hubbard correction, in order to build the final Hamiltonian for DMFT calculations, it is often convenient to integrate out or *downfold*, in part or completely, the weakly correlated states. There are different degrees of downfolding. The two opposite extreme limits are (i) *no downfolding*, i.e., keep explicitly in the Hamiltonian all weakly-correlated states (ii) *massive downfolding*, i.e., downfold all weakly correlated states. If we perform massive downfolding, e.g., downfold to the d (or e_g or t_{2g}) bands at the Fermi level, the Hamiltonian relevant for DMFT takes a simpler form. The LDA part is limited to the selected orbitals or bands, which, in the ideal case, are decoupled from the rest

$$\hat{H}^{LDA} = - \sum_{ii'} \sum_{\sigma\sigma'} \sum_{m_\alpha m_\alpha'} t_{m_\alpha \sigma, m_\alpha' \sigma'}^{i,i'} c_{im_\alpha \sigma}^\dagger c_{i'm_\alpha' \sigma'}. \tag{109}$$

The local *screened* Coulomb interaction for this set of orbitals is the on-site tensor

$$\hat{H}_U^l = \frac{1}{2} \sum_i \sum_{\sigma\sigma'} \sum_{m_\alpha m_\alpha'} \sum_{m_\beta m_\beta'} U_{m_\alpha m_\beta m_\alpha' m_\beta'} c_{im_\alpha \sigma}^\dagger c_{im_\beta \sigma'}^\dagger c_{im_\beta' \sigma'} c_{im_\alpha' \sigma}. \tag{110}$$

It is important to point out that the level of downfolding does not modify the hardness of the quantum-impurity problem. If, for example, in studying a transition-metal oxide, we plan to treat only $3d$ bands as correlated, it does not matter if we perform calculations with a Hamiltonian containing also, e.g., O p states, or we rather downfold all states but the $3d$ and work with a set of Wannier basis spanning the $3d$-like bands only. The number of correlated orbitals in the quantum-impurity problem is the same.[9]

One advantage of massive downfolding is that the double-counting correction typically becomes a shift of the chemical potential, and it is therefore not necessary to calculate it explicitly. A second important advantage is that the interpretation of the final results is simpler. Instead, a disadvantage is that the basis functions are less localized, and therefore the approximation of the Coulomb interaction to a local operator might be less justified, and in some cases it might be

---

[9]The choice might influence how severe the QMC sign problem is, however.
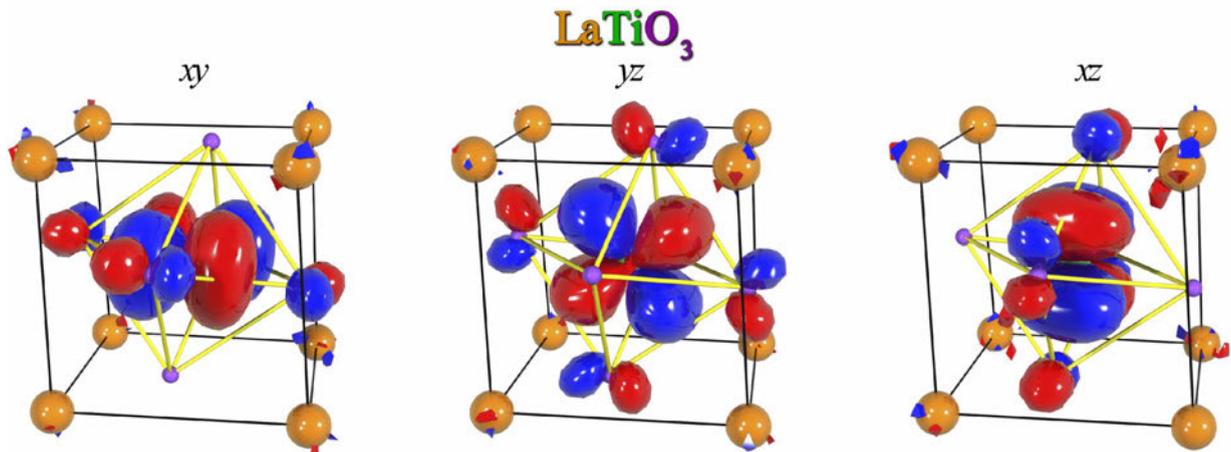
Fig. 10: *NMTO Wannier-like orbitals for t_{2g} states in LaTiO$_3$ obtained via massive downfolding to the t_{2g} bands. The t_{2g}-like orbitals have O p tails at the neighboring O sites reflecting the distortions of the lattice. The figure has been taken from Ref. [15].*

necessary to include non-local Coulomb terms. The effect of downfolding on the localization of Wannier functions is illustrated for example in Fig. 10. Finally, another disadvantage of massive downfolding is that the energy window in which the model is valid is more narrow.

Considered all advantages and disadvantages, what is then the best way of performing DMFT calculations? There is no universal answer to this question; it depends on the problem we are trying to solve and the system we are studying. Independently of the degree of downfolding we choose, it is important to point out that a clear advantage of Wannier functions in general is that they carry information about the lattice, bonding, chemistry and distortions. This can be seen once more in Fig. 10, where orbitals are tilted and deformed by the actual structure and chemistry of the compound. Indeed, one might naively think of using a "universal" basis, for example atomic functions, the same for all systems, and thus calculating the hopping integrals using simply the electron-nuclei interaction $v_{en}(\boldsymbol{r})$. Besides the complications arising from the lack of orthogonality, such a basis has no built-in materials-specific information, except lattice positions. It is therefore a worse starting point to describe the electronic structure, even in the absence of correlations; larger basis sets are required to reach the same accuracy. From the point of view of LDA+DMFT, an advantage of a universal basis would be that it is free from double-counting corrections; on the other hand, however, exactly because we do not use the LDA potential and LDA orbitals to calculate the hopping integrals, we also cannot count on the successes of LDA in the description of average and long-range Coulomb effects. For these reasons *ab-initio* Wannier functions remain so far the basis of choice. They can be built via the Nth-Order Muffin-Tin Orbital (NMTO) method [15], the maximal-localization scheme [16], or projectors. Fig. 10 shows examples of NMTO-based Wannier functions.

## 3.2   Localization of the basis and range of the Coulomb interaction

No matter what construction procedure is used, a common characteristic of *ab-initio* Wannier functions is that they are site-centered and localized.[10] A question naturally arises: How crucial is it to use localized functions as one-electron basis? This is an important point, since we have seen that strong-correlation effects arise in systems in which the on-site Coulomb interaction is much larger than longer-range terms. Let us consider therefore two opposite extreme limits. The first is the case in which the basis functions are independent of the lattice position (i.e., they are totally delocalized). For such a basis choice the Coulomb interaction parameters would be the same for every couple of lattice sites, no matter how distant. Thus a Hubbard-like model would be hard to justify. In the second extreme case, we adopt a hypothetical basis so localized that $\psi_{im\sigma}(\boldsymbol{r})\overline{\psi_{i'm'\sigma'}}(\boldsymbol{r}) \sim \delta_{i,i'}\delta(\boldsymbol{r}-\boldsymbol{T}_i)$. Even for such a basis choice, the unscreened Coulomb interaction is *not* local. It is given by

$$U^{iji'j'}_{mp\,m'p'} \propto \frac{\delta_{i,i'}\delta_{j,j'}}{|\boldsymbol{T}_i-\boldsymbol{T}_j|}, \tag{111}$$

hence it decays slowly with distance, although the (divergent) on-site term dominates. More generally, we can conclude that by increasing the localization of the basis we enhance the importance of the on-site Coulomb repulsion with respect to long-range terms; this better justifies Hubbard-like models—although we have to remember that most of the long-range part of the Coulomb interaction is in any case subtracted via the double-counting correction $\hat{H}_{\mathrm{DC}}$. The extreme case of the $\delta(\boldsymbol{r}-\boldsymbol{T}_i)$ functions also illustrates, however, how far we can go. A major problem with the extremely localized basis discussed above is that it would make it impossible to properly describe bonding, since the hopping integrals would be zero. Although such a basis is, of course, never used to build many-body models, there is a tempting approximation that has similar flaws. If one uses DFT-based electronic-structure techniques that tile the space in interstitial and *non*-overlapping atomic spheres (e.g., the LAPW method), it is tempting to use as basis for correlated electrons the atomic functions *defined inside the atomic spheres*. These functions are, by construction, much more localized than Wannier orbitals (even when no downfolding is performed in the Wannier construction). However, they *do not form a complete basis set* in the space of square-integrable functions. This is obvious because such a basis does not even span the LDA bands; to reproduce the bands we need, in addition, functions defined in the interstitial region. This is illustrated in Fig. 11 for a simple example of two quantum well potentials.[11] We therefore cannot use it to write the many-body Hamiltonian in the usual form $\hat{H}_0 + \hat{H}_U$. In conclusion, a basis which, as *ab-initio* Wannier functions, is complete and indeed spans the bands, is better justified, although we somewhat lose in localization.

---

[10]Differences in localizations between the various construction procedures are actually small for the purpose of many-body calculations, provided that the same bands are spanned in the same way.

[11]Another, but less severe, problem of atomic sphere truncations is that the results will depend on the sphere size, in particular when atomic spheres are small.
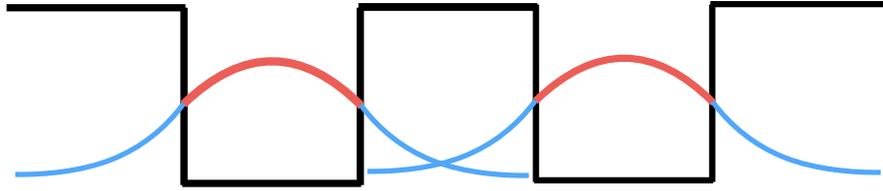
Fig. 11: *The problem of two quantum wells. The figure shows (schematically) for each well the wavefunction of a bound state. If we consider only the part of the wavefunction inside its own well (red in the figure), the differential overlap (and hence the hopping integral) between functions centered on different wells would be zero.*

3.3 Hubbard Hamiltonians for t_{2g} and e_g systems

Several strongly-correlated transition-metal oxides can be described via minimal materials-specific Hubbard-like models which involve only t_{2g} or only e_g bands. A representative system of this kind is the layered perovskite Sr_2RuO_4 with the $4d$ t_{2g}^4 electronic configuration. Its crystal structure is shown in Fig. 12 (left side), together with the associated LDA bands crossing the Fermi level (top-right panel). Due to the layered structure the xz and yz bands are quasi one-dimensional and the xy band is quasi two-dimensional. Thus, the t_{2g} bands give rise, in first approximation, to a Fermi surface made of four crossing lines (from the xz, yz bands) and a circle (from the xy band), shown schematically in the bottom-right panel of Fig. 12. Experimentally, Sr_2RuO_4 is a correlated metal down to 1.5 K; below this temperature it becomes an anomalous superconductor. Other representative cases of t_{2g} systems are the Mott insulating perovskites $LaTiO_3$ and $YTiO_3$, with the electronic configuration $3d$ t_{2g}^1. A paradigmatic e_g system is instead the orbitally ordered insulator $KCuF_3$, with the electronic configuration $t_{2g}^6 e_g^3$. For all these materials, if we massively downfold all LDA bands but the t_{2g} (or the e_g), the resulting 3-band (or 2-band) generalized Hubbard model takes the form

$$\hat{H} = \sum_{i\sigma} \sum_{mm'} \varepsilon_{m,m'}\, c^\dagger_{im\sigma} c_{im'\sigma} - \sum_\sigma \sum_{i\neq i'} \sum_{mm'} t^{i,i'}_{m,m'}\, c^\dagger_{im\sigma} c_{i'm'\sigma}$$

$$+ U \sum_{i\,m} \hat{n}_{im\uparrow}\hat{n}_{im\downarrow} + \frac{1}{2} \sum_{\substack{i\sigma\sigma' \\ m\neq m'}} \left(U - 2J - J\delta_{\sigma,\sigma'} \right) \hat{n}_{im\sigma}\hat{n}_{im'\sigma'}$$

$$- J \sum_{i\,m\neq m'} \left(c^\dagger_{im\uparrow}c^\dagger_{im\downarrow}c_{im'\uparrow}c_{im'\downarrow} + c^\dagger_{im\uparrow}c_{im\downarrow}c^\dagger_{im'\downarrow}c_{im'\uparrow} \right), \tag{112}$$

where $m, m' = xy, yz, xz$ for t_{2g} and $m, m' = 3z^2-r^2, x^2-y^2$ for e_g. The parameters U and J are the direct and exchange screened Coulomb integrals. The Coulomb interaction $\hat{H}_U$ is here assumed to have full $O(3)$ rotational symmetry, as in the atomic limit.[12] The first two terms of

---

[12] A derivation of the Coulomb interaction tensor for the free atom can be found in my chapter in Ref. [8]. There the difference in the values of U and J for the t_{2g} and e_g orbitals is also discussed.
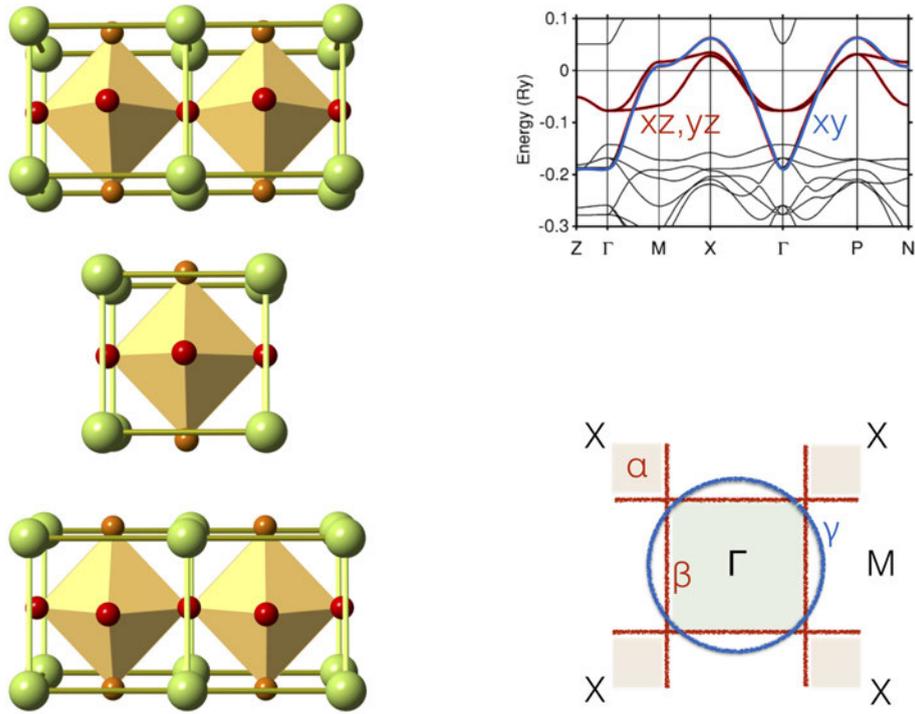
Fig. 12: *Left: Crystal structure of the tetragonal layered perovskite Sr_2RuO_4. Right: Low-energy LDA band structure (top) and schematic representation of the associated Fermi surface (bottom). The band structure was calculated using the Nth-Order Muffin-Tin Orbital (NMTO) method. The figure is rearranged from Ref. [17].*

$\hat{H}_U$ are the so-called density-density terms, and the last two are the pair-hopping and spin-flip interactions. We dropped the double-counting correction $\hat{H}_{DC}$, which in this case is a mere shift of the chemical potential. The energies $\varepsilon_{m,m'}$ are the elements of the crystal-field matrix. In the case of cubic symmetry, the crystal-field matrix, the self-energy, the Green function and the spectral function are all diagonal in orbital space. For low-symmetry systems, however, this is not true. It can be seen in Fig. 13, which shows the diagonal and off-diagonal elements of the spectral-function matrix for the orthorhombic Mott insulator $YTiO_3$.

3.4   Spin-orbit interaction and effects of the basis choice

In many interesting systems the spin-orbit interaction $\hat{H}_{SO}$ plays an important role. In the atomic limit, for the d shells the spin-orbit interaction is

$$\hat{H}_{SO} = \sum_{\mu} \lambda_\mu \sum_{mm'} \sum_{\sigma\sigma'} \epsilon^\mu_{m\sigma,m'\sigma'} \, c^\dagger_{m\sigma} c_{m'\sigma'}, \qquad \epsilon^\mu_{m\sigma,m'\sigma'} = \langle m\sigma|l_\mu s_\mu|m'\sigma'\rangle, \qquad (113)$$

where $\mu = x, y, z$, and λ_μ are the spin-orbit couplings, with $\lambda_\mu = \lambda$ in $O(3)$ symmetry, and

$$\lambda \sim g\mu_B^2 \left\langle \frac{1}{r}\frac{d}{dr}v_R(r) \right\rangle. \qquad (114)$$
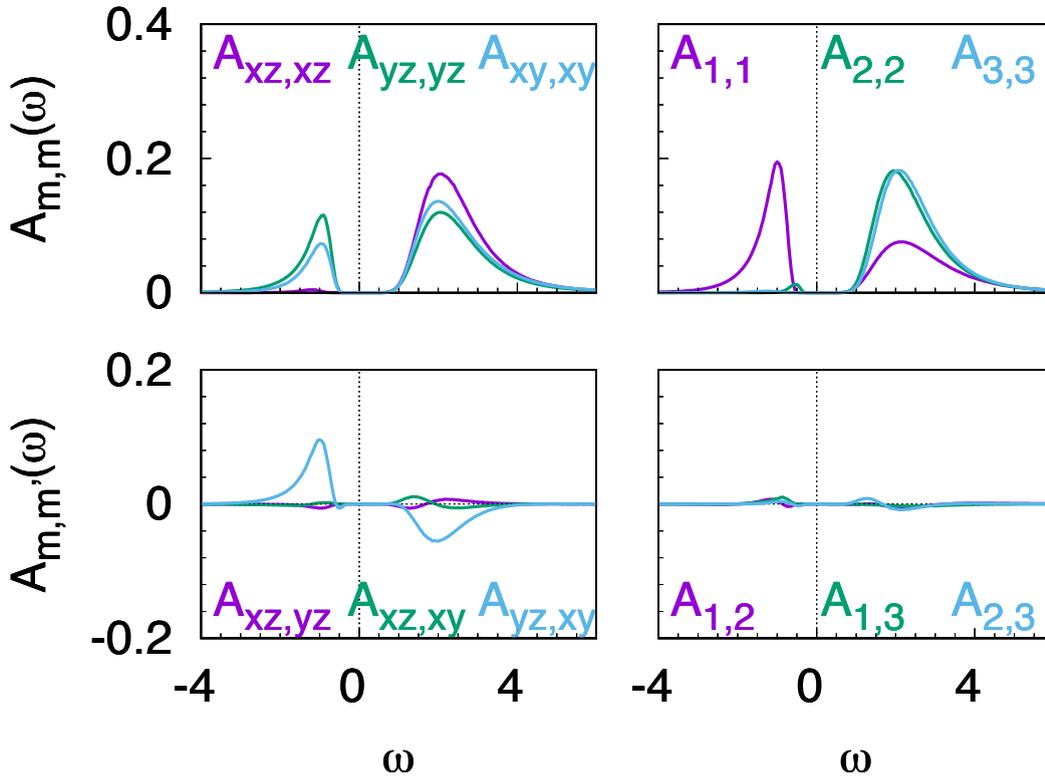
Fig. 13: *The LDA+DMFT spectral function matrix of the orbitally-ordered t_{2g}^1 system YTiO$_3$, in the (xz, yz, xy) basis (left panels) and in the crystal-field basis (right panels) [15, 22].*

For a given material, the on-site one-electron Hamiltonian is thus the matrix $\hat{\varepsilon}$ with elements $\hat{\varepsilon}_{m\sigma,m'\sigma'} = \varepsilon_{m,m'} + \sum_\mu \lambda_\mu \epsilon^\mu_{m\sigma,m'\sigma'}$, where the terms $\varepsilon_{m,m'}$ arise from the crystal field. More specifically, for a t_{2g} system with tetragonal site symmetry we have

$$
\hat{\varepsilon} = \begin{pmatrix}
\varepsilon_{xy} & 0 & 0 & 0 & \frac{\lambda_y}{2} & -\frac{i\lambda_x}{2} \\
0 & \varepsilon_{yz} & \frac{i\lambda_z}{2} & -\frac{\lambda_y}{2} & 0 & 0 \\
0 & -\frac{i\lambda_z}{2} & \varepsilon_{xz} & \frac{i\lambda_x}{2} & 0 & 0 \\
0 & -\frac{\lambda_y}{2} & -\frac{i\lambda_x}{2} & \varepsilon_{xy} & 0 & 0 \\
\frac{\lambda_y}{2} & 0 & 0 & 0 & \varepsilon_{yz} & -\frac{i\lambda_z}{2} \\
\frac{i\lambda_x}{2} & 0 & 0 & 0 & \frac{i\lambda_z}{2} & \varepsilon_{xz}
\end{pmatrix}.
\tag{115}
$$

Although $\hat{H}_{\mathrm{SO}}$ looks like an innocent one-body term, it turns out that, for materials, simulations including this term are more difficult. This has two reasons: (i) QMC calculations involve Green function matrices of larger size, e.g., 6×6 as in the case just discussed, hence they are from the start computationally more demanding; (ii) QMC calculations are often hampered by a much stronger sign problem; even when it can be tamed, this often happens at the price of further increasing the computational time. Thus, specific basis choices and approximations are used. A possible approach consists in working in the basis that diagonalizes the non-interacting local Green function or the non-interacting local Hamiltonian; such a choice is known to reduce
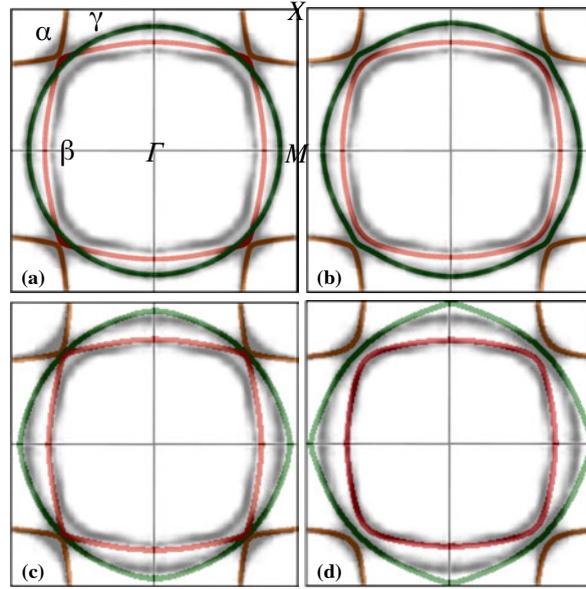
Fig. 14: *Fermi surface of Sr_2RuO_4 calculated with LDA (a), LDA+SO (b), LDA+DMFT (c) and LDA+SO+DMFT (d). Figure from [18]. The grey maps are experimental results from Ref. [21].*

the sign problem, as was first shown in Ref. [13] for the case without spin-orbit interaction. For a system with tetragonal symmetry, the states that diagonalize the local Green function belong either to the Γ_6 or to the Γ_7 irreducible representations, both 2-dimensional. There are two (coupled) Γ_7 representations, defining the space $\Gamma_7'\oplus\Gamma_7''$. The analytic expression of these states can be found in Refs. [17–19]. The transformation to the $\Gamma_6 \oplus \Gamma_7' \oplus \Gamma_7''$ basis is, of course, in principle, a mere basis change. Approximations are made, however, if all off-diagonal elements of the Green function are set to zero or the Coulomb tensor is truncated to further tame the sign problem or to reduce the computational time.

It has to be noticed that the Coulomb interaction of the t_{2g} Hubbard Hamiltonian is *only invariant under orthogonal transformations* of the basis. Thus if we change basis to the Γ_6-Γ_7'-Γ_7'' representation, the form of the interaction tensor changes. The exact expression of the Coulomb tensor in the angular momentum basis (i.e., the one relevant when the t_{2g} crystal-field splitting is zero) can be found in Ref. [20]. For the Coulomb interaction tensor in the basis of spherical harmonics you can instead look the derivation in Ref. [8].

In the presence of crystal-field splitting, if the spin-orbit interaction does not dominate, it is often preferable to perform the calculations in the t_{2g} basis. To this end, it is key to make QMC codes very efficient in order to reduce as much as possible statistical errors and increase the average sign. Exact LDA+SO+DMFT calculations in the t_{2g} basis have been successfully performed, e.g., for Sr_2RuO_4, using an interaction-expansion continuous-time quantum Monte Carlo solver, and an orbital-dependent phase which makes the Green function matrix real [18, 19]. This approach allowed us to study, for example, the effects of the spin-orbit interaction on the Fermi surface without approximations. The results are shown in Fig. 14 in comparison with experimental data; we will discuss them in the next section.

3.5 Non-spherical Coulomb terms and double-counting correction

While for a free atom the Coulomb tensor is spherical (symmetry $O(3)$), in a material the screened Coulomb tensor has, in general, the symmetry of the lattice. Taking into account non-spherical Coulomb terms is, in general hard, both because they make QMC calculations more difficult and can worsen the sign problem, and because in their presence the double-counting correction has to be explicitly accounted for, even when massive downfolding is used. For these reasons they are typically neglected. Recently it was shown that they can play, however, a very important role for the Fermi surface [18]. Let us therefore discuss how the double-counting correction can be treated with and without such terms, following the approach of Ref. [18]. One of the classical approximations for the double-counting correction is the so called "around mean-field" approximation. The idea is that LDA describes well the average Coulomb term, in the absence of orbital polarization. This is equivalent to using as double-counting correction the Hartree term of the Coulomb interaction tensor, i.e., the operator

$$\hat{H}_{\mathrm{U}}^{\mathrm{DC}} = U \sum_m \left(\hat{n}_{m\uparrow} \bar{n}_{m\downarrow} + \bar{n}_{m\uparrow} \hat{n}_{m\downarrow} \right) + (U - 2J) \sum_{m \neq m'} \left(\hat{n}_{m\uparrow} \bar{n}_{m'\downarrow} + \bar{n}_{m\uparrow} \hat{n}_{m'\downarrow} \right)$$

$$+ (U - 3J) \sum_\sigma \sum_{m > m'} \left(\hat{n}_{m\sigma} \bar{n}_{m'\sigma} + \bar{n}_{m\sigma} \hat{n}_{m'\sigma} \right) - \mu \hat{N}_d \tag{116}$$

$$- U \sum_m \bar{n}_{m\uparrow} \bar{n}_{m\downarrow} + (U - 2J) \sum_{m \neq m'} \bar{n}_{m\uparrow} \bar{n}_{m'\downarrow} + (U - 3J) \sum_\sigma \sum_{m > m'} \bar{n}_{m\sigma} \bar{n}_{m'\sigma}$$

where $\bar{n}_{m\sigma} = n/d$, if n is the number of the correlated electrons per site and d the orbital degeneracy. Within this approximation we have, after collecting all terms,

$$\hat{H}_{\mathrm{U}}^{\mathrm{DC}} = (\delta\mu - \mu) \hat{N}_d - \frac{n^2}{d} \big(U (2d - 1) - 5 (d - 1) \big)$$

$$\delta\mu = \frac{n}{d} \big(U(2d - 1) - 5J(d - 1) \big).$$

If we perform massive downfolding to the correlated bands, as previously mentioned, this is merely a shift of the chemical potential and can therefore be neglected. Let us now consider the case in which the Coulomb interaction has an additional term that does not change the average U but has tetragonal symmetry

$$\Delta\hat{H}_U = \frac{\Delta U}{3} \left(2\hat{n}_{xy\uparrow} \hat{n}_{xy\downarrow} - \hat{n}_{xz\uparrow} \hat{n}_{xz\downarrow} - \hat{n}_{yz\uparrow} \hat{n}_{yz\downarrow} \right)$$

We can now use the around mean-field approximation for this term as well. We find

$$\Delta\hat{H}_U^{\mathrm{DC}} = \frac{n}{6} \frac{\Delta U}{3} \sum_\sigma \left(2\hat{n}_{xy\sigma} - \hat{n}_{xz\sigma} - \hat{n}_{yz\sigma} \right) = \frac{n}{6} \Delta U \sum_\sigma \hat{n}_{xy\sigma} - \delta\mu' \hat{N}$$

$$\delta\mu' = \frac{n}{6} \frac{\Delta U}{3}.$$

This term, in addition to a shift of the chemical potential, yields an effective change of the crystal-field splitting $\varepsilon_{\mathrm{CF}}$, and has therefore to be accounted for explicitly.

How does ΔU change the Fermi surface of Sr_2RuO_4? The Fermi surface is determined by the poles of the Green function at zero frequency. These depend on the non-interacting Hamiltonian and the self-energy matrix at zero frequency. In the Fermi-liquid regime, and within the DMFT approximation, the effect of the self-energy is merely to modify the on-site part of the Hamiltonian, i.e., the crystal-field splitting $\varepsilon_{CF} = \varepsilon_{xz/yz} - \varepsilon_{xy}$ and the spin-orbit couplings λ_μ

$$\varepsilon_{CF} \rightarrow \varepsilon_{CF} + \Delta\varepsilon_{CF}(0),$$

$$\lambda_\mu \rightarrow \lambda_\mu + \Delta\lambda_\mu(0).$$

Both $\Delta\varepsilon_{CF}(0)$ and $\Delta\lambda_\mu(0)$ are positive for Sr_2RuO_4, and lead to an almost doubling of the LDA parameters. The positive $\Delta\varepsilon_{CF}(0)$ shrinks the β sheet (xz/yz bands) and enlarges the γ (xy band) sheet. This can be understood from the schematic Fermi surface and the LDA band structure in Fig. 12. Enhancing the crystal-field splitting corresponds to slightly moving the xy band downwards and the xz/yz bands upwards with respect to the Fermi level. The enhancement of the spin-orbit couplings has a large Hartree-Fock component [19], since the spin-orbit interaction yields a small but finite off-diagonal occupation matrix. For an $O(3)$-symmetric Coulomb tensor, the Hartree-Fock enhancement of the spin-orbit coupling is thus

$$\frac{\Delta\lambda_z}{2} = \quad i(U-3J)\, n^{\uparrow\uparrow}_{xz,yz}$$

$$\frac{\Delta\lambda_y}{2} = - \left(U-3J\right) n^{\uparrow\downarrow}_{xy,yz},$$

$$\frac{\Delta\lambda_x}{2} = -i\left(U-3J\right) n^{\uparrow\downarrow}_{xz,xy},$$

where $n^{\sigma\sigma'}_{m,m'}$ are the off-diagonal elements of the density matrix. The Coulomb-enhanced spin-orbit coupling improves the agreement with the experimental Fermi surface at the degeneracy points (e.g., along the Γ-X direction). The agreement with ARPES data, however, further deteriorates for the γ sheet. This can be seen in Fig. 14, in which the LDA and LDA+DMFT Fermi surface are shown on top of ARPES data from Ref. [21].

Including correlation effects has thus two opposite effects: on the one hand, the agreement with experiments improves (with respect to LDA) for the β sheet; on the other hand, it deteriorates for the γ sheet. This can be seen comparing either panels (a) and (c) or panels (b) and (d) in Fig. 14. Introducing tetragonal Coulomb terms, and in particular the term ΔU, however, reduces the crystal-field enhancement to

$$\varepsilon_{CF} \rightarrow \varepsilon_{CF} + \Delta\varepsilon'_{CF}(0),$$

where $\Delta\varepsilon'_{CF}(0)$ becomes almost zero for cRPA-based estimates of ΔU. This leads to an almost perfect Fermi surface, as shown in Fig. 15. Non-spherical Coulomb terms turn out to be more important for properties that reflect the point symmetry of the lattice, like the Fermi surface, than for properties that average over orbitals, like the total spectral function [19].
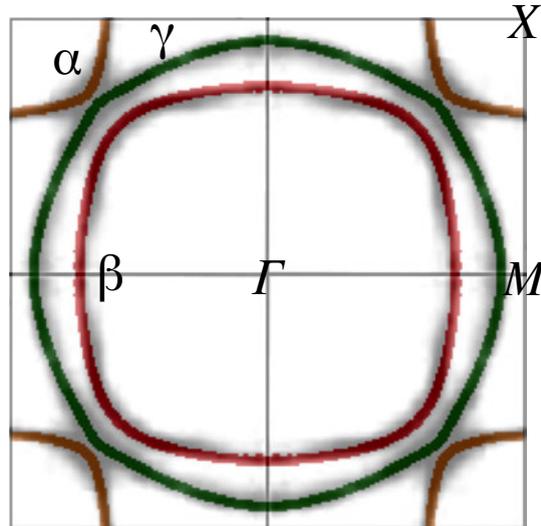
Fig. 15: *The LDA+SO+DMFT Fermi surface of Sr_2RuO_4 calculated including the effects of the non-spherical Coulomb term ΔU. Figure from [18].*

4 Conclusion

The LDA+DMFT approach and its extension has proved very successful for describing correlated materials. It has shown us that materials details do matter, contrarily to what often was assumed in the past; for example a crystal field much smaller than the bandwidth can favor the Mott metal-insulator transition [22]. The method is also becoming very versatile. It is now possible, e.g., to study multi-orbital models including the full Coulomb vertex and spin-orbit interaction, and to calculate response functions or bosonic excitations. Still, many challenges remain. Models with more than a few orbitals or sites and out-of-equilibrium phenomena remain, e.g., very hard to study. Furthermore, since the birth of DFT, Moore's law constantly helped as much as new algorithms in extending the frontier; that has come now slowly to a halt. Quantum computers and artificial intelligence, or other new, not yet foreseeable, technological advances might help us in the future. The present deceleration, however, urges us to think to what we should strive for. It is perhaps easier to discuss first what we *do not* need. We do not need a magical calculating machine that gives us, either via an "exact" first principles scheme or via artificial intelligence, answers with no explanations. Reproducing the data is, of course, the aim of theory, but not the only goal. As scientists we need to know why. The danger of giving this question up is evident if we look back at the historical controversy between copernican and ptolemaic system [23]. At the time, the ptolemaic system was the one which agreed better with experiments. Indeed, it had been fine-tuned along the years, via a series of ad hoc assumptions. The copernican system was initially not performing so well, because it was based on circular orbits. But, at the end, it is the copernican system that made a contribution to science, by identifying the correct picture. A theory should reproduce the generic aspects of a phenomenon, but providing at the same time, as Walter Kohn underlined, *understanding*, via a coherent description and the essential details. This should be our aim.

Appendices

A   Eigenstates of two-site models

A.1   Hubbard dimer

The Hamiltonian of the Hubbard dimer is given by

$$\hat{H} = \varepsilon_d \sum_\sigma \sum_{i=1,2} n_{i\sigma} - t \sum_\sigma \left(c_{1\sigma}^\dagger c_{2\sigma} + c_{2\sigma}^\dagger c_{1\sigma} \right) + U \sum_{i=1,2} \hat{n}_{i\uparrow} \hat{n}_{i\downarrow}.$$

It commutes with the number of electron operator $\hat{N}$, with the total spin $\hat{S}$, and with $\hat{S}_z$. Thus we can express the many-body states in the atomic limit as

$\lvert N, S, S_z \rangle$			N	S	$E(N, S)$
$\lvert 0, 0, 0 \rangle$	$=$	$\lvert 0 \rangle$	0	0	0
$\lvert 1, \frac{1}{2}, \sigma \rangle_1$	$=$	$c_{1\sigma}^\dagger \lvert 0 \rangle$	1	$\frac{1}{2}$	ε_d
$\lvert 1, \frac{1}{2}, \sigma \rangle_2$	$=$	$c_{2\sigma}^\dagger \lvert 0 \rangle$	1	$\frac{1}{2}$	ε_d
$\lvert 2, 1, 1 \rangle$	$=$	$c_{2\uparrow}^\dagger c_{1\uparrow}^\dagger \lvert 0 \rangle$	2	1	$2\varepsilon_d$
$\lvert 2, 1, -1 \rangle$	$=$	$c_{2\downarrow}^\dagger c_{1\downarrow}^\dagger \lvert 0 \rangle$	2	1	$2\varepsilon_d$
$\lvert 2, 1, 0 \rangle$	$= \frac{1}{\sqrt{2}} \left(c_{1\uparrow}^\dagger c_{2\downarrow}^\dagger + c_{1\downarrow}^\dagger c_{2\uparrow}^\dagger \right) \lvert 0 \rangle$		2	1	$2\varepsilon_d$
$\lvert 2, 0, 0 \rangle_0$	$= \frac{1}{\sqrt{2}} \left(c_{1\uparrow}^\dagger c_{2\downarrow}^\dagger - c_{1\downarrow}^\dagger c_{2\uparrow}^\dagger \right) \lvert 0 \rangle$		2	0	$2\varepsilon_d$
$\lvert 2, 0, 0 \rangle_1$	$=$	$c_{1\uparrow}^\dagger c_{1\downarrow}^\dagger \lvert 0 \rangle$	2	0	$2\varepsilon_d + U$
$\lvert 2, 0, 0 \rangle_2$	$=$	$c_{2\uparrow}^\dagger c_{2\downarrow}^\dagger \lvert 0 \rangle$	2	0	$2\varepsilon_d + U$
$\lvert 3, \frac{1}{2}, \sigma \rangle_1$	$=$	$c_{1\sigma}^\dagger c_{2\uparrow}^\dagger c_{2\downarrow}^\dagger \lvert 0 \rangle$	3	$\frac{1}{2}$	$3\varepsilon_d + U$
$\lvert 3, \frac{1}{2}, \sigma \rangle_2$	$=$	$c_{2\sigma}^\dagger c_{1\uparrow}^\dagger c_{1\downarrow}^\dagger \lvert 0 \rangle$	3	$\frac{1}{2}$	$3\varepsilon_d + U$
$\lvert 4, 0, 0 \rangle$	$=$	$c_{1\uparrow}^\dagger c_{1\downarrow}^\dagger c_{2\uparrow}^\dagger c_{2\downarrow}^\dagger \lvert 0 \rangle$	4	0	$4\varepsilon_d + 2U$

Let us order the $N = 1$ states as in the table above, first the spin up and then spin down block. For finite t the Hamiltonian matrix for $N = 1$ electrons takes then the form

$$\hat{H}_1 = \begin{pmatrix} \varepsilon_d & -t & 0 & 0 \\ -t & \varepsilon_d & 0 & 0 \\ 0 & 0 & \varepsilon_d & -t \\ 0 & 0 & -t & \varepsilon_d \end{pmatrix}.$$

This matrix can be easily diagonalized and yields the *bonding* $(-)$ and *antibonding* $(+)$ states

$\|1, S, S_z\rangle_\alpha$		$E_\alpha(1, S)$	$d_\alpha(1, S)$
$\|1, \frac{1}{2}, \sigma\rangle_+$	$= \frac{1}{\sqrt{2}}\left(\|1, \frac{1}{2}, \sigma\rangle_1 - \|1, \frac{1}{2}, \sigma\rangle_2\right)$	$\varepsilon_d + t$	2
$\|1, \frac{1}{2}, \sigma\rangle_-$	$= \frac{1}{\sqrt{2}}\left(\|1, \frac{1}{2}, \sigma\rangle_1 + \|1, \frac{1}{2}, \sigma\rangle_2\right)$	$\varepsilon_d - t$	2

where $d_\alpha(N)$ is the spin degeneracy of the α manifold.

For $N = 2$ electrons (half filling), the hopping integrals only couple the three $S = 0$ states, and therefore the Hamiltonian matrix is given by

$$\hat{H}_2 = \begin{pmatrix} 2\varepsilon_d & 0 & 0 & 0 & 0 & 0 \\ 0 & 2\varepsilon_d & 0 & 0 & 0 & 0 \\ 0 & 0 & 2\varepsilon_d & 0 & 0 & 0 \\ 0 & 0 & 0 & 2\varepsilon_d & -\sqrt{2}t & -\sqrt{2}t \\ 0 & 0 & 0 & -\sqrt{2}t & 2\varepsilon_d+U & 0 \\ 0 & 0 & 0 & -\sqrt{2}t & 0 & 2\varepsilon_d+U \end{pmatrix}.$$

The eigenvalues and the corresponding eigenvectors are

$\|2, S, S_z\rangle_\alpha$		$E_\alpha(2, S)$	$d_\alpha(2, S)$
$\|2, 0, 0\rangle_+$	$= a_1\|2, 0, 0\rangle_0 - \frac{a_2}{\sqrt{2}}\left(\|2, 0, 0\rangle_1 + \|2, 0, 0\rangle_2\right)$	$2\varepsilon_d + \frac{1}{2}\left(U+\Delta(t,U)\right)$	1
$\|2, 0, 0\rangle_o$	$= \frac{1}{\sqrt{2}}\left(\|2, 0, 0\rangle_1 - \|2, 0, 0\rangle_2\right)$	$2\varepsilon_d + U$	1
$\|2, 1, m\rangle_o$	$= \|2, 1, m\rangle$	$2\varepsilon_d$	3
$\|2, 0, 0\rangle_-$	$= a_2\|2, 0, 0\rangle_0 + \frac{a_1}{\sqrt{2}}\left(\|2, 0, 0\rangle_1 + \|2, 0, 0\rangle_2\right)$	$2\varepsilon_d + \frac{1}{2}\left(U-\Delta(t,U)\right)$	1

where

$$\Delta(t, U) = \sqrt{U^2 + 16t^2},$$

and

$$a_1^2 = a_1^2(t, U) = \frac{1}{\Delta(t,U)}\frac{\Delta(t,U) - U}{2} \qquad a_2^2 = a_2^2(t, U) = \frac{4t^2}{\Delta(t,U)}\frac{2}{\Delta(t,U) - U},$$

so that $a_1 a_2 = 2t/\Delta(t, U)$. For $U = 0$ we have $a_1 = a_2 = 1/\sqrt{2}$, and the two states $|2, 0, 0\rangle_-$ and $|2, 0, 0\rangle_+$ become, respectively, the state with two electrons in the bonding orbital and the state with two electrons in the antibonding orbital; they have energy $E_\pm(2, 0) = 2\varepsilon_d \pm 2t$; the remaining states have energy $2\varepsilon_d$ and are non-bonding. For $t > 0$, the ground state is unique and it is always the singlet $|2, 0, 0\rangle_-$; in the large U limit its energy is

$$E_-(2, 0) \sim 2\varepsilon_d - 4t^2/U.$$

In this limit the energy difference between the first excited state, a triplet state, and the singlet ground state is thus equal to the Heisenberg antiferromagnetic coupling

$$E_o(2,1) - E_-(2,0) \sim 4t^2/U = \Gamma.$$

Finally, for $N = 3$ electrons, eigenstates and eigenvectors are

$\|3, S, S_z\rangle_\alpha$		$E_\alpha(3)$	$d_\alpha(3,S)$
$\|3, \frac{1}{2}, \sigma\rangle_+$	$= \frac{1}{\sqrt{2}}\left(\|1, \frac{1}{2}, \sigma\rangle_1 + \|1, \frac{1}{2}, \sigma\rangle_2\right)$	$3\varepsilon_d + U + t$	2
$\|3, \frac{1}{2}, \sigma\rangle_-$	$= \frac{1}{\sqrt{2}}\left(\|1, \frac{1}{2}, \sigma\rangle_1 - \|1, \frac{1}{2}, \sigma\rangle_2\right)$	$3\varepsilon_d + U - t$	2

If we exchange holes and electrons, the $N = 3$ case is identical to the $N = 1$ electron case. This is due to the particle-hole symmetry of the model.

A.2 Anderson molecule

The Hamiltonian of the Anderson molecule is given by

$$\hat{H} = \varepsilon_s \sum_\sigma \hat{n}_{2\sigma} - t \sum_\sigma \left(c_{1\sigma}^\dagger c_{2\sigma} + c_{2\sigma}^\dagger c_{1\sigma}\right) + \varepsilon_d \sum_\sigma \hat{n}_{1\sigma} + U\hat{n}_{1\uparrow}\hat{n}_{1\downarrow}.$$

In the atomic limit, its eigenstates states can be classified as

$\|N, S, S_z\rangle$		N	S	$E(N,S)$
$\|0, 0, 0\rangle$	$= \quad \|0\rangle$	0	0	0
$\|1, \frac{1}{2}, \sigma\rangle_1$	$= \quad c_{1\sigma}^\dagger\|0\rangle$	1	$\frac{1}{2}$	ε_d
$\|1, \frac{1}{2}, \sigma\rangle_2$	$= \quad c_{2\sigma}^\dagger\|0\rangle$	1	$\frac{1}{2}$	ε_s
$\|2, 1, 1\rangle$	$= \quad c_{2\uparrow}^\dagger c_{1\uparrow}^\dagger\|0\rangle$	2	1	$\varepsilon_d + \varepsilon_s$
$\|2, 1, -1\rangle$	$= \quad c_{2\downarrow}^\dagger c_{1\downarrow}^\dagger\|0\rangle$	2	1	$\varepsilon_d + \varepsilon_s$
$\|2, 1, 0\rangle$	$= \frac{1}{\sqrt{2}}\left(c_{1\uparrow}^\dagger c_{2\downarrow}^\dagger + c_{1\downarrow}^\dagger c_{2\uparrow}^\dagger\right)\|0\rangle$	2	1	$\varepsilon_d + \varepsilon_s$
$\|2, 0, 0\rangle_0$	$= \frac{1}{\sqrt{2}}\left(c_{1\uparrow}^\dagger c_{2\downarrow}^\dagger - c_{1\downarrow}^\dagger c_{2\uparrow}^\dagger\right)\|0\rangle$	2	0	$\varepsilon_d + \varepsilon_s$
$\|2, 0, 0\rangle_1$	$= \quad c_{1\uparrow}^\dagger c_{1\downarrow}^\dagger\|0\rangle$	2	0	$2\varepsilon_d + U$
$\|2, 0, 0\rangle_2$	$= \quad c_{2\uparrow}^\dagger c_{2\downarrow}^\dagger\|0\rangle$	2	0	$2\varepsilon_s$
$\|3, \frac{1}{2}, \sigma\rangle_1$	$= \quad c_{1\sigma}^\dagger c_{2\uparrow}^\dagger c_{2\downarrow}^\dagger\|0\rangle$	3	$\frac{1}{2}$	$\varepsilon_d + 2\varepsilon_s$
$\|3, \frac{1}{2}, \sigma\rangle_2$	$= \quad c_{2\sigma}^\dagger c_{1\uparrow}^\dagger c_{1\downarrow}^\dagger\|0\rangle$	3	$\frac{1}{2}$	$2\varepsilon_d + \varepsilon_s + U$
$\|4, 0, 0\rangle$	$= \quad c_{1\uparrow}^\dagger c_{1\downarrow}^\dagger c_{2\uparrow}^\dagger c_{2\downarrow}^\dagger\|0\rangle$	4	0	$2\varepsilon_d + 2\varepsilon_s + U$

For $N = 1$ electrons the Hamiltonian can be written in the matrix form

$$\hat{H}_1 = \begin{pmatrix} \varepsilon_d & -t & 0 & 0 \\ -t & \varepsilon_s & 0 & 0 \\ 0 & 0 & \varepsilon_d & -t \\ 0 & 0 & -t & \varepsilon_s \end{pmatrix}.$$

The eigenstates are thus

$|1, S, S_z\rangle_\alpha$	$E_\alpha(1, S)$	$d_\alpha(1, S)$
$|1, \frac{1}{2}, \sigma\rangle_+ = \alpha_1|1, \frac{1}{2}, \sigma\rangle_1 - \alpha_2|1, \frac{1}{2}, \sigma\rangle_2$	$\frac{1}{2}\left(\varepsilon_d + \varepsilon_s + \sqrt{(\varepsilon_d - \varepsilon_s)^2 + 4t^2}\right)$	2
$|1, \frac{1}{2}, \sigma\rangle_- = \alpha_2|1, \frac{1}{2}, \sigma\rangle_1 + \alpha_1|1, \frac{1}{2}, \sigma\rangle_2$	$\frac{1}{2}\left(\varepsilon_d + \varepsilon_s - \sqrt{(\varepsilon_d - \varepsilon_s)^2 + 4t^2}\right)$	2

where $d_\alpha(N)$ is the spin degeneracy of the α manifold. For $\varepsilon_s = \varepsilon_d + U/2$ the eigenvalues are

$$E_\pm(1, S) = \varepsilon_d + \frac{1}{4}\left(U \pm \Delta(U, t)\right),$$

while the coefficients are $\alpha_1 = a_1(t, U)$ and $\alpha_2 = a_2(t, U)$.

For $N=2$ electrons, the hopping integrals only couple the $S=0$ states. The Hamiltonian is

$$\hat{H}_2 = \begin{pmatrix} \varepsilon_d + \varepsilon_s & 0 & 0 & 0 & 0 & 0 \\ 0 & \varepsilon_d + \varepsilon_s & 0 & 0 & 0 & 0 \\ 0 & 0 & \varepsilon_d + \varepsilon_s & 0 & 0 & 0 \\ 0 & 0 & 0 & \varepsilon_d + \varepsilon_s & -\sqrt{2}t & -\sqrt{2}t \\ 0 & 0 & 0 & -\sqrt{2}t & 2\varepsilon_d + U & 0 \\ 0 & 0 & 0 & -\sqrt{2}t & 0 & 2\varepsilon_s \end{pmatrix}$$

For $\varepsilon_s = \varepsilon_d + U/2$ the eigenvalues and the corresponding eigenvectors are

$|2, S, S_z\rangle_\alpha$	$E_\alpha(2, S)$	$d_\alpha(2, S)$
$|2, 0, 0\rangle_+ = b_1|2, 0, 0\rangle_0 - \frac{b_2}{\sqrt{2}}\left(|2, 0, 0\rangle_1 + |2, 0, 0\rangle_2\right)$	$2\varepsilon_d + \frac{U}{2} + \frac{1}{4}\left(U + 2\Delta(t, \frac{U}{2})\right)$	1
$|2, 0, 0\rangle_o = \frac{1}{\sqrt{2}}\left(|2, 0, 0\rangle_1 - |2, 0, 0\rangle_2\right)$	$2\varepsilon_d + U$	1
$|2, 1, m\rangle_o = |2, 1, m\rangle$	$2\varepsilon_d + \frac{U}{2}$	3
$|2, 0, 0\rangle_- = b_2|2, 0, 0\rangle_0 + \frac{b_1}{\sqrt{2}}\left(|2, 0, 0\rangle_1 + |2, 0, 0\rangle_2\right)$	$2\varepsilon_d + \frac{U}{2} + \frac{1}{4}\left(U - 2\Delta(t, \frac{U}{2})\right)$	1

where $b_1 = a_1(t, U/2)$ and $b_2 = a_2(t, U/2)$. These states have the same form as in the case of the Hubbard dimer; the ground state energy and the weight of doubly occupied states in $|2, 0, 0\rangle_-$ differ, however. Finally, for $N = 3$ electrons, the eigenstates are

$|3, S, S_z\rangle_\alpha$	$E_\alpha(3, S)$	$d_\alpha(3, S)$
$|3, \frac{1}{2}, \sigma\rangle_+ = \alpha_2|1, \frac{1}{2}, \sigma\rangle_1 + \alpha_1|1, \frac{1}{2}, \sigma\rangle_2$	$3\varepsilon_d + U + \frac{1}{4}\left(U + \Delta(t, U)\right)$	2
$|3, \frac{1}{2}, \sigma\rangle_- = \alpha_1|1, \frac{1}{2}, \sigma\rangle_1 - \alpha_2|1, \frac{1}{2}, \sigma\rangle_2$	$3\varepsilon_d + U + \frac{1}{4}\left(U - \Delta(t, U)\right)$	2

B Lehmann representation of the local Green function

For a single-orbital model, the local Matsubara Green function for a given site i is defined as

$$G_{i,i}^{\sigma}(i\nu_n) = -\int_0^{\beta} d\tau \, e^{i\nu_n\tau} \langle \mathcal{T} c_{i\sigma}(\tau) c_{i\sigma}^{\dagger}(0) \rangle, \tag{117}$$

where $\mathcal{T}$ is the time-ordering operator, $\beta = 1/k_B T$, and ν_n a fermionic Matsubara frequency. Let us assume to know all eigenstates $|N_l\rangle$ and their energy $E_l(N)$, for arbitrary number of electrons N. Thus, formally

$$G_{i,i}^{\sigma}(i\nu_n) = -\frac{1}{Z} \sum_{Nl} \int_0^{\beta} d\tau \, e^{i\nu_n\tau} e^{-\Delta E_l(N)\beta} \langle N_l | c_{i\sigma}(\tau) c_{i\sigma}^{\dagger}(0) | N_l \rangle, \tag{118}$$

where $Z = \sum_{Nl} e^{-\Delta E_l(N)\beta}$ is the partition function, $\Delta E_l(N) = E_l(N) - \mu N$ with μ the chemical potential, and $c_{i\sigma}^{\dagger}(0) = c_{i\sigma}^{\dagger}$. We now insert a complete set of states, obtaining

$$
\begin{aligned}
G_{i,i}^{\sigma}(i\nu_n) &= -\frac{1}{Z} \sum_{ll'NN'} \int_0^{\beta} d\tau \, e^{i\nu_n\tau} e^{-\Delta E_l(N)\beta} \langle N_l | c_{i\sigma}(\tau) | N_{l'}' \rangle \langle N_{l'}' | c_{i\sigma}^{\dagger} | N_l \rangle \\
&= -\frac{1}{Z} \sum_{ll'NN'} \int_0^{\beta} d\tau \, e^{-\Delta E_l(N)\beta} e^{(i\nu_n + \Delta E_l(N) - \Delta E_{l'}(N'))\tau} \left| \langle N_{l'}' | c_{i\sigma}^{\dagger} | N_l \rangle \right|^2 \\
&= \frac{1}{Z} \sum_{ll'NN'} \frac{e^{-\Delta E_{l'}(N')\beta} + e^{-\Delta E_l(N)\beta}}{i\nu_n + \Delta E_l(N) - \Delta E_{l'}(N')} \left| \langle N_{l'}' | c_{i\sigma}^{\dagger} | N_l \rangle \right|^2.
\end{aligned} \tag{119}
$$

Due to the weight $|\langle N_{l'}' | c_{i\sigma}^{\dagger}(0) | N_l \rangle|^2$ only the terms for which $N' = N+1$ contribute. Thus, after exchanging the labels $l'N' \leftrightarrow lN$ in the first addend, we obtain the Lehmann representation

$$G_{i,i}^{\sigma}(i\nu_n) = \sum_{ll'N} \frac{e^{-\beta \Delta E_l(N)}}{Z} \left(\frac{\left| \langle (N-1)_{l'} | c_{i\sigma} | N_l \rangle \right|^2}{i\nu_n - \Delta E_l(N) + \Delta E_{l'}(N-1)} + \frac{\left| \langle (N+1)_{l'} | c_{i\sigma}^{\dagger} | N_l \rangle \right|^2}{i\nu_n - \Delta E_{l'}(N+1) + \Delta E_l(N)} \right).$$

Let us consider as example the atomic limit of the Hubbard model at half filling. In this case all sites are decoupled; there are four eigenstates per site, the vacuum $|0\rangle$, with $\Delta E(0) = 0$, the doublet $|1_\sigma\rangle = c_{i\sigma}^{\dagger}|0\rangle$, with $\Delta E_\sigma(1) = -U/2$, and the doubly-occupied singlet $|2\rangle = c_{i\uparrow}^{\dagger} c_{i\downarrow}^{\dagger}|0\rangle$, with $\Delta E(2) = 0$. Furthermore, $Z = 2(1 + e^{\beta U/2})$ and

$$\left| \langle (N-1)_{l'} | c_{i\sigma} | N_l \rangle \right|^2 = \begin{cases} 1 & \text{if } |N_l\rangle = |2\rangle \vee |1_\sigma\rangle \\ 0 & \text{otherwise} \end{cases} \qquad \left| \langle (N+1)_{l'} | c_{i\sigma}^{\dagger} | N_l \rangle \right|^2 = \begin{cases} 1 & \text{if } |N_l\rangle = |0\rangle \vee |1_{-\sigma}\rangle \\ 0 & \text{otherwise} \end{cases}$$

Thus, after summing up the four non-zero contributions, we find

$$G_{i,i}^{\sigma}(\nu_n) = \frac{1}{2} \left(\frac{1}{i\nu_n + U/2} + \frac{1}{i\nu_n - U/2} \right). \tag{120}$$

References

[1] P. Hohenberg and W. Kohn, Phys. Rev. **136**, B864 (1964);
W. Kohn and L. J. Sham, Phys. Rev. **140**, A1133 (1965)

[2] W. Kohn, Rev. Mod. Phys. **71**, 1253 (1999)

[3] P.W. Anderson: *More and different – Notes from a thoughtful curmudgeon*
(World Scientific, Singapore, 2011)

[4] W. Metzner and D. Vollhardt, Phys. Rev. Lett. **62**, 324 (1989)

[5] E. Müller-Hartmann, Z. Phys. B **74**, 507 (1989);
Z. Phys. B **76**, 211 (1989); Int. J. Mod. Phys. B **3**, 2169 (1989)

[6] A. Georges and G. Kotliar, Phys. Rev. B **45**, 6479 (1992)

[7] M. Jarrell, Phys. Rev. Lett. **69**, 168 (1992)

[8] E. Pavarini, E. Koch, D. Vollhardt, A. Lichtenstein (Eds.):
The LDA+DMFT approach to strongly-correlated materials,
Reihe Modeling and Simulation, Vol. 1 (Forschungszentrum Jülich, 2011)
http://www.cond-mat.de/events/correl11

[9] E. Pavarini, E. Koch, A. Lichtenstein, D. Vollhardt (Eds.):
DMFT at 25: Infinite Dimensions,
Reihe Modeling and Simulation, Vol. 4 (Forschungszentrum Jülich, 2014)
http://www.cond-mat.de/events/correl14

[10] E. Pavarini, E. Koch, A. Lichtenstein, D. Vollhardt (Eds.):
DMFT: From Infinite Dimensions to Real Materials,
Reihe Modeling and Simulation, Vol. 8 (Forschungszentrum Jülich, 2018)
http://www.cond-mat.de/events/correl18

[11] E. Koch, G. Sangiovanni, and O. Gunnarsson, Phys. Rev. B **78**, 115102 (2008)

[12] E. Gull, A. J. Millis, A. I. Lichtenstein, A. N. Rubtsov, M. Troyer, and P. Werner,
Rev. Mod. Phys. **83**, 349 (2011)

[13] A. Flesch, E. Gorelov, E. Koch, E. Pavarini, Phys. Rev. B **87**, 195141 (2013)

[14] A. Kiani and E. Pavarini, Phys. Rev. B **94**, 075112 (2016)

[15] E. Pavarini, A. Yamasaki, J. Nuss, and O.K. Andersen,
New. J. Phys **7**, 188 (2005)

[16] N. Marzari, A.A. Mostofi, J.R. Yates, I. Souza, and D. Vanderbilt,
Rev. Mod. Phys. **84**, 1419 (2012)

[17] G. Zhang and E. Pavarini, Phys. Status Solidi RRL, 1800211 (2018)

[18] G. Zhang, E. Gorelov, E. Sarvestani, and E. Pavarini, Phys. Rev. Lett. **116**, 106402 (2016)

[19] E. Sarvestani, G. Zhang, E. Gorelov, and E. Pavarini, Phys. Rev. B **97**, 085141 (2018)

[20] G. Zhang and E. Pavarini, Phys. Rev. B **99**, 125102 (2019)

[21] A. Damascelli, D.H. Lu, K.M. Shen, N.P. Armitage, F. Ronning, D.L. Feng, C. Kim,
Z.-X. Shen, T. Kimura, Y. Tokura, Z.Q. Mao, and Y. Maeno,
Phys. Rev. Lett. **85**, 5194 (2000)

[22] E. Pavarini, S. Biermann, A. Poteryaev, A.I. Lichtenstein, A. Georges, and O.K. Andersen,
Phys. Rev. Lett. **92**, 176403 (2004)

[23] S. Singh: *Big Bang. The most important scientific discovery of all time
and why you need to know about it* (Harper Perennial, London, 2005)

6 Green Functions and Self-Energy Functionals

Robert Eder

Institute for Quantum Materials and Technologies

Karlsruhe Institute of Technology

Contents

1 Introduction

Green functions are quantities of central importance in the theory of interacting many-particle systems. In simplest terms they may be viewed as describing the propagation of some kind of 'perturbation' through a system of interacting particles. On one hand, by their very definition Green functions contain information about the system which can be directly compared to experiments, on the other hand they are a useful mathematical tool because there is a wide variety of techniques to calculate them approximately, and thus overcome the, in general, insoluble nature of the many-particle problem. Of particular importance is the single-particle Green function $G(\mathbf{k}, \omega)$, which describes the propagation of an added particle with wave number $\mathbf{k}$ and energy $\hbar\omega$ through the system and which is directly related to the experimentally measurable photoemission and inverse photoemission spectrum. The famous Dyson equation then expresses the single-particle Green function in terms of another central quantity in many-body physics, the self-energy $\Sigma(\mathbf{k}, \omega)$. This may be viewed as a $\mathbf{k}$- and ω-dependent potential which mimics the effect of the other particles on the propagation of the added particle (it is therefore hardly a surprise that to simplest approximation the self-energy equals the Hartree-Fock potential). However, the physical significance of the self-energy is considerably wider. Namely, in 1961 Luttinger and Ward (LW) published a seminal paper [1] which became the foundation of many important developments in the quantum theory of many-particle systems. They showed that the grand canonical potential Ω of an interacting Fermion system can be expressed as a functional of the single-particle Green function $G(\mathbf{k}, \omega)$ and the self-energy $\Sigma(\mathbf{k}, \omega)$. A key step thereby was the construction of the Luttinger-Ward functional $\Phi[G]$, a functional of the Green function which essentially describes the deviation of Ω from a non-interacting system with the same band structure as the interacting one. Luttinger and Ward gave an explicit expression for $\Phi[G]$ as a sum over infinitely many Feynman diagrams and also showed that Σ is the functional derivative of $\Phi[G]$ with respect to G and that Ω is stationary under variations of Σ. The expression for Ω and the properties of $\Phi[G]$ became the basis for many important results, such as the Luttinger theorem [2] which states that interactions between electrons do not change the volume of the Fermi surface, or the construction of conserving approximations by Baym and Kadanoff [3,4], where $\Phi[G]$ is approximated by keeping only a subclass of Feynman diagrams. While the representation of Green functions in terms of Feynman diagrams was highly successful for systems such as the electron gas, a new challenge arose with increasing interest in strongly correlated electron systems such as the Hubbard model. Namely any Feynman diagram expansion implicitly treats the interaction between the particles as a perturbation and assumes a continuous evolution from the noninteracting case, which is highly questionable for systems such as Mott-insulators. It is the purpose of the present lecture to sketch a further development of the ideas of Luttinger and Ward which is mainly due to Potthoff, the so-called self-energy functional theory. We present Potthoff's non-perturbative re-derivation of the results of Luttinger and Ward [5,6] and the application of their theorems to strongly correlated electron systems by combining them with numerical methods. As an application, we discuss the metal-insulator transition in the single-band Hubbard model.

2 Green functions and the self-energy

2.1 The Green function and its analytical properties

We start with a discussion of Green functions and their properties and use. We will not cover the representation of Green functions in terms of Feynman diagrams, since excellent introductions to this subject can be found in various textbooks [7–9]. In the present notes we try to be consistent with Fetter/Walecka (FW) [8].

We consider a system of interacting fermions and assume that there is some complete basis of single electron states $\varphi_\alpha(x)$. Here $x = (\mathbf{r}, \sigma)$ is the combined real-space and spin coordinate, whereas α is shorthand for a set of quantum numbers. For example, in an LCAO-type description of a solid – which is what we mostly have in mind – we would have $\alpha = (i, n, \nu, \sigma)$ where $i \in \{1, \ldots, N\}$ denotes the unit cell, $n \in \{1, \ldots, n_{Atom}\}$ the number of the atoms in the basis, $\nu \in \{s, p_x, p_y, p_z, d_{xy} \ldots\}$ the type of orbital on the respective atom, and σ the z-component of spin. We denote the number of orbitals in a unit cell by n_{orb}, the total number of α's thus is $N_\alpha = 2Nn_{orb}$. Upon Fourier transformation one would replace $i \to \mathbf{k}$, the wave vector.

In all that follows we consider a grand canonical ensemble with inverse temperature $\beta = 1/k_B T$ and chemical potential μ. Introducing fermionic creation/annihilation operators $c_\alpha^\dagger/c_\alpha$ for electrons in the states $\varphi_\alpha(x)$, the grand canonical Hamiltonian $K = H - \mu\hat{N}$ (with $\hat{N}$ the operator for the number of electrons) can be written as $K = K_0 + K_1$ with [7–9]

$$K_0 = \sum_{\alpha,\beta} \left(t_{\alpha,\beta} - \mu\, \delta_{\alpha,\beta}\right) c_\alpha^\dagger c_\beta \quad \text{and} \quad K_1 = \frac{1}{2} \sum_{\alpha,\beta,\gamma,\delta} V_{\alpha,\beta,\delta,\gamma}\, c_\alpha^\dagger c_\beta^\dagger c_\gamma c_\delta. \tag{1}$$

The matrix elements in this Hamiltonian are given by

$$t_{\alpha,\beta} = \int dx\, \varphi_\alpha^*(x)\left(-\frac{\hbar^2}{2m}\nabla^2 + V(\mathbf{r})\right)\varphi_\beta(x),$$

$$V_{\alpha,\beta,\delta,\gamma} = \int dx \int dx'\, \varphi_\alpha^*(x)\, \varphi_\beta^*(x')\, V(x-x')\, \varphi_\gamma(x')\, \varphi_\delta(x).$$

For later reference we calculate

$$[c_\alpha, K] = \sum_\beta \left(t_{\alpha,\beta} - \mu\delta_{\alpha,\beta}\right)c_\beta + \sum_{\beta,\gamma,\delta} V_{\alpha,\beta,\delta,\gamma}\, c_\beta^\dagger c_\gamma c_\delta, \tag{2}$$

where we have used the identity $V_{\alpha,\beta,\gamma,\delta} = V_{\beta,\alpha,\delta,\gamma}$ obtained by exchanging the integration variables $x \leftrightarrow x'$ in the definition of V. It obviously holds that $[H, \hat{N}] = 0$ so that eigenstates of H have a fixed particle number. The thermal average of any operator $\hat{O}$ is

$$\langle \hat{O} \rangle_{th} = \frac{1}{Z} \text{Tr}\left(e^{-\beta K}\hat{O}\right) = \frac{1}{Z} \sum_i e^{-\beta K_i}\, \langle i|\hat{O}|i\rangle. \tag{3}$$

Here $|i\rangle$ are the eigenstates of H, $H|i\rangle = E_i|i\rangle$, and $K_i = E_i - \mu N_i$ the corresponding eigenvalues of K. Also,

$$Z = \text{Tr}\left(e^{-\beta K}\right) = \sum_i e^{-\beta K_i} \tag{4}$$

is the grand partition function, which is a quantity of interest by itself, because the grand canonical potential of the system is given by $\Omega = -k_B T \, \log(Z)$.

We proceed to the definition of *Green functions* which basically describe the following *gedanken experiment*: the system is initially in thermal equilibrium, but at a certain time t we do something to the system by acting with an operator $\hat{A}$. $\hat{A}$ could add or remove an electron, flip a spin or similar. We then let the system evolve for some time and undo the change at a time t' by acting with an operator $\hat{B}$, which often is $\hat{A}^\dagger$. We then form the overlap with the state we would have obtained had the system evolved without perturbation. In other words, the Green function describes how the 'perturbation' created by $\hat{A}$ propagates in the interval $t \to t'$ before it is removed by $\hat{B}$.

We now formalize this idea, but for reasons which will become clear only later we make a digression and first introduce *imaginary time Green functions*. Moreover, we specialize to the *single particle Green function*, where the perturbation is removing or adding a particle, i.e. $\hat{A} = c_\alpha$ and $\hat{B} = c_\beta^\dagger$, or vice versa. For any operator $\hat{O}$ the imaginary time Heisenberg operator is $\hat{O}(\tau) = e^{\tau K/\hbar} \, \hat{O} \, e^{-\tau K/\hbar}$ and the imaginary time Green function is

$$
\begin{aligned}
G_{\alpha,\beta}(\tau,\tau') &= -\big\langle T \, c_\alpha(\tau) c_\beta^\dagger(\tau') \big\rangle_{th} \\
&= -\Theta(\tau-\tau') \big\langle c_\alpha(\tau) c_\beta^\dagger(\tau') \big\rangle_{th} + \Theta(\tau'-\tau) \big\langle c_\beta^\dagger(\tau') c_\alpha(\tau) \big\rangle_{th} \qquad (5) \\
&= \frac{1}{Z} \bigg(-\Theta(\tau-\tau') \sum_{i,j} e^{-\beta K_i} \, e^{\frac{\tau-\tau'}{\hbar}(K_i - K_j)} \, \langle i|c_\alpha|j\rangle \langle j|c_\beta^\dagger|i\rangle \\
&\qquad + \Theta(\tau'-\tau) \sum_{i,j} e^{-\beta K_i} \, e^{\frac{\tau-\tau'}{\hbar}(K_j - K_i)} \, \langle i|c_\beta^\dagger|j\rangle \langle j|c_\alpha|i\rangle \bigg). \qquad (6)
\end{aligned}
$$

T in the first line is the *time ordering operator*, which reorders the following Heisenberg operators such that their times decrease from left to right and multiplies by (-1) for each exchange of two Fermion operators, as can be seen in the second line. In going from the second to last line we have used (3), inserted a resolution of unity $\sum_j |j\rangle\langle j| = 1$, and used $\langle i|\hat{O}(\tau)|j\rangle = e^{\frac{\tau}{\hbar}(K_i - K_j)} \, \langle i|\hat{O}|j\rangle$. Eq. (6) shows that $G_{\alpha,\beta}$ really is a function of $\tau-\tau'$ only: $G_{\alpha,\beta}(\tau,\tau') = G_{\alpha,\beta}(\tau-\tau')$. To simplify the notation we henceforth replace $\tau-\tau' \to \tau$, which is equivalent to choosing $\tau' = 0$. The τ-dependence of both terms in (6) is $e^{(-\beta+\frac{|\tau|}{\hbar})K_i} \, e^{-\frac{|\tau|}{\hbar}K_j}$. Since the K_i are bounded from below, namely by K_0 for the ground state with the given μ, but unbounded from above in the thermodynamical limit, $\mathbf{G}$ is therefore well-defined only for $\tau \in [-\beta\hbar, \beta\hbar]$ [10]. It therefore can be written as a Fourier series with frequencies $n\pi/\hbar\beta$. However, it is easy to see from (6) that for $\tau \in [-\beta\hbar, 0]$ one has $G(\tau+\beta\hbar) = -G(\tau)$, so that only odd n can contribute. All in all we find the Fourier expansion

$$
G(\tau) = \frac{1}{\beta\hbar} \sum_{\nu=-\infty}^{\infty} e^{-i\omega_\nu \tau} \, G(i\omega_\nu), \qquad (7)
$$

$$
G(i\omega_\nu) = \int_0^{\beta\hbar} d\tau \, e^{i\omega_\nu \tau} \, G(\tau), \qquad (8)
$$

with $\omega_\nu = (2\nu + 1)\pi/\beta\hbar$ and integer ν. The ω_ν are the Fermionic *Matsubara frequencies*.

Performing the integral (8) with (6) for $G_{\alpha,\beta}(\tau)$, thereby using $e^{i\omega_\nu \beta\hbar} = -1$ for any ν, we obtain

$$G_{\alpha,\beta}(i\omega_\nu) = \frac{1}{Z} \sum_{i,j} \frac{e^{-\beta K_i} + e^{-\beta K_j}}{i\omega_\nu - \frac{1}{\hbar}(K_j - K_i)} \langle i|c_\alpha|j\rangle\langle j|c_\beta^\dagger|i\rangle. \tag{9}$$

This so-called *Lehmann representation* of the Green function is exact but not really helpful for practical computations because it requires knowledge of all eigenstates and energies of H. It can be used, however, for establishing certain properties of the Green function as will be seen in the following.

We proceed to the definition of the real-time Green function. Defining the real-time Heisenberg operator $\hat{O}(\tau) = e^{itK/\hbar}\, \hat{O}\, e^{-itK/\hbar}$ the *retarded real-time Green function* is

$$
\begin{aligned}
G_{\alpha,\beta}^R(t,t') &= -i\Theta(t-t')\Big(\big\langle c_\alpha(t) c_\beta^\dagger(t')\big\rangle_{th} + \big\langle c_\beta^\dagger(t') c_\alpha(t)\big\rangle_{th}\Big), \\
&= -i\Theta(t-t')\frac{1}{Z}\bigg(\sum_{i,j} e^{-\beta K_i}\, e^{i\frac{t-t'}{\hbar}(K_i-K_j)}\, \langle i|c_\alpha|j\rangle\langle j|c_\beta^\dagger|i\rangle \\
&\qquad\qquad + \sum_{i,j} e^{-\beta K_i}\, e^{i\frac{t-t'}{\hbar}(K_j-K_i)}\, \langle i|c_\beta^\dagger|j\rangle\langle j|c_\alpha|i\rangle \bigg).
\end{aligned}
\tag{10}
$$

Again this is a function of $t-t'$ only and, using the formula derived in Appendix A,

$$-i\Theta(t)\, e^{-iEt} = \lim_{\eta\to 0^+} \frac{1}{2\pi} \int_{-\infty}^{\infty} d\omega\, \frac{e^{-i\omega t}}{\omega - E + i\eta}$$

we find its Fourier transform

$$G_{\alpha,\beta}^R(\omega) = \frac{1}{Z} \lim_{\eta\to 0^+} \sum_{i,j} \frac{e^{-\beta K_i} + e^{-\beta K_j}}{\omega + i\eta - \frac{1}{\hbar}(K_j - K_i)} \langle i|c_\alpha|j\rangle\, \langle j|c_\beta^\dagger|i\rangle. \tag{11}$$

Comparison with Eq. (9) shows that $G_{\alpha,\beta}^R(\omega)$ can be obtained from $G_{\alpha,\beta}(i\omega_\nu)$ by replacing $i\omega_\nu \to \omega + i\eta$. In other words, there is one function $G_{\alpha,\beta}(z)$ of the complex variable z, often called *the* Green function, which gives $G_{\alpha,\beta}(i\omega_\nu)$ when evaluated for the Matsubara frequencies, and $G_{\alpha,\beta}^R(\omega)$ when evaluated on a line infinitesimally above the real axis. The existence of such a function is the very reason why the imaginary time Green function is introduced in the first place. In principle, the quantities of interest, of course, are the real-time Green functions. For example, the single-particle Green function (11) contains information about the photoemission and inverse photoemission spectrum of the system. On the other hand, the imaginary-time Green function (9) can be evaluated approximately by using the powerful technique of expansion in Feynman diagrams [7–9], which is *not* possible for the real-time Green function. The standard way to obtain the real-time Green functions, which is used again and again in the literature, is to first obtain an approximate $G_{\alpha,\beta}(i\omega_\nu)$ by doing an expansion in Feynman diagrams and then obtain the real-time Green function by continuing it analytically to a line infinitesimally above the real axis. If one has an analytical expression for $G_{\alpha,\beta}(i\omega_\nu)$ this can be done by simply replacing $i\omega_\nu \to \omega + i\eta$.

We now discuss some properties of *the* Green function. In Eq. (11) the product of matrix elements $\langle i|c_\alpha|j\rangle\langle j|c_\beta^\dagger|i\rangle$ can differ from zero only if $N_j = N_i+1$, whence $K_j-K_i = E_j-E_i-\mu$. $G_{\alpha,\beta}(z)$ therefore has poles on the real axis, which correspond to differences of energies of states whose electron number differ by one. Next, we rewrite the Green function as

$$\mathbf{G}(z) = \int_{-\infty}^{\infty} d\omega\, \frac{\boldsymbol{\rho}(\omega)}{z-\omega}, \tag{12}$$

where the elements of the *spectral density matrix* $\boldsymbol{\rho}(\omega)$ can be read off from (9)

$$\rho_{\alpha,\beta}(\omega) = \frac{1}{Z} \sum_{i,j} \left(e^{-\beta K_i}+e^{-\beta K_j}\right) \langle i|c_\alpha|j\rangle\langle j|c_\beta^\dagger|i\rangle\, \delta\left(\omega - \frac{K_i-K_j}{\hbar}\right). \tag{13}$$

Since ω is real we find $\rho_{\alpha,\beta}^*(\omega) = \rho_{\beta,\alpha}(\omega)$, i.e., $\boldsymbol{\rho}(\omega)$ is Hermitian for any ω. Next consider any vector $\mathbf{v}$ of length N_α and define the linear combination $c_\mathbf{v}^\dagger = \sum v_\alpha c_\alpha^\dagger$. Then

$$\sum_{\alpha,\beta} v_\alpha^* \,\rho_{\alpha,\beta}(\omega)\, v_\beta = \frac{1}{Z} \sum_{i,j} \left(e^{-\beta K_i}+e^{-\beta K_j}\right) \left|\langle j|c_\mathbf{v}^\dagger|i\rangle\right|^2 \delta\left(\omega - \frac{K_i-K_j}{\hbar}\right) > 0$$

i.e., $\boldsymbol{\rho}(\omega)$ is positive definite for each ω. It then follows from (12) that $\left(\mathbf{G}(z)\right)^+ = \mathbf{G}(z^*)$ so that $\mathbf{G}(z)$ is *not* Hermitian for complex z. Next consider

$$f(z) = \sum_{\alpha,\beta} v_\alpha^*\, G_{\alpha,\beta}(z)\, v_\beta = \frac{1}{Z} \sum_{i,j} \frac{e^{-\beta K_i} + e^{-\beta K_j}}{z - \frac{K_i-K_j}{\hbar}} \left|\langle j|c_\mathbf{v}^\dagger|i\rangle\right|^2. \tag{14}$$

We write $z = x+iy$ and find the imaginary part of this to be

$$\Im f(z) = -\frac{y}{Z} \sum_{i,j} \frac{e^{-\beta K_i} + e^{-\beta K_j}}{\left(x - \frac{K_i-K_j}{\hbar}\right)^2 + y^2} \left|\langle j|c_\mathbf{v}^\dagger|i\rangle\right|^2. \tag{15}$$

This expression cannot vanish unless $y = 0$, so that for z away from the real axis all eigenvalues of $\mathbf{G}(z)$ must have a nonvanishing imaginary part, otherwise we could choose $\mathbf{v}$ to be the normalized right-hand eigenvector belonging to a purely real eigenvalue λ and find that $f(z)=\lambda$, in contradiction to (15). This implies in particular that for z away from the real axis all eigenvalues of $\mathbf{G}(z)$ are different from zero so that the determinant of $\mathbf{G}(z)$ is different from zero [11] and its inverse $\mathbf{G}^{-1}(z)$ does exist. Using Cramer's rule we find the elements of the inverse Green function

$$G_{\alpha,\beta}^{-1}(z) = \frac{(-1)^{\alpha+\beta} \det \mathbf{M}_{\alpha,\beta}(z)}{\det \mathbf{G}(z)}$$

where $\mathbf{M}_{\alpha,\beta}(z)$ is the respective minor of $\mathbf{G}(z)$, i.e. the matrix $\mathbf{G}(z)$ with line α and column β discarded. Since for z away from the real axis all elements of $\mathbf{G}(z)$ are finite (see Eq. (9)) and the determinant of $\mathbf{G}(z)$ is different from zero it moreover follows that away from the real axis all elements of $\mathbf{G}^{-1}(z)$ are analytical functions of z.

We proceed to a discussion of the behavior of $\mathbf{G}(z)$ for large $|z|$. We assume that the range of ω where the elements of $\boldsymbol{\rho}(\omega)$ are different from zero is finite, which simply means that the change

in energy upon adding or removing an electron is bounded. To discuss the limit $|z| \to \infty$ we rewrite $\mathbf{G}(z)$ as

$$G_{\alpha,\beta}(z) = \frac{1}{Z} \sum_{i,j} e^{-\beta K_i} \left(\frac{\langle i|c_\alpha|j\rangle\langle j|c_\beta^\dagger|i\rangle}{z - \frac{K_j - K_i}{\hbar}} + \frac{\langle i|c_\beta^\dagger|j\rangle\langle j|c_\alpha|i\rangle}{z + \frac{K_j - K_i}{\hbar}} \right), \qquad (16)$$

and expand

$$\frac{1}{z \pm \frac{K_j - K_i}{\hbar}} \to \frac{1}{z} \mp \frac{K_j - K_i}{\hbar z^2} + \mathcal{O}\left(\frac{1}{z^3}\right).$$

Next use $(K_j - K_i)\langle j|c_\alpha|i\rangle = \langle j|Kc_\alpha|i\rangle - \langle j|c_\alpha K|i\rangle = \langle j|[K, c_\alpha]|i\rangle$ and find

$$G_{\alpha,\beta}(z) \to \frac{\delta_{\alpha,\beta}}{z} + \frac{\left\langle \{c_\beta^\dagger, [c_\alpha, K]\} \right\rangle_{th}}{\hbar z^2} + \mathcal{O}\left(\frac{1}{z^3}\right).$$

Using (2) we obtain

$$\left\langle \{c_\beta^\dagger, [c_\alpha, K]\} \right\rangle_{th} = t_{\alpha,\beta} - \mu\delta_{\alpha,\beta} + \sum_{\gamma,\delta} \left(V_{\alpha,\gamma,\beta,\delta} - V_{\alpha,\gamma,\delta,\beta}\right) \langle c_\gamma^\dagger c_\delta \rangle_{th}. \qquad (17)$$

The term involving V looks like the Hartree-Fock potential $V_{\alpha,\beta}^{(HF)}$, however, whereas for the true Hartree-Fock potential the thermal average has to be taken using the Hartree-Fock wave functions and energies, the thermal average in (17) has to be taken using the fully interacting eigenstates and energies. Keeping this subtle difference in mind we still call the third term the Hartree-Fock potential $V_{\alpha,\beta}^{(HF)}$ so that

$$\mathbf{G}(z) \to \frac{1}{z} + \frac{\mathbf{t} - \mu + \mathbf{V}^{(HF)}}{\hbar z^2} + \mathcal{O}\left(\frac{1}{z^3}\right). \qquad (18)$$

Eq. (16) also highlights the physical content of the Green function. We consider a single band of *non*-interacting electrons where $\alpha = (\mathbf{k}, \sigma)$, and $K = \sum_{\mathbf{k}} (\varepsilon_{\mathbf{k}} - \mu) c_{\mathbf{k},\sigma}^\dagger c_{\mathbf{k},\sigma}$. All eigenstates can then be characterized by the occupation numbers of the states $(\mathbf{k}, \sigma)$ being either 0 or 1. In

$$G_{\mathbf{k},\mathbf{k}}(z) = \frac{1}{Z} \sum_{i,j} e^{-\beta K_i} \left(\frac{\langle i|c_{\mathbf{k},\sigma}^\dagger|j\rangle\langle j|c_{\mathbf{k},\sigma}|i\rangle}{z + \frac{K_j - K_i}{\hbar}} + \frac{\langle i|c_{\mathbf{k},\sigma}|j\rangle\langle j|c_{\mathbf{k},\sigma}^\dagger|i\rangle}{z - \frac{K_j - K_i}{\hbar}} \right)$$

the matrix element $\langle j|c_{\mathbf{k},\sigma}|i\rangle$ in the first term is then different from zero only if $|i\rangle$ has an electron in the single-electron state $(\mathbf{k}, \sigma)$, whereas $|j\rangle$ has none, while all other momenta have identical occupation. It follows that $E_i = E_j + \varepsilon_{\mathbf{k}}$, whence $K_j - K_i = -\varepsilon_{\mathbf{k}} + \mu$. The first term therefore describes the removal of an electron with momentum $\mathbf{k}$ and spin σ. By analogous reasoning, in the second term $K_j - K_i = \varepsilon_{\mathbf{k}} - \mu$ and this term describes addition of an electron. In both terms $K_j - K_i$ is independent of both, $|i\rangle$ and $|j\rangle$, so that we can use $\sum_j |j\rangle\langle j| = 1$ and find

$$G_{\mathbf{k},\mathbf{k}}(z) = \frac{1}{Z} \sum_i e^{-\beta K_i} \left(\frac{\langle i|c_{\mathbf{k},\sigma}^\dagger c_{\mathbf{k},\sigma}|i\rangle}{z - \frac{\varepsilon_{\mathbf{k}} - \mu}{\hbar}} + \frac{\langle i|c_{\mathbf{k},\sigma} c_{\mathbf{k},\sigma}^\dagger|i\rangle}{z - \frac{\varepsilon_{\mathbf{k}} - \mu}{\hbar}} \right) = \frac{\langle n_{\mathbf{k},\sigma}\rangle_{th}}{z - \frac{\varepsilon_{\mathbf{k}} - \mu}{\hbar}} + \frac{\langle 1 - n_{\mathbf{k},\sigma}\rangle_{th}}{z - \frac{\varepsilon_{\mathbf{k}} - \mu}{\hbar}}.$$

Both terms have poles which trace the electrons' dispersion relation $\varepsilon_{\mathbf{k}} - \mu$, but the first term describes only the occupied part of the band, the second term the unoccupied part. The Green function is the combined photoemission and inverse photoemission spectrum and this holds true also for the interacting case.

2.2   The self-energy and its analytical properties

We proceed to the definition of another key quantity, the *self-energy*, and start by discussing the *equation of motion* of the imaginary time Green function Eq. (5). We set $G_{\alpha,\beta}(\tau,0)\rightarrow G_{\alpha,\beta}(\tau)$. It follows readily from the definition of the imaginary-time Heisenberg operator $\hat{O}(\tau)$ that $-\hbar\partial_\tau \hat{O}(\tau) = [\hat{O}(\tau), K]$. Moreover, using, e.g., the representation $\Theta(\tau) = \int_{-\infty}^{\tau} dx\, \delta(x)$ one finds $\partial_\tau \Theta(\pm\tau) = \pm\delta(\tau)$. Combining everything we get the equation of motion of the Green function

$$-\hbar\partial_\tau G_{\alpha,\beta}(\tau) = \hbar\,\delta(\tau)\left\langle\left\{c_\alpha,\, c_\beta^\dagger\right\}\right\rangle_{th} + \left\langle T\left[c_\alpha(\tau),\, K\right] c_\beta^\dagger(0)\right\rangle_{th}$$

$$= \hbar\,\delta(\tau)\,\delta_{\alpha,\beta} + \sum_\nu \left(t_{\alpha,\nu}-\mu\delta_{\alpha,\nu}\right) G_{\nu,\beta}(\tau) + F_{\alpha,\beta}(\tau), \tag{19}$$

$$F_{\alpha,\beta}(\tau) = -\sum_{\nu,\kappa,\lambda} V_{\alpha,\nu,\kappa,\lambda}\left\langle T\left[(c_\nu^\dagger c_\lambda c_\kappa)(\tau) c_\beta^\dagger(0)\right]\right\rangle_{th}, \tag{20}$$

where (2) was used. In the *noninteracting case*, i.e., all $V_{\alpha,\nu,\kappa,\lambda}=0$ we have $F_{\alpha,\beta}(\tau)=0$ and the equation closes. Using the representation of the δ-function in terms of Matsubara-frequencies [8]

$$\delta(\tau) = \frac{1}{\hbar\beta}\sum_{\nu=-\infty}^{\infty} e^{-i\omega_\nu\tau}$$

straightforward Fourier transform gives the noninteracting Green function

$$\left(i\omega_\nu - \frac{\mathbf{t}-\mu}{\hbar}\right)\mathbf{G}_0(i\omega_\nu) = 1. \tag{21}$$

We return to the case $V \neq 0$. We recall that $G(\tau)$ fulfills $G(\tau+\beta\hbar) = -G(\tau)$ for $\tau \in [-\beta\hbar, 0]$, which established its Fourier expansion (7). It follows that $\partial_\tau G(\tau+\beta\hbar) = -\partial_\tau G(\tau)$ whence $F(\tau)$ must obey the same boundary condition: $F(\tau+\beta\hbar) = -F(\tau)$. Accordingly, $F(\tau)$ has the same Fourier expansion (7) as $G(\tau)$ itself and we find

$$\left(i\omega_\nu - \frac{\mathbf{t}-\mu}{\hbar}\right)\mathbf{G}(i\omega_\nu) - \frac{1}{\hbar}\boldsymbol{F}(i\omega_\nu) = 1.$$

Now we define the *self-energy* $\boldsymbol{\Sigma}(i\omega_\nu)$ by $\boldsymbol{F}(i\omega_\nu) = \hbar\boldsymbol{\Sigma}(i\omega_\nu)\,\mathbf{G}(i\omega_\nu)$ (recall that $\mathbf{G}^{-1}(z)$ exists for all z away from the real axis so that $\boldsymbol{\Sigma}(i\omega_\nu)$ is well defined) whence

$$\left(i\omega_\nu - \frac{\mathbf{t}-\mu}{\hbar} - \boldsymbol{\Sigma}(i\omega_\nu)\right)\mathbf{G}(i\omega_\nu) = 1. \tag{22}$$

By analytical continuation, $i\omega_\nu \rightarrow z$, this equation defines $\boldsymbol{\Sigma}(z)$ for all z away from the real axis. Next, notice that the brackets on the left-hand side of (21) and (22) are $\mathbf{G}_0^{-1}(z)$ and $\mathbf{G}^{-1}(z)$, respectively, so that we immediately read off the famous *Dyson equation*

$$\mathbf{G}^{-1}(z) = \mathbf{G}_0^{-1}(z) - \boldsymbol{\Sigma}(z) = z - \frac{\mathbf{t}-\mu}{\hbar} - \boldsymbol{\Sigma}(z). \tag{23}$$
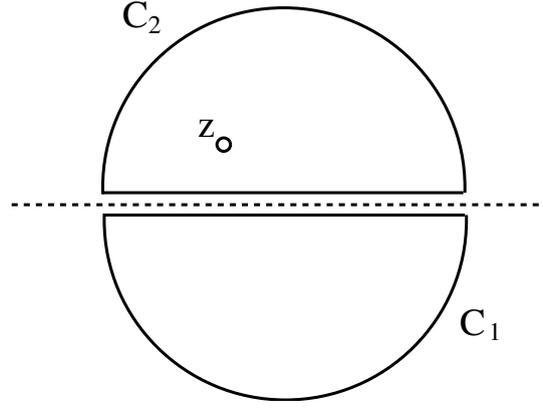
Fig. 1: *Integration contours for the proof of the spectral representation of Σ. The dashed line is the real z' axis.*

We discuss some properties of $\boldsymbol{\Sigma}(z)$ which follow from its definition. Since both $\mathbf{G}^{-1}(z)$ and $\mathbf{G}_0^{-1}(z)$ are analytical in the complex z-plane except for the real axis, the same must hold true for $\boldsymbol{\Sigma}(z)$. Next, it follows from (18) that

$$\mathbf{G}^{-1}(z) \to z - \frac{\mathbf{t}-\mu}{\hbar} - \frac{\mathbf{V}^{(HF)}}{\hbar} + \mathcal{O}\left(\frac{1}{z}\right) \Rightarrow \boldsymbol{\Sigma}(z) \to \frac{\mathbf{V}^{(HF)}}{\hbar} + \mathcal{O}\left(\frac{1}{z}\right).$$

The shifted function $\bar{\boldsymbol{\Sigma}}(z) = \boldsymbol{\Sigma}(z) - \frac{\mathbf{V}^{(HF)}}{\hbar}$ therefore vanishes as $1/z$ for large $|z|$. Now consider the equation $\mathbf{G}^{-1}(z)\,\mathbf{G}(z) = 1$, take the Hermitian conjugate and use $[\mathbf{G}(z)]^+ = \mathbf{G}(z^*)$. It follows that $[\mathbf{G}^{-1}(z)]^+ = \mathbf{G}^{-1}(z^*)$. Since trivially $[\mathbf{G}_0^{-1}(z)]^+ = \mathbf{G}_0^{-1}(z^*)$ and $\mathbf{V}^{HF}$ is Hermitian it follows that $\bar{\boldsymbol{\Sigma}}(z^*) = \bar{\boldsymbol{\Sigma}}^+(z)$. Next, for real ω, define the real matrices $\mathbf{K}(\omega)$ and $\mathbf{J}(\omega)$ by

$$\bar{\boldsymbol{\Sigma}}(\omega+i0^+) = \mathbf{K}(\omega) + i\mathbf{J}(\omega) \quad \Rightarrow \quad \bar{\boldsymbol{\Sigma}}(\omega-i0^+) = \mathbf{K}^T(\omega) - i\mathbf{J}^T(\omega). \tag{24}$$

We introduce the symmetrized/antisymmetrized linear combinations $\mathbf{K}^{(\pm)} = (\mathbf{K} \pm \mathbf{K}^T)/2$ and $\mathbf{J}^{(\pm)} = (\mathbf{J} \pm \mathbf{J}^T)/2$ whence

$$\bar{\boldsymbol{\Sigma}}^{(+)}(z) = \frac{1}{2}\left(\bar{\boldsymbol{\Sigma}}(z)+\bar{\boldsymbol{\Sigma}}^T(z)\right), \qquad \bar{\boldsymbol{\Sigma}}^{(-)}(z) = \frac{i}{2}\left(\bar{\boldsymbol{\Sigma}}(z)-\bar{\boldsymbol{\Sigma}}^T(z)\right). \tag{25}$$

The latter can be expressed in terms of $\mathbf{K}^{(\pm)}(z)$ and $\mathbf{J}^{(\pm)}(z)$ as

$$\begin{aligned}
\bar{\boldsymbol{\Sigma}}^{(+)}(\omega\pm i0^+) &= \mathbf{K}^{(+)}(\omega) \pm i\mathbf{J}^{(+)}(\omega), \\
\bar{\boldsymbol{\Sigma}}^{(-)}(\omega\pm i0^+) &= -\mathbf{J}^{(-)}(\omega) \pm i\mathbf{K}^{(-)}(\omega).
\end{aligned} \tag{26}$$

Now consider the integration contours in figure 1 which consist of lines infinitesimally above and below the real axis and semicircles at infinity. Since $\bar{\boldsymbol{\Sigma}}(z)$ is analytic away from the real axis we have for any z in the upper half-plane

$$\oint_{C_1} dz' \frac{\bar{\boldsymbol{\Sigma}}^{(\pm)}(z')}{z'-z} = 0 \quad \Rightarrow \quad \int_{-\infty}^{\infty} d\omega \frac{\bar{\boldsymbol{\Sigma}}^{(\pm)}(\omega-i0^+)}{\omega-z} = 0. \tag{27}$$

The second equation follows because the integrand is $\propto 1/z'^2$ for large $|z'|$ so that the contribution from the arc vanishes and only the line infinitesimally below the real axis contributes,

where $z = \omega - i0^+$, and $\omega - i0^+ - z = \omega - z$ whenever z has a finite imaginary part. We can now use (26) and obtain

$$\int_{-\infty}^{\infty} d\omega \, \frac{\mathbf{K}^{(\pm)}(\omega)}{\omega - z} = i \int_{-\infty}^{\infty} d\omega \, \frac{\mathbf{J}^{(\pm)}(\omega)}{\omega - z} \, . \tag{28}$$

Next we apply Cauchy's theorem to the contour C_2 in figure 1 and find

$$\bar{\boldsymbol{\Sigma}}^{(\pm)}(z) = \frac{1}{2\pi i} \oint_{C_2} dz' \, \frac{\bar{\boldsymbol{\Sigma}}^{(\pm)}(z')}{z' - z} \, .$$

Again the contribution from the arc vanishes. We use (28) to eliminate the integrals over $\mathbf{K}^{(+)}$ and $\mathbf{J}^{(-)}$, revert (25) to obtain $\bar{\boldsymbol{\Sigma}}(z)$ and arrive at the spectral representation of the self-energy, as derived by Luttinger [12]

$$\boldsymbol{\Sigma}(z) = \frac{\mathbf{V}^{(HF)}}{\hbar} + \int_{-\infty}^{\infty} d\omega \, \frac{\boldsymbol{\sigma}(\omega)}{\omega - z}. \tag{29}$$

Here, the Hermitian matrix $\boldsymbol{\sigma}(\omega) = \mathbf{J}^{(+)}(\omega) - i\mathbf{K}^{(-)}(\omega)$.

Lastly, we notice a property of the self-energy that will be of some importance later on: we will often be concerned with systems which contain both, 'correlated orbitals' and 'uncorrelated orbitals'. A given orbital α is 'uncorrelated' if all interaction matrix elements $V_{\kappa\lambda\mu\nu} = 0$ if at least one of the four indices equals α. In other words, electrons in an uncorrelated orbital do not interact with the other electrons. An example is the well-known Anderson model where one usually has correlated 'f-orbitals' hybridizing with uncorrelated 'conduction electrons'. It then follows from the definition (20) that $F_{\alpha,\beta}(z) = 0$ whenever α or β are uncorrelated, and the same holds true for $\Sigma_{\alpha,\beta}(z)$: *matrix elements of the self-energy involving uncorrelated orbitals are zero!*

2.3 Physical significance of the self-energy

We briefly recall the key results of our discussion so far: The Green function and self-energy are related by the Dyson equation (23), they are analytical functions on the complex frequency plane except for the real axis, and they have the spectral representations (12) and (29). The poles of the Green function on real axis give the ionization and affinity energies of the system, i.e., the energies it takes to remove or add an electron. We now want to discuss the physical consequences of this formal structure. For the remainder of this subsection we consider the case of a single band, set $\hbar = 1$ and call $t_{\mathbf{k}} - V_{\mathbf{k}}^{(HF)} - \mu = \varepsilon_{\mathbf{k}}$. Moreover, we drop the dependence on $\mathbf{k}$ and replace $\varepsilon_{\mathbf{k}} \to \varepsilon$, $G(\mathbf{k}, \omega) \to G(\omega)$ and so on. To begin with, we consider a system with finite N, where the spacing between eigenvalues K_i and hence between the poles of $G(\omega)$ is finite. We have

$$G(\omega) = \frac{1}{\omega - \varepsilon - \bar{\Sigma}(\omega)} = \sum_{i=1}^{n+1} \frac{Z_i}{\omega - \omega_i} \tag{30}$$

$$\bar{\Sigma}(\omega) = \sum_{i=1}^{n} \frac{\sigma_i}{\omega - \zeta_i} \tag{31}$$
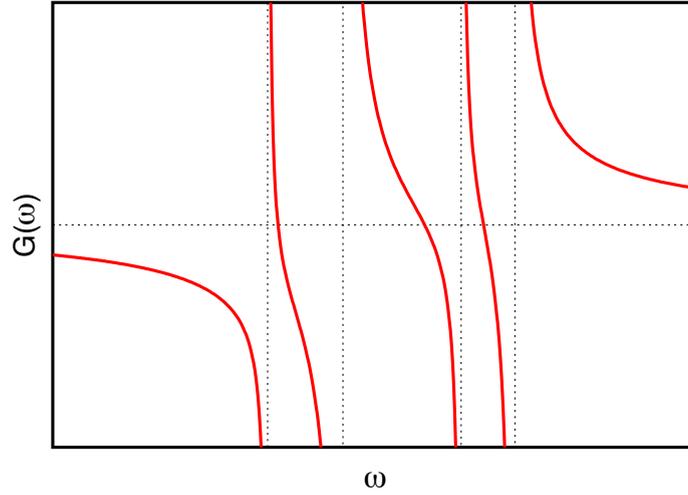
Fig. 2: *The Green function $G(\omega)$ for real ω. The dashed vertical lines give the poles, ω_i.*

where $Z_i > 0$ and ω_i, ζ_i real. On the real axis, $G(\omega)$ crosses zero precisely once in each interval $[\omega_i, \omega_{i+1}]$ with negative slope, see figure 2. It follows from (30) that $G(\zeta) = 0$ implies $\Sigma(\zeta) \to \infty$ so that the ζ_i in (31) must be the zeroes of $G(\omega)$. Moreover, the ζ_i are 'sandwiched' in between the poles ω_i and their number is indeed one less than the ω_i, see figure 2. Since $G^{-1}(\omega_i) = 0$ we find for ω close to ω_i

$$G^{-1}(\omega) = \left(1 - \left.\frac{\partial \Sigma}{\partial \omega}\right|_{\omega_i}\right)(\omega - \omega_i) \quad \Rightarrow \quad Z_i = \left(1 - \left.\frac{\partial \Sigma}{\partial \omega}\right|_{\omega_i}\right)^{-1}. \tag{32}$$

The residue Z_i, which equals the weight observed in photoemission/inverse photoemission, therefore is related to the slope of the self-energy, which is a well-known result.

We consider a situation where the self-energy has a single pole, $\sigma(\omega) = \sigma_0 \delta(\omega - \zeta)$, and reinsert the **k**-dependence

$$G^{-1}(\mathbf{k}, z) = z - \varepsilon_{\mathbf{k}} - \frac{\sigma_0}{z - \zeta} \quad \Rightarrow \quad G(\mathbf{k}, z) = \frac{Z_+}{z - \omega_{+,\mathbf{k}}} + \frac{Z_-}{z - \omega_{-,\mathbf{k}}} \tag{33}$$

where we have introduced

$$\omega_{\pm,\mathbf{k}} = \frac{1}{2}\left((\varepsilon_{\mathbf{k}}+\zeta) \pm \sqrt{(\varepsilon_{\mathbf{k}}-\zeta)^2 + 4\sigma_0}\right), \qquad Z_{\pm} = \pm\frac{\omega_{\pm} - \zeta}{\omega_+ - \omega_-}.$$

It is easy to see that $Z_{\pm} > 0$ and $Z_+ + Z_- = 1$ as it has to be. We can see from this that the single pole of the noninteracting Green function at $\omega = \varepsilon_{\mathbf{k}}$ is split into two poles at $\omega_{\pm,\mathbf{k}}$, i.e., the single band with dispersion $\varepsilon_{\mathbf{k}}$ becomes two bands with dispersions $\omega_{\pm,\mathbf{k}}$. Note that irrespective of the value of $\varepsilon_{\mathbf{k}}$ we find $\omega_{+,\mathbf{k}} - \omega_{-,\mathbf{k}} \geq 2\sqrt{\sigma_0}$ so that the two resulting bands are separated by a gap of width $\geq 2\sqrt{\sigma_0}$. Thus, a single pole of the self-energy with macroscopic residuum σ_0 'pushes open' a gap in the band structure around its position ζ. In fact, this is exactly the situation encountered in a Mott insulator, where the self-energy has a single dominant pole of strength $\approx U^2/4$ which 'pushes open' the Mott gap of width $\approx U$.

3 The Luttinger-Ward functional

3.1 The Green function as a functional integral

We start from the representation of the Green function in terms of a functional integral over *Grassmann variables*. An excellent introduction to Grassmann variables and their use in quantum field theory can be found in the textbook by Negele/Orland [9]. We give a brief summary for readers unfamiliar with Grassmann variables, but it should be noted that this is nowhere near sufficient to fully understand their use. Grassmann variables are objects (here we write them as φ_i^* or φ_j, where i and j distinguish different Grassmann variables) which anticommute: $\varphi_i^*\varphi_j^* = -\varphi_j^*\varphi_i^*$, $\varphi_i\varphi_j^* = -\varphi_j^*\varphi_i$, and $\varphi_i\varphi_j = -\varphi_j\varphi_i$. It follows immediately that the square of any Grassmann variable is zero. While we will be using Grassmann variables with (φ_i^*) and without (φ_j) an asterisk, it should be noted that there is no such thing as the complex conjugate of a Grassmann variable – just as the index, the asterisk is simply a part of the name of the Grassmann variable. Once we have defined a set of Grassmann variables, the corresponding *Grassmann algebra* consists of all possible sums of products of Grassmann variables with complex coefficients. For example, if we have the two Grassmann variables φ^* and φ, the corresponding algebra consists of all expressions $a_0+a_1\varphi+a_2\varphi^*+a_3\varphi\varphi^*$ with complex a_0, a_1, a_2, and a_3 (note that all higher powers of Grassmann variables vanish). The key property of the Grassmann variables, which is used in field theory, is the rule for 'integration' over Grassmann variables, which is

$$\int d\varphi\, \varphi = 1, \qquad \int d\varphi\, 1 = 0\,.$$

In other words, integration over Grassmann variables is the same as differentiation for ordinary numbers, the only difference being that there are just two 'functions' of a Grassmann variable. When we integrate over several Grassmann variables it has to be kept in mind that the differentials $d\varphi_i^*$ and $d\varphi_j$ anticommute as well. Transcendental functions of elements of the Grassmann variables are defined via their power series expansion. To illustrate the above, we evaluate

$$\int d\varphi^* d\varphi\, e^{a_0+a_1\varphi+a_2\varphi^*+a_3\varphi\varphi^*}$$

$$= \int d\varphi^* d\varphi \left(1 + \left(a_0 + a_1\varphi + a_2\varphi^* + a_3\varphi\varphi^*\right) + \frac{1}{2}\left(a_0 a_3\varphi\varphi^* + a_1 a_2(\varphi\varphi^*+\varphi^*\varphi)\right)\right)$$

$$= a_3 \left(1+\frac{a_0}{2}\right).$$

Note that the power series expansion of the exponential terminates very quickly due to the fact that all powers of Grassmann variables higher than the first vanish. Moreover, there is a nonvanishing contribution to the integral only from those terms in the integrand where each Grassmann variable to be integrated over appears precisely once.

After these preliminaries, we turn to the representation of the imaginary-time Green function as functional integral over Grassmann variables. The full derivation is too lengthy to present here but it is explained in a very understandable way by Negele/Orland [9]. Let the imaginary time interval $[0, \hbar\beta]$ be divided into M intervals of length $\varepsilon = \hbar\beta/M$, whereby we assume for

convenience that M is even. Define the imaginary time grid points $\tau_k = k \cdot \varepsilon$, $k = 1 \ldots M$. Then introduce Grassmann variables $\varphi^*_{\alpha,k}$ and $\varphi_{\alpha,k}$ where α is the 'compound index' that labels the Fermion operators $c^\dagger_\alpha$ and c_α, whereas $k = 1 \ldots M$ denotes the position in the imaginary time grid. Then, the partition function can be written as $Z = \lim_{M \to \infty} Z_M$, whereby [9]

$$Z_M = \prod_{k=1}^{M} \prod_{\gamma} \int d\varphi^*_{\gamma,k} d\varphi_{\gamma,k} \, e^{-S(\varphi^*,\varphi)}$$

$$S = \varepsilon \sum_{k=1}^{M} \left(\sum_{\gamma} \varphi^*_{\gamma,k} \frac{\varphi_{\gamma,k} - \varphi_{\gamma,k-1}}{\varepsilon} + \frac{1}{\hbar} K(\varphi^*_k, \varphi_{k-1}) \right). \tag{34}$$

Here the 'Grassmann Hamiltonian' $K(\varphi^*_k, \varphi_{k-1})$ is obtained from the Fermionic Hamiltonian (1) by replacing $c^\dagger_\gamma \to \varphi^*_{\gamma,k}$ and $c_\gamma \to \varphi_{\gamma,k-1}$. The imaginary time Green function (5) reads [9]

$$G_{\alpha,\beta}(\tau,\tau') = -\lim_{M \to \infty} \frac{1}{Z_M} \prod_{k=1}^{M} \prod_{\gamma} \int d\varphi^*_{\gamma,k} \, d\varphi_{\gamma,k} \, \varphi_{\alpha,k(\tau)} \varphi^*_{\beta,k(\tau')} \, e^{-S(\varphi^*,\varphi)}. \tag{35}$$

The symbols $k(\tau)$ and $k(\tau')$ denote those points on the imaginary-time grid which are closest to τ and τ'. Note that in the definition of S the term with $k=1$ also involves the variable $\varphi_{\gamma,0}$, which is *not* included in the set of integration variables. Rather one has to set $\varphi_{\gamma,0} = -\varphi_{\gamma,M}$ to account for Fermi statistics [9]. If we let $M \to \infty$ so that $\varepsilon \to 0$, S appears to become an integral whereas $(\varphi_{\gamma,k} - \varphi_{\gamma,k-1})/\varepsilon$ appears to become a derivative whence, apparently,

$$S \to \int_0^{\hbar\beta} d\tau \left(\sum_{\gamma} \varphi^*_\gamma \frac{\partial \varphi_\gamma}{\partial \tau} + \frac{1}{\hbar} K(\varphi^*, \varphi) \right).$$

This notation can often be found in the literature but, as stressed by Negele/Orland, this can be misleading because the 'trajectories' $\varphi(\tau)$ over which the functional integral is performed may not at all be expected to be 'smooth'.

Doing all calculations at finite M and taking the limit $M \to \infty$ in the end is quite unwieldy but fortunately there is an easy way to circumvent this. Namely we may always switch to the Fourier transforms $\tilde{\varphi}_{\gamma,\nu}$ and $\tilde{\varphi}^*_{\gamma,\nu}$, defined as

$$\tilde{\varphi}^*_{\gamma,\nu} = \frac{1}{\sqrt{M}} \sum_{k=1}^{M} e^{-i\omega_\nu \tau_k} \varphi^*_{\gamma,k}, \qquad \tilde{\varphi}_{\gamma,\nu} = \frac{1}{\sqrt{M}} \sum_{k=1}^{M} e^{i\omega_\nu \tau_k} \varphi_{\gamma,k}, \tag{36}$$

whereby the frequencies $\omega_\nu = (2\nu+1)\pi/\hbar\beta$ are the Fermionic Matsubara frequencies defined above. The second equation looks like the Hermitian conjugate of the first one but recall that there is no such thing as the Hermitian conjugate of a Grassmann variable, so this is actually a *definition*. If we restrict ν to $-M/2 + 1 \leq \nu \leq M/2$, so that the number of ω_ν equals the number of τ_k, the above transformations are unitary as shown in Appendix B, and can be reverted to give

$$\varphi^*_{\gamma,k} = \frac{1}{\sqrt{M}} \sum_{\nu} e^{i\omega_\nu \tau_k} \tilde{\varphi}^*_{\gamma,\nu}, \qquad \varphi_{\gamma,k} = \frac{1}{\sqrt{M}} \sum_{\nu} e^{-i\omega_\nu \tau_k} \tilde{\varphi}_{\gamma,\nu}. \tag{37}$$

Note that $e^{i\omega_\nu \tau_M} = e^{i(2\nu+1)\pi} = -1$. Accordingly, if we *define* $\varphi_{\gamma,0}$ to be (37) evaluated for $k=0$ we automatically have $\varphi_{\gamma,0} = -\varphi_{\gamma,M}$ which was implicit in the definition of S. Since the transformation from the $\varphi_{\gamma,k}$ to the $\tilde\varphi_{\gamma,\nu}$ is unitary the Jacobian is unity and

$$\prod_{k=1}^{M} \prod_\gamma \int d\varphi_{\gamma,k}^* \, d\varphi_{\gamma,k} \quad \rightarrow \quad \prod_{\nu=-\frac{M}{2}+1}^{\frac{M}{2}} \prod_\gamma \int d\tilde\varphi_{\gamma,\nu}^* \, d\tilde\varphi_{\gamma,\nu} \,.$$

We proceed to rewrite S in terms of the $\tilde\varphi^*$ and $\tilde\varphi$. First, consider the 'derivative term'

$$\varepsilon \sum_{k=1}^{M} \varphi_{\gamma,k}^* \frac{\varphi_{\gamma,k} - \varphi_{\gamma,k-1}}{\varepsilon} = \sum_{\nu,\nu'} \frac{\varepsilon}{M} \sum_{k=1}^{M} e^{i(\omega_\nu - \omega_{\nu'})\tau_k} \left(\frac{1 - e^{i\omega_{\nu'}\varepsilon}}{\varepsilon}\right) \tilde\varphi_\nu^* \tilde\varphi_{\nu'} = \varepsilon \sum_\nu \left(\frac{1 - e^{i\omega_\nu \varepsilon}}{\varepsilon}\right) \tilde\varphi_\nu^* \tilde\varphi_\nu.$$

In the limit of small ε (i.e. $M \to \infty$) the square bracket can be written as

$$-e^{i\omega_\nu \varepsilon/2} \frac{e^{i\omega_\nu \varepsilon/2} - e^{-i\omega_\nu \varepsilon/2}}{\varepsilon} = -e^{i\omega_\nu \varepsilon/2} \left(\left.\frac{de^{i\omega_\nu x}}{dx}\right|_{x=0} + \mathcal{O}(\varepsilon^2)\right) \to -i\omega_\nu \, e^{i\omega_\nu \varepsilon/2}$$

whence we obtain the final expression

$$\varepsilon \sum_{k=1}^{M} \varphi_{\gamma,k}^* \frac{\varphi_{\gamma,k} - \varphi_{\gamma,k-1}}{\varepsilon} = -\varepsilon \sum_\nu i\omega_\nu \, e^{i\omega_\nu \varepsilon/2} \, \tilde\varphi_\nu^* \tilde\varphi_\nu \,.$$

A typical term in K_0 becomes

$$\varepsilon \sum_{k=1}^{M} \left(t_{\alpha,\beta} - \mu\delta_{\alpha,\beta}\right) \varphi_{\alpha,k}^* \varphi_{\beta,k-1} = \varepsilon \sum_\nu e^{i\omega_\nu \varepsilon} \left(t_{\alpha,\beta} - \mu\delta_{\alpha,\beta}\right) \tilde\varphi_{\alpha,\nu}^* \tilde\varphi_{\beta,\nu}$$

whereas the products of 4 Grassmann variables in K_1 become

$$\varepsilon \sum_{k=1}^{M} \varphi_{\alpha,k}^* \varphi_{\beta,k}^* \varphi_{\gamma,k-1} \varphi_{\delta,k-1} = \frac{\varepsilon^2}{\hbar\beta} \sum_{\nu_1,\nu_2,\nu_3,\nu_4} \delta_{\nu_1+\nu_2,\,\nu_3+\nu_4} \, e^{i(\omega_{\nu_3}+\omega_{\nu_4})\varepsilon} \, \tilde\varphi_{\alpha,\nu_1}^* \tilde\varphi_{\beta,\nu_2}^* \tilde\varphi_{\gamma,\nu_3} \tilde\varphi_{\delta,\nu_4} \,.$$

The various powers of ε which show up as prefactors can be eliminated by introducing the rescaled Fourier transform $\varphi_{\gamma,\nu} = \sqrt{\varepsilon}\,\tilde\varphi_{\gamma,\nu}$. This transformation is no longer unitary, rather the Jacobian is ε^M which does not have a well-defined limit as $M \to \infty$. However, for any finite M the Jacobian is the same in both numerator and denominator in (35) and simply cancels out so that the limit $M \to \infty$ can be taken without problem. Having rewritten S in terms of the (rescaled) Fourier amplitudes the limit $M \to \infty$ becomes trivial: since we had $-M/2 + 1 \leq \nu \leq M/2$, we simply let each ν range over all integers. Our final result then becomes

$$\begin{aligned}
-S[\varphi^*,\varphi] = \quad & \sum_\nu \varphi_{\alpha,\nu}^* \, e^{i\omega_\nu \varepsilon} \, G_{0,\alpha,\beta}^{-1}(i\omega_\nu) \, \varphi_{\beta,\nu} \\
& - \frac{1}{2\hbar^2\beta} \sum_{\substack{\alpha,\beta,\gamma,\delta \\ \nu_1,\nu_2,\nu_3,\nu_4}} V_{\alpha\beta,\delta,\gamma} \, \delta_{\nu_1+\nu_2,\,\nu_3+\nu_4} \, e^{2i(\omega_{\nu_3}+\omega_{\nu_4})\varepsilon} \, \varphi_{\alpha,\nu_1}^* \varphi_{\beta,\nu_2}^* \varphi_{\gamma,\nu_3} \varphi_{\delta,\nu_4} \,,
\end{aligned} \tag{38}$$

whereby the limit $\varepsilon \to 0^+$ has to be taken and the matrix $\mathbf{G}_0^{-1}(i\omega_\nu) = i\omega_\nu - \frac{\mathbf{t}-\mu}{\hbar}$ is the inverse noninteracting Green function, see (21). Keeping the explicit factors of $e^{i\omega_\nu\varepsilon}$ and $e^{2i(\omega_{\nu_3}+\omega_{\nu_4})\varepsilon}$ while $\varepsilon \to 0$ may seem awkward, however, these factors are in fact crucial in some cases to obtain meaningful results (see Appendix C) whereas they may be safely replaced by unity in other cases. Next, using Eqs. (7) and (8) it is easy to show that

$$
\frac{1}{\hbar\beta} \int_0^{\hbar\beta} d\tau \int_0^{\hbar\beta} d\tau' \, e^{i\omega_\nu\tau} \, e^{-i\omega_{\nu'}\tau'} \, G(\tau, \tau') = \delta_{\nu,\nu'} \, G(i\omega_\nu) \, ,
$$

the 'finite-M-version' of which is

$$
G_{\alpha,\beta}(i\omega_\nu) = \lim_{M\to\infty} \frac{\varepsilon^2}{\hbar\beta} \sum_{k,k'=1}^M e^{i\omega_\nu\tau_k} \, e^{-i\omega_\nu\tau_{k'}} \, G_{\alpha,\beta}(\tau_k, \tau_{k'})
$$

$$
= -\frac{\prod_{\mu=-\infty}^{\infty} \prod_\gamma \int d\varphi_{\gamma,\mu}^* \, d\varphi_{\gamma,\mu} \; \varphi_{\alpha,\nu} \, \varphi_{\beta,\nu}^* \, e^{-S(\varphi^*,\varphi)}}{\prod_{\mu=-\infty}^{\infty} \prod_\gamma \int d\varphi_{\gamma,\mu}^* \, d\varphi_{\gamma,\mu} \; e^{-S(\varphi^*,\varphi)}} \, , \tag{39}
$$

because $\frac{\varepsilon^2}{\hbar\beta} = \left(\frac{\sqrt{\varepsilon}}{\sqrt{M}} \right)^2$. This expression readily lends itself to a perturbation expansion in K_1 which leads to the known representation of the Green function in terms of Feynman diagrams. However, we do not pursue this here but switch to our central objective, namely the construction of the Luttinger-Ward functional, thereby closely following Potthoff [5, 6].

3.2   Construction of the Luttinger-Ward functional

We start by slightly changing our point of view. We note that the various objects that we are concerned with (the noninteracting Green function $\mathbf{G}_0$, the full Green function $\mathbf{G}$ and the self-energy Σ) all are just sets of complex numbers: $F_{\alpha,\beta}(i\omega_\nu)$, $F \in \{G_0, G, \Sigma\}$. Then, we may consider (39) with (38) as the definition of a functional $\mathcal{G}[\mathbf{G}_0^{-1}]$, which maps one such set, $\mathbf{G}_0^{-1}(i\omega_\nu)$, to another one: $\mathbf{G}(i\omega_\nu)$. If the initial set happens to be a noninteracting Green function of the form $\mathbf{G}_0^{-1}(i\omega_\nu) = i\omega_\nu - (\mathbf{t}-\mu)/\hbar$ with some physical set of single particle elements $\mathbf{t}$, $\mathcal{G}[\mathbf{G}_0^{-1}]$ yields the corresponding interacting Green function, with interaction part K_1. Accordingly, K_1 in (38) may be viewed as an implicit parameter of the functional and we consider K_1 fixed from now on. One may wonder if the functional $\mathcal{G}[\mathbf{G}_0^{-1}]$ gives a well-defined result for any choice of $\mathbf{G}_0^{-1}$. This is probably not the case, but we simply restrict its domain those $\mathbf{G}_0^{-1}$ which give a well-defined result. Next consider the functional

$$
\Omega[\mathbf{G}_0^{-1}] = -\frac{1}{\beta} \ln \left(\prod_{\mu=-\infty}^{\infty} \prod_\gamma \int d\varphi_{\gamma,\mu}^* \, d\varphi_{\gamma,\mu} \; e^{-S(\varphi^*,\varphi)} \right) \, ,
$$

which is the grand canonical potential for a physical $\mathbf{G}_0^{-1}$ because the bracket is Z in this case, see (34). Its variation with respect to $\mathbf{G}_0^{-1}$ is

$$
\beta \, \frac{\partial \, \Omega[\mathbf{G}_0^{-1}]}{\partial \, G_{0,\alpha,\beta}^{-1}(i\omega_\nu)} = -e^{i\omega_\nu\varepsilon} \, \mathcal{G}[\mathbf{G}_0^{-1}]_{\beta,\alpha}(i\omega_\nu) \, . \tag{40}
$$

Note the 'inverted' order of indices of G on the right hand side, which follows by a comparison of (38) and (39). Next, for a given 'self energy' $\boldsymbol{\Sigma}$ and a given 'Green function' $\mathbf{G}$ consider

$$\mathbf{D}[\mathbf{G}, \boldsymbol{\Sigma}] = \mathcal{G}[\mathbf{G}^{-1} + \boldsymbol{\Sigma}] - \mathbf{G}\,.$$

Assume $\boldsymbol{\Sigma}$ is a true self-energy corresponding to some $\mathbf{G}_0^{-1}(i\omega_\nu) = i\omega_\nu - (\mathbf{t} - \mu)/\hbar$ (and interaction K_1) and $\mathbf{G}$ the corresponding interacting Green function. By the Dyson equation $\mathbf{G}^{-1} + \boldsymbol{\Sigma} = \mathbf{G}_0^{-1}$, and since $\mathcal{G}[\mathbf{G}_0^{-1}] = \mathbf{G}$ we find $\mathbf{D}[\mathbf{G}, \boldsymbol{\Sigma}] = 0$. Next, for a given 'Green function' $\mathbf{G}$ define the functional $\mathcal{S}[\mathbf{G}]$ to be the 'self energy' which minimizes the norm of $\mathbf{D}[\mathbf{G}, \boldsymbol{\Sigma}]$, defined as

$$\big|\mathbf{D}\big| = \frac{1}{N} \sum_{\alpha,\beta} \sum_\nu \big|D_{\alpha,\beta}(i\omega_\nu)\big|^2.$$

For a physical Green function $\mathbf{G}$ and the corresponding self-energy $\boldsymbol{\Sigma}$ we found $\mathbf{D} = 0$, which gives the minimal value of $|\mathbf{D}|$, whence $\mathcal{S}[\mathbf{G}] = \boldsymbol{\Sigma}$ and $\mathcal{S}$ simply maps the Green function to the self-energy. If $\mathbf{G}$ is not a physical Green function, but sufficiently 'reasonable' such that the above functionals can be defined, we expect

$$\mathcal{G}\big[\mathbf{G}^{-1} + \mathcal{S}[\mathbf{G}]\big] = \mathbf{G} + \delta\mathbf{G} \tag{41}$$

where $\delta\mathbf{G} \to 0$ whenever $\mathbf{G}$ approaches a physical Green function. We are now in the position to define the *Luttinger-Ward functional*, which is the following complex valued functional of a Green function

$$\Phi[\mathbf{G}] = \Omega\big[\mathbf{G}^{-1} + \mathcal{S}[\mathbf{G}]\big] + \frac{1}{\beta}\sum_\lambda e^{i\omega_\lambda \varepsilon}\Big(-\ln\det \mathbf{G}(i\omega_\lambda) + \operatorname{Tr}\mathbf{G}(i\omega_\lambda)\boldsymbol{\Sigma}[\mathbf{G}](i\omega_\lambda)\Big). \tag{42}$$

The logarithm of the determinant is the sum of the logarithms of the $2Nn_{orb}$ eigenvalues of $\mathbf{G}(i\omega_\lambda)$ and the limit $\varepsilon \to 0^+$ is understood (to shorten the notation we henceforth omit factors like $e^{i\omega_\lambda \varepsilon}$ and reinsert them only in the final result). Consider the variation of this functional under a change of $\mathbf{G}$: Using (40), (41) and the chain rule we find the variation of the first term

$$\beta\frac{\partial\Omega\big[\mathbf{G}^{-1} + \mathcal{S}[\mathbf{G}]\big]}{\partial G_{\alpha,\beta}(i\omega_\nu)} = -\sum_\lambda\sum_{\delta,\gamma}\mathcal{G}\big[\mathbf{G}^{-1} + \mathcal{S}[\mathbf{G}]\big]_{\delta,\gamma}(i\omega_\lambda)\frac{\partial(G^{-1} + \mathcal{S}[\mathbf{G}])_{\gamma,\delta}(i\omega_\lambda)}{\partial G_{\alpha,\beta}(i\omega_\nu)}$$

$$= -\sum_\lambda\sum_{\delta,\gamma}(G_{\delta,\gamma} + \delta G_{\delta,\gamma})(i\omega_\lambda)\frac{\partial(G^{-1} + \mathcal{S}[\mathbf{G}])_{\gamma,\delta}(i\omega_\lambda)}{\partial G_{\alpha,\beta}(i\omega_\nu)} \tag{43}$$

Next, notice that for each λ

$$\sum_{\gamma,\delta} G_{\delta,\gamma}(i\omega_\lambda)\, G_{\gamma,\delta}^{-1}(i\omega_\lambda) = 2Nn_{orb}\,, \tag{44}$$

and since the $G_{\alpha,\beta}(i\omega_\nu)$ for different α, β and ν must be considered as independent variables

$$\frac{\partial G_{\delta,\gamma}(i\omega_\lambda)}{\partial G_{\alpha,\beta}(i\omega_\nu)} = \delta_{\nu,\lambda}\,\delta_{\alpha,\delta}\,\delta_{\beta,\gamma}\,.$$

Differentiating (44) with respect to $G_{\alpha,\beta}(i\omega_\nu)$ we therefore obtain

$$\sum_{\gamma,\delta}\left(\delta_{\nu,\lambda}\delta_{\alpha,\delta}\,\delta_{\beta,\gamma}\,G_{\gamma,\delta}^{-1}(i\omega_\nu) + G_{\delta,\gamma}(i\omega_\lambda)\frac{\partial G_{\gamma,\delta}^{-1}(i\omega_\lambda)}{\partial G_{\alpha,\beta}(i\omega_\nu)}\right) = 0$$

$$\Rightarrow\quad -\sum_{\gamma,\delta}G_{\delta,\gamma}(i\omega_\lambda)\frac{\partial G_{\gamma,\delta}^{-1}(i\omega_\lambda)}{\partial G_{\alpha,\beta}(i\omega_\nu)} = \delta_{\nu,\lambda}\,G_{\beta,\alpha}^{-1}(i\omega_\nu)\,,$$

and inserting this into (43) we find

$$\beta\,\frac{\partial\Omega\left[\mathbf{G}^{-1}+\mathcal{S}[\mathbf{G}]\right]}{\partial G_{\alpha,\beta}(i\omega_\nu)} = G_{\beta,\alpha}^{-1}(i\omega_\nu) - \sum_\lambda\sum_{\delta,\gamma}G_{\delta,\gamma}(i\omega_\lambda)\frac{\partial\mathcal{S}[\mathbf{G}]_{\gamma,\delta}(i\omega_\lambda)}{\partial G_{\alpha,\beta}(i\omega_\nu)} + \mathcal{O}(\delta G). \qquad (45)$$

Using Appendix D the derivative of the second term on the right hand side of (42) becomes

$$\beta\,\frac{\partial}{\partial G_{\alpha,\beta}(i\omega_\nu)}\left(-\frac{1}{\beta}\sum_\lambda \ln\det \mathbf{G}(i\omega_\lambda)\right) = -G_{\beta,\alpha}^{-1}(i\omega_\nu)\,, \qquad (46)$$

whereas the derivative of the third term (multiplied by β) is

$$\mathcal{S}[\mathbf{G}]_{\beta,\alpha}(i\omega_\nu) + \sum_\lambda\sum_{\delta,\gamma}G_{\delta,\gamma}(i\omega_\lambda)\frac{\partial\mathcal{S}[\mathbf{G}]_{\gamma,\delta}(i\omega_\lambda)}{\partial G_{\alpha,\beta}(i\omega_\nu)}\,. \qquad (47)$$

Adding up (45), (46), and (47) and reinserting the exponential of $e^{i\omega_\nu\varepsilon}$ we obtain

$$\beta\,\frac{\partial\Phi[\mathbf{G}]}{\partial G_{\alpha,\beta}(i\omega_\nu)} = e^{i\omega_\nu\varepsilon}\mathcal{S}[\mathbf{G}]_{\beta,\alpha}(i\omega_\nu) + \mathcal{O}(\delta G). \qquad (48)$$

If we now let $\mathbf{G}$ become the physical Green function for some noninteracting Green function (and the fixed interaction K_1) $\mathcal{S}[\mathbf{G}]$ becomes the physical self-energy and δG vanishes. We arrive at the key result that the self-energy is the functional derivative of the Luttinger-Ward functional Φ with respect to the Green function (but note the inverted matrix indices on the right hand side). For a physical $\mathbf{G}$, $\Omega\left[\mathbf{G}^{-1}+\mathcal{S}[\mathbf{G}]\right]$ becomes the grand canonical potential and we arrive at the expression for Ω first derived by Luttinger and Ward

$$\Omega = -\lim_{\varepsilon\to 0}\frac{1}{\beta}\sum_\lambda e^{i\omega_\lambda\varepsilon}\Big(\ln\det \mathbf{G}^{-1}(i\omega_\lambda) + \mathrm{Tr}\,\mathbf{G}(i\omega_\lambda)\,\mathbf{\Sigma}(i\omega_\lambda)\Big) + \Phi[\mathbf{G}]\,. \qquad (49)$$

As it stands this expression is not really helpful for evaluating Ω, because if one wanted to use the definition (42) to evaluate $\Phi[\mathbf{G}]$ one would have to know Ω in the first place. However, Luttinger and Ward have shown that $\Phi[\mathbf{G}]$ can be represented as a sum over infinitely many suitably chosen Feynman diagrams [1], so that for example a partial summation over a subset of diagrams gives an explicit (approximate) expression for $\Phi[\mathbf{G}]$. The expression (49) gives Ω as a functional of $\mathbf{G}$ (the self-energy Σ can be eliminated using the Dyson equation) and in the

next step we want to write Ω as a functional of $\boldsymbol{\Sigma}$. Since the self-energy is the derivative of Φ with respect to $\mathbf{G}$

$$\frac{1}{\beta} e^{i\omega_\nu \varepsilon} \, \boldsymbol{\Sigma}_{\beta,\alpha}(i\omega_\nu) = \frac{\partial \Phi[\mathbf{G}]}{\partial G_{\alpha,\beta}(i\omega_\nu)} \,, \tag{50}$$

this can be done by Legendre transform. Assuming that the functional $\mathcal{S}[\mathbf{G}]$ can be inverted to yield $\mathbf{G}[\boldsymbol{\Sigma}]$, define the Legendre transform

$$F[\boldsymbol{\Sigma}] = \Phi\left[\mathbf{G}[\boldsymbol{\Sigma}]\right] - \sum_\lambda \sum_{\gamma,\delta} G[\boldsymbol{\Sigma}]_{\delta,\gamma}(i\omega_\lambda) \, \frac{\partial \Phi[\mathbf{G}]}{\partial G_{\delta,\gamma}(i\omega_\lambda)}$$

$$= \Phi\left[\mathbf{G}[\boldsymbol{\Sigma}]\right] - \frac{1}{\beta} \sum_\lambda \sum_{\gamma,\delta} e^{i\omega_\lambda \varepsilon} \, G[\boldsymbol{\Sigma}]_{\delta,\gamma}(i\omega_\lambda) \, \boldsymbol{\Sigma}_{\gamma,\delta}(i\omega_\lambda)$$

and inserting this into (49) we find

$$\Omega = -\lim_{\varepsilon \to 0} \frac{1}{\beta} \sum_\lambda e^{i\omega_\lambda \varepsilon} \ln \det\left(\mathbf{G}_0^{-1}(i\omega_\lambda) - \boldsymbol{\Sigma}(i\omega_\lambda)\right) + F[\boldsymbol{\Sigma}] \,. \tag{51}$$

By virtue of being a Legendre transform this functional obeys

$$\beta \, \frac{\partial F[\boldsymbol{\Sigma}]}{\partial \Sigma_{\alpha,\beta}(i\omega_\nu)} = -e^{i\omega_\nu \varepsilon} \, G_{\beta,\alpha}(i\omega_\nu), \tag{52}$$

which is easily verified directly. Using this and again the theorem from Appendix D we arrive at the key result

$$\frac{\partial \Omega}{\partial \Sigma_{\alpha,\beta}(i\omega_\nu)} = 0 \,. \tag{53}$$

Let us summarize what we found. First, there exists a functional $\Phi[\mathbf{G}]$ such that the grand potential Ω is given by (49). By itself this is not really spectacular because one could always define $\Phi[\mathbf{G}]$ via (49). What is highly nontrivial, however, is the fact that the self-energy can be obtained as the functional derivative of $\Phi[\mathbf{G}]$ at the exact $\mathbf{G}$, see (50). Similarly, there exists a functional $F[\boldsymbol{\Sigma}]$ such that Ω is given by (51) and the Green function is obtained as the derivative of $F[\boldsymbol{\Sigma}]$, see (52). Moreover, when expressed as a functional of the self-energy, Ω is stationary with respect to variations of $\boldsymbol{\Sigma}$, see (53), *at the exact self-energy*. Moreover, the functionals $\Phi[\mathbf{G}]$ and $F[\boldsymbol{\Sigma}]$ have an additional important property: they depend only on the interaction part K_1 in the Hamiltonian, but are completely independent of the noninteracting term K_0 or, equivalently, the noninteracting Green function $\mathbf{G}_0$. To see this, let us carefully go through our above construction of the Luttinger-Ward functional. The functionals $\mathcal{G}[\mathbf{G}_0^{-1}]$ and $\Omega[\mathbf{G}_0^{-1}]$ have the noninteracting Green function as their argument while there is no further 'intrinsic' dependence on $\mathbf{G}_0$ (these functional do depend on K_1, however!). It follows that the functional $\mathcal{S}[G]$, which is defined using only the functional $\mathcal{G}$, does not have any implicit dependence on $\mathbf{G}_0$ either, i.e., it can in principle be evaluated without knowledge of $\mathbf{G}_0$. Accordingly, $\Phi[\mathbf{G}]$ is a functional only of the $G_{\alpha,\beta}(i\omega_\lambda)$ with no implicit dependence on $\mathbf{t}$ and μ, so that the same holds true for its Legendre-transform $F[\boldsymbol{\Sigma}]$.

4 Self-energy functional theories

4.1 Dynamical mean-field theory

In the preceding section we have seen that the grand potential Ω of an interacting Fermi system can be represented as a functional of its self-energy, see Eq. (51), and that this functional is stationary at the true self-energy, see Eq. (53). This is a promising result: Such stationarity principles are put to use in almost every area of physics. In fact, one might come up with the following variational determination of the self-energy: choose a trial self-energy of the form (29), whence Ω ultimately becomes a functional of the spectral density $\boldsymbol{\sigma}(\omega)$ ($\mathbf{V}^{(HF)}$ is itself a functional of the Green function and hence the self-energy) and then use (53) to derive an Euler-Lagrange equation for $\boldsymbol{\sigma}(\omega)$. The problem is that the definition of the functional $\Phi[\mathbf{G}]$, Eq. (42), allowed to prove some of its properties, such as (50), but that it is completely impossible to actually evaluate it for a given 'trial $\mathbf{G}$' (this would, for example, necessitate knowledge of Ω). Accordingly, it is equally impossible to give an explicit expression for its Legendre transform $F[\boldsymbol{\Sigma}]$ and evaluate this for a given 'trial $\boldsymbol{\Sigma}$'.

However, we can circumvent this problem by making use of the fact that the functional $F[\boldsymbol{\Sigma}]$ does not depend on the noninteracting part of the Hamiltonian K_0, but only on the interaction part K_1. To illustrate the idea we consider the well-known Hubbard model on a lattice with N sites and periodic boundary conditions

$$H = \sum_{i,j}\sum_{\sigma} t_{i,j}\, c_{i,\sigma}^{\dagger}c_{i,\sigma} + U\sum_{i} n_{i,\uparrow}n_{i\downarrow} = \sum_{\mathbf{k},\sigma}\varepsilon_{\mathbf{k}}\, c_{\mathbf{k},\sigma}^{\dagger}c_{\mathbf{k},\sigma} + U\sum_{i} n_{i,\uparrow}n_{i\downarrow}\,.$$

Thereby $n_{i,\sigma} = c_{i,\sigma}^{\dagger}c_{i,\sigma}$ and $\varepsilon_{\mathbf{k}}$ is the Fourier transform of $t_{i,j}$. In addition we consider an artificial system, called the *reference system*, with Hamiltonian $\tilde{H} = \sum_i \tilde{H}_i$, where all H_i have the identical form of an Anderson impurity model

$$\tilde{H}_i = \sum_{\nu}\varepsilon_{\nu}\, l_{i,\nu,\sigma}^{\dagger}l_{i,\nu,\sigma} + \sum_{\nu}\left(V_{\nu}\, l_{i,\nu,\sigma}^{\dagger}c_{i,\sigma} + H.c.\right) + U\, n_{i,\uparrow}n_{i\downarrow} \tag{54}$$

where again $n_{i,\sigma} = c_{i,\sigma}^{\dagger}c_{i,\sigma}$. This describes a single 'Hubbard-site' (described by $c_{i,\sigma}^{\dagger}$ and $c_{i,\sigma}$) coupled to a number of 'ligand' sites (described by $l_{i,\nu,\sigma}^{\dagger}$ and $l_{i,\nu,\sigma}$). We assume that the impurity system can be solved, and denote the Green function and self-energy for this system by $\tilde{G}$ and $\tilde{\Sigma}$. We have seen above that all matrix elements of the self-energy involving uncorrelated sites vanish. Since the ligands in the Hamiltonian (54) are uncorrelated, the only nonvanishing element is $\tilde{\Sigma}_{c,c}(z)$.

After these preliminaries we come to the crucial point: since H and $\tilde{H}$ have the same interaction, namely $K_1 = U\sum_i n_{i,\uparrow}n_{i,\downarrow}$, the functional $F[\tilde{\Sigma}]$ is the same for the Hubbard model and the reference system. We now make use of this fact by taking the self-energy $\tilde{\Sigma}$ of the impurity model to be the 'trial self-energy' for the lattice system. Since the reference system consists of disconnected clusters its self-energy is diagonal in real space: $\tilde{\Sigma}_{(i,c),(j,c)}(z) = \delta_{i,j}\,\tilde{\Sigma}_{c,c}(z)$, whence its Fourier transform is $\mathbf{k}$-independent: $\tilde{\Sigma}(\mathbf{k},z) = \tilde{\Sigma}_{c,c}(z)$. The resulting Green function of the lattice therefore is $G^{-1}(\mathbf{k},z) = z - (\varepsilon_{\mathbf{k}}-\mu)/\hbar - \tilde{\Sigma}_{c,c}(z)$. Using (51) we thus obtain

an approximate Ω_{latt} for the Hubbard model (the factor of 2 is for spin)

$$\Omega_{latt} = F[\tilde{\Sigma}] - \lim_{\varepsilon \to 0} \frac{2}{\beta} \sum_{\mathbf{k}} \sum_{\lambda} e^{i\omega_\lambda \varepsilon} \ln\left(i\omega_\lambda - \frac{\varepsilon_{\mathbf{k}} - \mu}{\hbar} - \tilde{\Sigma}_{c,c}(i\omega_\lambda)\right). \tag{55}$$

Now we know that Ω is stationary under variations of the self-energy, see Eq. (53). We cannot perform a variation of the self-energy over *all* possible self-energies but we may restrict the domain to 'impurity model representable' ones, that means those self-energies which can be obtained by solution of the impurity model for some set of parameters $\{\varepsilon_\nu, V_\nu\}$. The variation of $\tilde{\Sigma}$ then amounts to a variation of the parameters ε_ν and V_ν in (54). Let us discuss how the value of $F[\tilde{\Sigma}]$ changes with the parameters of the impurity model, $t \in \{\varepsilon_\nu, V_\nu\}$. Using the chain rule and (52) we find

$$\begin{aligned}
\frac{\partial F[\tilde{\boldsymbol{\Sigma}}]}{\partial t} &= \sum_{\alpha,\beta} \sum_\lambda \frac{\partial F[\tilde{\boldsymbol{\Sigma}}]}{\partial \tilde{\Sigma}_{\alpha,\beta}(i\omega_\lambda)} \frac{\partial \tilde{\Sigma}_{\alpha,\beta}(i\omega_\lambda)}{\partial t} \\
&= -\frac{1}{\beta} \sum_{\alpha,\beta} \sum_\lambda e^{i\omega_\lambda \varepsilon} \tilde{G}_{\beta,\alpha}(i\omega_\lambda) \frac{\partial \tilde{\Sigma}_{\alpha,\beta}(i\omega_\lambda)}{\partial t} \\
&= -\frac{2N}{\beta} \sum_\lambda e^{i\omega_\lambda \varepsilon} \tilde{G}_{c,c}(i\omega_\lambda) \frac{\partial \tilde{\Sigma}_{c,c}(i\omega_\lambda)}{\partial t}.
\end{aligned}$$

The last equation follows from the fact that there are N lattice sites i and the two spin directions for each site. It follows that

$$\frac{\partial \Omega_{latt}}{\partial t} = -\frac{2}{\beta} \sum_{\mathbf{k},\lambda} e^{i\omega_\lambda \varepsilon} \left[\tilde{G}_{c,c}(i\omega_\lambda) - G(\mathbf{k}, i\omega_\lambda)\right] \frac{\partial \tilde{\Sigma}_{c,c}(i\omega_\lambda)}{\partial t} = 0. \tag{56}$$

We may now perform a limiting procedure by sending the number of ligands $\to \infty$ that means considering a continuum of ligands which hybridize with the correlated c-orbital. Then the number of parameters t for which (56) must be fulfilled becomes a continuum. The simplest way to fulfill all of these conditions at once is to set the square bracket equal to zero for each λ, that means

$$\tilde{G}_{c,c}(i\omega_\lambda) = \frac{1}{N} \sum_{\mathbf{k}} G(\mathbf{k}, i\omega_\lambda) = \frac{1}{N} \sum_{\mathbf{k}} \frac{1}{i\omega_\lambda - (\varepsilon_{\mathbf{k}} - \mu)/\hbar - \tilde{\Sigma}_{c,c}(i\omega_\lambda)}. \tag{57}$$

This equation must be solved simultaneously for each ω_λ by adjusting the hybridization function $V(E)$ and the density of states $\rho(E)$ for the ligands in the impurity model, and in fact is nothing but the well-known self-consistency equation for dynamical mean-field theory (DMFT) [13] . The derivation above shows that DMFT can be understood as approximate minimization of the grand potential as functional of the self-energy. The impurity model thereby acts as the 'self-energy preparation lab' to generate trial Green functions and the associated exact self-energy.

So far we have partitioned the lattice into single sites and each site was 'decorated' with a 'bath' of ligands. However, we also could have partitioned the lattice into small but finite clusters and decorated each cluster with a bath of noninteracting ligand sites. Going through similar steps as above one can easily derive the self-consistency equations for various cluster-generalizations of DMFT [6]. The variational principle for the grand potential as a functional of the self-energy thus provides a unifying principle to derive all of these theories.

4.2   Metal-insulator-transition in a dimer

We have seen that DMFT can be derived from the variational principle for the grand potential by restricting the domain of self-energies to those which are derivable from an impurity model. However, self-energy functional theory as outlined above allows for even simpler approaches and as an example we now study Potthoff's re-derivation of the phase diagram for the metal-insulator transition in the Hubbard model [14]. We again consider the single-band Hubbard model on a simple cubic N-site lattice with periodic boundary condition, but focus on the case of *particle-hole symmetry*. To develop this idea we first note that the simple cubic lattice can be divided into two *sublattices*, A and B, such that all neighbors of a site on the A sublattice are on the B-sublattice and vice versa. Also, we rewrite the Hubbard model as

$$K = H - \mu = \sum_{i,j} \sum_\sigma t_{i,j}\, c_{i,\sigma}^\dagger c_{i,\sigma} + \frac{U}{2} \sum_{i=1}^N \left(n_i - 1\right)\left(n_i - 1\right) - N\frac{U}{2}$$

$$= \sum_{\mathbf{k},\sigma} \left(\varepsilon_{\mathbf{k}} - \frac{U}{2}\right) c_{\mathbf{k},\sigma}^\dagger c_{\mathbf{k},\sigma} + U \sum_{i=1}^N n_{i,\uparrow}\, n_{i,\downarrow},$$

where $n_i = c_{i,\uparrow}^\dagger c_{i,\uparrow} + c_{i,\downarrow}^\dagger c_{i,\downarrow}$ and we assume that all $t_{i,j}$ are real so that $t_{i,j} = t_{j,i}$. Under the transformation $c^\dagger \leftrightarrow c$ we have $n_i - 1 \to 1 - n_i$ so that the interaction part is invariant, whereas the hopping term changes sign. If the hopping integral $t_{i,j}$ is different from zero only if the sites i and j belong to different sublattices, which is what we assume, this sign change can be compensated by the gauge transformation $c_{i,\sigma}^\dagger \to -c_{i,\sigma}^\dagger$ for all sites i of, say, sublattice B. It is straightforward to show that this transformation exchanges photoemission and inverse photoemission spectrum and implies $\mu = U/2$. We will now use particle-hole symmetry to construct a simplified reference system.

Namely for the reference system we follow Potthoff and choose N dimers with one 'Hubbard-site' hybridizing with one bath-site, i.e., the Hamiltonian for one dimer reads

$$\tilde{K} = \tilde{H} - \mu N = -V \sum_\sigma \left(c_\sigma^\dagger l_\sigma + l_\sigma^\dagger c_\sigma\right) + \left(\varepsilon_l - \frac{U}{2}\right)\sum_\sigma l_\sigma^\dagger l_\sigma + \frac{U}{2}\left(n_c - 1\right)\left(n_c - 1\right) - \frac{U}{2}. \quad (58)$$

Here $l_\sigma^\dagger$ creates an electron in the ligand site and $n_c = c_\uparrow^\dagger c_\uparrow + c_\downarrow^\dagger c_\downarrow$. Compared to the reference system (54) for DMFT that was discussed in the previous section, this amounts to retaining only a single ligand. We have to write $\varepsilon_l - U/2$ because $\mu = U/2$. Since we want to generate particle-hole symmetric self-energies we have to impose particle-hole symmetry also in the reference system. The transformation $c^\dagger \leftrightarrow c$, $l^\dagger \leftrightarrow -l$ indeed converts the Hamiltonian into itself *except* for the second term. Setting $\varepsilon_l = U/2$, however, eliminates this term and particle-hole symmetry is restored. The Hamiltonian thus becomes

$$\tilde{K} = -V \sum_\sigma \left(c_\sigma^\dagger l_\sigma + l_\sigma^\dagger c_\sigma\right) + \frac{U}{2}\left(n_c - 1\right)\left(n_c - 1\right) - \frac{U}{2}. \quad (59)$$

and the only remaining parameter to be varied therefore is V, the ligand energy ε_l having been eliminated by the requirement of particle-hole symmetry. The Fock space of the dimer has a

dimension of $2^4 = 16$ so that all eigenstates $|i\rangle$ and corresponding eigenenergies K_i can be obtained by numerical diagonalization of the matrix for $\tilde{K}$. If we construct basis functions with fixed particle number, spin and z-component of the spin, the problem in fact can be broken down to diagonalizing 2×2 matrices. We therefore can calculate the grand potential $\tilde{\Omega}$ by numerical evaluation of the grand partition function (4), the Green function $\tilde{G}_{\alpha,\beta}(z)$ by using the Lehmann representation (9) and the self-energy $\tilde{\Sigma}_{\alpha,\beta}(z)$ from the Dyson equation (23). Again, only the entry $\tilde{\Sigma}_{c,c}(z)$ may differ from zero for any z, which is a good check for the computer program. For concreteness, at $T = 0$ the self-energy of the dimer becomes [15]

$$\tilde{\Sigma}(z) = \frac{U}{2} + \frac{U^2}{8}\left(\frac{1}{z+3V} + \frac{1}{z-3V}\right). \tag{60}$$

Note that this has exactly the form (29), in particular the first term is indeed the Hartree-Fock potential $\langle n_\sigma\rangle U$ because $\langle n_\sigma\rangle = 1/2$ due to particle-hole symmetry. Reverting Eq. (51) we can now calculate the numerical value of the functional $F[\tilde{\Sigma}]$

$$F[\tilde{\Sigma}] = \tilde{\Omega} + \lim_{\varepsilon\to0}\frac{1}{\beta}\sum_\lambda e^{i\omega_\lambda\varepsilon}\ln\det\tilde{\mathbf{G}}^{-1}(i\omega_\lambda).$$

Notice that this is possible *only* because we could obtain the numerical value of $\tilde{\Omega}$ by full exact diagonalization of $\tilde{K}$. This procedure gives us a self-energy $\tilde{\Sigma}(z)$ and the corresponding numerical value of the functional $F[\tilde{\Sigma}]$ and we recall that both of these are functions of the hybridization matrix element V in (59). Next, we proceed as above: we use the self-energy $\tilde{\Sigma}(z)$ as a trial self-energy for the lattice model and write

$$\Omega_{latt} = -\frac{2}{\beta}\sum_\lambda e^{i\omega_\lambda\varepsilon}\int d\varepsilon\,\rho_0(\varepsilon)\ln\left(i\omega_\lambda - \varepsilon + \mu - \tilde{\Sigma}_{c,c}(i\omega_\lambda)\right) + F[\tilde{\Sigma}],$$

where $\rho_0(\varepsilon)$ is the density of states for the conduction band. Following Potthoff [14] we use a semi-elliptical density of states of width $W = 4$

$$\rho_0(\varepsilon) = \frac{1}{2\pi}\sqrt{4-\varepsilon^2}.$$

In this approximation Ω becomes a function of V and figure 3(a) shows $\Omega(V)$ at $T = 0$ for different U. For smaller U there are two stationary points: a maximum at $V = 0$ and a minimum at finite V, which is the physical solution. At $U_c \approx 5.82$ the two extrema coalesce into a single minimum at $V = 0$, which is the only stationary point for larger U. This change from finite V to $V = 0$ precisely corresponds to the metal-insulator transition. To see this we recall equation (60) for $\tilde{\Sigma}(z)$ and insert it into the **k**-integrated Green function

$$G(z) = 2\int_{-2}^{2} d\varepsilon\,\frac{\rho_0(\varepsilon)}{z + U/2 - \varepsilon - \tilde{\Sigma}(z)}. \tag{61}$$

This is shown in figure 4 together with $\Im\tilde{\Sigma}(z)$ for $z = \omega - i\eta$. The self-energy has two poles at $\zeta_1 = -3V$ and $\zeta_2 = 3V$ which give the two Lorentzian peaks in $\Im\tilde{\Sigma}(z)$. As discussed above
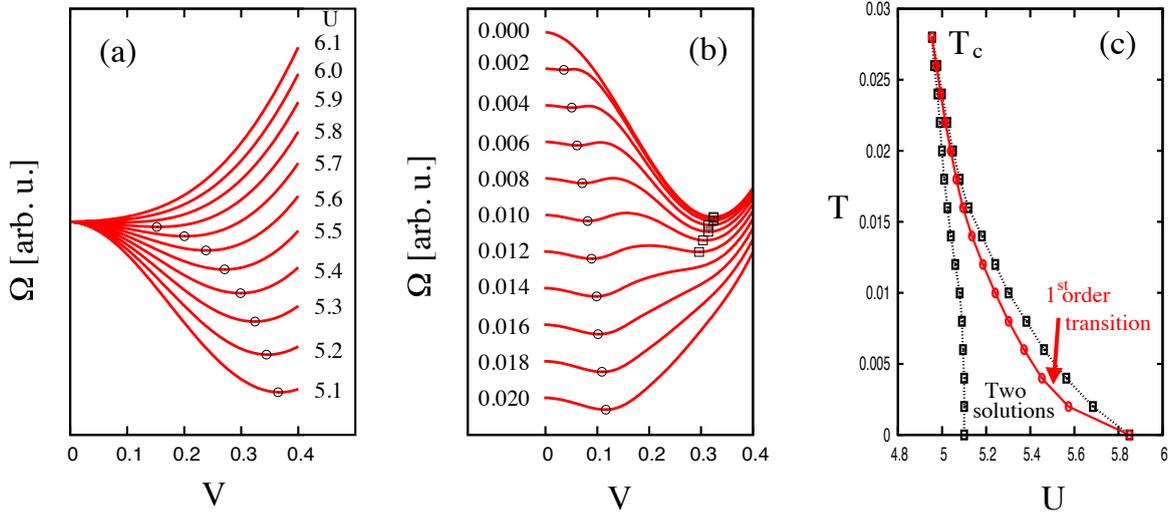
Fig. 3: *(a): $\Omega(V)$ versus V at $T = 0$, variation with U, (b): Ω versus V at $U = 5.2$, variation with T, (c): the resulting phase diagram.*

these two poles 'push open' gaps in the density of states around themselves, see the top panel of Fig. 4. There is still a finite spectral weight at the Fermi level, $\omega = 0$, i.e., the system is a metal. As V becomes smaller, see the center panel of Fig. 4, the slope of $\tilde{\Sigma}(z)$ in the energy range between ζ_1 and ζ_2 (which is $\frac{\partial \Sigma}{\partial \omega} = - \left(\frac{U}{6V}\right)^2$ at $\omega = 0$) becomes steeper and steeper so that according to (32) the spectral weight at the Fermi level becomes smaller and smaller. Finally, as $V \to 0$ the two poles coalesce, see the bottom panel of Fig. 4, and there remains only a single pole at $\omega = 0$ which pushes open a gap of order U and the spectral density at $\omega = 0$ vanishes – the system has turned into a Mott-insulator! This is precisely the scenario predicted by DMFT [13], whereby DMFT calculations find $U_c \approx 5.84$ [13] as compared to $U_c \approx 5.82$ from the simple dimer calculation.

Next, figure 3(b) shows $\Omega(V)$ for the fixed value of $U = 5.2$ and different temperatures T. For most temperatures there are three stationary points whereby the local maximum can be discarded. It follows, that there are actually two possible solutions for each temperature which cross in between $T = 0.10$ and $T = 0.12$. This implies that there is a first order phase transition between these two temperatures. Repeating the procedure for various U gives the phase diagram in figure 3(c). There is only a metallic solution for small U, at a first U_{c1} a second insulating solution starts to appear, at U_c there is a first order metal-insulator transition and on from U_{c2} there is only an insulating solution. The results obtained in this way by the solution of a dimer are qualitatively very similar to those obtained by extensive numerical renormalization group [16] and quantum Monte Carlo [17] calculations in the framework of DMFT. The main deficiency of the dimer calculation is the underestimation of the critical temperature T_c in figure 3(c) by a factor of ≈ 2.

This application of self-energy functional theory, whereby trial self-energies $\Sigma(z)$ and the numerical value of Ω and hence $F[\Sigma]$ are obtained by exact diagonalization of a suitably chosen reference system is called the *Variational Cluster Approximation*. This was first proposed by Potthoff and successfully applied to a large number of problems.
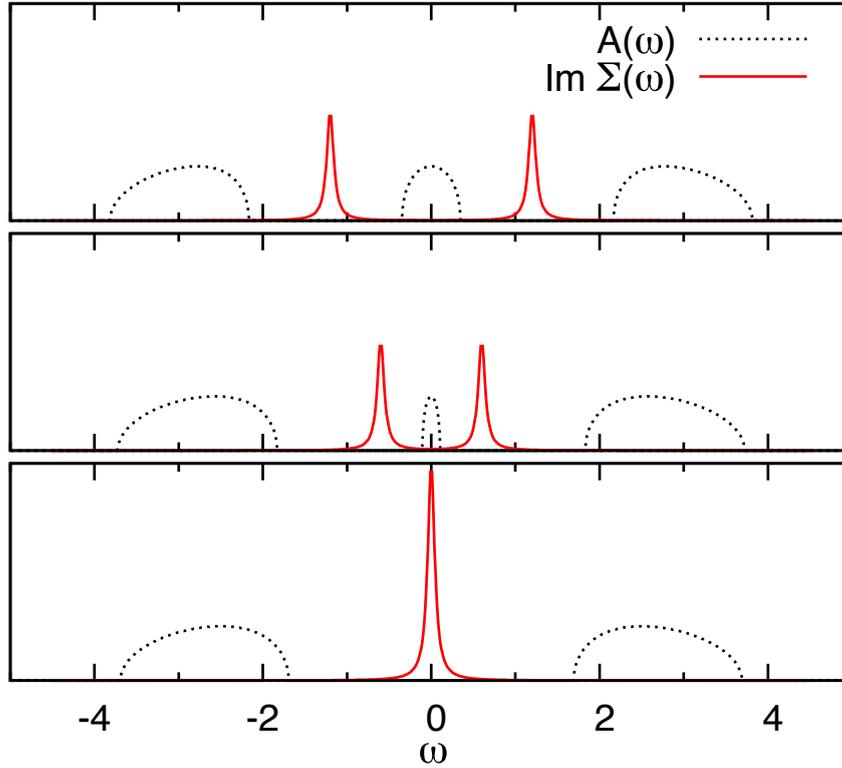
Fig. 4: *Single particle spectral function and imaginary part of the self-energy (calculated with an imaginary part of* 0.05 *for the frequency) obtained from the angle integrated Green function (61) with self-energy (60). Parameter values are* $U = 5$ *and* $V = 0.4$ *(top),* $V = 0.2$ *(center) and* $V = 0$ *(bottom).*

5   Summary and conclusion

We have discussed the single-particle Green function $\mathbf{G}(z)$ which describes the propagation of a particle added to a system of interacting fermions. It is a function of the complex frequency variable z which is analytical throughout the complex z-plane except for the real axis. On the real axis it has poles which give the energies needed to add or remove a particle. Via the Dyson equation it can be related to the self-energy $\mathbf{\Sigma}(z)$ which describes the effects of the interaction with the propagating particle with the other particles in the system. We have derived the spectral representations Eq. (12) and Eq. (29) for these quantities. We have then given a nonperturbative derivation of the results of Luttinger and Ward: the grand canonical potential Ω is a functional of the Green function and self-energy (see Eq. (49), the self-energy is the derivative of the Luttinger-Ward functional with respect to the Green function (see Eq. (50)) and Ω is stationary with respect to variations of the self-energy (see Eq. (53)). We have then seen that Ω can also be expressed as a functional of the self-energy alone (see Eq. (51)) which is stationary with respect to variations of the self-energy. This then is the basis of self-energy functional theory which provides a simple unifying framework for Dynamical Mean-Field Theory and its cluster generalizations and which also can be applied directly in the framework of the Variational Cluster Approximation.

Appendix A

We want to prove the formula

$$- i\Theta(t)\, e^{-iEt} = \lim_{\eta \to 0^+} \frac{1}{2\pi} \int_{-\infty}^{\infty} d\omega\, \frac{e^{-i\omega t}}{\omega - E + i\eta} \,. \tag{62}$$

We consider the integral on the right-hand-side as a contour integral in the complex ω-plane along the real axis. We initially limit the range of integration to be $\int_{-R}^{R} d\omega \cdots$ and take the limit $R \to \infty$ in the end. We augment this contour by a semicircle of radius R around the origin so that the resulting contour is closed. For any ω on the semicircle we have

$$e^{-i\omega t} = e^{\sin(\varphi)Rt}\, e^{-i\cos(\varphi)Rt}$$

where φ is the phase of ω. Assume that $t\sin(\varphi) < 0$. Then, for any $\varepsilon > 0$ we can find an R such that $R\, e^{\sin(\varphi)Rt} < \varepsilon$. It follows that the contour integral over the part of the semicircle where $t\sin(\varphi) < 0$ vanishes in the limit $R \to 0$. For $t > 0$ this means that the integral over the semicircle in the lower half-plane $\pi < \varphi < 2\pi$ vanishes, whereas it is the semicircle in the upper half-plane $0 < \varphi < \pi$ which gives vanishing contribution for $t < 0$. We can thus replace the integral on the right-hand-side by an integral along a *closed* contour which consists of the real axis and an infinitely large semicircle in the lower (upper) half-plane for $t > 0$ ($t < 0$). But this means we can invoke the *theorem of residues* which tells us that the integral is $\pm 2\pi i$ times the sum of residues of all poles within the integration contour. The integrand has one pole at $\omega_0 = E - i\eta$ with residuum $e^{-i\omega_0 t}$. This is in the lower half-plane so that we know immediately that for $t < 0$ the integral vanishes i.e., it is $\propto \Theta(t)$. For $t > 0$ we readily find that the integral is $-2\pi i\, e^{-i\omega_0 t}$ and inserting this into (62) and taking the limit $\eta \to 0$ proves (62), which shows that the Fourier transform of the left-hand side is $(\omega - E + i\eta)^{-1}$.

Appendix B

Call $\lambda = e^{i\frac{2m\pi}{M}}$ where m and M are integers. Then

$$\sum_{k=1}^{M} \lambda^k = \lambda \sum_{k=0}^{M-1} \lambda^k = \lambda \frac{\lambda^M - 1}{\lambda - 1}\,,$$

but since $\lambda^M = (e^{2\pi i})^m$ this is zero. Defining M-component vectors $\vec{\varphi}^* = (\varphi_1^*, \varphi_2^*, \ldots, \varphi_M^*)$ and $\vec{v}_\nu = \frac{1}{\sqrt{M}}(e^{-i\omega_\nu \tau_1}, e^{-i\omega_\nu \tau_2}, \ldots e^{-i\omega_\nu \tau_M})$ the first one of Equations (36) can be written as $\varphi_{\gamma,\nu}^* = \vec{v}_\nu^* \cdot \vec{\varphi}^*$. Introducing $\lambda = e^{2i\frac{\mu-\nu}{M}\pi}$ one has, using $\omega_\nu = (2\nu+1)\pi/\hbar\beta$ and $\tau_k = \hbar\beta k/M$,

$$\vec{v}_\nu^* \cdot \vec{v}_\mu = \frac{1}{M} \sum_{k=1}^{M} e^{i(\omega_\mu - \omega_\nu)\tau_k} = \frac{1}{M} \sum_{k=1}^{M} \lambda^k = \begin{cases} 1 & \text{for } \mu - \nu = nM, \\ \lambda \frac{\lambda^M - 1}{\lambda - 1} = 0 & \text{for } \mu - \nu \neq nM. \end{cases} \tag{63}$$

with integer n. The M vectors $\vec{v}_\nu$ with $-M/2 + 1 \leq \nu \leq M/2$ therefore are orthonormal. The matrix T, which transforms the M variables φ_k^* into the M variables, $\vec{\varphi}_\nu^* = T\, \vec{\varphi}_k^*$, therefore has the $\vec{v}_\mu$ as its lines, whence $T^+ = T^{-1}$ and the transformation is unitary. Eq. (37) follows immediately.

(a)   (b)   (c)
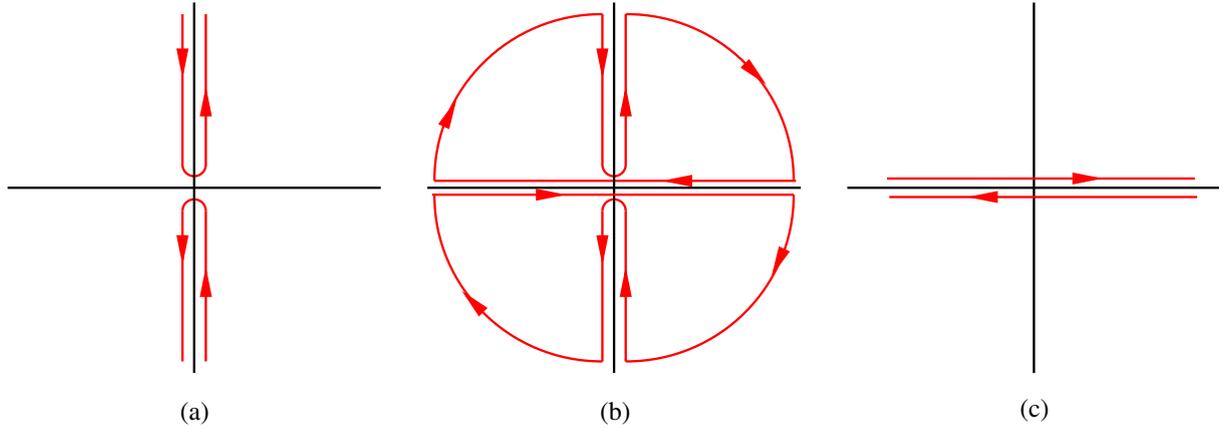
Fig. 5: *Integration contours for sums over Matsubara frequencies.*

Appendix C

In this Appendix we want to highlight the importance of the factors of $e^{i\omega_\lambda \varepsilon}$ and discuss the evaluation of sums of the form

$$S = -\lim_{\varepsilon \to 0} \frac{1}{\beta} \sum_\lambda e^{i\omega_\lambda \varepsilon} \, g(i\omega_\lambda) \,,$$

whereby we assume that $g(z)$ is an analytic function except for the real axis. Since $i\hbar\beta\omega_\lambda = (2\lambda+1)i\pi$ the Fermi function $f(z) = (e^{\beta\hbar z} + 1)^{-1}$ has poles at the Matsubara frequencies $i\omega_\lambda$. Straightforward calculation shows that for $z = i\omega_\lambda + \zeta$ we have $f(z) = -1/\beta\hbar\zeta$ so that the residuum is $-1/\beta\hbar$. Invoking the theorem of residues we can rewrite

$$S = \lim_{\varepsilon \to 0} \frac{\hbar}{2\pi i} \oint_{\mathcal{C}} dz \, f(z) \, e^{\varepsilon z} \, g(z) \,,$$

where $\mathcal{C}$ encircles the imaginary axis in counterclockwise fashion, see figure 5(a). Next we note that the integrals along the two clover-shaped contours in figure 5(b) are zero, *provided* the integrand is analytic in the interior of the two curves. Since the Fermi function has all of its poles along the imaginary axis, which is outside of the curves in figure 5(b), and since we assumed that $g(z)$ is analytic except on the real axis this is certainly true. The Fermi function $f(z)$ guarantees that the contribution from the semicircle with $\Re(z) > 0$ vanishes, whereas the factor $e^{z\varepsilon}$ does the same for the semicircle with $\Re(z) < 0$, see the discussion in Appendix A. It follows that the integral along the contour $\mathcal{C}$ in figure 5(a) is equal to that along the contour $\mathcal{C}'$ in figure 5(c) (note the inverted direction of the curves in figure 5(c) as compared to figure 5(b)!). We could thus convert the sum over Matsubara frequencies to an integral over a contour which runs counterclockwise around the real axis, which can again be evaluated using the theorem of residues whereby we pick up contributions from the singularities of $g(z)$. In particular, the limit $T \to 0$ can be taken without problem for this expression. Notice that the seemingly unimportant factor of $e^{i\omega_\lambda \varepsilon}$ was instrumental for this construction because it was only due to this factor that the arc with $\Re(z) < 0$ could be neglected. This is the reason why these factors have to be followed carefully in all calculations.

Appendix D

Here we prove the identity

$$\frac{\partial \ln \det A}{\partial A_{ij}} = A_{ji}^{-1}$$

We use Laplace's formula and expand $\det A$ in terms of minors

$$\det A = \sum_{l=1,n} (-1)^{i+l} \, A_{il} M_{il}$$

Since none of the minors M_{il} contains the element A_{ij} we find

$$\frac{\partial \ln \det A}{\partial A_{ij}} = \frac{(-1)^{i+j} M_{ij}}{\det A}$$

Next, the ith column of A^{-1} is the solution of the system of equations

$$Ac = E_i$$

where E_i is the ith column of the unit matrix. It has all elements equal to zero, except for the ith, which is one. We use Cramer's rule and find for the jth element of the ith column

$$A_{ji}^{-1} = \frac{\det \bar{A}_j}{\det A}$$

where $\bar{A}_j$ is the matrix where the jth column has been replaced by E_i. Now we use again Laplace's formula for $\det \bar{A}_j$ and obtain

$$A_{ji}^{-1} = \frac{(-1)^{i+j} M_{ij}}{\det A}$$

which proves the theorem.

As an application we assume that the matrix elements of A are functions of some parameter α. Then we find

$$\frac{\partial \ln \det A}{\partial \alpha} = \sum_{i,j} \frac{\partial \ln \det A}{\partial A_{ij}} \frac{\partial A_{ij}}{\partial \alpha} = \sum_{i,j} A_{ji}^{-1} \frac{\partial A_{ij}}{\partial \alpha} = \mathrm{Tr}\, A^{-1} \frac{\partial A}{\partial \alpha} \,.$$

References

[1] J.M. Luttinger and J.C. Ward, Phys. Rev. **118**, 1417 (1960)

[2] J.M. Luttinger, Phys. Rev. **119**, 1153 (1960)

[3] G. Baym and L.P. Kadanoff, Phys. Rev. **124**, 287 (1961)

[4] G. Baym, Phys. Rev. **127**, 1391 (1962)

[5] M. Potthoff, Condens. Mat. Phys. **9**, 557 (2006)

[6] M. Potthoff in A. Avella and F. Mancini (eds.): *Theoretical Methods for
     Strongly Correlated Systems*, (Springer, 2011); see also preprint arXiv:11082183

[7] A.A. Abrikosov, L.P. Gorkov, and I.E. Dzyaloshinksi:
     Methods of Quantum Field Theory in Statistical Physics
     (Prentice-Hall, New Jersey 1964)

[8] A.L. Fetter and J.D. Walecka: *Quantum Theory of Many-Particle Systems*
     (McGraw-Hill, San Francisco, 1971)

[9] J.W. Negele and H. Orland: *Quantum Many-Particle Systems*
     (Addison-Wesley, Redwood, 1988)

[10] G. Baym and N.D. Mermin, J. Math. Phys. **2**,232 (1961)

[11] I. Dzyaloshinskii, Phys. Rev. B **68**, 085113 (2003)

[12] J.M. Luttinger, Phys. Rev. **121**, 942 (1961)

[13] A. Georges, G. Kotliar, W. Krauth, and M.J. Rozenberg, Rev. Mod. Phys. **68**, 13 (1996)

[14] M. Potthoff, Eur. Phys. J. B**36**, 335 (2003)

[15] E. Lange, Mod. Phys. Lett.B **12**, 915 (1998)

[16] R. Bulla, T.A. Costi, and D. Vollhardt, Phys. Rev. B **64** 045103 (2001)

[17] J. Joo and V. Oudovenko, Phys. Rev. B **64** 103102 (2001)

7 Green Functions in the Renormalized Many-Body Perturbation Theory

Václav Janiš

Institute of Physics

The Czech Academy of Sciences

Na Slovance 1999/2, CZ-182 21 Praha

Contents

1   Renormalization of the many-body perturbation theory

The major objective of theoretical physics is to simplify the complexity of Nature in that one breaks the whole into separate individual phenomena, or situations for which one identifies the relevant degrees of freedom that decide about the observed specific behavior. At the end, the theory provides models that should explain, mathematically formalize, and quantify the observed phenomena. The relevance of each model is measured not only by its ability to reproduce the experimental data. The strength of theoretical models lies in their predictive power of the behavior in yet unexplored situations. The basic idea behind simplified models with only a few degrees of freedom is that one will be able to solve them without further approximations. It is, however, a rare case and mostly only in specific, little realistic limiting situations. That is why perturbation methods are ubiquitous in theoretical physics.

Quantum dynamics arises from our inability to measure simultaneously the precise values of the fundamental variables. They are particle coordinate and velocity (momentum) in quantum mechanics. The observables are then represented by self-adjoint operators in a Hilbert space. The operators of non-simultaneously measurable quantities do not commute. The lack of exact solutions of quantum models lies in our inability to find the exact spectrum of the generating Hamiltonian, being a sum of non-commuting operators. That is why time-dependent perturbation theory was introduced in single-particle quantum mechanics, in particular for the particle interacting with external fields [1].

Many-body quantum systems add to non-commutativity of the particle coordinates and momenta also indistinguishability of identical particles and non-commutativity of the kinetic energy and the interaction in the Hamilton operator. This forces us to introduce the Fock Hilbert space and the occupation-number representation with creation and annihilation operators. Finding the exact dynamics of the quantum many-body models is generally beyond our reach. The only reliable technique to obtain quantitative results then is the perturbation theory with the many-body Green functions [2].

Green functions were introduced in mathematics as a means to solve differential equations with boundary conditions [3]. The most attractive feature of Green functions are their analytic properties. The many-body Green functions are used in a slightly different context than in the solutions of differential equations. They solve exactly the unperturbed/noninteracting models with quadratic Hamiltonians, including boundary conditions, and enter as the fundamental ingredients in the perturbation expansion in powers of the non-quadratic particle interaction. The importance of Green functions was emphasized early during the creation of the relativistic quantum field theory [4–7]. The way towards the application of the many-body Green functions also in non-relativistic theories were set in Refs. [8, 9] and extensively discussed in Ref. [2]. The important part of the application of perturbation theory is its renormalization, inevitable in relativistic theories, being the only tool to extend the perturbation expansion from weak to strong coupling in many-body statistical models. The canonical way of performing renormalizations of the many-body perturbation theory systematically in terms of the one-particle Green function was proposed by Baym and Kadanoff [10, 11].

The Baym-Kadanoff approach addresses explicitly only the renormalization of the one-particle Green function. Explicit renormalization of the two-particle Green function was introduced in Refs. [12–15]. The latter approach was later extended to the so-called parquet construction with an explicit two-particle self-consistency [16–18]. The one- and two-particle Green functions cannot be renormalized independently. One has to obey two relations between them in order to keep the approximations conserving. One relation is established by the dynamical Schwinger-Dyson equation, the other is the Ward identity [11]. The generic problem of renormalized many-body perturbation theory is the inability to obey simultaneously the two relations between one and two-particle Green functions in approximate solutions [19].

The first level of the renormalization of many-body perturbation theory are mean-field-like approximations with a set of static parameters to be determined self-consistently from an approximate thermodynamic potential. Such approximations are semiclassical with classical order-parameters, and Green functions are mostly not needed. The only way to include the true quantum dynamical effects into the renormalizations is to employ Green functions and to utilize their analytic properties to keep the approximations consistent and free of spurious and unphysical behavior. I will review the way renormalizations of the many-body perturbation theory can be introduced in models of interacting fermions and show how to use the Green functions to derive consistent approximations, even having a mean-field character, in the strong-coupling regime.

2   Generic models of interacting electrons and quantum perturbations

There are a few generic models of strongly interacting electrons that offer exact solutions in specific limits. They may be used for testing the effectiveness and reliability of renormalized perturbation theory. The paradigm for strongly correlated electrons is the single-band Hubbard model, the tight-binding Hamiltonian of which can be represented in second quantization as

$$\widehat{H}_H = \sum_{\mathbf{k},\sigma} \varepsilon(\mathbf{k})\, c^\dagger_{\mathbf{k}\sigma} c_{\mathbf{k}\sigma} + U \sum_i \widehat{n}_{i\uparrow}\widehat{n}_{i\downarrow}\,, \tag{1}$$

where $\varepsilon(\mathbf{k})$ is the dispersion relation, $\widehat{n}_{i\sigma}$ is the operator of the density of particles with spin σ on lattice site $\mathbf{R}_i$, and U is the electron repulsion due to the screened Coulomb potential. This model can be solved exactly in the extreme limits of one and infinite dimensions. The exact solution in the former case can be reached at zero temperature via an algebraic Bethe ansatz [20] while the full solution in the latter limit can be obtained only numerically [21].

There is a simpler version of the Hubbard model that offers an analytic solution in infinite dimensions. It is the spinless Falicov-Kimball model

$$\widehat{H}_{FK} = -t \sum_{\langle ij \rangle} c^\dagger_i c_j + \sum_i \varepsilon_i f^\dagger_i f_i + U \sum_i c^\dagger_i c_i f^\dagger_i f_i\,, \tag{2}$$

where ε_i are the atomic levels of the immobile electrons, and $\langle ij \rangle$ indicates nearest neighbors. Unlike the Hubbard model, the Falicov-Kimball model does not describe a Fermi liquid. That is

why this model is rather limited in its applications and less suitable for testing the renormalized perturbation theory of correlated electrons [22].

The third generic model of interacting electrons with an exact solution is the single-impurity Anderson model (SIAM) for the formation of local magnetic moments. Its Hamiltonian reads

$$\widehat{H}_{SIAM} = -t \sum_{\langle ij \rangle \sigma} c_{i\sigma}^{\dagger} c_{j\sigma} + E_f \sum_{\sigma} f_{\sigma}^{\dagger} f_{\sigma} + U f_{\uparrow}^{\dagger} f_{\uparrow} f_{\downarrow}^{\dagger} f_{\downarrow} + \sum_{i,\sigma} \left(V_i \, c_{i\sigma}^{\dagger} f_{\sigma} + V_i^* \, f_{\sigma}^{\dagger} c_{i\sigma} \right), \quad (3)$$

where E_f is the impurity energy level and V_i is the hybridization between the local impurity f and the conduction electrons c_i. Its solution serves as the input for the self-consistency equation of the Hubbard model in infinite dimensions. It offers a local model with strong dynamical quantum fluctuations leading, at half filling, to quantum critical behavior and the strong coupling Kondo effect [23, 24].

All three Hamiltonians represent genuine many-body systems where the operator of the local particle interaction does not commute with the non-local operator of the kinetic energy, or the hybridization term of the SIAM. Quantum fluctuations are important and must be appropriately treated in the perturbation theory. Only sufficient renormalizations can allow to continue reliably the perturbation expansion from weak to strong coupling. Although we are interested in equilibrium properties of the many-body models we must introduce perturbations driving the systems out of equilibrium to explore all possible changes of the equilibrium state when crossing from weak to strong coupling. Most interestingly, the models may display quantum critical behavior at low temperatures driven by cooperative quantum fluctuations. One has to choose the perturbing forces as general as possible not to miss any, sometimes unexpected, quantum phase transition.

The fundamental quantity to be determined from the perturbation theory is the grand potential Ω of the systems with appropriate external excitations represented by a time-dependent Hamiltonian $\widehat{H}_{ext}$. The perturbation theory treats the non-quadratic part of the Hamiltonian $\widehat{H}_I$ and the external non-equilibrium term $\widehat{H}_{ext}$ as a perturbation of the exactly solved quadratic part $\widehat{H}_0$, a set of harmonic oscillators. The generating functional of the perturbation expansion is

$$\Omega[H_{ext}] = -\beta^{-1} \log \text{Tr} \exp \left(-\beta \Big(\widehat{H}_0 - \mu \widehat{N} + \underbrace{\widehat{H}_I + \widehat{H}_{ext}}_{\text{perturbation}} \Big) \right), \quad (4)$$

where $\widehat{N}$ is the number operator and $\beta = 1/k_B T$ the inverse temperature. The external part of the total perturbation is quadratic but it generally contains an arbitrary combination of the creation and annihilation operators. There are four general quadratic terms for spin-½ fermions. We denote the nonlocal external field perturbing the densities of particles with spin σ by $\eta_{\sigma}^{\parallel}(1, 2)$. We used a short-hand notation for the space-time and spin variables $l = (\mathbf{R}_l, \tau_l, \sigma_l)$. This field generates longitudinal spin fluctuations. Analogously we denote $\eta^{\perp}(1, 2)$ the field that generates transversal spin fluctuations. We further introduce fields $\xi^{\perp}(1, 2)$ and $\xi_{\sigma}^{\parallel}(1, 2)$ generating transversal and longitudinal charge fluctuations, respectively. Fields $\eta^{\perp}$, $\xi^{\perp}$, and $\xi_{\sigma}^{\parallel}$ are complex while $\eta_{\sigma}^{\parallel}$ is not. The complex character of the excitation field indicates that the perturbation breaks either conservation of spin, charge or both. Complex fields are not measurable but when

the linear response to them is broken they generate a quantum long-range order. The most general quantum perturbation can then be represented as

$$\widehat{H}_{ext} = \int d1 d2 \Bigg[\sum_{\sigma} \eta_{\sigma}^{\|}(1,2) c_{\sigma}^{\dagger}(1) c_{\sigma}(2) \qquad \text{(conserves charge\&spin)} \quad (5)$$

$$+ \left[\eta^{\perp}(1,2) c_{\uparrow}^{\dagger}(1) c_{\downarrow}(2) + \bar{\eta}^{\perp}(1,2) c_{\downarrow}^{\dagger}(2) c_{\uparrow}(1) \right] \qquad \text{(conserves charge)}$$

$$+ \left[\bar{\xi}^{\perp}(1,2) c_{\uparrow}(1) c_{\downarrow}(2) + \xi^{\perp}(1,2) c_{\downarrow}^{\dagger}(2) c_{\uparrow}^{\dagger}(1) \right] \qquad \text{(conserves spin)}$$

$$+ \sum_{\sigma} \left[\bar{\xi}_{\sigma}^{\|}(1,2) c_{\sigma}(1) c_{\sigma}(2) + \xi_{\sigma}^{\|}(1,2) c_{\sigma}^{\dagger}(1) c_{\sigma}^{\dagger}(2) \right] \Bigg] \quad \text{(changes charge\&spin)}$$

where the bar denotes complex conjugation. The possible long-range orders generated by the perturbations with fields $\eta_{\sigma}^{\|}$, $\eta^{\perp}$, are longitudinal and transversal magnetic order, and singlet and triplet superconductivity for fields $\xi^{\perp}$, and $\xi_{\sigma}^{\|}$, respectively [25].

3 Static renormalizations

Exactly solvable statistical models are mostly those with quadratic Hamiltonians. Perturbation theory uses them as unperturbed models and expands thermodynamic quantities in powers of the non-quadratic interacting Hamiltonians. The first step to improve upon such a bare perturbation expansion is to introduce a renormalization of the parameters characterizing the unperturbed system. This is the idea of mean-field theories. This static renormalization optimizes the initial state of the perturbation expansion.

3.1 Variational mean-field theories

There are several ways of deriving mean-field approximations. The most advanced construction of comprehensive mean-field theories is presently the limit to infinite spatial dimensions of a hypercubic lattice with an appropriate rescaling of the off-diagonal (nonlocal) elements in the model Hamiltonian [26]. This construction leads to a dynamical mean-field theory (DMFT) of quantum many-body models [21]. This limit is not analytically solvable for the Hubbard model and, hence, cannot be used as a renormalized starting point of the perturbation theory. The original idea behind the classical mean-field approximations is to create optimal upper or lower bounds on the equilibrium thermodynamic potential by renormalizing the parameters of the exactly solvable unperturbed Hamiltonian.

We split the total Hamiltonian into an exactly solvable part $\widehat{H}_0$ and a correction $\Delta\widehat{H}$

$$\widehat{H} = \widehat{H}_0 + \Delta\widehat{H} \qquad (6)$$

and use the Gibbs-Bogoliubov inequality for the grand potentials

$$\Omega\big[\widehat{H}\big] \leq \Omega\big[\widehat{H}_0\big] + \big\langle \Delta\widehat{H} \big\rangle_0. \qquad (7)$$

Here $\langle\Delta\widehat{H}\rangle_0$ is the statistical average of the correcting term in the unperturbed system. A mean-field approximation is obtained by optimizing the upper bound with spin-dependent energies E_σ renormalizing the chemical potential μ and the external magnetic field h. That is, we choose

$$\widehat{H}_0 = \sum_{\mathbf{k},\sigma} \varepsilon(\mathbf{k}) c^\dagger_{\mathbf{k}\sigma} c_{\mathbf{k}\sigma} + \sum_{\mathbf{i}\sigma} (E_\sigma - \mu - \sigma h)\, \widehat{n}_{\mathbf{i}\sigma}$$

and the correction

$$\langle\Delta\widehat{H}\rangle_0/N = U n_\uparrow n_\downarrow - \sum_\sigma E_\sigma n_\sigma \,,$$

where $n_\sigma = N^{-1} \sum_{\mathbf{i}} \langle\widehat{n}_{\mathbf{i}\sigma}\rangle_0$. The lowest upper bound is then produced by the Hartree mean-field solution $E_\sigma = U n_{-\sigma}$.

There is also a variational way for constructing a lower bound on the equilibrium grand potential [27]: We decompose the total Hamiltonian by using positive normalized parameters $\lambda_\alpha \geq 0$ and $\sum_\alpha \lambda_\alpha = 1$,

$$\widehat{H} = \sum_\alpha \lambda_\alpha \widehat{H}_\alpha \,. \tag{8}$$

Using the convexity property of the grand potential we obtain an inequality

$$\sum_\alpha \lambda_\alpha \Omega\big[\widehat{H}_\alpha\big] \leq \Omega\big[\widehat{H}\big]. \tag{9}$$

The grand potential of the Falicov-Kimball model, Eq. (2), can be expressed via analytic functions exactly in infinite spatial dimensions [28]. We can then use the following decomposition of the Hubbard Hamiltonian with two parameters λ_α, where $\alpha = 1, 2$:

$$\lambda_\alpha \widehat{H}_\alpha = \sum_{\mathbf{k}} \varepsilon(\mathbf{k}) c^\dagger_{\mathbf{k}\alpha} c_{\mathbf{k}\alpha} + \lambda_\alpha \sum_{\mathbf{i}\sigma} \big(E_\sigma - \mu_\sigma\big) \widehat{n}_{\mathbf{i}\sigma} + U \lambda_\alpha \sum_{\mathbf{i}} \widehat{n}_{\mathbf{i}\uparrow} \widehat{n}_{\mathbf{i}\downarrow} \,,$$

where $\mu_\sigma = \mu + \sigma h$. The grand potential of the component Hamiltonians is known analytically in the DMFT. We can hence maximize the lower bound on the Hubbard model by finding the optimal decomposition parameters λ_α. The derived mean-field approximation of the maximal lower bound is a thermodynamically consistent extension of the Hubbard III approximation [29].

3.2 Fermi liquid

Static mean-field approximations are short of an important feature of correlated electrons in metals. It is the concept of quasiparticles with a finite lifetime. They are generated by dynamical correlations of the low-lying excitations of the ground state. Quasiparticles were introduced by Landau in his theory of a Fermi liquid [30]. The Fermi liquid was initially presented as a phenomenological theory, but it had a profound impact on all theories of interacting fermions. It qualitatively correctly describes the behavior of the low-lying fermionic excitations if the actual interaction can be reached adiabatically from zero (Fermi gas) without passing through a phase transition or, equivalently, a divergence in the perturbation theory. Consequently, the

Fermi-liquid theory reduces the impact of particle interactions to only a renormalization of the parameters of the Fermi gas.

The fundamental assumption of the Landau Fermi-liquid theory is the existence of an energy functional depending only on squares of the instantaneous densities of the low-lying excitations $\delta n_{\mathbf{k},\sigma}(t)$ caused by a general weak external potential $V_{\mathbf{k}\sigma}$. The macroscopic generated averaged energy functional is

$$E\left[\delta n_{\mathbf{k},\sigma}\right] = \sum_{\mathbf{k},\sigma}\left(\varepsilon(\mathbf{k})+V_{\mathbf{k}\sigma}\right)\overline{\delta n_{\mathbf{k},\sigma}(t)} + \frac{1}{2V}\sum_{\mathbf{k}\mathbf{k}',\sigma\sigma'}f(\mathbf{k},\mathbf{k}';\sigma,\sigma')\,\overline{\delta n_{\mathbf{k},\sigma}(t)\,\delta n_{\mathbf{k}',\sigma'}(t)}\,,\quad(10)$$

where the bar denotes averaging over the microscopic time scales t. The bare-particle interaction of the model Hamiltonian was replaces by the Landau scattering function $f(\mathbf{k},\mathbf{k}';\sigma,\sigma')$ standing for the screened dynamical interaction of quasiparticle densities of the low-lying excitations. It is assumed as the input of the phenomenological Fermi liquid theory.

Due to the ergodic theorem the time averaging can be replaced by a statistical one. And since the energy functional should depend at most on squares of the densities of the excited states, the Hartree decoupling for the product of time-dependent densities of the excitations holds

$$\overline{\delta n_{\mathbf{k},\sigma}(t)\,\delta n_{\mathbf{k}',\sigma'}(t)} = \langle\delta n_{\mathbf{k},\sigma}\rangle\,\langle\delta n_{\mathbf{k}',\sigma'}\rangle\,.\qquad(11)$$

The elementary excitations correspond to the eigenstates of the Fermi gas and hence the statistical average has the fermionic form

$$\langle\delta n_{\mathbf{k},\sigma}\rangle = \frac{1}{\exp\left(-\beta(\varepsilon_{\mathbf{k}}+V_{\mathbf{k}\sigma}+U_{\mathbf{k},\sigma})\right)+1} - \Theta(k_F-k)\,,\qquad(12)$$

with the Fermi momentum k_F and an effective potential

$$U_{\mathbf{k},\sigma} = \frac{1}{V}\sum_{\mathbf{k}',\sigma'}f(\mathbf{k},\mathbf{k}';\sigma,\sigma')\,\langle\delta n_{\mathbf{k}',\sigma'}\rangle\,.\qquad(13)$$

The statistical averaging was chosen such that the density of the particle-like excitations ($k>k_F$) is positive while the density of the hole-like excitations ($k<k_F$) is negative. The low-lying excitations are affected only by the Landau scattering function at the Fermi energy E_F and $|k|\approx k_F$. That is, the only relevant physical scale in this theory is the Fermi energy. The Landau scattering function can either be determined from experimental data or can be calculated from a microscopic theory. At the end, the Fermi liquid is a Fermi gas with renormalized thermodynamic quantities [31]. In this sense it is a semi-classical theory with only averaged quantum dynamical fluctuations.

4   Dynamical corrections and Green functions

So far we introduced only static renormalizations of the equilibrium thermodynamic quantities. The genuine quantum fluctuations due to the non-commutativity of the kinetic-energy and particle-interaction operators can be obtained only from a fully dynamical perturbation theory. The only way to keep all the necessary information from the quantum fluctuations is to use the Matsubara formalism and many-body Green functions.

4.1   Green functions, Matsubara formalism, and analytic continuation

The dispersion relation between energy and momentum from the model Hamiltonian is generally obeyed only at the energy (mass) shell. Since we are unable to find the spectrum of the full Hamiltonian we have to go off the mass shell and to introduce time-dependent excitations for which the energy is detached from the momentum. We introduce an imaginary time $\tau \in (0, \beta)$ and let the creation and annihilation operators propagate with the unperturbed free-electron Hamiltonian $\widehat{H}_0 = \sum_{\mathbf{k}\sigma} \left(\varepsilon(\mathbf{k}) - \mu - \sigma h \right) c^{\dagger}_{\mathbf{k}\sigma} c_{\mathbf{k}\sigma}$, where μ is the chemical potential and h the external magnetic field. We define $c_{\mathbf{k}\sigma}(\tau) = \mathrm{e}^{\tau \widehat{H}_0} c_{\mathbf{k}\sigma} \, \mathrm{e}^{-\tau \widehat{H}_0}$ and analogously the time-dependent hermitian-conjugate creation operator, $c^{\dagger}_{\mathbf{k}\sigma}(\tau) = \mathrm{e}^{\tau \widehat{H}_0} c^{\dagger}_{\mathbf{k}\sigma} \, \mathrm{e}^{-\tau \widehat{H}_0}$. Notice that $c^{\dagger}_{\mathbf{k}\sigma}(\tau) \neq c_{\mathbf{k}\sigma}(\tau)^{\dagger} = c^{\dagger}_{\mathbf{k}\sigma}(-\tau)$. Moving the creation and annihilation operators off the mass shell we can introduce Green functions as time-ordered moments of the density-matrix operator

$$G_{(n)}(1, \ldots, n, \bar{n}, \ldots, \bar{1}) = \frac{(-1)^n}{\mathscr{Z} \, \hbar^n} \left\langle \mathrm{Tr}_0 \, \mathcal{T} c(1) \cdots c(n) \, c^{\dagger}(\bar{n}) \cdots c^{\dagger}(\bar{1}) \, \mathrm{e}^{-\int_0^{\beta} d\tau \, \widehat{H}_I(\tau)} \right\rangle_{av} \tag{14}$$

where we denoted $\mathrm{Tr}_0 \, \widehat{X} = \mathrm{Tr} \, \widehat{X} \mathrm{e}^{-\beta \widehat{H}_0}$ and $\mathscr{Z} = \mathrm{Tr}_0 \, \mathcal{T} \mathrm{e}^{-\int_0^{\beta} d\tau \, \widehat{H}_I(\tau)}$ is the partition sum.

The Matsubara formalism [32] uses the grand potential with a fixed chemical potential during the perturbation expansion of the functional of the partition sum. The propagation in imaginary time can then be diagonalized by a Fourier series of the periodic extensions of the interval $(-\beta, \beta)$ with imaginary even, bosonic $i\nu_m = 2m\pi i k_B T$, and odd, fermionic $i\omega_n = (2n+1)\pi i k_B T$, frequencies where n, m are integers.

We can represent the partition function, the generator of the perturbation expansion, via a functional integral over the anticommuting Grassmann variables ψ and ψ^* replacing the time ordering of the operators in the interaction picture by an unperturbed (inverse) Green function diagonal in momenta and Matsubara frequencies

$$\mathscr{Z} = \int \mathcal{D}\psi \mathcal{D}\psi^* \, \mathrm{e}^{\sum_{\mathbf{k}} \sum_{n\sigma} e^{i\omega_n 0^+} \psi^*_{n\sigma}(\mathbf{k}) \left(i\omega_n + \mu - \varepsilon(\mathbf{k}) \right) \psi_{n\sigma}(\mathbf{k}) - U \sum_i \int_0^{\beta} d\tau \, \widehat{n}^d_{\uparrow}(\tau, \mathbf{R}_i) \widehat{n}^d_{\downarrow}(\tau, \mathbf{R}_i)} . \tag{15}$$

The local interaction term is diagonal in imaginary time and does not commute with the unperturbed, kinetic part, which is diagonal in the momenta and Matsubara frequencies. The expansion of the partition sum in powers of the interaction strength is the gist of many-body perturbation theory.

The problem of the sums over Matsubara frequencies is that one must sometimes use the normalization factor $e^{i\omega_n 0^+}$ defining the proper limit to large frequency values. This can be avoided by analytic continuation from the discrete set of Matsubara frequencies on the imaginary axis to continuous real frequencies weighted by the appropriate statistical distribution. The sums over the fermionic and bosonic frequencies can be analytically continued to spectral integrals

as follows

$$\frac{1}{\beta} \sum_n F(i\omega_n) e^{i\omega_n 0^+} \rightarrow -\int_{-\infty}^{\infty} \frac{d\omega}{\pi} f(\omega) \Im F(\omega + i0) + \sum_i f(\zeta_i) \operatorname{Res}[F, \zeta_i] , \qquad (16a)$$

$$\frac{1}{\beta} \sum_m F(i\nu_m) e^{i\omega_m 0^+} \rightarrow P\int_{-\infty}^{\infty} \frac{d\omega}{\pi} b(\omega) \Im F(\omega + i0) - \sum_i b(\zeta_i) \operatorname{Res}[F, \zeta_i] , \qquad (16b)$$

where P stands for the principal value of the integral and we denoted $f(x) = 1/(e^{\beta x} + 1)$ and $b(x) = 1/(e^{\beta x} - 1)$ the Fermi and Bose distribution functions, respectively. Further on, ζ_i will be the poles of the complex function $F(z)$ outside the real axis. One can uniquely analytically continue from the set of the values at the Matsubara frequencies only if infinity is a point of analyticity of the continued function.

4.2   One-particle Green function – Schwinger and Dyson equations

The basic ingredient of the perturbation theory is the one-particle Green function. Its operator definition in the Heisenberg picture without splitting the full Hamiltonian into the unperturbed part and interaction reads

$$\widehat{G}(\tau, \sigma; \bar{\tau}, \bar{\sigma}) = -\frac{1}{\hbar} \operatorname{Tr} \widehat{\rho}_H \, \mathcal{T} \, \widehat{\psi}_\sigma(\tau) \, \widehat{\psi}_{\bar{\sigma}}^\dagger(\bar{\tau}) . \qquad (17)$$

We introduced the full density matrix $\widehat{\rho}_H = e^{-\beta \widehat{H}} / \operatorname{Tr} e^{-\beta \widehat{H}}$ while $\widehat{\psi}$ and $\widehat{\psi}^\dagger$ are the field operator and its hermitian conjugate. The time evolution is controlled by the full Hamiltonian, that is $\widehat{\psi}_\sigma(\tau) = e^{\tau \widehat{H}} \widehat{\psi}_\sigma e^{-\tau \widehat{H}}$. The time-dependent Green function from Eq. (17) is an operator (matrix) in the spatial coordinates. The number Green function then is $G(1, \bar{1}) = \langle \mathbf{R}_1 | \widehat{G}(\tau_1, \sigma_1; \tau_{\bar{1}}, \sigma_{\bar{1}}) | \mathbf{R}_{\bar{1}} \rangle$.

We cannot directly evaluate the Green functions in the Heisenberg picture since the full Hamiltonian is not diagonalizable. We separate the quadratic part of the total Hamiltonian from the non-quadratic one to go to Dirac's interaction picture with the time propagation controlled by the unperturbed Hamiltonian as in Eq. (14). The impact of the particle interaction U on the one-particle Green function can be expressed via a Schwinger integral equation [10]

$$\int d\bar{1} \, G^{(0)-1}(1, \bar{1}) \, G(\bar{1}, 1') = \delta(1 - 1') - \int d\bar{1} \, U(1 - \bar{1}) \, G_{(2)}(1\bar{1}^-, 1'\bar{1}^+) , \qquad (18)$$

where we introduced a two-particle Green function

$$G_{(2)}(1\bar{1}, 3\bar{3}) = \frac{1}{\hbar^2} \operatorname{Tr} \widehat{\rho} \, \mathcal{T} \, \widehat{\psi}_{\sigma_1}(\mathbf{R}_1, \tau_1) \widehat{\psi}_{\sigma_3}(\mathbf{R}_3, \tau_3) \widehat{\psi}_{\sigma_{\bar{3}}}^\dagger(\mathbf{R}_{\bar{3}}, \tau_{\bar{3}}) \widehat{\psi}_{\sigma_{\bar{1}}}^\dagger(\mathbf{R}_{\bar{1}}, \tau_{\bar{1}}) . \qquad (19)$$

The superscripts $\pm$ indicate whether we approach the equal-time limit of two time variables from above or below. The unperturbed Green function has an explicit algebraic expression in the Matsubara formalism

$$G_\sigma^{(0)}(\mathbf{k}, i\omega_n) = \frac{1}{i\omega_n + \mu + \sigma h - \varepsilon(\mathbf{k})} . \qquad (20)$$

The Schwinger equation does not determine the one-particle Green function in closed form. One also must know the impact of the interaction on the two-particle Green function. If we go on with the two-particle Green function as in the Schwinger equation, we obtain a relation between the two-particle and a three-particle Green function. This is generally not an effective way to evaluate Green functions. It is better to formally close the dynamical equations for the Green functions in the same particle space by introducing irreducible functions. The one-particle irreducible function is a self-energy $\Sigma(\bar{1}, 2)$. The self-energy is used to close the equation for the one-particle Green function within the one-particle representation space via a Dyson equation

$$G(1, \bar{1}) = G^{(0)}(1, \bar{1}) + \sum_{3, \bar{3}} G^{(0)}(1, \bar{3}) \, \Sigma(\bar{3}, 3) \, G(3, \bar{1}) \, . \tag{21}$$

Since the self-energy has the same dependence on the internal variables as the Green function, the Dyson equation becomes algebraic in momentum and frequency representation in equilibrium. The full equilibrium Green function in the Matsubara formalism then is

$$G_\sigma(\mathbf{k}, i\omega_n) = \frac{1}{i\omega_n + \mu + \sigma h - \varepsilon(\mathbf{k}) - \Sigma_\sigma(\mathbf{k}, i\omega_n)} \, . \tag{22}$$

The Dyson equation is only a formal relation determining the Green function from the self-energy. The latter must be obtained from perturbation theory.

4.3 Two-particle vertex – Bethe-Salpeter equations

Although we formally do not need the two-particle Green function to determine the one-particle one, the perturbation theory for the self-energy contains contributions from two-particle Green functions, or better two-particle vertices. The two-particle vertex Γ, that is, a one-particle irreducible two-particle function, is related to the two-particle Green function via a defining equation

$$G_{\sigma\sigma'}(k, k'; q) = G_\sigma(k) \, G_{\sigma'}(k+q) \Big(\delta(k-k') + \Gamma_{\sigma\sigma'}(k, k'; q) \, G_\sigma(k') \, G_{\sigma'}(k'+q) \Big). \tag{23}$$

We used a simplified, four-vector, notation of the dynamical variables, momenta and frequencies, the fermionic ones $k = (\mathbf{k}, i\omega_n)$ and the bosonic ones $q = (\mathbf{q}, i\nu_m)$. The two-particle functions obey conservation of momentum and energy and hence they contain only three independent dynamical variables. The attachment of the three variables to four corners of the two-particle vertex is graphically shown in Fig. 1, where we used the definition of the direct and a transposed two-particle vertices $\Gamma_{\sigma\sigma'}(k, k'; q)$ and $\Gamma^t_{\sigma\sigma'}(k, k'; q)$, respectively.

The two-particle vertex is only one-particle irreducible. We can introduce a two-particle irreducible vertex Λ in analogy with the self-energy in order to formally close the dynamical equation for the two-particle vertex. The two-particle analogue of the Dyson equation is a Bethe-Salpeter equation. It is an integral equation generally of the following form

$$\Gamma_{\sigma\sigma'}(k, k'; q) = \Lambda_{\sigma\sigma'}(k, k'; q) - \frac{1}{\beta N} \sum_{k''} \Lambda_{\sigma\sigma'}(k, k''; q) \, G_\sigma(k'') \, G_{\sigma'}(k''+q) \, \Gamma^t_{\sigma\sigma'}(k'', k'; q). \tag{24}$$
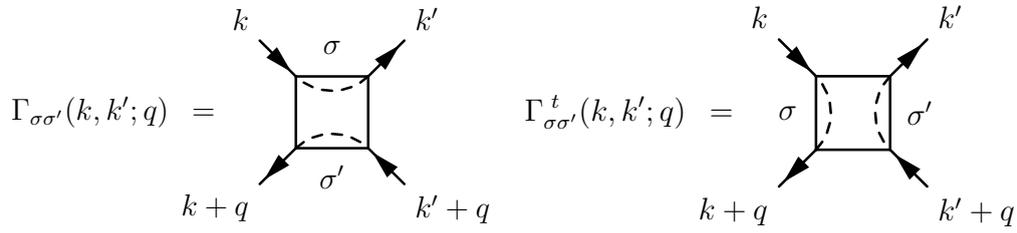
Fig. 1: *Assignment of the dynamical variables to the two-particle vertex as used in the text. The dashed line expresses the charge and spin conservation of the vertex, which means that the incoming line goes continuously through the vertex and goes out on the other side. The left figure stands for the direct propagation (left to right), the right one for the transposed one (up to down).*
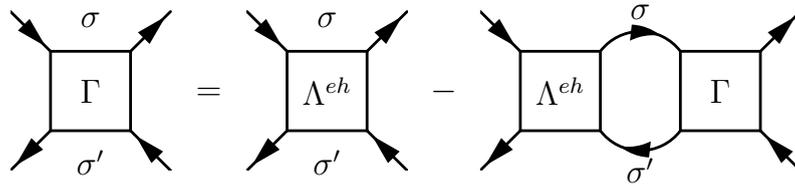

Fig. 2: *Bethe-Salpeter equation in the horizontal electron-hole channel. The direct and transposed vertices do not mix in this channel.*

Unlike the one-particle irreducibility, the two-particle irreducibility is not uniquely defined. The irreducibility is best demonstrated graphically with the solid oriented line standing for the one-particle Green function. The Bethe-Salpeter equation (24) is diagrammatically represented in Fig. 2. This equation is characterized by a simultaneous propagation of an electron of spin σ, the upper line, and a hole with spin σ', the lower line. The vertex is electron-hole, two-particle irreducible when cutting simultaneously electron and hole lines does not break the diagram into two disconnected parts. In this case they are horizontal electron and hole lines. Vertex Λ^{eh} is the electron-hole irreducible vertex.

There are more than one Bethe-Salpeter equations. Due to the orientation of the lines representing the charge propagation, cutting simultaneously parallel or antiparallel pairs of fermion lines is not the same operation and leads to a different result with a different conserving dynamical variable. Each of the two-particle irreducibilities can actually be characterized by a bosonic dynamical variable that is conserved, that is, it is the same whenever we perform the cut. It is $q = (\mathbf{q}, i\nu_m)$ in Eq. (24) for vertex $\Gamma_{\sigma\sigma'}(k, k'; q)$ with the attachment of the variables defined in Fig. 1.

Another option of the horizontal two-particle propagation is in connecting the vertices by parallel lines. The corresponding Bethe-Salpeter equation is graphically represented in Fig. 3. Unlike Eq. (24), the direct and transposed vertices are now mixed up. We can see that the transposed vertices are connected in the same way as the direct ones, only the upper and lower intercon-
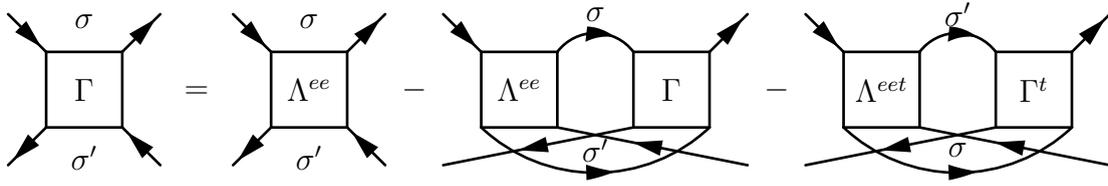
Fig. 3: *Graphical representation of the Bethe-Salpeter equation with the simultaneous propagation of two electrons. The direct and transposed vertices contribute with the same diagram with only interchanged spins in the intermediate propagation.*
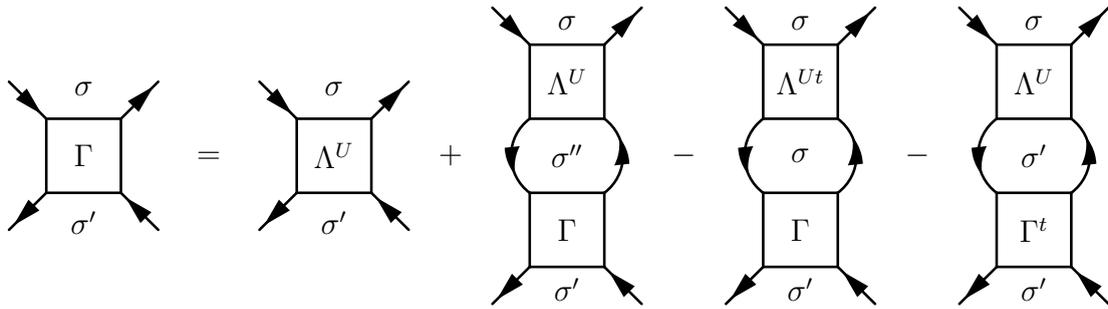
Fig. 4: *Bethe-Salpeter equation for the vertical (transposed) propagation of the electron and the hole with the same spin. The double primed variables are dummy integration variables. Notice, that vertex $\Gamma_{\uparrow\downarrow}$ is coupled to $\Gamma_{\uparrow\uparrow}$ and $\Gamma_{\downarrow\downarrow}$.*

necting propagators are interchanged. Checking the conservation laws in the vertices we easily find that the conserving dynamical variable in this channel is $Q = q+k'+k$. Vertex Λ^{ee} is electron-electron irreducible and differs from vertex Λ^{eh}, being irreducible in the electron-hole channel of Fig. 2.

There is yet another Bethe-Salpeter equation and another two-particle irreducibility. It is an electron-hole irreducibility propagating vertically (in the transposed sense) an electron and a hole carrying the same spin. It differs from the horizontal electron-hole propagation in Fig. 2 where the spins of the particle and the hole are independent. The graphical representation of such a Bethe-Salpeter equation is shown in Fig. 4. The double primed variable indicates that it is summed over. The direct and transposed vertices are mixed in this channel in a more complex way than in Fig. 3. The sign at each diagram in the graphical representation accounts for the anticommuting character of the one-particle operators. The conserving dynamical variable in this vertical channel is $\Delta k = k-k'$. The irreducible vertex Λ^{U} differs from both preceding vertices Λ^{eh} and Λ^{ee}.

The full two-particle vertex Γ is the same in all three Bethe-Salpeter equations. We thus have three inequivalent representations of the two-particle vertex via irreducible ones. Simultaneously we could construct three Bethe-Salpeter equations for the transposed vertex Γ^{t}. We obtain for the equal-spin vertex $\Gamma^{tot}_{\sigma\sigma}(k, k'; q) = \Gamma_{\sigma\sigma}(k, k'; q) + \Gamma^{t}_{\sigma\sigma}(k, k'; q)$ with the symmetry relation $\Gamma^{t}_{\sigma\sigma}(k, k'; q) = -\Gamma_{\sigma\sigma}(k, k+q; k'-k)$.

5 Baym-Kadanoff construction of the renormalized perturbation theory

Perturbation theory can be constructed independently for Green functions of any order. The one-particle Green function is an input to the perturbation theory for higher-order Green functions. It is only expected to obey the desired analytic properties. To keep the whole perturbation theory for all types of Green functions consistent and conserving we must relate the one-particle Green function with the higher-order ones. The renormalizations of the one-particle and higher-order Green functions cannot be done independently. The canonical way to construct renormalized and conserving approximations was proposed by Baym and Kadanoff [10, 11].

5.1 Generating Luttinger-Ward functional and irreducible functions

The basic element of the perturbation theory is the one-particle Green function. Its behavior is essential since it enters all physical quantities. It is hence the primary task of the perturbation theory to evaluate the one-particle Green function. It is sufficient to know the self-energy since the Dyson equation determines the Green function from the self-energy. The fundamental quantity of the perturbation theory becomes then the self-energy. The principal assumption of the Baym-Kadanoff approach is that the self-energy Σ can be expressed as a functional of the renormalized one-particle Green function G and the bare interaction U, $\Sigma[G, U]$.

The conserving character of the perturbation theory demands the existence of a generating functional from which we can determine all physical quantities via functional derivatives. The Baym-Kadanoff self-energy is obtained from the Luttinger-Ward generating functional $\Phi[G, U]$. The thermodynamic functional of the Baym-Kadanoff theory is the grand potential in the Matsubara formalism

$$\frac{\Omega[G, \Sigma]}{N} = \frac{-1}{\beta N} \sum_{\sigma} \sum_{\omega_n, \mathbf{k}} e^{i\omega_n 0^+} \Big(\ln \big[G_\sigma^{(0)\,-1}(\mathbf{k}, i\omega_n) - \Sigma_\sigma(\mathbf{k}, i\omega_n) \big] + G_\sigma(\mathbf{k}, i\omega_n) \Sigma_\sigma(\mathbf{k}, i\omega_n) \Big) + \Phi[G, U].$$

(25)

The equilibrium value of the functional $\Omega[G, \Sigma]$ is stationary with respect to variations of its functional variables, $\Sigma_\sigma(\mathbf{k}, i\omega_n), G_\sigma(\mathbf{k}, i\omega_n)$. Functional derivatives of the Luttinger-Ward functional with respect to Green function $G_\sigma(\mathbf{k}, i\omega_n)$ lead to the irreducible functions. The first and second derivatives lead to the self-energy and the two-particle irreducible vertex

$$\Sigma_\sigma(k) = \frac{\delta \Phi[G, U]}{\delta G_\sigma(k)}, \quad \Lambda_{\sigma\sigma'}(k, k'; q) = \frac{\delta \Sigma_\sigma(k, k')}{\delta G_{\sigma'}(k'+q, k+q)}.$$

(26)

Both, the self-energy and the Green function have two frequency-momentum variables in the second derivative since the variations drag the system out of equilibrium, where energy and momentum are not conserved. The Green function in the first derivative of the grand potential has only one variable since the derivatives determine the equilibrium values.

Stationarity of the grand potential $\Omega[G, \Sigma]$ with respect to variations of $\Sigma_\sigma(\mathbf{k}, i\omega_n)$ leads to the Dyson equation for the one-particle Green function $G_\sigma(\mathbf{k}, i\omega_n)$ renormalized by the self-energy
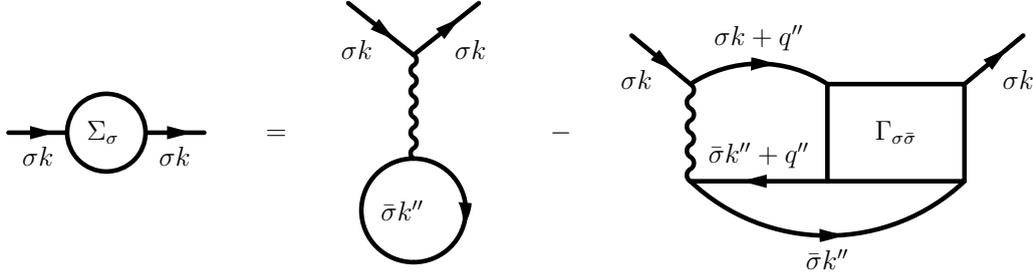
Fig. 5: *Graphical representation of the Schwinger-Dyson equation of the Hubbard model. The first term on the right-hand-side is the Hartree term and the second is the contribution from the two-particle vertex Γ. We kept the variables of one-particle propagators. The double-prime indices are summed (integrated) over. The bar denotes the inverse value.*

$\Sigma_\sigma(\mathbf{k}, i\omega_n)$ from Eq. (26). Notice that combinations of the independent variables in the second derivative of Eq. (26) lead to different two-particle irreducible vertices. It holds for all higher-order irreducible functions that they are not unique and depend on the way we use the internal variables out of equilibrium in the functional derivatives. The Baym-Kadanoff perturbation theory is hence fully one-particle renormalized. The higher-order Green and irreducible functions do not enter the generating functional and are not determined self-consistently.

The fundamental quantity of the Baym-Kadanoff construction is the Luttinger-Ward functional. Its existence is guaranteed by interchangeable second derivatives in Φ-derivable theories. The Luttinger-Ward functional can be formally obtained from the bare perturbation theory via a Legendre transformation by replacing the inverse of the bare propagator by the fully renormalized Green function

$$\Phi[G, U] = -k_B T \ln \mathcal{Z}\big[G^{(0)\,-1}, U\big] - \int d\,\bar{1} \left(G^{(0)\,-1}(1, \bar{1}) - G^{-1}(1, \bar{1}) \right) G(\bar{1}, 1'). \qquad (27)$$

It is, however, only a formal representation that does not help us find the functional dependence of the Luttinger-Ward functional on the full Green function. The Luttinger-Ward functional is not the primary object of interest in the Baym-Kadanoff construction. It is replaced by the self-energy, the contributions to which from the perturbation expansion are better controlled.

5.2 Schwinger-Dyson equation, Ward identity, and Schwinger field-theory

The contributions from perturbation theory to the self-energy functional can be regrouped so that one singles out the static Hartree contribution and represent the dynamical part via the two-particle vertex. Its graphical representation is plotted in Fig. 5. Mathematically it is represented for Hubbard-like models as

$$\Sigma_\sigma[G, U](k) = \frac{U}{\beta N} \sum_{k'} G_{\bar{\sigma}}(k') \left(1 - \frac{1}{\beta N} \sum_q \Gamma_{\sigma\bar{\sigma}}[G, U](k, k'; q)\, G_\sigma(k+q)\, G_{\bar{\sigma}}(k'+q) \right). \qquad (28)$$

The two-particle vertex $\Gamma[G, U]$ contains the unspecified dependence on the one-particle Green function that has to be also determined from the perturbation theory. Its form is, however, fully determined by the Luttinger-Ward functional $\Phi[G, U]$, if known.
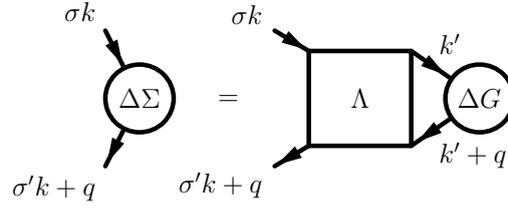
Fig. 6: *Ward identity matching a difference $\Delta\Sigma$ of the self-energy with the two-particle irreducible vertex Λ.*

The two-particle vertex can be represented by the two-particle irreducible vertices in the corresponding Bethe-Salpeter equations. The two-particle irreducible functions do not enter the Luttinger-Ward functional, but they are determined from its functional derivatives. The second functional derivative in Eq. (26) is a differential form of the Ward identity that is a sufficient microscopic condition that guarantees validity of the continuity equation of the macroscopic system. The differential Ward identity can be integrated to [33, 34]

$$\Sigma_\sigma(k+q) - \Sigma_\sigma(k) = \frac{1}{\beta N} \sum_{k'} \Lambda_{\sigma\sigma}^{eh}(k, k'; q) \Big(G_\sigma(k'+q) - G_\sigma(k') \Big) \tag{29}$$

and is plotted graphically in Fig. 6. If we use one of the Bethe-Salpeter equations to determine the full two-particle vertex and the differential form of the Ward identity for the two-particle irreducible vertex in the Schwinger-Dyson equation (28) we end up with an integro-differential functional equation for the self-energy

$$\Sigma = U \left\langle G - G \left(1 + \frac{\delta\Sigma}{\delta G} GG\star \right)^{-1} \frac{\delta\Sigma}{\delta G} GG \right\rangle, \tag{30}$$

where the star denotes the appropriate two-particle convolution from the Bethe-Salpeter equation and the angular brackets stand for the summation over the one-particle integration variables. Equation (30) represents the Schwinger field theory for the self-energy [5]. Unlike the Luttinger-Ward functional, the Schwinger field theory explicitly utilizes the exact properties of both the one and two-particle Green functions. The solution of Eq. (30) can be reached only iteratively via an expansion in the interaction strength, which is equivalent to the standard perturbation theory for the thermodynamic potential.

Although the Luttinger-Ward functional guarantees a conserving theory, none of the self-energy functionals $\Sigma[G, U]$ determined from the perturbation theory is fully conserving. A fully conserving theory should also obey conservation of the particle interaction. Namely, the strength of the particle interaction is fully generated by the electrons present in the system. This conservation is mathematically expressed as a sum rule [35]

$$\frac{\partial\Omega(U, \mu_{i\sigma})}{\partial U} = \sum_{\mathbf{i}} \left(\frac{\delta^2\Omega}{\delta\mu_{i\uparrow}\delta\mu_{i\downarrow}} + \frac{\delta\Omega}{\delta\mu_{i\uparrow}} \frac{\delta\Omega}{\delta\mu_{i\downarrow}} \right) = \sum_{i} \left(\frac{k_B T}{4} (\kappa_{ii} - \chi_{ii}) + n_{i\uparrow} n_{i\downarrow} \right), \tag{31}$$

where $\mu_{i\sigma}$ are the local spin-dependent chemical potentials, modifying the number operator $\widehat{N} = \sum_{i,\sigma} \mu_{i\sigma} c_{i\sigma}^\dagger c_{i\sigma}$, and κ_{ii} and χ_{ii} are local compressibility and susceptibility, respectively.

This identity expresses that the charges behind the Coulomb repulsion are entirely carried by the present electrons. The meaning of this identity is that mass and charge of the electrons cannot be separated.

The above sum rule can be extended to a gauge transformation by making interaction and mass of the electrons dynamical. The corresponding generalized Ward identity then reads

$$\underbrace{\frac{\delta\Phi[U,G]}{\delta U(\mathbf{q},i\nu_m)}}_{\text{Schwinger-Dyson}} = \underbrace{-\frac{1}{\beta N}\sum_{\mathbf{k},\omega_n}\frac{\delta G_\sigma(\mathbf{k}+\mathbf{q},i\omega_n+i\nu_m)}{\delta\mu_{-\sigma}(\mathbf{k},i\omega_n)}}_{\text{Ward}}, \tag{32}$$

where $U(\mathbf{q},i\nu_m)$ is a dynamical interaction and $\mu_\sigma(\mathbf{k},i\omega_n)$ is the spin-dependent local chemical potential in the frequency-momentum representation. Both sides of this dynamical equation should lead to the same two-particle correlation function. The left-hand side results in a correlation function obtained from the vertex of the Schwinger-Dyson equation, while the right-hand side determines a correlation function from the Bethe-Salpeter equation with the irreducible vertex satisfying the differential Ward identity of Eq. (26). The Ward identity (32) complies with the Schwinger-Dyson equation only if the irreducible vertex obeys an integro-differential functional equation [19]

$$\Lambda_{\sigma\bar{\sigma}}^{eh} = U - U\left(1 + G_\sigma G_{\bar{\sigma}}\Lambda_{\sigma\bar{\sigma}}^{eh}\star\right)^{-1}G_\sigma\left(\Lambda_{\sigma\bar{\sigma}}^{eh} + G_{\bar{\sigma}}\frac{\delta\Lambda_{\sigma\bar{\sigma}}^{eh}}{\delta G_{\bar{\sigma}}}\right)\left(1 + \star G_\sigma G_{\bar{\sigma}}\Lambda_{\sigma\bar{\sigma}}^{eh}\right)^{-1}\circ G_{\bar{\sigma}}, \tag{33}$$

where we denoted $\bar{\sigma} = -\sigma$. We recall that $\star$ denotes a summation over the intermediate variables during the simultaneous electron-hole propagation (antiparallel particle lines) and $\circ$ is a sum over the variables in the convolution from the propagation of two electrons (parallel lines). The two propagations differ in attaching the variables of the conected two-particle functions. Finding its solution is equivalent to solving the Schwinger field theory. Consequently, the Schwinger-Dyson equation (28) and the differential Ward identity from Eq. (26) can never be fully satisfied in approximate solutions in many-body perturbation theory.

5.3   Simple approximations: Hartree, RPA, FLEX

Having set the general rules for the renormalized perturbation theory, we proceed to use them to derive approximate solutions. The simplest is the Hartree approximation. It is a static mean-field theory that can be derived from the grand potential of Eq. (25) by choosing the simplest Luttinger-Ward functional

$$\Phi_{Hartree}[G,U] = \frac{U}{\beta N}\sum_{\mathbf{k},\omega_n} G_\uparrow(\mathbf{k},i\omega_n)\,G_\downarrow(\mathbf{k},i\omega_n)\,.$$

The resulting Hartree self-energy is

$$\Sigma_\sigma[G,U] = \frac{U}{\beta N}\sum_{\mathbf{k},\omega_n} e^{i\omega_n 0^+} G_{\bar{\sigma}}(\mathbf{k},i\omega_n) = Un_{\bar{\sigma}}\,, \tag{34}$$

where n_σ is the spin density. Consequently, $\Gamma_{\sigma\sigma'}[G, U] = 0$ in the Schwinger-Dyson equation (28). The resulting theory is not trivial because the thermodynamic properties are derived from the Ward identity and the irreducible two-particle vertex from Eq. (26), $\Lambda_{\uparrow\downarrow}[G, U] = U$. This irreducible vertex leads to a nontrivial full two-particle vertex

$$\Gamma_{\uparrow\downarrow}(\mathbf{q}, i\nu_m) = \frac{U}{1 + U\phi_{\uparrow\downarrow}(\mathbf{q}, i\nu_m)} \tag{35}$$

when we use it in the Bethe-Salpeter equation (24). We introduced a two-particle (electron-hole) bubble

$$\phi_{\uparrow\downarrow}(\mathbf{q}, i\nu_m) = \frac{1}{\beta N} \sum_{\mathbf{k}, \omega_n} G_\uparrow(\mathbf{k}+\mathbf{q}, i\omega_n+i\nu_m) \, G_\downarrow(\mathbf{k}, i\omega_n) \tag{36}$$

$$= -\frac{1}{N} \sum_{\mathbf{k}} \int_{-\infty}^{\infty} \frac{dx}{\pi} f(x) \Big(G(\mathbf{k}+\mathbf{q}, x+\omega_+) + G(\mathbf{k}-\mathbf{q}, x-\omega_+) \Big) \Im G(\mathbf{k}, x_+).$$

We denoted $\omega_\pm = \omega \pm i0^+$. Vertex $\Gamma_{\uparrow\downarrow}$ from Eq. (35) generates the thermodynamic behavior of the Hartree mean-field approximation. We can further use it in the Schwinger-Dyson equation to derive a new dynamical, spin-symmetric self-energy

$$\Sigma^{Sp}(\mathbf{k}, \omega_+) = \tag{37}$$
$$\frac{U}{N} \sum_{\mathbf{q}} P \int_{-\infty}^{\infty} \frac{dx}{\pi} \Bigg(b(x) G(\mathbf{k}+\mathbf{q}, \omega_++x) \Im \frac{1}{1+U\phi(\mathbf{q}, x_+)} - \frac{f(x+\omega)}{1+U\phi(\mathbf{q}, x_-)} \Im G(\mathbf{k}+\mathbf{q}, x+\omega_+) \Bigg),$$

where the Green functions are renormalized by the Hartree self-energy from Eq. (34). Only the linear term reproduces the Hartree self-energy. The self-energy $\Sigma^{Sp}(\mathbf{k}, \omega_+)$ from this equation represents the random-phase approximation (RPA). The RPA is not Φ-derivable, since the Green functions in the Schwinger-Dyson equation are not one-particle self-consistent. If we replace the Hartree self-energy with $\Sigma^{Sp}(\mathbf{k}, \omega_+)$ from Eq. (37) and the Hartree propagators in Eqs. (36) and on the right-hand side of Eq. (37) by the fully renormalized one

$$G(\mathbf{k}, \omega_+) = \frac{1}{\omega_++\mu-\varepsilon(\mathbf{k}) - \Sigma^{Sp}(\mathbf{k}, \omega_+)}, \tag{38}$$

the self-energy $\Sigma^{Sp}(\mathbf{k}, \omega_+)$ then generates a fluctuation-exchange approximation (FLEX). This approximation is fully one-particle self-consistent and its Luttinger-Ward functional reads [35]

$$\Phi_{FLEX}[G, U] = \frac{1}{N} \sum_{\mathbf{q}} P \int_{-\infty}^{\infty} \frac{d\omega}{\pi} b(\omega) \Im \Big(U\phi_{\uparrow\downarrow}(\mathbf{q}, \omega_+) - \ln\big(1+U\phi_{\uparrow\downarrow}(\mathbf{q}, \omega_+)\big) \Big). \tag{39}$$

These simple approximations derived within the Baym-Kadanoff construction and the generating Luttinger-Ward functional demonstrate the inability to obey simultaneously the Ward identity and the Schwinger-Dyson equation. They also demonstrate that the Ward identity is important for deriving thermodynamic properties averaged over Matsubara frequencies, while the Schwinger-Dyson equation is responsible for the dynamics and dynamical effects. The level of self-consistency in the Schwinger-Dyson equation may significantly determine the quality of

the approximations. The RPA shares the thermodynamic properties with the Hartree approximation and introduces the corresponding dynamical corrections in the spectral function. The FLEX theory changes both the thermodynamic and also dynamical properties of the Hartree approximation but the two are derived from different vertex functions and hence, inconsistent. An alternative approach should be chosen to reconcile the thermodynamic and spectral properties of self-consistent theories.

6 Two-particle approach and two-particle renormalizations

The Baym-Kadanoff approach leads directly to the Schwinger-Dyson equation determining the one-particle self-energy. It contains only one-particle functions and includes only one-particle renormalizations. The two-particle functions are derived indirectly. There are two vertex functions to a single self-energy. One is the vertex extracted from the Schwinger-Dyson equation and the other is constructed from a Bethe-Salpeter equation with the two-particle irreducible vertex related to the self-energy via the Ward identity. The two vertices are different in all approximate schemes and the critical behavior cannot be determined uniquely in such a construction.

The critical behavior connected with a phase transition is real and unique. That is why it must also be identified uniquely in theoretical models. It is then of utmost importance to have only a single two-particle vertex that would lead to the experimentally observed critical behavior. Moreover, a direct two-particle self-consistency is needed to suppress the unphysical and spurious critical behavior of weak-coupling approximations and to gain full control of the critical behavior. Since we cannot satisfy simultaneously the Ward identity and the Schwinger-Dyson equation we should accept the existence of two self-energies to a single two-particle vertex. The generating functional of such an approach cannot be a thermodynamic potential or the self-energy but rather the two-particle irreducible vertex from the singular Bethe-Salpeter equation of the studied critical behavior. It will be determined from the perturbation theory. One self-energy derived from this vertex will represent a thermodynamic order parameter and will obey the Ward identity. The other self-energy will be derived from the Schwinger-Dyson equation without changing the critical behavior of the two-particle vertex and the order parameter.

6.1 Symmetry-breaking field – odd and even functions

The basic characteristic quantity that distinguishes the two self-energies derived from a single two-particle vertex is the symmetry-breaking field in which the linear-response theory breaks down at the critical point. It is related to the order parameter in the low-temperature ordered phase via a Legendre transformation. We separate quantities with even and odd symmetry with respect to the reversal of this field. The order parameter is a typical quantity with odd symmetry. Let us assume, e. g., a symmetry-breaking field $\eta^\perp$ generating spin-flip processes. Its Legendre conjugate order parameter is

$$\Delta_{\uparrow\downarrow} = \frac{1}{N} \sum_i \left\langle c_\downarrow^\dagger(\mathbf{R}_i) c_\uparrow(\mathbf{R}_i) \right\rangle. \tag{40}$$

It describes the transverse magnetic order. Both the field and the order parameter are generally complex. It is sufficient to keep only the leading terms in the symmetry-breaking field to describe qualitatively correctly the critical behavior. Only the symmetric two-particle functions remain then relevant in the critical region. We hence define a symmetric two-particle propagator with a general external field η

$$
\begin{aligned}
\left[G(\mathbf{k}, i\omega_n)\, G(\mathbf{k+q}, i\omega_n+i\nu_m)\right]_\eta = \frac{1}{2}\Big(& G_\uparrow(\mathbf{k}, i\omega_n; +\eta)\, G_\downarrow(\mathbf{k+q}, i\omega_n+i\nu_m; +\eta) \\
+ & G_\downarrow(\mathbf{k}, i\omega_n; -\eta)\, G_\uparrow(\mathbf{k+q}, i\omega_n+i\nu_m; -\eta)\Big),
\end{aligned} \tag{41}
$$

where index η denotes the field with respect to which the symmetrization is performed.
The one-particle functions must be considered both with odd and even symmetries. The odd and even components of the one-particle Green function are

$$
\Delta_\eta G(\mathbf{k}, i\omega_n) = \frac{1}{2}\Big(G_\sigma(\mathbf{k}, i\omega_n; \eta) - G_{\bar\sigma}(\mathbf{k}, i\omega_n; -\eta)\Big), \tag{42a}
$$

$$
\bar{G}_\eta(\mathbf{k}, i\omega_n) = \frac{1}{2}\Big(G_\sigma(\mathbf{k}, i\omega_n; \eta) + G_{\bar\sigma}(\mathbf{k}, i\omega_n; -\eta)\Big). \tag{42b}
$$

The odd propagator will determine the thermodynamic order parameter while the even propagator will enter the Schwinger-Dyson equation to complete the description of the dynamical and spectral behavior of the chosen approximation without affecting its thermodynamic critical behavior.

6.2 Two-particle self-consistency and charge renormalization

The main qualitative difference between the two-particle approach and the Baym-Kadanoff construction is a two-particle self-consistency introduced via a renormalization of the two-particle irreducible vertices. We know that there are three two-particle irreducible vertices generating three independent Bethe-Salpeter equations for a single full two-particle vertex. A two-particle self-consistency in the perturbation theory for the two-particle irreducible vertices can be expressed functionally $\Lambda^\alpha_{ren}[G, \Gamma]$. It means that we replaced the bare interaction U by the full two-particle vertex Γ. The approximate functional dependence must be, however, chosen carefully to avoid multiple summations of diagrams. The two-particle self-consistency is introduced by an equation eliminating the full vertex in favor of the irreducible ones and the bare interaction

$$
F\left(\{\Lambda^\alpha_{ren}[G, \Gamma]\}_{\alpha=1}^l, U\right) = 0. \tag{43}
$$

Replacing the bare interaction of the Baym-Kadanoff perturbation theory with the two-particle vertex Γ in the two-particle approach, that is a replacement $\Lambda^\alpha[G, U] \to \Lambda^\alpha_{ren}[G, \Gamma]$, corresponds to a charge renormalization since the bare interaction is proportional to the square of the charge of the electrons.
Straightforward two-particle renormalizations are induced by the parquet approach and its simplifying variants introduced in the many-body perturbation theory by De Dominicis and Martin [14, 15]. A review of the recent developments of the parquet theory can be found in

Refs. [18, 36]. Its main idea is to use the ambiguity in the definition of the two-particle ir-reducibility. The reducible vertex in one scattering channel becomes irreducible in the others. If Λ^α is the irreducible vertex and $\mathcal{K}^\alpha$ its corresponding reducible counterpart in scattering channel α then the parquet equations can be written as

$$\Gamma = \Lambda^\alpha + \mathcal{K}^\alpha = \mathcal{I}_l + \sum_{\alpha=1}^{l} \mathcal{K}^\alpha, \tag{44}$$

where $\mathcal{I}_l$ is the fully irreducible vertex in the selected l scattering channels in the parquet theory. The full vertex Γ can be excluded from Eq. (44) and the parquet equations are closed for either the irreducible Λ^α or the reducible $\mathcal{K}^\alpha$ vertices. The input to the parquet equations are the one-particle propagators G_σ and the fully irreducible vertex $\mathcal{I}_l$. The latter is usually replaced by the bare interaction, $\mathcal{I}_l = U$. It is important to mention that the parquet decomposition does not hold always, but only when the overlap of the sets of the reducible diagrams from different channels is empty [37].

6.3   Order parameter and mass renormalization

The perturbation theory for the two-particle vertex functions is initially independent of the perturbation theory for the one-particle Green functions. The one-particle Green functions enter the perturbation theory for the two-particle functions only as an input with the expected analytic properties. One needs, however, to match the perturbation theories for the one and two-particle Green function in order to keep the approximations conserving. We already know that we cannot simultaneously obey all the exact relations between the one and two-particle functions. We must hence decide which relation in which situation is relevant and must not be neglected. Approximate fulfillment of the exact relations need not have a qualitative impact on the perturbative solutions. The critical regions of the phase transitions are, however, different. We must be very careful in breaking the relations between the one and two-particle functions there.

The first step was already made by separating the one-particle functions with odd and even symmetry with respect to the symmetry-breaking field of the studied critical behavior. Thermodynamic consistency demands that the one-particle order parameter starts to grow from zero at the critical point of the two-particle response function. This is achieved only when the Ward identity is obeyed. Qualitative consistency is reached already when the Ward identity is satisfied in the leading linear order in the symmetry-breaking field. The linear dependence of the self-energy on perturbation $\eta^\perp$ is plotted in Fig. 7. This is the odd self-energy and it will be related to the two-particle vertex via the Ward identity.

The Ward identity linearized with respect to the static homogeneous field $\eta^\perp$ as in Fig. 7 is

$$\Delta_\eta \Sigma(\mathbf{k}, i\omega_n) = \frac{1}{\beta N} \sum_{\mathbf{k}', \omega_{n'}} \Lambda_\eta^{eh}(\mathbf{k}, i\omega_n, \mathbf{k}', i\omega_{n'}; 0, 0) \, \Delta_\eta G(\mathbf{k}', i\omega_{n'}), \tag{45}$$

where we used the definitions of Eqs. (42).

The Ward identity is a microscopic relation guaranteeing macroscopic conservation laws. It has no direct relation to the microscopic quantum dynamics. The latter is governed by the
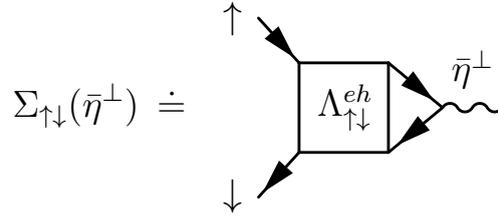
Fig. 7: *The leading linear order of the contribution from the symmetry-breaking field, $\eta^\perp$ in this case, to the self-energy.*

Schwinger-Dyson equation. The dynamics is not directly connected with the thermodynamic critical behavior. The only consistency requirement is that the vertex in the Schwinger-Dyson equation is built from the same irreducible vertex used in the Ward identity via the corresponding Bethe-Salpeter equation. We hence demand that the even self-energy be determined from the following Schwinger-Dyson dynamical equation

$$\bar{\Sigma}_\eta(\mathbf{k}, i\omega_n) = \frac{U}{2}n - \frac{U}{N^2}\sum_{\mathbf{k}'\mathbf{q}}\frac{1}{\beta^2}\sum_{\omega_{n'}\nu_m}\bar{G}_\eta(\mathbf{k}', i\omega_{n'})\,\bar{G}_\eta(\mathbf{k}'+\mathbf{q}, i\omega_{n'}+i\nu_m) \tag{46}$$

$$\times\,\Gamma_\eta(\mathbf{k}, i\omega_n, \mathbf{k}', i\omega_{n'}; \mathbf{q}, i\nu_m)\,\bar{G}_\eta(\mathbf{k}+\mathbf{q}, i\omega_n+i\nu_m),$$

where n is the total charge density.

The self-energy is split into odd and even parts. The odd part plays the role of the order parameter and is determined from the linearized Ward identity. The even part obeys the symmetrized Schwinger-Dyson equation and is responsible for the dynamical behavior and the spectral properties. This general construction of two self-energies is an extension of the Hartree thermodynamics and the RPA dynamics. At the end, however, all the physical quantities must be determined from the full one-particle Green function with the total self-energy $\Sigma(\mathbf{k}, i\omega_n) = \Delta\Sigma(\mathbf{k}, i\omega_n) + \bar{\Sigma}(\mathbf{k}, i\omega_n)$. The way we separate the odd and even self-energy depends on the critical behavior and the controlling symmetry-breaking field. The construction is fitted just to the investigated critical behavior. The order parameter can be anomalous with an anomalous Green function in the ordered phase breaking macroscopic conservation laws.

7 Mean-field theory with a two-particle self-consistency

The main difference between the Baym-Kadanoff construction and the two-particle approach is the selection of the functional generating the perturbation theory. The former starts with the Luttinger-Ward functional and takes the self-energy as the fundamental object of the perturbation theory. The latter makes the two-particle irreducible vertices the central objects of the perturbation theory. The two approaches formally coincide in the high-temperature phase with no odd self-energy. They differ in the critical regions of the phase transitions where the Ward identity must be obeyed, at least in the leading order of the symmetry-breaking field. This is guaranteed only in the direct perturbation theory for the two-particle functions.

The perturbation theory for the self-energy is much easier to handle than the theory of the two-particle irreducible vertices. It is evident from the equations in which they enter the one and the two-particle Green functions. The one-particle Green function is determined from an algebraic Dyson equation, while the two-particle vertex from integral Bethe-Salpeter equations. It means that it is still a cumbersome way to determine the physical response functions from the generating two-particle irreducible functions. The major problem of the two-particle functions is their complexity with three independent dynamical variables and an unknown analytic structure. This is the main hurdle in the application of the two-particle approach. That is why most two-particle theories are based on heavy numerics [38–40].

The starting point of the perturbation theory is a reliable mean-field approximation with static renormalizations of the input parameters as discussed in Sec. 3. The Baym-Kadanoff approach leads only to a weak-coupling mean-field approximation. Moreover, due to the lack of the two-particle self-consistency, it contains spurious transitions. One expects that this flaw will be removed by the two-particle approach. The first task of the two-particle perturbation theory is then to construct a mean-field theory with a two-particle self-consistency.

7.1   Reduced parquet equations

We discussed that the most straightforward way to introduce a two-particle self-consistency is to use the parquet equations interconnecting the two-particle irreducible/reducible vertices. The two-particle approach must be able to reach the critical region of the weak-coupling theory in which the two-particle self-consistency suppresses the spurious crossing of the critical point. Unfortunately, the full set of parquet equations misses the critical point of the RPA and is unable to reach the Kondo regime in the SIAM [41]. That is why we developed a simplified analytic theory with reduced parquet equations that we used to construct a mean-field theory with a two-particle self-consistency [42, 19, 43].

The first step in the reduction of the parquet equations is to select the Bethe-Salpeter equation with a critical point of the unrenormalized perturbation theory. It is the equation with multiple electron-hole scatterings as plotted in Fig. 2 for systems with the repulsive interaction. In order to keep the analytic control we resort only to two scattering channels for the direct vertex. The second channel to be selected must be able to suppress the spurious transition and it is the Bethe-Salpeter equation with multiple electron-electron scatterings of Fig. 3.

In the next step we separate the critical from the non-critical fluctuations. We know that the irreducible vertex from the electron-hole channel remains finite and only the reducible vertex of this channel becomes singular. The full parquet equation for the singlet irreducible vertex $\Lambda_{\uparrow\downarrow}$ contains a convolution of two singular reducible vertices $\mathcal{K}_{\uparrow\downarrow}$, which is the reason why the full set of parquet equations misses completely the critical region of the RPA pole and the Kondo regime in the SIAM. Since we know that the Kondo effect is exact in the SIAM, we assume that the superdivergent term, the convolution of two divergent terms, is compensated by higher-order contributions beyond the parquet equations with the bare interaction. With this assumption we can reduce the parquet equation for the irreducible vertex from the electron-hole channel to
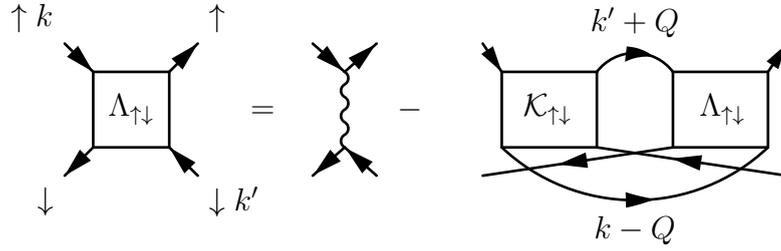
Fig. 8: *The reduced parquet equation for the irreducible vertex from the electron-hole channel in which the convolution of the divergent vertices $\mathcal{K}_{\uparrow\downarrow}$ is assumed to be compensated by higher order terms beyond the parquet equations.*
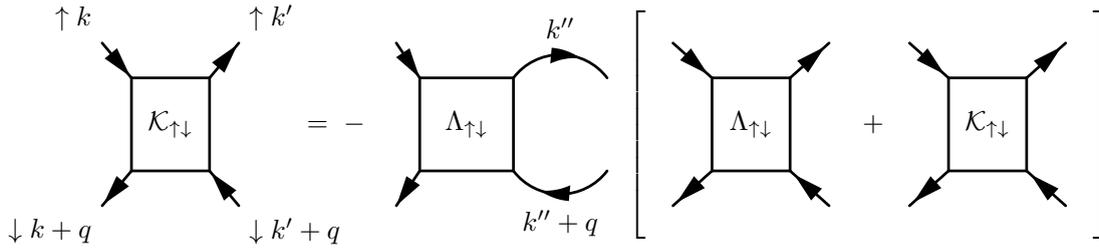
Fig. 9: *Bethe-Salpeter equation for the reducible vertex from the singular, electron-hole, scattering channel. The diagrams within the brackets are attached to the two-particle propagator in front of the brackets.*

$$\Lambda_{\sigma\bar{\sigma}}(\mathbf{k}, i\omega_n; \mathbf{k}', i\omega_{n'}) = U - \frac{1}{N}\sum_{\mathbf{Q}}\frac{1}{\beta}\sum_{\nu_l} K_{\sigma\bar{\sigma}}(\mathbf{k}, i\omega_n, \mathbf{k}'+\mathbf{Q}, i\omega_{n'}+i\nu_l; -\mathbf{Q}, -i\nu_l)$$

$$\times\, G_\sigma(\mathbf{k}'+\mathbf{Q}, i\omega_{n'}+i\nu_l)\, G_{\bar{\sigma}}(\mathbf{k}-\mathbf{Q}, i\omega_n-i\nu_l)\, \Lambda_{\sigma\bar{\sigma}}(\mathbf{k}'+\mathbf{Q}, i\omega_{n'}+i\nu_l, \mathbf{k}-\mathbf{Q}, i\omega_n-i\nu_l), \quad (47)$$

the diagrammatic representation of which is shown in Fig. 8. The reducible vertex $\mathcal{K}_{\uparrow\downarrow}$ is determined from the unrestricted Bethe-Salpeter equation in the electron-hole channel. It reads

$$K_{\sigma\bar{\sigma}}(\mathbf{k}, i\omega_n, \mathbf{k}', i\omega_{n'}; \mathbf{q}, i\nu_m) = -\frac{1}{N}\sum_{\mathbf{k}''}\frac{1}{\beta}\sum_{\omega_l} \Lambda_{\sigma\bar{\sigma}}(\mathbf{k}, i\omega_n; \mathbf{q}+\mathbf{k}'', i\omega_{m+l})\, G_{\bar{\sigma}}(\mathbf{k}''+\mathbf{q}, i\omega_{m+l})$$

$$\times\, G_\sigma(\mathbf{k}'', i\omega_l)\Big(\Lambda_{\sigma\bar{\sigma}}(\mathbf{k}'', i\omega_l; \mathbf{q}+\mathbf{k}', i\omega_{m+n'}) + K_{\sigma\bar{\sigma}}(\mathbf{k}'', i\omega_l, \mathbf{k}', i\omega_{n'}; \mathbf{q}, i\nu_m)\Big) \quad (48)$$

and is shown in Fig. 9.

Equations (47) and (48) are the simplest parquet-like equations introducing a two-particle self-consistency without missing the weak-coupling critical behavior. They are solvable only numerically in their full generality. We still need a simplification in order not to lose the analytic control of the approximation. We use the fact that we are essentially interested in the critical behavior in the proximity of the RPA pole. We hence divide the dynamical fluctuations of the vertex functions into relevant ones, controlling the critical behavior, and irrelevant ones, that do not affect the universal critical behavior. We further neglect the irrelevant frequency and momentum dependence of the noncritical functions. The irrelevant variables are the fermionic

ones. If we neglect them in the irreducible vertex we reduce it to a static effective interaction Λ. Using the solution for the reducible vertex $\mathcal{K}(\mathbf{q}, i\nu_m)$ from Eq. (48) in Eq. (47) we obtain

$$\left(1 - \frac{\Lambda^2}{N} \sum_{\mathbf{q}} \frac{1}{\beta} \sum_{\nu_m} \phi(-\mathbf{q}, -i\nu_m) \frac{G_\uparrow(\mathbf{k}+\mathbf{q}, i\omega_{n+m}) \, G_\downarrow(\mathbf{k}'-\mathbf{q}, i\omega_{n'-m})}{1 + \Lambda\phi(-\mathbf{q}, -i\nu_m)}\right) \Lambda = U \,, \qquad (49)$$

where

$$\phi(\mathbf{q}, i\nu_m) = \frac{1}{2N} \sum_{\sigma} \sum_{\mathbf{k}} \frac{1}{\beta} \sum_{\omega_n} \Big(G_{\bar{\sigma}}(\mathbf{k}+\mathbf{q}, i\omega_{n+m}) + G_{\bar{\sigma}}(\mathbf{k}-\mathbf{q}, i\omega_{n-m}) \Big) G_\sigma(\mathbf{k}, i\omega_n) \,. \qquad (50)$$

It is evident that this equation cannot hold point-wise for all fermionic momenta and frequencies. It means that we can satisfy Eq. (49) only approximately unless we decorate the effective interaction Λ with frequencies and momenta. The dynamical vertex Λ would make the resulting renormalization extremely complicated and would lead to losing analytic control of the critical behavior, which we do not want. If we cannot obey Eq. (49) fully we resort to an approximate solution. There are two options how to close the equation for the effective interaction Λ. The first one is suitable for metallic systems at very low temperatures. It uses analytic continuation to real frequencies where we put the fermionic frequencies on the Fermi level. This approximation works well in the strong-coupling limit of the SIAM at zero temperature [44,45]. The other option is to use the fact that the universal critical behavior is not qualitatively affected by fluctuations in the fermionic variables since they are irrelevant in the critical region of the pole in the response function. We can then average Eq. (49) over the fermionic momenta and Matsubara frequencies. The selection of the averaging procedure is not, however, unambiguous [46]. One way, particularly suitable for extended lattice systems, is to multiply both sides of Eq. (49) by the product of the one-particle thermodynamic propagators $G_\downarrow(-\mathbf{k}, -i\omega_n)G_\uparrow(-\mathbf{k}', -i\omega_{n'})$ and sum/integrate over the fermionic variables $\mathbf{k}, \omega_n$ $\mathbf{k}', \omega_{n'}$. Equation (49) reduces after this averaging to [47]

$$\Lambda = \frac{U \, (n^2 - m^2)}{n^2 - m^2 + 4\Lambda^2 \mathcal{X}} \,, \qquad (51)$$

where

$$\mathcal{X} = -\frac{1}{N} \sum_{\mathbf{q}} \frac{\psi(\mathbf{q}, i\nu_m)\psi(-\mathbf{q}, -i\nu_m)\phi(-\mathbf{q}, -i\nu_m)}{1 + \Lambda\phi(-\mathbf{q}, -i\nu_m)} \,, \qquad (52a)$$

$$\psi(\mathbf{q}, \omega_+) = \frac{1}{N} \sum_{\mathbf{k}} \frac{1}{\beta} \sum_{\omega_n} \Big(G_{\bar{\sigma}}(\mathbf{q}+\mathbf{k}, i\omega_{m+n}) + G_{\bar{\sigma}}(\mathbf{q}-\mathbf{k}, i\omega_{m-n}) \Big) G_\sigma(\mathbf{k}, i\omega_n). \qquad (52b)$$

We denoted the charge and spin densities $n = (\beta N)^{-1} \sum_\sigma \sum_{\mathbf{k},\omega_n} G_\sigma(\mathbf{k}, i\omega_n)e^{i\omega_n 0^+}$ and $m = (\beta N)^{-1} \sum_\sigma \sigma \sum_{\mathbf{k},\omega_n} G_\sigma(\mathbf{k}, i\omega_n)e^{i\omega_n 0^+}$, respectively. Positivity of integral $\mathcal{X}$ leads to a screening of the bare interaction. Equation (51) self-consistently determines the effective interaction Λ that controls the critical behavior near the pole, a singularity in the integrand of Eq. (52). The singularity emerges when $a(\mathbf{Q}) = 1 + \Lambda\phi(\mathbf{Q}, 0) = 0$. Vector $\mathbf{Q}$ is the momentum at which the static bubble $\phi(\mathbf{q}, 0)$ has a minimum, maximum of its modulus. It characterizes the type of the critical behavior we investigate. The critical point can be reached and crossed to

an ordered phase only if $\mathcal{X} < \infty$. It means that the physical singularity must be integrable. The self-consistent equation for the effective interaction then suppresses the spurious poles of the random-phase approximation with the bare interaction U and allows only for integrable singularities in the response functions.

7.2 Spectral function

Equations (51) and (52) determine fully the effective interaction from which we derive most of the thermodynamic properties of the model. All calculations can be performed in the Matsubara formalism without the necessity to use analytic continuation to real frequencies. We showed that this thermodynamic mean-field approximation suppresses the spurious phase transition of the Hartree approximation. It is the desired extension of the Hartree weak-coupling mean-field theory to the strong-coupling regime. This thermodynamic theory remains essentially at the two-particle level. The one-particle propagators are an input and can be approximated via a separate scheme, except for the odd self-energy that reduces to a static value $\Delta\Sigma = -\Lambda m/2$. The even self-energy is obtained from an approximation to the corresponding Schwinger-Dyson equation.

The Schwinger-Dyson dynamical equation for the static effective interaction reads

$$\bar{\Sigma}(\mathbf{k}, \omega_+) = U\frac{n}{2} - \frac{U\Lambda}{N}\sum_{\mathbf{q}} P \int_{-\infty}^{\infty} \frac{dx}{\pi}\left(b(x)\,\bar{\mathcal{G}}(\mathbf{k+q}, \omega_+ + x)\,\Im\frac{\bar{\Phi}(\mathbf{q}, x_+)}{1 + \Lambda\phi(\mathbf{q}, x_+)} \right.$$
$$\left. - \frac{f(x+\omega)\bar{\Phi}(\mathbf{q}, x_-)}{1 + \Lambda\phi(\mathbf{q}, x_-)}\,\Im\bar{\mathcal{G}}(\mathbf{q+k}, x+\omega_+) \right), \quad (53a)$$

where we introduced a two-particle bubble with the renormalized one-particle propagators

$$\bar{\Phi}(\mathbf{q}, \omega_+) = -\frac{1}{N}\sum_{\mathbf{k}} \int_{\infty}^{\infty} \frac{dx}{\pi} f(x)\Big(\bar{\mathcal{G}}(\mathbf{k+q}, x+\omega_+) + \bar{\mathcal{G}}(\mathbf{k-q}, x-\omega_+) \Big)\Im\bar{\mathcal{G}}(\mathbf{k}, x_+). \quad (53b)$$

We used new symbols for the one-particle Green function $\bar{\mathcal{G}}$ and for the two-particle bubble $\bar{\Phi}$ on the right-hand side of Eq. (53). Independently of which even self-energy we used in the thermodynamic Green functions $G_\sigma(\mathbf{k}, i\omega_n)$ in Eqs (51) and (52) to determine Λ and $\phi(\mathbf{q}, \omega_+)$, the Green function $\bar{\mathcal{G}}(\mathbf{q}, \omega_+)$ must be at least partly renormalized by the resulting self-energy $\bar{\Sigma}(\mathbf{k}, \omega_+)$ from Eq. (53). The simplest renormalization would be the Hartree self-consistency where the self-energy in the one-particle propagator $\bar{\mathcal{G}}$ on the right-hand side of Eq. (53) is approximated by the linear term in the interaction strength. That is,

$$\bar{\Sigma}(\mathbf{k}, \omega_+) = U\frac{n}{2} = -\frac{U}{N}\sum_{\mathbf{k}} \int_{-\infty}^{\infty} \frac{dx}{\pi} f(x)\,\Im\bar{\mathcal{G}}(\mathbf{k}, x_+) \quad (54)$$

is used in the Green function $\bar{\mathcal{G}}$ in Eq. (53). It is the mean-field selection of the even self-energy in the two-particle thermodynamic calculations and it closes the static mean-field approximation with a two-particle self-consistency.

The importance of the Schwinger-Dyson equation lies in its dynamical structure that is affected in the critical region by the singular two-particle propagator. If we go beyond the static Hartree approximation for $\bar{\Sigma}(\mathbf{k}, \omega_+)$ the full one-particle self-consistency in Eq. (53) demands that we use the following fully renormalized one-particle Green function in models with a magnetic critical behavior

$$\mathcal{G}_\sigma(\mathbf{k}, i\omega_n) = \frac{1}{i\omega_n + \mu - \sigma\Delta\Sigma - \varepsilon(\mathbf{k}) - \bar{\Sigma}(\mathbf{k}, i\omega_n)} \ . \tag{55}$$

The advantage of the two-particle approach is the possibility to separate the one-particle self-consistency from the two-particle one. It means that the one-particle Green functions G_σ determining the effective interaction and the two-particle bubble can differ from the Green function $\bar{\mathcal{G}}$ in Eq. (55). We demonstrated that the best approximation of the Kondo limit and the three-peak structure of the spectral function of the SIAM deliver the thermodynamic propagators with only the static Hartree renormalization [19].

If we renormalize the one-particle Green functions in the parquet equations differently from the Schwinger-Dyson equation then the thermodynamic propagators in the two-particle approach play the role of the bare propagators from the unrenormalized perturbation theory. The physical self-energy and the Green function are those determined from Eqs. (53) and (55). An important restriction on the even self-energy from the Schwinger-Dyson equation is that it depends only on even powers of the symmetry-breaking field and hence, does not affect the critical behavior derived from the two-particle irreducible vertex Λ from the critical Bethe-Salpeter equation.

8   Conclusions

It is generally difficult to calculate thermodynamic properties of interacting many-body systems even for simplified models. Exact solutions are rare and available only in specific limiting situations. Understanding the impact of the particle interaction on the collective macroscopic behavior is of great importance for our ability to control and utilize materials properties for our convenience. Methods of classical statistical physics are sufficient to reliably describe macroscopic phenomena at high, i.e. room, temperatures. Quantum physics comes into play at lower temperatures where quantum many-body models must be used to explain the long-range effects in solids.

Microscopic quantum dynamics, non-commutativity of the fundamental operators, and indistinguishability of the identical particles makes it extremely difficult to get quantitative results when the interaction strength is dominant over the kinetic energy. It is one of the most important tasks of the condensed-matter theory to develop reliable and generally applicable techniques in the strong-coupling regime of quantum many-body models. The quantum perturbation theory with Feynman diagrams and many-body Green functions becomes one of the most powerful means to reach the goal.

The only way to use perturbation theory in strong coupling is to use renormalizations and self-consistent summations of classes of Feynman diagrams. This can be done only by using many-body Green functions and their analytic properties. Renormalizations of the perturbation theory

must be done carefully and in a controlled way not to lose causality and/or not to break conservation laws. The major problem of quantum interacting models is the two-fold interconnectivity of one and two-particle functions. The first one is the dynamical equation of motion, being the Schwinger-Dyson equation for the Green functions. The other is the Ward identity.

The standard way to introduce renormalizations into the many-body perturbation theory is the Baym-Kadanoff construction with the Luttinger-Ward functional generating the self-energy as the fundamental object of this approach. It formally guarantees the conserving character of the theory but no approximate self-energy from the Schwinger-Dyson equation obeys the Ward identity: There are two two-particle vertices to the approximate self-energy. That is why this approach cannot be continued beyond the critical points to the ordered phases.

An alternative way to introduce renormalizations into the perturbation theory is to build the theory from the two-particle vertex. After identifying the critical behavior of the model, one chooses the irreducible vertex of the singular Bethe-Salpeter equation as the generating functional. One splits the Green functions into either odd or even symmetric parts with respect to the reflection of the symmetry-breaking field responsible for the critical behavior. Only the two-particle functions with even symmetry become relevant when we use the Ward identity valid up to linear order of the symmetry-breaking field. The odd part of the one-particle self-energy is related with the two-particle irreducible vertex via a linearized Ward identity. The even self-energy then obeys the symmetrized Schwinger-Dyson equation. The separation of the odd and even self-energies seems to be the only way to reconcile at least qualitatively the Ward identity and the Schwinger-Dyson equation in approximate theories.

The two-particle approach is for obvious reasons much more complicated than the one-particle one of Baym and Kadanoff. We nevertheless succeeded to reduce the complexity of the two-particle functions by neglecting noncritical fluctuations and keeping only the critical ones. In this way we were able to construct a mean-field theory with a static effective interaction being a consistent extension of the RPA to strong coupling. It naturally includes a two-particle self-consistency in the effective interaction suppressing thereby the spurious pole of the RPA. It separately allows for various levels of renormalizations of the even dynamical self-energy in the Schwinger-Dyson equation. Last but not least, the two-particle mean-field approximation is consistent with the Mermin-Wagner theorem and distinguishes between zero and non-zero temperatures in low spatial dimensions.

Acknowledgment

References

[1] R. Shankar: *Principles of Quantum Mechanics* (Plenum Press, New York, 1980)

[2] A.A. Abrikosov, L.P. Gorkov, and I.E. Dzyaloshinski: *Methods of Quantum Field Theory in Statistical Physics* (Dover Publications, New York, 1963)

[3] F. Byron and R.W. Fuller: *Mathematics of Classical and Quantum Physics* (Dover Publications, New York, 1992)

[4] S. Tomonaga, Prog. Theor. Phys. **1**, 27 (1946)

[5] J. Schwinger, Phys. Rev. **75**, 651 (1949)

[6] R.P. Feynman, Phys. Rev. **76**, 769 (1949)

[7] F.J. Dyson, Phys. Rev. **75**, 486 (1949)

[8] P.C. Martin and J. Schwinger, Phys. Rev. **115**, 1342 (1959)

[9] J. Schwinger, J. Math. Phys. **2**, 407 (1961)

[10] G. Baym and L.P. Kadanoff, Phys. Rev. **124**, 287 (1961)

[11] G. Baym, Phys. Rev. **127**, 1391 (1962)

[12] C.D. Dominicis, J. Math. Phys. **3**, 983 (1962)

[13] C.D. Dominicis, J. Math. Phys. **4**, 255 (1963)

[14] C.D. Dominicis and P.C. Martin, J. Math. Phys. **5**, 14 (1964)

[15] C.D. Dominicis and P.C. Martin, J. Math. Phys. **5**, 31 (1964)

[16] A.D. Jackson, A. Lande, and R.A. Smith, Phys. Rep. **86**, 55 (1982)

[17] N.E. Bickers and S.R. White, Phys. Rev. B **43**, 8044 (1991)

[18] N. Bickers, Int. J. Mod. Phys. B **05**, 253 (1991)

[19] V. Janiš, A. Kauch, and V. Pokorný, Phys. Rev. B **95**, 045108 (2017)

[20] F.H.L. Essler, V.E. Korepin, and K. Schoutens, Phys. Rev. Lett. **67**, 3848 (1991)

[21] A. Georges, G. Kotliar, W. Krauth, and M.J. Rozenberg, Rev. Mod. Phys. **68**, 13 (1996)

[22] J.K. Freericks and V. Zlatić, Rev. Mod. Phys. **75**, 1333 (2003)

[23] A. Tsvelick and P. Wiegmann, Adv. Phys. **32**, 453 (1983)

[24] A.C. Hewson: *The Kondo Problem to Heavy Fermions*,
     Cambridge Studies in Magnetism, Vol. 2 (Cambridge University Press, 1993)

[25] V. Janiš, Phys. Rev. B **60**, 11345 (1999)

[26] C.J. Thompson, Commun. Math. Phys. **36**, 255 (1974)

[27] V. Janiš and D. Vollhardt, Z. Phys. B **91**, 317 (1993)

[28] V. Janiš, Z. Phys. B **83**, 227 (1991)

[29] V. Janiš, J. Mašek, and D. Vollhardt, Z. Phys. B **91**, 325 (1993)

[30] L.D. Landau, Sov. Phys. JETP **3**, 920 (1957)

[31] G. Baym and C. Pethick: *Landau Fermi-Liquid Theory: Concepts and Applications*
     (Wiley VCH, Weinheim, 1991)

[32] T. Matsubara, Prog. Theor. Phys. **14**, 351 (1955)

[33] V. Janiš, J. Phys.: Condens. Matter **15**, L311 (2003)

[34] F. Krien, E.G.C.P. van Loon, H. Hafermann, J. Otsuki, M.I. Katsnelson, and
     A.I. Lichtenstein, Phys. Rev. B **96**, 075155 (2017)

[35] V. Janiš, J. Phys.: Condens. Matter **10**, 2915 (1998)

[36] G. Rohringer, H. Hafermann, A. Toschi, A. Katanin, A. Antipov, M. Katsnelson,
     A. Lichtenstein, A. Rubtsov, and K. Held, Rev. Mod. Phys. **90**, 025003 (2018)

[37] V. Janiš, J. Phys.: Condens. Matter **21**, 485501 (2009)

[38] K.M. Tam, H. Fotso, S.-X. Yang, T.W. Lee, J. Moreno, J. Ramanujam, and M. Jarrell,
     Phys. Rev. E **87**, 013311 (2013)

[39] G. Li, A. Kauch, P. Pudleiner, and K. Held, Comp. Phys. Commun. **241**, 146 (2019)

[40] C.J. Eckhardt, C. Honerkamp, K. Held, and A. Kauch, Phys. Rev. B **101**, 155104 (2020)

[41] V. Janiš, Condens. Matter Phys. **9**, 499 (2006)

[42] V. Janiš and P. Augustinský, Phys. Rev. B **75**, 165108 (2007)

[43] V. Janiš, P. Zalom, V. Pokorný, and A. Klíč, Phys. Rev. B **100**, 195114 (2019)

[44] V. Janiš, V. Pokorný, and A. Kauch, Phys. Rev. B **95**, 165113 (2017)

[45] V. Janiš and A. Klíč, JPS Conference Proceedings **30**, 011124 (2020)

[46] V. Janiš and P. Augustinský, Phys. Rev. B **77**, 085106 (2008)

[47] V. Janiš, J. Yan, and A. Klíč, AIP Adv. **10**, 125127 (2020)

8   An Essential Introduction to NEGF Methods for Real-Time Simulations

Gianluca Stefanucci
University of Rome Tor Vergata
via della Ricerca Scientifica 1
00173 Rome, Italy

Contents

1   Introduction

We often hear about *strongly correlated systems* as opposed to weakly correlated ones. Strictly speaking, however, the adjective "correlated" is not a feature of the system, rather of the *state of the system*. Consider for instance a Hubbard dimer at half-filling with on-site repulsion U and hopping integral t. For $U/t \to \infty$ the ground state is a singlet with no double occupancy; such singlet is certainly a strongly correlated state since mean-field treatments predict that the ground state has a finite and U-independent double occupation. Does this mean that the Hubbard dimer is a strongly correlated system? Of course not. The same system does indeed admit a triplet excited state of zero energy which is identical to the triplet excited state of the noninteracting ($U = 0$) Hubbard dimer. Another example is provided by organic molecules. The majority of them have a weakly correlated ground state but highly correlated excited states.

In dealing with out-of-equilibrium problems it is crucial to have some physical intuition about the amount of correlation carried by *all* eigenstates involved in the dynamics. Not only that, different excited states may experience different correlation effects, meaning that several state-specific correlation mechanisms must be simultaneously taken into account. For these reasons the development of approximated methods is generally more difficult than for equilibrium problems.

In this chapter we introduce a versatile formalism to deal with any quantum system in arbitrary nonequilibrium situations. The formalism is dubbed Nonequilibrium Green Functions (NEGF) [1] and it is essentially the extension of many-body diagrammatic theory to systems driven by external time-dependent fields. We show how to convert a generic nonequilibrium process into a mathematical expression and hence how to build approximation schemes from our physical intuition. Finally we present recent advances for efficient real-time NEGF simulations of systems of interacting electrons and bosons, e.g., phonons or photons [2–6]. These progresses make NEGF competitive with the fastest quantum method today available, i.e., time-dependent density functional theory. Implementations in high performance computer facilities will more likely open the door to first-principles investigations of a wide range of nonequilibrium correlated phenomena.

2   The contour idea

In almost all approaches to quantum matter the very first approximation is the truncation of the one-particle Hilbert space. For solids this is usually done by ignoring planewaves with momentum higher than a certain cutoff and by choosing a certain discretization of momenta in the first Brillouin zone. In finite systems like atoms and molecules the truncation consists in considering only a certain number of localized orbitals, e.g., Slater type orbitals or Gaussian type orbitals or splines etc. Many kinds of one-particle bases are of course available in the market, their suitability depending on the system under investigation *and* on the external perturbing fields. In this chapter we do not specify the basis set and let the reader choose his/her favorite one. Only in the last section we shall introduce two different kind of bases for the discussion of recent

implementation strategies of the NEGF equations. We assume, however, that the chosen basis is orthonormal and we denote by $\hat{d}_i$ and $\hat{d}_i^\dagger$ the fermionic operators annihilating and creating an electron in the i-th basis function: hence the anticommutation rules read $\{\hat{d}_i, \hat{d}_j^\dagger\} = \delta_{ij}$. Notice that the label i includes, in general, both orbital and spin degrees of freedom.

In second quantization the fermionic operators are used to construct operators associated to observable quantities, hence the Hamiltonian too. For a self-contained presentation we consider a system of interacting electrons subject to external classical fields. However, we mention that the NEGF formalism can deal with more realistic situations where an interaction between electrons and quantized phonons and photons is present [7–9]. The purely electronic Hamiltonian reads

$$\hat{H}(t) = \hat{H}_0(t) + \hat{H}_{\text{int}} = \sum_{ij} h_{ij}(t)\, \hat{d}_i^\dagger \hat{d}_j + \frac{1}{2} \sum_{ijmn} v_{ijmn}\, \hat{d}_i^\dagger \hat{d}_j^\dagger \hat{d}_m \hat{d}_n\,. \tag{1}$$

Henceforth we shall use the hat symbol "ˆ" for *all* operators written in second quantization. The noninteracting part $\hat{H}_0(t)$ is a quadratic form of fermionic operators and it contains information on how electrons are coupled to external static potentials, e.g., the nuclear potential, and time-dependent fields, e.g., laser pulses. The interacting part $\hat{H}_{\text{int}}$ is a two-body operator describing, e.g., the Coulomb interaction between electrons. We specialize the discussion to an initial state which is the ground state $|\Psi_g\rangle$ of $\hat{H}_0 + \hat{H}_{\text{int}}$ and, without any loss of generality, we take $t = 0$ as the initial time. The average of any operator $\hat{O}$ at times $t > 0$ is given by

$$O(t) = \langle \Psi_g | \hat{U}(0,t)\, \hat{O}\, \hat{U}(t,0) | \Psi_g \rangle, \tag{2}$$

where $\hat{U}(t, t')$ is the evolution operator from time t' to time t. Let us manipulate Eq. (2). Although the assumption of the adiabatic connection is not necessary to develop the NEGF formalism we here assume that it is fulfilled as it shortens the derivations. What is this assumption about? Let us first define it mathematically and then explore its physical content. The adiabatic Hamiltonian

$$\hat{H}_\eta(t) = \hat{H}_0 + e^{-\eta|t|} \hat{H}_{\text{int}} \tag{3}$$

coincides with the noninteracting part $\hat{H}_0$ in the remote past ($t \to -\infty$) and, for an infinitesimal energy η, it approaches (adiabatically) the full interacting Hamiltonian at time $t = 0$. Let $|\Phi_g\rangle$ be the (noninteracting) ground state of $\hat{H}_0$ and let $\hat{U}_\eta(t, t')$ be the evolution operator from time t' to time t associated to the Hamiltonian $\hat{H}_\eta(t)$. According to the Gell-Mann-Low theorem [10–12] the state $|\Psi\rangle = \hat{U}_\eta(0, -\infty)|\Phi_g\rangle$ is an eigenstate of $\hat{H}_0 + \hat{H}_{\text{int}}$. The adiabatic connection is fulfilled if $|\Psi\rangle = |\Psi_g\rangle$, i.e., if the interacting ground state can be obtained from the noninteracting one by an adiabatic switch-on of the interaction. The adiabatic connection allows for rewriting Eq. (2) in terms of the *non*-interacting state $|\Phi_g\rangle$, the price to pay being that the evolution starts at $t = -\infty$ instead of $t = 0$:

$$O(t) = \langle \Phi_g | \hat{U}_\eta(-\infty, 0)\, \hat{U}(0, t)\, \hat{O}\, \hat{U}(t, 0)\, \hat{U}_\eta(0, -\infty) | \Phi_g \rangle. \tag{4}$$

We could compress this result if we extend the definition of the time-dependent Hamiltonian in Eq. (1) to negative times: $\hat{H}(t < 0) = \hat{H}_\eta(t)$. Then the group property of the evolution operator
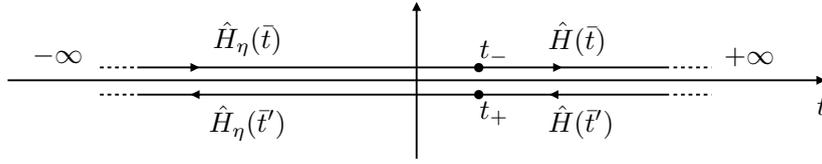
Fig. 1: *The contour γ, starting at $t = -\infty$, going all the way to $t = +\infty$ and then back to $t = -\infty$. By definition, any point lying on the forward branch is earlier than a point lying on the backward branch.*

implies $\hat{U}(t,0)\hat{U}_\eta(0,-\infty) = \hat{U}(t,-\infty)$ and Eq. (4) becomes

$$O(t) = \langle \Phi_g | \hat{U}(-\infty,t)\,\hat{O}\,\hat{U}(t,-\infty)|\Phi_g\rangle. \tag{5}$$

The *forward* evolution operator has a simple mathematical form in terms of the time-ordering operator $\mathcal{T}$. For any $t > t'$ (forward evolution)

$$\hat{U}(t,t') = \mathcal{T}\left\{ e^{-\mathrm{i}\int_{t'}^{t} d\bar{t}\,\hat{H}(\bar{t})} \right\}. \tag{6}$$

In fact, $\mathcal{T}$ is not at all an operator, rather it is a rule according to which the operators in the curly bracket must be ordered with *later* times to the *left* (or equivalently earlier times to the right). We can better visualize the action of $\mathcal{T}$ if we write the integral in Eq. (6) as a Riemann sum over the discrete times $t_n = t' + n\delta$, where n varies from zero to $N = \mathrm{Int}[(t-t')/\delta]$ and $\delta \to 0$. Then t_n is later than t_m if $n > m$ and

$$\mathcal{T}\left\{ e^{-\mathrm{i}\int_{t'}^{t} d\bar{t}\,\hat{H}(\bar{t})} \right\} = \lim_{\delta \to 0} \mathcal{T}\left\{ e^{-\mathrm{i}\delta\sum_{n=0}^{N}\hat{H}(t_n)} \right\} = \lim_{\delta \to 0} e^{-\mathrm{i}\delta\hat{H}(t_N)}e^{-\mathrm{i}\delta\hat{H}(t_{N-1})}\cdots e^{-\mathrm{i}\delta\hat{H}(t_1)}e^{-\mathrm{i}\delta\hat{H}(t_0)}. \tag{7}$$

From this "unzipped" expression of the forward operator $\hat{U}(t,t')$ we can immediately find an expression for the *backward* evolution operator $\hat{U}(t',t)$. Taking into account the group property $\hat{U}(t,t')\hat{U}(t',t) = \hat{1}$ we have

$$\hat{U}(t',t) = \lim_{\delta \to 0} e^{\mathrm{i}\delta\hat{H}(t_0)}e^{\mathrm{i}\delta\hat{H}(t_1)}\cdots e^{\mathrm{i}\delta\hat{H}(t_{N-1})}e^{\mathrm{i}\delta\hat{H}(t_N)} = \bar{\mathcal{T}}\left\{ e^{\mathrm{i}\int_{t'}^{t} d\bar{t}\,\hat{H}(\bar{t})} \right\} = \bar{\mathcal{T}}\left\{ e^{-\mathrm{i}\int_{t}^{t'} d\bar{t}\,\hat{H}(\bar{t})} \right\}, \tag{8}$$

where $\bar{\mathcal{T}}$ is the so called anti-time-ordering operator, i.e., a rule according to which the operators in the curly bracket must be ordered with later times to the right. Inserting these results into Eq. (5) we get

$$O(t) = \langle \Phi_g | \bar{\mathcal{T}}\left\{ e^{-\mathrm{i}\int_{t}^{-\infty} d\bar{t}'\,\hat{H}(\bar{t}')} \right\} \hat{O}\,\mathcal{T}\left\{ e^{-\mathrm{i}\int_{-\infty}^{t} d\bar{t}\,\hat{H}(\bar{t})} \right\} |\Phi_g\rangle. \tag{9}$$

Pay now attention to the ordering of times. If we define the oriented contour $\gamma = (-\infty, +\infty) \cup (+\infty, -\infty)$, see Fig. 1, and we place the times $\bar{t}$ on the upper, or forward, branch and the times $\bar{t}'$ on the lower, or backward, branch then the string of operators in Eq. (9) appears ordered on the contour γ. This observation is at the basis of the *contour idea* developed independently by Keldysh [13], Schwinger [14], and Konstantinov and Perel' [15], see also Refs. [16, 17] for a more recent discussion. Let us introduce the contour-variable, or better the contour-time $z \in \gamma$; z can lie either on the forward branch or on the backward branch and once the branch is specified it can assume any value between $-\infty$ and $+\infty$. To specify the branch we add a "+"

or "−" subscript to the times; thus $z = t_-$ is a time t on the forward branch and $z = t_+$ is a time t on the backward branch, see again Fig. 1. We also define operators with argument on the contour like

$$\hat{O}(t_-) = \hat{O}(t_+) \equiv \hat{O}(t) \quad \Rightarrow \quad \hat{O}(z) = \hat{O}(t). \tag{10}$$

In Fig. 1 we show how the Hamiltonian $\hat{H}(z)$ varies along the contour. Equation (9) can then be rewritten as

$$O(t) = \langle \Phi_g | \mathcal{T}_\gamma \left\{ e^{-i \int_\gamma d\bar{z}\, \hat{H}(\bar{z})} \hat{O}(z) \right\} | \Phi_g \rangle, \tag{11}$$

where $\mathcal{T}_\gamma$ is the contour-ordering operator, i.e., a rule according to which the operators in the curly bracket must be ordered with later contour-times to the left. A contour-time is earlier than another if it is closer to the starting point, which in our notation is $\lim_{t \to -\infty} t_-$. Therefore, $\mathcal{T}_\gamma$ acts like the time-ordering operator $\mathcal{T}$ for arguments on the forward branch and like the anti-time-ordering operator $\bar{\mathcal{T}}$ for arguments on the backward branch. Let us verify Eq. (11). Suppose that $z = t_-$. Then Eq. (11) implies

$$O(t) = \langle \Phi_g | \underbrace{\bar{\mathcal{T}} \left\{ e^{-i \int_\infty^{-\infty} d\bar{t}'\, \hat{H}(\bar{t}')} \right\}}_{\hat{U}(-\infty,\infty)} \underbrace{\mathcal{T} \left\{ e^{-i \int_t^\infty d\bar{t}\, \hat{H}(\bar{t})} \right\}}_{\hat{U}(\infty,t)} \hat{O} \underbrace{\mathcal{T} \left\{ e^{-i \int_{-\infty}^t d\bar{t}\, \hat{H}(\bar{t})} \right\}}_{\hat{U}(t,-\infty)} | \Phi_g \rangle$$
$$= \langle \Phi_g | \hat{U}(-\infty,t)\, \hat{O}\, \hat{U}(t,-\infty) | \Phi_g \rangle, \tag{12}$$

which is the same as Eq. (5). Similarly the reader can verify that choosing $z = t_+$ the result does not change.

A remark about Eq. (11) is important at this point. If the operator $\hat{O}$ does not depend explicitly on time, like it is our operator, then we can safely write $\hat{O}(t) = \hat{O}$ in Eq. (12). However, if we do so in Eq. (11) then it is not possible to establish where to place the operator $\hat{O}$ when acted upon by $\mathcal{T}_\gamma$. The reason to give a contour argument even to operators that do not have an explicit time dependence (like the fermionic operators $\hat{d}_i$ and $\hat{d}_i^\dagger$) stems from the need of specifying their position along the contour, thus rendering unambiguous the action of $\mathcal{T}_\gamma$. Once the operators are ordered we can omit the time arguments if there is no time dependence.

We conclude this section with a brief comment on the necessity of introducing a contour for nonequilibrium situations. In the *absence* of external fields the Hamiltonian at positive times is constant and given by $\hat{H} = \hat{H}_0 + \hat{H}_{int}$. For any finite $t > 0$ we can choose the infinitesimal energy η such that the equality $\hat{H} = \hat{H}_\eta(t)$ is fulfilled with arbitrary precision. Hence we can calculate time-dependent averages using the Hamiltonian $\hat{H}(t) = \hat{H}_\eta(t)$ for negative *and* positive times. For a nondegenerate ground state the Gell-Mann-Low theorem implies that $\langle \Phi_g | \hat{U}(\infty, -\infty) = \langle \Phi_g | e^{i\alpha_g}$ where $e^{i\alpha_g}$ is a phase factor. Physically this means that by switching on and then off the interaction we end up in the same state up to a phase factor $e^{i\alpha_g} = \langle \Phi_g | \hat{U}(\infty, -\infty) | \Phi_g \rangle$. Substituting this result into Eq. (5) and using the group property of the evolution operator we get

$$O(t) = \frac{\langle \Phi_g | \hat{U}(\infty, t) \hat{O} \hat{U}(t, -\infty) | \Phi_g \rangle}{\langle \Phi_g | \hat{U}(\infty, -\infty) | \Phi_g \rangle}. \tag{13}$$

Reading the time arguments from right to left we see that they are ordered on the real axis. In equilibrium there is no need of introducing a contour. A more detailed discussion can be found in Ref. [1].

3 Nonequilibrium Green function

The NEGF formalism is a *nonperturbative* approach to calculate averages like in Eq. (11). Its power and versatility stems from the possibility of including only a (well thought) selection of scattering channels in the time-evolution. The fundamental bit in NEGF is the contour Green function

$$G_{ij}(z, z') \equiv \frac{1}{i} \langle \Phi_g | \mathcal{T}_\gamma \left\{ e^{-i \int_\gamma d\bar{z} \, \hat{H}(\bar{z})} \, \hat{d}_i(z) \, \hat{d}_j^\dagger(z') \right\} | \Phi_g \rangle, \tag{14}$$

where $\mathcal{T}_\gamma$ is the contour-ordering operator with an extra rule: after the reordering the sign changes if z' is later than z. This extra rule can be shown to simplify the math enormously [1]. Equation (14) is a two-point correlator on the contour. For both z and z' on the forward branch the contour Green function coincides with the more familiar time-ordered Green function. However other choices of contour-times are possible. Let us get acquainted with Eq. (14).

If z is earlier than z' we have (notice the sign change due to the extra rule)

$$G_{ij}(z, z') = -\frac{1}{i} \langle \Phi_g | \hat{U}(-\infty, t') \, \hat{d}_j^\dagger \, \hat{U}(t', t) \, \hat{d}_i \, \hat{U}(t, -\infty) | \Phi_g \rangle \equiv G_{ij}^<(t, t'). \tag{15}$$

The last equality defines the *lesser* Green function. Notice that $G^<$ is a function of the physical times t and t'. One way to get this function for *all* times t and t' consists in evaluating the contour Green function for $z = t_-$ (forward branch) and $z' = t'_+$ (backward branch); in this case z would indeed be always earlier than z'. However, if $t < t'$ then we can get $G^<$ also choosing $z = t_-$ and $z' = t'_-$ whereas if $t > t'$ then we can get $G^<$ also choosing $z = t_+$ and $z' = t'_+$. The lesser Green function is proportional to the probability amplitude that a hole created at time t in the basis function i is found at time t' in the basis function j. In other words $G^<$ describes how an added hole (or a removed electron) propagates in the system.

The *greater* Green function is defined as the contour Green function evaluated at the contour-time z later than z'

$$G_{ij}(z, z') = \frac{1}{i} \langle \Phi_g | \hat{U}(-\infty, t) \, \hat{d}_i \, \hat{U}(t, t') \, \hat{d}_j^\dagger \, \hat{U}(t', -\infty) | \Phi_g \rangle \equiv G_{ij}^>(t, t'). \tag{16}$$

Again this is a function of the physical times t and t' and it is proportional to the probability amplitude that an electron created at time t' in the basis function j is found at time t in the basis function i. Hence $G^>$ describes how an added electron propagates in the system. The lesser and greater Green functions can be used to rewrite the contour Green function as

$$G_{ij}(z, z') \equiv \Theta(z, z') \, G_{ij}^>(t, t') + \Theta(z', z) \, G_{ij}^<(t, t'), \tag{17}$$

where the Heaviside function on the contour $\Theta(z, z')$ has value 1 if z is later than z' and zero otherwise. In Eq. (17) the contour time z can be either t_- or t_+ and similarly the contour time z' can be either t'_- or t'_+.

From the equal-time lesser Green function we can calculate the time-dependent average of any one-body operator $\hat{O} = \sum_{ij} O_{ij} \hat{d}_i^\dagger \hat{d}_j$. To show it we observe that Eq. (15) for $t = t'$ yields

$$G_{ij}^<(t, t) = -\frac{1}{i} \langle \Phi_g | \hat{U}(-\infty, t) \, \hat{d}_j^\dagger \, \hat{d}_i \, \hat{U}(t, -\infty) | \Phi_g \rangle = i \rho_{ij}(t), \tag{18}$$

where $\rho(t)$ is the one-particle density matrix. Taking into account Eq. (5)

$$O(t) = \sum_{ij} O_{ij} \langle \Phi_g | \hat{U}(-\infty, t)\, \hat{d}_i^\dagger\, \hat{d}_j \hat{U}(t, -\infty) | \Phi_g \rangle = -\mathrm{i} \sum_{ij} O_{ij} G_{ji}^<(t, t) = \sum_{ij} O_{ij} \rho_{ji}(t). \quad (19)$$

Examples of one-body operators are the noninteracting part of the Hamiltonian, the particle density, the particle current, the local magnetic moment, the dipole moment, etc. From the time off-diagonal values of $G^<$ it is also possible to calculate the average of the interaction part of the Hamiltonian. This non trivial result is known as the Galitskii-Migdal formula

$$H_{\mathrm{int}}(t) = \langle \Phi_g | \hat{U}(-\infty, t)\hat{H}_{\mathrm{int}}\hat{U}(t, -\infty) | \Phi_g \rangle = \frac{1}{4\mathrm{i}} \sum_{ij} \left[\mathrm{i}\left(\frac{d}{dt} - \frac{d}{dt'}\right)\delta_{ij} - 2h_{ij}(t)\right] G_{ji}^<(t, t')\bigg|_{t=t'}. \quad (20)$$

The lesser and greater Green functions contain also information on the spectral properties, such as those probed in photoemission or inverse photoemission experiments. Let $D_{\mathbf{k}i}(t)$ be the matrix element of the light-matter interaction operator between the i-th state of our basis set and a photoelectron state of momentum $\mathbf{k}$ and energy $\varepsilon_{\mathbf{k}}$. The current of photoelectrons of momentum $\mathbf{k}$ measured at time t is then given by [18]

$$I_{\mathbf{k}}(t) = 2 \sum_{ij} \int d\bar{t}\, \mathrm{Re}\left(\Sigma_{ij,\mathbf{k}}(t, \bar{t})\, G_{ji}^<(\bar{t}, t)\right) \quad (21)$$

where $\Sigma_{ij,\mathbf{k}}(t, \bar{t}) = -\mathrm{i}\Theta(t-\bar{t})\, D_{i\mathbf{k}}(t)D_{j\mathbf{k}}^*(t)e^{-\mathrm{i}\varepsilon_{\mathbf{k}}(t-\bar{t})}$.
In the next sections we lay down the basis for the calculation of the lesser and greater Green function.

4 Noninteracting systems

A noninteracting system is described by a Hamiltonian with $\hat{H}_{\mathrm{int}} = 0$. In this case the calculation of the Green function is elementary. The evolution operator in Eqs. (6) and (8) satisfies *for all t and t'*

$$\mathrm{i}\frac{d}{dt}\hat{U}(t, t') = \hat{H}(t)\hat{U}(t, t'), \qquad -\mathrm{i}\frac{d}{dt'}\hat{U}(t, t') = \hat{U}(t, t')\hat{H}(t'). \quad (22)$$

We then see that the derivative of Eq. (15) with respect to, e.g., t generates a commutator between $\hat{H}(t)$ and $\hat{d}_i$. For noninteracting Hamiltonians this commutator is simply given by $[\hat{H}_0(t), \hat{d}_i] = -\sum_m h_{im}(t)\, \hat{d}_m$. Similarly, the derivative with respect to t' generates the commutator between $\hat{H}(t')$ and $\hat{d}_j^\dagger$ which for noninteracting Hamiltonians is simply $[\hat{H}_0(t'), \hat{d}_j^\dagger] = \sum_m h_{mj}(t')\, \hat{d}_m^\dagger$. Therefore

$$\mathrm{i}\frac{d}{dt}G_{ij}^<(t, t') = \sum_m h_{im}(t)\, G_{mj}^<(t, t'), \qquad -\mathrm{i}\frac{d}{dt'}G_{ij}^<(t, t') = \sum_m G_{im}^<(t, t')\, h_{mj}(t'). \quad (23)$$

An analogous derivation for $G^>$ leads to the same equations of motion (23). Let us rewrite them in matrix form

$$\mathrm{i}\frac{d}{dt}G^{\lessgtr}(t, t') = h(t)G^{\lessgtr}(t, t'), \qquad -\mathrm{i}\frac{d}{dt'}G^{\lessgtr}(t, t') = G^{\lessgtr}(t, t')h(t'). \quad (24)$$

The most general solution of these equations is $G^{\lessgtr}(t,t') = u(t)\, Q^{\lessgtr} u^\dagger(t')$ where $Q^<$ and $Q^>$ are arbitrary matrices whereas u is the unitary time-evolution matrix in the *one-particle* Hilbert space

$$u(t) \equiv \mathcal{T}\left\{ e^{-i \int_{-\infty}^{t} d\bar{t}\, h(\bar{t})} \right\} \qquad \Rightarrow \qquad i\frac{d}{dt}u(t) = h(t)u(t). \qquad (25)$$

To find the matrices $Q^{\lessgtr}$ we need an initial condition. We observe that $\lim_{t\to-\infty} u(t) = 1$ and therefore $Q^{\lessgtr} = \lim_{t\to-\infty} G^{\lessgtr}(t,t)$. From Eq. (15) this limit is given by

$$Q^<_{ij} = \lim_{t\to-\infty} G^<_{ij}(t,t) = i\langle \Phi_g | \hat{d}^\dagger_j \hat{d}_i | \Phi_g \rangle \equiv i\rho^g_{ij}, \qquad (26)$$

$$Q^>_{ij} = \lim_{t\to-\infty} G^>_{ij}(t,t) = -i\langle \Phi_g | \hat{d}_i \hat{d}^\dagger_j | \Phi_g \rangle = -i\big(\delta_{ij} - \rho^g_{ij}\big), \qquad (27)$$

where ρ^g_{ij} is the one-particle density matrix in the remote past, which is also the one-particle density matrix associated to the noninteracting ground state $|\Phi_g\rangle$. The noninteracting Green function is therefore known once we know ρ^g.

The ρ^g can easily be calculated from the eigenvectors of the (equilibrium) one-particle hamiltonian: $h\, \vec{\varphi}^{(\lambda)} = \varepsilon_\lambda \vec{\varphi}^{(\lambda)}$. Let us see how. We construct the fermionic operators $\hat{c}^\dagger_\lambda \equiv \sum_m \varphi^{(\lambda)}_m \hat{d}^\dagger_m$ that create an electron in the basis vector $\vec{\varphi}^{(\lambda)}$. Using the orthonormality of the eigenvectors the inverse relation reads $\hat{d}^\dagger_m = \sum_\lambda \varphi^{(\lambda)*}_m \hat{c}^\dagger_\lambda$ and the noninteracting Hamiltonian can be rewritten as

$$\hat{H}_0 = \sum_{\lambda\lambda'} \sum_{ij} \hat{c}^\dagger_\lambda \varphi^{(\lambda)*}_i h_{ij} \varphi^{(\lambda')}_j \hat{c}_{\lambda'} = \sum_{\lambda\lambda'} \sum_i \hat{c}^\dagger_\lambda \varphi^{(\lambda)*}_i \varepsilon_{\lambda'} \varphi^{(\lambda')}_i \hat{c}_{\lambda'} = \sum_{\lambda\lambda'} \hat{c}^\dagger_\lambda \varepsilon_\lambda \delta_{\lambda\lambda'} \hat{c}_{\lambda'} = \sum_\lambda \varepsilon_\lambda \hat{c}^\dagger_\lambda \hat{c}_\lambda. \qquad (28)$$

According to the aufbau principle the noninteracting ground-state $|\Phi_g\rangle$ of the system with N particles is constructed by filling the first N levels of h, i.e., $|\Phi_g\rangle = \hat{c}^\dagger_1 \ldots \hat{c}^\dagger_N |0\rangle$ where $|0\rangle$ is the empty state. We then have

$$\rho^g_{ij} = \langle 0| \hat{c}_N \ldots \hat{c}_1\, \hat{d}^\dagger_j \hat{d}_i\, \hat{c}^\dagger_1 \ldots \hat{c}^\dagger_N |0\rangle = \sum_{\lambda=1}^{N} \varphi^{(\lambda)*}_j \varphi^{(\lambda)}_i. \qquad (29)$$

To summarize the noninteracting lesser and greater Green functions have the following analytic expression (in matrix form)

$$G^<(t,t') = i\, u(t)\, \rho^g\, u^\dagger(t'), \qquad G^>(t,t') = -i\, u(t)\big(1-\rho^g\big) u^\dagger(t'). \qquad (30)$$

We can use the property of the evolution operator $u^\dagger(\tau)u(\tau) = 1$ for any time τ to rewrite Eq. (30) in terms of the *equal-time* lesser and greater Green functions $G^{\lessgtr}(t,t)$

$$G^{\lessgtr}(t,t') = \Big(\Theta(t-t') + \Theta(t'-t)\Big) G^{\lessgtr}(t,t')$$
$$= \Theta(t-t')\, u(t)u^\dagger(t') G^{\lessgtr}(t',t') + \Theta(t'-t)\, G^{\lessgtr}(t,t)\, u(t)u^\dagger(t'). \qquad (31)$$

This rewriting brings out two functions, i.e., the retarded and advanced Green functions

$$G^{\mathrm{R}}(t,t') = -i\Theta(t-t')\, u(t)\, u^\dagger(t') = -i\Theta(t-t')\, \mathcal{T}\left\{ e^{-i \int_{t'}^{t} d\bar{t}\, h(\bar{t})} \right\}, \qquad (32)$$

$$G^{\mathrm{A}}(t,t') = i\Theta(t'-t)\, u(t)\, u^\dagger(t') = i\Theta(t'-t)\, \bar{\mathcal{T}}\left\{ e^{-i \int_{t'}^{t} d\bar{t}\, h(\bar{t})} \right\} = \big(G^{\mathrm{R}}(t',t)\big)^\dagger. \qquad (33)$$

The retarded and advanced Green functions carry no information on how the noninteracting levels are initially populated. They only contain information on how to propagate one-particle states – sometimes we shall refer to G^R and G^A as propagators. Using the propagators we can rewrite Eq. (31) as

$$G^{\lessgtr}(t,t') = \mathrm{i}G^R(t,t')\,G^{\lessgtr}(t',t') - \mathrm{i}G^{\lessgtr}(t,t)\,G^A(t,t'). \tag{34}$$

This result has inspired an important ansatz in NEGF; we come back to it in section 8.

5   Dyson equation on the contour

The analytic calculation of the interacting Green function defined in Eq. (14) is possible only in special cases like, e.g., integrable models or systems with only a few particles. In most cases the interacting Green function must be approximated. In this section we discuss a scheme to evaluate $G(z,z')$ using an arbitrary subset of scattering processes. Accurate approximations can then be generated by selecting those processes that dominate over the others.
The starting point is the observation that inside the contour ordering the operators can be treated as commuting operators. Consider for instance the contour ordered product of $\hat{H}_0(z)$ (noninteracting part of the Hamiltonian) and $\hat{H}_{\mathrm{int}}(z')$ (interaction Hamiltonian). Then

$$\mathcal{T}_\gamma\left\{\hat{H}_0(z)\hat{H}_{\mathrm{int}}(z')\right\} = \mathcal{T}_\gamma\left\{\hat{H}_{\mathrm{int}}(z')\hat{H}_0(z)\right\}. \tag{35}$$

Indeed for, e.g., z later than z' Eq. (35) yields $\hat{H}_0(t)\hat{H}_{\mathrm{int}}(t')$ no matter if we use the expression in the left hand side or in the right hand side – remember the rule: operators with later contour-times must be placed to the left. We can then manipulate the interacting Green function in Eq. (14) as follows

$$G_{ij}(z,z') = \frac{1}{\mathrm{i}}\langle\Phi_g|\mathcal{T}_\gamma\left\{e^{-\mathrm{i}\int_\gamma d\bar{z}\,\hat{H}_0(\bar{z})}e^{-\mathrm{i}\int_\gamma d\bar{z}\,\hat{H}_{\mathrm{int}}(\bar{z})}\hat{d}_i(z)\hat{d}_j^\dagger(z')\right\}|\Phi_g\rangle,$$

$$= \frac{1}{\mathrm{i}}\sum_{n=0}^\infty\frac{(-\mathrm{i})^n}{n!}\int_\gamma dz_1\cdots dz_n\langle\Phi_g|\mathcal{T}_\gamma\left\{e^{-\mathrm{i}\int_\gamma d\bar{z}\,\hat{H}_0(\bar{z})}\hat{H}_{\mathrm{int}}(z_1)\cdots\hat{H}_{\mathrm{int}}(z_n)\hat{d}_i(z)\hat{d}_j^\dagger(z')\right\}|\Phi_g\rangle. \tag{36}$$

In the first equality we used that for two commuting operators $\hat{A}$ and $\hat{B}$ we have $e^{\hat{A}+\hat{B}} = e^{\hat{A}}e^{\hat{B}}$. In the second equality we expanded the exponent containing the interaction Hamiltonian in a Taylor series. Comparing Eq. (36) with the expansion of the more familiar time-ordered Green function we notice that the only difference is in the domain of integration: in Eq. (36) all integrals are over the contour while in the time-ordered Green function all integrals are between $-\infty$ and $+\infty$ (real axis). We can then recycle all results of the time-ordered formalism; it will be enough to change the time domain from the real axis to the contour. In particular the integrand in Eq. (36) is the noninteracting average of a string of fermionic operators, which can be broken into products of Green functions using the Wick theorem [19]. This innocent-looking observation implies that we can represent the expansion of Eq. (36) in terms of the same Feynman diagrams as the time-ordered Green function! The only difference in NEGF is that the

oriented lines are contour Green functions and the times of each internal vertex are integrated over the contour. A few diagrammatic examples are given in the next section.

It is textbook knowledge that the diagrammatic expansion of G highlights the occurrence of an important mathematical unit repeated to infinite order, i.e., the self-energy Σ. In NEGF the self-energy, like the Green function, depends on two contour-times and the relation between G and Σ is given by the Dyson equation (in matrix form)

$$
\begin{aligned}
G(z, z') &= G_0(z, z') + \int_\gamma dz_1 dz_2 \, G_0(z, z_1) \Sigma(z_1, z_2) G(z_2, z') \\
&= G_0(z, z') + \int_\gamma dz_1 dz_2 \, G(z, z_1) \Sigma(z_1, z_2) G_0(z_2, z'),
\end{aligned}
\tag{37}
$$

where the Green function G_0 is the noninteracting Green function discussed in section 4. We can transform the Dyson equation into two integro-differential equations that, as we shall see, are easier to handle. For this purpose we derive below the equation of motion of $G_0(z, z')$ on the contour. Using the decomposition in Eq. (17) we have

$$
\mathrm{i}\frac{d}{dz}G_0(z, z') = \mathrm{i}\delta(z, z')\Big[G_0^>(t, t) - G_0^<(t, t)\Big] + \Theta(z, z')\frac{d}{dt}G_0^>(t, t') + \Theta(z', z)\frac{d}{dt}G_0^<(t, t'),
\tag{38}
$$

where

$$
\delta(z, z') = \frac{d}{dz}\Theta(z, z') = -\frac{d}{dz}\Theta(z', z)
\tag{39}
$$

is the Dirac delta on the contour. From Eq. (30) the term in the square bracket is simply

$$
G_0^>(t, t) - G_0^<(t, t) = -\mathrm{i}u(t)\Big(1 - \rho^g + \rho^g\Big)u^\dagger(t) = -\mathrm{i}.
\tag{40}
$$

Taking into account Eq. (24), i.e., the time derivative of $G_0^{\lessgtr}$, we can then rewrite Eq. (38) as

$$
\mathrm{i}\frac{d}{dz}G_0(z, z') = \delta(z, z') + h(t)G_0(z, z').
\tag{41}
$$

With similar steps we can calculate the derivative with respect to z' and find

$$
-\mathrm{i}\frac{d}{dz'}G_0(z, z') = \delta(z, z') + G_0(z, z')h(t').
\tag{42}
$$

These last two equations are the equations of motion (on the contour) for the noninteracting Green function. As anticipated, they are useful to transform the Dyson equation into two integro-differential equations for G. Deriving the first line of Eq. (37) with respect to z and the second line of the same equation with respect to z' we find

$$
\left(\mathrm{i}\frac{d}{dz} - h(t)\right)G(z, z') = \delta(z, z') + \int_\gamma d\bar{z}\,\Sigma(z, \bar{z})G(\bar{z}, z'),
\tag{43}
$$

$$
G(z, z')\left(-\mathrm{i}\frac{\overleftarrow{d}}{dz'} - h(t')\right) = \delta(z, z') + \int_\gamma d\bar{z}\,G(z, \bar{z})\Sigma(\bar{z}, z').
\tag{44}
$$

Before discussing the numerical strategies to solve the equations of motion (43) and (44) let us have a closer look at the self-energy and its lesser and greater components.
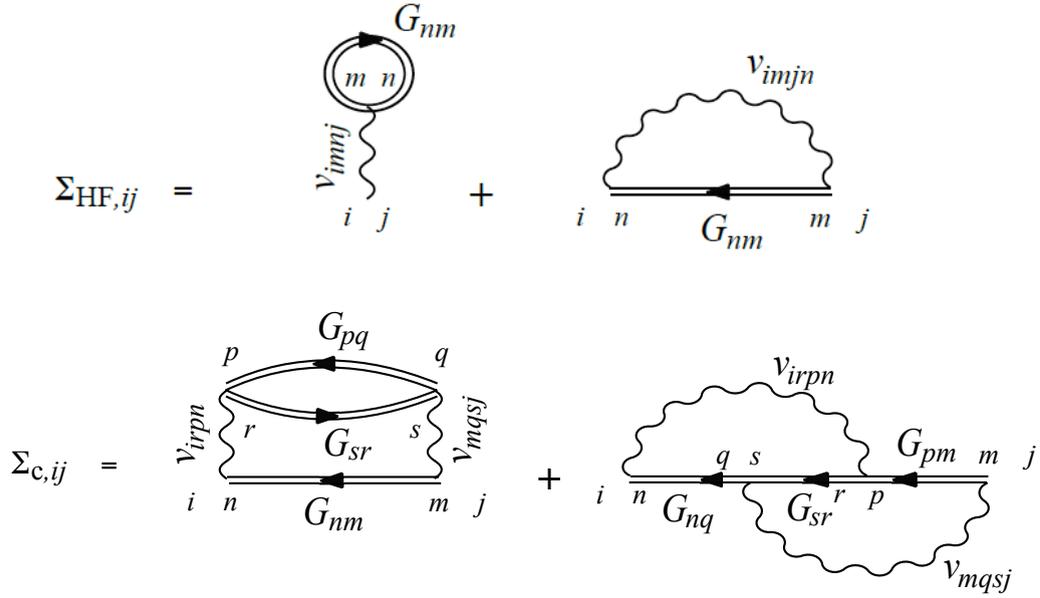
Fig. 2: *Diagrams for the Hartree-Fock self-energy (top) and for the correlation self-energy in the 2nd Born approximation (bottom).*

6 Simple diagrammatic approximations

In Fig. 2 we show a couple of diagrammatic approximations to Σ. To first order in the electron-electron interaction v only two diagrams contribute, see Fig. 2 (top). The resulting Σ is the so called Hartree-Fock (HF) self-energy

$$\Sigma_{\text{HF},ij}(z,z') = \underbrace{-\mathrm{i}\,\delta(z,z')\sum_{mn} v_{imnj}\, G_{nm}(z,z^+)}_{\text{Hartree}} + \underbrace{\mathrm{i}\delta(z,z')\sum_{mn} v_{imjn}\, G_{nm}(z,z^+)}_{\text{Fock}}$$

$$\equiv \delta(z,z')\, V_{\text{HF},ij}(t), \tag{45}$$

where we have denoted by z^+ a contour-time infinitesimally later than z and we have defined the HF potential in the second line of Eq. (45). From Eq. (17) we see that $G(z,z^+) = G^<(t,t) = \mathrm{i}\rho(t)$. The HF potential is therefore a linear function of the one-particle density matrix; explicitly we have

$$V_{\text{HF},ij}(t) = \sum_{mn} \big(v_{imnj} - v_{imjn}\big)\rho_{nm}(t). \tag{46}$$

The HF self-energy diagrams are the only self-energy diagrams proportional to the Dirac delta on the contour. This time-locality of Σ_{HF} prevents the description of, e.g., quasi-particle lifetimes (which are always infinite in HF) and quasi-particle satellites like those emerging from the dressing of electrons with plasmons. The Green function in the HF approximation is the solution of the equations of motion (43) and (44) when Σ is approximated with Σ_{HF}. The contour integral is in this case trivial and the equations of motion reduce to

$$\left(\mathrm{i}\frac{d}{dz} - h(t) - V_{\text{HF}}(t)\right)G(z,z') = \delta(z,z'), \tag{47}$$

$$G(z, z') \left(-\mathrm{i} \frac{\overleftarrow{d}}{dz'} - h(t') - V_{\mathrm{HF}}(t') \right) = \delta(z, z'). \tag{48}$$

These equations have the same mathematical structure as those of the noninteracting Green function, see Eqs. (41) and (42). The only difference is that the one-particle Hamiltonian $h(t)$ is replaced by the HF Hamiltonian

$$h_{\mathrm{HF}}(t) \equiv h(t) + V_{\mathrm{HF}}(t). \tag{49}$$

In essence the HF world is a world where an electron does not collide with other electrons but it rather moves in the mean-field potential V_{HF} generated by all other electrons. The lesser and greater components are therefore given by Eq. (30) with evolution operator $u(t) = \mathcal{T}\{e^{-\mathrm{i}\int_{-\infty}^{t} d\bar{t}\, h_{\mathrm{HF}}(\bar{t})}\}$. This implies that the HF retarded and advanced Green functions read

$$G^{\mathrm{R}}(t, t') = \mathrm{i}\Theta(t-t')\mathcal{T}\{e^{-\mathrm{i}\int_{t'}^{t} d\bar{t}\, h_{\mathrm{HF}}(\bar{t})}\}, \qquad G^{\mathrm{A}}(t, t') = \left(G^{\mathrm{R}}(t', t)\right)^{\dagger}, \tag{50}$$

and that Eq. (34) for $G^{\lessgtr}$ is valid in the HF approximation too.

Higher-order self-energy diagrams are nonlocal in time and contribute to the so called *correlation* self-energy Σ_{c}. The splitting of the full self-energy $\Sigma = \Sigma_{\mathrm{HF}} + \Sigma_{\mathrm{c}}$ into a HF part and a correlation part is extremely convenient for computational purposes, see section 10. In Fig. 2 we show the second-order (in the interaction) diagrams for the correlated self-energy, also known as the 2nd Born (2B) approximation. In the 2B world an electron can collide only once with another electron; this is however enough to change its quantum number like, e.g., the momentum, and hence to generate a finite life-time.

Converting the diagrams of Fig. 2 into a mathematical expression we get

$$\begin{aligned}
\Sigma_{\mathrm{c},ij}(z, z') &= \\
&= \mathrm{i}^2 \sum_{rpn} \sum_{mqs} v_{irpn} v_{mqsj} \big[-G_{nm}(z, z') G_{sr}(z', z) G_{pq}(z, z') + G_{nq}(z, z') G_{sr}(z', z) G_{pm}(z, z') \big] \\
&= \mathrm{i}^2 \sum_{rpn} \sum_{mqs} v_{irpn} \big(v_{qmsj} - v_{mqsj} \big) G_{nm}(z, z') G_{sr}(z', z) G_{pq}(z, z'), \tag{51}
\end{aligned}$$

where in the last step we renamed $m \leftrightarrow q$ in the second term of the square bracket. As anticipated this self-energy is nonlocal in time, i.e., it is not proportional to $\delta(z, z')$, and the equations of motion for G remain integro-differential equations. The corresponding greater and lesser Green functions cannot be written as in Eq. (30) and, consequently, Eq. (34) is no longer valid. The lesser and greater components of the self-energy are defined similarly to the lesser and greater components of the Green function

$$\Sigma_{\mathrm{c}}^{<}(t, t') \equiv \Sigma_{\mathrm{c}}(t_-, t'_+), \qquad \Sigma_{\mathrm{c}}^{>}(t, t') \equiv \Sigma_{\mathrm{c}}(t_+, t'_-). \tag{52}$$

Both $\Sigma^{<}$ and $\Sigma^{>}$ are functions of the real times t and t'. From their definition we see that these functions are simply obtained from Eq. (51) with the replacement

$$G_{nm}(z, z') G_{sr}(z', z) G_{pq}(z, z') \;\rightarrow\; G_{nm}^{\lessgtr}(t, t') G_{sr}^{\gtrless}(t', t)^{\lessgtr} G_{pq}^{\lessgtr}(t, t'). \tag{53}$$

Like the Green function, see discussion below Eq. (15), if $t < t'$ then the lesser self-energy is also given by $\Sigma_{\rm c}^<(t, t') = \Sigma_{\rm c}^<(t_-, t'_-)$ whereas if $t > t'$ then we have $\Sigma_{\rm c}^<(t, t') = \Sigma_{\rm c}^<(t_+, t'_+)$. Analogous considerations apply to the greater self-energy. Choosing z and z' on different branches, like we have done in Eq. (52), returns the lesser and greater self-energy for all times t and t'.

In the next section we describe how to calculate the Green function with a nonvanishing correlation self-energy.

7 Kadanoff-Baym equations

Let us start by rewriting the equations of motion (43), (44) with the self-energy $\Sigma = \Sigma_{\rm HF} + \Sigma_{\rm c}$

$$\left({\rm i}\frac{d}{dz} - h_{\rm HF}(t) \right) G(z, z') = \delta(z, z') + \int_\gamma d\bar{z}\, \Sigma_{\rm c}(z, \bar{z})\, G(\bar{z}, z'), \qquad (54)$$

$$G(z, z') \left(-{\rm i}\frac{\overleftarrow{d}}{dz'} - h_{\rm HF}(t') \right) = \delta(z, z') + \int_\gamma d\bar{z}\, G(z, \bar{z})\, \Sigma_{\rm c}(\bar{z}, z'). \qquad (55)$$

As pointed out in section 3, see discussion below Eq. (15), the lesser Green function $G^<(t, t')$ is equal (for all t and t') to the contour Green function $G(z, z')$ when $z = t_-$ and $z' = t'_+$. Making this choice of contour-times in, e.g., Eq. (54) we find

$$\left({\rm i}\frac{d}{dt} - h_{\rm HF}(t) \right) G^<(t, t') = \int_\gamma d\bar{z}\, \Sigma_{\rm c}(t_-, \bar{z})\, G(\bar{z}, t'_+). \qquad (56)$$

The Dirac delta vanishes since z lies on the forward branch and z' lies on the backward branch (hence they can never coincide). To work out the integral over the contour we break it up into four different pieces, two per branch. The integral over the forward branch is performed from $-\infty$ to t and then from t to $+\infty$ whereas the integral over the backward branch is performed from $+\infty$ to t' and then from t' to $-\infty$

$$\int_\gamma d\bar{z}\, \Sigma_{\rm c}(t_-, \bar{z}) G(\bar{z}, t'_+) = \int_{-\infty}^t d\bar{t}\, \underbrace{\Sigma_{\rm c}(t_-, \bar{t}_-) G(\bar{t}_-, t'_+)}_{\Sigma_{\rm c}^>(t,\bar{t}) G^<(\bar{t},t')} + \int_t^\infty d\bar{t}\, \underbrace{\Sigma_{\rm c}(t_-, \bar{t}_-) G(\bar{t}_-, t'_+)}_{\Sigma_{\rm c}^<(t,\bar{t}) G^<(\bar{t},t')}$$

$$+ \int_\infty^{t'} d\bar{t}\, \underbrace{\Sigma_{\rm c}(t_-, \bar{t}_+) G(\bar{t}_+, t'_+)}_{\Sigma_{\rm c}^<(t,\bar{t}) G^<(\bar{t},t')} + \int_{t'}^{-\infty} d\bar{t}\, \underbrace{\Sigma_{\rm c}(t_-, \bar{t}_+) G(\bar{t}_+, t'_+)}_{\Sigma_{\rm c}^<(t,\bar{t}) G^>(\bar{t},t')}. \quad (57)$$

In this equation the integrand of the second and third terms is the same. We can then use $\int_t^\infty + \int_\infty^{t'} = \int_t^{t'} = \int_{-\infty}^{t'} - \int_{-\infty}^t$ and rewrite the contour integral as

$$\int_\gamma d\bar{z}\, \Sigma_{\rm c}(t_-, \bar{z}) G(\bar{z}, t'_+) = \int_{-\infty}^t d\bar{t}\left(\Sigma_{\rm c}^>(t, \bar{t}) - \Sigma_{\rm c}^<(t, \bar{t}) \right) G^<(\bar{t}, t')$$

$$- \int_{-\infty}^{t'} d\bar{t}\, \Sigma_{\rm c}^<(t, \bar{t}) \left(G^>(\bar{t}, t') - G^<(\bar{t}, t') \right). \qquad (58)$$

For any two-times correlator $C(z, z')$ we define the retarded and advanced components as

$$C^{\mathrm{R}}(t, t') = \Theta(t - t')\Big(C^>(\bar{t}, t') - C^<(\bar{t}, t')\Big), \tag{59}$$

$$C^{\mathrm{A}}(t, t') = -\Theta(t' - t)\Big(C^>(\bar{t}, t') - C^<(\bar{t}, t')\Big). \tag{60}$$

One important property following from these definitions is that

$$C^{\mathrm{R}} - C^{\mathrm{A}} = C^> - C^<. \tag{61}$$

Using the retarded and advanced functions we can transform the equation of motion (56) in a form containing only integrals and functions on the real axis

$$\left(\mathrm{i}\frac{d}{dt} - h_{\mathrm{HF}}(t)\right)G^<(t, t') = \int_{-\infty}^{\infty} d\bar{t}\left(\Sigma_{\mathrm{c}}^{\mathrm{R}}(t, \bar{t})G^<(\bar{t}, t') + \Sigma_{\mathrm{c}}^<(t, \bar{t})G^{\mathrm{A}}(\bar{t}, t')\right). \tag{62}$$

With similar manipulations we obtain the equation of motion for the greater Green function. We choose $z = t_+$ and $z' = t'_-$, use Eq. (55), and find

$$G^>(t, t')\left(-\mathrm{i}\frac{\overleftarrow{d}}{dt'} - h_{\mathrm{HF}}(t')\right) = \int_{-\infty}^{\infty} d\bar{t}\left(G^{\mathrm{R}}(t, \bar{t})\Sigma_{\mathrm{c}}^>(\bar{t}, t') + G^>(t, \bar{t})\Sigma_{\mathrm{c}}^{\mathrm{A}}(\bar{t}, t')\right). \tag{63}$$

Equations (62) and (63) are known as the *Kadanoff-Baym equations* (KBE) [20]. They form a closed system of integro-differential equations since (i) the lesser and greater self-energies are functions (or better functionals) of $G^<$ and $G^>$, see for instance the 2B self-energy in Eq. (51), and (ii) the lesser and greater Green functions are anti-hermitian, see the definitions in Eqs. (15) and (16), i.e.,

$$G^{\lessgtr}(t', t) = -\Big(G^{\lessgtr}(t, t')\Big)^{\dagger}. \tag{64}$$

Due to the cubic scaling with the maximum propagation time, the KBE are rather burdensome to solve numerically. Their use has been so far restricted to atoms, diatomic molecules, or model systems [21–24]. Details on available implementations strategies can be found in [1, 25, 26]. Before concluding this section we would like to observe that the retarded and advanced correlators defined in Eqs. (59) and (60) agree with the previous definition of G^{R} and G^{A} in noninteracting systems. The noninteracting lesser and greater Green functions are given in Eq. (30) and therefore the noninteracting retarded Green function calculated according to Eq. (59) is

$$G^{\mathrm{R}}(t, t') = -\mathrm{i}\Theta(t - t')u(t)\big(1 - \rho^g + \rho^g\big)u^{\dagger}(t') = -\mathrm{i}\Theta(t - t')u(t)u^{\dagger}(t'), \tag{65}$$

which is the same as Eq. (32). Similarly one can show that the advanced noninteracting Green functions defined as in Eq. (60) agrees with Eq. (33).

8   The Generalized Kadanoff-Baym Ansatz

In the mid-1980s Lipavsky *et al.* [27] proposed the so called Generalized Kadanoff-Baym Ansatz (GKBA) to collapse the KBE for the two-times Green functions into a single equation for the one-particle density matrix $\rho(t)$, reducing the computational cost drastically. The

NEGF+GKBA approach has been successfully applied to the nonequilibrium dynamics [28,29] and many-body localization [30] of Hubbard clusters, time-dependent quantum transport [31, 32] equilibrium absorption of sodium clusters [33], real-time dynamics of the Auger decay [34], transient absorption [35–38] and carrier dynamics [18, 39] of semiconductors, excitonic insulators out of equilibrium [40] as well as charge transfer [41] and charge migration [42–44] in molecular systems.

The basic idea of the GKBA is to approximate the lesser and greater Green functions *inside* the collision integral with the expression in Eq. (34), which we have demonstrated to be valid only for noninteracting systems or in the HF approximation. In terms of the one-particle density matrix $\rho(t) = -\mathrm{i}G^<(t,t) = 1 - \mathrm{i}G^>(t,t)$ defined in Eq. (18) we can write the GKBA as

$$G^<(t,t') = -G^{\mathrm{R}}(t,t')\,\rho(t') \quad + \quad \rho(t) \quad G^{\mathrm{A}}(t,t'), \tag{66}$$

$$G^>(t,t') = -G^{\mathrm{R}}(t,t')(\rho(t')-1) + (\rho(t)-1)G^{\mathrm{A}}(t,t'). \tag{67}$$

Through the GKBA the time off-diagonal lesser and greater Green functions are expressed in terms of ρ *and* the propagators. Assuming that the average time between two consecutive collisions of an electron in the medium is longer than the quasiparticle life-time we can further approximate the propagators with their HF expression, see Eq. (50). In this way the full $G^{\lessgtr}(t,t')$ depends only on the density matrix since h_{HF} is a functional of ρ through the HF potential, see again Eq. (46). We mention here that other approximations to the propagators have been proposed in the literature with the aim of accounting for finite quasi-particle life-times [31, 45–47]. In all cases, however, the approximated propagators are functionals of ρ only.

Let us see how to reduce the KBE to a single equation for $\rho(t)$ using the GKBA. Consider Eq. (62) and the adjoint equation where the lesser Green function $G^<(t,t')$ is derived with respect to t'. The adjoint equation is the same as Eq. (63) with $> \to <$. Subtracting the two equations and setting $t = t'$ we get

$$\mathrm{i}\left(\frac{d}{dt} + \frac{d}{dt'}\right) G^<(t,t')\big|_{t=t'} - \big[h_{\mathrm{HF}}(t),\, G^<(t,t)\big] = I(t) + I^{\dagger}(t), \tag{68}$$

where $I(t)$ is the collision integral on the right hand side of Eq. (62) calculated at $t = t'$. To show that the collision integral of the adjoint equation is the hermitian conjugate of $I(t)$ one can use the anti-hermiticity of the Green function, i.e., Eq. (64), and of the self-energy. In this chapter there is not enough space for the general proof of the property $\Sigma^<(t,t') = -\big(\Sigma^<(t',t)\big)^{\dagger}$; however, the reader can verify that this property is fulfilled by the 2B self-energy in Eq. (51); see Ref. [1] for the general proof. The crucial observation is now that the first term in Eq. (68) is nothing but the time derivative of the one-particle density matrix ρ, whereas the second term is the commutator between the HF Hamiltonian and ρ. Hence

$$\frac{d}{dt}\rho(t) + \mathrm{i}\big[h_{\mathrm{HF}}[\rho](t),\, \rho(t)\big] = -I[\rho](t) - I^{\dagger}[\rho](t). \tag{69}$$

We have highlighted that h_{HF} is a functional of ρ through the HF potential in Eq. (46) and that the collision integral I is a functional of ρ through the GKBA. Therefore Eq. (69) is a closed

equation for the one-particle density matrix! The numerical solution scales quadratically with the maximum propagation time since ρ depends on one time only. To better appreciate the computational gain let us work out the collision integral $I(t)$ for the 2B self-energy.

We begin by observing that for $t = t'$ the right hand side of Eq. (62) can be written as

$$
I(t) = \int_{-\infty}^{t} d\bar{t} \left(\left(\Sigma_{\mathrm{c}}^{>}(t,\bar{t}) - \Sigma_{\mathrm{c}}^{<}(t,\bar{t}) \right) G^{<}(\bar{t},t) - \Sigma_{\mathrm{c}}^{<}(t,\bar{t}) \left(G^{>}(\bar{t},t) - G^{<}(\bar{t},t) \right) \right)
$$

$$
= \int_{-\infty}^{t} d\bar{t} \left(\Sigma_{\mathrm{c}}^{>}(t,\bar{t}) \, G^{<}(\bar{t},t) - \Sigma_{\mathrm{c}}^{<}(t,\bar{t}) \, G^{>}(\bar{t},t) \right). \tag{70}
$$

Using Eq. (51) a matrix element of the product $\Sigma_{\mathrm{c}}^{>}(t,\bar{t}) \, G^{<}(\bar{t},t)$ reads

$$
\left(\Sigma_{\mathrm{c}}^{>}(t,\bar{t}) G^{<}(\bar{t},t) \right)_{il} = \sum_{j} \Sigma_{\mathrm{c},ij}^{>}(t,\bar{t}) \, G_{jl}^{<}(\bar{t},t)
$$

$$
= \mathrm{i}^2 \sum_{rpn} v_{irpn} \sum_{jmqs} \left(v_{qmsj} - v_{mqsj} \right) G_{nm}^{>}(t,\bar{t}) G_{sr}^{<}(\bar{t},t) G_{pq}^{>}(t,\bar{t}) G_{jl}^{<}(\bar{t},t). \tag{71}
$$

Similarly, the matrix element of the product $\Sigma_{\mathrm{c}}^{<}(t,\bar{t}) \, G^{>}(\bar{t},t)$ is obtained from Eq. (71) by interchanging $> \leftrightarrow <$. The mathematical structure underlying these expressions emerges clearly if we introduce the Coulomb tensor

$$
w_{\substack{qj \\ sm}} \equiv v_{mqsj} - v_{qmsj} = w_{\substack{jq \\ ms}}^{*} \tag{72}
$$

and the response function

$$
\chi_{\substack{pq \\ rs}}^{0,\gtrless}(t,t') \equiv -\mathrm{i} G_{pq}^{\gtrless}(t,t') G_{sr}^{\lessgtr}(t',t). \tag{73}
$$

We then see that Eq. (70) becomes [2–4]

$$
I_{il}(t) = \mathrm{i}^2 \sum_{rpn} v_{irpn} \int_{-\infty}^{t} d\bar{t} \sum_{jmqs} \left[\chi_{\substack{pq \\ rs}}^{0,>}(t,\bar{t}) w_{\substack{qj \\ sm}} \chi_{\substack{jl \\ mn}}^{0,<}(\bar{t},t) - \chi_{\substack{pq \\ rs}}^{0,<}(t,\bar{t}) w_{\substack{qj \\ sm}} \chi_{\substack{jl \\ mn}}^{0,>}(\bar{t},t) \right]
$$

$$
\equiv -\mathrm{i} \sum_{rpn} v_{irpn} \, \mathcal{G}_{\substack{pl \\ rn}}(t). \tag{74}
$$

The square bracket is the sum of simple products between matrices in the two-particle space. Using greek letters for superindices composed by pairs of one-particle indices, e.g., $\alpha = (p,r)$, $\beta = (l,n)$, etc., the matrix elements of $\mathcal{G}$ can also be written as [4]

$$
\mathcal{G}_{\alpha\beta}(t) = -\mathrm{i} \int_{-\infty}^{t} d\bar{t} \sum_{\mu\nu} \left[\chi_{\alpha\mu}^{0,>}(t,\bar{t}) w_{\mu\nu} \chi_{\nu\beta}^{0,<}(\bar{t},t) - \chi_{\alpha\mu}^{0,<}(t,\bar{t}) w_{\mu\nu} \chi_{\nu\beta}^{0,>}(\bar{t},t) \right]. \tag{75}
$$

We point out that up to this point we have not yet used the GKBA to transform the collision integral, or equivalently $\mathcal{G}$, into a functional of the density matrix. Evaluating the greater response function for $t > t'$ using the GKBA we get

$$
\chi_{\substack{pq \\ rs}}^{0,>}(t,t') = \mathrm{i} \underbrace{\sum_{a} G_{pa}^{\mathrm{R}}(t,t') \left(\rho_{aq}(t') - \delta_{aq} \right)}_{-G_{pq}^{>}(t,t')} \underbrace{\sum_{b} \rho_{sb}(t') G_{br}^{\mathrm{A}}(t',t)}_{G_{sr}^{<}(t',t)} = \sum_{ab} P_{\substack{pa \\ rb}}^{\mathrm{R}}(t,t') \rho_{\substack{aq \\ bs}}^{(2)>}(t'), \tag{76}
$$

where we have defined

$$P^{\mathrm{R}}_{\substack{pa\\rb}}(t,t') \equiv \mathrm{i}\, G^{\mathrm{R}}_{pa}(t,t')\, G^{\mathrm{A}}_{br}(t',t), \qquad \rho^{(2)>}_{\substack{aq\\bs}}(t') \equiv \big(\rho_{aq}(t')-\delta_{aq}\big)\rho_{sb}(t'). \qquad (77)$$

The two-time function P^{R} can be interpreted as the propagator of an electron-hole pair. Notice that $G^{\mathrm{R}}(t^+,t) = -\mathrm{i}$ and $G^{\mathrm{A}}(t,t^+) = \mathrm{i}$, and hence

$$P^{\mathrm{R}}_{\substack{pa\\rb}}(t^+,t) = \mathrm{i}\delta_{pa}\delta_{rb} \qquad (78)$$

or equivalently

$$P^{\mathrm{R}}_{\alpha\beta}(t^+,t) = \mathrm{i}\delta_{\alpha\beta}. \qquad (79)$$

For $t < t'$ the GKBA implies

$$\chi^{0,>}_{\substack{pq\\rs}}(t,t') = \mathrm{i}\underbrace{\sum_a \big(\rho_{pa}(t)-\delta_{pa}\big)G^{\mathrm{A}}_{aq}(t,t')}_{G^{>}_{pq}(t,t')}\underbrace{\sum_b G^{\mathrm{R}}_{sb}(t',t)\rho_{br}(t)}_{-G^{<}_{sr}(t',t)} = -\sum_{ab}\rho^{(2)>}_{\substack{pa\\rb}}(t)P^{\mathrm{A}}_{\substack{aq\\bs}}(t,t'), \quad (80)$$

where

$$P^{\mathrm{A}}_{\substack{aq\\bs}}(t,t') \equiv -\mathrm{i}\, G^{\mathrm{A}}_{aq}(t,t')G^{\mathrm{R}}_{sb}(t',t) = \Big(P^{\mathrm{R}}_{\substack{qa\\sb}}(t',t)\Big)^*. \qquad (81)$$

Using the superindex convention, the greater response function in GKBA for any t and t' then reads

$$\chi^{0,>}_{\alpha\beta}(t,t') = \sum_\mu \Big(P^{\mathrm{R}}_{\alpha\mu}(t,t')\rho^{(2)>}_{\mu\beta}(t') - \rho^{(2)>}_{\alpha\mu}(t)P^{\mathrm{A}}_{\mu\beta}(t,t')\Big). \qquad (82)$$

An analogous derivation can be carried out for the lesser response function. The final result is identical to Eq. (82) but the matrix $\rho^{(2)>}$ is replaced by the matrix

$$\rho^{(2)<}_{\substack{aq\\bs}}(t) \equiv \rho_{aq}(t)\big(\rho_{sb}(t)-\delta_{sb}\big). \qquad (83)$$

Hence

$$\chi^{0,<}_{\alpha\beta}(t,t') = \sum_\mu \Big(P^{\mathrm{R}}_{\alpha\mu}(t,t')\rho^{(2)<}_{\mu\beta}(t') - \rho^{(2)<}_{\alpha\mu}(t)P^{\mathrm{A}}_{\mu\beta}(t,t')\Big). \qquad (84)$$

We are now ready to transform $\mathcal{G}$ into an explicit functional of the one-particle density matrix. Taking into account that $\bar{t} < t$ in Eq. (75), we obtain (in matrix form) [2–4]

$$\boldsymbol{\mathcal{G}}(t) = \mathrm{i}\int_{-\infty}^t d\bar{t}\, \boldsymbol{P}^{\mathrm{R}}(t,\bar{t})\Big(\boldsymbol{\rho}^{(2)>}(\bar{t})\boldsymbol{w}\boldsymbol{\rho}^{(2)<}(\bar{t}) - \boldsymbol{\rho}^{(2)<}(\bar{t})\boldsymbol{w}\boldsymbol{\rho}^{(2)>}(\bar{t})\Big)\boldsymbol{P}^{\mathrm{A}}(\bar{t},t), \qquad (85)$$

where boldface letters are used to distinguish matrices in the two-particle space from matrices like G, h or Σ in the one-particle space. The quadratic scaling of the NEGF+GKBA approach is evident from Eq. (85): a time step from t to $t + \delta t$ necessitates the calculation of $\mathcal{G}(t)$, and $\mathcal{G}(t)$ contains an integral whose upper limit grows like t.

$$\begin{cases} I_{il} = -\mathrm{i} \sum_{rpn} v_{irpn} \, \mathcal{G}_{\substack{pl \\ rn}} \\[2ex] \Psi \equiv \rho^{(2)>} w \rho^{(2)<} - \rho^{(2)<} w \rho^{(2)>} \\[2ex] \rho^{(2)<}_{\substack{aq \\ bs}} \equiv \rho_{aq}(\rho_{sb} - \delta_{sb}) \\[2ex] \rho^{(2)>}_{\substack{aq \\ bs}} \equiv (\rho_{aq} - \delta_{aq})\rho_{sb} \\[2ex] h^{(2)}_{\mathrm{HF},\substack{pc \\ rd}} = h_{\mathrm{HF},pc}\delta_{rd} - \delta_{pc}h_{\mathrm{HF},dr} \end{cases}$$

$$\frac{d}{dt}\rho + \mathrm{i}\Big[h_{\mathrm{HF}}, \rho\Big] = -(I + I^{\dagger})$$

$$\frac{d}{dt}\mathcal{G} + \mathrm{i}\Big[h^{(2)}_{\mathrm{HF}}, \mathcal{G}\Big] = \mathrm{i}\Psi$$

Fig. 3: *Summary of the fundamental equations and definitions for NEGF+GKBA simulations in the 2B approximation.*

9 Time-linear scaling and state-of-the-art approximations

Important progress has been recently achieved in reducing the computational scaling of the NEGF+GKBA equations to the ideal linear law [2], and in establishing that the time-linear scaling holds for the 2B approximation as well as for state-of-the-art diagrammatic methods like GW and T-matrix (both in the particle-hole and particle-particle channels) [3]. In Ref. [4] the time-linear scaling formulation has been further extended to GW plus exchange, T-matrix plus exchange and self-energies with three-particle correlations. Furthermore, in Ref. [5] a GKBA has been introduced also for *bosonic* Green functions, and a time-linear scaling formulation for real-time simulations of nonequilibrium systems of interacting electrons and bosons, e.g., phonons or photons, has been established here too.

The fundamental observation is that the two-particle propagator $\boldsymbol{P}^{\mathrm{R}}$ satisfies an elementary equation of motion. Taking into account that G^{R} and G^{A} are approximated at the HF level, see Eq. (50), we get for any $t > \bar{t}$

$$\mathrm{i}\frac{d}{dt}P^{\mathrm{R}}_{\substack{pa \\ rb}}(t,\bar{t}) = \sum_c h_{\mathrm{HF},pc}(t) P^{\mathrm{R}}_{\substack{ca \\ rb}}(t,\bar{t}) - \sum_d h_{\mathrm{HF},dr}(t) P^{\mathrm{R}}_{\substack{ca \\ db}}(t,\bar{t}). \tag{86}$$

Introducing the HF Hamiltonian in the two-particle space

$$h^{(2)}_{\mathrm{HF},\substack{pc \\ rd}}(t) = h_{\mathrm{HF},pc}(t)\delta_{rd} - \delta_{pc}h_{\mathrm{HF},dr}(t), \tag{87}$$

we can rewrite the equation of motion for $\boldsymbol{P}^{\mathrm{R}}$ in matrix form as follows

$$\mathrm{i}\frac{d}{dt}\boldsymbol{P}^{\mathrm{R}}(t,\bar{t}) = \boldsymbol{h}^{(2)}_{\mathrm{HF}}(t)\boldsymbol{P}^{\mathrm{R}}(t,\bar{t}), \qquad t > \bar{t}. \tag{88}$$

Let us now come to $\boldsymbol{P}^{\mathrm{A}}$. In matrix form Eq. (81) reads $\boldsymbol{P}^{\mathrm{A}}(\bar{t},t) = \big(\boldsymbol{P}^{\mathrm{R}}(t,\bar{t})\big)^{\dagger}$. Taking the hermitian conjugate of Eq. (88) we then get

$$-\mathrm{i}\frac{d}{dt}\boldsymbol{P}^{\mathrm{A}}(\bar{t},t) = \boldsymbol{P}^{\mathrm{A}}(\bar{t},t)\boldsymbol{h}^{(2)}_{\mathrm{HF}}(t), \qquad t > \bar{t}, \tag{89}$$
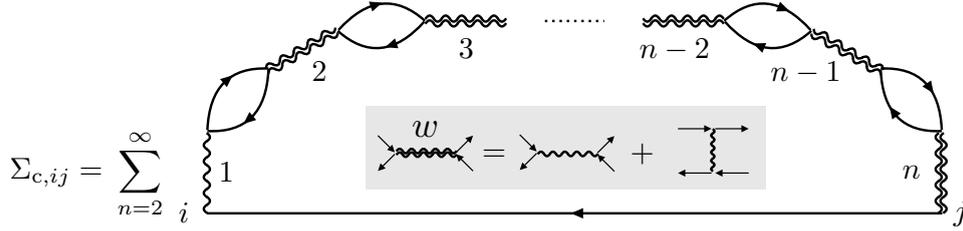
Fig. 4: *Diagrams for the GW+X self-energy.*

where we have observed that the matrix $\boldsymbol{h}_{\mathrm{HF}}^{(2)}$ is hermitian in the two-particle space, i.e., $h_{\mathrm{HF},\alpha\beta}^{(2)} = h_{\mathrm{HF},\beta\alpha}^{(2)*}$. The equations of motion for $\boldsymbol{P}^{\mathrm{R}}$ and $\boldsymbol{P}^{\mathrm{A}}$ can be used to construct an equation of motion for $\boldsymbol{\mathcal{G}}$. Recalling the rule

$$\frac{d}{dt} \int^t d\bar{t}\, f(t,\bar{t}) = f(t^+,t) + \int^t d\bar{t}\, \frac{d}{dt} f(t,\bar{t}), \tag{90}$$

where f is an arbitrary function of two times, we find from Eq. (85)

$$\mathrm{i}\frac{d}{dt}\boldsymbol{\mathcal{G}}(t) = -\boldsymbol{\Psi}(t) + \boldsymbol{h}_{\mathrm{HF}}^{(2)}(t)\boldsymbol{\mathcal{G}}(t) - \boldsymbol{\mathcal{G}}(t)\boldsymbol{h}_{\mathrm{HF}}^{(2)}(t), \tag{91}$$

with

$$\boldsymbol{\Psi}(t) \equiv \boldsymbol{\rho}^{(2)>}(t)\boldsymbol{w}\boldsymbol{\rho}^{(2)<}(t) - \boldsymbol{\rho}^{(2)<}(t)\boldsymbol{w}\boldsymbol{\rho}^{(2)>}(t). \tag{92}$$

Equation (91) together with the equation of motion for ρ, see Eq. (69), form a closed system of ordinary differential equations [2, 3]. Thus the numerical solution of the time-dependent 2B approximation in NEGF+GKBA scales linearly with the maximum propagation time, which was to be demonstrated. For the benefit of the reader we summarize in Fig. 3 the main equations and definitions.

We have already mentioned that the linear scaling of the NEGF+GKBA equations is not limited to the 2B approximation. In what follows we derive the NEGF+GKBA equations for the GW plus exchange (GW+X) approximation. As we shall see the difference with the 2B approximation, Eq. (91), is only minor. Readers who wish to immediately compare 2B with GW+X or who prefer to go through the derivation in a second reading can jump directly to Eq. (110).

The GW+X self-energy is displayed in Fig. 4 where the double wiggly lines represent the tensor w defined in Eq. (72), see also the diagrammatic representation of w in the grey box of Fig. 4. The well known GW self-energy is recovered by neglecting the exchange contribution in w, i.e., by setting $w_{\substack{qj \\ sm}} = v_{mqsj}$ (first term on the right hand side of the diagrammatic equation in the grey box). The figure shows the diagrams of order n in the interaction strength. The first term of the sum has $n = 2$ and it coincides with the 2B self-energy of Fig. 2. Thus, the GW+X self-energy is obtained from the 2B self-energy of Eq. (51) upon replacing the bare response function $\chi_{\substack{pq \\ rs}}^0(z,z') \equiv -\mathrm{i}G_{pq}(z,z')G_{sr}(z',z)$, cf. Eq. (73), with the RPA response function (in matrix form)

$$\boldsymbol{\chi}(z,z') = \boldsymbol{\chi}^0(z,z') + \int_\gamma d\bar{z}\, \boldsymbol{\chi}^0(z,\bar{z})\, \boldsymbol{w}\, \boldsymbol{\chi}(\bar{z},z'). \tag{93}$$

This implies that the collision integral can again be written as in Eq. (74), but the function $\mathcal{G}$ changes into

$$\mathcal{G}(t) = -\mathrm{i} \int_{-\infty}^{t} d\bar{t} \left(\boldsymbol{\chi}^{>}(t,\bar{t}) \, \boldsymbol{w} \, \boldsymbol{\chi}^{0,<}(\bar{t},t) - \boldsymbol{\chi}^{<}(t,\bar{t}) \, \boldsymbol{w} \, \boldsymbol{\chi}^{0,>}(\bar{t},t) \right). \tag{94}$$

We point out that at this point we have not yet used the GKBA to transform $\mathcal{G}$ into a functional of the density matrix.

Before using the GKBA we extract the lesser and greater components of the RPA response function. They follows from Eq. (93) when setting $z = t_{-/+}$ and $z' = t_{+/-}$. Manipulating the contour integral as we did in Eq. (57) until Eq. (62) we get

$$\boldsymbol{\chi}^{\lessgtr}(t,t') = \boldsymbol{\chi}^{0,\lessgtr}(t,t') + \int d\bar{t} \left(\boldsymbol{\chi}^{0,\mathrm{R}}(t,\bar{t}) \, \boldsymbol{w} \, \boldsymbol{\chi}^{\lessgtr}(\bar{t},t') + \boldsymbol{\chi}^{0,\lessgtr}(t,\bar{t}) \, \boldsymbol{w} \, \boldsymbol{\chi}^{\mathrm{A}}(\bar{t},t') \right). \tag{95}$$

Unless otherwise stated undefined integrals are over the entire real axis, i.e., $\int \equiv \int_{-\infty}^{\infty}$. We can use Eq. (95) to calculate the retarded and advanced components which, we recall, are defined for any two-times correlator in Eqs. (59) and (60). For the retarded response function we find

$$\boldsymbol{\chi}^{\mathrm{R}}(t,t') = \boldsymbol{\chi}^{0,\mathrm{R}}(t,t') + \Theta(t-t') \int d\bar{t} \, \boldsymbol{\chi}^{0,\mathrm{R}}(t,\bar{t}) \, \boldsymbol{w} \left[\boldsymbol{\chi}^{>}(\bar{t},t') - \boldsymbol{\chi}^{<}(\bar{t},t') \right]$$

$$+ \Theta(t-t') \int d\bar{t} \left[\boldsymbol{\chi}^{0,>}(t,\bar{t}) - \boldsymbol{\chi}^{0,<}(t,\bar{t}) \right] \boldsymbol{w} \, \boldsymbol{\chi}^{\mathrm{A}}(\bar{t},t'). \tag{96}$$

Consider the last term in this expression. It vanishes unless $t > t'$, due to the theta function $\Theta(t-t')$, and $t' > \bar{t}$, due to the theta function hidden in $\boldsymbol{\chi}^{\mathrm{A}}$. We can then multiply the integrand by $\Theta(t-\bar{t})$ and hence replace the square bracket with $\boldsymbol{\chi}^{0,\mathrm{R}}(t,\bar{t})$. Taking into account Eq. (61) to rewrite the square bracket in the second term we then see that the products $\boldsymbol{\chi}^{0,\mathrm{R}} \, \boldsymbol{w} \, \boldsymbol{\chi}^{\mathrm{A}}$ cancel off and we remain with

$$\boldsymbol{\chi}^{\mathrm{R}}(t,t') = \boldsymbol{\chi}^{0,\mathrm{R}}(t,t') + \int d\bar{t} \, \boldsymbol{\chi}^{0,\mathrm{R}}(t,\bar{t}) \, \boldsymbol{w} \, \boldsymbol{\chi}^{\mathrm{R}}(\bar{t},t'). \tag{97}$$

The advanced response function can be worked out similarly; the result is the same as Eq. (97) with $\mathrm{R} \to \mathrm{A}$.

The equations for $\boldsymbol{\chi}^{\mathrm{R/A}}$ are useful to isolate $\boldsymbol{\chi}^{\lessgtr}$ in Eq. (95). To lighten the notation let us denote with a dot the convolution between two functions. Thus Eq. (95) can be shorten into $\boldsymbol{\chi}^{\lessgtr} = \boldsymbol{\chi}^{0,\lessgtr} + \boldsymbol{\chi}^{0,\mathrm{R}} \, \boldsymbol{w} \cdot \boldsymbol{\chi}^{\lessgtr} + \boldsymbol{\chi}^{0,\lessgtr} \, \boldsymbol{w} \cdot \boldsymbol{\chi}^{\mathrm{A}}$ and similarly Eq. (97) becomes $\boldsymbol{\chi}^{\mathrm{R}} = \boldsymbol{\chi}^{0,\mathrm{R}} + \boldsymbol{\chi}^{0,\mathrm{R}} \, \boldsymbol{w} \cdot \boldsymbol{\chi}^{\mathrm{R}}$. The dot can of course go to the left of $\boldsymbol{w}$ as well. Notice that the retarded equation can be solved iteratively to give

$$\begin{aligned}
\boldsymbol{\chi}^{\mathrm{R}} &= \boldsymbol{\chi}^{0,\mathrm{R}} + \boldsymbol{\chi}^{0,\mathrm{R}} \, \boldsymbol{w} \cdot \boldsymbol{\chi}^{0,\mathrm{R}} + \boldsymbol{\chi}^{0,\mathrm{R}} \, \boldsymbol{w} \cdot \boldsymbol{\chi}^{0,\mathrm{R}} \, \boldsymbol{w} \cdot \boldsymbol{\chi}^{0,\mathrm{R}} + \dots \\
&= \boldsymbol{\chi}^{0,\mathrm{R}} + \left(\boldsymbol{\chi}^{0,\mathrm{R}} + \boldsymbol{\chi}^{0,\mathrm{R}} \, \boldsymbol{w} \cdot \boldsymbol{\chi}^{0,\mathrm{R}} + \dots \right) \boldsymbol{w} \cdot \boldsymbol{\chi}^{0,\mathrm{R}} \\
&= \boldsymbol{\chi}^{0,\mathrm{R}} + \boldsymbol{\chi}^{\mathrm{R}} \boldsymbol{w} \cdot \boldsymbol{\chi}^{0,\mathrm{R}}.
\end{aligned} \tag{98}$$

In other words $\boldsymbol{\chi}^{\mathrm{R}} \, \boldsymbol{w} \cdot \boldsymbol{\chi}^{0,\mathrm{R}} = \boldsymbol{\chi}^{0,\mathrm{R}} \, \boldsymbol{w} \cdot \boldsymbol{\chi}^{\mathrm{R}}$. Let us go back to Eq. (95). Isolating $\boldsymbol{\chi}^{\lessgtr}$ we get

$$\left(\boldsymbol{\delta} - \boldsymbol{\chi}^{0,\mathrm{R}} \, \boldsymbol{w} \right) \cdot \boldsymbol{\chi}^{\lessgtr} = \boldsymbol{\chi}^{0,\lessgtr} \cdot \left(\boldsymbol{\delta} + \boldsymbol{w} \, \boldsymbol{\chi}^{\mathrm{A}} \right), \tag{99}$$

where $\boldsymbol{\delta}$ stands for the Dirac delta, hence for any two-times correlator $\mathcal{C}$ we have $[\boldsymbol{\delta} \cdot \mathcal{C}](t, t') = \int d\bar{t}\, \boldsymbol{\delta}(t - \bar{t})\, \mathcal{C}(\bar{t}, t') = \mathcal{C}(t, t')$. Next we observe that

$$\left(\boldsymbol{\delta} + \boldsymbol{\chi}^{\mathrm{R}}\, \boldsymbol{w}\right) \cdot \left(\boldsymbol{\delta} - \boldsymbol{\chi}^{0,\mathrm{R}}\, \boldsymbol{w}\right) = \boldsymbol{\delta} + \left(\boldsymbol{\chi}^{\mathrm{R}} - \boldsymbol{\chi}^{0,\mathrm{R}} - \boldsymbol{\chi}^{\mathrm{R}}\, \boldsymbol{w} \cdot \boldsymbol{\chi}^{0,\mathrm{R}}\right)\boldsymbol{w} = \boldsymbol{\delta}, \qquad (100)$$

since the term in parenthesis vanish, see Eq. (98). Convoluting Eq. (99) with $\left(\boldsymbol{\delta} + \boldsymbol{\chi}^{\mathrm{R}}\, \boldsymbol{w}\right)$ on the right we then find

$$\boldsymbol{\chi}^{\lessgtr} = \left(\boldsymbol{\delta} + \boldsymbol{\chi}^{\mathrm{R}}\, \boldsymbol{w}\right) \cdot \boldsymbol{\chi}^{0,\lessgtr} \cdot \left(\boldsymbol{\delta} + \boldsymbol{w}\, \boldsymbol{\chi}^{\mathrm{A}}\right). \qquad (101)$$

At this point we have all ingredients to evaluate $\mathcal{G}$ using the GKBA. From Eqs. (82) and (84) we first obtain the GKBA expression of the retarded/advanced bare response functions

$$\boldsymbol{\chi}^{0,\mathrm{R}}(t, t') = \boldsymbol{P}^{\mathrm{R}}(t, t')\boldsymbol{\rho}^{(2),\Delta}(t'), \qquad \boldsymbol{\chi}^{0,\mathrm{A}}(t, t') = \boldsymbol{\rho}^{(2),\Delta}(t)\boldsymbol{P}^{\mathrm{A}}(t, t'), \qquad (102)$$

where we have defined

$$\boldsymbol{\rho}^{(2),\Delta}(t) \equiv \boldsymbol{\rho}^{(2),>}(t) - \boldsymbol{\rho}^{(2),<}(t). \qquad (103)$$

Inserting Eq. (102) into Eq. (97) and in the analogous equation for $\boldsymbol{\chi}^{\mathrm{A}}$ we obtain the GKBA expression for the retarded/advanced RPA response functions

$$\boldsymbol{\chi}^{\mathrm{R}}(t, t') = \boldsymbol{\Pi}^{\mathrm{R}}(t, t')\boldsymbol{\rho}^{(2),\Delta}(t'), \qquad \boldsymbol{\chi}^{\mathrm{A}}(t, t') = \boldsymbol{\rho}^{(2),\Delta}(t)\boldsymbol{\Pi}^{\mathrm{A}}(t, t'), \qquad (104)$$

where the dressed electron-hole propagators satisfy the integral equation

$$\boldsymbol{\Pi}^{\mathrm{R}} = \boldsymbol{P}^{\mathrm{R}} + \boldsymbol{P}^{\mathrm{R}} \cdot \boldsymbol{\rho}^{(2),\Delta}\, \boldsymbol{w}\, \boldsymbol{\Pi}^{\mathrm{R}} = \boldsymbol{P}^{\mathrm{R}} + \boldsymbol{\Pi}^{\mathrm{R}} \cdot \boldsymbol{\rho}^{(2),\Delta}\, \boldsymbol{w}\, \boldsymbol{P}^{\mathrm{R}}, \qquad (105a)$$

$$\boldsymbol{\Pi}^{\mathrm{A}} = \boldsymbol{P}^{\mathrm{A}} + \boldsymbol{P}^{\mathrm{A}} \cdot \boldsymbol{w}\, \boldsymbol{\rho}^{(2),\Delta}\, \boldsymbol{\Pi}^{\mathrm{A}} = \boldsymbol{P}^{\mathrm{A}} + \boldsymbol{\Pi}^{\mathrm{A}} \cdot \boldsymbol{w}\, \boldsymbol{\rho}^{(2),\Delta}\, \boldsymbol{P}^{\mathrm{A}}. \qquad (105b)$$

Here and below the product of a one-time function A and a two-times function B is intended as $[AB](t, t') \equiv A(t)B(t, t')$ and $[BA](t, t') = B(t, t')A(t')$. Thus in Eqs. (105) the convolution dot could actually be placed anywhere between $\boldsymbol{P}^{\mathrm{R/A}}$ and $\boldsymbol{\Pi}^{\mathrm{R/A}}$. Using the GKBA expression for $\boldsymbol{\chi}^{0,\lessgtr}$ in Eqs. (82) and (84) as well as the GKBA expression for $\boldsymbol{\chi}^{\mathrm{R/A}}$ in Eq. (104) the lesser/greater RPA response function in Eq. (101) becomes

$$\boldsymbol{\chi}^{\lessgtr} = \left(\boldsymbol{\delta} + \boldsymbol{\Pi}^{\mathrm{R}}\boldsymbol{\rho}^{(2),\Delta}\, \boldsymbol{w}\right) \cdot \left(\boldsymbol{P}^{\mathrm{R}}\boldsymbol{\rho}^{(2),\lessgtr} - \boldsymbol{\rho}^{(2),\lessgtr}\boldsymbol{P}^{\mathrm{A}}\right) \cdot \left(\boldsymbol{\delta} + \boldsymbol{w}\, \boldsymbol{\rho}^{(2),\Delta}\boldsymbol{\Pi}^{\mathrm{A}}\right)$$

$$= \boldsymbol{\Pi}^{\mathrm{R}}\boldsymbol{\rho}^{(2),\lessgtr} \cdot \left(\boldsymbol{\delta} + \boldsymbol{w}\, \boldsymbol{\rho}^{(2),\Delta}\boldsymbol{\Pi}^{\mathrm{A}}\right) - \left(\boldsymbol{\delta} + \boldsymbol{\Pi}^{\mathrm{R}}\boldsymbol{\rho}^{(2),\Delta}\, \boldsymbol{w}\right) \cdot \boldsymbol{\rho}^{(2),\lessgtr}\boldsymbol{\Pi}^{\mathrm{A}}. \qquad (106)$$

This result allows for rewriting $\mathcal{G}$ in Eq. (94) in a very elegant form. Taking into account that

for any $\bar{t} < t$ Eqs. (82) and (84) imply $\boldsymbol{\chi}^{0,\lessgtr}(\bar{t},t) = -[\boldsymbol{\rho}^{(2),\lessgtr}\boldsymbol{P}^{\mathrm{A}}](\bar{t},t)$ we find

$$
\boldsymbol{\mathcal{G}}(t) = \mathrm{i}\bigg[\bigg(\underbrace{\boldsymbol{\Pi}^{\mathrm{R}}\boldsymbol{\rho}^{(2),>}\cdot(\boldsymbol{\delta}+\boldsymbol{w}\,\boldsymbol{\rho}^{(2),\varDelta}\boldsymbol{\Pi}^{\mathrm{A}}) - (\boldsymbol{\delta}+\boldsymbol{\Pi}^{\mathrm{R}}\boldsymbol{\rho}^{(2),\varDelta}\,\boldsymbol{w})\cdot\boldsymbol{\rho}^{(2),>}\boldsymbol{\Pi}^{\mathrm{A}}}_{\boldsymbol{\chi}^>}\bigg)\cdot\boldsymbol{w}\,\underbrace{\boldsymbol{\rho}^{(2),<}\boldsymbol{P}^{\mathrm{A}}}_{-\boldsymbol{\chi}^{0,<}}\bigg](t,t)
$$

$$
- \Big[> \leftrightarrow < \Big]
$$

$$
= \mathrm{i}\Big[\boldsymbol{\Pi}^{\mathrm{R}}\boldsymbol{\rho}^{(2),>}\boldsymbol{w}\boldsymbol{\rho}^{(2),<}\cdot\boldsymbol{P}^{\mathrm{A}} + \boldsymbol{\Pi}^{\mathrm{R}}\big(\underbrace{\boldsymbol{\rho}^{(2),>}\boldsymbol{w}\boldsymbol{\rho}^{(2),\varDelta}-\boldsymbol{\rho}^{(2),\varDelta}\boldsymbol{w}\boldsymbol{\rho}^{(2),>}}_{-\boldsymbol{\Psi}}\big)\cdot\boldsymbol{\Pi}^{\mathrm{A}}\cdot\boldsymbol{w}\boldsymbol{\rho}^{(2),<}\boldsymbol{P}^{\mathrm{A}}\Big](t,t)
$$

$$
- \mathrm{i}\Big[\boldsymbol{\Pi}^{\mathrm{R}}\boldsymbol{\rho}^{(2),<}\boldsymbol{w}\boldsymbol{\rho}^{(2),>}\cdot\boldsymbol{P}^{\mathrm{A}} + \boldsymbol{\Pi}^{\mathrm{R}}\big(\underbrace{\boldsymbol{\rho}^{(2),<}\boldsymbol{w}\boldsymbol{\rho}^{(2),\varDelta}-\boldsymbol{\rho}^{(2),\varDelta}\boldsymbol{w}\boldsymbol{\rho}^{(2),<}}_{-\boldsymbol{\Psi}}\big)\cdot\boldsymbol{\Pi}^{\mathrm{A}}\cdot\boldsymbol{w}\boldsymbol{\rho}^{(2),>}\boldsymbol{P}^{\mathrm{A}}\Big](t,t)
$$

$$
= \mathrm{i}\Big[\boldsymbol{\Pi}^{\mathrm{R}}\boldsymbol{\Psi}\cdot\boldsymbol{P}^{\mathrm{A}} + \boldsymbol{\Pi}^{\mathrm{R}}\boldsymbol{\Psi}\cdot\boldsymbol{\Pi}^{\mathrm{A}}\cdot\boldsymbol{w}\,\boldsymbol{\rho}^{(2),\varDelta}\boldsymbol{P}^{\mathrm{A}}\Big](t,t)
$$

$$
= \mathrm{i}\Big[\boldsymbol{\Pi}^{\mathrm{R}}\boldsymbol{\Psi}\cdot\boldsymbol{\Pi}^{\mathrm{A}}\Big](t,t), \tag{107}
$$

where in the second equality we have observed that $[\boldsymbol{\rho}^{(2),\gtrless}\boldsymbol{\Pi}^{\mathrm{A}}\cdot\boldsymbol{w}\,\boldsymbol{\rho}^{(2),\lessgtr}\boldsymbol{P}^{\mathrm{A}}](t,t) = 0$ since $\boldsymbol{\Pi}^{\mathrm{A}}$ contains a $\Theta(\bar{t}-t)$ and $\boldsymbol{P}^{\mathrm{A}}$ contains a $\Theta(t-\bar{t})$. We have also recognized the quantity $\boldsymbol{\Psi}$ defined in Eq. (92). Making explicit the time integration, the function $\boldsymbol{\mathcal{G}}$ in the GW+X approximation has the following compact and elegant form

$$
\boldsymbol{\mathcal{G}}(t) = \mathrm{i}\int_{-\infty}^{t} d\bar{t}\,\boldsymbol{\Pi}^{\mathrm{R}}(t,\bar{t})\,\boldsymbol{\Psi}(t)\boldsymbol{\Pi}^{\mathrm{A}}(\bar{t},t). \tag{108}
$$

It is now easy to prove that also the GW+X method scales linearly in time. Taking into account the equation of motion (88) for $\boldsymbol{P}^{\mathrm{R}}$ and the rule in Eq. (90) we find from Eq. (105a)

$$
\mathrm{i}\frac{d}{dt}\boldsymbol{\Pi}^{\mathrm{R}}(t,t') = \boldsymbol{h}_{\mathrm{HF}}^{(2)}(t)\boldsymbol{P}^{\mathrm{R}}(t,t') + \mathrm{i}\frac{d}{dt}\int_{-\infty}^{t} d\bar{t}\,\boldsymbol{P}^{\mathrm{R}}(t,\bar{t})\boldsymbol{\rho}^{(2),\varDelta}(t)\,\boldsymbol{w}\,\boldsymbol{\Pi}^{\mathrm{R}}(\bar{t},t')
$$

$$
= \Big(\boldsymbol{h}_{\mathrm{HF}}^{(2)}(t) - \boldsymbol{\rho}^{(2),\varDelta}(t)\,\boldsymbol{w}\Big)\boldsymbol{\Pi}^{\mathrm{R}}(t,t'). \tag{109}
$$

Equation (105a) also implies that $\boldsymbol{\Pi}^{\mathrm{R}}(t^+,t) = \mathrm{i}$ and that $\boldsymbol{\Pi}^{\mathrm{A}}(t',t) = [\boldsymbol{\Pi}^{\mathrm{R}}(t,t')]^\dagger$. Thus, using again the rule in Eq. (90)

$$
\mathrm{i}\frac{d}{dt}\boldsymbol{\mathcal{G}}(t) = -\boldsymbol{\Psi}(t) + \boldsymbol{h}_{\mathrm{eff}}^{(2)}(t)\boldsymbol{\mathcal{G}}(t) - \boldsymbol{\mathcal{G}}(t)\boldsymbol{h}_{\mathrm{eff}}^{(2)\dagger}(t), \tag{110}
$$

where

$$
\boldsymbol{h}_{\mathrm{eff}}^{(2)}(t) \equiv \boldsymbol{h}_{\mathrm{HF}}^{(2)}(t) - \boldsymbol{\rho}^{(2),\varDelta}(t)\,\boldsymbol{w}. \tag{111}
$$

Comparing this result with the 2B equation of motion (91) we conclude that the only change brought about by the GW+X approximation is the replacement of $\boldsymbol{h}_{\mathrm{HF}}^{(2)}$ with the effective Hamiltonian $\boldsymbol{h}_{\mathrm{eff}}^{(2)}$. The effective Hamiltonian is not hermitian and therefore the last two terms in Eq. (110) cannot be grouped to form a commutator.

Similar derivations can be carried out for the T-matrix approximation in the particle-particle and particle-hole channels (with and without exchange diagrams), see Refs. [2–4]. In Ref. [4] an

extension of the GKBA to higher order Green functions has been put forward to include three-particle correlations while preserving the linear time-scaling. Another promising extension is the GKBA for bosonic Green functions to deal with systems of electrons interacting with quantized photons or phonons [5]. In this case too it is possible to build propagation algorithms that scale linearly in time [5]. Importantly, these methodological advances can be merged to treat the electron-electron, electron-phonon and electron-photon interactions on equal footing [6], thus opening the door for the investigation of a broad range of nonequilibrium correlated phenomena. Implementations of the NEGF+GKBA equations in high performance computer facilities are therefore foreseeable in the next few years.

10 First-principles NEGF+GKBA implementations

The NEGF+GKBA equations can be applied to finite systems like atoms and molecules as well as to extended systems like solids and interfaces. Of course, the most suitable basis to describe a certain phenomenon depends on the system *and* on the external driving. For the sake of definiteness we consider a finite system subject to an external time-dependent electric field $\mathbf{E}(t)$. Treating the light-matter interaction in the dipole approximation the one-particle Hamiltonian reads

$$h_{ij}(t) = h_{ij}^{\text{eq}} + \mathbf{E}(t) \cdot \mathbf{D}_{ij}, \tag{112}$$

where $\mathbf{D}_{ij} = (D_{ij}^{x}, D_{ij}^{y}, D_{ij}^{z})$ is a matrix element of the dipole vector.

In general a finite system is described by a one-particle basis made of active states and core states. The population of the active states is different from 0 or 1 because of dynamical correlations or thermal fluctuations or external fields whereas the population of the core states is frozen to unity. We can work in the truncated space spanned by the active states provided that the HF potential of the core electrons is added to h^{eq}. Henceforth we use the letter c for indices running in the space of core states and the letters i, j, m, n for indices running in the active space. We split the Hartree and exchange potentials into a core-electrons (ce) contribution and an active-electrons (ae) contribution

$$\left(V_{\text{H,ce}}[\rho]\right)_{ij} = \sum_{cc'} v_{icc'j}\rho_{c'c}, \qquad \left(V_{\text{H,ae}}[\rho]\right)_{ij} = \sum_{mn} v_{imnj}\rho_{nm}, \tag{113}$$

$$\left(V_{\text{x,ce}}[\rho]\right)_{ij} = -\sum_{cc'} v_{icjc'}\rho_{c'c}, \qquad \left(V_{\text{x,ae}}[\rho]\right)_{ij} = -\sum_{mn} v_{imjn}\rho_{nm}. \tag{114}$$

The full HF potential with indices in the active space is simply given by $V_{\text{HF}} = V_{\text{H,ce}} + V_{\text{H,ae}} + V_{\text{x,ce}} + V_{\text{x,ae}}$, see Eq. (46). Taking into account that $\rho_{cc'} = \delta_{cc'}$, the equilibrium HF Hamiltonian in Eq. (49) can be rewritten as

$$h_{\text{HF}}[\rho] = h^{\text{eq+ce}} + V_{\text{H,ae}}[\rho] + V_{\text{x,ae}}[\rho], \tag{115}$$

where

$$h^{\text{eq+ce}} = h^{\text{eq}} + V_{\text{H,ce}} + V_{\text{x,ce}} \tag{116}$$

is the one-particle Hamiltonian plus the HF potential generated by the frozen core-electrons. Thus, replacing h^{eq} with $h^{\text{eq+ce}}$ in Eq. (112) we can solve the NEGF+GKBA equations directly in the active space.

In the next sections we shall describe how to perform first-principles NEGF+GKBA simulations using two different types of basis. More details can be found in Ref. [48].

10.1 Kohn-Sham basis

We here consider the case of a Kohn-Sham (KS) basis [49–51] and assume that electrons in the KS core orbitals remain frozen and do not participate to the dynamics. The equilibrium KS one-particle density matrix in the KS basis reads $\rho_{\text{KS},nm} = \delta_{nm}$. The equilibrium KS Hamiltonian in the same basis is diagonal and reads

$$h_{\text{KS}} = h^{\text{eq}} + V_{\text{H,ce}} + V_{\text{H,ae}}[\rho_{\text{KS}}] + V_{\text{xc}}, \tag{117}$$

where V_{xc} is the exchange-correlation (xc) potential of Density Functional Theory (DFT). In general, $V_{\text{H,ce}} + V_{\text{xc}}$ is given by the sum of the pseudopotential and the xc potential generated by the active electrons. A comparison with Eq. (115) allows us to express $h^{\text{eq+ce}}$ in terms of the KS Hamiltonian according to

$$h^{\text{eq+ce}} = h_{\text{KS}} - V_{\text{xc}} - V_{\text{H,ae}}[\rho_{\text{KS}}] + V_{\text{x,ce}}. \tag{118}$$

Thus a first-principles NEGF+GKBA simulation needs as input the KS eigenvalues $\varepsilon_i^{\text{KS}}$ (needed to construct the KS Hamiltonian $h_{\text{KS},ij} = \delta_{ij}\varepsilon_i^{\text{KS}}$), the matrix elements $V_{\text{xc},ij}$, $\mathbf{D}_{ij}$ and the Coulomb integrals v_{ijmn} for the evaluation of the Hartree potential $V_{\text{H,ae}}[\rho_{\text{KS}}]$ generated by the active KS electrons, see Eq. (118), as well as for the evaluation of the functionals $V_{\text{H,ae}}[\rho]$ and $V_{\text{x,ae}}[\rho]$, see Eq. (115), and for the quantities $\boldsymbol{\Psi}$, see Eq. (92), and $\boldsymbol{h}_{\text{eff}}^{(2)}$, see Eq. (111). In this way the only remaining unknown is $V_{\text{x,ce}}$ which, however, is usually small and can be neglected. One could estimate this quantity by performing an all-electron KS calculation without pseudopotentials.

10.2 Localized basis

For a description in terms of N one-particle localized states $\{|i\rangle\}$ like, e.g., the Slater type orbitals (STO) [52, 53] or the Gaussian type orbitals (GTO) [54], we need the matrix elements of the equilibrium Hamiltonian $h_{ij}^{\text{eq}} = \langle i|\frac{\hat{p}^2}{2m} + \hat{V}_{\text{n}}|j\rangle$ (V_{n} being the nuclear potential), dipole vector $\mathbf{D}_{ij} = \langle i|\hat{\mathbf{r}}|j\rangle$, overlap matrix $S_{ij} = \langle i|j\rangle$ and Coulomb integrals $v_{ijmn} = \langle ij|\hat{v}|mn\rangle$. As our equations have been formulated in an *orthonormal* basis the very first step consists in the orthonormalization of the localized (STO or GTO) basis

$$|i\rangle \rightarrow \sum_m |m\rangle\, S_{mi}^{-1/2}, \tag{119}$$

and in expressing the matrices h^{eq}, $\mathbf{D}$ and the Coulomb tensor v in the new orthonormal basis. To reduce the dimensionality of the one-particle Hilbert space we must perform a preliminary

self-consistent HF calculation in the orthonormal basis of Eq. (119), and then construct the orthonormal HF vectors $|i_{\mathrm{HF}}\rangle = \sum_m \varphi_m^{(i)}|m\rangle$ with HF energies $\varepsilon_i^{\mathrm{HF}}$. The HF states $|i_{\mathrm{HF}}\rangle = |c_{\mathrm{HF}}\rangle$ of energy $\varepsilon_c^{\mathrm{HF}} < \Lambda$ are considered as core states. Setting the vacuum energy at zero the energy cut-off Λ is typically of the order of -10^2 eV. The best way to exploit the fixed occupation of the core states is then to work in the HF basis since in this basis $\rho_{cc'} = \delta_{cc'}$. This means that we must calculate the matrix elements h_{ij}^{eq}, $\mathbf{D}_{ij}$ and the Coulomb tensor v_{ijmn} in the HF basis. To determine $h^{\mathrm{eq+ce}}$ we use its definition in Eq. (116) which in the HF basis yields

$$h_{ij}^{\mathrm{eq+ce}} = h_{ij}^{\mathrm{eq}} + \sum_{cc'} \left(v_{icc'j} - v_{icjc'}\right)\rho_{c'c} = h_{ij}^{\mathrm{eq}} + \sum_c \left(v_{iccj} - v_{icjc}\right). \tag{120}$$

This equation tells us that in addition to v_{ijmn} with all indices in the active space we also need to calculate v_{iccj} and v_{icjc} for all core indices c and for all active indices i, j.

The main limitation of the STO or GTO basis is that the continuum part of the one-particle spectrum is, in general, poorly described and hence phenomena like photo-induced ionization and Auger decay cannot be simulated. In phenomena like electron transport or photoabsorption the electrons do instead remain bound to the system and a description in terms of localized orbitals can be made accurate at will.

References

[1] G. Stefanucci and R. van Leeuwen: *Nonequilibrium Many-Body Theory of Quantum Systems: A Modern Introduction* (Cambridge University Press, 2013)

[2] N. Schlünzen, J.P. Joost, and M. Bonitz, Phys. Rev. Lett. **124**, 076601 (2020)

[3] J.P. Joost, N. Schlünzen, and M. Bonitz, Phys. Rev. B **101**, 245101 (2020)

[4] Y. Pavlyukh, E. Perfetto, and G. Stefanucci, Phys. Rev. B, in press (2021)

[5] D. Karlsson, R. van Leeuwen, Y. Pavlyukh, E. Perfetto, and G. Stefanucci, Phys. Rev. Lett., in press (2021)

[6] Y. Pavlyukh, D. Karlsson, R. van Leeuwen, E. Perfetto, and G. Stefanucci, in preparation

[7] N. Säkkinen, Y. Peng, H. Appel, and R. van Leeuwen, J. Chem. Phys. **143**, 234102 (2015)

[8] P.M.M.C. de Melo and A. Marini, Phys. Rev. B **93**, 155102 (2016)

[9] M. Schüler, J. Berakdar, and Y. Pavlyukh, Phys. Rev. B **93**, 054303 (2016)

[10] M. Gell-Mann and F. Low, Phys. Rev. **84**, 350 (1951)

[11] A.L. Fetter and J.D. Walecka: *Quantum Theory of Many-Particle Systems* (McGraw-Hill, New York, 1971)

[12] L.G. Molinari, J. Math. Phys. **48**, 052113 (2007)

[13] L.V. Keldysh et al., Sov. Phys. JETP **20**, 1018 (1965)

[14] J. Schwinger, J. Math. Phys. **2**, 407 (1961)

[15] O. Konstantinov and V. Perel, Sov. Phys. JETP **12**, 142 (1961)

[16] M. Wagner, Phys. Rev. B **44**, 6104 (1991)

[17] G. Stefanucci and C.O. Almbladh, Phys. Rev. B **69**, 195318 (2004)

[18] E. Perfetto, D. Sangalli, A. Marini, and G. Stefanucci, Phys. Rev. B **94**, 245303 (2016)

[19] R. van Leeuwen and G. Stefanucci, Phys. Rev. B **85**, 115119 (2012)

[20] L.P. Kadanoff and G.A. Baym: *Quantum statistical mechanics: Green's function methods in equilibrium and nonequilibirum problems* (Benjamin, 1962)

[21] N.H. Kwong and M. Bonitz, Phys. Rev. Lett. **84**, 1768 (2000)

[22] N.E. Dahlen and R. van Leeuwen, Phys. Rev. Lett. **98**, 153004 (2007)

[23] P. Myöhänen, A. Stan, G. Stefanucci, and R. van Leeuwen, EPL **84**, 67001 (2008)

[24] M.P. von Friesen, C. Verdozzi, and C.O. Almbladh, Phys. Rev. Lett. **103**, 176404 (2009)

[25] A. Stan, N.E. Dahlen, and R. van Leeuwen, The J. Chem. Phys. **130**, 224101 (2009)

[26] K. Balzer and M. Bonitz: *Nonequilibrium Green's Functions Approach to Inhomogeneous Systems* (Springer, 2013)

[27] P. Lipavský, V. Špička, and B. Velický, Phys. Rev. B **34**, 6933 (1986)

[28] S. Hermanns, N. Schlünzen, and M. Bonitz, Phys. Rev. B **90**, 125111 (2014)

[29] N. Schlünzen and M. Bonitz, Contrib. Plasma Phys. **56**, 5 (2016)

[30] Y. Bar Lev and D.R. Reichman, Phys. Rev. B **89**, 220201 (2014)

[31] S. Latini, E. Perfetto, A.M. Uimonen, R. van Leeuwen, and G. Stefanucci,
Phys. Rev. B **89**, 075306 (2014)

[32] R. Tuovinen, R. van Leeuwen, E. Perfetto, and G. Stefanucci,
J. Chem. Phys. **154**, 094104 (2021)

[33] G. Pal, Y. Pavlyukh, W. Hübner, and H.C. Schneider, Eur. Phys. J. B **79**, 327 (2011)

[34] F. Covito, E. Perfetto, A. Rubio, and G. Stefanucci, Phys. Rev. A **97**, 061401 (2018)

[35] E. Perfetto, A.M. Uimonen, R. van Leeuwen, and G. Stefanucci,
Phys. Rev. A **92**, 033419 (2015)

[36] E. Perfetto, D. Sangalli, A. Marini, and G. Stefanucci, Phys. Rev. B **92**, 205304 (2015)

[37] D. Sangalli, S. Dal Conte, C. Manzoni, G. Cerullo, and A. Marini,
Phys. Rev. B **93**, 195205 (2016)

[38] E.A.A. Pogna, M. Marsili, D. De Fazio, S. Dal Conte, C. Manzoni, D. Sangalli, D. Yoon,
A. Lombardo, A.C. Ferrari, A. Marini, G. Cerullo, and D. Prezzi,
ACS Nano **10**, 1182 (2016)

[39] Sangalli, D. and Marini, A., EPL **110**, 47004 (2015)

[40] R. Tuovinen, D. Golež, M. Eckstein, and M.A. Sentef, Phys. Rev. B **102**, 115157 (2020)

[41] E.V. Boström, A. Mikkelsen, C. Verdozzi, E. Perfetto, and G. Stefanucci,
Nano Lett. **18**, 785 (2018)

[42] E. Perfetto, D. Sangalli, A. Marini, and G. Stefanucci,
J. Physical Chem. Lett. **9**, 1353 (2018)

[43] E. Perfetto, D. Sangalli, M. Palummo, A. Marini, and G. Stefanucci,
     J. Chem. Theory Comput. **15**, 4526 (2019)

[44] E. Perfetto, A. Trabattoni, F. Calegari, M. Nisoli, A. Marini, and G. Stefanucci,
     J. Phys. Chem. Lett. **11**, 891 (2020)

[45] H. Haug, Phys. Status Solidi B **173** (1992)

[46] M. Bonitz, D. Semkat, and H. Haug, Eur. Phys. J. B **9**, 309 (1999)

[47] A. Marini, Phys. Rev. Lett. **101**, 106405 (2008)

[48] E. Perfetto and G. Stefanucci, J. Phys: Condens. Matter **30**, 465901 (2018)

[49] P. Giannozzi, S. Baroni, N. Bonini, M. Calandra, R. Car, C. Cavazzoni, D. Ceresoli,
     G.L. Chiarotti, M. Cococcioni, I. Dabo, A.D. Corso, S. de Gironcoli, S. Fabris, G. Fratesi,
     R. Gebauer, U. Gerstmann, C. Gougoussis, A. Kokalj, M. Lazzeri, L. Martin-Samos,
     N. Marzari, F. Mauri, R. Mazzarello, S. Paolini, A. Pasquarello, L. Paulatto, C. Sbraccia,
     S. Scandolo, G. Sclauzero, A.P. Seitsonen, A. Smogunov, P. Umari, and R.M. Wentzcov-
     itch, J. Phys.: Condens. Matter **21**, 395502 (2009)

[50] X. Andrade, D. Strubbe, U. De Giovannini, A.H. Larsen, M.J.T. Oliveira, J. Alberdi-
     Rodriguez, A. Varas, I. Theophilou, N. Helbig, M.J. Verstraete, L. Stella, F. Nogueira,
     A. Aspuru-Guzik, A. Castro, M.A.L. Marques, and A. Rubio,
     Phys. Chem. Chem. Phys. **17**, 31371 (2015)

[51] D. Sangalli, A. Ferretti, H. Miranda, C. Attaccalite, I. Marri, E. Cannuccia, P. Melo,
     M. Marsili, F. Paleari, A. Marrazzo, G. Prandini, P. Bonfà, M.O. Atambo, F. Affinito,
     M. Palummo, A. Molina-Sánchez, C. Hogan, M. Grüning, D. Varsano, and A. Marini,
     J. Phys.: Condens. Matter **31**, 325902 (2019)

[52] J. Fernández Rico, I. Ema, R. López, G. Ramírez and K. Ishida, in *Recent Advances in
     Computational Chemistry: Molecular Integrals over Slater Orbitals*, eds. T. Ozdogan and
     M.B. Ruiz (Transworld Research Network, 2008), pp. 145.

[53] J.F. Rico, R. López, I. Ema, and G. Ramírez, J. Comp. Chem. **25**, 1987 (2004)

[54] Y. Pavlyukh and J. Berakdar, Comp. Phys. Commun. **184**, 387 (2013)

9 Orbital Entanglement and Correlation

Christian Schilling
Arnold Sommerfeld Centre for Theoretical Physics
LMU Munich
Theresienstr. 37, 80333 München, Germany

Contents

1   Introduction

The development of quantum many-body physics has been strongly influenced in recent years by quantum information theory with a particular emphasis on the concept of entanglement. From a general point of view, entanglement is one of the most fascinating concepts of physics and there are at least three distinctive reasons for its significance in various fields of the quantum sciences:

(i) It provides important insights into the properties and behavior of quantum systems such as quantum phase transitions [1–3] and the formation/breaking of chemical bonds [4].

(ii) It serves as a diagnostic tool for the description of quantum many-body states. Hence, its rigorous quantification facilitates the development of more efficient descriptions of strongly interacting systems [5, 6]

(iii) It is an important resource used in the quantum information sciences for realizing, e.g., quantum cryptography [7, 8], superdense coding [9] and possibly even quantum computing [10].

In the more traditional fields such as condensed matter physics and quantum chemistry, however, point (iii) is not sufficiently well acknowledged. In particular, the quantification of entanglement and correlation is often flawed or at least operationally meaningless and the significance of the respective numbers for quantum information processing tasks is therefore unclear. This is due to the fact that the fundamental superselection rule ("nature does not allow one to superpose even and odd fermion number states") is erroneously ignored. In quantum information theory, however, entanglement is often studied in an abstract mathematical context, often decoupled from concrete physical systems. It is not unlikely that this huge separation between the worlds of quantum many-body physicists and quantum information theorists will have rather unpleasant consequences for the interface between those two fields. As a matter of fact, this interface is gaining a lot of relevance in recent years due to the ongoing second quantum revolution which may shape the 21st century as much as the first quantum revolution has shaped the 20th century: Individual quantum systems, such as atoms and molecules shall be controlled to a much greater extent than before to enable more powerful applications of quantum information. This apparently would necessitate a thorough understanding of entanglement and various other correlations types in the context of fermionic quantum systems both on a fundamental and an applied level. Due to the expected transformative impact of this second quantum revolution this challenging task can even be seen as a key strategic goal for the near-term future (see also the illustration in figure 1).

Accordingly, the main motivation of these lecture notes is to provide an introduction into the concept of entanglement and correlation in the context of fermionic quantum systems taking into account the needs of both quantum information scientists and quantum many-body physicists. For this, we recall and discuss on a more elementary level concepts that were already
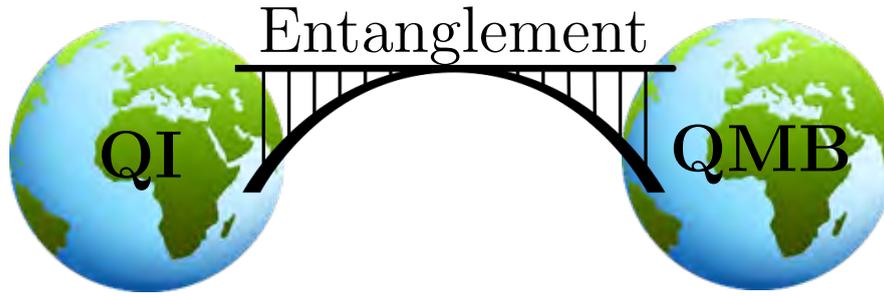
Fig. 1: *Strategic ambition for the quantum sciences: The connection between the worlds of quantum information (QI) and quantum many body physics (QMB) needs to be strengthened with a particular focus on entanglement as the unifying concept.*

presented in our recent articles [11, 12]. In section 2, we first recall the definition of entanglement and correlation in systems of *distinguishable* particles and then explain how those key concepts can be applied in the context of *identical* particles (mainly electrons). In particular, we explain the superselection rule and demonstrate that ignoring it would mean to violate fundamental laws of physics. Then, in section 3 we illustrate those concepts by applying them to smaller model systems which facilitate a fully analytical treatment. In section 4 we finally study more realistic systems (water, naphthalene and dichromium molecules) by exact numerical means and quantify the orbital correlation and its separation into quantum and classical parts.

2   Concept of correlation and entanglement

2.1   The quantum information theoretical formalism

The notion of correlation and entanglement plays a central role in quantum physics. In this section, we review those concepts and their quantification in the context of *distinguishable* subsystems as commonly studied in quantum information theory. We restrict ourselves to the most important case of bipartite settings and refer the reader to Refs. [13,14] for an introduction into the concept of multipartite correlation and entanglement.

To introduce the concepts of entanglement and correlation, we first recall a few important aspects regarding quantum states and their geometry. Although it is illustrative to deal with wave functions, e.g., $\psi(\vec{r}, \sigma)$, as one can use them to construct probability clouds for atomic and molecular orbitals visualization, it is advantageous to adopt the representation-free formalism of density operators, acting on an underlying (for simplicity finite-dimensional) Hilbert space $\mathcal{H}$. This facilitates more direct and compact definitions of correlation and entanglement. As a matter of fact, both concepts refer solely to a decomposition of the system into two (or more) subsystems and do not depend on any possible choice of basis states for those subsystems. In this formalism, a quantum state is represented by a Hermitian operator ρ that is positive semi-definite (i.e., having non-negative eigenvalues) and trace-normalized to unity, $\mathrm{Tr}[\rho] = 1$, reflecting the probabilistic nature of quantum mechanics. For the following considerations it

will prove convenient to introduce and briefly discuss the set $\mathcal{D}$ of all density operators on a given finite-dimensional complex Hilbert space $\mathcal{H}$:

$$\mathcal{D} \equiv \{\rho : \mathcal{H} \xrightarrow{\text{linear}} \mathcal{H} \,|\, \rho^\dagger = \rho \,\wedge\, \rho \geq 0 \,\wedge\, \text{Tr}[\rho] = 1\}. \tag{1}$$

Exercise 2.1

Prove that in case of finite-dimensional complex Hilbert spaces $\mathcal{H}$ the Hermiticity of ρ is a direct mathematical consequence of its positive semi-definiteness (and therefore would not need to be imposed separately), i.e., show that $\rho \geq 0$ implies $\rho^\dagger = \rho$.

Exercise 2.2

Prove that the set $\mathcal{D}$ of density operators is convex.

Equipped with the common notion of density operators, we can now discuss the concept of expectation values of physical observables. The expectation value $\langle \hat{A} \rangle_\rho$ of an observable represented by a Hermitian operator $\hat{A}$ follows according to Born's rule as

$$\langle \hat{A} \rangle_\rho = \text{Tr}[\rho \hat{A}]. \tag{2}$$

The set of all Hermitian operators generated through multiplication gives rise to the algebra $\mathcal{B}(\mathcal{H})$ of all linear operators on $\mathcal{H}$. For the sake of mathematical elegance one typically refers to $\mathcal{B}(\mathcal{H})$ as the *algebra of observables* despite the fact that it contains also non-Hermitian operators. It is also worth noticing that — in contrast to $\mathcal{B}(\mathcal{H})$ — the real vector space of Hermitian operators on $\mathcal{H}$ does not exhibit any algebraic structure since this set is not closed under multiplication, i.e., the product of two Hermitian operators is not necessarily Hermitian anymore. While the expression (2) of the expectation value of an observable is one of the key concepts thought in any quantum mechanics course, a crucial observation is often left out. To be more specific, the compact form (2) reveals a more comprehensive and systematic notation of quantum states: A quantum state is a linear, positive semi-definite map $\langle \cdot \rangle_\rho$ from the algebra of observables to the complex numbers, normalized to unity $\langle \hat{1} \rangle_\rho = 1$. The density operator just defines this map according to (2). At first sight, this comment seems to be a bit pedantic and overly mathematical. Yet, this more comprehensive notion of quantum states will allow one to define the concept of reduced states in a rather straightforward manner (as we will see below) while in the concrete formalism based on density operators and wave functions several obstacles may arise. The latter often leads in practice to confusion and occasionally even to wrong expressions for the reduced density operators of subsystems.

Exercise 2.3

Let $\rho_1, \rho_2 \in \mathcal{D}$ be two density operators on the finite dimensional Hilbert space $\mathcal{H}$. Show that the following two statements are equivalent:

1. $\rho_1 = \rho_2$,

2. $\langle \hat{A} \rangle_{\rho_1} = \langle \hat{A} \rangle_{\rho_2}$, for all $\hat{A} \in \mathcal{B}(\mathcal{H})$.

Remark. The equivalence described in Exercise 2.3 is not valid anymore if the algebra $\mathcal{A}$ of observables is restricted, i.e., it does not contain all linear operators on the Hilbert space, $\mathcal{A} \subsetneq \mathcal{B}(\mathcal{H})$. As we will learn in the next section, this will be the case for fermionic quantum systems whose algebras of observables are restricted by the fundamental superselection rule to only those operators that are not altering the particle number parity.

To develop some intuition for the convex space of density operators and quantum states, respectively, we observe that the boundary of $\mathcal{D}$ is given by those $\rho \in \mathcal{D}$ which have at least one vanishing eigenvalue. In particular, the extreme points (those that cannot be written as a convex combination of others) are given by the pure states, $\rho \equiv |\Psi\rangle\langle\Psi|$. From a general point of view, the space $\mathcal{D}$ of quantum states could be interpreted as a subset of the Hermitian matrices with $\dim(\mathcal{H})$ many rows and columns. In that sense the space $\mathcal{D}$ can be equipped with a suitable metric. Examples include the distance metric based on the Frobenius norm, $d_F(\rho, \sigma) = \|\rho - \sigma\|_F \equiv \sqrt{\mathrm{Tr}(\rho - \sigma)^2}$, or the Bures distance $d_B(\rho, \sigma) = \mathrm{Tr}[\sqrt{\sqrt{\rho}\,\sigma\sqrt{\rho}}]^2$. For further details on the geometry of density matrices and respective metrics we refer the reader to Refs. [15–17].

One of the important conclusions from those geometric considerations is that the possible similarity of two density operators ρ, σ can be quantified in a universal way, i.e., without referring to a specific observable, despite the fact that ρ, σ do not carry any physical unit. In particular, whenever two quantum states are close to each other in the state space $\mathcal{D}$, their expectation values will be close to each other for any observable as well. This follows directly from the Cauchy-Schwarz inequality, $|\langle \hat{A}, \hat{B}\rangle| \leq \sqrt{|\langle \hat{A}, \hat{A}\rangle|}\sqrt{|\langle \hat{B}, \hat{B}\rangle|}$ applied to the Hilbert-Schmidt inner product, $\langle \hat{A}, \hat{B}\rangle \equiv \mathrm{Tr}\hat{A}^\dagger\hat{B}$,

$$\left|\langle \hat{A}\rangle_\rho - \langle \hat{A}\rangle_\sigma\right| = \left|\mathrm{Tr}\hat{A}(\rho - \sigma)\right| \leq \|\hat{A}\|_F \, d_F(\rho, \sigma). \tag{3}$$

To fully appreciate relation (3) let us recall that two quantum states with, e.g., the same energy can still differ in their expectation values of other relevant observables.

All considerations so far were just referring to the total system. The discussion of interesting physics refers, however, to a notion of subsystems. Let us consider in the following a quantum system which can be split into two subsystems A and B, occasionally also called Alice's and Bob's subsystem. In the common quantum information theoretical formalism those two subsystems are assumed to be distinguishable and its states are described by density operators ρ_{AB} on the total Hilbert space $\mathcal{H}_{AB} \equiv \mathcal{H}_A \otimes \mathcal{H}_B$, where $\mathcal{H}_{A/B}$ denotes the local Hilbert space of subsystem A/B. The underlying algebra $\mathcal{A}_{AB}$ of observables of the total system follows in the same way from the local algebras, $\mathcal{A}_{AB} \equiv \mathcal{A}_A \otimes \mathcal{A}_B$. The presence of a multipartite quantum system in particular allows us to introduce the important notion of reduced states corresponding to subsystems. To work this out, we consider a local measurement corresponding to $\hat{A} \in \mathcal{B}(\mathcal{H}_A)$. Its expectation value follows directly as

$$\langle \hat{A} \otimes \hat{1}_B\rangle_\rho = \mathrm{Tr}\rho(\hat{A} \otimes \hat{1}_B). \tag{4}$$

Since such a measurement is essentially restricted to only Alice's subsystem, there exists a local description of the quantum state, with respect to which the expectation of any local operator $\hat{A}$

is the same as (4). This is the commonly used reduced density operator defined as

$$\rho_A \equiv \mathrm{Tr}_B\,\rho, \tag{5}$$

which satisfies

$$\langle \hat{A}\rangle_{\rho_A} = \langle \hat{A}\otimes\hat{1}_B\rangle_\rho, \quad \forall \hat{A}\in\mathcal{B}(\mathcal{H}_A). \tag{6}$$

It is exactly the content of Exercise 2.3 which proves the existence and uniqueness of this reduced density operator. In this context, it is also worth noticing that the more abstract notion of a quantum state as a linear map from the algebra of observables to the complex numbers would allow one to define on a mathematical level the reduced state in a particularly simple manner: The reduced state is given by the reduction of the total state to the subalgebra $\mathcal{A}_A\otimes\hat{1}$ (effectively $\mathcal{A}_A$). Then, by referring to the Riesz representation theorem, the existence of a corresponding density operator ρ_A follows directly.

Exercise 2.4

Calculate the reduced density operator ρ_A on the subsystem A of the two-qubit state

$$|\Psi\rangle = \frac{1}{\sqrt{3}}|0\rangle_A\otimes|0\rangle_B + \frac{1}{\sqrt{3}}|1\rangle_A\otimes|0\rangle_B + \frac{1}{\sqrt{3}}|0\rangle_A\otimes|1\rangle_B.$$

To proceed, we notice that a particularly relevant class of observables in $\mathcal{A}_{AB}$ are the local ones, i.e, those of the form $\hat{A}\otimes\hat{B}$. As a matter of fact, they correspond to simultaneous measurements of $\hat{A}$ on subsystem A and $\hat{B}$ on subsystem B. To understand the relation between both subsystems, one would be interested in understanding how the respective measurements of both local measurements are correlated. As a matter of definition, they are uncorrelated if the expectation value of $\hat{A}\otimes\hat{B}$ factorizes,

$$\begin{aligned}
\langle \hat{A}\otimes\hat{B}\rangle_{\rho_{AB}} &\equiv \mathrm{Tr}_{AB}\,\rho_{AB}\,\hat{A}\otimes\hat{B}\\
&= \mathrm{Tr}_{AB}[\rho_{AB}\,\hat{A}\otimes\hat{1}_B]\,\mathrm{Tr}_{AB}[\rho_{AB}\,\hat{1}_A\otimes\hat{B}]\\
&\equiv \mathrm{Tr}_A[\rho_A\,\hat{A}]\,\mathrm{Tr}_B[\rho_B\,\hat{B}] \equiv \langle\hat{A}\rangle_{\rho_A}\langle\hat{B}\rangle_{\rho_B}.
\end{aligned} \tag{7}$$

In the second line we introduced the identity operator $\hat{1}_{A/B}\in\mathcal{A}_{A/B}$ and the last line gives rise to the reduced density operators $\rho_{A/B}\equiv\mathrm{Tr}_{B/A}\,\rho_{AB}$ of subsystems A/B obtained by tracing out the complementary subsystem B/A. To quantify the correlation between the measurements of $\hat{A}$ and $\hat{B}$ one thus introduces the correlation function

$$C_{\rho_{AB}}(\hat{A},\hat{B}) \equiv \langle\hat{A}\otimes\hat{B}\rangle_{\rho_{AB}} - \langle\hat{A}\rangle_{\rho_A}\langle\hat{B}\rangle_{\rho_B}. \tag{8}$$

Popular examples are the spin-spin or the density-density correlation functions, i.e., the local operators $\hat{A}$, $\hat{B}$ are given by some spin-component operator $\hat{S}_\tau(\vec{x})$ or the particle density operator $\hat{n}(\vec{x})$ at two different positions $\vec{x}_{A/B}$ in space.

The vanishing of the correlation function for a specific pair of observables $\hat{A}$, $\hat{B}$ does not imply by any means that the same will be the case for any other pair $\hat{A}'$, $\hat{B}'$ of local observables. A

prominent example would be the dissociated hydrogen state

$$|\Psi\rangle = \frac{1}{\sqrt{2}} \left(f_{L\uparrow}^\dagger f_{R\downarrow}^\dagger - f_{L\downarrow}^\dagger f_{R\uparrow}^\dagger \right) |\Omega\rangle, \tag{9}$$

where $f_{L/R\sigma}^\dagger$ denotes the fermionic creation operator for an electron at the left(L)/right(R) nucleus with spin σ, and $|\Omega\rangle$ the vacuum state. Its electron density-density correlation function between the left (L) and right (R) side vanishes in contrast to the respective spin-spin correlation functions. Inspired by this example, one would like to introduce a measure for the correlation between both subsystems without referring to a specific pair of local observables. One idea would be to determine an average of the correlation function $C_{\rho_{AB}}(\hat{A}, \hat{B})$ or its maximal possible value with respect to all possible choices of local observables $\hat{A}, \hat{B}$. At first sight, those two possible measures of total correlation seem to be very difficult (if not impossible) to calculate for a given ρ_{AB}. Yet, by referring to the geometric picture of density operators the introduction of a total correlation measure turns into a rather simple task. To explain this, we first define

Definition 2.1 (Uncorrelated States) *Let $\mathcal{H}_{AB} \equiv \mathcal{H}_A \otimes \mathcal{H}_B$ be the Hilbert space and $\mathcal{A}_{AB} \equiv \mathcal{A}_A \otimes \mathcal{A}_B$ the algebra of observables of a bipartite system AB, with local Hilbert spaces $\mathcal{H}_{A/B}$ and local algebras $\mathcal{A}_{A/B}$. A state ρ_{AB} on $\mathcal{H}_{AB}$ is called uncorrelated, if and only if*

$$\langle \hat{A} \otimes \hat{B} \rangle_{\rho_{AB}} = \langle \hat{A} \rangle_{\rho_A} \langle \hat{B} \rangle_{\rho_B}, \tag{10}$$

for all local observables $\hat{A} \in \mathcal{A}_A$, $\hat{B} \in \mathcal{A}_B$. The set of uncorrelated states is denoted by $\mathcal{D}_0$ and states $\rho_{AB} \notin \mathcal{D}_0$ are said to be correlated.

A comment is in order regarding the local algebras $\mathcal{A}_{A/B}$ that play a crucial role in definition 2.1. In the context of distinguishable subsystems one typically assumes that $\mathcal{A}_{A/B}$ comprises all Hermitian operators on the local space $\mathcal{H}_{A/B}$. As a consequence, a state ρ_{AB} is then uncorrelated if and only if it is a product state, $\rho_{AB} = \rho_A \otimes \rho_B$. This conclusion is, however, not true anymore if one would consider in definition 2.1 smaller subalgebras [18]. Actually, exactly this will be necessary in fermionic quantum systems due to the number parity superselection rule [19].

By referring to the geometric picture of density operators a measure for the total correlation between A and B follows naturally. It is given by the distance of ρ_{AB} to the set $\mathcal{D}_0$ of uncorrelated states (see also figure 2 for an illustration). In principle one could base such a measure on any possible distance-function. Yet, the notion of correlation and entanglement is formalized in quantum information theory by imposing plausible axioms defining valid measures, complemented by preferable features to guarantee an operational meaning [13, 14]. While further details on that subject matter would go beyond the scope of these lecture notes, we just would like to stress that the quantum relative entropy,

$$S(\rho||\sigma) = \operatorname{Tr}\rho\left(\log(\rho) - \log(\sigma)\right), \tag{11}$$

emerges as the preferable underlying function for a geometric correlation (and entanglement) measure (despite the fact that it is not a distance function in the strict mathematical sense) [20].

Besides its information theoretical meaning, the quantum relative entropy has additional appealing properties. For instance, it is invariant under unitary transformations,

$$S(\rho||\sigma) = S(U\rho U^\dagger || U\sigma U^\dagger) \tag{12}$$

and it is convex in both arguments. The total correlation measures follow as [21, 22]

$$I(\rho_{AB}) \equiv \min_{\sigma_{AB} \in \mathcal{D}_0} S(\rho_{AB}||\sigma_{AB}) = S(\rho_{AB}||\rho_A \otimes \rho_B). \tag{13}$$

Remarkably, the distinguished properties of the quantum relative entropy allow one to determine the minimizer $\sigma_{AB} \in \mathcal{D}_0$ of ρ_{AB}'s distance to $\mathcal{D}_0$ analytically. It follows as $\sigma_{AB} = \rho_A \otimes \rho_B$ and the correlation is nothing else than the quantum mutual information $I(\rho_{AB})$. The latter has a clear information theoretical meaning which emphasizes the significance of the total correlation measure (13). It quantifies the information content in the state ρ_{AB} which is not yet contained in the local states ρ_A, ρ_B.

> **Exercise 2.5**
>
> Prove that the following three definitions of the mutual information I are equivalent:
>
> 1. $I(\rho_{AB}) = S(\rho_A) + S(\rho_B) - S(\rho_{AB})$,
>
> 2. $I(\rho_{AB}) = S(\rho_{AB}||\rho_A \otimes \rho_B)$,
>
> 3. $I(\rho_{AB}) = \min_{\sigma_A, \sigma_B} S(\rho||\sigma_A \otimes \sigma_B)$.

We proceed by stating a crucial relation [23] between the total correlation (13) and individual correlation functions (8),

$$\frac{C_{\rho_{AB}}(\hat{A}, \hat{B})}{\|\hat{A}\|_F \|\hat{B}\|_F} \leq \sqrt{2\log(2)}\sqrt{I(\rho_{AB})}. \tag{14}$$

This means in particular that the correlation function of *any* two local observables $\hat{A}, \hat{B}$ is small whenever the quantum mutual information is small.

> **Exercise 2.6**
>
> Prove the crucial inequality (14). Hint: Combine (3) applied to the observable $\hat{A} \otimes \hat{B}$ with a well-known relation between the quantum relative entropy and the Frobenius norm (see, e.g., Theorem 10.6 in Ref. [24]).

A possibly large total correlation suggests that the accurate description of the total system AB requires significantly more computational effort than the one of both individual subsystems A, B (in case they were entirely decoupled). While this is rather unfortunate for a quantum chemist or a condensed matter theorist (they are interested in an accurate description of such systems) the opposite is true from a quantum informational point of view. To be more specific, primarily the quantum part of the total correlation represents an important resource for realizing quantum information processing tasks such as quantum cryptography [7, 8], superdense coding [9],

quantum teleportation [25] and possibly even quantum computing [10]. Typical protocols for realizing such fascinating tasks utilize so-called Bell pairs, i.e., maximally entangled pure state of two qubits (two-level quantum systems), e.g.,

$$|\Psi\rangle = \frac{1}{\sqrt{2}}\Big(|\uparrow\rangle_A \otimes |\downarrow\rangle_B - |\downarrow\rangle_A \otimes |\uparrow\rangle_B\Big). \tag{15}$$

It is thus one of the most important challenges to rigorously quantify the number of such Bell pairs that could be extracted from a given correlated quantum state ρ_{AB}. It is not hard to imagine that a correlated quantum state $\rho_{AB} = \sum_i p_i \, \rho_A^{(i)} \otimes \rho_B^{(i)}$ which is given as the *classical mixture* of uncorrelated states $\rho_A^{(i)} \otimes \rho_B^{(i)}$ does not offer any useful resource in that context: The system AB is found in uncorrelated states $\rho_A^{(i)} \otimes \rho_B^{(i)}$ yet there is a classical probabilistic uncertainty in which of them it will be in. To elaborate further on the quantification of entanglement one defines

Definition 2.2 (Separable States) *A state ρ_{AB} is called separable/non-entangled if ρ_{AB} can be expressed as a convex linear combination of uncorrelated states, that is $\rho_{AB} \in \mathrm{Conv}(\mathcal{D}_0) \equiv \mathcal{D}_{sep}$. Otherwise a state is called entangled.*

Here, $\mathrm{Conv}(\cdot)$ stands for the convex hull and the term *separable* is frequently used in quantum information theory for denoting non-entangled states. In these lecture notes, we will use these two terms interchangeably.

In complete analogy to the concept of total correlation one has formulated plausible axioms for valid and operationally meaningful entanglement measures [13, 14]. By referring the reader to Ref. [22] for more details, it is again the geometric picture which leads to a prominent entanglement measure, the

$$E(\rho_{AB}) \equiv \min_{\sigma_{AB} \in \mathcal{D}_{sep}} S(\rho_{AB}||\sigma_{AB}). \tag{16}$$

It measures in terms of the quantum relative entropy (11) the minimal distance of ρ_{AB} to the set $\mathcal{D}_{sep}$ of separable states. This and the general geometric picture is illustrated in figure 2. The set $\mathcal{D}_0$ of uncorrelated states (recall definition 2.1) is shown as a black curve. According to definition 2.2, its convex hull $\mathcal{D}_{sep} \equiv \mathrm{Conv}(\mathcal{D}_0)$ comprises all separable/non-entangled states while the remaining density operators (gray area) are entangled. The geometric correlation and entanglement measures are given by the closest distance from a general state $\rho \equiv \rho_{AB}$ to the sets $\mathcal{D}_0$ (red dashed) and $\mathcal{D}_{sep}$ (red), respectively. Since the uncorrelated states are in particular non-entangled, $\mathcal{D}_0 \subset \mathcal{D}_{sep}$, the entanglement can never exceed the total correlation,

$$I(\rho_{AB}) \geq E(\rho_{AB}). \tag{17}$$

In contrast to the total correlation, there is no explicit analytical expression known for the relative entropy of entanglement in case of general mixed states and even its numerical calculation is typically quite demanding. That is quite different in case of pure states, $\rho_{AB} = |\Psi_{AB}\rangle\langle\Psi_{AB}|$, since (16) then simplifies to the entanglement entropy which is defined as the von Neumann entropy of the reduced density operators of subsystem A and B, respectively [26, 27],

$$E(|\Psi_{AB}\rangle\langle\Psi_{AB}|) = S(\rho_{A/B}) = -\mathrm{Tr}\,\rho_{A/B} \log(\rho_{A/B}). \tag{18}$$
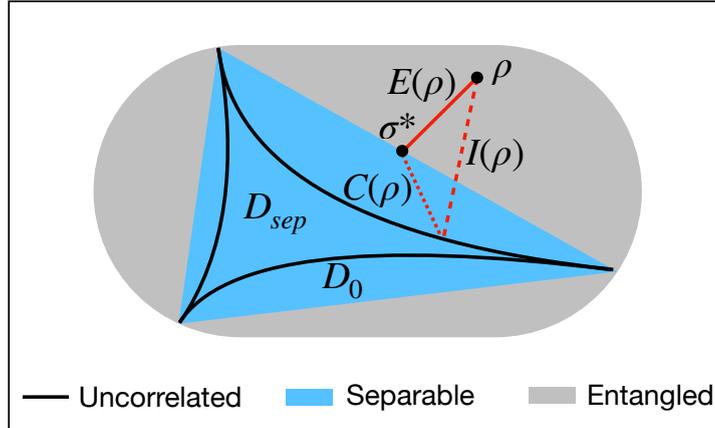
Fig. 2: *Schematic illustration of the space $\mathcal{D}$ of quantum states. Family $\mathcal{D}_0$ of uncorrelated states shown as thick black line and the separable states (its convex hull $\mathcal{D}_{sep}$) reside in the blue area. The grey area represents the entangled states and the red (dashed) line the geometric entanglement (classical correlation) measure $E(\rho)$ ($I(\rho)$). From a more heuristic point of view, one defines the classical correlation $C(\rho)$ as the quantum relative entropy between the closest separable and closest uncorrelated state.*

It is equivalent to calculate the entanglement entropy with either ρ_A or ρ_B, as they have the same eigenvalues in case of pure total states [28] and one has $E(|\Psi_{AB}\rangle\langle\Psi_{AB}|) = 0$ if and only if $|\Psi_{AB}\rangle$ factorizes. In that context, we also would like to recall that for mixed states ρ_{AB} the entanglement entropy (18) is obviously not a good measure for entanglement anymore since the mixedness of the reduced density operators $\rho_{A/B}$ could originate just from possible mixedness in ρ_{AB} (classical correlation).

Actually, knowing the closest separable state, the *classical correlation* of ρ can be quantified geometrically (see figure 2), namely as the distance from the closest separable state σ^* to the closest uncorrelated state $\rho_A \otimes \rho_B$ [29],

$$C(\rho) \equiv S(\sigma^* || \rho_A \otimes \rho_B). \tag{19}$$

We conclude this section with two crucial comments. The first one is concerned with the relation between the different types of correlation. In general, entanglement and classical correlation do not sum to the total correlation. This is because mixed quantum states typically contain quantum correlations beyond entanglement as it is concisely described by the concept of quantum discord [30]. Moreover, a known exact relation including quantum discord refers to an alternative definition of classical correlation which is more technical than our simple geometric one (see Eq. (19)) [30]. Due to its particular significance for quantum information tasks and for the sake of simplicity we focus in our lecture notes on entanglement, however, and refer to it occasionally as quantum correlation.

Last but not least, we would like to stress that for pure total states a remarkable operational meaning of the entanglement entropy (to the base 2) has been found [31, 26]: In the asymptotic limit of n identical two-qubit systems, each in the same pure quantum state shared between two parties A and B with an entanglement entropy S, the number m of maximally entangled

Bell pairs that can be extracted follows as $m = n\,S$. It is exactly this operational meaning of entanglement between distinguishable subsystems which raises some doubts about the common approach to entanglement and correlation in condensed matter physics and quantum chemistry: Applying some partial trace-like map to obtain some type of reduced density operator, possibly even not normalized to unity, and then plugging it into the formula for the von Neumann entropy does not necessarily mean to quantify correlation or entanglement.

2.2 Fermionic quantum systems

The concepts of entanglement and correlation, as reviewed in the previous section, refer to a well-defined separation of the total system into two (or more) distinguishable subsystems. In the simplest case, this separation emerges naturally from the physical structure of the total system, namely by referring to a possible spatial separation of two subsystems. In that case, it will be also easier to experimentally access both subsystems to eventually extract the entanglement from their joint quantum state. Nonetheless, the notion of bipartite correlation and entanglement is by no means unique for a given system since one just needs to identify some tensor product structure in the total system's Hilbert space, $\mathcal{H} \equiv \mathcal{H}_A \otimes \mathcal{H}_B$. In the most general approach, one even defines subsystems by choosing two commuting subalgebras $\mathcal{A}_A, \mathcal{A}_B$ of observables [18]. This also highlights the crucial fact that entanglement and correlation are relative concepts since they refer to a choice of subsystems/subalgebras of observables.

In case of identical fermions the identification of subsystems is not obvious at all. For instance, how could one decompose the underlying N-fermion Hilbert space $\mathcal{H}_N \equiv \wedge^N[\mathcal{H}_1]$ or the Fock space $\mathcal{F} \equiv \oplus_{N \geq 0} \mathcal{H}_N$? Actually, there exist two natural routes which look promising. The first one refers naturally to the 2nd quantized formalism and leads to a notion of *orbital* (sometimes also called mode or site) entanglement and correlation [32–34]. A second and more subtle route [11] which is not covered here is related more to first quantization and tries to define correlation and entanglement in the *particle* picture.

A natural tensor product structure emerges in the formalism of second quantization, facilitating a bipartition on the set of spin-orbitals. To explain this, let us fix a reference basis for the one-particle Hilbert space $\mathcal{H}_1$. We then introduce the corresponding fermionic creation ($f_i^\dagger$) and annihilation operators (f_j), fulfilling the fermionic commutation relations,

$$\{f_i^{(\dagger)}, f_j^{(\dagger)}\} = 0, \quad \{f_i^\dagger, f_j\} = \delta_{ij}. \tag{20}$$

In the quantum information community the one-particle reference states are often referred to as *modes*, or (lattice) sites by condensed matter physicists. Each spin-orbital or generally mode i can be either empty or occupied by a fermion. In this picture, the quantum states are naturally represented in the occupation number basis. The respective *configuration states*

$$|n_1, n_2, \ldots, n_d\rangle = (f_1^\dagger)^{n_1}(f_2^\dagger)^{n_2} \cdots (f_d^\dagger)^{n_d}|\Omega\rangle \tag{21}$$

with $n_1, n_2 \ldots, n_d \in \{0, 1\}$ form a basis for the underlying Fock space

$$\mathcal{F}(\mathcal{H}_1) = \bigoplus_{N=0}^{d} \wedge^N[\mathcal{H}^{(1)}]. \tag{22}$$

Bipartitions naturally arise as separations of the basis $\mathcal{B} = \{|\varphi_j\rangle\}_{j=1}^d$ of reference spin-orbitals into two disjoint subsets $\mathcal{B}_A = \{|\varphi_j\rangle\}_{j=1}^m$, $\mathcal{B}_B = \{|\varphi_j\rangle\}_{j=m+1}^d$. This in turn suggests a splitting of the configuration state according to

$$|n_1, \ldots, n_m, n_{m+1}, \ldots, n_d\rangle \mapsto |n_1, n_2, \ldots n_m\rangle_A \otimes |n_{m+1}, n_{m+2}, \ldots, n_d\rangle_B. \tag{23}$$

The total Fock space $\mathcal{F}(\mathcal{H}_1)$ thus admits the tensor product structure

$$\mathcal{F}_{AB} \equiv \mathcal{F}(\mathcal{H}_1) = \mathcal{F}(\mathcal{H}_1^{(A)}) \otimes \mathcal{F}(\mathcal{H}_1^{(B)}) \equiv \mathcal{F}_A \otimes \mathcal{F}_B, \tag{24}$$

with respect to the given ordering of the spin-orbitals, where $\mathcal{H}_1^{(A/B)}$ denotes the one-particle Hilbert space spanned by the first m and last $d-m$ spin-orbitals, respectively. Actually, any splitting of the one-particle Hilbert space into two complementary subspaces,

$$\mathcal{H}_1 = \mathcal{H}_1^{(A)} \oplus \mathcal{H}_1^{(B)}, \tag{25}$$

induces a respective splitting (24) on the Fock space level.[1] Moreover, such a decomposition of the total Fock space into two factors allows us to introduce orbital reduced density operators $\rho_{A/B}$ for the respective orbital subsystem A/B. They are obtained by taking the partial trace of the total state ρ with respect to the complementary factor $\mathcal{F}_{B/A}$. Consequently, $\rho_{A/B}$ is defined as an operator on the local space $\mathcal{F}_{A/B}$ and in general does not have a definite particle number anymore.

It seems that we can now readily apply the common quantum information theoretical formalism referring to distinguishable subsystems. Yet there is one crucial obstacle. Not every Hermitian operator acting on a fermionic Fock space is a physical observable. For instance, nature does not allow one to coherently superpose even and odd fermion number states [19]. The significance of this *number parity superselection rule* (SSR) is rather obvious as it will be explained in the subsequent section since its violation would equivalently make superluminal signalling possible in contradiction to special relativity. The number parity SSR implies that the algebra of observables on any Fock space comprises only those operators which are block-diagonal with respect to the even and odd fermion number sectors, $\hat{A} = \hat{A}_{ee} + \hat{A}_{oo}$ [35].

2.3   Superselection rules

A key ingredient in the physics of fermionic systems is the so-called *parity superselection rule* (P-SSR). In its original form, P-SSR forbids coherent superpositions of even and odd fermion-numbers states. In a more modern version, P-SSR states that the operators belonging to physically measurable quantities must commute with the parity operator of the particle number. This means they have to be linear combinations of even degree monomials of the fermionic creation and annihilation operators. This in turn implies that a superposition of two pure states with even

---

[1]For the sake of mathematical rigor and conclusiveness, we would like to stress that the corresponding isomorphism $\mathcal{F}_{AB} \to \mathcal{F}_A \otimes \mathcal{F}_B$ is by no means unique. Yet, this changes when we take into account the parity superselection rule as discussed below.
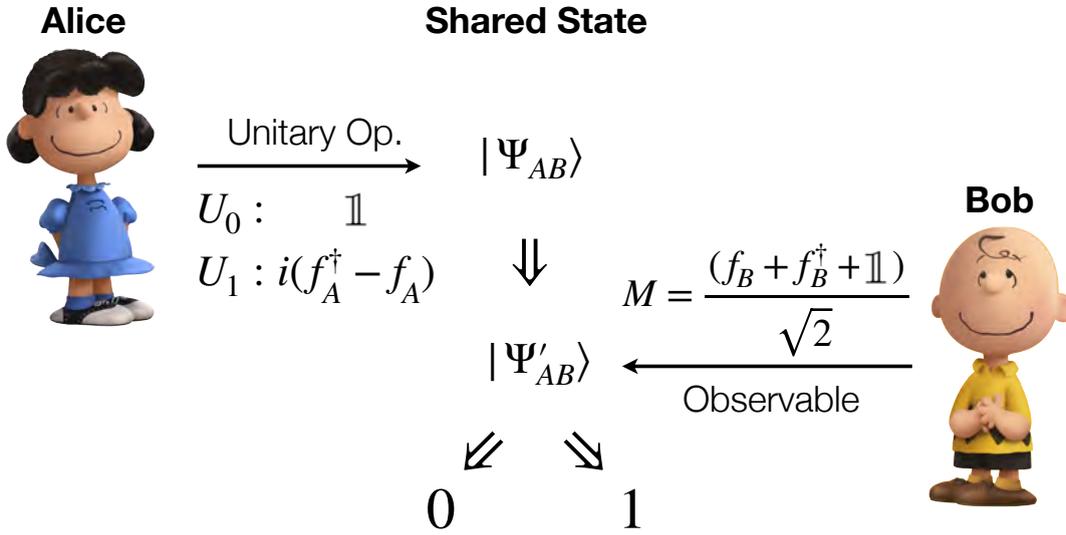
Fig. 3: *The protocol showing how superluminal signaling is possible when parity superselection rule is broken: Alice communicates the bit value $b \in \{0,1\}$ by applying the corresponding unitary U_b, Bob measures the observable M and obtains instantaneously that bit value, as explained in the text.*

and odd particle numbers cannot be distinguished from an incoherent classical mixture of those states, thus one recovers the original formulation as a consequence.

The idea that the laws of nature impose P-SSR on fermionic systems was originally derived based on group theoretical arguments [19, 36, 37]. However, the pertinence of P-SSR is also obvious from the fundamental fact that violation of P-SSR would lead to a violation of the no-signaling theorem, as we will explain in the following. The no-signaling theorem states that two spatially separated parties cannot communicate faster than the speed of light. To relate this fundamental law of physics to the P-SSR, let us assume that two distant parties Alice and Bob could violate the P-SSR. For our argument it is sufficient for Alice and Bob to have each access to one mode (e.g., an atomic spin-orbital). Their local Fock spaces are thus generated by the fermionic annihilation and creation operators $(f_A, f_A^\dagger)$ and $(f_B, f_B^\dagger)$, respectively. Assume now that they can share the state $|\psi\rangle_{AB} = \frac{1}{\sqrt{2}}(|0\rangle_A |0\rangle_B + |0\rangle_A |1\rangle_B)$, which is a superposition of odd and even number states. The procedure for Alice to communicate instantaneously one bit $b = 0, 1$ of classical information to Bob would be the following (see also figure 3): both of them synchronize the clocks in their labs, and they pre-decide to perform local operations at a particular time. If Alice wants to communicate 1, she does nothing (i.e., formally applies the unitary $U_1 = \mathbb{1}$), so $|\psi\rangle_{AB}$ remains unchanged; to communicate 0, Alice applies the unitary $U_0 = i(f_A^\dagger - f_A)$, and the state becomes $|\psi'\rangle_{AB} = \frac{i}{\sqrt{2}}(|1\rangle_A |0\rangle_B + |1\rangle_A |1\rangle_B)$. At the same instant Bob measures the observable $\frac{1}{2}(f_B + f_B^\dagger + \mathbb{1})$. One easily verifies that in both cases $b = 0, 1$ the outcome of that measurement is deterministic and will be nothing else than the value of b. Hence, this proposed procedure allows Alice to communicate instantaneously a bit b of information in contradiction to the no-signaling theorem and the laws of relativity.

> **Exercise 2.7**
>
> Recap various steps of the quantum protocol outlined above and calculate various intermediate quantum states to confirm that violation of the P-SSR would indeed make superluminal signalling possible.

Beside the parity superselection rule, it is often pertinent to consider superselection rules due to some experimental limitations. One such rule is the fermion *particle number superselection rule* (N-SSR). Measurable quantities obeying N-SSR must commute with the particle parity operators [36]. This, in the form of lepton number conservation, was once considered to be an exact symmetry of Nature. Recently, however, there have been indications that fundamental Majorana particles may exist which could lead to a violation of the N-SSR. Nevertheless, in a usual quantum chemistry set-up, we can safely regard N-SSR to hold. Indeed, the energies of common molecular systems are (in contrast to systems studied in high energy physics) sufficiently low to entirely suppress the emergence of electrons and other particles from vacuum fluctuations. In the following parts of the lecture notes we will in particular discuss the consequences of *both* superselection rules, but we assume that the N-SSR is the more relevant one in quantum chemistry.

Having established the fundamental importance of superselection rules, we will now elucidate how they affect our description of quantum states, and consequently change the physically accessible correlation and entanglement in a quantum state. Accordingly, the SSRs will have important consequences for the realization of quantum information processing tasks.

In the following, we will explain on a more abstract level superselection rules by referring to the concept of local symmetries and present a general scheme for taking them into account. The examples provided in Section 3 will then demonstrate those general concepts on a more elementary level by applying them to the particle number and number parity symmetry for electronic quantum systems. From a general point of view, SSRs are restrictions on local algebras of observables, resulting in physical algebras $\mathcal{A}_A$ and $\mathcal{A}_B$. If the SSR is related to some locally conserved quantity $Q_{A/B}$, then local operators must also preserve this quantity. That is, all local observables satisfy

$$\mathcal{A}_{A/B} \ni \mathcal{O}_{A/B} = \sum_q P_q \, \mathcal{O}_{A/B} P_q, \tag{26}$$

where q ranges over all possible value of $Q_{A/B}$ and P_q's are projectors onto the eigensubspaces, i.e., $\mathcal{O}_{A/B}$ are block diagonal in any eigenbasis of $Q_{A/B}$. It follows that different SSRs will lead to drastically different $\mathcal{A}_{A/B}$. The fact that we cannot physically implement every mathematical operator changes the accessibility of quantum states. The fully accessible states are called the physical states, and they satisfy

$$\rho = \sum_{q,q'} P_q \otimes P_{q'} \, \rho \, P_q \otimes P_{q'}, \tag{27}$$

or equivalently

$$\left[\rho, \, Q_{A/B} \right] = 0. \tag{28}$$
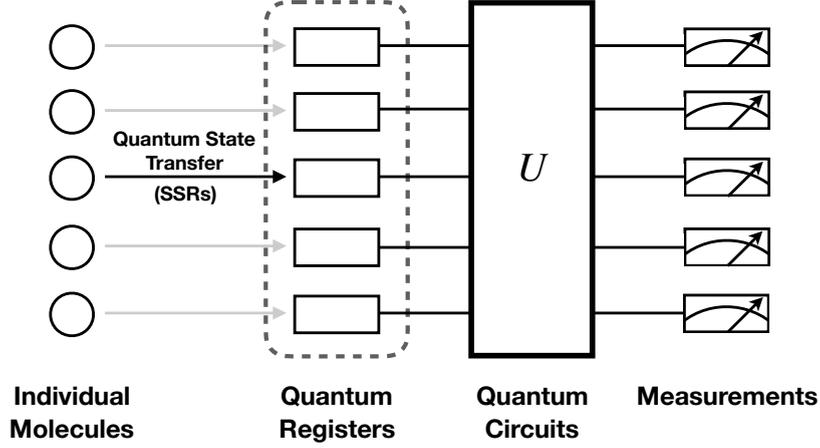
Fig. 4: *Schematic protocol for utilizing entanglement from molecular systems (see text for more details).*

For a general state ρ which does not satisfy (28), we can obtain its physical part by the following projection

$$\rho^{\mathrm{Q}} \equiv \sum_{q,q'} P_q \otimes P_{q'} \, \rho \, P_q \otimes P_{q'}. \tag{29}$$

The physical state ρ^{Q} gives the same expectation value as ρ for all *physical* observables. Therefore we can define a new class of uncorrelated states to be the ones with uncorrelated physical parts with respect to the physical algebra:

$$\mathcal{D}_0^{\mathrm{Q\text{-}SSR}} = \left\{ \rho \,\middle|\, \langle \mathcal{O}_A \otimes \mathcal{O}_B \rangle_\rho = \langle \mathcal{O}_A \rangle_{\rho_A} \langle \mathcal{O}_B \rangle_{\rho_B} \; \forall \mathcal{O}_A \in \mathcal{A}_A, \mathcal{O}_B \in \mathcal{A}_B \right\}. \tag{30}$$

It is clear that the new set of uncorrelated states includes the one of the distinguishable setting, i.e., $\mathcal{D}_0 \subseteq \mathcal{D}_0^{\mathrm{Q\text{-}SSR}}$. Consequently also more states are deemed separable. Relating to figure 2, both the correlation and entanglement measure become smaller in the presence of an SSR. There are two key messages here. First of all, correlation and entanglement are relative concepts. They depend not only on the particular division of the total system into two (or more) subsystems but also on the underlying SSRs, which eventually defines the physical local algebras of observables $\mathcal{A}_{A/B}$ and the global algebra $\mathcal{A}_A \otimes \mathcal{A}_B$. Secondly, by ignoring the fundamentally important SSRs, one may radically overestimate the amount of physical correlation and entanglement in a quantum state.

One of the biggest motivations for correctly identifying the amount of physical correlation and entanglement in a quantum state is its value for information processing tasks. An operationally meaningful quantification of entanglement does not only reveal non-local properties of a quantum state, but should also measure the amount of resource that can be extracted for performing various quantum information tasks mentioned in section 1. In figure 4 we illustrate the schematic protocol for utilizing entanglement from molecular systems. The quantum states of individual molecules are transferred to SSR-free quantum registers through local measurements and classical communication. A quantum circuit represented by a unitary gate U in figure 4 then acts on these quantum register states to perform computations. Finally, the end results of the computation are retrieved with carefully designed measurements. The key step that limits

the extraction of entanglement is the transferring of the quantum state, which is constrained by the underlying SSR [38]. What remains on the quantum registers after the transfer are the *physical* parts defined in Eq. (29). From this perspective, the Q-SSR-constrained total correlation, entanglement, and classical correlation of a single system in a state ρ follow as

$$
\begin{aligned}
I^{\text{Q-SSR}}(\rho) &= I(\rho^{\text{Q}}), \\
E^{\text{Q-SSR}}(\rho) &= E(\rho^{\text{Q}}), \\
C^{\text{Q-SSR}}(\rho) &= C(\rho^{\text{Q}}).
\end{aligned}
\tag{31}
$$

All quantum information theoretical concepts discussed so far are applicable to any *arbitrary* orthonormal basis of $D \geq 2$ spin orbitals. In particular, they then refer to any *arbitrary* separation of them into subsystems A and B defined by spin-orbitals $\{|\varphi_j\rangle\}_{j=1}^{D_A}$ and $\{|\varphi_j\rangle\}_{j=D_A+1}^{D}$, respectively. As far as the description of electronic structure is concerned, there are two particularly relevant separations. To explain them, let us first observe that the underlying one-particle Hilbert space. $\mathcal{H}^{(1)}$ consists of orbital and spin degrees of freedom, i.e., $\mathcal{H}^{(1)} \equiv \mathcal{H}_l^{(1)} \otimes \mathcal{H}_s^{(1)}$, where $\dim(\mathcal{H}_l^{(1)}) \equiv d$, $\dim(\mathcal{H}_s^{(1)}) \equiv 2$ and $\dim(\mathcal{H}^{(1)}) \equiv D = 2d$. The first partition picks one orbital $|\chi\rangle \in \mathcal{H}_l^{(1)}$ and then defines subsystem A through the two spin-orbitals $|\chi\rangle \otimes |\sigma\rangle$, $\sigma = \uparrow, \downarrow$. Subsystem B follows accordingly and comprises the remaining $D-2$ spin-orbitals. The corresponding measures for entanglement and correlation can be referred to as single-orbital entanglement and correlation. As we will show in section 3.1, the fact that the total N-electron ground state of a molecular system is pure drastically simplifies the respective measures and in particular leads to closed formulas. The second more elaborated separation quantifies entanglement and correlation between two orbitals $|\chi_i\rangle, |\chi_j\rangle \in \mathcal{H}_l^{(1)}$. This means to first trace out the complementary $D-4$ spin-orbitals to obtain a two-orbital reduced density matrix $\rho_{i,j}$ which is "living" on a sixteen-dimensional Fock space as illustrated in figure 5. Then, one applies to this new "total state" $\rho_{i,j}$ the formalism of bipartite entanglement and correlation for the separation $i \leftrightarrow j$ (see also the subsequent section).

Finally, let us also illustrate how the SSRs are implemented in the calculation of pairwise orbital entanglement. According to the previous comments, particularly Eq. (29), we just need to replace $\rho_{i,j}$ by its physical part $\rho_{i,j}^{\text{Q}}$. For the case of P-SSR and N-SSR this is illustrated in figure 5. $\rho_{i,j}^{\text{P}}$ is obtained by cutting out all light gray parts and $\rho_{i,j}^{\text{N}}$ follows after removing two additional entries (gray).

To avoid confusion, we recall that the quantum state on the algebra of observables based on two orbitals i, j is described by the full 2RDM $\rho_{i,j}$, including the gray and light gray entries as well. Yet, if we ask about the true physical correlation and entanglement between orbitals i and j this means to restrict in a first step the quantum state to the subalgebra

$$
\mathcal{A}_i \otimes \mathcal{A}_j \subsetneq \mathcal{A}_{i,j} .
\tag{32}
$$

Indeed, $\mathcal{A}_i \otimes \mathcal{A}_j$ is smaller than the full two-orbital algebra $\mathcal{A}_{i,j}$ because of the Q-SSR which is applied for the former on both single-orbital algebras individually. Just to illustrate this in more concrete terms, we observe for instance that the operator $f_{i\sigma}^\dagger f_{j\tau}$ belongs to $\mathcal{A}_{i,j}$ but not to $\mathcal{A}_i \otimes \mathcal{A}_j$, neither for P-SSR nor N-SSR, since $f_{i\sigma}^\dagger$ and $f_{j\tau}$ change locally the number parity.

N,m	0, 0	1, $-1/2$		1, 1/2		2,-1	2, 0					2, 1	3, $-1/2$		3, 1/2		4, 0
	$-\,-$	$-\downarrow$	$\downarrow\,-$	$-\uparrow$	$\uparrow\,-$	$\downarrow\downarrow$	$-\uparrow\downarrow$	$\downarrow\uparrow$	$\uparrow\downarrow$	$\uparrow\downarrow\,-$		$\uparrow\uparrow$	$\downarrow\uparrow\downarrow$	$\uparrow\downarrow\downarrow$	$\uparrow\uparrow\downarrow$	$\uparrow\downarrow\uparrow$	$\uparrow\downarrow\uparrow\downarrow$

(matrix grid: diagonal black blocks; off-diagonal gray/light-gray entries as in figure)

Fig. 5: *Illustration of two-orbital reduced density matrix $\rho_{i,j}$ and its superselected variants $\rho_{i,j}^{Q}$, $Q = N, P$. Most entries vanish due to spin and particle symmetry (white). According to (29) the P-SSR sets light gray entries to zero while N-SSR removes in addition two entries (gray).*

Legend: No SSR, P-SSR, N-SSR

3 Analytic treatment

3.1 Closed formulas for entanglement and correlation

We first look at the single-orbital total correlation and entanglement and assume a pure quantum state $\rho = |\Psi\rangle\langle\Psi|$ for the total N-electron system (typically it will be the ground state or an excited state of a molecular system). The one-orbital reduced density matrix associated with the orbital $|\chi_j\rangle$ is obtained by tracing out all remaining orbitals [34]

$$\rho_j = \mathrm{Tr}_{\backslash\{j\}}[|\Psi\rangle\langle\Psi|]. \tag{33}$$

We reiterate that the partial trace $\mathrm{Tr}_{\backslash\{j\}}[\cdot]$ does not mean to trace out particles but instead refers to the tensor product in the second quantization, i.e., it exploits the structure $\mathcal{F} = \mathcal{F}_j \otimes \mathcal{F}_{\backslash\{j\}}$. From a practical point of view, the non-vanishing entries of the single-orbital reduced density matrix can be determined by calculating expectation values of $|\Psi\rangle$ involving only fermionic creation and annihilation operators referring to orbital $|\chi_j\rangle$. For more details we refer the reader to Refs. [39,40,34]. Due to the fixed particle number and the spin symmetry of $|\Psi\rangle$ the one-orbital reduced density matrix will be always diagonal in the local reference basis $\{|\Omega\rangle, |\uparrow\rangle, |\downarrow\rangle, |\uparrow\downarrow\rangle\}$ of orbital $|\chi_j\rangle$:

$$\rho_j = \begin{pmatrix} p_1 & 0 & 0 & 0 \\ 0 & p_2 & 0 & 0 \\ 0 & 0 & p_3 & 0 \\ 0 & 0 & 0 & p_4 \end{pmatrix}. \tag{34}$$

By referring to the so-called Schmidt decomposition, the total state then takes the form

$$|\Psi\rangle = \sqrt{p_1}|\Omega\rangle \otimes |\Psi_{N,M}\rangle + \sqrt{p_2}|\uparrow\rangle \otimes |\Psi_{N-1,M-\frac{1}{2}}\rangle \tag{35}$$
$$+ \sqrt{p_3}|\downarrow\rangle \otimes |\Psi_{N-1,M+\frac{1}{2}}\rangle + \sqrt{p_4}|\uparrow\downarrow\rangle \otimes |\Psi_{N-2,M}\rangle,$$

where $|\Psi_{n,m}\rangle$ is a quantum state with particle number n and magnetization m of the complementary subsystem comprising the remaining $D-2$ spin-orbitals. Now we can readily determine the physical part ρ^Q in the presence of P-SSR or N-SSR. In the absence of SSRs, the single-orbital entanglement of $|\Psi\rangle$ is simply given by the von Neumann entropy of ρ_j, and the single-orbital total correlation is simply twice the entanglement,

$$E(|\Psi\rangle\langle\Psi|) = S(\rho_j) = -\sum_{i=1}^{4} p_i \ln(p_i).$$
$$I(|\Psi\rangle\langle\Psi|) = 2E(|\Psi\rangle\langle\Psi|). \tag{36}$$

In the case of Q-SSR, we need to consider the physical part ρ^Q of $\rho = |\Psi\rangle\langle\Psi|$, which is no longer a pure state. Consequently the single-orbital entanglement cannot be quantified by the von Neumann entropy of ρ_j anymore. Instead we have to invoke the geometric picture in figure 2. We first calculate the physical states with respect to P-SSR and N-SSR according to (29), and then their correlation and entanglement are quantified using (13) and (16). Remarkably, despite the fact that ρ^Q is not a pure state anymore the single-orbital correlation and entanglement under P-SSR and N-SSR still involves the spectrum of ρ_j only:

$$I(\rho^P) = (p_1 + p_4)\ln(p_1 + p_4) + (p_2 + p_3)\ln(p_2 + p_3)$$
$$- 2(p_1 \ln(p_1) + p_2 \ln(p_2) + p_3 \ln(p_3) + p_4 \ln(p_4)),$$
$$I(\rho^N) = p_1 \ln(p_1) + (p_2 + p_3)\ln(p_2 + p_3) + p_4 \ln(p_4)$$
$$- 2(p_1 \ln(p_1) + p_2 \ln(p_2) + p_3 \ln(p_3) + p_4 \ln(p_4)), \tag{37}$$
$$E(\rho^P) = (p_1 + p_4)\ln(p_1 + p_4) + (p_2 + p_3)\ln(p_2 + p_3)$$
$$- p_1 \ln(p_1) - p_2 \ln(p_2) - p_3 \ln(p_3) - p_4 \ln(p_4),$$
$$E(\rho^N) = (p_2 + p_3)\ln(p_2 + p_3) - p_2 \ln(p_2) - p_3 \ln(p_3).$$

In particular, this implies immediately for both SSRs (Q=P,N)

$$I^{\text{Q-SSR}}(\rho) = E^{\text{Q-SSR}}(\rho) + E(\rho). \tag{38}$$

For the case of no SSR, this is consistent with Eq. (36).

As already explained in the previous section, the second particularly relevant partitioning of the total system leads to a notion of orbital-orbital correlation and entanglement. It is fully described by the two-orbital reduced density matrix associated with orbital $|\chi_i\rangle$ and $|\chi_j\rangle$

$$\rho_{i,j} = \text{Tr}_{\backslash\{i,j\}}[|\Psi\rangle\langle\Psi|]. \tag{39}$$

For the specific case of a total system consisting of just two orbitals, the only two-orbital "reduced" density operator is given by the total (pure) state. Consequently, the orbital-orbital

correlation and entanglement thus coincide with the single-orbital ones and the above results (36), (37) immediately apply. Due to the electron interaction, the two-orbital reduced density matrices $\rho_{i,j}$ of *general* systems are, however, not pure anymore. This makes the calculation of orbital-orbital entanglement and classical correlation highly non-trivial: According to the definition of the relative entropy of entanglement (16) one needs to minimize the distance between $\rho_{i,j}$ and $\sigma_{i,j} \in \mathcal{D}_{sep}$ which *a priori* involves 255 parameters. Yet, $\rho_{i,j}$ inherits particle and spin symmetries from the molecular ground state $\rho = |\Psi\rangle\langle\Psi|$ which changes the general situation drastically. As a consequence almost all of its entries vanish as it is shown in figure 5 (see also Refs. [39]). Based on elaborated ideas the respective minimization (16) can be simplified accordingly by transferring those symmetries to $\mathcal{D}_{sep}$ [41,42]. The latter simplification eventually allows us to calculate below the entanglement between $|\chi_1\rangle, |\chi_2\rangle \in \mathcal{H}_l^{(1)}$ for any $\rho_{i,j}$.

In the following, we will illustrate those concepts in the form of several analytical examples.

3.2 Single electron state

At first glance it might seem somewhat bizarre to examine the correlation and entanglement in a system with only one particle. However, the reader shall bear in mind that the separation into subsystems is not referring to particles but *orbitals*. The total Fock space $\mathcal{F}$ in our case of two orbitals ($|1\rangle, |2\rangle$) has indeed a natural tensor product structure between the Fock spaces of the first and second orbital, i.e., $\mathcal{F} = \mathcal{F}_1 \otimes \mathcal{F}_2$. Therefore the notion of correlation and entanglement between two physically distinct orbitals is entirely legitimate even in the case of one single electron.

In the following we consider the specific one-electron state

$$|\Psi\rangle = \frac{1}{\sqrt{2}}(f_{1\uparrow}^\dagger + f_{2\uparrow}^\dagger)|\Omega\rangle \equiv \frac{|\uparrow\rangle \otimes |\Omega_2\rangle + |\Omega_1\rangle \otimes |\uparrow\rangle}{\sqrt{2}}. \tag{40}$$

Here, $f_{j\sigma}^\dagger$ denotes the fermionic creation operator for the spin-orbital $|j\sigma\rangle$, $j = 1, 2, \sigma = \uparrow, \downarrow$ and $|\Omega\rangle$ and $|\Omega_{1/2}\rangle$ the global and local vacuum states, respectively. If the SSRs are ignored, state (40) is certainly entangled. Yet, as we will show now this entanglement is artificial since it disappears when the P-SSR is taken into account. To prove this, recall that the P-SSR physical part of ρ is obtained by projecting onto fixed local parity sectors

$$\rho^P = \sum_{\tau,\tau'=\text{odd, even}} P_\tau \otimes P_{\tau'} \rho P_\tau \otimes P_{\tau'} = \frac{1}{2}|\Omega_1\rangle\langle\Omega_1| \otimes |\uparrow\rangle\langle\uparrow| + \frac{1}{2}|\uparrow\rangle\langle\uparrow| \otimes |\Omega_2\rangle\langle\Omega_2|, \tag{41}$$

which is correlated but not entangled. Indeed, it is a classical mixture of two uncorrelated states. For the sake of completeness, we would like to stress that for single electron states there is no difference between P-SSR and N-SSR. In particular for the state (40) we find

$$\rho^N = \sum_{m,n=0}^{2} P_m \otimes P_n \rho P_m \otimes P_n$$

$$= \frac{1}{2}|\Omega_1\rangle\langle\Omega_1| \otimes |\uparrow\rangle\langle\uparrow| + \frac{1}{2}|\uparrow\rangle\langle\uparrow| \otimes |\Omega_2\rangle\langle\Omega_2| = \rho^P. \tag{42}$$

	No SSR	P-SSR	N-SSR
Total	$2\ln(2)$	$\ln(2)$	$\ln(2)$
Quantum	$\ln(2)$	0	0
Classical	$0.208\ln(2)$	$\ln(2)$	$\ln(2)$

Table 1: *Total, quantum and classical correlation between the two orbitals in the one-electron state $|\Psi\rangle$ in (40), for the case without SSR, with P-SSR and with N-SSR.*

We present in table 1 the orbital total correlation ("Total"), entanglement ("Quantum") and classical correlation ("Classical") between $|1\rangle$ and $|2\rangle$ contained in state (40) which can easily be calculated based on the physical states (41), (42).

The number 0.208 in table 1 is the constant $\ln(4/3)/2$. When P-SSR or N-SSR is present (they are equivalent in the case of only one electron), all entanglement is wiped out and all correlation is classical, as it is shown by the second and third column. This striking example shows that one can never extract any entanglement from a single one-electron quantum state even if it appears at first sight as being entangled.

> **Exercise 3.1**
>
> Recalculate various entries of table 1.

> **Exercise 3.2**
>
> Building up on Exercise 3.1, explain why single electron quantum states are never P-SSR or N-SSR entangled (i.e., for any dimension of the underlying one-particle Hilbert space $\mathcal{H}^{(1)}$ and any splitting (25)).

3.3 Dissociated hydrogen

Having studied the orbital-orbital correlation and entanglement in a one-electron state, we now add a second electron to our two-orbital system. As an example, we consider the ground state of the hydrogen molecule in the dissociation limit. The two orbital system now consists of the $1s$ orbital at each nucleus (both orthonormal as we assume almost infinite separation) and the ground state follows as

$$|\Psi\rangle = \frac{1}{\sqrt{2}}(f^\dagger_{1\uparrow}f^\dagger_{2\downarrow} - f^\dagger_{1\downarrow}f^\dagger_{2\uparrow})|\Omega\rangle. \tag{43}$$

In table 2 we list the total correlation, entanglement and classical correlation between $|1\rangle$ and $|2\rangle$. When no SSR is considered, all three types of correlation equal those of the one-electron state in table 1. However, in contrast to the latter, the ground state $|\Psi\rangle$ of the dissociated hydrogen molecule is already a physical state, with respect to both P-SSR and N-SSR. From (43) we infer that $|\Psi\rangle$ is a pure state with definite local parities (odd, odd) and definite local particle numbers $(1,1)$. The projection (29) therefore does not change the state $|\Psi\rangle\langle\Psi|$ and thus all three types of correlation are unaffected by P-SSR and N-SSR according to (31).

	No SSR	P-SSR	N-SSR
Total	$2\ln(2)$	$2\ln(2)$	$2\ln(2)$
Quantum	$\ln(2)$	$\ln(2)$	$\ln(2)$
Classical	$0.208\ln(2)$	$0.208\ln(2)$	$0.208\ln(2)$

Table 2: *Total, quantum and classical correlation between both orbitals* $|1\rangle, |2\rangle$ *in the dissociated hydrogen ground state* $|\Psi\rangle$ *in (43), for the case without SSR, with P-SSR and N-SSR.*

> **Exercise 3.3**
>
> Recalculate various entries of table 2.

3.4 Hubbard dimer

The dissociated hydrogen molecule described in the previous section is a very special case with a definite local particle number (and of course, parity). If we consider intermediate bond length, however, different local particle number or parity sectors will start to mix, and hence the behavior of the orbital correlation and entanglement will be more interesting. To elaborate on this, we turn to an elementary model system. The Hamiltonian of this Hubbard dimer which comprises two sites reads

$$H = -t \sum_{\sigma=\uparrow,\downarrow} f_{1\sigma}^{\dagger} f_{2\sigma} + \text{H.c.} + U \sum_{j=1,2} \hat{n}_{j\uparrow}\hat{n}_{j\downarrow}, \tag{44}$$

where $f_{j\sigma}^{(\dagger)}$ are annihilation (creation) operators associated with a spin σ electron on site $j = 1, 2$. It is worth recalling that small hopping rates t correspond to larger inter-nuclei separations. The repulsive potential U penalizes any doubly occupied site, effectively describing the Coulomb repulsion of two electrons in the same $1s$ orbital. Exploiting the symmetries of (44) one easily determines the ground state of the Hubbard dimer

$$|\Psi\rangle = \frac{a}{\sqrt{2}}\big(f_{1\uparrow}^{\dagger} f_{2\downarrow}^{\dagger} - f_{1\downarrow}^{\dagger} f_{2\uparrow}^{\dagger}\big)|\Omega\rangle + \frac{b}{\sqrt{2}}\big(f_{1\uparrow}^{\dagger} f_{1\downarrow}^{\dagger} - f_{2\downarrow}^{\dagger} f_{2\uparrow}^{\dagger}\big)|\Omega\rangle, \tag{45}$$

where

$$a = \sqrt{\frac{W + \frac{U}{2}}{2W}}, \quad b = \frac{2t}{\sqrt{2W\left(W + \frac{U}{2}\right)}}, \quad W = \sqrt{\frac{U^2}{4} + 4t^2}. \tag{46}$$

The orbital-orbital total correlation I, entanglement E and classical correlation C in the ground state (45) are plotted in figure 6, for the case without SSR, with P-SSR and N-SSR [11], as a function of the parameter t/U. In this special case of just two orbitals in total and a pure state, the single-orbital and orbital-orbital correlation and entanglement coincide.

In the case without any SSR, the orbital-orbital entanglement E (red solid) is exactly half of the total correlation I. For finite t/U, i.e., when $b > 0$ in (45), P-SSR and N-SSR drastically reduce
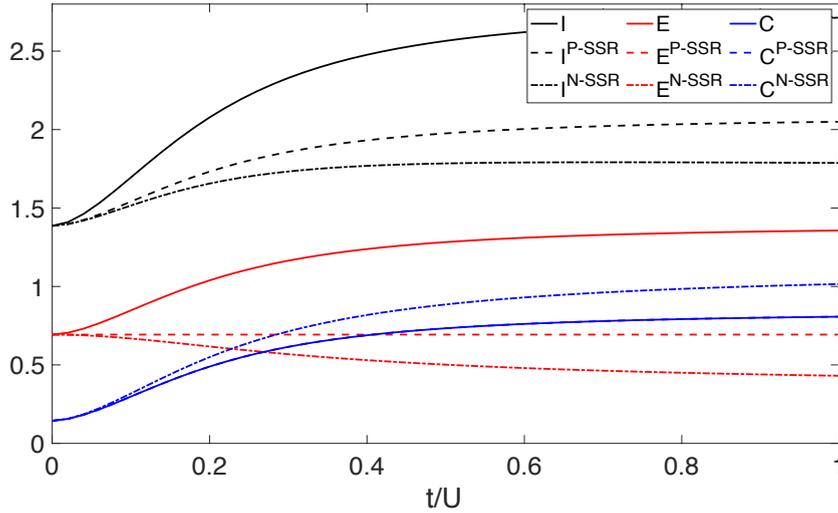
Fig. 6: *Total correlation I (black), entanglement E (red) and classical correlation C (blue) between both sites for the ground state of the Hubbard dimer (44) as functions of the ratio t/U. The curves for C and $C^{P\text{-}SSR}$ coincide.*

the orbital-orbital total correlation and entanglement, as is shown by the curves corresponding to $I^{\text{P-SSR}}$ (black dashed), $I^{\text{N-SSR}}$ (black dot-dashed), $E^{\text{P-SSR}}$ (red dashed) and $E^{\text{N-SSR}}$ (red dot-dashed). N-SSR being the stronger rule, reduces correlation and entanglement the most. However, when we take $t/U \to 0$, corresponding to the dissociation limit, the effect of P-SSR and N-SSR disappears. This is due to the vanishing coefficient b in (45) in the dissociation limit, which results in a ground state that is physical in the presence of both P-SSR and N-SSR, as it has already been pointed out in section 3.3.

In the weak coupling limit, $U \to 0$, the Hamiltonian (44) reduces to the hopping Hamiltonian. Since the latter is a one-particle operator it is a particularly simple task to understand the form of its ground state: Both electrons just occupy (in different spin states) the energetically lower one-particle state $1/\sqrt{2}\big(|L\rangle + |R\rangle\big)$. This is nothing else than the bonding orbital which maximizes relative to the antibonding orbital $1/\sqrt{2}\big(|L\rangle - |R\rangle\big)$ the electron density between both nuclei/sites. The corresponding ground state therefore reads

$$|\Psi(U{=}0)\rangle = \frac{1}{2}\Big(f_{1\uparrow}^{\dagger}f_{1\downarrow}^{\dagger} + f_{1\uparrow}^{\dagger}f_{2\downarrow}^{\dagger} + f_{2\uparrow}^{\dagger}f_{1\downarrow}^{\dagger} + f_{2\uparrow}^{\dagger}f_{2\downarrow}^{\dagger}\Big)|\Omega\rangle \,. \tag{47}$$

Exercise 3.4

Calculate for the state (47) all nine correlation quantities (in analogy to Table 2) and verify their correctness by comparison with the numerical results presented in Figure 6.

All these previous elementary examples already reveal the drastic effect of SSRs on orbital correlation and entanglement. In the following section we will apply the quantum information theoretical concepts to systems with more orbitals.

4   Numerical application to molecular ground states

In this section we investigate the correlation and entanglement in the ground states of molecules. We consider exemplarily three chemical systems, the water molecule H_2O, naphthalene $C_{10}H_8$ and the chromium dimer Cr_2, each containing different levels of correlation. Accurate ground states are found by using the density matrix renormalization group (DMRG) method as outlined in the following section 4.1. The single-orbital and orbital-orbital correlation and entanglement are studied in sections 4.2 and 4.3 with respect to two sets of orbitals, the Hartree Fock molecular orbitals and the so-called natural orbitals. To avoid any confusion, it is worth noticing that the choice of orbitals with respect to which those quantities are eventually calculated is made only *after* having obtained a good approximation of the molecule's quantum state. Only for illustrative purposes we will choose in the following for this the Hartree-Fock orbitals which at the same time already play some role in the calculation of the ground state. Hence, in complete analogy to expectation values of more conventional observables, the orbital entanglement and correlation depend on both the molecule's quantum state $|\Psi\rangle$ and the choice of orbitals. Yet, they do not depend on the numerical method that is used to obtain the concrete quantum state $|\Psi\rangle$.

4.1   Computational details

In order to find a ground state, and from it compute the required orbital reduced density matrices, we start with a preceding Hartree-Fock calculation to establish the molecular orbitals. For our post-Hartree-Fock DMRG calculation we construct an active space consisting of the most relevant molecular orbitals and compute integral elements with the one- and two-particle Hamiltonian T and V, respectively. Those respective integral elements define the electronic Hamiltonian at hand by referring to second quantization

$$H = \sum_{ij\sigma} T_{ij}\, f_{i\sigma}^{\dagger} f_{j\sigma} + \sum_{ijkl\sigma\tau} V_{ijkl}\, f_{i\sigma}^{\dagger} f_{j\tau}^{\dagger} f_{k\tau} f_{l\sigma}\,. \tag{48}$$

For our DMRG calculations we do not fix any molecular symmetries. Yet, the total particle number and the z-component of the total spin are always assumed to be conserved, with the latter one always fixed to be zero. Furthermore, we did not employ exceedingly large active spaces for two reasons. First, the ground states are almost exactly found. Second, for the purpose of demonstration, our findings do not qualitatively hinge on the tiny improvement found by resorting to larger active spaces. In particular, the reduction in correlation and entanglement due to the regularly ignored superselection rules turns out to exceed by several orders of magnitude the truncation error of our active spaces.

To obtain for each ground state $|\Psi\rangle$ the required one- (ρ_j) and two-orbital reduced density matrices ($\rho_{i,j}$) we trace all orbitals except one and two, respectively (recall Eqs. (33), (39)).
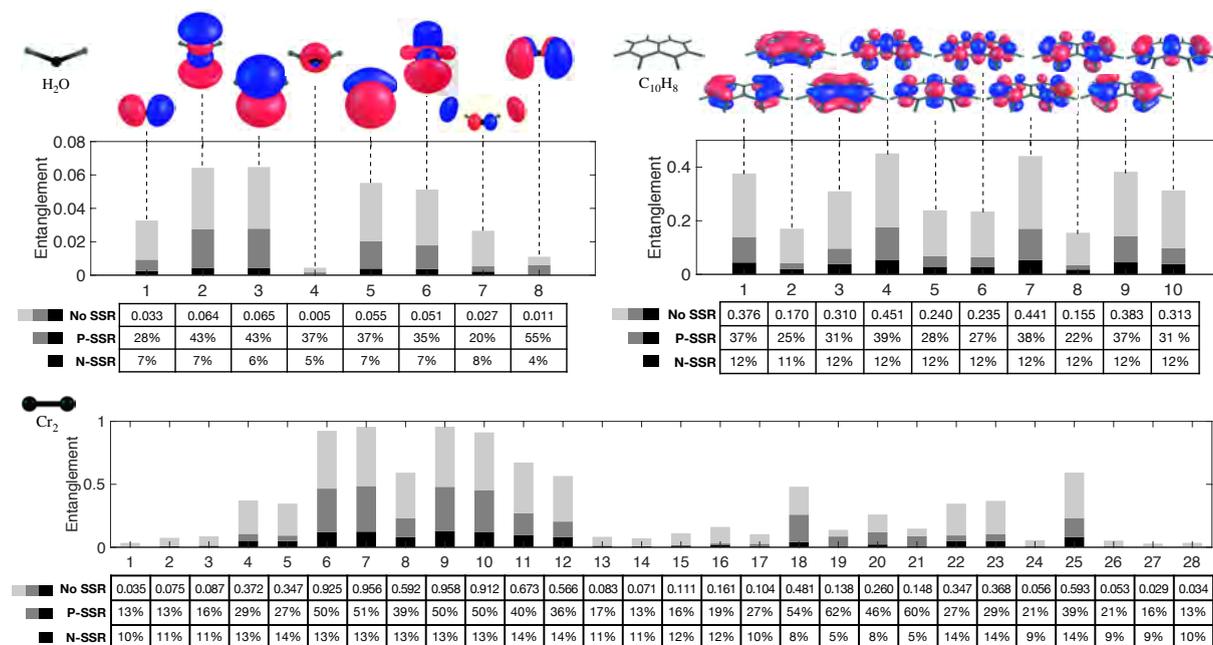
Fig. 7: *Single-orbital entanglement of the Hartree-Fock molecular orbitals (as visualized) in the ground states of H_2O, $C_{10}H_8$ and Cr_2 for the three cases of no, P- and N-SSR. Exact values of entanglement and the remaining entanglement in terms of percentage of the No SSR case in the presence of P-SSR and N-SSR are listed in the table below each plot.*

4.2 Single-orbital entanglement and correlation

After having obtained the ground states of the desired molecules, we can now explore single-orbital correlation and entanglement by applying the respective formulas from section 3.1. Since the states ρ at hand are all *pure* states, the single-orbital total correlation without any SSR is always exactly twice the single-orbital entanglement, as stated in (36). When P-SSR or N-SSR is taken into account, the respective physical states ρ^P and ρ^N are no longer pure, but in general mixtures of fixed parity or particle number states. However, in the form of Eq. (38) there still exists an exact relation between total correlation and entanglement in the presence of SSRs. Because of this, we focus in this section on the entanglement.

In figure 7 we plotted the single-orbital entanglement in the ground state of the H_2O, $C_{10}H_8$ and Cr_2, respectively, for the case without SSR, with P-SSR and with N-SSR, using the analytic formulas (36) and (37). Below each figure we listed the exact values of single-orbital entanglement in the absence of SSRs, and also the remaining entanglement in the presence of P-SSR and N-SSR, in percentage. All these results refer here and in the following to the Hartree-Fock molecular orbitals which are for the sake of completeness also visualized for H_2O and $C_{10}H_8$.

Generally speaking, the single-orbital entanglement of Hartree-Fock orbitals is quite small compared to the one of *atomic* orbitals in a bond (see sections 3.3 and 3.4), particularly for H_2O and $C_{10}H_8$. This confirms that the Hartree-Fock orbitals give rise to a much more local structure than that the atomic orbitals and in that sense define a much better starting point for high precision ground state methods. Comparing the three systems, the water molecule contains the

weakest single-orbital entanglement, less than 10^{-1} for all eight orbitals, whereas the strongest single-orbital entanglement in naphthalene and the chromium dimer have the values 0.451 and 0.958, respectively. This already emphasizes the different levels of correlation in those systems. Yet, it is worth noticing that any type of orbital entanglement and correlation (e.g., single- or two-orbital entanglement) strongly depends on the chosen reference basis. Even for a configuration state (21) one could find large orbital entanglement and correlation if one referred to orbitals which differ a lot from the natural orbitals.

From a quantum information perspective, the effect of SSRs on the single-orbital entanglement is drastic. The presence of P-SSR and N-SSR considerably reduces the amount of physical entanglement. According to the accompanying tables in figure 7, P-SSR eliminates at least 45% of it and occasionally even up to 87%. Taking into account the more relevant N-SSR eliminates between 86% and 96%. Intriguingly, the entanglement hierarchy, however, remains almost intact. That is, if one orbital is more entangled with the rest than another orbital, the same will likely hold in the presence of P-SSR and N-SSR. It is also worth noting that even the stronger N-SSR does never wipe out the entire entanglement, which we shall see below can happen in the context of orbital-orbital entanglement.

From a quantum chemistry point of view, in figure 7 the single-orbital entanglement varies significantly from orbital to orbital. In particular, some orbitals are barely correlated with the others. Since we have chosen our active spaces systematically by taking into account various Hartree-Fock orbitals energetically closest to the Fermi level, this is a good indicator that our actives spaces were large enough to cover most of the correlation contained in the three molecules. On the other hand, if most orbitals were strongly entangled, the respective active space probably would have been too small. This is also the reason why the single-orbital correlation could help to automate the selection of active orbital spaces in quantum chemistry, as has been suggested and worked out in Refs. [43, 44]. Our refined analytic results (36) and (37) demonstrated in figure 7 are able to identify exactly the quantum part of the total correlation while also taking into account the important superselection rules. These additional facets make precise the usage of quantum information theoretic concepts in the context of quantum chemistry, and may offer new perspectives into the selection of active space.

4.3   Orbital-orbital entanglement and correlation

To provide more detailed insights into the correlation and entanglement structure of molecular ground states, we also study the pairwise correlation and entanglement between two orbitals. This can be done in general in three steps:

1. Obtain the two-orbital reduced density matrix $\rho_{i,j}$ by tracing out all orbital degrees of freedom but orbital i and j as described in (39).

2. Apply the suitable projection to obtain the physical part $\rho_{i,j}^{Q}$ of $\rho_{i,j}$ under Q-SSR, as explained in section 2.3.

3. Calculate the correlation and entanglement between the two orbitals using (31).

Hartree-Fock Orbitals   **Natural Orbitals**
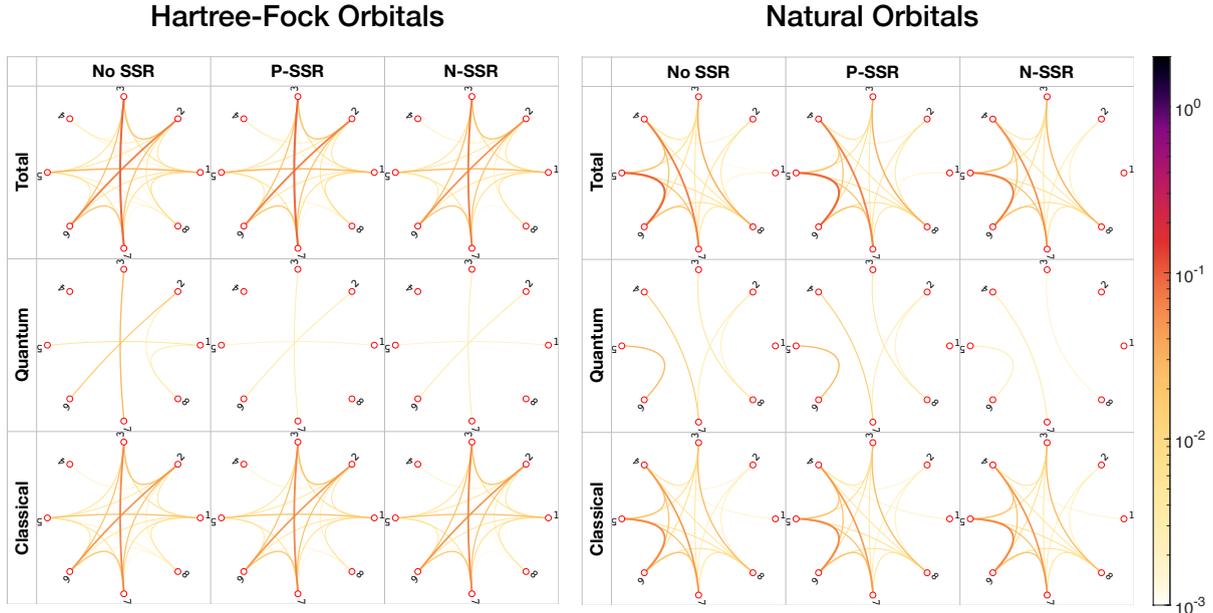
Fig. 8: *Total correlation, entanglement ("Quantum") and classical correlation between any two Hartree-Fock (left) and natural (right) orbitals in the ground state of H_2O for the case with no, P- and N-SSR.*

It is worth recalling that the two-orbital reduced density matrices $\rho_{i,j}$ are typically highly mixed, which is due to the coupling between different Hartree-Fock orbitals in the Hamiltonian (48). The total correlation for a mixed state, measured by the distance to the closest uncorrelated state (13), can always be calculated analytically, as it coincides with the quantum mutual information (13). However, the entanglement quantified as the distance to the closest separable state (16) is immensely difficult to obtain by analytic means due to two reasons. One is the challenge imposed by the high dimensionality, even if we are interested in the entanglement between just two orbitals. The respective total system in that case has a Hilbert space isomorphic to $\mathbb{C}^4 \otimes \mathbb{C}^4$ (see also figure 5). A generic density matrix is then described by $16 \times 16 - 1 = 255$ real-valued parameters. In order to find the closest separable state to a two-orbital state $\rho_{i,j}$, one already needs to navigate through 255 parameters. The second difficulty lies in the complexity of the boundary of the set of separable states $\mathcal{D}_{sep}$. So far exact criteria for separability known are only for Hilbert spaces with dimensions up to 2×3 [45, 46]. In some cases when the total state exhibits many symmetries, the closest separable state for the two-orbital reduced state can still be found analytically [42]. In general, however, one has no choice but to resort to a combination of analytic tools and numerical methods, which is here the case.

The quantities calculated are the total correlation, entanglement and classical correlation between two Hartree-Fock orbitals, for the case without SSR, with P-SSR and with N-SSR. All those nine quantities are calculate for all pairwise combinations of orbitals, for the ground states of all three molecules introduced in section 4.1. Since each ground state is a singlet with a fixed electron number, any two-orbital reduced state $\rho_{i,j}$ is also symmetric with respect to the total two-orbital spin, magnetization and particle number [42]. Using the symmetry argument [41],
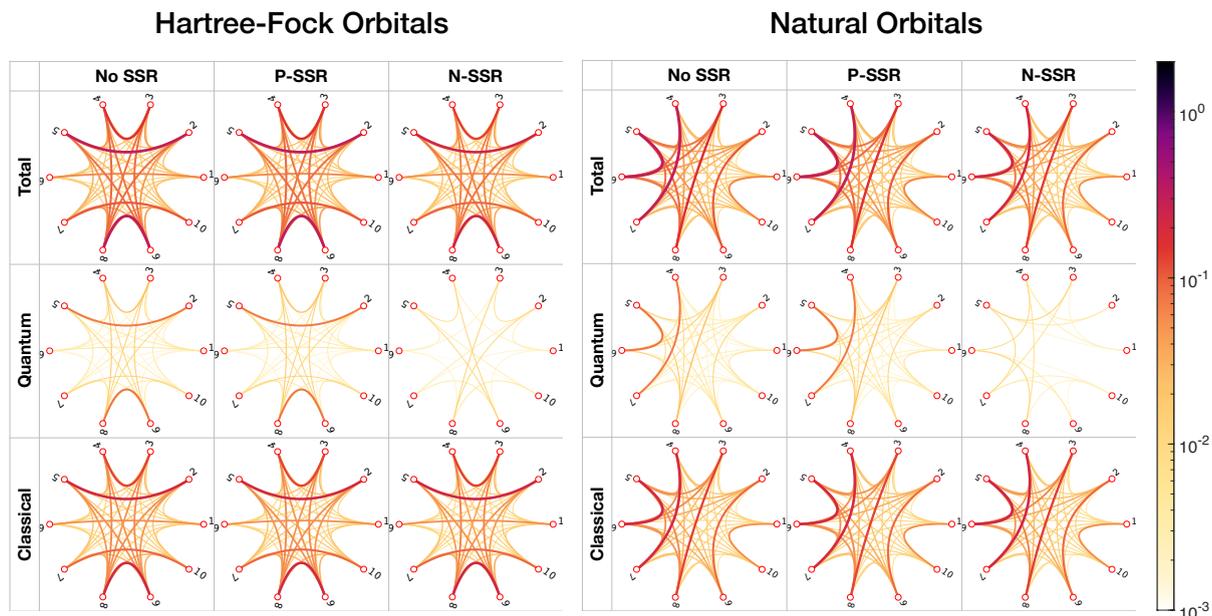
Fig. 9: *Total correlation, entanglement ("Quantum") and classical correlation between any two Hartree-Fock (left) and natural (right) orbitals in the ground state of $C_{10}H_8$ for the case with no, P- and N-SSR.*

the closest separable state $\sigma_{i,j}^*$ is block diagonal in the simultaneous eigenbasis of the respective two-orbital spin and particle number operators (as also illustrated in figure 5). In the case of N-SSR, the projections used for calculating the physical state further increase the symmetry of $\sigma_{i,j}^*$, which eventually allows us to determine it analytically [42]. For the case without SSR and with P-SSR, we developed an algorithm based on semidefinite programming to find the closest separable state and calculate the entanglement in an numerically exact way [42].

In figure 8, 9 and 10 we present the different types of correlation of the ground state of H_2O constructed with 8 orbitals, $C_{10}H_8$ with 10 orbitals and Cr_2 with 28 orbitals, respectively.

There are several important messages to get across. First of all, similar to the results for the single-orbital entanglement, the water molecule contains the weakest orbital-orbital correlation, and the chromium dimer the strongest. Most importantly, our comprehensive analysis then reveals that the quantum part of the total correlation plays only a minor role. In fact, the orbital-orbital entanglement is usually one order of magnitude smaller than the total correlation, and the molecular structure is thus dominated by classical correlation. This key result of the analysis emphasizes that the quantum mutual information (13) is not a suitable tool for quantifying orbital entanglement, as it leads to a gross overestimation. From a general point of view, our findings raise questions about the significance of entanglement in chemical bonding and quantum chemistry in general.

Similar to the single-orbital entanglement, SSRs also have a drastic effect on the orbital-orbital entanglement, yet in a qualitatively different way. In the molecular systems we considered, P-SSR preserved almost all of the orbital-orbital entanglement, whereas in the case of N-SSR, almost no orbital-orbital entanglement is left, and consequently almost all orbital-orbital corre-
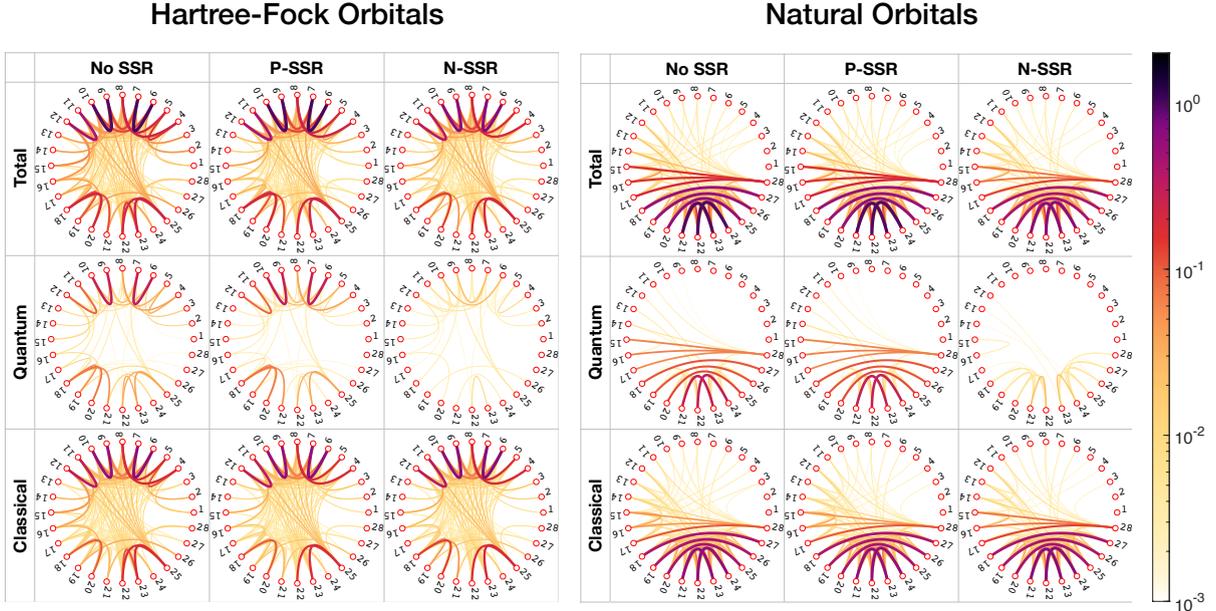
Fig. 10: *Total correlation, entanglement ("Quantum") and classical correlation between any two Hartree-Fock (left) and natural (right) orbitals in the ground state of Cr_2 for the case with no, P- and N-SSR.*

lation is classical. Furthermore, in some instances even the *entire* orbital-orbital entanglement is destroyed by the N-SSR. Referring to figure 5, this indicates that most of the contribution to orbital-orbital correlation and entanglement comes from superposing $f_{i\downarrow}^\dagger f_{i\uparrow}^\dagger|\Omega\rangle$ and $f_{j\downarrow}^\dagger f_{j\uparrow}^\dagger|\Omega\rangle$, which are marked as the dark grey blocks. These states describe either empty or doubly occupied orbitals. In fact, in all three molecules, single excitations are highly suppressed in any of the molecular orbitals we consider. This is qualitatively different to the analysis of a single bond in section 3.3 which was referring to *localized atomic* orbitals, each singly occupied. In agreement with valence bonding theory, this observation confirms that two-orbital correlation and entanglement are suitable tools for describing bonding orders only if they are applied to localized atomic orbitals.

Lastly we would like to compare the correlation patterns of the Hartree-Fock orbitals with those of the natural orbitals (see Figure 8, 9 and 10). To recap, the natural orbitals are the eigenstates of the orbital one-particle reduced matrix

$$\gamma_{i,j}^{(l)} \equiv \sum_{\sigma=\uparrow,\downarrow} \langle\Psi|f_{j\sigma}^\dagger f_{i\sigma}|\Psi\rangle \,. \tag{49}$$

The natural orbitals inherit the ordering of the natural orbital occupation numbers (eigenvalues of $\rho^{(l)}$) which are arranged decreasingly. Previous observations regarding the correlation patterns with respect to the Hartree-Fock orbitals is still present. Entanglement takes up only a small fraction of the total correlation, and the presence of SSRs drastically reduce the entanglement. In contrast to the more scrambled pattern of the Hartree-Fock orbitals, however, an additional pairing structure emerges among the natural orbitals. To be more precise, orbitals in the neighbourhood of the Fermi level are strongly correlated but they share this entanglement

only within pairs. After all, these pairs are symmetrical relative to the Fermi level. This suggests a potential simplified description of the ground state in the natural orbital basis. At the same time, the qualitative difference between the correlation patterns of the two sets of orbitals demonstrates again that correlation and entanglement are relative concepts.

Acknowledgment

References

[1] T.J. Osborne and M.A. Nielsen, Phys. Rev. A **66**, 032110 (2002)

[2] G. Vidal, J.I. Latorre, E. Rico, and A. Kitaev, Phys. Rev. Lett. **90**, 227902 (2003)

[3] S.J. Gu, S.S. Deng, Y.Q. Li, and H.Q. Lin, Phys. Rev. Lett. **93**, 086402 (2004)

[4] S. Szalay, G. Barcza, T. Szilvási, L. Veis, and Ö. Legeza, Sci. Rep **7**, 1 (2017)

[5] T.J. Osborne and M.A. Nielsen, Quantum Inf. Process. **1**, 45 (2002)

[6] G. Vidal, Phys. Rev. Lett. **99**, 220405 (2007)

[7] A.K. Ekert, Phys. Rev. Lett. **67**, 661 (1991)

[8] T. Jennewein, C. Simon, G. Weihs, H. Weinfurter, and A. Zeilinger,
Phys. Rev. Lett. **84**, 4729 (2000)

[9] C.H. Bennett and S.J. Wiesner, Phys. Rev. Lett. **69**, 2881 (1992)

[10] R. Jozsa and N. Linden, Proc. R. Soc. Lond **459**, 2011 (2003)

[11] L. Ding and C. Schilling, J. Chem. Theory Comput. **16**, 4159 (2020)

[12] L. Ding, S. Mardazad, S. Das, S. Szalay, U. Schollwöck, Z. Zimborás, and C. Schilling,
J. Chem. Theory Comput. **17**, 79 (2021)

[13] O. Gühne and G. Tóth, Phys. Rep. **474**, 1 (2009)

[14] R. Horodecki, P. Horodecki, M. Horodecki, and K. Horodecki,
Rev. Mod. Phys. **81**, 865 (2009)

[15] M. Hübner, Phys. Lett. A **163**, 239 (1992)

[16] D. Petz and C. Sudár, J. Math. Phys. **37**, 2662 (1996)

[17] D.C. Brody, J. Phys. A **44**, 252002 (2011)

[18] P. Zanardi, Phys. Rev. Lett. **87**, 077901 (2001)

[19] G.C. Wick, A.S. Wightman, and E.P. Wigner, Phys. Rev. **88**, 101 (1952)

[20] V. Vedral, Rev. Mod. Phys. **74**, 197 (2002)

[21] G. Lindblad, Commun. Math. Phys. **33**, 305 (1973)

[22] V. Vedral, M.B. Plenio, M.A. Rippin, and P.L. Knight, Phys. Rev. Lett. **78**, 2275 (1997)

[23] M.M. Wolf, F. Verstraete, M.B. Hastings, and J.I. Cirac,
Phys. Rev. Lett. **100**, 070502 (2008)

[24] J. Watrous: *Lecture notes on the Theory of Quantum Information* (U. of Waterloo, 2011)
     `https://cs.uwaterloo.ca/˜watrous/TQI-notes/`

[25] C.H. Bennett, G. Brassard, C. Crépeau, R. Jozsa, A. Peres, and W.K. Wootters,
     Phys. Rev. Lett. **70**, 1895 (1993)

[26] S. Popescu and D. Rohrlich, Phys. Rev. A **56**, R3319 (1997)

[27] G. Vidal, J. Mod. Opt. **47**, 355 (2000)

[28] M.A. Nielsen and I. Chuang: *Quantum computation and quantum information*
     (Cambridge University Press, 2002)

[29] L. Henderson and V. Vedral, J. Phys. A **34**, 6899 (2001)

[30] G. Adesso, M. Cianciaruso, and T.R. Bromley: *Quantum Discord and Nonclassical
     Correlations Beyond Entanglement* (John Wiley & Sons, 2016), chap. 9, pp. 175–194

[31] C.H. Bennett, H.J. Bernstein, S. Popescu, and B. Schumacher,
     Phys. Rev. A **53**, 2046 (1996)

[32] N. Friis, A.R. Lee, and D.E. Bruschi, Phys. Rev. A **87**, 022338 (2013)

[33] N. Friis, New J. Phys. **18**, 033014 (2016)

[34] G.G. Amosov and S.N. Filippov, Quantum Inf. Process. **16**, 2 (2017)

[35] M.C. Bañuls, J.I. Cirac, and M.M. Wolf, Phys. Rev. A **76**, 022311 (2007)

[36] G.C. Wick, A.S. Wightman, and E.P. Wigner, Phys. Rev. D **1**, 3267 (1970)

[37] G.C. Wick, A.S. Wightman, and E.P. Wigner: In *Part I: Particles and Fields;
     Part II: Foundations of Quantum Mechanics* (Springer, 1997), p. 102

[38] S.D. Bartlett and H.M. Wiseman, Phys. Rev. Lett. **91**, 097903 (2003)

[39] K. Boguslawski, P. Tecmer, G. Barcza, Ö. Legeza, and M. Reiher,
     J. Chem. Theory Comput. **9**, 2959 (2013)

[40] K. Boguslawski and P. Tecmer, Int. J. Quantum Chem. **115**, 1289 (2015)

[41] K.G.H. Vollbrecht and R.F. Werner, Phys. Rev. A **64**, 062307 (2001)

[42] L. Ding, Z. Zimboras, and C. Schilling: *Entanglement between orbitals or sites*
     (in preparation)

[43] G. Barcza, Ö. Legeza, K.H. Marti, and M. Reiher, Phys. Rev. A **83**, 012508 (2011)

[44] K. Boguslawski, P. Tecmer, Ö. Legeza, and M. Reiher, J. Phys. Chem. Lett **3**, 3129 (2012)

[45] M. Horodecki, P. Horodecki, and R. Horodecki, Phys. Lett. A **223**, 1 (1996)

[46] A. Peres, Phys. Rev. Lett **77**, 1413 (1996)

10 Analog Quantum Simulations of the Hubbard Model

Walter Hofstetter
Institute for Theoretical Physics
Goethe-University Frankfurt
Max-von-Laue-Strasse 1
D-60438 Frankfurt/Main

Contents

1 Introduction

Ultracold quantum gases in optical lattices are highly tunable quantum many-body systems, which allow investigation of strongly correlated synthetic quantum matter [1,2]. They illustrate Feynman's visionary idea of a universal quantum simulator [3], and give access to (analog) quantum simulation of strongly correlated electronic systems, for example high-temperature superconductors [4,5], Mott insulators, or quantum magnets. Also bosonic quantum phases and phase transitions can be studied, for example the paradigmatic superfluid to Mott insulator (MI) transition [6]. Even more exotic types of quantum matter, such as Fermi-Hubbard models with higher internal SU(N) symmetry can be emulated using optical lattices [7,8].

Ideally, quantum simulations of the Hubbard model should address regimes or (universal) aspects of a complex and less tunable quantum system (e.g. a quantum material), which are hard to investigate on classical computers due to the exponential growth of many-body Hilbert space with increasing particle number, which limits diagonalization-based methods, and due to the (dynamical) sign problem in quantum Monte Carlo (QMC) simulations [9,10]. Highly tunable model parameters, flexible preparation of initial states, and efficient measurement techniques are key distinguishing features of optical lattice emulators, which allow observing quantum many-body dynamics on the intrinsic length and time scales of these systems.

In these lecture notes we will focus on analog, rather than digital quantum simulation [11].

2 Optical lattice emulation of the Hubbard model

The Hubbard model [12] is the simplest microscopic lattice model of itinerant, interacting electrons in a solid. It has been successfully applied to describe, for example magnetic ordering, metal-insulator transitions and d-wave superconductivity [4,5]. For spin-½ fermions in a single band it is given by the Hamiltonian

$$\hat{H} = -t \sum_{\langle ij \rangle, \sigma} \left(\hat{c}_{i\sigma}^\dagger \hat{c}_{j\sigma} + \text{h.c.} \right) + U \sum_i \hat{n}_{i\uparrow} \hat{n}_{i\downarrow} + \sum_{i\sigma} \varepsilon_i \hat{n}_{i\sigma} \tag{1}$$

containing a kinetic energy (hopping) with matrix element t between nearest-neighbor lattice sites $\langle ij \rangle$ and a purely local (on-site) Hubbard interaction term of strength U. A schematic illustration is shown in Fig. 1. $\sigma = \uparrow, \downarrow$ labels spin, $\hat{c}_{i\sigma}^\dagger$ denotes the creation operator on lattice site i, and $\hat{n}_{i\sigma}$ is the local number operator for spin σ. We have included an additional single-particle potential ε_i, which could arise due to spatial randomness or due to an external potential, such as an optical or magnetic trap for ultracold atoms.

This simple version of the Hubbard model (1) is highly idealized. In solids, even in metals, the screening length of the Coulomb interaction can be significantly larger than the lattice constant, which leads to further terms in the Hamiltonian, for example longer-range interactions [12]. The coupling to lattice phonons can be relevant as well. In optical lattice realizations of the Hubbard model, to be discussed below, these additional terms are in general absent, but can be introduced in a controlled way, e.g., by dressing with Rydberg-excited states [13] or by coupling to dynamical phonons of trapped ion crystals [14].
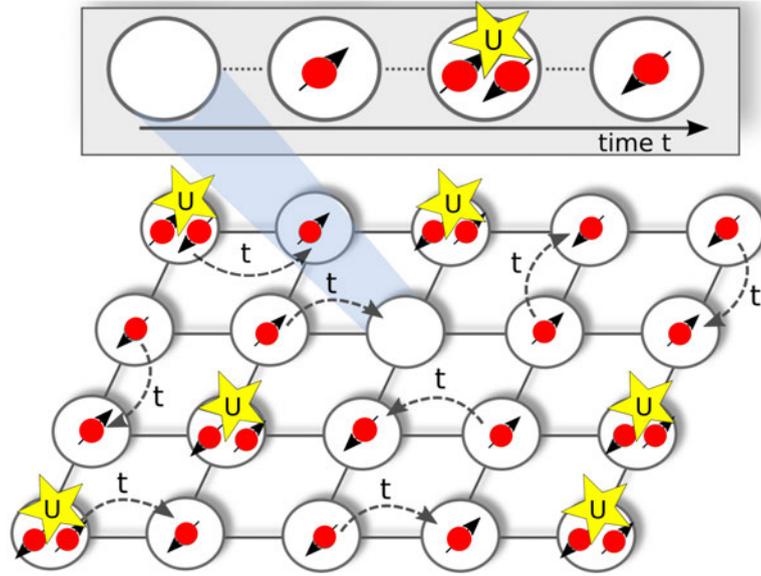
Fig. 1: *Single-band Fermi-Hubbard model on the square lattice.*
Figure reprinted from [2], ©IOP Publishing Ltd. CC BY 3.0.

(Numerically) exact solutions of the Fermi-Hubbard model exist only in one spatial dimension (Bethe Ansatz, Density-Matrix Renormalization Group (DMRG)) and in infinite dimensions (Dynamical Mean-Field Theory (DMFT)) [15]. In particular, due to basic limitations of simulation techniques (Quantum Monte-Carlo, DMRG, exact diagonalization) many questions remain open regarding the low-temperature phase diagram of the 2d Hubbard model, which is believed to be highly relevant for the description of high-temperature superconductivity [16]. On the other hand, interacting fermions [17] or bosons [18] in optical lattices provide a controlled and tunable analog quantum simulator of the pure Hubbard model. Quantum-gas microscopy techniques [19] allow single-site resolved measurements of charge and spin order, for example in (doped) Mott insulators [20–22], and give access to measurements of nonequilibrium particle and spin dynamics in real time [23–25].

Optical lattices are standing light-waves created by interfering, pairwise counterpropagating laser beams; see for example Fig. 2 (left). Neutral atoms interact with the optical lattice via the AC Stark effect, which results in an effective (time-averaged) lattice potential, see the schematic illustration in Fig. 2 (right). For a simple cubic lattice with infinite extension this potential is separable and given by

$$V_{\text{lat}}(x, y, z) = V_0 \left(\sin^2(kx) + \sin^2(ky) + \sin^2(kz) \right) \tag{2}$$

where $k = 2\pi/\lambda$ is the wavenumber of the lattice-lasers. The lattice amplitude V_0 depends on the atomic polarizability and the intensity of the light [26], and is positive (negative) for blue (red) detuning of the lasers. The characteristic energy scale is set by the recoil energy $E_r = \hbar^2 k^2/2m$, with typical values of order $O(\text{kHz})$. Many different lattice geometries have been realized in this way, including triangular [27], Kagome [28], and artificial graphene [29].
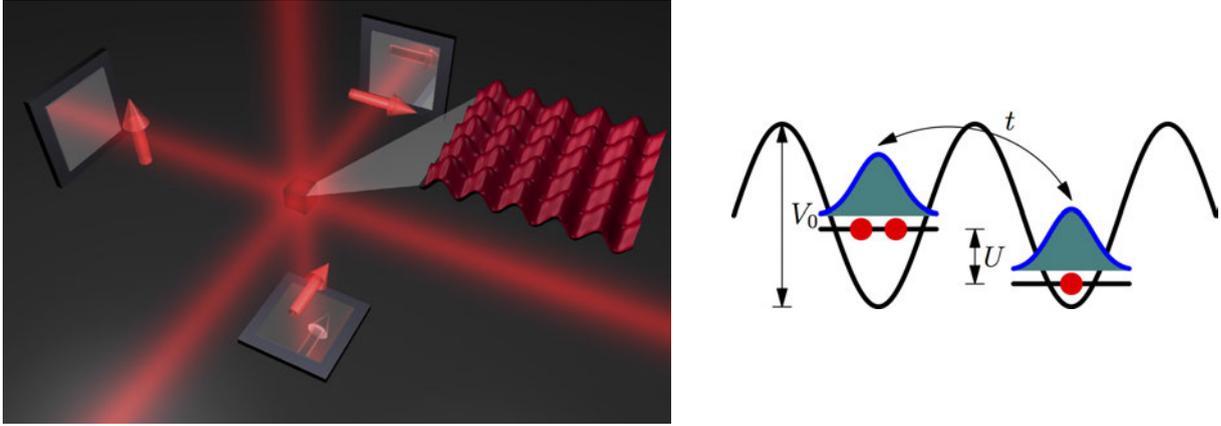
Fig. 2: *Left: Cubic optical lattice. For illustration purposes, a 2d slice is shown. The three lattice lasers have mutually orthogonal polarizations indicated by the arrows, and are each retroreflected from a mirror. Figure reprinted from [30] with permission. Right: Schematic illustration of spinless bosons in an optical lattice with hopping t and on-site Hubbard interaction U. Figure reprinted from [2], ©IOP Publishing Ltd. CC BY 3.0.*

Compared to solid-state crystals, the lattice constant of an optical lattice is much larger ($a = O(100\,\mathrm{nm})$ instead of $O(\text{Å})$), and the resulting energy-scales are much lower (kHz instead of eV). This results in much slower quantum dynamics than in electronic solids, which has made it possible to observe in-situ the quantum phases and nonequilibrium dynamics of ultracold atoms on their intrinsic time-scales with single-site, single-atom resolution, via quantum-gas microscopy [19].

Ultracold gases in optical lattices are almost ideal closed quantum systems, highly isolated from their environment, with the residual dissipation mostly arising from spontaneous emission [26], which leads to heating that typically starts to dominate after times of several 100 ms. Note that optical lattices are very clean, i.e., free of defects, but they are intrinsically finite (typical lengths of $O(100)$ lattice sites) and typically inhomogeneous due to the profile of the Gaussian laser beams, although quasi-flat "box potentials" can also be engineered. This confinement-induced inhomogeneity can often be well described within a local density approximation, where each lattice site i is treated as part of an infinite homogeneous system with an effective chemical potential $\mu_i = \mu - \varepsilon_i$ that depends on the lattice site.

Let us now show that the low-energy effective Hamiltonian of an ensemble of ultracold atoms in an optical lattice is given – under suitable conditions – by the single-band Hubbard model. We consider, for the moment, a homogeneous lattice without external confinement potential. According to Bloch's theorem, the single-particle eigenstates in an optical lattice can be written as

$$\phi_{\boldsymbol{q}}^{(\alpha)}(\boldsymbol{r}) = e^{i\boldsymbol{q}\cdot\boldsymbol{r}}\, u_{\boldsymbol{q}}^{(\alpha)}(\boldsymbol{r}). \tag{3}$$

The index α labels different bands, and $\boldsymbol{q} = (q_x, q_y, q_z)$ is the quasimomentum. On a simple cubic lattice its components are in the range $q_{x,y,z} \in (-\pi/a, \pi/a]$, with the lattice constant $a = \lambda/2$ determined by the laser wavelength. $u_{\boldsymbol{q}}^{(\alpha)}(\boldsymbol{r})$ is a lattice-periodic function.
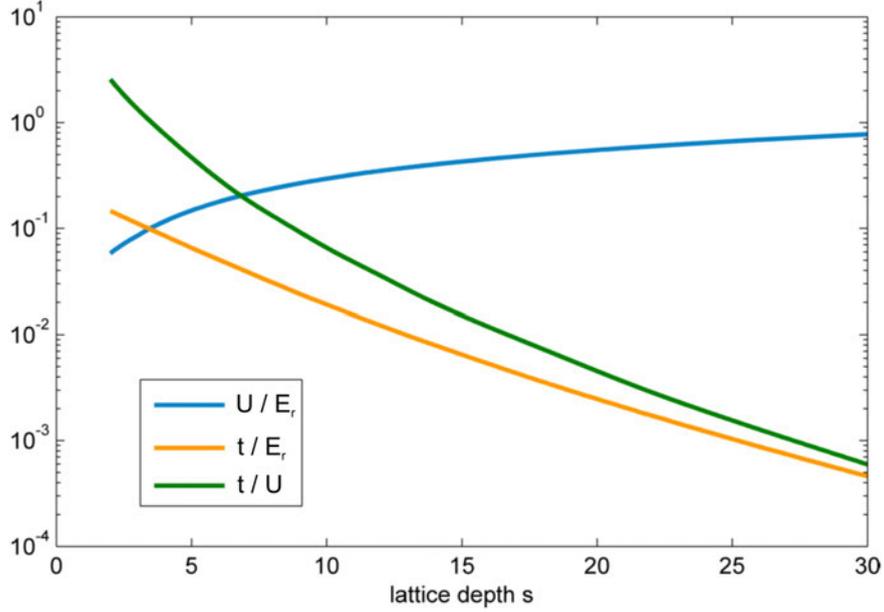
Fig. 3: *Hubbard parameters t and U and their ratio, shown here as a function of the dimensionless lattice depth s for ^{87}Rb in a 812 nm optical lattice. Both the hopping t and the ratio t/U decay approximately exponentially for deep lattices. Figure adapted from [30] with permission.*

To formulate a tight-binding Hamiltonian we use Wannier functions, which also form an orthonormal single-particle basis and are maximally localized at the respective lattice sites. They are related to the Bloch functions by

$$w^{(\alpha)}(\boldsymbol{r}-\boldsymbol{r}_i) = N^{-1/2} \sum_{\boldsymbol{q}} e^{-i\boldsymbol{q}\cdot\boldsymbol{r}_i} \phi_{\boldsymbol{q}}^{(\alpha)}(\boldsymbol{r}) \tag{4}$$

with $\boldsymbol{r}_i$ the position of the i-th lattice site and N the total number of sites. Note that computing the maximally localized Wannier functions usually involves numerical optimization of the phases of the Bloch states. An efficient alternative is calculating Wannier functions as eigenfunctions of the band-projected position operator [29, 30], which can also be done for systems with broken lattice translational invariance, for example due to disorder.

If the filling (the number of particles per site), the temperature T, and the Hubbard interaction strength U are low enough, it is sufficient to consider only the lowest Bloch band with $\alpha = 1$. This will be assumed in the following discussion, where the band index will be omitted. We write the kinetic energy as $\hat{H}_{\text{kin}} = -t \sum_{\langle ij\rangle,\sigma} \hat{c}_{i\sigma}^{\dagger} \hat{c}_{j\sigma} + \text{h.c.}$, where $\hat{c}_{i\sigma}^{\dagger} = \int d^3r\, w(\boldsymbol{r}-\boldsymbol{r}_i)\, \hat{\Psi}_{\sigma}^{\dagger}(\boldsymbol{r})$ creates a particle with mass m and internal (hyperfine) state σ in the lowest Wannier state on site i. The resulting tunneling matrix element between neighboring sites i and j is given by $t = -\int d^3r\, w^*(\boldsymbol{r}-\boldsymbol{r}_i) \left(-\hbar^2\boldsymbol{\nabla}^2/2m+V_{\text{lat}}(\boldsymbol{r})\right) w(\boldsymbol{r}-\boldsymbol{r}_j)$. For sufficiently deep optical lattices with a dimensionless depth $s \equiv V_0/E_r \gg 1$, tunneling beyond nearest neighbors $\langle ij\rangle$ can in most cases be neglected. If the lattice is also separable, one obtains approximately $t = (4/\sqrt{\pi})E_r\, s^{3/4} \exp\left(-2s^{1/2}\right)$ [1].

Two-particle interactions between ultracold neutral atoms are usually dominated by s-wave scattering and can be described by a contact interaction [1]

$$\hat{H}_{\text{int}} = g \int d^3r \, \hat{\Psi}_\uparrow^\dagger(\boldsymbol{r}) \hat{\Psi}_\downarrow^\dagger(\boldsymbol{r}) \hat{\Psi}_\downarrow(\boldsymbol{r}) \hat{\Psi}_\uparrow(\boldsymbol{r})$$

of strength $g = 4\pi\hbar^2 a_s/m$ (where a_s is the scattering length), which has been written here for fermions with two hyperfine ("spin") states $\uparrow, \downarrow$. For a sufficiently deep optical lattice with $s \gg 1$ and in the absence of Feshbach resonances we can again use the single-band approximation. The dominant interaction term is then given by $\hat{H}_{int} = U \sum_i \hat{n}_{i\uparrow} \hat{n}_{i\downarrow}$ with the Hubbard interaction parameter $U = g \int d^3r \, |w(\boldsymbol{r})|^4 \approx \sqrt{8/\pi}(2\pi a_s/\lambda)s^{3/4} E_r$. We have thus obtained the single-band Fermi-Hubbard model as given in Eq. (1) [17]. The additional onsite energy ε_i describes the confinement potential, or additional optical potentials (e.g. superlattices or spatially fluctuating optical Speckle potentials) which may be superimposed onto the primary optical lattice. Experimentally the correlation strength U/t is highly tunable from values $U/t \approx 0$ to $|U|/t > 1000$, either by varying the optical lattice depth as shown in Fig. 3, or by using Feshbach resonances [1] to change a_s.

The bosonic Hubbard model [31]

$$\hat{H} = -t \sum_{\langle ij \rangle} \left(\hat{b}_i^\dagger \hat{b}_j + \text{h.c.} \right) + \frac{U}{2} \sum_i \hat{n}_i(\hat{n}_i - 1) + \sum_i \varepsilon_i \hat{n}_i \tag{5}$$

can analogously be derived for ultracold bosons [18], and has been first implemented in a pioneering experiment exploring the superfluid – MI transition [6].

Corrections to the standard single-band Hubbard models (1) and (5) become important for strong contact interactions, for example close to Feshbach resonances or in shallow lattices. A density dependence of the Hubbard interaction parameter U has been measured [32]. It can be described, together with other corrections such as density-dependent hopping, pair tunneling, and next-neighbor interactions, by including contributions of higher Bloch bands in an effective single-band model [33]. Independently, it is also possible to populate higher bands of an optical lattice and to study multi-band phenomena.

Let us now give a brief overview of techniques for measuring observables (e.g. particle- or spin-density excitation spectra) in cold atom quantum simulators. Time-of-flight (TOF) spectroscopy is performed by ballistic expansion of the atomic cloud in the absence of interactions, followed by measurement of the density via absorption imaging. It allows to extract the in-trap momentum distribution of the initial many-body state as $\langle \hat{n}(\boldsymbol{r}) \rangle_{\text{TOF}} \propto \langle \hat{n}(\boldsymbol{k}) \rangle_{\text{trap}}$ where $\boldsymbol{k} = m\boldsymbol{r}/\hbar t$ [1]. Using a slow initial ramp-down of the optical lattice that is adiabatic with respect to the band gap, one can also directly image the Bloch quasimomentum distribution, including higher Brillouin zones [34]. Moreover, spatial correlations of the noise in single-shot TOF images can be used to infer momentum correlations in the initial many-body state, and thus to detect for example MI states or magnetic long-range order [35, 36].

Interaction effects can be studied by radio-frequency (RF) spectroscopy [37], where the atoms initially in the hyperfine state $|g\rangle$ are excited to state $|e\rangle$ by an applied RF field, and the fraction of excited atoms is then detected. This has allowed, for example, to measure the pairing

gap in a strongly interacting superfluid Fermi gas [38], similar to tunneling experiments in superconductors. Using a momentum-resolved version of RF spectroscopy [39] the fermionic spectral function $A(\boldsymbol{k}, \omega) = -\frac{1}{\pi}\mathrm{Im}\, G^R(\boldsymbol{k}, \omega)$ at frequency ω and momentum $\boldsymbol{k}$ has been measured experimentally, where $G^R(\boldsymbol{k}, t) = -i\Theta(t)\,\langle\Psi_0|\{\hat{c}_{\boldsymbol{k}}(t), \hat{c}_{\boldsymbol{k}}^\dagger(0)\}|\Psi_0\rangle$. This is an analog of angle-resolved photoemission spectroscopy (ARPES) in solids.

Two-photon Bragg spectroscopy allows probing dynamical correlation functions such as the dynamical structure factor $S(\boldsymbol{k}, \omega) \propto \sum_f \left|\langle f|\hat{\rho}^\dagger(\boldsymbol{k})|g\rangle\right|^2 \delta\big(\hbar\omega - (E_f - E_g)\big)$ given here at zero temperature. $\hat{\rho}(\boldsymbol{k})$ is the Fourier transform of the density, and $|f(g)\rangle$ the initial (final) state of the many-body system. This is achieved by a two-photon transition, where atoms absorb a photon from one laser and emit a photon into a second laser mode, which leads to a momentum and energy "kick" $\hbar\boldsymbol{k}_{\mathrm{Bragg}} = \hbar(\boldsymbol{k}_1 - \boldsymbol{k}_2)$ and $\hbar\delta = \hbar(\omega_1 - \omega_2)$, where $\hbar\boldsymbol{k}_i$ and $\hbar\omega_i$ with $i = 1, 2$ denote the momenta and energies of the two lasers. Bragg scattering has also been applied in the strongly correlated regime and beyond linear response, where the amplitude mode of strongly interacting bosons in a cubic lattice has been observed [40]. A related approach is lattice amplitude modulation spectroscopy, which has been applied, for example, to identify the Mott-insulator phase of fermions in a cubic optical lattice [41].

Optical quantum-gas microscopy, first realized for bosonic ^{87}Rb [19], has revolutionized quantum simulators based on ultracold atoms. Fluorescence photons created by in-trap laser cooling are detected with a high-resolution imaging objective, which allows imaging of single atoms on individual sites of an optical lattice. This technique also allows local control and manipulation, for example performing spin-flips of individual atoms [42]. It is also applicable to fermionic quantum gases, where it has for example been applied to image the fermionic Mott insulator [43], including the "wedding cake structure" of the density profile corresponding to spatial domains of different phases (Fermi liquid, band- and Mott-insulator).

3 Mott insulator transition

Mott insulators and the associated metal-insulator transitions are of fundamental relevance in strongly correlated electronic systems, for example in transition metal oxides and organic conductors, and – with additional doping – in cuprate high-temperature superconductors [4].

Ultracold gases in optical lattices have allowed for a highly controlled experimental realization of the Mott transition, both fermionic and bosonic, which clearly separates the itinerant degrees of freedom from other effects such as phonons and defects, and which is more easily tunable than solid-state realizations. In particular, the correlation strength (the ratio U/t of Hubbard interaction and hopping) can be tuned all the way from the limit of a noninteracting Fermi gas in a lattice [34], to the "atomic limit", i.e., the deep Mott-insulator regime, where tunneling can be considered a small perturbation.

On the other hand, the theoretical description of Mott transitions has made strong progress due to advances in numerical techniques such as DMRG, QMC and, in higher spatial dimensions, DMFT [15] and its real-space generalization to inhomogeneous systems [44]. DMFT is based on a mapping of each lattice site of the Hubbard model to an (Anderson-) quantum impurity

model with the same effective local action

$$S_{\mathrm{eff}}^{(i)} = - \iint d\tau d\tau' \sum_\sigma c_{i\sigma}^\dagger(\tau)\, \mathcal{G}_0^{(i)}(\sigma, \tau-\tau')^{-1}\, c_{i\sigma}(\tau') - U \int d\tau\, n_{i\uparrow}(\tau)n_{i\downarrow}(\tau) \qquad (6)$$

that is determined self-consistently. This yields a non-perturbative description of local quantum dynamics in the original correlated lattice problem. The DMFT self-consistency loop is formed by the local Dyson equation $\mathcal{G}_0^{(i)}(\sigma, i\omega_n)^{-1} = G^{(i)}(\sigma, i\omega_n)^{-1} + \Sigma^{(i)}(\sigma, i\omega_n)$ and the lattice Dyson equation $\boldsymbol{G}(\sigma, i\omega_n)^{-1} = \boldsymbol{G}_0(\sigma, i\omega_n)^{-1} - \boldsymbol{\Sigma}(\sigma, i\omega_n)$, complemented by the requirement that the interacting local (impurity) Green's function is equal to the respective diagonal element of the full lattice Green's function: $G^{(i)}(\sigma, i\omega_n) = G_{ii}(\sigma, i\omega_n)$. Above, boldface objects are matrices with entries labeled by two lattice site indices. Calculating the self-energy $\Sigma^{(i)}$ from the local action (6) is a computationally demanding task which is performed by a quantum impurity solver, e.g., exact diagonalization, the Numerical Renormalization Group (NRG), or continuous-time Quantum Monte-Carlo (CT-QMC) [15, 45]. The full real-space extension of DMFT [44] allows simulation of inhomogeneous, correlated fermionic and bosonic lattice gases for experimentally relevant system sizes [46], even in situations where other simulation methods are not applicable. DMFT has been very successful in describing the Mott metal-insulator transition, see for example the DMFT phase diagram of the single-band Fermi-Hubbard model at half filling in Fig. 4. In particular, it has provided theoretical understanding of the narrow quasiparticle resonance in the spectral function of the correlated metallic phase close to the transition [47]. On bipartite lattices (e.g. cubic) at half filling, antiferromagnetism emerges at low temperatures for any value of the Hubbard interaction, and typically hides the paramagnetic Mott transition. On generic lattices with frustration the antiferromagnetic phase is reduced and the Mott transition can be recovered to some extent, see Fig. 4.

A Mott transition also occurs in the Bose-Hubbard model at integer filling, in this case between superfluid and Mott insulator [31]. It is captured qualitatively by a static (Gutzwiller) mean-field theory, based on a variational wavefunction that is a product over all lattice sites and connects two limiting cases: At vanishing hopping, the Mott insulator wavefunction for integer filling n can be written as $|\Psi_{\mathrm{Mott}}\rangle \propto \prod_{i=1}^N \left(\hat{b}_i^\dagger\right)^n|0\rangle$, while in the noninteracting case ($U{=}0$) and for arbitrary filling n the condensate can be written as a product of coherent states at the individual lattice sites: $|\Psi_{\mathrm{cond}}\rangle \propto \left(\sum_{i=1}^N \hat{b}_i^\dagger\right)^{nN}|0\rangle \propto \prod_{i=1}^N \exp\left(\sqrt{n}\,\hat{b}_i^\dagger\right)|0\rangle_i$. The development of bosonic DMFT [48] has improved theoretical understanding of the bosonic Mott insulator, capturing particle-hole excitations which lead to short-range coherence, as well as superexchange interactions in multi-component systems. Independently, large-scale QMC simulations of bosonic lattice models became feasible using the Worm algorithm [49].

The Bose-Hubbard model has been realized experimentally [6], following the proposal [18], using ^{87}Rb on a cubic optical lattice. The superfluid-Mott insulator quantum phase transition has been observed in measurements of the momentum distribution and the excitation spectrum, at a correlation strength $U/t = 5.8\,z$, with the lattice coordination number $z = 2d$, which agrees reasonably well with the static mean-field prediction. Later, a *validation* of this quantum simulator for the model (5) has been performed by finite-temperature measurements of the momentum
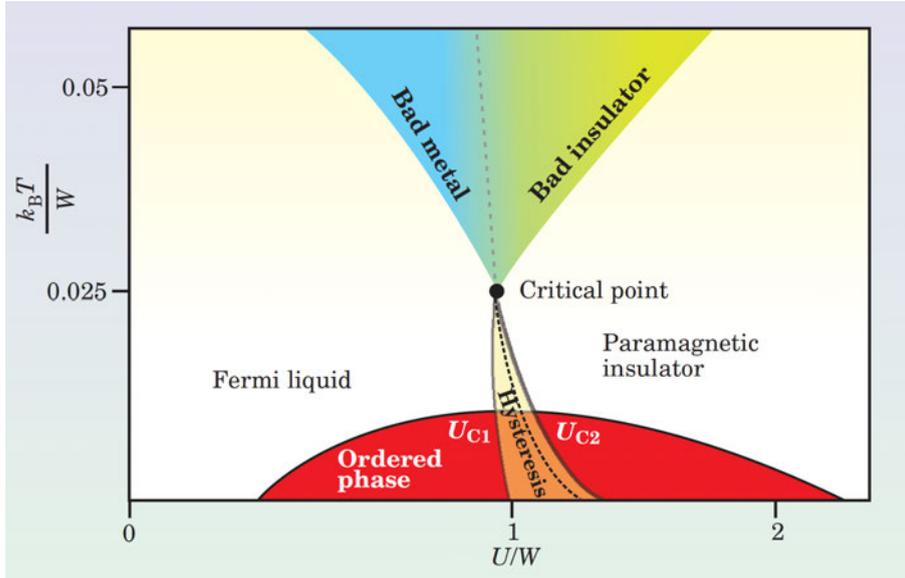
Fig. 4: *Schematic DMFT phase diagram of the homogeneous Fermi-Hubbard model (1) at half filling on a generic 3d lattice with bandwidth W. At low temperatures long-range order emerges (indicated in red), for example antiferromagnetism, depending on the lattice structure. In the orange region metallic and Mott-insulating phases coexist. At the dashed line a first-order transition occurs, which ends in a second-order critical point. At higher temperatures the Mott metal-insulator transition becomes a crossover. Figure reproduced from [47], with the permission of the American Institute of Physics.*

distribution and comparison to QMC calculations [50], which allowed determining the finite-temperature phase diagram. More recently, optical quantum-gas microscopy has given access to in-situ imaging and control with single-atom, single-site resolution [19], opening up new possibilities for optical lattice quantum simulators. It allows, for example, to image superfluid and Mott insulating domains, and to determine temperature and entropy directly from the local particle-number statistics.

The fermionic Mott transition has also been observed in ultracold gases. In [51] this was achieved by measuring the size and compressibility of the fermionic ^{40}K cloud as a function of the confinement potential, and by comparison to DMFT simulations. On the other hand, in [41] the double occupancy and particle-hole excitation energies have been determined. The crossover from the "metallic" to the Mott insulating regime was also studied for spinful ultra-cold fermions in artificial graphene [29]. The fermionic Mott insulator has also been imaged with quantum-gas microscopy [43], which has allowed to determine from the local particle number statistics the entropy per site, which was found to be $s_i \approx k_B \ln 2$, in agreement with theoretical expectations.

Mott insulators with larger spin $S > 1/2$ or higher symmetry groups such as SU(N) can also be implemented in optical lattices, using multiple hyperfine states. For example, an SU(6) Mott insulator of ^{173}Yb has been realized [52], with an increased spin entropy per site $s = k_B \ln N$ due to the larger number of internal states.
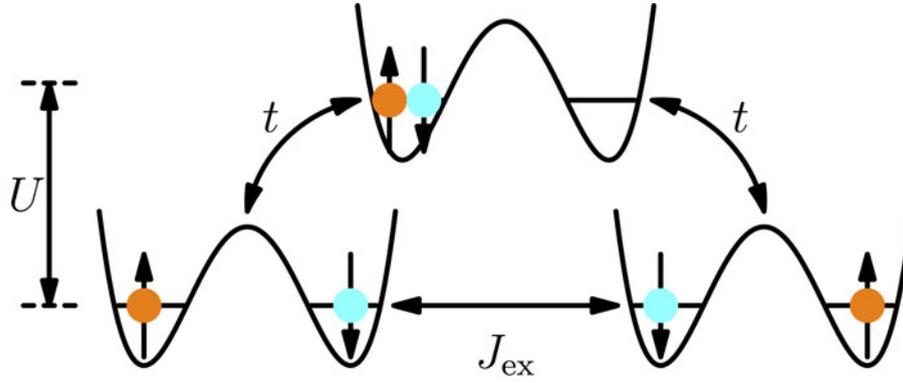
Fig. 5: *Superexchange couplings due to virtual second-order tunneling.*
Figure reprinted from [2], ©IOP Publishing Ltd. CC BY 3.0.

4 Quantum magnetic correlations

For spin-½ fermions and in the "atomic" limit of vanishing tunneling $t \to 0$ the paramagnetic spin-½ Mott insulator discussed above has an extensive residual entropy $S = N k_B \ln 2$ due to spin fluctuations. At finite t, magnetic superexchange couplings, illustrated in Fig. 5, will induce spin-spin correlations and possibly long-range magnetic order, depending on temperature.

Quantum magnetism, although studied for a long time, still poses intriguing open questions, for example whether quantum spin liquids on frustrated lattices exist, and what their properties are. In many cases it is challenging to investigate quantum magnetic correlations by numerically exact techniques, due to the sign problem (QMC), system size (exact diagonalization), or spatial dimensionality (DMRG). The same holds true for simulations of real-time nonequilibrium spin dynamics in Hubbard-type models.

Optical-lattice quantum simulators are well suited for investigating quantum spin systems. On the one hand this is due to the high tunability of lattice geometry, dimensionality and (effective) exchange couplings. On the other hand, novel observation techniques such as quantum-gas microscopy allow to measure spin ordering, magnetic correlations, and nonequilibrium spin dynamics with single-site resolution and in real-time [19].

Let us consider a two-component version of the Hubbard model for ultracold atoms [53]

$$\hat{H} = -\sum_{\langle ij \rangle \sigma} \left(t_\sigma \hat{a}_{i\sigma}^\dagger \hat{a}_{j\sigma} + \text{h.c.} \right) + U_{\uparrow\downarrow} \sum_i \hat{n}_{i\uparrow} \hat{n}_{i\downarrow} + \frac{1}{2} \sum_{i,\sigma} U_\sigma \, \hat{n}_{i\sigma} (\hat{n}_{i\sigma} - 1), \qquad (7)$$

where $\sigma = \uparrow, \downarrow$ is a pseudospin index, labeling either different hyperfine states or atomic species. All interactions are repulsive $U_{\uparrow\downarrow}, U_\sigma \geq 0$. This model is applicable both for bosonic and for fermionic atoms, created by $\hat{a}_{i\sigma}^\dagger$. For fermions, it is equivalent to the standard spin-½ Fermi Hubbard model, and the repulsion U_σ between equal species should then be set to infinity in the equations below. The hopping amplitudes t_σ are tunable and can be spin-dependent, e.g., due to a mass imbalance of the two species $\sigma = \uparrow, \downarrow$ [54] or spin-dependent optical lattices. Changing the s-wave scattering lengths $a_{\sigma\sigma'}$, e.g., via Feshbach resonances, allows tuning of the interactions $U_{\sigma\sigma'}$.
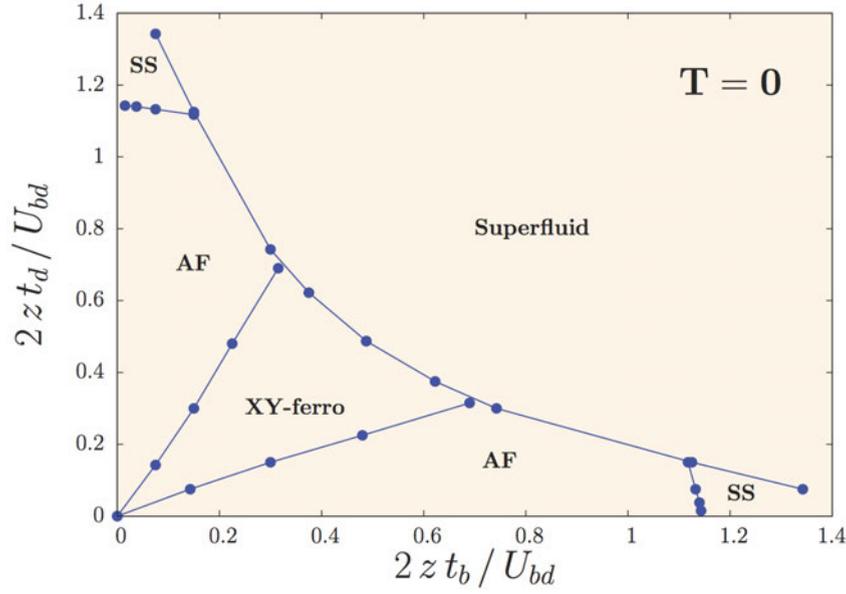
Fig. 6: *Tunable ground-state magnetic order of two-component bosons in a cubic, spin-dependent lattice, obtained by bosonic DMFT. xy-ferromagnetic, z-Néel antiferromagnetic (AF) and supersolid (SS) phases are found, in addition to the homogeneous superfluid. Here $t_{b(d)}$ corresponds to $t_{\uparrow(\downarrow)}$ in Eq. (7), $U_{b(d)}$ corresponds to $U_{\uparrow(\downarrow)}$, and U_{bd} corresponds to $U_{\uparrow\downarrow}$. Ratios between the different interactions have been fixed as $U_b = U_d = 12U_{bd}$. The total filling per site is one, with $n_b = n_d = 0.5$. Reprinted figure with permission from [55]. Copyright 2011 by the American Physical Society.*

In the Mott insulator for total filling $n_{i\uparrow} + n_{i\downarrow} = 1$ per site, and to leading order in $t_\sigma/U_{\uparrow\downarrow}$ and t_σ/U_σ the low-energy effective Hamiltonian

$$\hat{H} = \sum_{\langle ij \rangle} J_z \hat{\sigma}_i^z \hat{\sigma}_j^z \pm J_\perp (\hat{\sigma}_i^x \hat{\sigma}_j^x + \hat{\sigma}_i^y \hat{\sigma}_j^y) \tag{8}$$

is an XXZ spin model [53], with the sign $+(-)$ for fermions (bosons), and with longitudinal and transverse superexchange couplings given by

$$J_z = \frac{t_\uparrow^2 + t_\downarrow^2}{2U_{\uparrow\downarrow}} - \frac{t_\uparrow^2}{U_\uparrow} - \frac{t_\downarrow^2}{U_\downarrow} \qquad \text{and} \quad J_\perp = \frac{t_\uparrow t_\downarrow}{U_{\uparrow\downarrow}} . \tag{9}$$

For fermions these couplings are always antiferromagnetic ($t_\sigma \geq 0$ is assumed). However, for bosons, the sign of J_z can be tuned, leading, in a spin-dependent cubic lattice at unit filling, to a quantum phase transition between xy-ferromagnetism and z-Néel antiferromagnetism [53, 55], see Fig. 6. Finite-temperature DMFT calculations for the same model [56] have, in addition, found a Pomeranchuk effect, where heating the system leads to a transition from the superfluid phase to a paramagnetic Mott insulator and, as a result, non-monotonic behavior of the local particle number variance $(\Delta n_i)^2 = \left\langle \left(\hat{n}_i - \langle \hat{n}_i \rangle \right)^2 \right\rangle$, which should be observable by quantum-gas microscopy.
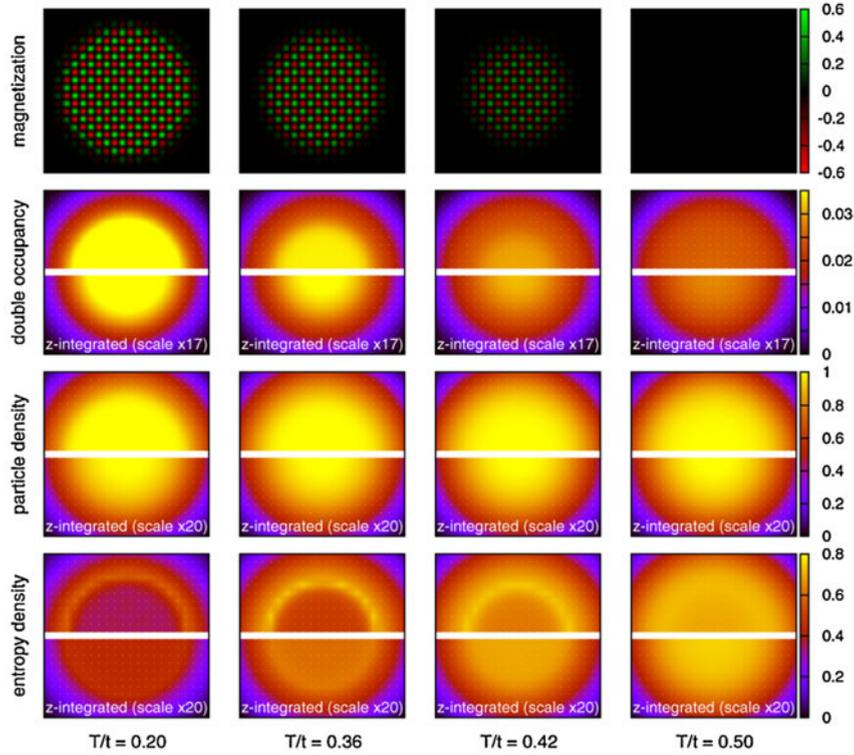
Fig. 7: *Real-space DMFT simulation of a Fermi-Hubbard model in a harmonic trap. Shown are antiferromagnetic order (first row), double occupancy D (second row), particle (3rd row) and entropy (4th row) densities per site, in the central plane of the Fermi-Hubbard model (1) on a cubic lattice with $U = 12t$ and a harmonic trapping potential $\varepsilon_i = V_0 \mathbf{r}_i^2/a^2$ with $V_0 = 0.05t$. At low temperature (left column) a large antiferromagnetic core is visible; with increasing temperature the AF order decays. In the 2nd, 3rd and 4th row the top half displays the respective observables in the central plane of the lattice, and the bottom half the corresponding values after integration along the z-axis. Reprinted figure with permission from [46]. Copyright 2010 by the American Physical Society.*

The formation of antiferromagnetic (AF) order of spin-½ ultracold fermions in a half-filled optical lattice was first proposed in [17]. It was later studied by cluster DMFT [57], which provided an estimate $s_{\text{Néel}} \approx 0.42\,k_B$ for the critical entropy per particle. Experiments with 3d optical lattices have yielded higher values $s \approx 0.77\,k_B$ in the Mott core [58], indicating that in these measurements the AF ordered regime has not yet been reached. Magnetization and entropy profiles for realistic system sizes in a harmonic trap have been obtained by real-space DMFT [46], see Fig. 7, and an enhanced double occupancy $D = \langle \hat{n}_{i\uparrow} \hat{n}_{i\downarrow} \rangle$ was found in the Néel-ordered phase.

Ultracold atoms also allow realizing multi-flavor mixtures with more than two hyperfine states and higher internal symmetry groups. This has for example been achieved with ^{173}Yb, a fermionic alkaline-earth-like element, which has been cooled into an SU(6) Mott-insulating state [52]. DMFT studies of three-component fermionic mixtures in optical lattices have predicted exotic spin and density order [59]. Note that due to enhanced Pomeranchuk cooling, adiabatic lattice loading of fermions with multiple flavors can achieve lower temperatures than for spin-½ systems [60].

Experimentally, tunable superexchange interactions in ultracold atoms, as given in Eq. (9) and shown in Fig. 5, were first seen in the spin dynamics of a mixture of two hyperfine states of ^{87}Rb in a superlattice [61]. Achieving sufficiently low entropies and temperatures of quantum gases in an optical lattice in order to observe superexchange-induced magnetic order is an experimental challenge [62], although much progress has been made. Adiabatic spin gradient demagnetization has allowed to cool a mixture of two hyperfine states of bosonic ^{87}Rb in a cubic lattice to temperatures as low as 350 pK [63]. Real-space bosonic DMFT calculations for this experimental setup have provided quantitative modeling of these results [56] and predicted that long-range magnetic order can indeed be reached by adiabatic demagnetization.

Early measurements of spin-spin correlations included a detection scheme for singlets and triplets based on merging pairs of lattice sites, which allowed to observe short-range AF correlations in dimerized and simple cubic lattices [64]. Another powerful approach is given by spin-sensitive Bragg scattering, which yields the spin structure factor

$$S_{\boldsymbol{q}}^z = \frac{1}{N} \sum_{i,j} e^{i\boldsymbol{q} \cdot (\boldsymbol{r}_i - \boldsymbol{r}_j)} \langle \hat{\sigma}_i^z \hat{\sigma}_j^z \rangle$$

and is analogous to neutron scattering in solid-state physics. In the experiment [58] a strong enhancement of $S_{\boldsymbol{q}}^z$ at the wavevector $\boldsymbol{q} = (\pi/a)(-1, -1, 1)$ was observed for fermionic ^{6}Li in a cubic optical lattice, indicating Néel-type spin-spin correlations. Comparison to numerical simulations (QMC and linked-cluster expansion) allowed to estimate the temperature in this setup as 1.4-times the critical temperature of long-range AF order.

More recently, optical quantum-gas microscopy has allowed to detect spin-spin- and density-density-correlations in-situ. The spin-spin correlator $C_{\boldsymbol{d}} \propto \sum_{\boldsymbol{r}} \langle \hat{\sigma}_{\boldsymbol{r}}^z \hat{\sigma}_{\boldsymbol{r}+\boldsymbol{d}}^z \rangle - \langle \hat{\sigma}_{\boldsymbol{r}}^z \rangle \langle \hat{\sigma}_{\boldsymbol{r}+\boldsymbol{d}}^z \rangle$ has been measured for a mixture of two hyperfine states of fermionic ^{6}Li in a square optical lattice [20]. At half filling, long-range AF correlations extending throughout the lattice (size 10×10 sites) were observed at temperatures as low as $T/T_F \approx 0.06$, where $T_F = 4t/k_B$ is the Fermi temperature in the lattice.

Ultracold atom quantum simulators allow to directly control and tune the spin-imbalance (spin polarization) of the system, which in the case of the half-filled Fermi-Hubbard model induces canted antiferromagnetic correlations, as observed in [21] using ^{6}Li. Note that very large magnetic fields would be required for observing this effect in solid-state materials. Very recently, a bilayer Hubbard model was realized with ^{40}K, where tomographic imaging allowed to address both layers individually [65]. With increasing interlayer tunneling a crossover from a planar antiferromagnetic Mott insulator to a band insulator of interlayer spin-singlets was observed, confirming previous theoretical expectations. Also the attractive ($U < 0$) Fermi-Hubbard model has been realized with ^{6}Li, where quantum-gas microscopy of doublon density correlations, in combination with QMC simulations, made it possible to estimate the strength of s-wave pairing correlations [22]. Major progress has thus been made in quantum simulations of magnetism and superconductivity in Fermi-Hubbard systems, as first proposed in [17].

Cold atom quantum simulators also allow observing out-of-equilibrium particle- and spin-dynamics in real time. For example, using ^{87}Rb a one-dimensional two-component Bose-Hubbard model (see Eq. (7)) was realized, which for strong coupling maps onto an effective

ferromagnetic Heisenberg spin chain. In this system, propagation of magnons and of two-magnon bound states was observed by quantum-gas microscopy [23]. More recently, spin-charge deconfinement was observed in ^{6}Li Fermi-Hubbard chains, where after sudden removal of one particle the spin and charge excitations (spinons and holons) were found to propagate with different, interaction-dependent velocities [24]. Spin diffusion and spin conduction were measured in a 2d fermionic Mott insulator of ultracold ^{40}K, using quantum-gas microscopy [25], thus opening up the possibility to gain further insight into the interplay of charge and spin in strongly correlated fermion systems.

Recent progress with Rydberg-excited and Rydberg-dressed quantum gases allows engineering long-range interactions, both in quantum spin systems and in itinerant lattice models. Spinless fermions with next-neighbor interaction on an anisotropic square lattice, with hopping only in one direction, were realized with Rydberg-dressed ^{6}Li [13], and the effect of the next-neighbor interaction on the decay dynamics of initially prepared charge-density waves was investigated. Quantum simulations of extended Fermi-Hubbard models are thus within reach of current experiments. For itinerant bosons with Rydberg excitations in an optical lattice, an extended 2-component Bose-Hubbard model description is appropriate, which includes, in addition to Eq. (7), a long-range van der Waals interaction $H_{vdW} = (C_6/2) \sum_{i \neq j} \hat{n}_{i\uparrow} \hat{n}_{j\uparrow} / |\boldsymbol{i} - \boldsymbol{j}|^6$. Here the pseudospin states $\uparrow$ ($\downarrow$) denote the Rydberg state (ground state), respectively, $\boldsymbol{i}$ and $\boldsymbol{j}$ are the positions of lattice sites i, j and C_6 is the van der Waals coefficient. Coherent driving by a laser populates the Rydberg state, which leads (within the rotating wave approximation) to an additional Rabi term $H_R = (\Omega/2) \sum_i \left(a_{i\uparrow}^\dagger a_{i\downarrow} + a_{i\downarrow}^\dagger a_{i\uparrow} \right) - \Delta \hat{n}_{i\uparrow}$ with Rabi frequency Ω and detuning Δ. Bosonic DMFT simulations yield a rich phase diagram including a devil's staircase of crystalline phases which extends into the supersolid regime, where crystalline and condensate long-range order coexist [66], see Fig. 8.

Alternatively, optical microtraps can be arranged in arbitrary geometries and loaded with single atoms, which can be individually addressed and excited to a Rydberg state. In this way, the quantum many-body dynamics of Ising-type quantum-spin models has been investigated for systems with up to 51 qbits [67].

5 Topological (many-body) states of ultracold atoms

Topological states of matter provide a new paradigm beyond Landau's approach towards classifying phases of matter [68]. A prime example in two spatial dimensions is the integer quantum Hall effect. According to the TKNN formula [69] its quantized transverse conductivity is determined by a topological invariant, the Chern number $n = (1/2\pi) \sum_m \int d^2 \boldsymbol{k}\, \Omega_m(\boldsymbol{k})$, where the summation is over all occupied bands. Here $\Omega_m = i \big(\langle \partial_{k_x} u_m(\boldsymbol{k}) | \partial_{k_y} u_m(\boldsymbol{k}) \rangle - \langle \partial_{k_y} u_m(\boldsymbol{k}) | \partial_{k_x} u_m(\boldsymbol{k}) \rangle \big)$ is the Berry curvature, and $|u_m(\boldsymbol{k})\rangle$ is the lattice-periodic part of the Bloch state with quasimomentum $\boldsymbol{k}$ in band m. Laughlin's argument [70] proves that in systems of finite width a quantized Hall conductivity $\sigma_{xy} = ne^2/h$ implies the existence of chiral edge states. As shown by Haldane, time-reversal symmetry breaking can induce a quantum Hall state even if no net magnetic flux is applied to the 2d system [71].
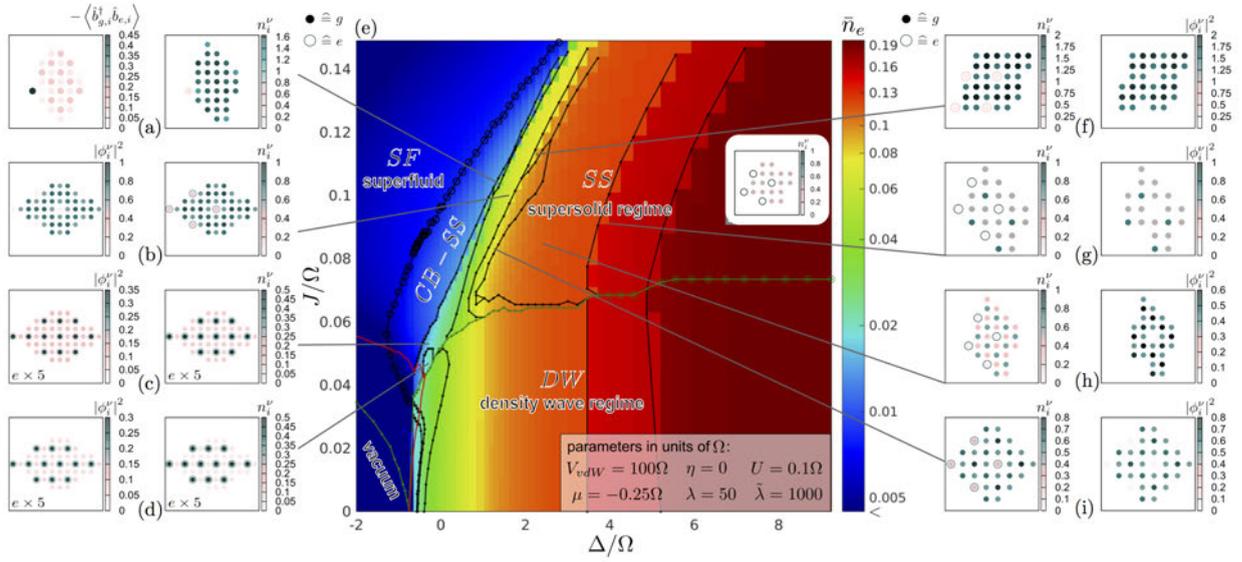
Fig. 8: *(e) Ground state phase diagram of a two-species extended bosonic Hubbard model with long-range (van der Waals) interaction of the excited Rydberg state, as a function of hopping amplitude (here denoted as J) and detuning Δ, in units of the Rabi frequency Ω. $\bar{n}_e$ is the lattice-averaged Rydberg fraction. The green (gray) line marks the emergence of a finite condensate order parameter. Black lines indicate transitions between different supersolid (SS) or density wave (DW) ordered phases, where circles denote second order and points first order. CB-SS indicates the checkerboard supersolid, and SF the homogeneous superfluid. Subfigures (a)-(d), (f)-(i) and the inset of (e) show the spatial distribution of different observables: density n_i^ν and condensate density $|\phi_i^\nu|^2$, where i is the lattice site index and $\nu = g(e)$ here denotes the ground (Rydberg excited) state. In addition, the correlation function $\langle b_{g,i}^\dagger b_{e,i} \rangle$, sensitive to checkerboard order, is shown, where $b^\dagger(b)$ denote the bosonic creation (annihilation) operators. Parameters given in the inset of (e) are: the ratio η of excited state hopping and ground state hopping, the van der Waals interaction strength $V_{vdW} = C_6/a^3$, and the onsite interaction ratios $\lambda = U_{\uparrow\downarrow}/U_\downarrow$ and $\tilde{\lambda} = U_\uparrow/U_\downarrow$, see Eq. (7), where we use the notation $\uparrow \,\hat{=}\, e$ and $\downarrow \,\hat{=}\, g$. Reprinted figure with permission from [66]. Copyright 2017 by the American Physical Society.*

More recently, time-reversal invariant topological insulators have been discovered, such as the quantum spin Hall (QSH) state, which is characterized by a Z_2 topological invariant and helical edge states inside the bulk band gap. An important model system featuring a QSH state is the Kane-Mele model [72], which consists of time-reversed copies of Haldane's model [71], discussed below. In solid-state systems quantum (spin-) Hall states can be detected by measuring band structures via angle-resolved photoemission or by measuring the Hall conductivity. But in these systems it is hard to measure the Berry curvature, or to study topological states of matter in the presence of tunable two-particle interactions.

Synthetic gauge fields, i.e., synthetic flux or spin-orbit coupling, have been realized in neutral ultracold atoms. Here we will focus on gauge fields in optical lattices achieved by time-periodic driving, in particular by laser-induced tunnelling [73–76] and in shaken lattices [77–79]. These techniques allow creating strong effective magnetic flux and topologically non-trivial states.

They are examples for Floquet engineering, which allows to design and tune band structures, interactions, quantum states and effective (Floquet-) Hamiltonians, by time-periodic driving [80]. Important model systems have already been realized in this way, in particular the Harper-Hofstadter (HH) [74, 75] and Haldane Hamiltonians [78].

The topological Haldane model [71] describes a quantum anomalous Hall state in the absence of a net flux and has the form

$$\hat{H} = -\sum_{\langle ij \rangle} t_{ij} \, \hat{a}_i^\dagger \hat{a}_j - \sum_{\langle\langle ij \rangle\rangle} t'_{ij} \, e^{i\phi_{ij}} \hat{a}_i^\dagger \hat{a}_j + \text{h.c.} + \Delta_{AB} \sum_{i \in A} \hat{a}_i^\dagger \hat{a}_i \tag{10}$$

where the indices $i(j)$ label the sites of a honeycomb lattice, t_{ij} and t'_{ij} are real hopping amplitudes between pairs of nearest neighbors $\langle ij \rangle$ and next-nearest neighbors $\langle\langle ij \rangle\rangle$, respectively, ϕ_{ij} is a phase, and Δ_{AB} is a staggered energy offset between the two sublattices A and B. The Haldane model has been realized experimentally [78] by "lattice shaking", i.e., by accelerated motion of a two-dimensional optical honeycomb lattice on an elliptical orbit $\boldsymbol{r}_{\text{lat}} = A\big(\cos(\omega t)\boldsymbol{e}_x + \cos(\omega t - \varphi)\boldsymbol{e}_y \big)$. The Berry curvature $\Omega_m(\boldsymbol{k})$ was measured semiclassically via the quasimomentum drift of a cloud of ultracold ^{40}K in the lowest band. More recently, a tomographic measurement of the full quasimomentum dependence of the Berry curvature of a tunable honeycomb lattice has been performed by monitoring the dynamics of the fermionic cloud after a sudden quench of the periodic driving [79].

The HH Hamiltonian describes a quantum particle on a tight-binding square lattice

$$\hat{H} = -\sum_{m,n} t \left(e^{i\phi_{mn}} \hat{a}_{m+1,n}^\dagger \hat{a}_{m,n} + \hat{a}_{m,n+1}^\dagger \hat{a}_{m,n} \right) + \text{h.c.}, \tag{11}$$

where the sites of the lattice are labeled by (m, n), in the presence of a strong magnetic flux, which is described by the Peierls phase ϕ_{mn}. It has been realized in optical lattices [74, 75], following the proposal [73], where the Peierls phase is imprinted by laser-assisted tunneling, as shown in the setup in Fig. 9. Due to a magnetic field gradient the energy offset Δ between neighboring sites in x-direction is much larger than the bare tunneling amplitude, suppressing hopping in this direction. Two additional laser beams with frequency difference $\omega = \omega_1 - \omega_2 = \Delta/\hbar$ and wave vector difference $\boldsymbol{q} = \boldsymbol{k}_1 - \boldsymbol{k}_2$ then induce resonant, laser-assisted tunneling in the x-direction. In the limit of high driving frequency ω this system can be described by an effective time-independent (Floquet-) Hamiltonian of the HH type as given in Eq. (11). The resulting Peierls phase is given by $\phi_{mn} = \boldsymbol{q} \cdot \boldsymbol{R}_{mn}$, where $\boldsymbol{R}_{mn}$ is the position of lattice site (m, n). One defines a dimensionless flux per plaquette of the lattice as $\alpha = \Phi/2\pi$, where Φ is the accumulated Peierls phase on a closed path around the plaquette. The Chern number of the lowest band of this system has been measured for $\alpha = 1/4$ in a modified, all-optical set-up [76]. Realizing a QSH state by filling the Chern bands with ultracold fermions and detecting the associated edge states remains an open challenge for experiments. Note, however, that edge states, and also a local Chern marker characterizing bulk topology, have been recently observed in setups where one spatial dimension is replaced by a "synthetic dimension" encoded in different internal (hyperfine) states, see for example [81].
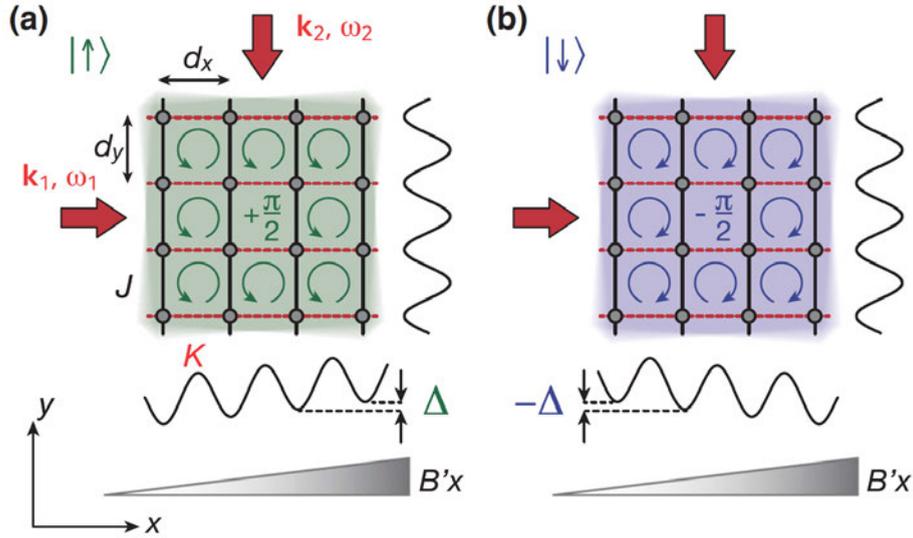
Fig. 9: *Experimental set-up for the realization of the Harper-Hofstadter Hamiltonian [74]. Two time-reversed copies of the HH-Hamiltonian (11) with opposite flux were realized for two hyperfine states labeled by $|\uparrow\rangle, |\downarrow\rangle$. Reprinted figure with permission from [74]. Copyright 2013 by the American Physical Society.*

Cold atoms with synthetic gauge fields are well suited for studying interacting topological many-body states. From a theoretical perspective, noninteracting topological insulators have been studied intensely and are quite well understood [68], but many open questions remain regarding the effect of two-particle interactions on topological bands. One promising approach [82] allows to extract (integer) topological invariants of interacting lattice systems from the zero-frequency Green's function alone, via an effective noninteracting "topological Hamiltonian" $h_{\text{top}}(\boldsymbol{k}) = -G^{-1}(\boldsymbol{k}, i\omega{=}0)$. It can be conveniently combined with (real-space) DMFT and allows to calculate topological invariants for strongly correlated fermionic systems, e.g., for interacting QSH states in Hubbard-type lattice models. This approach has been applied to calculate the phase diagram of the time-reversal-symmetric fermionic Hofstadter-Hubbard model

$$\hat{H} = -t \sum_{j} \left(\hat{c}^{\dagger}_{j+\boldsymbol{e}_x} e^{i2\pi\gamma\sigma^x} \hat{c}_j + \hat{c}^{\dagger}_{j+\boldsymbol{e}_y} e^{i2\pi\alpha x\sigma^z} \hat{c}_j + \text{h.c.} \right) + \sum_{j} \left((-1)^x \lambda \hat{c}^{\dagger}_j \hat{c}_j + U \hat{n}_{i\uparrow} \hat{n}_{i\downarrow} \right) \quad (12)$$

with a staggered potential λ and additional spin-orbit coupling γ. Here $\boldsymbol{e}_x, \boldsymbol{e}_y$ are the primitive lattice vectors in x- and y-direction of a square lattice and $c^{\dagger}_j = (c^{\dagger}_{j\uparrow}, c^{\dagger}_{j\downarrow})$ denotes the creation operator at site $j = (x, y)$. An interaction-driven transition into the QSH state has been observed and the bulk-edge correspondence has been verified [83]. Moreover, the formation of a smooth topological interface in the bulk of the optical lattice has been proposed and studied theoretically by ramping up the staggered potential $\lambda(x)$ in the model (12) as a function of the x-coordinate [84], as shown in Fig. 10. By real-space DMFT simulations it was found that the gapless edge states at the interface are visible in an enhanced local compressibility. The latter can be directly related to non-local density-density correlations, which could in principle be measured by quantum-gas microscopy [19].
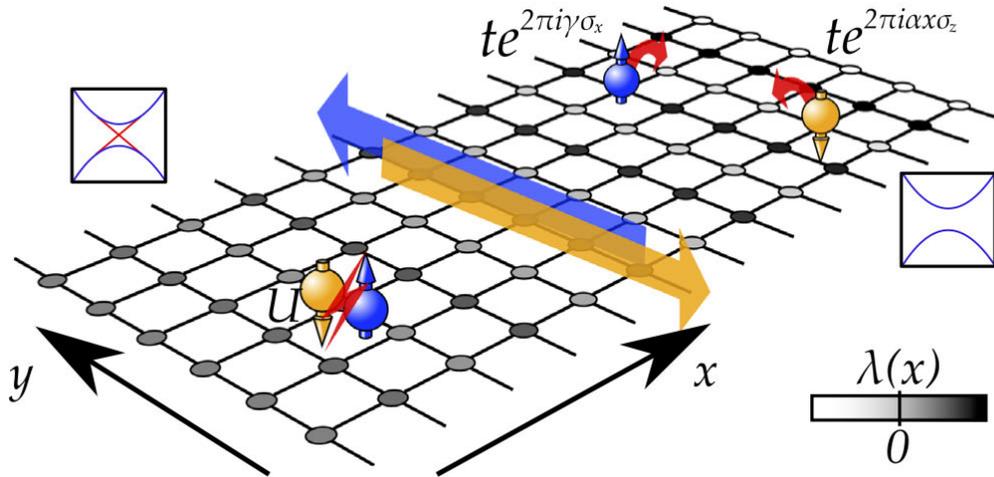
Fig. 10: *Topological Hofstadter interface: Schematic representation of the Hofstadter-Hubbard model, given by Eq. (12), in a cylinder geometry, with a staggered potential $\lambda(x)$ linearly increasing across the lattice in x-direction. Reprinted figure with permission from [84]. Copyright 2019 by the American Physical Society.*

The measurement of topological invariants in interacting quantum gases is challenging. In [85] it was shown for a spin-½ Haldane-Hubbard model that from the single-particle density-matrix (SPDM) of the system the effective topological Hamiltonian $h_{\text{top}}(\boldsymbol{k})$ can be extracted, and thus the Chern number calculated and the topological phase transition determined. Furthermore, in this work a general experimental tomography scheme was proposed for measuring the SPDM of interacting fermions in bipartite lattices, based on a sudden quench of the system to a non-interacting lattice Hamiltonian, and subsequent time-of-flight measurement.

Topological band insulators are symmetry-protected topological (SPT) phases, with a bulk gap and nontrivial surface states which are protected by symmetry. Alternatively, a many-body system may have intrinsic topological order, with topological ground state degeneracy and fractional excitations [86]. Optical flux lattices may be a promising experimental platform for realizing fractional Chern insulators in ultracold atoms [87]. Topological order could be observed by measuring nonlocal correlation functions, for example string order, which has already been detected in a 1d bosonic Mott insulator [88].

6 Disorder and localization

Effects of disorder, such as localization or glassiness, are important in solid-state materials, where defects are intrinsically present and unavoidable. In particular, conducting properties of electronic systems are strongly affected by scattering from defects. In itinerant electronic systems metal-insulator transitions can occur which are driven by the interplay between spatial randomness and two-particle interactions. Noninteracting, disordered systems are rather well understood, see for example the review [89]. This is due to techniques such as the scaling theory of localization, which considers the dimensionless conductance $g \equiv G/(e^2/\hbar)$ and argues that
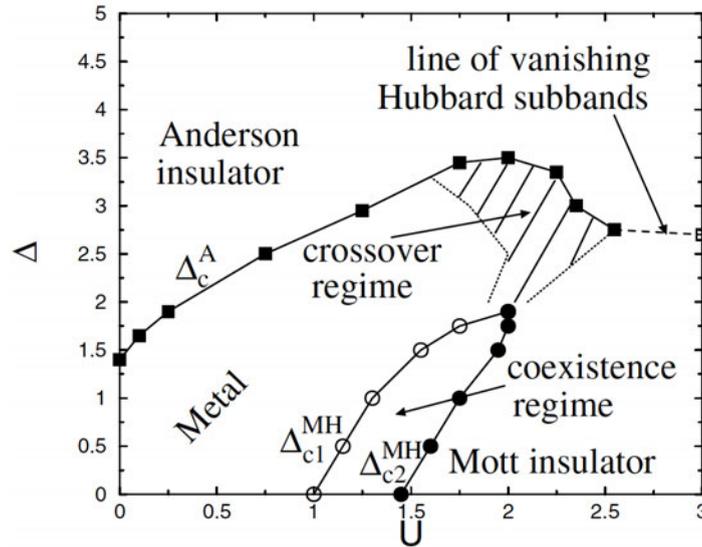
Fig. 11: *Paramagnetic ground state phase diagram of the fermionic Anderson-Hubbard model at half filling, determined by DMFT in combination with typical-medium theory. Reprinted figure with permission from [94]. Copyright 2005 by the American Physical Society.*

its dependence on the linear system size can be expressed as $\frac{d\ln g}{d\ln L} = \beta(g)$. In spatial dimensions $d = 1$ and 2 this leads in the thermodynamic limit $L \to \infty$ always to insulating behavior, corresponding to completely localized single-particle states, since $\beta(g) < 0$. On the other hand, in $d = 3$ one finds that $\beta(g_c) = 0$ at a critical value g_c of the conductance. This implies a mobility edge between (Anderson-)localized and extended single-particle states, and a metal-insulator transition as a function of disorder strength or chemical potential, as already predicted by Anderson in his seminar paper [90].

Ultracold atomic quantum simulations of relevant theoretical models offer high tunability of the type and strength of disorder, via quasi-periodic optical lattices or optical speckle potentials. In addition, two-particle interactions are tunable via Feshbach resonances, and also the (bosonic or fermionic) quantum statistics can be tuned by an appropriate choice of the atomic species. Moreover, non-equilibrium dynamics can be monitored in-situ in real time, which allows to probe many-body localization (MBL), as will be discussed below. We will, in the following, only consider quenched disorder potentials, corresponding to static, randomly placed defects which do not change on the experimental timescales.

Ultracold bosons have for the first time allowed direct observation in real space of an exponentially localized matter wave $\Psi_{\text{BEC}}(x) \sim e^{-|x|/\xi}$, for example by imaging an expanding, non-interacting Bose-Einstein condensate in a 1d disordered optical Speckle potential [91]. Three-dimensional Anderson localization has been observed in ultracold fermionic ^{40}K, where an exponentially localized component of the cloud was detected, corresponding to particles below the mobility edge [92].

Major theoretical challenges remain in studies of quantum many-body systems with (strong) disorder and interaction. It has been predicted that two-particle interactions can lead to a metal-insulator transition in 2d disordered Fermi gases [93], in contrast to the non-interacting case.

Optical lattice quantum simulations are well suited for studying the interplay between strong local correlations, captured by the Hubbard model and leading e.g., to a Mott metal-insulator transition, and Anderson localization induced by strong disorder. Developments in DMFT have led to theoretical progress on this topic. The fermionic Anderson-Hubbard model is a disordered version of Eq. (1), where the onsite energies ε_i are independently sampled from a probability distribution $p(\varepsilon)$ of width Δ. Important disorder types are box disorder with a flat, bounded distribution $p(\varepsilon) = \Theta\big(\Delta/2 - |\varepsilon|\big)/\Delta$, or optical Speckle disorder with $p(\varepsilon) = \Theta(\varepsilon)\exp(-\varepsilon/\Delta)/\Delta$, where $\Theta(x)$ is the Heaviside function. The fermionic Anderson-Hubbard model with box disorder has been studied at half filling by DMFT in combination with typical-medium theory (TMT) [94]. TMT is built on the concept that the typical (i.e. most probable) value of the local density of states (LDOS) $A_{i\sigma}(\omega) = -\frac{1}{\pi}\mathrm{Im}G_{ii\sigma}(\omega+i0^+)$ can be considered as a mean-field for the Anderson localization transition. In particular, the typical LDOS vanishes inside the Anderson insulator, in contrast to the average density of states. The resulting non-magnetic ground state phase diagram, see Fig. 11, clearly shows that weak interactions can induce delocalization in the Anderson insulator. This corresponds to re-entrant metallic behavior, which also occurs when disorder is added to the Mott insulator. Later DMFT studies also considered the experimentally realistic disorder distribution for optical Speckle potentials [95], and included the possibility of antiferromagnetic ordering, which leads to a novel antiferromagnetic metallic phase [96].

A quantum simulation of the fermionic Anderson-Hubbard model on a cubic optical lattice has been performed with ^{40}K, where disorder was induced by an additional optical Speckle potential [97]. A transport-type measurement of localization properties was performed where the center-of-mass velocity was detected after applying a magnetic field gradient. This velocity was found to decrease with increasing disorder, and to vanish at a critical disorder strength Δ_c, in agreement with an Anderson metal-insulator transition. Increasing the Hubbard interaction in the Anderson insulator led to delocalization, as shown in Fig. 12, which qualitatively confirms the DMFT prediction [94].

On the other hand, the disordered Bose-Hubbard model [31] describes effects of randomness in strongly correlated bosonic systems, for example in superfluid ^{4}He immersed in random pores of Vycor. It is given by Eq. (5) with onsite energies ε_i sampled from a probability distribution of width Δ. In the ground state, an insulating and compressible Bose glass (BG) phase has been predicted, in addition to the Mott insulator (MF) and the superfluid (SF) [31]. The properties of the BG have been the subject of numerous theoretical studies. In one spatial dimension, DMRG simulations have provided early insight [98], but less has been known in higher dimensions. Simple arithmetic averaging over disorder cannot describe the BG phase, since it effectively restores translational invariance. This has motivated development of a stochastic mean-field theory (SMFT), which maps the inhomogeneous system with spatial fluctuations of the condensate onto an ensemble of effective single-site problems, each coupled to a mean-field bath with condensate order parameter ψ, subject to a probability distribution $P(\psi)$ that is determined self-consistently [99, 100], as shown in Fig. 13 (left). In this way, the BG phase with its disorder-induced localization is captured, with a non-trivial dependence on spatial dimen-
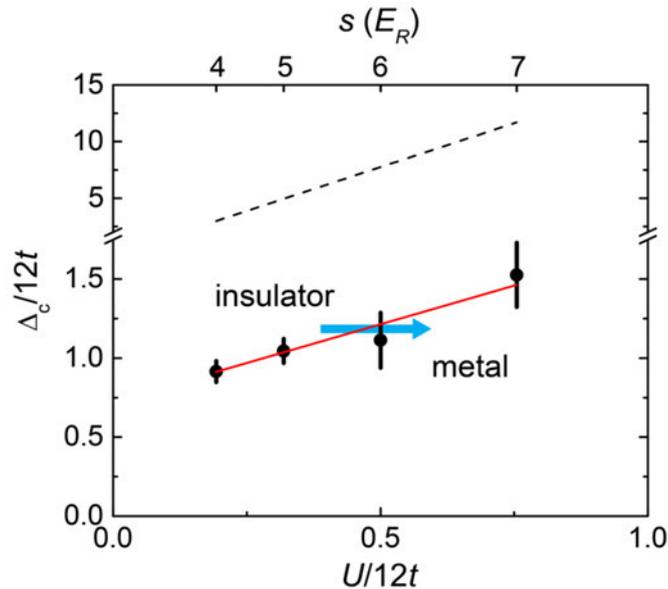
Fig. 12: *Critical disorder-strength of the disorder-driven fermionic metal-insulator transition measured for ultracold ^{40}K in a cubic lattice with Speckle disorder. Interaction-induced delocalization can be clearly seen. Reprinted figure with permission from [97]. Copyright 2015 by the American Physical Society.*

sion beyond mean-field scaling. The method can be applied to realistic disorder types such as optical Speckle potentials, and is formulated directly in the thermodynamic limit, thus avoiding finite-size effects. The MI, SF and BG phases are distinguished by their values of the average condensate order parameter ψ and the compressibility $\partial n/\partial \mu$. When including collective excitations of the BG in the SMFT calculation [100], one observes that the transition from MI to SF in the ground state of the disordered Bose-Hubbard model always occurs via an intermediate BG phase. This has been independently shown by QMC studies and a "theorem of inclusions" [101]. In the strongly interacting regime, at constant filling, increasing the disorder strength can lead to re-entrant superfluidity, i.e., drive the system from the insulator back into the superfluid phase. This was observed in SMFT calculations with a finite lattice coordination number $z = 6$ (see Fig. 13 (right)) [100] and in QMC simulations on a cubic lattice [101].

The disordered Bose-Hubbard model has been realized experimentally in a cubic optical lattice with an additional short-wavelength optical Speckle potential [102]. After switching on the Speckle potential, a strong reversible decrease of the condensate fraction was observed, which indicates that the interacting Bose-Einstein condensate is indeed localized by disorder. This was confirmed by measurement of mass transport in the lattice. Distinguishing the MI and BG phases would require additional measurements of the excitation spectrum or the compressibility, which were not performed in this experiment. Also, presumably due to finite temperature, no disorder-induced re-entrant superfluidity was observed.

Our discussion of localization transitions so far has focused on thermodynamic equilibrium and low temperatures. However, disordered and isolated quantum many-body systems may fail to thermalize, thus violating ergodicity, as was found in a perturbative study [103]. This so-called
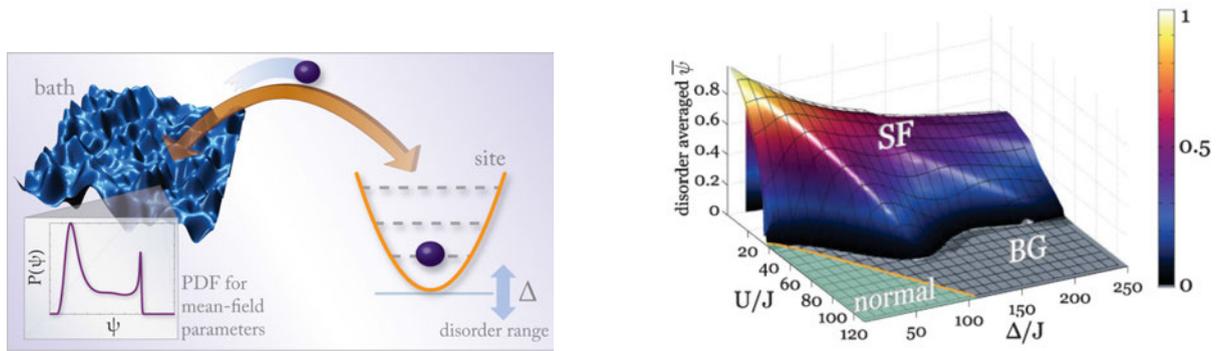
Fig. 13: *(left) Schematic illustration of SMFT. The lattice model is mapped onto an ensemble of effective single-site problems, each of which is coupled to a condensate mean-field bath. Spatially random fluctuations are captured by a statistical distribution of the condensate order parameter ψ. Reprinted figure with permission from [99]. (right) Phase diagram of the Bose-Hubbard model with lattice coordination number $z = 6$ and box disorder at filling $n = 1$ and $T = 0.03U$ (J denotes the hopping). At the protruding Mott lobe re-entrant superfluidity occurs, i.e., increasing the disorder strength drives a series of SF-insulator transitions. Reprinted figure with permission from [100]. Copyright 2010 by the American Physical Society.*

many-body localization (MBL) has since been the subject of numerous theoretical studies using different numerical and analytical approaches; for a review see [104]. Remarkably, a many-body localized system can remain fully insulating even at $T > 0$, different from an interacting Anderson insulator, which is only strictly insulating at $T = 0$. In the out-of equilibrium real-time dynamics of MBL systems, when initialized in a non-entangled state, entanglement spreads logarithmically, in contrast to thermal states or noninteracting Anderson insulators [104]. For a 1d quantum spin chain with short-range interactions a quasi-rigorous proof for the existence of MBL has been given [105]. Much less is known in $d > 1$, due to a lack of exact analytical solutions or reliable numerical simulation of quantum many-body dynamics. There have been arguments that MBL may be absent in $d > 1$ [106] and even MBL in disordered, interacting quantum spin chains has recently been challenged [107].

Quantum simulations with ultracold atoms have provided new insight into MBL. For fermions in a 1d incommensurate optical superlattice, described by the Aubry-André model which contains quasi-random disorder, it was observed that an initially prepared particle-density wave state does not decay in time, provided randomness is sufficiently strong [108]. This indicates a breakdown of thermalization. In a later measurement the real-time dynamics of a bosonic ^{87}Rb ensemble in a 2d disordered optical lattice after a quantum quench was observed. It was found that an initially prepared density domain wall fails to decay completely if the disorder strength is above a critical value, leading to a non-thermalized (quasi-) steady state [109]. The spatial decay length of the density distribution in the steady state was found to diverge at the critical disorder strength, i.e., at the (possible) MBL transition observed here. However, it remains to be seen whether the MBL phenomena observed on the time scales accessible in these experiments represent a stable localized quantum phase, or whether they correspond to a metastable transient regime that emerges before thermalization sets in at much longer time scales [104].

7 Outlook

Analog quantum simulations of Hubbard-type models with ultracold atoms in optical lattices have already been very successful. One future goal will be to achieve even lower temperature (entropy) in optical lattices, in order to reach exotic low-temperature phases such as d-wave superfluidity in the Fermi-Hubbard model [17]. Hybrid quantum simulators with degenerate fermionic clouds coupled to phonons of trapped ion crystals can provide insight into the effect of additional electron-phonon coupling in strongly correlated systems [14].

Tunable long-range interactions in ultracold atomic ensembles will lead to novel physics compared to strongly correlated electronic systems. They can be induced by different approaches, including Rydberg excitations, heteronuclear molecules, magnetic dipolar moments, and coupling of quantum gases to single- or few-mode optical cavities. In this way, for example, supersolid phases have already been realized [110, 111].

Fermionic alkaline-earth-like elements (for example ^{173}Yb or ^{87}Sr) with their large nuclear spin decoupled from electronic angular momentum have emerged as platforms for simulating itinerant lattice models with orbital degeneracy or higher internal symmetries, which could allow quantum simulation of more exotic states of matter [112, 7, 8].

Due to the unprecedented local access in preparation and measurement of quantum states that is provided by optical quantum-gas microscopy, optical lattice quantum simulators are also ideally suited to study far-from-equilibrium quantum many-body dynamics. Fundamental open questions that will be further investigated in this way range from many-body-localization to quantum chaos.

Acknowledgments

References

[1] I. Bloch, J. Dalibard, and W. Zwerger, Rev. Mod. Phys. **80**, 885 (2008)

[2] W. Hofstetter and T. Qin, J. Phys. B: At. Mol. Opt. Phys. **51**, 082001 (2018)

[3] R.P. Feynman, Int. J. Theor. Phys. **21**, 467 (1982)

[4] P.A. Lee, N. Nagaosa, and X.-G. Wen, Rev. Mod. Phys. **78**, 17 (2006)

[5] K. Le Hur and T.M. Rice, Ann. Phys. **324**, 1452 (2009)

[6] M. Greiner, O. Mandel, T. Esslinger, T.W. Hänsch, and I. Bloch, Nature **415**, 39 (2002)

[7] C. Honerkamp and W. Hofstetter, Phys. Rev. Lett. **92**, 170403 (2004)

[8] A. Rapp, G. Zarand, C. Honerkamp, and W. Hofstetter,
Phys. Rev. Lett. **98**, 160405 (2007)

[9] M. Troyer and U.-J. Wiese, Phys. Rev. Lett. **94**, 170201 (2005)

[10] G. Cohen, E. Gull, D.R. Reichman, and A.J. Millis, Phys. Rev. Lett. **115**, 266802 (2015)

[11] I.M. Georgescu, S. Ashhab, and F. Nori, Rev. Mod. Phys. **86**, 153 (2014)

[12] J. Hubbard, Proc. R. Soc. Lond. A **276**, 238 (1963)

[13] E. Guardado-Sanchez, B.M. Spar, P. Schauss, R. Belyansky, J.T. Young, P. Bienias,
A.V. Gorshkov, T. Iadecola, W.S. Bakr, Phys. Rev. X **11**, 021036 (2021)

[14] U. Bissbort, D. Cocks, A. Negretti, Z. Idziaszek, T. Calarco, F. Schmidt-Kaler,
W. Hofstetter, R. Gerritsma, Phys. Rev. Lett. **111**, 080501 (2013)

[15] A. Georges, G. Kotliar, W. Krauth, and M.J. Rozenberg, Rev. Mod. Phys. **68**, 13 (1996)

[16] P.W. Anderson, Science **235**, 1196 (1987)

[17] W. Hofstetter, J.I. Cirac, P. Zoller, E. Demler, and M.D. Lukin,
Phys. Rev. Lett. **89**, 220407 (2002)

[18] D. Jaksch, C. Bruder, J.I. Cirac, C.W. Gardiner, and P. Zoller,
Phys. Rev. Lett. **81**, 3108 (1998)

[19] W.S. Bakr, A. Peng, M.E. Tai, R. Ma, J. Simon, J.I. Gillen, S. Fölling, L. Pollet,
and M. Greiner, Science **329**, 547 (2010); J.F. Sherson, C. Weitenberg, M. Endres,
M. Cheneau, I. Bloch, and S. Kuhr, Nature **467**, 68 (2010)

[20] A. Mazurenko, C.S. Chiu, G. Ji, M.F. Parsons, M. Kanasz-Nagy, R. Schmidt, F. Grusdt,
E. Demler, D. Greif and M. Greiner, Nature **545**, 462 (2017)

[21] P.T. Brown, D. Mitra, E. Guardado-Sanchez, P. Schauß, S.S. Kondov, E. Khatami,
T. Paiva, N. Trivedi, D.A. Huse, W.S. Bakr, Science **357**, 1385 (2017)

[22] D. Mitra, P.T. Brown, E. Guardado-Sanchez, S.S. Kondov, T. Devakul, D.A. Huse,
P. Schauß and W.S. Bakr, Nat. Phys. **14**, 173 (2018)

[23] T. Fukuhara, P. Schauß, M. Endres, S. Hild, M. Cheneau, I. Bloch and C. Gross,
Nature **502**, 76 (2013)

[24] J. Vijayan, P. Sompet, G. Salomon, J. Koepsell, S. Hirthe, A. Bohrdt, F. Grusdt, I. Bloch,
and C. Gross, Science **367**, 186 (2020)

[25] M.A. Nichols, L.W. Cheuk, M. Okan, T.R. Hartke, E. Mendez, T. Senthil, E. Khatami,
H. Zhang, and M.W. Zwierlein, Science **363**, 383 (2019)

[26] R. Grimm, M. Weidemüller and Y.B. Ovchinnikov,
Adv. At. Mol. Opt. Phys. **42**, 95 (2000)

[27] J. Struck, C. Ölschläger, R. Le Targat, P. Soltan-Panahi, A. Eckardt, M. Lewenstein,
P. Windpassinger, and K. Sengstock, Science **333**, 996 (2011)

[28] G.-B. Jo, J. Guzman, C.K. Thomas, P. Hosur, A. Vishwanath, and D.M. Stamper-Kurn,
Phys. Rev. Lett. **108**, 045305 (2012)

[29] T. Uehlinger, G. Jotzu, M. Messer, D. Greif, W. Hofstetter, U. Bissbort, and T. Esslinger,
Phys. Rev. Lett. **111**, 185307 (2013)

[30] U. Bissbort: *Dynamical effects and disorder in ultracold bosonic matter*,
PhD Thesis, Johann Wolfgang Goethe-Universität, Frankfurt am Main (2013)

[31] M.P.A. Fisher, P.B. Weichman, G. Grinstein, and D.S. Fisher, Phys. Rev. B **40**, 546 (1989)

[32] S. Will, T. Best, U. Schneider, L. Hackermüller, D.-S. Lühmann, and I. Bloch,
Nature **465**, 197 (2010)

[33] U. Bissbort, F. Deuretzbacher, and W. Hofstetter, Phys. Rev. A **86**, 023617 (2012)

[34] M. Köhl, H. Moritz, T. Stöferle, K. Günter, and T. Esslinger,
Phys. Rev. Lett. **94**, 080403 (2005)

[35] E. Altman, E. Demler, and M.D. Lukin, Phys. Rev. A **70**, 013603 (2004)

[36] J. Simon, W.S. Bakr, R. Ma, M.E. Tai, P.M. Preiss, and M. Greiner,
Nature **472**, 307 (2011)

[37] C.A. Regal and D.S. Jin, Phys. Rev. Lett. **90**, 230404 (2003);
S. Gupta, Z. Hadzibabic, M.W. Zwierlein, C.A. Stan, K. Dieckmann, C.H. Schunck,
E.G.M. van Kempen, B.J. Verhaar, and W. Ketterle, Science **300**, 1723 (2003)

[38] A. Schirotzek, Y.-il Shin, C.H. Schunck, and W. Ketterle,
     Phys. Rev. Lett. **101**, 140403 (2008)

[39] J.T. Stewart, J.P. Gaebler, and D.S. Jin, Nature **454**, 744 (2008)

[40] U. Bissbort, S. Götze, Y. Li, J. Heinze, J.S. Krauser, M. Weinberg, C. Becker,
     K. Sengstock, and W. Hofstetter, Phys. Rev. Lett. **106**, 205303 (2011)

[41] R. Jördens, N. Strohmaier, K. Günter, H. Moritz, and T. Esslinger,
     Nature **455**, 204 (2008)

[42] C. Weitenberg, M. Endres, J.F. Sherson, M. Cheneau, P. Schauß, T. Fukuhara, I. Bloch
     and S. Kuhr, Nature **471**, 319 (2011)

[43] D. Greif, M.F. Parsons, A. Mazurenko, C.S. Chiu, S. Blatt, F. Huber, G. Ji,
     and M. Greiner, Science **351**, 953 (2016)

[44] M. Snoek, I. Titvinidze, C. Toke, K. Byczuk, and W. Hofstetter,
     New J. Phys. **10**, 093008 (2008)

[45] E. Gull, A.J. Millis, A. Lichtenstein, A.N. Rubtsov, M. Troyer, and P. Werner,
     Rev. Mod. Phys. **83**, 349 (2011)

[46] E.V. Gorelik, I. Titvinidze, W. Hofstetter, M. Snoek, and N. Blümer,
     Phys. Rev. Lett. **105**, 065301 (2010)

[47] G. Kotliar and D. Vollhardt, Phys. Today **57**, 53 (2004)

[48] K. Byczuk and D. Vollhardt, Phys. Rev. B **77**, 235106 (2008); A. Hubener, M. Snoek,
     and W. Hofstetter, Phys. Rev. B **80**, 245109 (2009)

[49] N. Prokof'ev and B. Svistunov, Phys. Rev. Lett. **92**, 15703 (2004)

[50] S. Trotzky, L. Pollet, F. Gerbier, U. Schnorrberger, I. Bloch, N. Prokof'ev, B. Svistunov,
     and M. Troyer, Nat. Phys. **6**, 998 (2010)

[51] U. Schneider, L. Hackermüller, S. Will, Th. Best, I. Bloch, T.A. Costi, R.W. Helmes,
     D. Rasch, and A. Rosch, Science **322**, 1520 (2008)

[52] S. Taie, R. Yamazaki, S. Sugawa, and Y. Takahashi, Nat. Phys. **8**, 825 (2012)

[53] E. Altman, W. Hofstetter, E. Demler, and M.D. Lukin, New J. Phys. **5**, 113 (2003)

[54] A. Sotnikov, D. Cocks, and W. Hofstetter, Phys. Rev. Lett. **109**, 065301 (2012)

[55] Y. Li, R. Bakhtiari, L. He, and W. Hofstetter, Phys. Rev. B **84**, 144411 (2011)

[56] Y. Li, M.R. Bakhtiari, L. He, and W. Hofstetter, Phys. Rev. A **85**, 023624 (2012)

[57] S. Fuchs, E. Gull, L. Pollet, E. Burovski, E. Kozik, T. Pruschke, and M. Troyer,
Phys. Rev. Lett. **106**, 030401 (2011)

[58] R.A. Hart, P.M. Duarte, T.-L. Yang, X. Liu, T. Paiva, E. Khatami, R.T. Scalettar,
N. Trivedi, D.A. Huse, and R.G. Hulet, Nature **519**, 211 (2015)

[59] A. Sotnikov and W. Hofstetter, Phys. Rev. A **89**, 063601 (2014); M. Hafez-Torbati
and W. Hofstetter, Phys. Rev. B **100**, 035133 (2019)

[60] L. Bonnes, K.R.A. Hazzard, S.R. Manmana, A.M. Rey, and S. Wessel,
Phys. Rev. Lett. **109**, 205305 (2012)

[61] S. Trotzky, P. Cheinet, S. Fölling, M. Feld, U. Schnorrberger, A.M. Rey, A. Polkovnikov,
E.A. Demler, M.D. Lukin, and I. Bloch, Science **319**, 295 (2008)

[62] D.C. McKay and B. DeMarco, Rep. Prog. Phys. **74**, 054401 (2011)

[63] P. Medley, D.M. Weld, H. Miyake, D.E. Pritchard, and W. Ketterle,
Phys. Rev. Lett. **106**, 195301 (2011)

[64] D. Greif, T. Uehlinger, G. Jotzu, L. Tarruell, and T. Esslinger, Science **340**, 1307 (2013)

[65] M. Gall, N. Wurz, J. Samland, C.F. Chan, and M. Köhl, Nature **589**, 40 (2021)

[66] A. Geißler, I. Vasić, and W. Hofstetter, Phys. Rev. A **95**, 063608 (2017)

[67] H. Bernien, S. Schwartz, A. Keesling, H. Levine, A. Omran, H. Pichler, S. Choi,
A.S. Zibrov, M. Endres, M. Greiner, V. Vuletic, and M.D. Lukin, Nature **551**, 579 (2017)

[68] M.Z. Hasan and C.L. Kane, Rev. Mod. Phys. **82**, 3045 (2010)

[69] D.J. Thouless, M. Kohmoto, M.P. Nightingale, and M. den Nijs,
Phys. Rev. Lett. **49**, 405 (1982)

[70] R.B. Laughlin, Phys. Rev. B **23**, 5632 (1981)

[71] F.D.M. Haldane, Phys. Rev. Lett. **61**, 2015 (1988)

[72] C.L. Kane and E.J. Mele, Phys. Rev. Lett. **95**, 226801 (2005)

[73] D. Jaksch and P. Zoller, New J. Phys. **5**, 56 (2003)

[74] M. Aidelsburger, M. Atala, M. Lohse, J.T. Barreiro, B. Paredes, and I. Bloch,
Phys. Rev. Lett. **111**, 185301 (2013)

[75] H. Miyake, G.A. Siviloglou, C.J. Kennedy, W.C. Burton, and W. Ketterle,
Phys. Rev. Lett. **111**, 185302 (2013)

[76] M. Aidelsburger, M. Lohse, C. Schweizer, M. Atala, J.T. Barreiro, S. Nascimbene, N.R. Cooper, I. Bloch, and N. Goldman, Nat. Phys. **11**, 162 (2015)

[77] J. Struck, M. Weinberg, C. Ölschläger, P. Windpassinger, J. Simonet, K. Sengstock, R. Höppner, P. Hauke, A. Eckardt, M. Lewenstein, and L. Mathey, Nat. Phys. **9**, 738 (2013)

[78] G. Jotzu, M. Messer, R. Desbuquois, M. Lebrat, T. Uehlinger, D. Greif, and T. Esslinger, Nature **515**, 237 (2014)

[79] N. Fläschner, B.S. Rem, M. Tarnowski, D. Vogel, D.-S. Lühmann, K. Sengstock, and C. Weitenberg, Science **352**, 1091 (2016)

[80] A. Eckardt, Rev. Mod. Phys. **89**, 011004 (2017)

[81] T. Chalopin, T. Satoor, A. Evrard, V. Makhalov, J. Dalibard, R. Lopes, and S. Nascimbene, Nat. Phys. **16**, 1017 (2020)

[82] Z. Wang and S.-C. Zhang, Phys. Rev. X **2**, 031008 (2012)

[83] D. Cocks, P.P. Orth, S. Rachel, M. Buchhold, K. Le Hur, and W. Hofstetter, Phys. Rev. Lett. **109**, 205303 (2012); P. Kumar, T. Mertz, and W. Hofstetter. Phys. Rev. B **94**, 115161 (2016)

[84] B. Irsigler, J.-H. Zheng, and W. Hofstetter, Phys. Rev. Lett. **122**, 010406 (2019)

[85] J.-H. Zheng, B. Irsigler, L. Jiang, C. Weitenberg, and W. Hofstetter, Phys. Rev. A **101**, 013631 (2020)

[86] T. Senthil, Annu. Rev. Condens. Matter Phys. **6**, 299 (2015)

[87] N.R. Cooper and J. Dalibard, Phys. Rev. Lett. **110**, 185301 (2013)

[88] M. Endres, M. Cheneau, T. Fukuhara, C. Weitenberg, P. Schauss, C. Gross, L. Mazza, M.C. Banuls, L. Pollet, I. Bloch, and S. Kuhr, Science **334**, 200 (2011)

[89] P.A. Lee and T.V. Ramakrishnan, Rev. Mod. Phys. **57**, 287 (1985)

[90] P.W. Anderson, Phys. Rev. **109**, 1492 (1958)

[91] J. Billy, V. Josse, Z. Zuo, A. Bernard, B. Hambrecht, P. Lugan, D. Clement, L. Sanchez-Palencia, P. Bouyer, and A. Aspect, Nature **453**, 891 (2008)

[92] S.S. Kondov, W.R. McGehee, J.J. Zirbel, and B. DeMarco, Science **334**, 66 (2011)

[93] S.V. Kravchenko and M.P. Sarachik, Rep. Prog. Phys. **67**, 1 (2003)

[94] K. Byczuk, W. Hofstetter, and D. Vollhardt, Phys. Rev. Lett. **94**, 056404 (2005)

[95] D. Semmler, J. Wernsdorfer, U. Bissbort, K. Byczuk, and W. Hofstetter,
      Phys. Rev. B **82**, 235115 (2010)

[96] K. Byczuk, W. Hofstetter, and D. Vollhardt, Phys. Rev. Lett. **102**, 146403 (2009)

[97] S.S. Kondov, W.R. McGehee, W. Xu, and B. DeMarco,
      Phys. Rev. Lett. **114**, 083002 (2015)

[98] S. Rapsch, U. Schollwöck, and W. Zwerger, Europhys. Lett. **46**, 559 (1999)

[99] U. Bissbort and W. Hofstetter, EPL **86**, 50007 (2009)

[100] U. Bissbort, R. Thomale, and W. Hofstetter, Phys. Rev. A **81**, 063643 (2010)

[101] V. Gurarie, L. Pollet, N.V. Prokof'ev, B.V. Svistunov, and M. Troyer,
      Phys. Rev. B **80**, 214519 (2009)

[102] M. White, M. Pasienski, D. McKay, S.Q. Zhou, D. Ceperley, and B. DeMarco,
      Phys. Rev. Lett. **102**, 055301 (2009);
      M. Pasienski, D. McKay, M. White, and B. DeMarco, Nat. Phys. **6**, 677 (2010)

[103] D.M. Basko, I.L. Aleiner, and B.L. Altshuler, Ann. Phys. **321**, 1126 (2006)

[104] R. Nandkishore and D.A. Huse, Annu. Rev. Condens. Matter Phys. **6**, 15 (2015)

[105] J.Z. Imbrie, Phys. Rev. Lett. **117**, 027201 (2016)

[106] W. De Roeck and F. Huveneers, Phys. Rev. B **95**, 155129 (2017)

[107] J. Suntajs, J. Bonca, T. Prosen, and L. Vidmar, Phys. Rev. E **102**, 062144 (2020)

[108] M. Schreiber, S.S. Hodgman, P. Bordia, H.P. Lüschen, M.H. Fischer, R. Vosk, E. Altman,
      U. Schneider, and I. Bloch, Science **349**, 842 (2015)

[109] J.-y. Choi, S. Hild, J. Zeiher, P. Schauß, A. Rubio-Abadal, T. Yefsah, V. Khemani,
      D.A. Huse, I. Bloch, and C. Gross, Science **352**, 1547 (2016)

[110] F. Böttcher, J. Schmidt, M. Wenzel, J. Hertkorn, M. Guo, T. Langen, and T. Pfau,
      Phys. Rev. X **9**, 011051 (2019);
      L. Tanzi, E. Lucioni, F. Fama, J. Catani, A. Fioretti, C. Gabbanini, R.N. Bisset, L. Santos,
      and G. Modugno, Phys. Rev. Lett. **122**, 130405 (2019);
      L. Chomaz, D. Petter, P. Ilzhöfer, G. Natale, A. Trautmann, C. Politi, G. Durastante,
      R.M.W. van Bijnen, A. Patscheider, M. Sohmen, M.J. Mark, and F. Ferlaino,
      Phys. Rev. X **9**, 021012 (2019)

[111] J. Léonard, A. Morales, P. Zupancic, T. Esslinger and T. Donner, Nature **543**, 87 (2017)

[112] A.V. Gorshkov, M. Hermele, V. Gurarie, C. Xu, P.S. Julienne, J. Ye, P. Zoller, E. Demler,
      M.D. Lukin, and A.M. Rey, Nat. Phys. **6**, 289 (2010)

11 Programming Quantum Computers

Kristel Michielsen, Madita Willsch, Dennis Willsch
Jülich Supercomputing Centre
Forschungszentrum Jülich

Contents

1   Introduction

Quantum computing is a new emerging computer technology. Current quantum computing devices are at a development stage where they gradually become suitable for small real-world applications. This lecture is devoted to the practical aspects of programming such quantum computing devices.

Over the past twenty years, two major paradigms of quantum computing have emerged. The first is the *gate-based model of quantum computing* (also known as *universal quantum computing*), and the second is *quantum annealing* (also known as *adiabatic quantum computing*). From a mathematical point of view, both models have the same computational power, but in practice they operate in a fundamentally different way.

The first part of this lecture focuses on gate-based quantum computers. We will define the basic unit of computation, the quantum bit (qubit), and how a quantum computer processes information. Subsequently, basic quantum circuits (i.e., the *programs* for gate-based quantum computers) are discussed and simulated. Finally, a more complex algorithm called the *quantum approximate optimization algorithm* (QAOA), which is considered to be an approach to address small optimization problems, is introduced and discussed.

In the second part of this lecture, we give an introduction to quantum annealing and discuss how to program a quantum annealer, i.e., the quantum processing unit (QPU) that performs the quantum annealing process. The introductory part starts with a discussion of discrete optimization problems and a formulation of the particular set of problems that can be solved on currently available quantum annealers. Subsequently, we describe the working principles of quantum annealers and the architecture of the currently available quantum annealers by D-Wave Systems Inc. We also discuss physical aspects including some limitations. Finally, we demonstrate how to program a D-Wave quantum annealer by means of some example programs.

2   Gate-based quantum computing

This section provides a hands-on introduction to the programming of gate-based quantum computers. After introducing the basic notions of qubits and gates, several examples of quantum circuits are programmed and discussed. These are either fundamental building blocks in disruptive quantum circuit scenarios, such as the quantum Fourier transform in Shor's factoring algorithm [1], or potentially relevant for near-term applications such as the QAOA [2]. In this section, the term *quantum computer* always refers to the gate-based model of quantum computing.

2.1   Quantum bits and gates

2.1.1   Single qubits

A gate-based quantum computer is designed to process information in terms of quantum bits (qubits). The word *qubit* is derived from the basic unit of computation in a digital computer, a
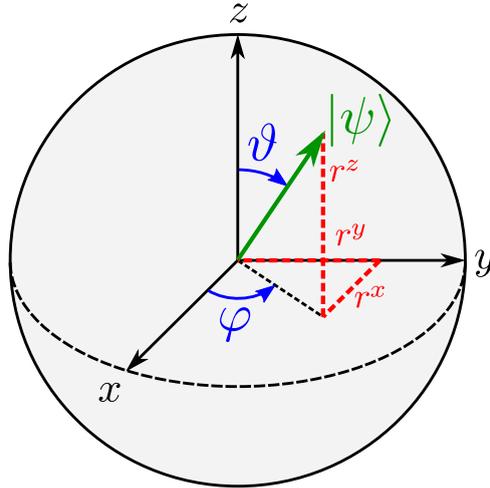
Fig. 1: *Bloch sphere representation of a pure single-qubit state $|\psi\rangle$. The azimuthal angle $\vartheta \in [0, \pi]$ and the polar angle $\varphi \in [0, 2\pi)$ are defined in Eq. (3), and the Cartesian coordinates r^x, r^y, and r^z are given by Eq. (5).*

binary digit or *bit*. While a bit in a digital computer can only ever be either 0 or 1, a qubit is a generalization of a bit in the sense that it can also be in a superposition of 0 and 1.

We describe a qubit $|\psi\rangle$ in terms of two complex numbers $\psi_0, \psi_1 \in \mathbb{C}$,

$$|\psi\rangle = \psi_0|0\rangle + \psi_1|1\rangle = \begin{pmatrix} \psi_0 \\ \psi_1 \end{pmatrix}, \tag{1}$$

which are normalized such that the norm of $|\psi\rangle$ is $\langle\psi|\psi\rangle = |\psi_0|^2 + |\psi_1|^2 = 1$. In the quantum computer model, the notions of 0 and 1 are represented by the standard vectors

$$|0\rangle = \begin{pmatrix} 1 \\ 0 \end{pmatrix}, \qquad |1\rangle = \begin{pmatrix} 0 \\ 1 \end{pmatrix}. \tag{2}$$

For the sake of programming quantum computers, these two notations are equivalent. We call $|\psi\rangle$ the *state vector* of the qubit.

Informally, a complex superposition like Eq. (1) is sometimes described as "0 and 1 at the same time", although it is important to realize that the notion of time plays no role here. Equation (1) is a well-defined mathematical object that completely describes the state of a single qubit.

A very useful representation of the general single-qubit state $|\psi\rangle$ in Eq. (1) is called the *Bloch sphere representation* that is shown in Fig. 1. It is particularly convenient to visualize the states and operations on a single qubit. We obtain the Bloch sphere representation by using the fact that $\langle\psi|\psi\rangle = |\psi_0|^2 + |\psi_1|^2 = 1$, which implies that there exists an angle $\vartheta \in [0, \pi]$ such that $|\psi_0| = \cos(\vartheta/2)$ and $|\psi_1| = \sin(\vartheta/2)$. Furthermore, as the global phase of a quantum state is irrelevant, we can choose without loss of generality $\psi_0 = \cos(\vartheta/2)$ and $\psi_1 = e^{i\varphi}\sin(\vartheta/2)$, where $\varphi \in [0, 2\pi)$ represents the relative phase between the complex coefficients. We thus obtain

$$|\psi\rangle = \cos\frac{\vartheta}{2}\,|0\rangle + e^{i\varphi}\sin\frac{\vartheta}{2}\,|1\rangle. \tag{3}$$

For all values of ϑ and φ, this state can be drawn on the surface of a 3D sphere with radius one as shown in Fig. 1.

When a qubit is measured, one always obtains one of the two discrete, digital outcomes "0" and "1". The complex coefficients of $|\psi\rangle$ determine the corresponding *probabilities* $p_0 = |\psi_0|^2$ and $p_1 = |\psi_1|^2$ to measure one of the two outcomes. On the Bloch sphere, the probabilities p_0 and p_1 can be obtained from the projection of $|\psi\rangle$ onto the z axis.

Exercise 1: Calculate ϑ and φ for the following states, visualize them on the Bloch sphere with radius one, and compute the probabilities to measure the qubit in $|0\rangle$ and $|1\rangle$:
(a) $|0\rangle$, **(b)** $|1\rangle$, **(c)** $(|0\rangle + |1\rangle)/\sqrt{2}$, **(d)** $(|0\rangle + i|1\rangle)/\sqrt{2}$, **(e)** $(\sqrt{3}/2)|0\rangle + ((1+i)/2\sqrt{2})|1\rangle$,
(f) $((1+i)/2)|0\rangle + ((1-\sqrt{3}i)/\sqrt{8})|1\rangle$ (hint: remove the global phase here first).

The Cartesian coordinates r^x, r^y, and r^z of the single-qubit state $|\psi\rangle$ in Fig. 1 can be computed as expectation values of the Pauli matrices,

$$\sigma^x = \begin{pmatrix} 0 & 1 \\ 1 & 0 \end{pmatrix}, \qquad \sigma^y = \begin{pmatrix} 0 & -i \\ i & 0 \end{pmatrix}, \qquad \sigma^z = \begin{pmatrix} 1 & 0 \\ 0 & -1 \end{pmatrix}. \qquad (4)$$

A short calculation yields

$$\vec{r} = \begin{pmatrix} r^x \\ r^y \\ r^z \end{pmatrix} = \begin{pmatrix} \langle\psi|\sigma^x|\psi\rangle \\ \langle\psi|\sigma^y|\psi\rangle \\ \langle\psi|\sigma^z|\psi\rangle \end{pmatrix} = \begin{pmatrix} \sin\vartheta\cos\varphi \\ \sin\vartheta\sin\varphi \\ \cos\vartheta \end{pmatrix}. \qquad (5)$$

2.1.2 Quantum gates

A *quantum gate* is a unitary operation that can be performed on a qubit. All single-qubit quantum gates can be visualized as rotations of $|\psi\rangle$ on the Bloch sphere in Fig. 1. One defines three elementary qubit rotations as matrix exponentials of the Pauli matrices in Eq. (4)

$$R^x(\theta) = e^{-i\theta\sigma^x/2} = \begin{pmatrix} \cos(\theta/2) & -i\sin(\theta/2) \\ -i\sin(\theta/2) & \cos(\theta/2) \end{pmatrix}, \qquad (6)$$

$$R^y(\theta) = e^{-i\theta\sigma^y/2} = \begin{pmatrix} \cos(\theta/2) & -\sin(\theta/2) \\ \sin(\theta/2) & \cos(\theta/2) \end{pmatrix}, \qquad (7)$$

$$R^z(\theta) = e^{-i\theta\sigma^z/2} = \begin{pmatrix} \exp(-i\theta/2) & 0 \\ 0 & \exp(i\theta/2) \end{pmatrix}. \qquad (8)$$

Here, the quantum gate $R^\alpha(\theta)$ for $\alpha = x, y, z$ rotates the qubit $|\psi\rangle$ by an angle θ around the axis α according to the *right-hand rule*. This means that if the thumb of the right hand points along the corresponding axis α in Fig. 1, the sense of rotation is given by the curl of the remaining fingers, i.e., counter-clockwise when looking at the top of the thumb. An example for the gate $R^y(\pi)$ is shown in Fig. 2.
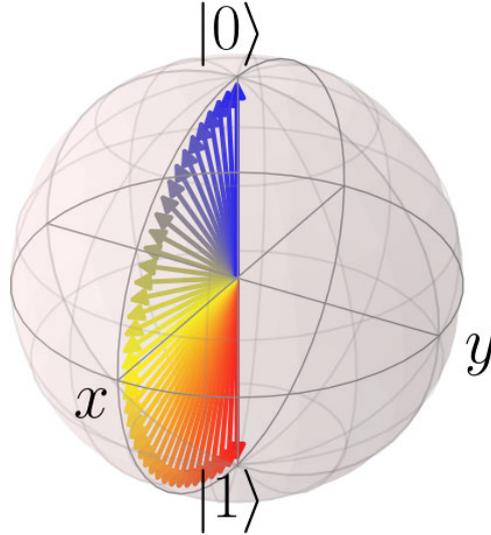
Fig. 2: *Visualization of the single-qubit gate $R^y(\pi)$ (see Eq. (7)) applied to the state $|0\rangle$ on the Bloch sphere defined in Fig. 1. The gate represents a counter-clockwise rotation around the y axis by an angle of π. Shown is the time evolution of a qubit during the application of a pulse designed to implement the gate $R^y(\pi)$. The time is encoded in the color of the arrows (from blue at the beginning over yellow to red at the end of the pulse). The data is taken from a simulation of transmon qubits [3].*

Often, at least one of these elementary qubit rotations is implemented in a hardware realization of a gate-based quantum computer. When programming quantum computers, the quantum gates are internally decomposed into products of such elementary rotations. For instance, for the current generation quantum processors of the IBM Q (which are based on superconducting transmon qubits [4]), the elementary rotations are $R^x(\pi/2)$ and $R^z(\theta)$ [5,6].

A general single-qubit rotation by an angle θ around a unit axis $\vec{n} = (n^x, n^y, n^z)$ is given by

$$R^{\vec{n}}(\theta) = e^{-i\theta\vec{n}\cdot\vec{\sigma}/2} = \cos\frac{\theta}{2} I - i\sin\frac{\theta}{2}\,\vec{n}\cdot\vec{\sigma}, \tag{9}$$

where $\vec{n}\cdot\vec{\sigma} = n^x\sigma^x + n^y\sigma^y + n^z\sigma^z$, and I is the $2{\times}2$ identity matrix. All single-qubit gates can be written in this form, up to an arbitrary global phase factor of the form $e^{i\alpha}$.

Besides the elementary single-qubit rotations, there are six other important gates that belong to the so-called standard gate set

$$X = \sigma^x, \qquad\qquad Y = \sigma^y, \qquad\qquad Z = \sigma^z, \tag{10}$$

$$H = \frac{1}{\sqrt{2}}\begin{pmatrix} 1 & 1 \\ 1 & -1 \end{pmatrix}, \qquad S = \begin{pmatrix} 1 & 0 \\ 0 & i \end{pmatrix}, \qquad T = \begin{pmatrix} 1 & 0 \\ 0 & e^{i\pi/4} \end{pmatrix}. \tag{11}$$

Especially the X gate (also known as the NOT gate or *bit flip* gate) and the Hadamard gate H (which maps a state $|0\rangle$ to a uniform superposition of $|0\rangle$ and $|1\rangle$ and back) are used in many applications. A comprehensive list of common quantum gates is given in appendix A.

As each quantum gate U is unitary (i.e., $U^{-1} = U^\dagger$ where $U^\dagger$ denotes the Hermitian conjugate), the inverse of a quantum gate U is again a quantum gate.

Exercise 2: For all single-qubit gates in Eqs. (10) and (11) and their inverses, find the corresponding axes $\vec{n}$ and angles θ (and optionally the global phase factors $e^{i\alpha}$) to express them in the form of Eq. (9) and visualize their operations as rotations on the Bloch sphere, as in Fig. 2.

2.1.3 Multiple qubits

While a single-qubit state is described by two complex coefficients ψ_0 and ψ_1 (see Eq. (1)), a multi-qubit state $|\psi\rangle$ with $n > 1$ qubits is described by 2^n complex coefficients $\psi_0, \ldots, \psi_{2^n-1}$,

$$|\psi\rangle = \psi_0|0\cdots00\rangle + \psi_1|0\cdots01\rangle + \cdots + \psi_{2^n-1}|1\cdots11\rangle = \begin{pmatrix} \psi_0 \\ \psi_1 \\ \vdots \\ \psi_{2^n-1} \end{pmatrix}, \qquad (12)$$

The corresponding basis vectors $|q_0q_1\cdots q_{n-1}\rangle$ for $q_i = 0, 1$ and $i = 0, \ldots, n-1$ are constructed from the single-qubit standard basis in Eq. (2) by means of the *tensor product* "$\otimes$" (also known as *Kronecker product*), $|q_0q_1\cdots q_{n-1}\rangle = |q_0\rangle \otimes |q_1\rangle \otimes \cdots \otimes |q_{n-1}\rangle$. For simplicity, we often do not write the tensor product explicitly. Consequently, for two qubits, the computational basis reads

$$|00\rangle = \begin{pmatrix} 1 \\ 0 \\ 0 \\ 0 \end{pmatrix}, \qquad |01\rangle = \begin{pmatrix} 0 \\ 1 \\ 0 \\ 0 \end{pmatrix}, \qquad |10\rangle = \begin{pmatrix} 0 \\ 0 \\ 1 \\ 0 \end{pmatrix}, \qquad |11\rangle = \begin{pmatrix} 0 \\ 0 \\ 0 \\ 1 \end{pmatrix}. \qquad (13)$$

One may notice that in Eq. (12), the basis state $|q_0q_1\cdots q_{n-1}\rangle$ corresponding to the coefficient ψ_j for $j = 0, \ldots, 2^n-1$ contains the binary representation of j, i.e., $\mathrm{bin}(j) = q_0q_1\cdots q_{n-1}$, or equivalently, $j = \sum_{i=0}^{n-1} q_i \times 2^{n-i-1}$. For this reason, we identify the notations $|j\rangle \equiv |\mathrm{bin}(j)\rangle \equiv |q_0q_1\cdots q_{n-1}\rangle$ so that the state in Eq. (12) is also written as

$$|\psi\rangle = \sum_{j=0}^{2^n-1} \psi_j|j\rangle. \qquad (14)$$

This notation is needed for the example of the quantum Fourier transform discussed below. Quantum gates on multiple qubits are, like single-qubit gates, unitary operations on the multi-qubit state $|\psi\rangle$. In practice, most multi-qubit gates are actually single-qubit gates acting on certain qubits in the multi-qubit state. For instance, a single-qubit gate U from Eqs. (10) or (11) acting on a certain qubit i (denoted by U_i) transforms a basis vector $|q_0\cdots q_{n-1}\rangle$ according to

$$U_i|q_0\cdots q_{n-1}\rangle = |q_0\cdots q_{i-1}\rangle(U|q_i\rangle)|q_{i+1}\cdots q_{n-1}\rangle. \qquad (15)$$

In other words, U_i is given by the tensor product $U_i = I \otimes \cdots \otimes U \otimes \cdots \otimes I$.

Another common set of multi-qubit gates derived from single-qubit gates are *controlled* quantum gates. For a single-qubit gate U, the controlled-U gate (denoted by CU) acts on two qubits

i_1 and i_2 in a multi-qubit state. Its action on a basis vector $|q_0 \cdots q_{n-1}\rangle$ is defined by

$$CU_{i_1 i_2}|q_0 \cdots q_{n-1}\rangle = \begin{cases} |q_0 \cdots q_{n-1}\rangle & (\text{if } q_{i_1} = 0) \\ |q_0 \cdots q_{i_2-1}\rangle(U|q_{i_2}\rangle)|q_{i_2+1} \cdots q_{n-1}\rangle & (\text{if } q_{i_1} = 1) \end{cases}. \tag{16}$$

In other words, the action is controlled by qubit q_{i_1}: Only if the control qubit q_{i_1} is in state 1, the target qubit q_{i_2} experiences the single-qubit gate U. On the two-qubit space spanned by the four basis states in Eq. (13), the matrix representation of the controlled-U gate is given by

$$CU = \begin{pmatrix} I & \mathbf{0} \\ \mathbf{0} & U \end{pmatrix}, \tag{17}$$

where $\mathbf{0}$ denotes a 2×2 matrix with all elements equal to zero.

It is important to realize that for controlled quantum gates constructed in this way, the global phase of the single-qubit gate U becomes a relative phase. In particular, this means that, even though the single-qubit gates S and $R^z(\pi/2)$ are equivalent, the controlled gates CS and $CR^z(\pi/2)$ are different two-qubit gates.

Two very important two-qubit gates constructed like this are the controlled-NOT (CNOT or CX) and the controlled-phase (CZ) gates. Their matrix representations with respect to the two-qubit basis in Eq. (13) are given by

$$\text{CNOT} = \begin{pmatrix} 1 & 0 & 0 & 0 \\ 0 & 1 & 0 & 0 \\ 0 & 0 & 0 & 1 \\ 0 & 0 & 1 & 0 \end{pmatrix}, \qquad CZ = \begin{pmatrix} 1 & 0 & 0 & 0 \\ 0 & 1 & 0 & 0 \\ 0 & 0 & 1 & 0 \\ 0 & 0 & 0 & -1 \end{pmatrix}. \tag{18}$$

The CNOT gate and the CZ gate can be converted into one another using the identity $\text{CNOT} = (I \otimes H)\,CZ\,(I \otimes H)$, which can be verified by computing the product of the corresponding matrix representations. On a space with more than two qubits, the same identity reads $\text{CNOT}_{i_1 i_2} = H_{i_2}\,CZ_{i_1 i_2}\,H_{i_2}$. More of such *circuit identities* that are useful when programming quantum computers can be found in the following exercise and in [7].

Exercise 3: Verify the following circuit identities, e.g. by computing their matrix representations on a suitable space and then confirming that they are equivalent (up to a global phase):
(a) $X = HZH$, **(b)** $Y = HYH$, **(c)** $Z = HXH$, **(d)** $I = XX = YY = ZZ = HH$,
(e) $S = TT$, **(f)** $H = SR^x(\pi/2)S$, **(g)** $HTH = R^x(\pi/4)$, **(h)** $XR^y(\theta)X = R^y(-\theta)$,
(i) $\text{CNOT}_{i_1 i_2} = H_{i_2}\,CZ_{i_1 i_2}\,H_{i_2}$,
(j) $\text{CNOT}_{i_2 i_1} = H_{i_1}H_{i_2}\,\text{CNOT}_{i_1 i_2}\,H_{i_1}H_{i_2}$,
(k) $\text{CNOT}_{i_2 i_1} = H_{i_1}H_{i_2}\,\text{CNOT}_{i_1 i_2}\,H_{i_1}H_{i_2}$,
(l) $CZ_{i_1 i_2} = CZ_{i_2 i_1}$, **(m)** $CS_{i_1 i_2} = CS_{i_2 i_1}$,
(n) $C(e^{i\alpha}I) = R^z(\alpha) \otimes I$,
(o) $R^z_{i_1}(\theta)\,\text{CNOT}_{i_1 i_2} = \text{CNOT}_{i_1 i_2}\,R^z_{i_1}(\theta)$,
(p) $R^x_{i_2}(\theta)\,\text{CNOT}_{i_1 i_2} = \text{CNOT}_{i_1 i_2}\,R^x_{i_2}(\theta)$.
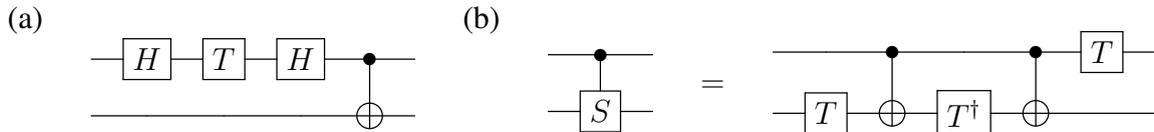
Fig. 3: *Example quantum circuit diagrams. Note that the diagrams are read from left to right. (a) Quantum circuit that generates the state $\cos(\pi/8)|00\rangle - i\sin(\pi/8)|11\rangle$ (which can be computed using the circuit identity from exercise 3 (g)) when starting with the initial state $|00\rangle$ on the left. (b) Schematic way of writing a circuit identity for the CS gate.*

2.2 Programming and simulating quantum circuits

A program for a gate-based quantum computer is called a *quantum circuit*. A quantum circuit is a sequence of several quantum gates. It is often expressed with a diagrammatic language that uses horizontal lines to represent the qubits and boxes to represent the quantum gates. The order of execution in the quantum gate sequence is from left to right. Controlled quantum gates such as $CU_{i_1 i_2}$ in Eq. (16) are visualized with a filled dot on the control qubit and the single-qubit gate U on the target qubit. The CNOT gate in particular is visualized with an encircled plus symbol on the target qubit. Two examples using this schematic language are shown in Fig. 3.

As described in the previous section, each gate in a quantum circuit represents a unitary matrix. By multiplying all quantum gate matrices in a quantum circuit, we could, in principle, obtain a large unitary matrix that is equivalent to the quantum circuit. Note that, as the order of execution in a quantum circuit diagram is from left to right, the corresponding quantum gate matrices must be multiplied in reverse order. For the right circuit in Fig. 3(a), for instance, this matrix product would read $\text{CNOT}\,(H \otimes I)\,(T \otimes I)\,(H \otimes I)$.

To simulate a quantum circuit, one could use the thus obtained matrix and apply it to a certain initial state, which is typically chosen as $|0\cdots0\rangle = (1, 0, \ldots, 0)^T$. This method works for small quantum circuits. However, it quickly becomes prohibitive because the size of the quantum circuit matrix for N qubits is $2^N \times 2^N$.

Larger quantum circuits with, say, $N \geq 30$ qubits can be simulated on supercomputers such as the GPU-cluster JUWELS Booster using JUQCS–G [8], which is a GPU-accelerated version of the Jülich Universal Quantum Computer Simulator (JUQCS) [9, 10] that was also used for benchmarking purposes in Google's quantum supremacy experiment [11]. For reference, the standard gate set implemented by JUQCS is given in appendix A.

A `qiskit` [12] interface to JUQCS including the conversion from the `qiskit` gate-set to the JUQCS gate-set is available through the Jülich UNified Infrastructure for Quantum computing (JUNIQ) service at `http://jugit.fz-juelich.de/qip/juniq-platform`.

An example program to simulate the circuit in Fig. 3(a) using this interface is shown in listing 1. It simulates the quantum circuit by propagating the state vector, sampling from the resulting probability, and returning the counts for all sampled events (in this case "00" and "11"). Furthermore, instead of sampling, JUQCS also provides an option to return the full state vector up to a certain number of qubits. An example program for this mode of operation is shown in listing 2.

```
1  import qiskit
2
3  circuit = qiskit.QuantumCircuit(2)
4  circuit.h(0)
5  circuit.t(0)
6  circuit.h(0)
7  circuit.cx(0,1)
8  circuit.measure_all()
9
10 from juqcs import Juqcs
11 backend = Juqcs.get_backend('qasm_simulator')
12 backend.allocate(minutes=10, max_qubits=2)
13
14 job = qiskit.execute(circuit.reverse_bits(), backend=backend, shots=1000)
15 result = job.result()
16
17 print(result.get_counts())
18
19 backend.deallocate()
```

Listing 1: *Example program to simulate the quantum circuit shown in Fig. 3(a). As the result of this circuit is $\cos(\pi/8)|00\rangle - i\sin(\pi/8)|11\rangle$, the printed counts should correspond to the probabilities $p_{00} = \cos(\pi/8)^2 \approx 0.85$ and $p_{11} = \sin(\pi/8)^2 \approx 0.15$. Note also the usage of* `circuit.reverse_bits()`, *because* `qiskit` *uses the ordering $|q_{n-1}\cdots q_0\rangle$ while all standard text books as well as these lecture notes use $|q_0\cdots q_{n-1}\rangle$.*

```
1  import qiskit
2
3  circuit = qiskit.QuantumCircuit(2)
4  circuit.h(0)
5  circuit.t(0)
6  circuit.h(0)
7  circuit.cx(0,1)
8
9  from juqcs import Juqcs
10 backend = Juqcs.get_backend('statevector_simulator')
11 backend.allocate(minutes=10, max_qubits=2)
12
13 job = qiskit.execute(circuit.reverse_bits(), backend=backend)
14 result = job.result()
15
16 print(result.get_statevector())
17
18 backend.deallocate()
```

Listing 2: *Example program to simulate the quantum circuit shown in Fig. 3(a) using the state vector simulator. The result of this program is a numerical representation of the state $\cos(\pi/8)|00\rangle - i\sin(\pi/8)|11\rangle$, up to a global phase.*
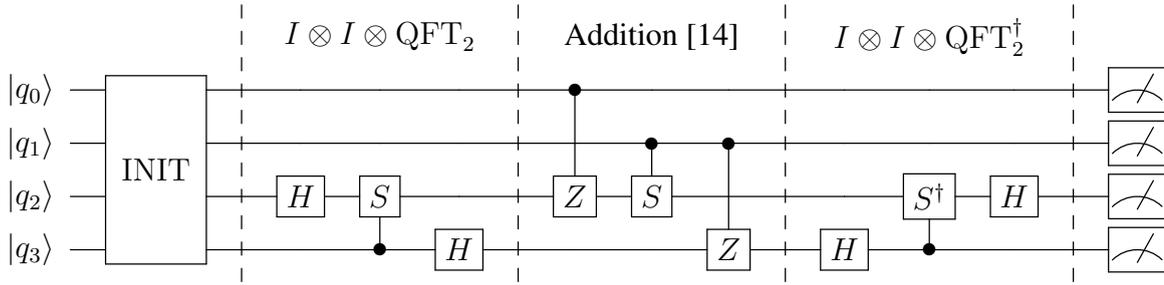
Fig. 4: *Circuit for a quantum adder [14] that adds two two-qubit registers modulo four, according to the rule Eq. (19). The circuit consists of four parts: Initialization of the qubit registers, QFT on the last two registers, the phase addition transform from [14], and another QFT on the last two registers. Note that the swaps that are part of typical QFT circuits (see [7]) are left out. Finally, a measurement of the qubits, which produces a "0" or a "1" for each qubit, is indicated at the end. To rewrite the gates, one can use identities from exercise 3 or [7].*

Instead of the JUQCS backend, one can also use a simulator from `qiskit` via the function `qiskit.Aer.get_backend`. This one only works for circuits with a small number of qubits, but it does not need the calls to `backend.allocate` and `backend.deallocate` as it does not run on a supercomputer. Furthermore, backends for real quantum devices can be accessed in a similar manner through the IBM Q Experience [13].

2.3   Example: Quantum adder

As a first "real-world" example, we consider a four-qubit quantum computer program that adds two two-qubit registers according to the rule

$$|q_0 q_1\rangle |q_2 q_3\rangle \mapsto |q_0 q_1\rangle |q_0 q_1 + q_2 q_3\rangle, \tag{19}$$

where the expression $q_0 q_1 + q_2 q_3$ is to be understood as integer addition (modulo 4) of the two-bit integers with binary representations $q_0 q_1$ and $q_2 q_3$, respectively. After the application of the quantum circuit, the second register contains the sum in binary notation. Some examples of the operation of the quantum adder are

$$|2\rangle |1\rangle \qquad\qquad \mapsto \qquad\qquad |2\rangle |3\rangle, \tag{20}$$

$$|2\rangle \frac{|0\rangle + |1\rangle}{\sqrt{2}} \qquad\qquad \mapsto \qquad\qquad |2\rangle \frac{|2\rangle + |3\rangle}{\sqrt{2}}, \tag{21}$$

$$|2\rangle \frac{|0\rangle + |1\rangle + |2\rangle}{\sqrt{3}} \qquad\qquad \mapsto \qquad\qquad |2\rangle \frac{|2\rangle + |3\rangle + |0\rangle}{\sqrt{3}}. \tag{22}$$

The interesting thing is that it can also add superpositions in parallel, as done in Eqs. (21) and (22) (note that this works because quantum circuits are linear maps, so a circuit U applied to a state $|\psi_1\rangle + |\psi_2\rangle$ produces the state $U|\psi_1\rangle + U|\psi_2\rangle$).

Exercise 3: Use the rule Eq. (19) for the quantum adder to work out the result when the initial state is given by $(|0\rangle + |3\rangle)/\sqrt{2} \otimes (|1\rangle + |2\rangle + |3\rangle)/\sqrt{3}$.

The quantum circuit for the adder consists of four stages that are shown in Fig. 4. The purpose of the INIT block at the beginning is to initialize the registers in a certain initial state, such as the states on the left-hand side in Eqs. (20)–(22).

The second and the fourth stage contain a quantum Fourier transform (QFT) on the second register. The QFT is an operation that, loosely speaking, moves information from the registers to the phases of exponential prefactors and vice versa. For an initial N-qubit basis state $|j\rangle$ ($j = 0, \ldots, 2^N-1$), the QFT is defined as the unitary transformation

$$|j\rangle \stackrel{\text{QFT}}{\mapsto} \frac{1}{2^{N/2}} \sum_{k=0}^{2^N-1} e^{2\pi i j k/2^N} |k\rangle, \tag{23}$$

where we identified j and its binary representation $q_0 \cdots q_{N-1}$ as done in Eq. (14). There is a generic quantum circuit [7] to implement this transformation using only H gates and conditional z rotations in a number of steps *polynomial* in N, as opposed to the *Fast Fourier Transform* that requires $\mathcal{O}(N2^N)$ steps. It is an important component of many quantum algorithms for which a theoretical exponential speedup is known. One such algorithm is Shor's factorization algorithm [1] in which the QFT is basically used to find the period of a suitable function (note that finding periods is a generic feature of any Fourier transform).

The third part of the quantum adder circuit in Fig. 4 is the addition transform from [14]. It uses conditional phase shifts from the first to the second register so that an addition is effectively performed in the exponent of the phase factors. For instance, if the first register represents an integer l (e.g. $|l\rangle \equiv |q_0 q_1\rangle$ above), and the second register is given by the QFT of an integer j (i.e. $\text{QFT}|j\rangle \propto \sum_k e^{2\pi i j k/2^N} |k\rangle$), the addition transform performs the operation

$$\sum_{k=0}^{2^N-1} e^{2\pi i j k/2^N} |l\rangle|k\rangle \mapsto \sum_{k=0}^{2^N-1} e^{2\pi i (j+l)k/2^N} |l\rangle|k\rangle. \tag{24}$$

After this step, the inverse QFT (given by $\text{QFT}^\dagger$ in Fig. 4) can be used to move the result $(j+l)$ of the addition from the exponent back into the second register. Note that the addition is automatically implemented modulo 2^N, because the complex exponential function is periodic with period $2\pi i$.

As an example, we consider an implementation of the quantum adder using the single-qubit gate set defined in Eqs. (9)–(11) and the CNOT gate as the only two-qubit gate. This requires rewriting (also known as *transpiling*) the gates using the circuit identities from exercise 3 and Fig. 3(b). The result is shown in Fig. 5 and listing 3. Note that the initial state in this example is chosen to be $|2\rangle(|0\rangle + |1\rangle)/\sqrt{2}$, i.e., the example from Eq. (21) above. As the output contains a superposition of the results, each result occurs as separate event in the simulation.

Fig. 5: *Example circuit for the quantum adder in Fig. 4 after transpiling some of the quantum gates using appropriate circuit identities. Note that in this example, an X and an H gate have been used to explicitly create the initial state for the example in Eq. (21).*

```python
1  import qiskit
2
3  circuit = qiskit.QuantumCircuit(4)
4  circuit.x(0)
5  circuit.h(3)
6  circuit.barrier()
7  circuit.t(1)
8  circuit.h(2)
9  circuit.t(3)
10 circuit.cx(2,3)
11 circuit.tdg(3)
12 circuit.t(2)
13 circuit.cx(2,3)
14 circuit.h(2)
15 circuit.cx(0,2)
16 circuit.h(2)
17 circuit.cx(2,1)
18 circuit.tdg(1)
19 circuit.cx(2,1)
20 circuit.cx(1,3)
21 circuit.cx(2,3)
22 circuit.t(3)
23 circuit.cx(2,3)
24 circuit.h(2)
25 circuit.tdg(3)
26 circuit.measure_all()
27
28 from juqcs import Juqcs
29 backend = Juqcs.get_backend('qasm_simulator')
30 backend.allocate(minutes=10, max_qubits=circuit.num_qubits)
31
32 job = qiskit.execute(circuit.reverse_bits(), backend=backend, shots=1000)
33 result = job.result()
34
35 print(result.get_counts())
36
37 backend.deallocate()
```

Listing 3: *Example program for the quantum adder circuit shown in Fig. 5 for the case given by Eq. (21) with initial state $|2\rangle(|0\rangle + |1\rangle)/\sqrt{2}$. The circuit is simulated with JUQCS as shown in listing 1. The output should be the events "1010" (corresponding to state $|2\rangle|2\rangle$) and "1011" (corresponding to state $|2\rangle|3\rangle$) with roughly 50% frequency each.*

Repeat for $k = 1, \ldots, p$ QAOA steps

Fig. 6: *General QAOA circuit [2]. Initially, the qubits are brought into a uniform superposition over all states using H gates. Then, $k = 1, \ldots, p$ QAOA steps with variational parameters $\beta_1, \ldots, \beta_p$ and $\gamma_1, \ldots, \gamma_p$ are applied. Each QAOA step k consists of a "weighting step" using z rotations scaled with γ_k and the parameters $\{h_i\}$ and $\{J_{ij}\}$ that define the optimization problem (see Eq. (25)), followed by a "mixing step" using x rotations with angle $2\beta_k$. Finally, the qubits are measured. The result can then be used to update the variational parameters until the energy is sufficiently low.*

2.4 Example: Quantum approximate optimization algorithm

In this section, we consider an approach to address optimization problems on gate-based quantum computers. Gate-based quantum computers are not made to solve optimization problems by design, which is a key difference to the adiabatic quantum computers covered in the next section. However, there is a standard (and by now rather common) way of addressing optimization problems in QUBO/Ising form on gate-based quantum computers, namely the quantum approximate optimization algorithm (QAOA) [2].

The optimization problems considered here are discrete Ising problems. The goal of such problems is to find the minimum of an energy function (or cost function)

$$E(s_0, \ldots, s_{N-1}) = \sum_{i=0}^{N-1} h_i s_i + \sum_{i<j} J_{ij} s_i s_j, \tag{25}$$

where $s_0, \ldots, s_{N-1} = \pm 1$ are the discrete, two-valued variables, N is the number of variables (which is equal to the number of required qubits), and $\{h_i\}$ and $\{J_{ij}\}$ are real numbers that define the optimization problem instance (for more information see the following section).

The QAOA is a quantum algorithm to find minima (or low-energy states) of Eq. (25). It is a variational quantum algorithm, which means that it has a number of variational parameters $\beta_1, \ldots, \beta_p$ and $\gamma_1, \ldots, \gamma_p$ that are varied during the iterations of the algorithm. The order of the QAOA, denoted by p, determines the number of variational parameters. It is worth mentioning that for large p, the QAOA can be related to approximate quantum annealing, which also provides a method to find a useful initialization of the variational parameters (see [8]).
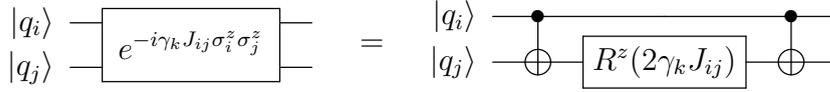
Fig. 7: *Circuit identity to implement the second part of the weighting step in Fig. 6.*

In each iteration of the QAOA, one executes the quantum circuit in Fig. 6 for a given set of variational parameters $\beta_1, \ldots, \beta_p$ and $\gamma_1, \ldots, \gamma_p$ (note that the quantum circuit depends on the fixed problem instance given by $\{h_i\}$ and $\{J_{ij}\}$). To execute the gate $\prod_{i,j} e^{-i\gamma_k J_{ij}\sigma_i^z\sigma_j^z}$ in the weighting step of the QAOA circuit in Fig. 6 using the standard gate set defined above, we need another circuit identity. This identity is shown in Fig. 7.

Exercise 4: Prove the circuit identity in Fig. 7, e.g. by computing the matrix representations of both sides and verifying that they are equivalent.

Each measurement at the end of the circuit produces a string of discrete variables $s_0, \ldots, s_{N-1} = \pm 1$, where the qubit measurement $q_i = 0$ corresponds to $s_i = +1$ and $q_i = -1$ corresponds to $s_i = -1$. Note that this convention, $q_i = (1-s_i)/2$, is standard for gate-based quantum computers [7]; for quantum annealers, one often uses $q_i = (1+s_i)/2$ instead (see below).

From several executions of the circuit, an expectation value for the energy in Eq. (25) can be computed. This result can be used to update the variational parameters and perform the next iteration. This process is continued as long as necessary until it converges.

Note that, when the QAOA is simulated using a state vector simulator (see listing 2), the expectation value can also be computed directly from the state vector $|\psi\rangle$. This is done by replacing the problem variables s_i in Eq. (25) by the Pauli matrices σ_i^z (which yields the *Ising Hamiltonian* of the problem) and computing the expectation value

$$\langle E \rangle = \langle \psi | E(\sigma_0^z, \ldots, \sigma_{N-1}^z) | \psi \rangle. \tag{26}$$

As an example, we consider a three-qubit problem characterized by the energy function

$$E(s_0, s_1, s_2) = -s_0 + \frac{1}{2}s_1 - \frac{1}{2}s_2 + \frac{1}{2}s_0 s_1 + \frac{1}{2}s_1 s_2. \tag{27}$$

In this case, the problem parameters for Eq. (25) are given by $(h_0, h_1, h_2) = (-1, 1/2, -1/2)$ and $(J_{01}, J_{02}, J_{12}) = (1/2, 0, 1/2)$. The minimum is given by $(s_0, s_1, s_2) = (+1, -1, +1)$ and corresponds to the state vector $|010\rangle$. The energy at the minimum is $E(+1, -1, +1) = -3$.

Constructing the QAOA circuit for $p = 1$ according to Figs. 6 and 7 yields the quantum circuit in Fig. 8. The program to simulate this circuit for a certain range of values for β_1 and γ_1 is shown in listing 4.

Figure 9 shows the expectation value of the energy, computed from the state vector $|\psi\rangle$ according to Eq. (26), and the success probability $|\langle 010|\psi\rangle|^2$. In this case, the energy minimum (see Fig. 9(a)) is very close to the point with maximum success probability (see Fig. 9(b)). Note that this is not guaranteed for larger QAOA applications [8, 15].
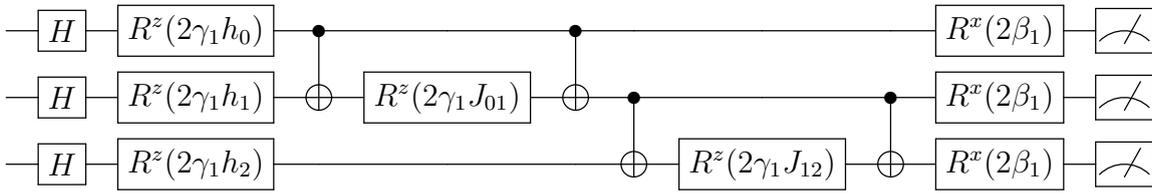
Fig. 8: *Example QAOA circuit for $p = 1$ to find the minimum of the energy function given by Eq. (27). The circuit has three qubits (one for each problem variable s_i). The qubit values q_i after the measurement at the end are related to the problem variables via $q_i = (1 - s_i)/2$ (gate-based convention). Note that only two of the blocks in Fig. 7 are necessary for the weighting step, because the third coupling parameter $J_{02} = 0$.*
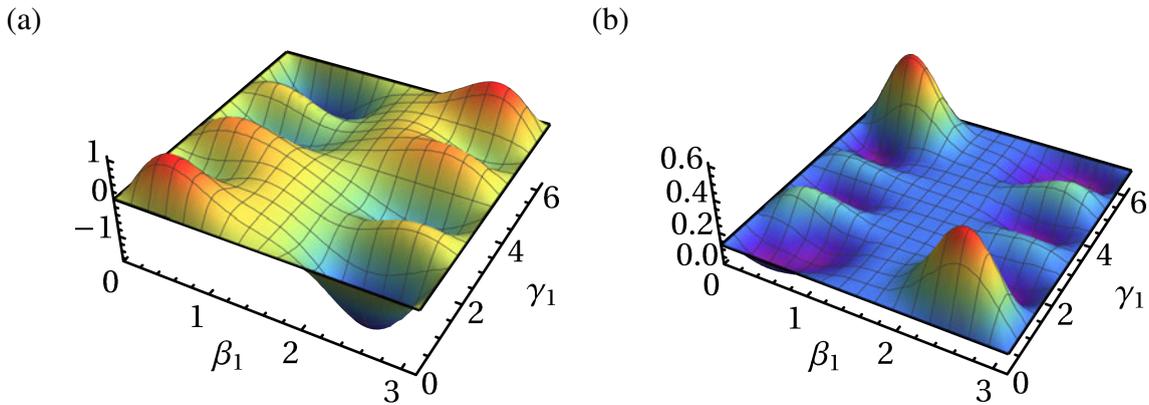
Fig. 9: *Example QAOA result for $p = 1$ that shows (a) the expectation value of the energy $\langle E \rangle$ (see Eq. (26)) and (b) the probability to measure the solution state $|\langle 010|\psi \rangle|^2$. In this case, the energy minimum at $(\beta_1, \gamma_1) \approx (2.505, 0.681)$ is very close to the point $(\beta_1, \gamma_1) \approx (2.524, 0.713)$ where the success probability is maximal. The state vector $|\psi\rangle$ has been obtained by simulating the QAOA circuit in Fig. 8 for the whole range of $\beta_1 \in [0, \pi)$ and $\gamma_1 \in [0, 2\pi)$. Beyond this range, the landscapes can be continued periodically; the periodicity in β_1 and γ_1 is due to the periodicity of the R^x and R^z gates in Fig. 8.*

Exercise 5: Run the $p = 1$ QAOA for the energy function in Eq. (27) by simulating the circuit in Fig. 8. Either perform a grid scan over $\beta_1 \in [0, \pi)$ and $\gamma_1 \in [0, 2\pi)$ (as done to produce Fig. 9), or write an optimization program to find the location of the minimum (e.g. by using the `scipy` package [16]).

Exercise 6: Construct the $p = 2$ QAOA circuit and run it to improve upon the $p = 1$ result. One way to do this is to take the best (β_1, γ_1) from exercise 5 or Fig. 9, and optimize for (β_2, γ_2). Another way would be to consider a case with larger p and take values for (β_k, γ_k) from a quantum annealing schedule as described in [8].

```python
import qiskit

h = [-1, 1/2, -1/2]
J = [1/2, 1/2]

def E(s0, s1, s2):
    return h[0]*s0 + h[1]*s1 + h[2]*s2 + J[0]*s0*s1 + J[1]*s1*s2

qaoa_circuits = []
qaoa_parameters = []

for beta1 in [2.0, 2.5]:
    for gamma1 in [0.5, 0.7, 1.0]:
        circuit = qiskit.QuantumCircuit(3)
        circuit.h(0)
        circuit.h(1)
        circuit.h(2)
        circuit.rz(2*gamma1*h[0], 0)
        circuit.rz(2*gamma1*h[1], 1)
        circuit.rz(2*gamma1*h[2], 2)
        circuit.cx(0,1)
        circuit.rz(2*gamma1*J[0], 1)
        circuit.cx(0,1)
        circuit.cx(1,2)
        circuit.rz(2*gamma1*J[1], 2)
        circuit.cx(1,2)
        circuit.rx(2*beta1, 0)
        circuit.rx(2*beta1, 1)
        circuit.rx(2*beta1, 2)
        qaoa_circuits.append(circuit.reverse_bits())
        qaoa_parameters.append([beta1, gamma1])

from juqcs import Juqcs
backend = Juqcs.get_backend('statevector_simulator')
backend.allocate(minutes=30, max_qubits=3)

job = qiskit.execute(qaoa_circuits, backend=backend)
result = job.result()

print('beta1\tgamma1\tenergyexpectation\tsuccessprobability')
for i,(beta1,gamma1) in enumerate(qaoa_parameters):
    psi = result.get_statevector(i)
    prob = abs(psi)**2
    energy  = E(+1,+1,+1)*prob[0b000] + E(+1,+1,-1)*prob[0b001]
    energy += E(+1,-1,+1)*prob[0b010] + E(+1,-1,-1)*prob[0b011]
    energy += E(-1,+1,+1)*prob[0b100] + E(-1,+1,-1)*prob[0b101]
    energy += E(-1,-1,+1)*prob[0b110] + E(-1,-1,-1)*prob[0b111]
    probability = prob[0b010]
    print(f'{beta1}\t{gamma1}\t{energy}\t{probability}')

backend.deallocate()
```

Listing 4: *Example program for the $p = 1$ QAOA circuit shown in Fig. 8. Separate circuits are simulated for all given values of β_1 and γ_1. From the resulting state vector, both energy and success probability are evaluated. The best result in the output should be at $\beta_1 = 2.5$ and $\gamma_1 = 0.7$ with energy -1.69 and success probability 58.9%.*

3   Quantum annealing

The second part of these lecture notes focuses on quantum annealing. Besides gate-based quantum computers, quantum annealing has emerged as the second major paradigm of quantum computing. As quantum annealers are somewhat simpler to manufacture, much larger devices of 5000+ qubits are already available and the technology is closer to the verge of technological maturity.

For this reason, the quantum annealing programs discussed in section 3.5 of these lecture notes exclusively target real devices, in contrast to the simulators discussed in the gate-based case above. Furthermore, with the garden optimization problem [17] as an application, the program type reflects the typical kind of problems solved on current quantum annealers that are a little bit closer to actual real-world applications.

3.1   Optimization problems with binary variables

Optimization of parameters in high-dimensional spaces can, in general, be a (computationally) demanding task. Gradient-based algorithms as well as non-gradient based algorithms usually require many evaluations of the cost function or its gradient. Typically, they rely on the continuity of the parameter space and often also on the continuity of the function itself. In high dimensional spaces, cost functions usually have many local optima in which optimization algorithms can get stuck as well as plateaus which slow down the convergence. There exist algorithms that use an adaptive step size to mitigate these effects. However, usually it is still necessary to start the optimizer with different (random) initial parameters and take at the end the overall best solution that was returned. In that sense, these algorithms also do not guarantee that the globally optimal solution has been found.

For cost functions of discrete or binary variables, these optimization algorithms are not applicable because the functions are only defined at discrete values. In general such optimization problems are NP-hard, and only a brute-force search over all possible inputs can deliver the optimal solution. For large configuration spaces, however, this is not feasible. For many discrete optimization problems, heuristic algorithms have been developed which work well for many cases. A heuristic algorithm may find the globally optimal solution but it may also return just a locally optimal solution as the outcome usually depends on the initialization. The advantage of heuristic algorithms is that the run time is much shorter than for a brute-force search. An example for such a heuristic algorithm is the simulated annealing algorithm [18].

A common discrete optimization problem in physics is to find the ground state of the Ising spin Hamiltonian

$$H_{\text{Ising}} = \sum_{i=1}^{N} h_i \sigma_i^z + \sum_{i<j} J_{ij} \sigma_i^z \sigma_j^z, \tag{28}$$

where N denotes the number of spins, h_i denotes the local field for spin i, J_{ij} denotes the

coupling strength between spins i and j, and σ_i^z denotes the Pauli z matrix

$$\sigma^z = \begin{pmatrix} 1 & 0 \\ 0 & -1 \end{pmatrix} \tag{29}$$

for spin i with eigenstates $|{\uparrow}\rangle$ and $|{\downarrow}\rangle$ such that $\sigma^z|{\uparrow}\rangle = |{\uparrow}\rangle$ and $\sigma^z|{\downarrow}\rangle = -|{\downarrow}\rangle$. This kind of problems can be solved on the D-Wave quantum annealer.

Another form of discrete optimization that can be solved on the D-Wave quantum annealer is Quadratic Unconstrained Binary Optimization (QUBO). The QUBO cost function to minimize is given in the form

$$C(\mathbf{x}) = \sum_{i=1}^{N} a_i x_i + \sum_{i<j} b_{ij} x_i x_j, \tag{30}$$

where N is the number of binary variables $x_i \in \{0,1\}$, $\mathbf{x} = x_1 x_2 \ldots x_N$ denotes the bitstring obtained by concatenating the problem variables, $a_i x_i$ are the linear terms and $b_{ij} x_i x_j$ are the quadratic terms in the binary variables, and $a_i, b_{ij} \in \mathbb{R}$ are the parameters that define the problem instance to be solved. In the definition of a QUBO, the term "Unconstrained" means that there are no constraints in the optimization of $C(\mathbf{x})$ such as "subject to $f(\mathbf{x}) = 0$". Solving a QUBO is equivalent to solving for the ground state of an Ising Hamiltonian Eq. (28). Many optimization problems that can be formulated in terms of an Ising or QUBO model are discussed in Ref. [19].

3.2   Working principle of a quantum annealer

Initially, quantum annealing was invented as an heuristic algorithm for a classical computer [20–22]. It was inspired by the simulated annealing algorithm [18] where thermal fluctuations are replaced by quantum fluctuations. For simulated annealing, thin but high energy barriers are difficult to overcome as thermal hopping processes become unlikely for high barriers. Therefore, the idea was that quantum fluctuations in quantum annealing allow for tunneling through these thin but high energy barriers. The quantum annealing Hamiltonian can be expressed as

$$H_{\mathrm{QA}}(t/t_{\max}) = \Gamma(t/t_{\max}) H_{\mathrm{QF}} + H_{\mathrm{problem}}, \tag{31}$$

where H_{problem} encodes the optimization problem to be solved, and H_{QF} denotes the Hamiltonian introducing the quantum fluctuations. The function $\Gamma(t/t_{\max})$ controls the strength of these fluctuations. It has to satisfy $\Gamma(0) \gg$ energy scale of H_{problem} and $\Gamma(1) \approx 0$.

Later, adiabatic quantum computation was proposed [23, 24]. The idea to perform the computation is based on the adiabatic theorem: The quantum system is to be initialized in the known ground state of an initial Hamiltonian H_{init}. Then, the time-dependent Hamiltonian of the system

$$H(t/t_{\max}) = A(t/t_{\max}) H_{\mathrm{init}} + B(t/t_{\max}) H_{\mathrm{final}} \tag{32}$$

is changed over time into the Hamiltonian H_{final} which encodes an optimization problem (e.g., the Ising Hamiltonian Eq. (28)). The annealing functions $A(t/t_{\max})$ and $B(t/t_{\max})$ satisfy
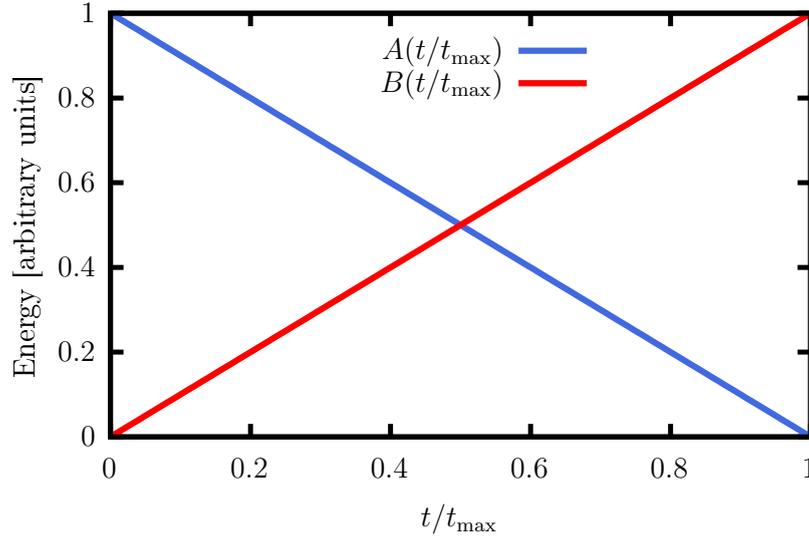
Fig. 10: *The annealing functions $A(t/t_{max})$ and $B(t/t_{max})$ for a linear annealing schedule.*

$A(0) \gg B(0)$ and $B(1) \gg A(1)$. An example for a linear annealing schedule is shown in Fig. 10. With $H_{\text{final}} = H_{\text{problem}}$, $H_{\text{init}} = H_{\text{QF}}$, $A(t/t_{\text{max}}) = \Gamma(t/t_{\text{max}})$ and $B(t/t_{\text{max}}) = 1$, Hamiltonian Eq. (32) implements the quantum annealing Hamiltonian Eq. (31). The adiabatic theorem [25] states that if the Hamiltonian $H(t/t_{\text{max}})$ changes sufficiently slowly with time, the system stays in the instantaneous ground state so that a measurement at the end of the process yields the state that encodes the solution to the optimization problem. A detailed review on the ideal (i.e., closed-system) model of adiabatic quantum computation is given in Ref. [26].

For a single spin-1/2 particle in a time-dependent external magnetic field, the closed-system model can be solved analytically exactly and is described by the Landau-Zener theory [27]: The Hamiltonian describing the spin in the external field $h_z = vt$ which changes with time t from $-\infty$ to ∞ with sweep velocity v and a time-independent transverse field h_x is given by

$$H_{\text{LZ}}(t) = -h_x \sigma^x - h_z(t)\sigma^z = -h_x \sigma^x - vt\sigma^z \tag{33}$$

where σ^x is the Pauli x matrix

$$\sigma^x = \begin{pmatrix} 0 & 1 \\ 1 & 0 \end{pmatrix}, \tag{34}$$

with eigenstates $|+\rangle = (|\uparrow\rangle + |\downarrow\rangle)/\sqrt{2}$ and $|-\rangle = (|\uparrow\rangle - |\downarrow\rangle)/\sqrt{2}$. The spin is prepared in the ground state of $H_{\text{LZ}}(t \to -\infty)$ which is the state $|\psi_{\text{init}}\rangle = |\downarrow\rangle$. The spin then evolves with the Hamiltonian $H_{\text{LZ}}(t)$ and the Landau-Zener theory gives the probability to find the spin in the ground ($|\uparrow\rangle$) or excited state ($|\downarrow\rangle$) of $H_{\text{LZ}}(t)$ for $t \to \infty$

$$P_\uparrow = 1 - e^{-\pi h_x^2/v}, \quad P_\downarrow = e^{-\pi h_x^2/v}. \tag{35}$$

These probabilities show that for fast sweeping (large v), $P_\uparrow \to 0$ and $P_\downarrow \to 1$. They also show that for $h_x \to 0$, $P_\uparrow \to 0$ and $P_\downarrow \to 1$. Since the minimal energy gap is proportional to $|h_x|$, the probabilities scale not only with the sweep velocity but also with the minimal energy gap squared.
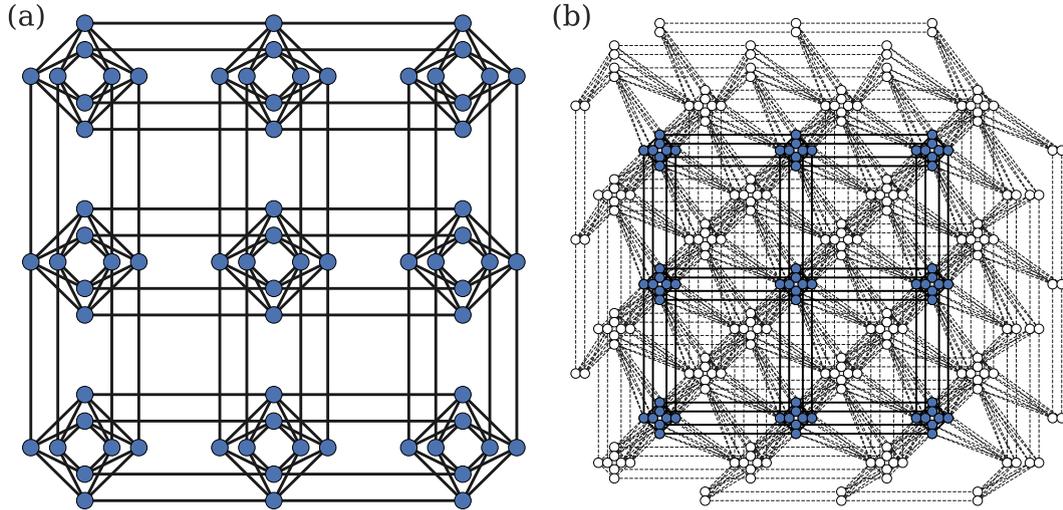
Fig. 11: *Small-size examples of the connectivity graphs of the (a) Chimera topology of the D-Wave 2000Q processors and (b) Pegasus topology of the Advantage processors. Blue nodes in the Pegasus graph show the embedding of the Chimera graph onto the Pegasus graph.*

In practice however, the annealing system is always connected to an environment at a finite temperature. This means that some sources of noise can never be removed completely. So not only a too rapid change of the Hamiltonian but also a too slow annealing procedure may excite the system.

3.3 Architecture of D-Wave quantum annealers

There are currently two generations of D-Wave quantum annealers available: The previous generation (D-Wave 2000Q) with about 2000 qubits and up to 6 couplers per qubit, and the current generation (Advantage) with more than 5000 qubits and up to 15 couplers per qubit. The qubits of the D-Wave 2000Q quantum processors are arranged in the so-called Chimera topology and the qubits of the Advantage systems are arranged in the so-called Pegasus topology (see Fig. 11). The Chimera graph is a subgraph of the Pegasus graph.

In the case of D-Wave quantum annealers, the final Hamiltonian is given by the Ising Hamiltonian

$$H_{\text{final}} = H_{\text{Ising}} = \sum_{i=1}^{N} h_i \sigma_i^z + \sum_{\substack{i<j \\ i,j \text{ neighbors}}} J_{ij} \sigma_i^z \sigma_j^z, \tag{36}$$

and the initial Hamiltonian is given by

$$H_{\text{init}} = -\sum_{i=1}^{N} \sigma_i^x. \tag{37}$$

The ground state of the initial Hamiltonian is given by the equal superposition of all computa-
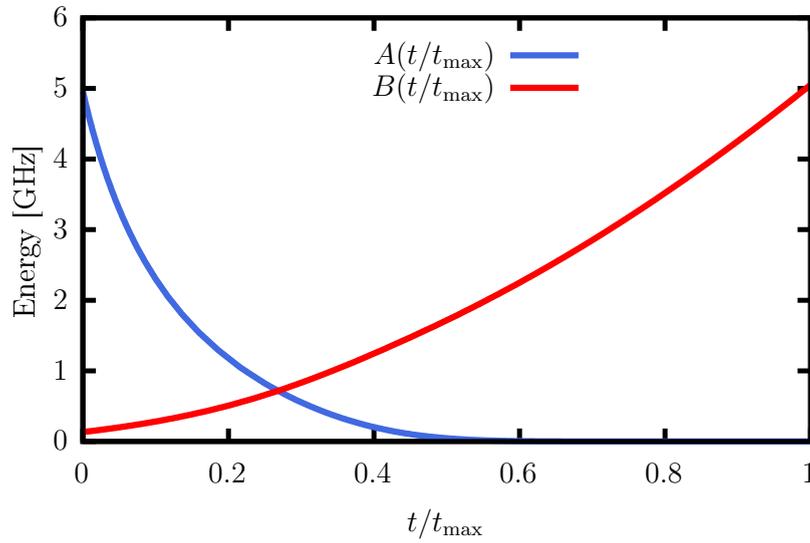
Fig. 12: *The annealing functions $A(t/t_{max})$ and $B(t/t_{max})$ of the annealing schedule of D-Wave's 5000+ qubit processor* `Advantage_system1.1`.

tional basis states,

$$|\psi_{\text{init}}\rangle = |+\rangle^{\otimes N} = \frac{1}{\sqrt{2^N}} \sum_{z_i \in \{\uparrow, \downarrow\}} |z_1 z_2 \dots z_N\rangle. \tag{38}$$

The qubits (two-level systems) of the Hamiltonians in Eqs. (36) and (37) are built of superconducting circuits. The particular design of these circuits is called flux qubits. The flux qubits as well as the couplers which allow for a tunable coupling between the qubits are controlled via external fluxes. The parameters h_i and J_{ij} of the final Hamiltonian given in Eq. (36) are controlled by time-independent external magnetic fluxes. The annealing process is controlled through time-dependent external magnetic fluxes which change the effective Hamiltonian from the initial Hamiltonian to the final Hamiltonian. As an example, in Fig. 12 we show the annealing schedule of the processor `Advantage_system1.1`. The annealing schedule is obviously different from the linear annealing schedule shown in Fig. 10. The reason for this is that the hardware design of the flux qubits does not allow for an independent control of the functions $A(t/t_{\max})$ and $B(t/t_{\max})$ [28]. Like all superconducting qubits, these systems are actually multi-level systems of which only a two-dimensional subspace (spanned by the two lowest energy eigenstates) functions as the qubit. More detailed information can be found in, for instance, Refs. [28–30].

3.4   Limitations

Current quantum annealers are subject to various limitations which may have an impact on the performance. For instance, due to the limited connectivity of the qubits (up to 6 connections per qubit on the Chimera architecture; up to 15 connections per qubit on the Pegasus architecture), the variables of a given problem may not be directly mappable to the qubits. In that case, an

embedding of the problem graph onto the hardware graph is necessary. Finding an (optimal) embedding is in general a hard problem itself. However, there exist heuristic methods to find embeddings and the `Ocean` package provides such an algorithm (cf. section 3.5.4). The need to find an embedding limits the performance due to the time overhead required to generate an embedding and it often also increases the required number of qubits (see section 3.5.4 for more details). Thus, although problem instances that feature the native hardware graphs (Chimera or Pegasus graphs) can be put on the D-Wave 2000Q and Advantage systems with sizes of 2000+ and 5000+ qubits, respectively, only 64- and 124-qubit fully-connected problems can be placed on these systems, respectively.

Other limiting factors are the restricted range and the limited precision of the parameters h_i and J_{ij}. In order for the parameter values to fit into the available range they have to be rescaled (see section 3.5.1). Thus, for problem instances which cover a large range of values but at the same time include parameters with small differences, these differences may not be resolvable anymore within the available precision, i.e., configured parameters on the hardware may differ from the specified ones.

A general limiting factor in practical quantum annealing is that in practice the quantum system can never be completely isolated from the environment and noise sources. As a consequence, the system can be thermally excited. In particular, for theoretical closed-system quantum annealing, the annealing time cannot be too long. However, for open systems, a long annealing time means long time for the system to interact with the environment and a higher probability to leave the ground state.

Apart from these practical limitations, there are also theoretical issues. The adiabatic theorem states that the quantum system stays in its instantaneous ground state if the Hamiltonian changes sufficiently slowly in time. In particular, the annealing time should satisfy ($s = t/t_{\max}$) [31]

$$ t_{\max} \gg \max_{s \in [0,1]} \frac{\left| \langle E_n(s) | \frac{\partial H}{\partial s} | E_0(s) \rangle \right|}{\left(E_0(s) - E_n(s) \right)^2} \quad \text{for } n \neq 0. \tag{39} $$

Thus, for an adiabatic evolution and for exponentially small energy gaps, the annealing time is expected to also increase exponentially.

3.5 Programming a D-Wave quantum annealer

In this section, we focus on programming the D-Wave quantum annealer using D-Wave's python package `Ocean-SDK` [32, 33], as well as some practical aspects which are useful when programming a D-Wave quantum annealer. It is worth mentioning that, even though the previous sections contain useful technical details for background information, the only knowledge required to program a quantum annealer is about the kind of optimization problem (Ising or QUBO) that it solves. This makes quantum annealers particularly attractive for non-physicists.

3.5.1 Problem specification

Optimization problems that can be put onto D-Wave quantum annealers have to be formulated as QUBO

$$\min_{x_i=0,1} \left(\sum_{i=0}^{N-1} a_i x_i + \sum_{i<j}^{N-1} b_{ij} x_i x_j \right) = \min_{x_i=0,1} \left(\sum_{i\leq j}^{N-1} x_i Q_{ij} x_j \right), \tag{40}$$

or as an Ising Hamiltonian

$$\min_{s_i=\pm 1} \left(\sum_{i=0}^{N-1} h_i s_i + \sum_{i<j}^{N-1} J_{ij} s_i s_j \right), \tag{41}$$

where $s_i \in \{-1, +1\}$ are the eigenvalues of the Pauli-z matrix σ_i^z. Reformulating a QUBO as Ising Hamiltonian can be done by substituting

$$x_i = \frac{1+s_i}{2}. \tag{42}$$

This convention is commonly used in quantum annealing and maps $x_i = 0$ and $x_i = 1$ to $s_i = -1$ and $s_i = 1$, respectively. Note that this convention is different from the one commonly used for gate-based quantum computing (see above). When converting problems between QUBO and Ising formulation, constants which arise from the substitution Eq. (42) can be neglected as they only lead to an energy shift but do not change the solution of the optimization.

To specify the problem instance using the `Ocean-SDK`, the coefficients can be stored in a dictionary `Q = {(i,j):`Q_{ij}`}` (QUBO) or two dictionaries `h = {`i`:`h_i`}` and `J = {(i,j):`J_{ij}`}` (Ising).

In practice, the coupling strength J_{ij} can only be set to values in a certain interval $[J_{\min}, J_{\max}]$, where usually $J_{\min} = -J_{\max}$, with a limited precision. The same applies to the single-qubit bias h_i with interval $[h_{\min}, h_{\max}]$. Thus, all h_i and J_{ij} need to be rescaled by a factor [34]

$$r = \max \left\{ \max\left[\frac{\max\{h_i\}}{h_{\max}}, 0 \right], \max\left[\frac{\min\{h_i\}}{h_{\min}}, 0 \right], \max\left[\frac{\max\{J_{ij}\}}{J_{\max}}, 0 \right], \max\left[\frac{\min\{J_{ij}\}}{J_{\min}}, 0 \right] \right\},$$

$$\tag{43}$$

to fit into the ranges $h_{\min} \leq h_i \leq h_{\max}$ and $J_{\min} \leq J_{ij} \leq J_{\max}$. If $r < 1$, rescaling is optional, but it may be useful to exhaust a larger parameter range and potentially improve the performance. When `auto_scale` is set to `true` (default), the rescaling is performed automatically when submitting a problem through `Ocean`. When auto-scaling is disabled and the problem parameters do not fit into the parameter range, the submission of the problem fails. Note that rescaling does not change the solution of the problem. In general, it is advised to have the auto-scaling feature enabled (default). However, there may be certain cases where it has to be disabled. If in such a study, unexpected results are obtained, one should check to disable the auto-scaling feature.

```
1 from dwave.system import DWaveSampler
2
3 sampler = DWaveSampler(solver='DW_2000Q_6', token='insert_your_token_here')
4 h = {0:1, 4:-0.5}
5 J = {(0,4):1, (0,5):-1}
6
7 response = sampler.sample_ising(h, J)
8 print(response)
```

Listing 5: *A minimal working example to run a program on a D-Wave quantum annealer.*

```
1 from dwave.system import DWaveSampler, EmbeddingComposite
2
3 sampler = EmbeddingComposite(DWaveSampler(solver='DW_2000Q_6', token='
      insert_your_token_here'))
4 Q = {(0,0):1, (0,1):1, (0,2):-1, (1,2):-0.8}
5
6 response = sampler.sample_qubo(Q, num_reads=100, chain_strength=2,
      annealing_time=5)
7 print(response)
```

Listing 6: *Example showing how to use an* `EmbeddingComposite`*.*

3.5.2 Submitting a problem to the D-Wave quantum annealer through the Ocean package

Listing 5 shows a minimal working example of a submission to the D-Wave quantum annealer. The class `DWaveSampler` takes a solver (for example the current hardware solvers, at the time of writing, 'DW_2000Q_6' or 'Advantage_system1.1') to which to submit the problem. If one did not create a `config`-file during or after the installation of the `Ocean-SDK`, the personal token also has to be provided to `DWaveSampler`. Depending on the formulation of the problem (Ising or QUBO), one has to create the `h` and `J` or `Q` dictionaries, respectively. The example code in listing 5 shows the case for the Ising formulation. For larger problems, the dictionaries should be generated algorithmically. The class `DWaveSampler` has the member functions `sample_ising` and `sample_qubo` which submit the specified problem to the QPU. The function `sample_ising` takes the `h` and `J` dictionaries and the function `sample_qubo` takes the `Q` dictionary.

Optional parameters of the functions `sample_ising` and `sample_qubo` are for instance the number of samples obtained per submission (`num_reads`), the `annealing_time` (in µs), or the `chain_strength` (see section 3.5.4). An example is shown in listing 6.

Listing 6 also illustrates how to use an `EmbeddingComposite` (see section 3.5.4). The return value contains the solutions returned by the quantum annealer as well as some additional information. An example output is shown in listing 7: The first column labels the different solutions returned (rows). The following N_{qubit} (in this case $N_{\text{qubit}} = 3$) columns give the values

```
1    0   1   2 energy num_oc. chain_.
2 0  0   1   1   -0.8      79      0.0
3 1  0   0   1    0.0       5      0.0
4 2  1   0   1    0.0       5      0.0
5 3  0   0   0    0.0       7      0.0
6 4  0   1   0    0.0       1      0.0
7 5  1   1   1    0.2       2      0.0
8 6  1   0   0    1.0       1      0.0
9 ['BINARY', 7 rows, 100 samples, 3 variables]
```

Listing 7: *Example output of the program given in listing 6.*

```
1 import dwave.inspector
2
3 #################
4 #  previous code #
5 #################
6
7 dwave.inspector.show(response)
```

Listing 8: *Example showing how to use* dwave.inspector *to visualize the result. A screenshot using the Leap IDE is shown in Fig. 13.*

of the qubits in the returned solution. The next three columns contain the energy, the number of occurrences of this solution in all samples, and the chain break fraction (see section 3.5.4), respectively. In our example output, we obtained 79 times the solution no. 0 with energy -0.8 (the energy of the ground state) and no chain breaks. In addition, the response also contains the information that the result is given in BINARY, i.e. QUBO, format (in the Ising representation it would be SPIN), that 7 distinct answers were returned by the quantum annealer (the number of rows), that the number of samples is 100 (equals num_reads), and that the number of qubits (variables) is three. Further information can be accessed through response.info.

Another tool of the Ocean package which can be handy when studying the returned results is dwave.inspector. With this tool, the response object can be visualized. The usage is illustrated in listing 8 and Fig. 13.

3.5.3 Implementing constraints

As mentioned previously, D-Wave quantum annealers are designed to solve QUBO or Ising problems by minimizing the corresponding energy function without constraints. However, in practice optimization problems often require constrained optimization, i.e., the objective function $C(\mathbf{x})$ needs to be minimized under a certain constraint $f(\mathbf{x}) = c$, where f is a function that takes a string of bits $\mathbf{x}$ and returns a scalar, and c is a scalar, i.e., the optimization task is to "minimize $C(\mathbf{x})$ subject to $f(\mathbf{x}) = c$".

We can consider such a constraint by formulating it as a QUBO (or Ising Hamiltonian) and adding it to the objective function: We can write the constraint $f(\mathbf{x}) = c$ as $f(\mathbf{x}) - c = 0$. The
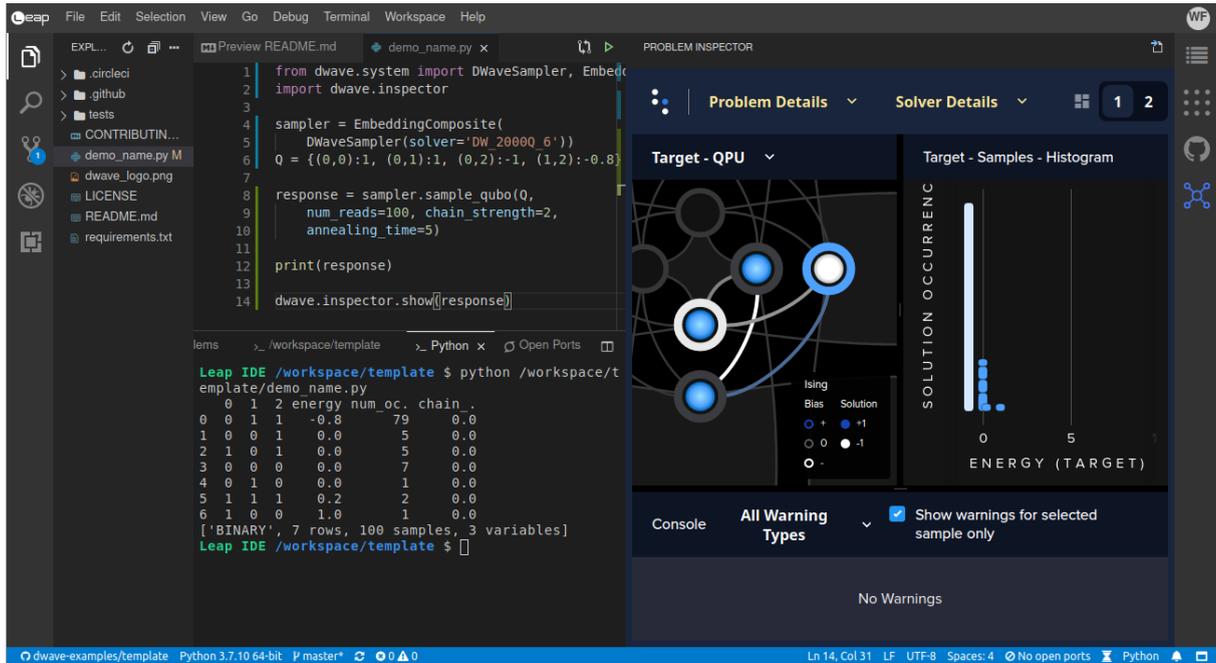
Fig. 13: *Running the example program from listing 6 and visualizing the result on the D-Wave using the inspector (see listings 7 and 8). The Leap IDE with an example template to run such an experiment can be opened at* `https://ide.dwavesys.io/#https://github.com/dwave-examples/template`*.*

square $(f(\mathbf{x}) - c)^2$ is always greater than zero, except if the constraint $f(\mathbf{x}) = c$ is satisfied in which case the square is equal to zero and thus minimal. By adding the square term $(f(\mathbf{x}) - c)^2$ to the objective function, we effectively add a penalty to the objective function if the constraint is not satisfied. To keep things simple, we assume that $f(\mathbf{x})$ is a linear function in the bits x_i (further information can be found in [35]). We add the penalty term to the objective function $C(\mathbf{x})$ so that the new/modified objective function reads $C(\mathbf{x}) + \lambda(f(\mathbf{x}) - c)^2$, where λ is a scalar called Lagrange multiplier and has to be chosen reasonably. The optimization task is now "minimize $C(\mathbf{x}) + \lambda(f(\mathbf{x}) - c)^2$".

A "reasonable" choice for λ means that λ should neither be too small nor too large. If λ is chosen too small, the constraint will likely not be satisfied in the optimal solution for $C(\mathbf{x}) + \lambda(f(\mathbf{x}) - c)^2$ as it may be more favorable to accept a penalty multiplied by a small λ than to return a state with a larger cost function value $C(\mathbf{x})$. On the other hand, a too large λ will force the constraint to be satisfied but due to the rescaling of the parameters (see section 3.5.1), the problem parameters might become so small that they cannot be represented accurately enough with the limited precision, and also the energy differences become so small that excitations to higher energy states, which do not encode the optimal solution to the original problem anymore, become very likely.
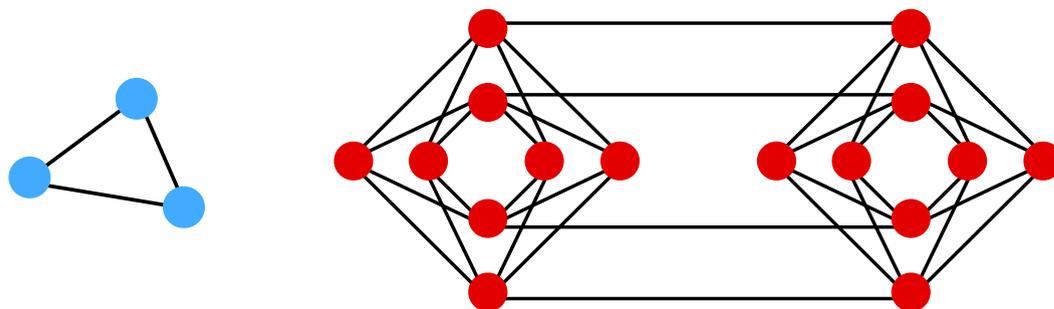
Fig. 14: *A graph with triangular connectivity (left) cannot be directly mapped onto the Chimera hardware graph (right).*

3.5.4   Embedding of problem graphs onto the hardware graph

As soon as problem sizes become larger so that we cannot immediately find a mapping of the problem graph onto the hardware graph, it is convenient to call a dedicated routine to find this mapping for us. Generating the optimal embedding of a graph onto another one is in general NP-hard, but a heuristic algorithm is provided by the `Ocean-SDK`. This algorithm uses probabilistic methods, which means that each time we call the function, it may return a different embedding and these may be of different quality. Thus, one typically tries several different embeddings and chooses the best one (see also [15, 17]). It may also be possible that the problem graph requires connectivities which are not present on the hardware graph. For instance, a triangular connectivity as shown in Fig. 14 cannot be mapped onto the Chimera graph. In such a case, we have to use more than a single physical qubit (the ones on the hardware) to represent a logical qubit (the ones in the problem specification), see Fig. 15. If we have more than a single physical qubit representing a logical qubit, i.e., a chain of two or more physical qubits represents a single logical qubit, the physical qubits should behave as a single entity, i.e., at the end of the annealing process, they should all have the same value.

To achieve this, the couplings J_{ij} between these physical qubits are set to a negative value with large magnitude. The magnitude (also called chain strength) determines how strongly these qubits couple and how easily the chain may "break". In this context, a "chain break" means that different qubits of a chain representing the same logical qubit end up in different states. The Ocean package includes post-processing procedures which, in this case, determine the value to return for the logical qubit by majority vote of the physical qubits. Thus, the values returned will always be valid for the original problem, although they could be far from optimal. Too many chain breaks should be avoided as the returned solutions become "randomized" and may be rather poor.

The optimal value of the chain strength depends on the particular problem and possibly also on the particular embedding. If the chain strength is chosen too weak, the optimal and close-to-optimal solutions may likely contain chain breaks as it is energetically favorable to break these couplings instead of the ones that encode the actual problem instance. In theory, the chain strength should be chosen as large as possible to satisfy the constraints. In practice however,

Fig. 15: *A graph with triangular connectivity (left) can be mapped onto the Chimera hardware graph (right) by using two physical qubits for one of the logical qubits.*

we have to keep in mind that the coupling strength J_{ij} can only be set to values in the interval $[J_{\min}, J_{\max}]$ with a limited precision (cf. section 3.5.1). Thus, all h_i and J_{ij} are rescaled by the factor r (see Eq. (43)). If the chain strength is chosen too strong, all parameters defining the problem instance will be rescaled to small values which might be no longer resolvable with the given precision. Moreover, the energy differences of the original problem are also rescaled and become very small which could more likely lead to excitations to higher energy states. This, in turn, would lead to worse results for the original problem than if a weaker chain strength had been chosen. The chain strength is a parameter called `chain_strength` that can be given to the `sample_qubo` or `sample_ising` functions.

The `Ocean` package provides several `EmbeddingComposite` classes [33] to handle the generation of embeddings:

- `EmbeddingComposite` tries to find an embedding each time one of the `sample` functions (`sample_qubo` or `sample_ising`) is called. This can be useful when submitting different problems or when studying the dependence on different embeddings.

- `LazyFixedEmbeddingComposite` tries to find an embedding the first time one of the `sample` functions is called. Later, it reuses this embedding. This can be useful when submitting the same problem with different hyperparameters such as annealing time or chain strength.

- `FixedEmbeddingComposite` takes an embedding as argument which is then used each time one of the `sample` functions is called. This can be useful when we already have an embedding for a particular problem (either by generating it ourselves or by loading a previously stored embedding) and we want to reuse it again.

- `TilingComposite` can be passed to any of the `EmbeddingComposites` to place several copies of small embedded graphs.

	Leek	Celery	Peas	Corn
Leek	○	♡	×	○
Celery	♡	○	○	×
Peas	×	○	○	♡
Corn	○	×	♡	○

Table 1: *Companion planting example of good (♡), neutral (○), and bad (×) neighbors.*
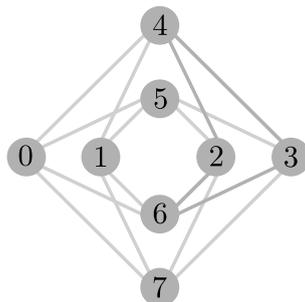
Fig. 16: *Labeling of the qubits in a Chimera graph unit cell of the D-Wave 2000Q quantum processors.*

3.6   Example: Garden optimization

As an example, we consider a simplified four-qubit problem from the garden optimization problem presented in [17]. The task is to place four plants in two pots such that good neighbors are in the same pot and bad neighbors are not. The relationships between the four plants that we consider in this example are shown in table 1.

The two pots have the labels -1 and $+1$ and the value s_i of qubit i denotes into which pot we place the plant of type i ($i \in \{$leek, celery, peas, corn$\}$). Since we consider minimization problems, we want to minimize the energy when good neighbors are placed in the same pot. Assume we place plants i and j in the same pot (i.e., $s_i = s_j$). According to Eq. (41), the energy is lowered if we choose J_{ij} negative (which we want for good neighbors i and j), and the energy is increased if we choose J_{ij} positive (which we want for bad neighbors i and j). Thus, we set $J_{\text{leek, celery}} = J_{\text{peas, corn}} = -1$ and $J_{\text{leek, peas}} = J_{\text{celery, corn}} = 1$. The energy function is then given by

$$E\big(s_{\text{leek}}, s_{\text{celery}}, s_{\text{peas}}, s_{\text{corn}}\big) = s_{\text{leek}} s_{\text{peas}} + s_{\text{celery}} s_{\text{corn}} - s_{\text{leek}} s_{\text{celery}} - s_{\text{peas}} s_{\text{corn}}. \quad (44)$$

The next step is to map the qubits onto the hardware graph. The labeling of the qubits in the first unit cell of the Chimera topology used in the D-Wave 2000Q processors is shown in Fig. 16. Since the problem is small and can be directly mapped onto the hardware graph, we define the mapping without an `EmbeddingComposite`. We use the mapping

$$\text{leek} \to 0, \quad \text{corn} \to 3, \quad (45)$$

$$\text{celery} \to 4, \quad \text{peas} \to 7, \quad (46)$$

which gives

$$J_{04} = J_{37} = -1 \quad \text{and} \quad J_{07} = J_{34} = 1. \quad (47)$$

The program to submit and solve the problem on the D-Wave 2000Q chip `DW_2000Q_6` is shown in listing 9.

Exercise 7: Consider the case that leek has already been placed in the pot with label "−1". Replanting it would require additional work. How could this additional cost be considered in the energy function? Modify the program in listing 9 accordingly. How does the result change?

```python
from dwave.system import DWaveSampler
import dwave.inspector

sampler = DWaveSampler(solver='DW_2000Q_6', token='insert_your_token_here')

h = {}

# We choose:
# 0 = leek
# 4 = celery
# 7 = peas
# 3 = corn
J = { (0,4): -1, (0,7): +1, (3,4): +1, (3,7): -1 }

response = sampler.sample_ising(h, J, num_reads=100)

dwave.inspector.show(response)
```

Listing 9: *Example code solving the four-qubit garden problem.*

Appendix

A   JUQCS standard gate set

This appendix contains the standard gate set implemented by the Jülich Universal Quantum Computer Simulator (JUQCS) [10]. JUQCS is a large-scale simulator for gate-based quantum computers that was also used for Google's quantum supremacy experiment [11]. A GPU-accelerated version was recently used to benchmark JUWELS Booster [8] with over 2048 GPUs across 512 compute nodes. A `qiskit` [12] interface to JUQCS including the conversion from the `qiskit` gate set to the JUQCS gate set is available through the Jülich UNified Infrastructure for Quantum computing (JUNIQ) service at `https://jugit.fz-juelich.de/qip/juniq-platform`. This interface was used for the example programs in this lecture.

I gate

Description	performs an identity operation on qubit n.	$I = \begin{pmatrix} 1 & 0 \\ 0 & 1 \end{pmatrix}$
Syntax	I n	
Qiskit syntax	`circuit.id(n)`	
Argument	n integer, $0 \leq n < N$ with N the number of qubits.	$—\boxed{I}—$

H gate

Description	performs a Hadamard operation on qubit n.	$H = \frac{1}{\sqrt{2}} \begin{pmatrix} 1 & 1 \\ 1 & -1 \end{pmatrix}$
Syntax	H n	
Qiskit syntax	`circuit.h(n)`	
Argument	n integer, $0 \leq n < N$ with N the number of qubits.	$—\boxed{H}—$

X gate

Description	performs a bit flip operation on qubit n.	$X = \begin{pmatrix} 0 & 1 \\ 1 & 0 \end{pmatrix}$
Syntax	X n	
Qiskit syntax	`circuit.x(n)`	
Argument	n integer, $0 \leq n < N$ with N the number of qubits.	$—\boxed{X}—$
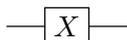
Y gate

Description	performs a bit and phase flip operation on qubit n.	$Y = \begin{pmatrix} 0 & -i \\ i & 0 \end{pmatrix}$
Syntax	Y n	
Qiskit syntax	`circuit.y(n)`	
Argument	n integer, $0 \leq n < N$ with N the number of qubits.	$—\boxed{Y}—$
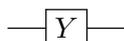
Z gate

Description	performs a phase flip operation on qubit n.	$Z = \begin{pmatrix} 1 & 0 \\ 0 & -1 \end{pmatrix}$
Syntax	Z n	
Qiskit syntax	`circuit.z(n)`	
Argument	n integer, $0 \leq n < N$ with N the number of qubits.	$—\boxed{Z}—$
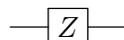
S gate

Description	rotates qubit n about the z-axis by $\pi/2$.	$S = \begin{pmatrix} 1 & 0 \\ 0 & i \end{pmatrix}$
Syntax	S n	
Qiskit syntax	`circuit.s(n)`	
Argument	n integer, $0 \leq n < N$ with N the number of qubits.	$—\boxed{S}—$

S† gate

Description	rotates qubit n about the z-axis by $-\pi/2$	$S^\dagger = \begin{pmatrix} 1 & 0 \\ 0 & -i \end{pmatrix}$
Syntax	S+ n	
Qiskit syntax	`circuit.sdg(n)`	
Argument	n integer, $0 \le n < N$ with N the number of qubits.	$-\boxed{S^\dagger}-$

T gate

Description	rotates qubit n about the z-axis by $\pi/4$	$T = \begin{pmatrix} 1 & 0 \\ 0 & (1+i)/\sqrt{2} \end{pmatrix}$
Syntax	T n	
Qiskit syntax	`circuit.t(n)`	
Argument	n integer, $0 \le n < N$ with N the number of qubits.	$-\boxed{T}-$

T† gate

Description	rotates qubit n about the z-axis by $-\pi/4$	$T^\dagger = \begin{pmatrix} 1 & 0 \\ 0 & (1-i)/\sqrt{2} \end{pmatrix}$
Syntax	T+ n	
Qiskit syntax	`circuit.tdg(n)`	
Argument	n integer, $0 \le n < N$ with N the number of qubits.	$-\boxed{T^\dagger}-$

U1 gate

Description	performs a U1(λ) operation [6] on qubit n.	$U1(\lambda) = \begin{pmatrix} 1 & 0 \\ 0 & e^{i\lambda} \end{pmatrix}$
Syntax	U1 n λ	
Qiskit syntax	`circuit.p(lam, n)`	
Arguments	n integer, $0 \le n < N$ with N the number of qubits, λ angle in radians (floating point or integer).	$-\boxed{U1(\lambda)}-$

U2 gate

Description	performs a U2(ϕ, λ) operation [6] on qubit n.	$U2(\phi, \lambda) = \frac{1}{\sqrt{2}}\begin{pmatrix} 1 & -e^{i\lambda} \\ e^{i\phi} & e^{i(\phi+\lambda)} \end{pmatrix}$
Syntax	U2 n ϕ λ	
Qiskit syntax	`circuit.u(pi/2, phi, lam, n)`	
Arguments	n integer, $0 \le n < N$ with N the number of qubits, ϕ, λ angles in radians (floating point or integer).	$-\boxed{U2(\phi, \lambda)}-$
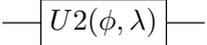
U3 gate

Description	performs a U3(θ, ϕ, λ) operation [6] on qubit n.	$U3(\theta, \phi, \lambda) =$
Syntax	U3 n θ ϕ λ	$\begin{pmatrix} \cos(\frac{\theta}{2}) & -e^{i\lambda}\sin(\frac{\theta}{2}) \\ e^{i\phi}\sin(\frac{\theta}{2}) & e^{i(\phi+\lambda)}\cos(\frac{\theta}{2}) \end{pmatrix}$
Qiskit syntax	`circuit.u(theta, phi, lam, n)`	
Arguments	n integer, $0 \le n < N$ with N the number of qubits, θ, ϕ, λ angles in radians (floating point or integer).	$-\boxed{U3(\theta, \phi, \lambda)}-$
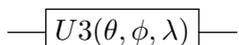
+X gate

Description	rotates qubit n by $-\pi/2$ about the x-axis.	$+X = \frac{1}{\sqrt{2}}\begin{pmatrix} 1 & i \\ i & 1 \end{pmatrix}$
Syntax	+X n	
Qiskit syntax	`circuit.rx(-pi/2, n)`	
Argument	n integer, $0 \le n < N$ with N the number of qubits.	$-\boxed{+X}-$

-X gate

Description	rotates qubit n by $+\pi/2$ about the x-axis.	$-X = \frac{1}{\sqrt{2}}\begin{pmatrix} 1 & -i \\ -i & 1 \end{pmatrix}$
Syntax	-X n	
Qiskit syntax	`circuit.rx(pi/2, n)`	
Argument	n integer, $0 \le n < N$ with N the number of qubits.	$-\boxed{-X}-$

+Y gate

Description	rotates qubit n by $-\pi/2$ about the y-axis.	
Syntax	+Y n	
Qiskit syntax	`circuit.ry(-pi/2, n)`	
Argument	n integer, $0 \le n < N$ with N the number of qubits.	

$$+Y = \frac{1}{\sqrt{2}} \begin{pmatrix} 1 & 1 \\ -1 & 1 \end{pmatrix}$$

$$-\boxed{+Y}-$$

-Y gate

Description	rotates qubit n by $+\pi/2$ about the y-axis.
Syntax	-Y n
Qiskit syntax	`circuit.ry(pi/2, n)`
Argument	n integer, $0 \le n < N$ with N the number of qubits.

$$-Y = \frac{1}{\sqrt{2}} \begin{pmatrix} 1 & -1 \\ 1 & 1 \end{pmatrix}$$

$$-\boxed{-Y}-$$

R(k) gate

Description	changes the phase of qubit n by $2\pi/2^k$.
Syntax	R n k
Qiskit syntax	`circuit.p(2*pi/2**k, n)`
Arguments	n integer, $0 \le n < N$ with N the number of qubits, k is non-negative integer.

$$R(k) = \begin{pmatrix} 1 & 0 \\ 0 & e^{2\pi i/2^k} \end{pmatrix}$$

$$-\boxed{R(k)}-$$

$R^{\dagger}$(k) gate

Description	changes the phase of qubit n by $-2\pi/2^k$.
Syntax	R n $-k$
Qiskit syntax	`circuit.p(-2*pi/2**k, n)`
Arguments	n integer, $0 \le n < N$ with N the number of qubits, k is non-negative integer.

$$R^{\dagger}(k) = \begin{pmatrix} 1 & 0 \\ 0 & e^{-2\pi i/2^k} \end{pmatrix}$$

$$-\boxed{R^{\dagger}(k)}-$$

Two-qubit gates

CNOT gate

Description	flips the target qubit if the control qubit is 1.
Syntax	CNOT *control target*
Qiskit syntax	`circuit.cx(control, target)`
Arguments	*control* $\ne$ *target* integers in the range $0, \ldots, N-1$ with N the number of qubits.
Note	The matrix looks different from the `qiskit` documentation as `qiskit` uses the ordering $\lvert q_{n-1} \cdots q_0 \rangle$ while all standard text books as well as these lecture notes use $\lvert q_0 \cdots q_{n-1} \rangle$. To fix this, the supplied example programs invoke the `circuit.reverse_bits()` function.

$$\text{CNOT} = \begin{pmatrix} 1 & 0 & 0 & 0 \\ 0 & 1 & 0 & 0 \\ 0 & 0 & 0 & 1 \\ 0 & 0 & 1 & 0 \end{pmatrix}$$
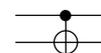
U(k) gate

Description	shifts the phase of the target qubit by $2\pi/2^k$ if the control qubit is 1.
Syntax	U *control target* k
Qiskit syntax	`circuit.cp(2*pi/2**k, control, target)`
Arguments	*control* $\ne$ *target* integers in the range $0, \ldots, N-1$ with N the number of qubits, k non-negative integer.

$$U(k) = \begin{pmatrix} 1 & 0 & 0 & 0 \\ 0 & 1 & 0 & 0 \\ 0 & 0 & 1 & 0 \\ 0 & 0 & 0 & e^{2\pi i/2^k} \end{pmatrix}$$

$$-\boxed{U(k)}-$$

U†(k) gate

Description	shifts the phase of the target qubit by $-2\pi/2^k$ if the control qubit is 1.	$$U^\dagger(k) =$$ $$\begin{pmatrix} 1 & 0 & 0 & 0 \\ 0 & 1 & 0 & 0 \\ 0 & 0 & 1 & 0 \\ 0 & 0 & 0 & e^{-2\pi i/2^k} \end{pmatrix}$$
Syntax	U *control target* $-k$	
Qiskit syntax	`circuit.cp(-2*pi/2**k, control,target)`	
Arguments	*control* $\neq$ *target* integers in the range $0, \dots, N-1$ with N the number of qubits, k non-negative integer.	

Toffoli gate

Description	flips the target qubit if both control qubits are 1.	$$\text{TOFFOLI} =$$ $$\begin{pmatrix} 1 & 0 & 0 & 0 & 0 & 0 & 0 & 0 \\ 0 & 1 & 0 & 0 & 0 & 0 & 0 & 0 \\ 0 & 0 & 1 & 0 & 0 & 0 & 0 & 0 \\ 0 & 0 & 0 & 1 & 0 & 0 & 0 & 0 \\ 0 & 0 & 0 & 0 & 1 & 0 & 0 & 0 \\ 0 & 0 & 0 & 0 & 0 & 1 & 0 & 0 \\ 0 & 0 & 0 & 0 & 0 & 0 & 0 & 1 \\ 0 & 0 & 0 & 0 & 0 & 0 & 1 & 0 \end{pmatrix}$$
Syntax	TOFFOLI *control$_1$ control$_2$ target*	
Qiskit syntax	`circuit.ccx(control1,control2,target)`	
Arguments	*control$_1$* $\neq$ *control$_2$* $\neq$ *target* $\neq$ *control$_1$* integers in the range $0, \dots, N-1$ with N the number of qubits.	
Note	The matrix looks different from the `qiskit` documentation because `qiskit` uses the ordering $|q_{n-1} \cdots q_0\rangle$ while all standard text books as well as these lecture notes use $|q_0 \cdots q_{n-1}\rangle$. To fix this, the supplied example programs invoke the `circuit.reverse_bits()` function.	

References

[1] P.W. Shor, in *Proceedings 35th Annual Symposium on Foundations of Computer Science* (1994), pp. 124–134

[2] E. Farhi, J. Goldstone, and S. Gutmann, arXiv:1411.4028

[3] D. Willsch: *Supercomputer simulations of transmon quantum computers* Ph.D. thesis, RWTH Aachen University, Aachen (2020)

[4] J. Koch, T.M. Yu, J. Gambetta, A.A. Houck, D.I. Schuster, J. Majer, A. Blais, M.H. Devoret, S.M. Girvin, and R.J. Schoelkopf, Phys. Rev. A **76**, 042319 (2007)

[5] D.C. McKay, C.J. Wood, S. Sheldon, J.M. Chow, and J.M. Gambetta, Phys. Rev. A **96**, 022330 (2017)

[6] A.W. Cross, L.S. Bishop, J.A. Smolin, and J.M. Gambetta, arXiv:1707.03429

[7] M. Nielsen and I. Chuang: *Quantum Computation and Quantum Information* (Cambridge University Press, 2010), 10th anniversary edition ed.

[8] D. Willsch, M. Willsch, F. Jin, K. Michielsen, and H. De Raedt, arXiv:2104.03293

[9] K. De Raedt, K. Michielsen, H. De Raedt, B. Trieu, G. Arnold, M. Richter, Th. Lippert, H. Watanabe, and N. Ito, Comput. Phys. Commun. **176**, 121 (2007)

[10] H. De Raedt, F. Jin, D. Willsch, M. Willsch, N. Yoshioka, N. Ito, S. Yuan, and K. Michielsen, Comput. Phys. Commun. **237**, 47 (2019)

[11] F. Arute, K. Arya, R. Babbush, D. Bacon, J.C. Bardin, R. Barends, R. Biswas, S. Boixo, F.G.S.L. Brandao, D.A. Buell, B. Burkett, Y. Chen, Z. Chen, B. Chiaro, R. Collins, W. Courtney, A. Dunsworth, E. Farhi, B. Foxen, A. Fowler, C. Gidney, M. Giustina, R. Graff, K. Guerin, S. Habegger, M.P. Harrigan, M.J. Hartmann, A. Ho, M. Hoffmann, T. Huang, T.S. Humble, S.V. Isakov, E. Jeffrey, Z. Jiang, D. Kafri, K. Kechedzhi, J. Kelly, P.V. Klimov, S. Knysh, A. Korotkov, F. Kostritsa, D. Landhuis, M. Lindmark, E. Lucero, D. Lyakh, S. Mandrà, J.R. McClean, M. McEwen, A. Megrant, X. Mi, K. Michielsen, M. Mohseni, J. Mutus, O. Naaman, M. Neeley, C. Neill, M.Y. Niu, E. Ostby, A. Petukhov, J.C. Platt, C. Quintana, E.G. Rieffel, P. Roushan, N.C. Rubin, D. Sank, K.J. Satzinger, V. Smelyanskiy, K.J. Sung, M.D. Trevithick, A. Vainsencher, B. Villalonga, T. White, Z.J. Yao, P. Yeh, A. Zalcman, H. Neven, and J.M. Martinis, Nature **574**, 505 (2019)

[12] *Qiskit: An Open-source Framework for Quantum Computing* (2019)
http://doi.org/10.5281/zenodo.2562110

[13] IBM Q team: *Quantum Experience* (2016)
http://quantum-computing.ibm.com/

[14] T.G. Draper, arXiv:quant-ph/0008033

[15] M. Willsch, D. Willsch, F. Jin, H. De Raedt, and K. Michielsen, Quantum Inf. Process. **19**, 197 (2020)

[16] E. Jones, T. Oliphant, P. Peterson et al.: *SciPy: Open source scientific tools for Python* (2001) `http://www.scipy.org/`

[17] C.D.G. Calaza, D. Willsch, and K. Michielsen, arXiv:2101.10827

[18] S. Kirkpatrick, C.D. Gelatt, and M.P. Vecchi, Science **220**, 671 (1983)

[19] A. Lucas, Front. Phys. **2**, 5 (2014)

[20] B. Apolloni, C. Carvalho, and D. de Falco, Stoch. Process. Their Appl. **33**, 233 (1989)

[21] A. Finnila, M. Gomez, C. Sebenik, C. Stenson, and J. Doll, Chem. Phys. Lett. **219**, 343 (1994)

[22] T. Kadowaki and H. Nishimori, Phys. Rev. E **58**, 5355 (1998)

[23] E. Farhi, J. Goldstone, S. Gutmann, and M. Sipser, arXiv:quant-ph/0001106

[24] A.M. Childs, E. Farhi, and J. Preskill, Phys. Rev. A **65**, 012322 (2001)

[25] M. Born and V. Fock, Z. Phys. **51**, 165 (1928)

[26] T. Albash and D.A. Lidar, Rev. Mod. Phys. **90**, 015002 (2018)

[27] C. Zener, Proc. R. Soc. London, Ser A **137**, 696 (1932)

[28] R. Harris, M.W. Johnson, T. Lanting, A.J. Berkley, J. Johansson, P. Bunyk, E. Tolkacheva, E. Ladizinsky, N. Ladizinsky, T. Oh, F. Cioata, I. Perminov, P. Spear, C. Enderud, C. Rich, S. Uchaikin, M.C. Thom, E.M. Chapple, J. Wang, B. Wilson, M.H.S. Amin, N. Dickson, K. Karimi, B. Macready, C.J.S. Truncik, and G. Rose, Phys. Rev. B **82**, 024511 (2010)

[29] R. Harris, T. Lanting, A.J. Berkley, J. Johansson, M.W. Johnson, P. Bunyk, E. Ladizinsky, N. Ladizinsky, T. Oh, and S. Han, Phys. Rev. B **80**, 052506 (2009)

[30] R. Harris, J. Johansson, A.J. Berkley, M.W. Johnson, T. Lanting, S. Han, P. Bunyk, E. Ladizinsky, T. Oh, I. Perminov, E. Tolkacheva, S. Uchaikin, E.M. Chapple, C. Enderud, C. Rich, M. Thom, J. Wang, B. Wilson, and G. Rose, Phys. Rev. B **81**, 134510 (2010)

[31] M.H.S. Amin, Phys. Rev. Lett. **102**, 220401 (2009)

[32] *D-Wave Ocean SDK* `https://github.com/dwavesystems/dwave-ocean-sdk`

[33] *D-Wave Ocean Software Documentation* `https://docs.ocean.dwavesys.com/en/stable/`

[34] D-Wave Systems: *D-Wave Solver Properties and Parameters*. Tech. rep., D-Wave Systems Inc., Burnaby, BC, Canada (2021). D-Wave User Manual 09-1169A-S `https://docs.dwavesys.com/docs/latest/doc_solver_ref.html`

[35] *Problem-Solving Handbook: Reformulating a Problem* `https://docs.dwavesys.com/docs/latest/handbook_reformulating.html`

12   Quantum Chemistry on Quantum Computers

Libor Veis

J. Heyrovský Institute of Physical Chemistry

Academy of Sciences of the Czech Republic, v.v.i.

Dolejškova 3, 18223 Prague 8, Czech Republic

Contents

1   Introduction

An exact simulation of quantum systems, including those in quantum chemistry, on a classical computer is computationally hard. The problem lies in the dimensionality of the Hilbert space needed for the description of a studied system that in fact grows exponentially with the size of this system, which is illustrated in Fig. 1. No matter if we simulate the dynamics or calculate some static property, e.g. the energy, this limitation is always present. Richard Feynman came up with an alternative to the classical simulation [1]. His idea was to convert the aforementioned drawback of quantum systems into their benefit. He suggested to map the Hilbert space of a studied quantum system on another one (both of them being exponentially large) and thus to *efficiently* simulate one quantum system on another one (i.e. on a quantum computer).

Although developing small quantum computers has taken over 30 years, we may soon benefit from Feynman's suggestion.[1] Indeed, quantum chemistry is supposed to be one of the first practical applications of small noisy quantum computers, named noisy intermediate-scale quantum (NISQ) devices [4]. Moreover, it is believed that quantum computers will eventually allow us to tackle classically intractable problems in chemistry, physics, and materials science [5–7]. In particular, *strongly correlated systems*, such as catalysts or high temperature superconductors, belong to problems of high socio-economic importance, which might be solved with the help of quantum hardware.

So far, several quantum algorithms have been proposed to solve computationally hard problems in chemistry *efficiently* (i.e. in polynomial time with polynomial resources with respect to size of the studied system and accuracy). Some of them have also been demonstrated experimentally [6]. However, due to limited quantum hardware capabilities, these experiments represent "only" proof-of-principle simulations of small chemical systems, which we can easily simulate classically. In order to make them scalable, there is a need for quantum error correction, which requires lower error rates than are currently available and moreover orders of magnitude more (physical) qubits. This field, on the other hand, grows very rapidly and we might see error-corrected digital quantum simulations of molecules in not so far future.

As mentioned above, several quantum algorithms which can solve different kinds of problems in chemistry have already been proposed [6]. In fact, quantum computational chemistry [5] has achieved enormous progress in the last 15 years.[2] In this chapter, we mention some of the algorithms, but most of the time restrict ourselves to the electronic structure problem of molecular Hamiltonians, i.e., the problem of finding the low lying energy spectrum of molecules. These algorithms can serve as subroutines for geometry optimization, calculation of optical properties, or determination of reaction rates [5]. Moreover, the methodology elaborated here can be easily applied to other problems (e.g. vibrational analysis). We focus on digital quantum simulation (analog quantum simulation is a subject of a different chapter), which means that the

---

[1]In fact, quantum computers with more than about 50 qubits are supposed to outperform the largest classical supercomputers and the first papers presenting the so called *quantum supremacy* have already appeared [2, 3]. However, the problems which they solved are rather artificial and not directly usable in chemistry simulations.

[2]The pioneering work of Aspuru-Guzik *et al.* [8] is being considered as the beginning of the quantum computational chemistry.

100 $\approx 10^7$ $\approx 10^{46}$
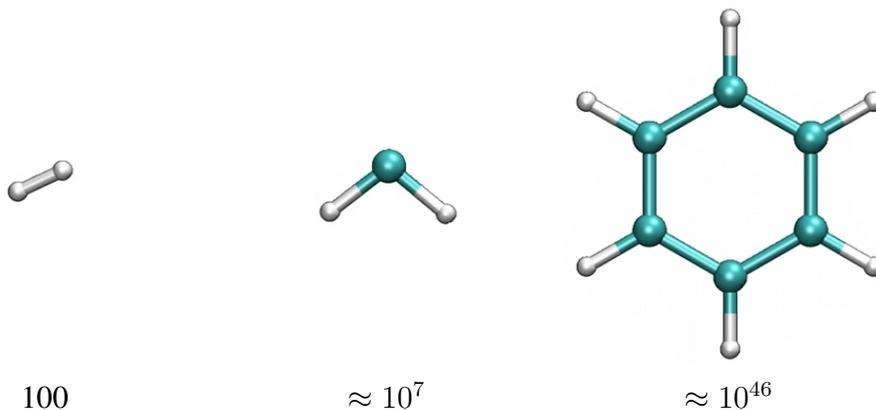
Fig. 1: *Exponential scaling of the Hilbert space dimension demonstrated on the examples of H_2, CH_2, and C_6H_6 molecules. The numbers below the molecular structures represent the number of Slater determinants in the full configuration interaction method (exact diagonalization) in double-ζ basis.*

original problem is mapped on a set of (quantum) gates which can be implemented on an universal quantum computer (i.e. not purpose specific). The chapter is meant to be a pedagogical introduction. For more details and references to original papers, we refer readers to the recent extensive reviews [5,6], from which we also draw a lot of information.

The chapter is organized as follows: we start with the basic elements of quantum computing in Sec. 2 and quantum chemistry in Sec. 3. We are aware of the fact that these topics are covered also in other chapters, however to make this chapter self-contained, we very briefly mention the basics, which are necessary for subsequent discussion of quantum algorithms for chemistry. In Sec. 4, we describe how to map the quantum chemistry problems onto a register of qubits (both in first and second quantization) and in Sec. 5 we present quantum algorithms for chemistry, both for the ultimate error-corrected applications (phase estimation, Sec. 5.1) as well as for NISQ devices (variational quantum eigensolver, Sec. 5.2). We end up with conclusions in Sec. 6.

2 Quantum computing in a nutshell

2.1 Qubit-based circuit model

We work with the qubit-based circuit model of quantum computation [9]. Similarly as the fundamental entity of classical computation and classical information is one bit, the fundamental entity of quantum computation and quantum information is one qubit. It is a quantum two-state system in a normalized state

$$|\psi\rangle = \alpha|0\rangle + \beta|1\rangle, \qquad |\alpha|^2 + |\beta|^2 = 1, \tag{1}$$

where α and β are complex-valued amplitudes. The orthonormal computational basis $\mathcal{B} = \{|0\rangle, |1\rangle\}$ is defined as

$$|0\rangle = \begin{pmatrix} 1 \\ 0 \end{pmatrix}, \quad |1\rangle = \begin{pmatrix} 0 \\ 1 \end{pmatrix}, \quad \text{therefore} \quad |\psi\rangle = \begin{pmatrix} \alpha \\ \beta \end{pmatrix}. \tag{2}$$

When going to n qubits, the system is described by a vector from the 2^n dimensional Hilbert space, which is formed by the tensor product of the Hilbert spaces of individual qubits. For example, a two-qubit system has four computational basis states

$$|00\rangle = \begin{pmatrix} 1 \\ 0 \end{pmatrix} \otimes \begin{pmatrix} 1 \\ 0 \end{pmatrix} = \begin{pmatrix} 1 \\ 0 \\ 0 \\ 0 \end{pmatrix}, \qquad |01\rangle = \begin{pmatrix} 1 \\ 0 \end{pmatrix} \otimes \begin{pmatrix} 0 \\ 1 \end{pmatrix} = \begin{pmatrix} 0 \\ 1 \\ 0 \\ 0 \end{pmatrix},$$

$$|10\rangle = \begin{pmatrix} 0 \\ 1 \end{pmatrix} \otimes \begin{pmatrix} 1 \\ 0 \end{pmatrix} = \begin{pmatrix} 0 \\ 0 \\ 1 \\ 0 \end{pmatrix}, \qquad |11\rangle = \begin{pmatrix} 0 \\ 1 \end{pmatrix} \otimes \begin{pmatrix} 0 \\ 1 \end{pmatrix} = \begin{pmatrix} 0 \\ 0 \\ 0 \\ 1 \end{pmatrix} \tag{3}$$

and a general two-qubit state has the form

$$|\psi\rangle = \alpha|00\rangle + \beta|01\rangle + \gamma|10\rangle + \delta|11\rangle. \tag{4}$$

Multi-qubit states can be classified as either product states or entangled states. Product states can be written as tensor products of fewer qubit (subsystem) wave functions, for example

$$\frac{1}{\sqrt{2}}\big(|00\rangle + |01\rangle\big) = |0\rangle \otimes \frac{1}{\sqrt{2}}\big(|0\rangle + |1\rangle\big) \tag{5}$$

is one of the two-qubit states from Eq. (4), which is a product state. On the other hand

$$\frac{1}{\sqrt{2}}\big(|00\rangle + |11\rangle\big) \tag{6}$$

cannot be written as a tensor product of subsystem wave functions and thus is entangled. The entanglement is a very interesting property stemming from the foundation of quantum mechanics, which does not have a classical counterpart, and is a key ingredient in quantum computation and quantum information, e.g., in quantum teleportation [9] (more about entanglement is given in other chapters). Each of the computational basis states can represent one decimal number in its binary form, e.g. $|4\rangle = |100\rangle$ (we employ the notation that the rightmost qubit is the first one).

A quantum circuit is composed of quantum gates acting on qubits, which are usually initialized in a $|\text{zero}\rangle = |0 \ldots 0\rangle$ state. Since the time evolution of quantum systems must be unitary, these gates are unitary operators. Quantum gates manipulate all components of a state vector, such as the one in Eq. (4), at the same time. This is so called quantum parallelism, which is however measurement limited.

Every multi-qubit unitary operation can be decomposed into single-, and entangling two-qubit gates [9]. Among the most important single qubit gates belong Pauli operators

$$X = \begin{pmatrix} 0 & 1 \\ 1 & 0 \end{pmatrix}, \quad Y = \begin{pmatrix} 0 & -i \\ i & 0 \end{pmatrix}, \quad Z = \begin{pmatrix} 1 & 0 \\ 0 & -1 \end{pmatrix}. \tag{7}$$

The Pauli matrices when exponentiated give rise to rotation operators about x, y and z axes, defined by the equations

$$R_x(\vartheta) = e^{-i\vartheta X/2} = \cos\frac{\vartheta}{2}\, I - i\sin\frac{\vartheta}{2}\, X = \begin{pmatrix} \cos\frac{\vartheta}{2} & -i\sin\frac{\vartheta}{2} \\ -i\sin\frac{\vartheta}{2} & \cos\frac{\vartheta}{2} \end{pmatrix}, \tag{8}$$

$$R_y(\vartheta) = e^{-i\vartheta Y/2} = \cos\frac{\vartheta}{2}\, I - i\sin\frac{\vartheta}{2}\, Y = \begin{pmatrix} \cos\frac{\vartheta}{2} & -\sin\frac{\vartheta}{2} \\ \sin\frac{\vartheta}{2} & \cos\frac{\vartheta}{2} \end{pmatrix}, \tag{9}$$

$$R_z(\vartheta) = e^{-i\vartheta Z/2} = \cos\frac{\vartheta}{2}\, I - i\sin\frac{\vartheta}{2}\, Z = \begin{pmatrix} e^{-i\frac{\vartheta}{2}} & 0 \\ 0 & e^{i\frac{\vartheta}{2}} \end{pmatrix}, \tag{10}$$

where I is the identity. Other very important single qubit gates include the Hadamard (denoted as Had not to confuse with the Hamiltonian) and T gates

$$\text{Had} = \frac{1}{\sqrt{2}} \begin{pmatrix} 1 & 1 \\ 1 & -1 \end{pmatrix}, \quad \text{T} = \begin{pmatrix} 1 & 0 \\ 0 & e^{i\pi/4} \end{pmatrix}. \tag{11}$$

The most common entangling two-qubit gate is the controlled-NOT (CNOT), which is a generalization of the classical XOR gate. Its action can be written as $|A, B\rangle \longrightarrow |A, B \oplus A\rangle$, where $\oplus$ is addition modulo two. The CNOT gate has the following circuit notation and matrix representation
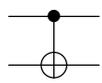
$$\begin{pmatrix} 1 & 0 & 0 & 0 \\ 0 & 1 & 0 & 0 \\ 0 & 0 & 0 & 1 \\ 0 & 0 & 1 & 0 \end{pmatrix}$$

and the action in the computational basis can be summarized as

$$|00\rangle \longrightarrow |00\rangle; \quad |01\rangle \longrightarrow |01\rangle; \quad |10\rangle \longrightarrow |11\rangle; \quad |11\rangle \longrightarrow |10\rangle. \tag{12}$$

One can see, that the NOT operation (X gate) is applied on the first qubit (rightmost in the ket, bottommost in the circuit), if the so called control qubit is in the state $|1\rangle$.

A final part of quantum circuits is a measurement that reveals some information. In quantum mechanics, a measurement is destructive, because it destroys superpositions. For example, when measuring the two-qubit state in Eq. (4) in the computational basis, the outcome will be one of the four possible states with the probability equal to the square of the absolute value of the expansion coefficient, e.g., the state $|00\rangle$ will be measured with probability $|\alpha|^2$.

wire carrying a qubit	$\|q\rangle$ ———————
measurement: projection onto $\|0\rangle$ and $\|1\rangle$	$\|q\rangle$ —[measure]=
single-qubit unitary gate U	$\|q\rangle$ —[U]—
controlled-NOT operation	$\|q_2\rangle$ ——•—— $\|q_1\rangle$ ——⊕——
controlled-U operation	$\|q_2\rangle$ ——•—— $\|q_1\rangle$ —[U]—
qubits ordering convention: $\|q_n \ldots q_2 q_1\rangle$	$\|q_n\rangle$ —————— $\vdots$ $\|q_2\rangle$ —————— $\|q_1\rangle$ ——————
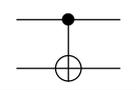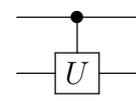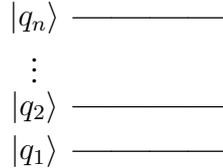
Fig. 2: *The quantum circuit model notation.*

Generally, having a register of qubits in the state $|\psi\rangle$, we can measure some observable O, which is represented by a Hermitian matrix. One is usually interested in an average value over many measurements, i.e., the expectation value of O

$$\langle O \rangle = \langle \psi | O | \psi \rangle. \tag{13}$$

Measuring in the computational basis of ith qubit corresponds to the expectation value of the Pauli Z operator, $\langle \psi | Z_i | \psi \rangle$. This expectation value is in practice obtained by repeated measurement of qubit i (each time the state $|\psi\rangle$ must be reinitialized) and averaging the outcomes of individual measurements ($+1$ for $|0\rangle$ and -1 for $|1\rangle$). As we will see in Sec. 4, strings of fermionic second quantized operators can be represented as strings of the Pauli operators. Therefore, in order to measure the expectation value of molecular Hamiltonians, we need also to measure in X and Y bases. These measurements can be realized by first applying single qubit rotations changing the basis, e.g., from X to Z and then measuring in the Z basis. One can easily verify that the Hadamard gate with the matrix representation in Eq. (11) transforms X eigenstates to Z eigenstates (and vice versa)

$$\frac{1}{\sqrt{2}} \begin{pmatrix} 1 & 1 \\ 1 & -1 \end{pmatrix} \cdot \frac{1}{\sqrt{2}} \begin{pmatrix} 1 \\ 1 \end{pmatrix} = \begin{pmatrix} 1 \\ 0 \end{pmatrix}, \tag{14}$$

$$\frac{1}{\sqrt{2}} \begin{pmatrix} 1 & 1 \\ 1 & -1 \end{pmatrix} \cdot \frac{1}{\sqrt{2}} \begin{pmatrix} 1 \\ -1 \end{pmatrix} = \begin{pmatrix} 0 \\ 1 \end{pmatrix}. \tag{15}$$

In Fig. 2, we summarize the quantum circuit model notation that is used throughout this chapter.
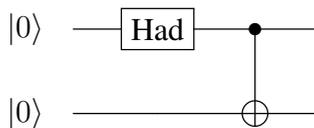
Fig. 3: *A quantum circuit which generates the Bell state $\frac{1}{\sqrt{2}}\big(|00\rangle + |11\rangle\big)$.*

As an example of a simple quantum circuit, we show in Fig. 3 the circuit, which generates the entangled state from Eq. (6) (the so called Bell state [9]). We employ the standard convention that time flows from left to right, i.e., first the Hadamard gate is applied on $|00\rangle$ forming

$$\frac{1}{\sqrt{2}}\big(|00\rangle + |10\rangle\big), \tag{16}$$

then the CNOT gate produces the final Bell state.

2.2 Quantum simulation

Quantum simulation can be either analog or digital. In case of analog simulators [10], a Hamiltonian of a studied system is mapped onto a tunable purpose-built quantum device (described by the same type of Hamiltonian), which then emulates the original system's dynamics. Any observable can be read out using suitable measurements. Analog simulators are very attractive as they are generally more robust to noise, which makes them suitable candidates for the near term quantum devices. However, in a long run, the lack of error correction is problematic for simulations of larger systems.

On the other hand, digital quantum simulation is realized by a quantum circuit (composed of single and two-qubit gates) implemented on an universal quantum computer. Digital quantum simulation can concern time evolution (dynamics) as well as computations of some static properties, such as the ground state energy.

The quantum algorithms for simulation of quantum dynamics were originally developed by Abrams and Lloyd [11, 12]. In order to time-evolve the studied system wave function on a register of qubits, one has to first map the initial system wave function (at time $t = 0$) onto the register, as well as map the system Hamiltonian to its qubit representation (H_q). The time evolution is then performed by the unitary propagator e^{-itH_q}, which is decomposed to elementary single and two-qubit gates. In quantum chemistry, we are interested in cases, when the system Hamiltonian contains polynomial number of terms (due to the two-body nature of molecular Hamiltonians)

$$H = \sum_j h_j, \tag{17}$$

which, however, mutually do not commute. The exponential of a Hamiltonian thus cannot be written as a product of the exponentials of individual h_j terms, but a numerical approximation must be used [11].

The first-order Trotter approximation [13] can be expressed as

$$e^{-itH} = e^{-it \sum_{j=1} h_j} = \left(\prod_{j=1} e^{-ih_j t/N} \right)^N + \mathcal{O}(t^2/N). \qquad (18)$$

We would like to note that Trotterization is not the only possible way to simulate a Hamiltonian time evolution. Other approaches, which are however much more involved, will be briefly mentioned in Sec. 5.1 in the context of phase estimation algorithm. It has also been shown that time evolution can be simulated using variational algorithms [14]. Variational algorithms are discussed in Sec. 5.2.

As a simple example of quantum simulation, let us consider a spin chain model with an Ising Hamiltonian of the following form, which we adopted from [5]

$$H_{\text{Ising}} = \sum_{\langle i,j \rangle} J_{ij} Z_i Z_j + \sum_i B_i X_i, \qquad (19)$$

where the first sum is over nearest-neighbor spins. In this spin case, the qubit representations of the wave function as well as the Hamiltonian are simple; $|0\rangle$ represents α spin, $|1\rangle$ represents β spin and the Hamiltonian in Eq. (19) has already a proper qubit form. After Trotterization, the Hamiltonian time evolution can be implemented by means of the terms

$$e^{-iJ_{ij}Z_iZ_j\delta t} \quad \text{and} \quad e^{-iB_iX_i\delta t}, \quad \text{where} \quad \delta t = t/N. \qquad (20)$$

The second one corresponds to a rotation about x axis (Eq. (8)) applied on the ith qubit, $R_x^i(2B_i\delta t)$. The first term in Eq. (20) has a diagonal form in the computational basis with $e^{\pm iJ_{ij}\delta t}$ on the diagonal. The sign depends on the parity of the corresponding basis state and the exponential can be implemented with the following circuit [9]

$$(21)$$

where CNOTs assure the correct sign of the exponent according to the parity of the state and rotation about z axis is defined in Eq. (10).

In Fig. 4, we show a quantum circuit corresponding to the time evolution governed by the Ising Hamiltonian (Eq. (19)), which uses the first-order Trotter approximation [13]. The sequence of Hadamard gates in the beginning constitutes the state preparation and effectively aligns the spins along the x axis. The unitaries U_{m} change the basis before the measurement and their form depends on what exactly is measured (e.g. spin correlation functions) [12].

The original quantum algorithm for obtaining static properties of quantum systems by means of digital quantum simulation was developed by Abrams and Lloyd [15] and is based on the phase estimation algorithm [9]. We will discuss this approach in detail in the context of quantum chemistry and molecular Hamiltonians in Sec. 5.1.
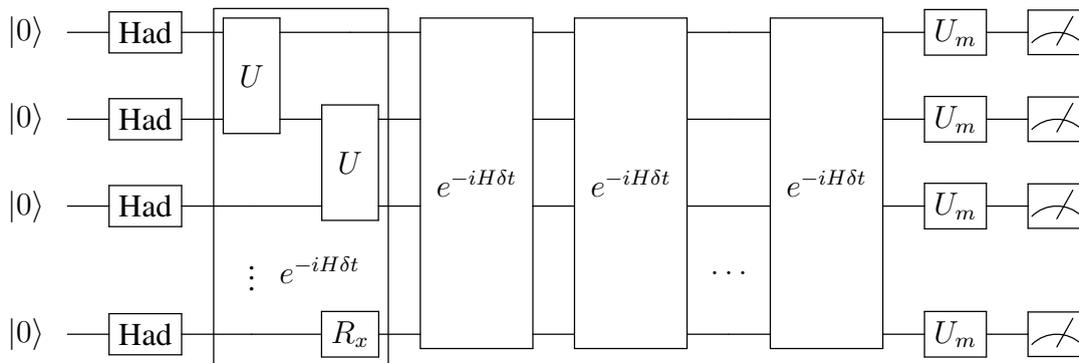
Fig. 4: *Scheme of a digital quantum simulation of the dynamics of a spin chain (Eq. (19)), which employs the first-order Trotter approximation. The two-qubit unitary gates correspond to $U_{ij} = CNOT^{i,j} R_z^j(2J_{ij}\delta t) CNOT^{i,j} R_x^i(2B_i\delta t)$.*

3   Quantum chemistry in a nutshell

We are predominantly interested in the electronic structure of molecules, whose Hamiltonians can be written (in atomic units) as

$$H = -\sum_i \frac{\nabla_i^2}{2} - \sum_I \frac{\nabla_I^2}{2M_I} - \sum_{i,I} \frac{Z_I}{|\mathbf{r}_i - \mathbf{R}_I|} + \frac{1}{2}\sum_{i\neq j} \frac{1}{|\mathbf{r}_i - \mathbf{r}_j|} + \frac{1}{2}\sum_{I\neq J} \frac{Z_I Z_J}{|\mathbf{R}_I - \mathbf{R}_J|}, \qquad (22)$$

where M_I, $\mathbf{R}_I$, and Z_I are the mass, position, and charge of the Ith nucleus and $\mathbf{r}_i$ is the position of ith electron. Taking into account that nuclei are more than 1000 times heavier than electrons, we can employ the Born-Oppenheimer approximation, which separates the electronic and nuclear parts of the Hamiltonian in Eq. (22) and solves them separately. Nuclei are then treated as classical point charges fixed at given positions in the electronic Hamiltonian

$$H_{\text{el.}} = -\sum_i \frac{\nabla_i^2}{2} + \frac{1}{2}\sum_{i\neq j} \frac{1}{|\mathbf{r}_i - \mathbf{r}_j|} - \sum_{i,I} \frac{Z_I}{|\mathbf{r}_i - \mathbf{R}_I|}. \qquad (23)$$

The Born-Oppenheimer approximation gives rise to the concept of the potential energy surfaces. Most of the quantum algorithms for chemical problems use this approximation, but there are exceptions. They comprise the first-quantized (Sec. 4.1) grid-based method [16] as well as the second-quantized (Sec. 4.2) nuclear and electron orbitals approach [17]. Both approaches treat nuclei and electrons on an equal footing.

3.1   Hartree-Fock method

The standard starting point of most of the electronic structure methods is the Hartree-Fock approximation. By using a wave function in the form of a single Slater determinant (see below) and applying the variational principle, it converts the N-electron problem in Eq. (23) to one-electron problems [18]. Electrons in the Hartree-Fock approximation are moving in an effective mean field of all the others. It is a so called mean-field approach.

As was mentioned above, the essence of the Hartree-Fock approximation is a wave function in the form of a single Slater determinant (or spin-adapted combination of few of them in case of open-shell problems)

$$\Phi(\mathbf{x}_1, \mathbf{x}_2, \ldots, \mathbf{x}_N) = \frac{1}{\sqrt{N!}} \begin{vmatrix} \chi_1(\mathbf{x}_1) & \chi_1(\mathbf{x}_2) & \ldots & \chi_1(\mathbf{x}_N) \\ \chi_2(\mathbf{x}_1) & \chi_2(\mathbf{x}_2) & \ldots & \chi_2(\mathbf{x}_N) \\ \vdots & \vdots & \vdots & \vdots \\ \chi_N(\mathbf{x}_1) & \chi_N(\mathbf{x}_2) & \ldots & \chi_N(\mathbf{x}_N) \end{vmatrix} \equiv |\chi_1 \chi_2 \ldots \chi_N\rangle. \tag{24}$$

Here $\mathbf{x}_i$ are composite spatial and spin coordinates of the ith electron, $\mathbf{x}_i = (\mathbf{r}_i, \sigma_i)$ and χ_j are one-electron wave functions, molecular spin-orbitals, which are obtained by solution of the Fock operator eigenvalue problem

$$f(\mathbf{x}_1)\chi_i(\mathbf{x}_1) = \varepsilon_i \chi_i(\mathbf{x}_1). \tag{25}$$

The Fock operator $f(\mathbf{x}_1)$ has the form [18]

$$f(\mathbf{x}_1) = -\frac{\nabla_1^2}{2} - \sum_I \frac{Z_I}{|\mathbf{r}_1 - \mathbf{R}_I|} + v^{\text{HF}}(\mathbf{x}_1), \tag{26}$$

where $v^{\text{HF}}(\mathbf{x}_1)$ represents the operator of a mean field potential of the remaining electrons

$$v^{\text{HF}}(\mathbf{x}_1) = \sum_i \int \chi_i^*(\mathbf{x}_2) \frac{1}{|\mathbf{r}_1 - \mathbf{r}_2|}(1 - P_{12})\chi_i(\mathbf{x}_2)\mathrm{d}\mathbf{x}_2, \tag{27}$$

and the permutation operator P_{12} permutes indices of both electrons. The eigenvalues ε_i in Eq. (25) are spin-orbital energies.

The Slater determinant form of a wave function, Eq. (24), correctly accounts for the exchange symmetry stemming from the fermionic nature of electrons. In fact, swapping any two electrons is equivalent to interchanging two columns of the determinant, which changes the sign of the wave function.

The Hartree-Fock equations, Eq. (25), are in fact nonlinear integro-differential equations, which are usually solved numerically via expansion of molecular orbitals[3] in an atomic orbital basis

$$\psi_i(\mathbf{r}) = \sum_\mu C_{\mu i} \varphi_\mu(\mathbf{r}). \tag{28}$$

The expansion coefficients $C_{\mu i}$ then represent variational parameters optimized during the self-consistent-field (SCF) procedure [18]. The most common atomic orbital basis functions $\varphi_\mu(\mathbf{r})$ are Gaussian-type orbitals (GTOs). GTOs obey the usual radial-angular decomposition

$$\varphi(\mathbf{r}) = R_{nl}(r)Y_{lm}(\vartheta, \varphi), \tag{29}$$

---

[3]Since the non-relativistic electronic Hamiltonian (Eq. (23)) does not contain spin-dependent operators, the spin can be effectively integrated out, transforming the original problem of molecular spin-orbitals to the problem of molecular orbitals.

with $Y_{lm}(\vartheta, \varphi)$ being spherical harmonic functions and the radial part is of the form

$$R_{nl}^{\text{GTO}}(r) \propto (\sqrt{\alpha_{nl}}r)^l e^{-\alpha_{nl}r^2}, \tag{30}$$

where l denotes the angular momentum quantum number of the orbital and α_{nl} is a fitting parameter. Gaussian-type orbitals do not form as compact basis sets as Slater-type orbitals (STOs), which have the correctly behaving radial part of the hydrogen atom solution

$$R_n^{\text{STO}}(r) \propto (\zeta r)^{n-1} e^{-\zeta r}, \tag{31}$$

however, two-electron integral evaluation with GTOs is much easier. For this reason, the most common basis sets used in quantum chemistry are contracted GTOs. In this case, each basis function is a fixed linear combination (contraction) of Gaussian functions (so called primitives). The contraction coefficients as well as exponents of Gaussian functions are pre-optimized for standard basis sets [19]. Regarding the flexibility of basis sets, the minimal basis (e.g. STO-3G) contains all orbitals involved in the Hartree-Fock Slater determinant (occupied ones) plus orbitals of the same/similar energy (e.g. all orbitals of a given open shell). For atoms such as lithium, basis functions of p type are also added to the $1s$ and $2s$ orbitals, because lithium also has a $1s2p$ bound state. The lithium minimal basis thus contains $\{1s, 2s, 2p_x, 2p_y, 2p_z\}$.

Since the valence electrons are the most important ones for chemistry (they participate in bonding), it is not surprising that valence orbitals are commonly represented by more than one basis function. These basis sets are denoted as split-valence and according to the number of basis functions per valence orbital are called valence double, triple, quadruple-ζ, etc. basis sets. Additional polarization functions (with higher angular momentum) or diffuse functions (with small exponents) can further increase the flexibility of GTO basis sets.

In spite of the fact that GTOs have been used in mainstream quantum chemistry for decades, it turns out that they may not be the best basis sets for use in connection with quantum algorithms. Their problem lies in a number of terms in a second-quantized form of a Hamiltonian (see Sec. 3.3), which scales as $\mathcal{O}(M^4)$, where M is the basis set size. The number of terms in a Hamiltonian largely influences the cost of quantum algorithms, as will be discussed below. Babbush et $al.$ [20] pointed out this problem and suggested the use of the plane wave basis and its dual representation. The plane wave basis functions have the form

$$\varphi_{\mathbf{G}}^{\mathbf{k}}(\mathbf{r}) = \frac{1}{\sqrt{\Omega}} e^{i(\mathbf{k}+\mathbf{G})\mathbf{r}}, \tag{32}$$

where Ω is the computational cell volume, $\mathbf{k}$ the wave vector, and $\mathbf{G}$ denote the reciprocal lattice vectors. The Fourier transform of the complete plane wave basis would lead to a basis of delta functions (a grid), thus by applying the discrete Fourier transform on an incomplete plane wave basis, one obtains a so called plane wave dual basis [20], which resembles a smooth approximation to a grid. Direct use of the plane wave basis leads to a reduction of the Hamiltonian terms from $\mathcal{O}(M^4)$ to $\mathcal{O}(M^3)$ (due to the momentum conservation). The plane wave dual basis which diagonalizes the two-body potential operator reduces the number of Hamiltonian terms to $\mathcal{O}(M^2)$ [20]. The plane wave basis sets have been traditionally used for density functional

theory (DFT) calculations of periodic systems. They can also be used for isolated molecules, however, for a given accuracy about hundred times more plane wave basis functions than GTOs are necessary.

The basis set methods exploit some suitable basis in order to make the wave function expansion as compact as possible (or decrease the number of terms in the Hamiltonian, or ideally both). Alternatively, one can employ grid based methods. In this case, the wave function is expanded on a discretized spatial grid (basis of delta functions at given positions $\{|r\rangle\}$) and has a form

$$|\Psi\rangle = \sum_{\mathbf{x}_1 \ldots \mathbf{x}_N} \psi(\mathbf{x}_1, \mathbf{x}_2, \ldots \mathbf{x}_N) \mathcal{A}(|\mathbf{x}_1, \mathbf{x}_2, \ldots \mathbf{x}_N\rangle), \tag{33}$$

where $|\mathbf{x}_i\rangle$ is the composite spatial and spin coordinate ($|\mathbf{r}_i\rangle|\sigma_i\rangle$) of the ith electron and $\mathcal{A}$ is the operator assuring proper antisymmetrization of the wave function. Classically, such approaches (without further approximations) are exponentially costly, because they naturally face the original problem of exponentially large Hilbert space. If each of the $3N$ coordinate axis is discretized to P equidistant points, then the number of expansion coefficients $\psi(\mathbf{x}_1, \mathbf{x}_2, \ldots \mathbf{x}_N)$ scales as $P^{3N} \times 2^N$. On the other hand, the grid-based quantum simulations can be *efficient*, as will be briefly discussed in Sec. 4.1.

3.2   Correlation energy

The Hartree-Fock method is derived based on the approximation of the N-electron wave function in the form of a single Slater determinant (or their spin-adapted combination) as shown in Eq. (24). Even if we solve the Hartree-Fock equations (Eq. (25)) exactly (in the limit of the complete basis set), we will certainly not get the exact energy, because the movement of electrons is not properly correlated at a single determinant level (e.g. electrons with opposite spins are allowed to be at the same place).

The exact wave function, for a given one-particle basis, which were discussed above, can be written as

$$|\Psi\rangle_{\text{FCI}} = c|\Phi\rangle + \sum_{ia} c_i^a |\Phi_i^a\rangle + \sum_{\substack{a<b \\ i<j}} c_{ij}^{ab} |\Phi_{ij}^{ab}\rangle + \cdots, \tag{34}$$

where $|\Phi\rangle$ is the Hartree-Fock Slater determinant (Eq. (24)), $i, j, \ldots$ are indices of occupied orbitals, $a, b, \ldots$ are indices of virtual orbitals (at the Hartree-Fock level), and $\Phi_{ij\ldots}^{ab\ldots}$ denote excited Slater determinants with respect to the Hartree-Fock one (singly excited $i \to a$, doubly excited $ij \to ab$, \ldots, up to N-electron excited). This exact wave function form corresponds to the full configuration interaction (FCI) method. Since the number of Slater determinants in the FCI expansion (Eq. (34)) scales exponentially with the number of electrons (see Fig. 1), only the smallest molecules can be treated by FCI (up to approx. 20 electrons in 20 orbitals).

The correlation energy is defined as the difference between the FCI energy in the limit of a complete basis set and the Hartree-Fock energy in the same limit

$$\Delta E_{\text{corr}} = E^{\text{FCI-lim.}} - E^{\text{HF-lim.}}. \tag{35}$$

In spite of the fact that the correlation energy is only about 1 % of the Hartree-Fock energy, it is orders of magnitude larger than reaction or activation enthalpies of chemical reactions even for small molecules and its, at least approximative, treatment is absolutely essential for chemically relevant results. The correlation energy is calculated by post-Hartree-Fock methods (we will briefly mention two of them, the configuration interaction method in Sec. 3.3.1 and the coupled cluster approach in Sec. 3.3.2). We can formally express the transition from the reference (Hartree-Fock) wave function to the exact one by means of the wave operator Ω

$$|\Psi\rangle = \Omega|\Phi_{\mathrm{HF}}\rangle. \tag{36}$$

A widely used accuracy threshold of 1 kcal/mol ($1.6 \cdot 10^{-3}$ Hartree) is known as "chemical accuracy". If the energy difference between the transition state of a chemical reaction and the reactant ($\Delta E^\dagger$) is given within this accuracy threshold, then the reaction rate at room temperature can be predicted to within an order of magnitude with the Eyring equation

$$v \propto e^{-\Delta E^\dagger/k_B T}, \tag{37}$$

where T denotes the temperature and k_B is the Boltzmann constant. The concept of the chemical accuracy is also widely used in the quantum computational chemistry community [5]. Usually, the experimental realizations of quantum algorithms for chemistry (or their simulations) are compared against the chemical accuracy [5,6].

As was mentioned above, electrons are not properly correlated at the Hartree-Fock level. Very often, the correlation effects (and their contributions to the correlation energy) are divided into dynamic (or weak) electron correlation and static (or strong) electron correlation. The former one is usually a small correction to the wave function (the Hartree-Fock determinant is by far the most dominant one) and is a result of improper treatment of Coulomb repulsion in the single-determinant Hartree-Fock approach. The dynamic electron correlation can be accounted for by an expansion into a large number of Slater determinants systematically formed from the Hartree-Fock reference (single excitations, single and double excitations, etc.), e.g., via the configuration interaction or coupled cluster methods (see Sec. 3.3), or to a large extent also by means of density functional theory. These methods are called single reference and they work very well, when the wave function can be qualitatively described by a single Slater determinant. DFT has a favorable scaling and can treat hundreds of atoms. If spectroscopic accuracy is desired, coupled cluster theory is often the first choice with CCSD(T) being the "gold standard" of quantum chemistry [21].

The static correlation is a result of quasidegeneracy of molecular orbitals and manifests itself by several equally dominant Slater determinants in a wave function expansion. Many important chemical problems fall into this category, e.g. homolytic bond breaking/formation, open-shell and excited electronic states, transition-metal complexes, and transition states of chemical reactions [22]. They are called multireference or strongly correlated. When the manifold of quasidenerate orbitals is small and can be treated by FCI, the active space methods (e.g. complete active space self consistent field, CASSCF) with perturbative dynamic electron correlation extensions can be used. However, when tens of orbitals are strongly correlated, the situation is
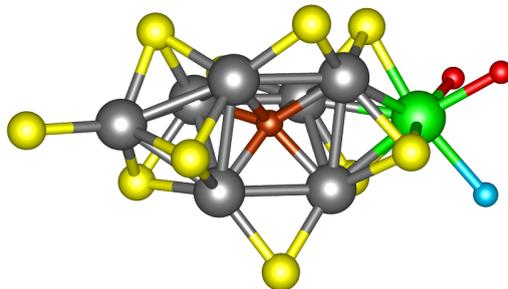
Fig. 5: *Structure of the FeMoco cluster. For clarity, only the atoms of the ligands which are directly bonded to Fe and Mo atoms are displayed. Atom colors: nitrogen - blue, sulphur - yellow, oxygen - red, carbon - brown, iron - grey, molybdenum - green.*

much more complicated. The classical computational methods like tensor networks with the density matrix renormalization group (DMRG), different flavors of quantum Monte Carlo, or e.g., selected configuration interaction approaches, which can treat larger active spaces than exact diagonalization allows, in fact have their own limitations. These are the situations, where quantum algorithms are believed to become a game changer [6].

We have already mentioned in the introduction that catalysts or high temperature superconductors belong to the class of very important strongly correlated problems. As a concrete example, let us mention the electronic structure problem of the Mo-dependent nitrogenase active site (Fe-Mo cofactor, FeMoco), whose structure is depicted in Fig. 5. It has been suggested by Reiher *et al.* [23] as a prominent candidate for quantum simulation algorithms. Enzyme nitrogenase is transforming N_2 into two NH_3 molecules under ambient conditions and understanding of this very complex process, whose mechanism is still not known, is of very high scientific and economic importance. In fact, 2 % of the annual energy production is consumed in the energetically demanding industrial Haber-Bosch synthesis of ammonia. The electronic structure problem of FeMoco is one of the most challenging problems of current computational chemistry.

3.3 Second quantization

Quantum mechanics can be formulated either in the first, or in the second quantization. In the former case, operators are assigned to variables like position or momentum. In the later one, fields rather than variables are quantized. The formalism of second quantization is widely used also in quantum chemistry [18]. Using this formalism, we can transform properties of determinants into algebraic properties of creation and annihilation operators. We restrict ourselves to orthonormal bases of spin orbitals.

The creation operator $a_p^\dagger$ creates an electron in the pth spin orbital. On the contrary, the annihilation operator a_q destroys an electron in the qth spin orbital. These operators obey fermionic anti-commutation rules

$$\{a_p,\, a_q^\dagger\} \;=\; a_p a_q^\dagger + a_q^\dagger a_p = \delta_{pq}, \tag{38}$$

$$\{a_p,\, a_q\} \;=\; \{a_p^\dagger,\, a_q^\dagger\} = 0, \tag{39}$$

which ensure proper anti-symmetry of a wave function and also satisfy the Pauli exclusion principle (if $p = q$, then $a_p^\dagger a_p^\dagger = 0$).

Slater determinants are represented in the occupation basis

$$\Phi(\mathbf{x}_1, \mathbf{x}_2, \ldots, \mathbf{x}_N) = |o_1, \ldots, o_p, \ldots, o_M\rangle, \tag{40}$$

where o_p is equal to 1, when χ_p is occupied, or 0, when it is unoccupied. In other words, kets in the occupation basis representation are binary strings with the length of the number of spin orbitals, in which ones define which spin orbitals are occupied. In order to demonstrate the action of second-quantized operators on determinants, let us take a simple example of the hydrogen molecule (H_2) in a minimal basis (we will use this example also further). Each of the two hydrogen atoms is described with one $1s$ atomic orbital, which are combined into the two molecular orbitals: bonding (denoted as *gerade*, 'g'), which is lower in energy, and antibonding (denoted as *ungerade*, 'u'), which is higher in energy. If we order orbitals in occupation binary strings according to the energy from the left to the right (α spin preceding β), the H_2 determinants in a minimal basis are represented as $|o_{g\uparrow}o_{g\downarrow}o_{u\uparrow}o_{u\downarrow}\rangle$. The Hartree-Fock state is given by

$$\Phi_{\mathrm{HF}} = |1100\rangle = a_{g\uparrow}^\dagger a_{g\downarrow}^\dagger |\rangle, \tag{41}$$

where $|\rangle$ denotes the normalized vacuum state, which does not contain any electrons and thus $a_p|\rangle = 0$. If we now apply, e.g., $a_{g\downarrow}$ on Φ_{HF}, we have

$$a_{g\downarrow}|1100\rangle = a_{g\downarrow}a_{g\uparrow}^\dagger a_{g\downarrow}^\dagger|\rangle = -a_{g\uparrow}^\dagger a_{g\downarrow}a_{g\downarrow}^\dagger|\rangle = -a_{g\uparrow}^\dagger(1 - a_{g\downarrow}^\dagger a_{g\downarrow})|\rangle = -a_{g\uparrow}^\dagger|\rangle = -|1000\rangle \tag{42}$$

where we have used Eq. (38) twice and the aforementioned property of $|\rangle$. The minus sign in Eq. (42) is the result of fermionic exchange anti-symmetry. In fact, the action of creation and annihilation operators on general determinants can be summarized as

$$a_p|o_1, \ldots, o_p, \ldots, o_M\rangle = \delta_{o_p,1}(-1)^{\sum_{i=1}^{p-1} o_i}|o_1, \ldots, o_p \oplus 1, \ldots, o_M\rangle, \tag{43}$$

$$a_p^\dagger|o_1, \ldots, o_p, \ldots, o_M\rangle = \delta_{o_p,0}(-1)^{\sum_{i=1}^{p-1} o_i}|o_1, \ldots, o_p \oplus 1, \ldots, o_M\rangle, \tag{44}$$

where $\oplus$ stands for addition modulo 2 ($0 \oplus 1 = 1$, $1 \oplus 1 = 0$).

Slater determinants excited with respect to the Hartree-Fock state as used in Eq. (34) can be written as

$$|\Phi_i^a\rangle = a_a^\dagger a_i|\Phi\rangle, \tag{45}$$

$$|\Phi_{ij}^{ab}\rangle = a_a^\dagger a_b^\dagger a_j a_i|\Phi\rangle, \quad \text{etc.} \tag{46}$$

As mentioned above, in second quantization, the proper anti-symmetry of a wave function is maintained by properties of creation and annihilation operators applied on it. On the other hand in first quantization, the operators applied on a wave function retain its anti-symmetry, which must be explicitly created during an initialization (see Sec. 4.1).

An arbitrary one-electron operator O_1, which can be written as a sum of one-electron contributions $\sum_i^N o_1(\mathbf{x}_i)$, has the following second-quantized representation [18]

$$O_1 = \sum_{pq} \langle p|o_1|q \rangle \, a_p^\dagger a_q, \tag{47}$$

where $\langle p|o_1|q \rangle$ denote the one-electron integrals

$$\langle p|o_1|q \rangle \equiv \int \chi_p(\mathbf{x}_1)^* o_1(\mathbf{x}_1) \chi_q(\mathbf{x}_1) \, d\mathbf{x}_1. \tag{48}$$

Analogously a two-electron operator O_2, which is expressed as a sum of two-electron contributions $\sum_{i<j}^N o_2(\mathbf{x}_i, \mathbf{x}_j)$, can be written as [18]

$$O_2 = \frac{1}{2} \sum_{pqrs} \langle pq|\, o_2 |rs \rangle a_p^\dagger a_q^\dagger a_s a_r, \tag{49}$$

with

$$\langle pq|o_2|rs \rangle \equiv \int \chi_p(\mathbf{x}_1)^* \chi_q(\mathbf{x}_2)^* o_2(\mathbf{x}_1, \mathbf{x}_2) \chi_r(\mathbf{x}_1) \chi_s(\mathbf{x}_2) \, d\mathbf{x}_1 d\mathbf{x}_2. \tag{50}$$

One can easily verify that such definitions satisfy the general Slater-Condon rules for matrix elements [18]. Based on these definitions, we can write the electronic Hamiltonian from Eq. (23) in the second-quantized form as

$$H = \sum_{pq} h_{pq} \, a_p^\dagger a_q + \frac{1}{2} \sum_{pqrs} \langle pq|rs \rangle \, a_p^\dagger a_q^\dagger a_s a_r, \tag{51}$$

where the one and two-electron integrals have the form

$$h_{pq} = \int \chi_p(\mathbf{x}_1)^* \left(-\frac{\nabla^2}{2} - \sum_I \frac{Z_I}{|\mathbf{r}_1 - \mathbf{R}_I|} \right) \chi_q(\mathbf{x}_1) \, d\mathbf{x}_1, \tag{52}$$

$$\langle pq|rs \rangle = \int \frac{\chi_p(\mathbf{x}_1)^* \chi_q(\mathbf{x}_2)^* \chi_r(\mathbf{x}_1) \chi_s(\mathbf{x}_2)}{|\mathbf{r}_1 - \mathbf{r}_2|} \, d\mathbf{x}_1 d\mathbf{x}_2. \tag{53}$$

One can see in Eq. (51) that the Hamiltonian contains up to M^4 terms (depending on the basis functions used) and these terms contain only up to four second-quantized operators (Coulomb interaction is two-body).

The formalism of second-quantization is commonly used in the derivation of computational methods. In what follows, we will very briefly mention two approaches, which are important for further discussion, namely the configuration interaction (CI) and coupled cluster (CC) methods.

3.3.1 Configuration interaction method

The configuration interaction is a variational method, which unlike the Hartree-Fock approach is not restricted to a single Slater determinant, but the wave function has the form of a linear

combination of the ground and excited Slater determinants. The wave function of the full con-figuration interaction (FCI) was already shown in Eq. (34). The wave operator, Eq. (36), can be written as

$$\Omega_{\mathrm{CI}} = c + \sum_{\alpha} C_{\alpha}, \tag{54}$$

where

$$C_1 = \sum_{ia} c_i^a a_a^\dagger a_i, \tag{55}$$

$$C_2 = \sum_{\substack{a<b \\ i<j}} c_{ij}^{ab} a_a^\dagger a_b^\dagger a_j a_i, \tag{56}$$

$$\vdots$$

with c, $c_{ij\ldots}^{ab\ldots}$ being the variational parameters. The FCI wave function contains all possible Slater determinants formed by placing N_α and N_β electrons in $M/2$ orbitals and is exact within a given orbital basis. However, its computational cost scales exponentially with the system size. Therefore, the CI method is typically restricted to including only certain excitations, most commonly single excitations (C_1, denoted as CIS) or single and double excitations (C_1, C_2, denoted as CISD).

The consequences of the linear form of the wave operator (Eq. (54)) are slow convergence to the FCI with increasing excitation rank as well as incorrect scaling of the energy with the system size (truncated CI is not size-extensive).

3.3.2 Coupled cluster method

The aforementioned limitations of the linear CI expansion are avoided in the coupled cluster (CC) theory. The CC wave operator has an exponential form

$$\Omega_{\mathrm{CC}} = e^T, \tag{57}$$

where T is the so called cluster operator

$$T = \sum_{\alpha} T_{\alpha} \tag{58}$$

and for T_α, it holds

$$T_1 = \sum_{ia} t_i^a a_a^\dagger a_i, \tag{59}$$

$$T_2 = \sum_{\substack{a<b \\ i<j}} t_{ij}^{ab} a_a^\dagger a_b^\dagger a_j a_i, \tag{60}$$

$$\vdots$$

where t parameters are CC amplitudes. Similarly to CI, the CC method is normally truncated to only certain excitations, e.g. single and double excitations, CCSD. The CCSD(T) method with

perturbative triple excitations and $\mathcal{O}(M^7)$ scaling is considered the "gold standard" of quantum chemistry [21].

The standard CC theory is unlike CI not variational, because direct application of the Rayleigh-Ritz variational principle on the wave function from Eq. (57) would lead to an infinite commutator expansion.[4] Instead, a projection technique is employed, which leads to closed explicit algebraic equations for the CC amplitudes, the so called amplitude equations.

The starting point in the derivation of the amplitude equations is the Schrödinger equation written using the CC wave function

$$H|\Psi\rangle = E|\Psi\rangle = Ee^T|\Phi_{\mathrm{HF}}\rangle. \tag{61}$$

If we multiply the above Schrödinger equation on the left by e^{-T} and then project on Φ_{HF}, we get the CC energy formula

$$\langle\Phi_{\mathrm{HF}}|e^{-T}He^T|\Phi_{\mathrm{HF}}\rangle = E\langle\Phi_{\mathrm{HF}}|\Phi_{\mathrm{HF}}\rangle = E. \tag{62}$$

If we project onto the entire set of up to m-tuply excited determinants Φ^* (Φ_i^a, Φ_{ij}^{ab}, etc.), where m is the highest excitation rank in T, we get the amplitude equations mentioned above

$$\langle\Phi^*|e^{-T}He^T|\Phi_{\mathrm{HF}}\rangle = E\langle\Phi^*|\Phi_{\mathrm{HF}}\rangle = 0. \tag{63}$$

The unitary coupled cluster (UCC) approach employs the following unitary form of the wave operator

$$\Omega_{\mathrm{UCC}} = e^{T-T^\dagger}. \tag{64}$$

The UCC method is superior to the standard CC [24], however for the same reason as the variational coupled cluster approach, it cannot be implemented efficiently on a classical computer. On the other hand, as we will discuss in Sec. 5.2, on a quantum computer the unitary ansatz is clearly advantageous as the wave function parametrization then straightforwardly and efficiently translates to a (unitary) quantum circuit.

4 Quantum chemistry to quantum computing mappings

In this section, we will discuss methods for encoding fermionic problems into qubits in both first and second quantization. In order to keep the text self-contained, we will mention in some detail also the most widely employed Jordan-Wigner mapping (Sec. 4.2), which is also discussed in a different chapter.

---

[4]The problem lies in the fact that a variational approach requires computation of $e^{T^\dagger}He^T$, which when employing the Baker-Campbell-Hausdorff formula does not produce a finite commutator expansion, because $T^\dagger$ contains de-excitations.

4.1   First quantized methods

First quantized methods can be grid based or employ the single-particle basis. We will follow the presentation given in the fantastic pedagogical review [5] and adopt some illustrative examples from there.

Let us start with grid based methods. In this case, the wave function is expanded on a discretized spatial grid and has the form shown in Eq. (33). Classically, it is not possible to store all the $P^{3N} \times 2^N$ complex amplitudes for larger systems, where P is the number of equidistant points in each axis. However, it can be done efficiently on a quantum computer. If P is expressed as power of 2, $P = 2^m$, then the number of complex amplitudes is equal to $P^{3N} \times 2^N = 2^{(3m+1)N}$. Taking into account properties of composite quantum systems discussed in Sec. 2.1, it is clear that $(3m+1)N$ qubits can store the wave function from Eq. (33).

As a simple example, we consider two spinless electrons on a four-point one-dimensional grid. Four points of a grid can be represented using 2 qubits: $|0\rangle \equiv |00\rangle$, $|1\rangle \equiv |01\rangle$, $|2\rangle \equiv |10\rangle$, and $|3\rangle \equiv |11\rangle$. As in [5], we distinguish two types of wave functions denoted as 'n' and 'u' shaped (according to the shape of amplitudes distribution). They have the form

$$|\varphi_n\rangle = \frac{1}{\sqrt{6}}|0\rangle + \frac{1}{\sqrt{3}}|1\rangle + \frac{1}{\sqrt{3}}|2\rangle + \frac{1}{\sqrt{6}}|3\rangle, \tag{65}$$

$$|\varphi_u\rangle = \frac{1}{\sqrt{3}}|0\rangle + \frac{1}{\sqrt{6}}|1\rangle + \frac{1}{\sqrt{6}}|2\rangle + \frac{1}{\sqrt{3}}|3\rangle. \tag{66}$$

In order to properly account for the fermionic exchange symmetry, one has to initially prepare the two-electron anti-symmetric wave function, such as

$$
\begin{aligned}
|\Phi\rangle &= \frac{1}{\sqrt{2}}\Big(|\varphi_n\rangle_1|\varphi_u\rangle_2 - |\varphi_u\rangle_1|\varphi_n\rangle_2\Big) \\
&= \frac{1}{6\sqrt{2}}\Big(|1\rangle_1|0\rangle_2 - |0\rangle_1|1\rangle_2 + |1\rangle_1|3\rangle_2 - |3\rangle_1|1\rangle_2 + |2\rangle_1|0\rangle_2 - |0\rangle_1|2\rangle_2 + |2\rangle_1|3\rangle_2 - |3\rangle_1|2\rangle_2\Big),
\end{aligned}
\tag{67}
$$

where ket subscripts label the electrons. The wave function is then maintained anti-symmetric during the time evolution. We have already mentioned the Trotterized time evolution in Sec. 2.2 and will comment on other approaches in Sec. 5.1.

Grid-based approaches have certain advantages, but also certain disadvantages. Regarding the advantages, they achieve a good scaling and it is easy to generalize them for equal treatment of nuclei and electrons on a grid, thus avoiding the Born-Oppenheimer approximation. On the other hand, they require a lot more qubits (to represent a grid) than basis set approaches, which makes them unsuitable for near-term devices.

The original first-quantized basis set based algorithm for quantum simulation was developed by Abrams and Lloyd [12]. It uses $N\lceil\log_2 M\rceil$ qubits to represent N electrons in M basis functions. For each of the electrons, $\lceil\log_2 M\rceil$ qubits are necessary to assign a basis function, they are ordered from $|0\ldots00\rangle$ to $|1\ldots11\rangle$. The product of N-electron wave function then has to be antisymmetrized. The original approach [12] requires $\mathcal{O}(N^2 \log_2^2 M)$ gates and also $\mathcal{O}(N \log_2 M)$ ancilla qubits.

As an illustrative example, we adopt the H_2 molecule in a minimal basis from Sec. 3.3 and label the molecular spin orbitals as $|g_\uparrow\rangle = |00\rangle = |0\rangle$, $|g_\downarrow\rangle = |01\rangle = |1\rangle$, $|u_\uparrow\rangle = |10\rangle = |2\rangle$, and $|u_\downarrow\rangle = |11\rangle = |3\rangle$. The simple product of one electron in the $|g_\uparrow\rangle$ spin orbital and the other in $|g_\downarrow\rangle$ representing the Hartree-Fock state is clearly not anti-symmetric. The properly anti-symmetrized Hartree-Fock state looks like

$$|\Phi_{\mathrm{HF}}\rangle = \frac{1}{\sqrt{2}}\big(|0\rangle_1|1\rangle_2 - |1\rangle_1|0\rangle_2\big). \tag{68}$$

The exact ground state wave function of the H_2 molecule in a minimal basis can be written as a linear combination of only two Slater determinants (we use the compact determinant notation from Eq. (24))

$$|\Psi\rangle = \alpha|g_\uparrow g_\downarrow\rangle + \beta|u_\uparrow u_\downarrow\rangle = \frac{\alpha}{\sqrt{2}}\big(|0\rangle_1|1\rangle_2 - |1\rangle_1|0\rangle_2\big) + \frac{\beta}{\sqrt{2}}\big(|2\rangle_1|3\rangle_2 - |3\rangle_1|2\rangle_2\big), \tag{69}$$

because the remaining two fulfilling the $s_z = 0$ $\big(|g_\uparrow u_\downarrow\rangle, |g_\downarrow u_\uparrow\rangle\big)$ have different spatial symmetry ("ungerade") and thus does not contribute to the ground state wave function.

The Hamiltonian can be obtained by projection onto the single-particle basis

$$H = \sum_{i=1}^{N} \sum_{p,q=1}^{M} h_{pq}|\chi_p\rangle_i\langle\chi_q|_i + \frac{1}{2} \sum_{i\neq j}^{N} \sum_{p,q,r,s}^{M} \langle pq|rs\rangle|\chi_p\rangle_i|\chi_q\rangle_j\langle\chi_s|_j\langle\chi_r|_i, \tag{70}$$

where one and two-electron integrals h_{qp} and $\langle pq|qs\rangle$ were already defined in Eqs. (52) and (53). Individual operators from Eq. (70) can be straightforwardly expressed by means of the Pauli operators, Eq. (7), leading to the total number of $\mathcal{O}(N^2 M^6)$ Pauli terms, which are up to $2\log_2 M$-local [5]. The Hamiltonian can then be used to time evolve the anti-symmetrized wave function [12]. We will discuss the time evolution, which is a key part in many quantum simulation algorithms, in more detail in Sec. 5.1.

4.2 Second quantized methods

In this subsection, we will describe how to express the creation and annihilation operators of indistinguishable electrons in terms of the Pauli operators acting on distinguishable qubits, which can be achieved in multiple ways.

In case of the Jordan-Wigner (JW) mapping [25], qubit states encode the occupation vector (Eq. (40))

$$|o_1 \ldots o_M\rangle \to |q_M \ldots q_1\rangle, \qquad q_p = o_{M-p+1} \in \{0, 1\}. \tag{71}$$

Since we employ the standard conventions used in quantum chemistry and quantum computing communities, i.e., orbitals in occupation vectors are ordered from the left [18] and qubits in kets are ordered from the right [9], in what follows, we will use the primed indices for qubit labels with a simple conversion

$$p' = M - p + 1. \tag{72}$$

The second-quantized operators can be expressed as

$$a_p^\dagger = \left(\bigotimes_{j=1}^{p-1} Z_{j'} \right) \otimes Q_{p'}^\dagger, \quad a_p = \left(\bigotimes_{j=1}^{p-1} Z_{j'} \right) \otimes Q_{p'}, \tag{73}$$

where $Q = |0\rangle\langle 1| = (X+iY)/2$ and $Q^\dagger = |1\rangle\langle 0| = (X-iY)/2$. The strings of Pauli Z operators ensure the right phase factor / "parity of the state" as summarized in Eqs. (43) and (44), Q and $Q^\dagger$ then decrease or increase the occupation of a given spin orbital. One can easily verify that such a representation of the second quantized operators satisfies their anti-commutation relations (Eq. (38)).

The electronic Hamiltonian, Eq. (51), can be rewritten using strings of Pauli operators

$$H = \sum_j h_j P_j = \sum_j h_j \prod_i \sigma_{i'}^j, \tag{74}$$

where σ_i^j stands for one of the Pauli operators (X, Y, Z) or the identity acting on i^{th} qubit, the sum over j runs over all one and two-electron terms and h_j formally represent one and two-electron integrals. Finally the exponentials of these strings, which are required by some time evolution algorithms, can be build up from single qubit gates and CNOTs [9], similarly to the time evolution of the simple Ising model presented in Sec. 2.2. We will demonstrate this approach on the one-electron part of the non-relativistic (real) Hamiltonian

$$H_1 = \sum_{pq} h_{pq} a_p^\dagger a_q = \sum_p h_{pp} a_p^\dagger a_p + \sum_{p<q} \left(h_{pq} a_p^\dagger a_q + h_{qp} a_q^\dagger a_p \right). \tag{75}$$

Employing the JW transform, the diagonal terms can be written as

$$h_{pp} a_p^\dagger a_p = h_{pp} Q_{p'}^\dagger Q_{p'} = h_{pp} |1\rangle_{p'} \langle 0|_{p'} |0\rangle_{p'} \langle 1|_{p'} = h_{pp} |1\rangle_{p'} \langle 1|_{p'} = \frac{h_{pp}}{2} \left(I_{p'} - Z_{p'} \right). \tag{76}$$

For the exponential it holds

$$e^{-ih_{pp} a_p^\dagger a_p \delta t} = e^{\frac{-ih_{pp}\delta t}{2}} R_z(-h_{pp}\delta t)_{p'}. \tag{77}$$

Similarly, the off-diagonal terms read

$$h_{pq} a_p^\dagger a_q + h_{qp} a_q^\dagger a_p = \frac{h_{pq}}{2} \left[X_{p'} \otimes Z_{p' \to q'} \otimes X_{q'} + Y_{p'} \otimes Z_{p' \to q'} \otimes Y_{q'} \right], \tag{78}$$

where $Z_{p' \to q'}$ represents the direct product

$$Z_{p' \to q'} \equiv Z_{(p+1)'} \otimes Z_{(p+2)'} \otimes \ldots \otimes Z_{(q-2)'} \otimes Z_{(q-1)'}. \tag{79}$$

The exponential of the string of Z operators $\exp[-i\delta t(Z \otimes \ldots \otimes Z)]$ is in fact diagonal in the computational basis with the phase shift $e^{\pm i\delta t}$ on the diagonal. The sign of this phase shift depends on the parity of the corresponding basis state ("+" if the number of ones in the binary

representation is odd, "−" otherwise). The exponential can be implemented with the following circuit [9]

$$(80)$$
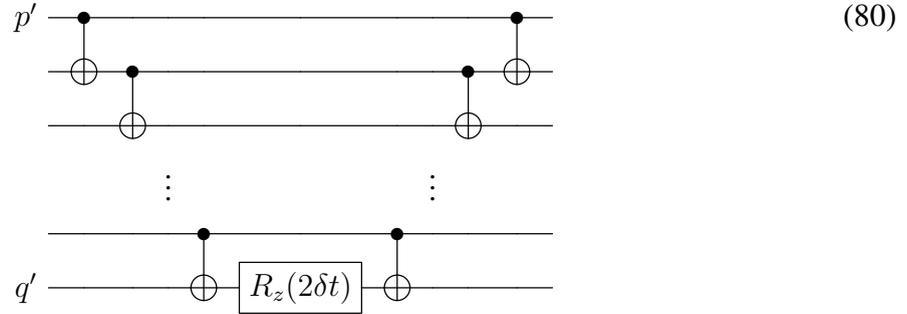
where CNOTs assure the correct sign of the phase shift according to the parity of the state and z-rotations were defined in Eq. (10). Generalization to the cases with X or Y operators acting on p' and q' qubits (Eq. (78)) can be easily realized with change-of-basis operators applied on p' and q' qubit before and after the action of the quantum circuit from Eq. (80). We have already shown in Eqs. (14) and (15) that, e.g., the Hadamard gate changes the basis from X to Z (and vice versa). The procedure for the two-electron part of the Hamiltonian is more elaborate, but completely analogous and can be found in [26].

The JW mapping is simple, but not the most economic one, when it comes to the number of gates required. As can be seen in Eq. (80), the quantum gates overhead scales as $\mathcal{O}(M)$. This is because the parity unlike the occupation of spin orbitals is not stored locally and must be collected by means of CNOT's before the single qubit rotation is applied. An alternative, which however has the same $\mathcal{O}(M)$ scaling, is the parity encoding. In this approach, the parity is stored locally and the occupation of spin orbitals non-locally

$$|o_1 \ldots o_M\rangle \to |q_M \ldots q_1\rangle, \qquad q_{p'} = \left[\sum_{i=1}^{p} o_i \right] (\mathrm{mod}\ 2).$$

$$(81)$$

The same scaling as for the JW mapping stems from the fact that when the occupation of a given orbital is changed, all the parities to which it contributes have to be updated, e.g. the first contributes to all of them.

More efficient than the JW mapping is the Bravyi-Kitaev (BK) mapping [27], which is a combination of the Jordan-Wigner and parity mappings. It compromises on the locality of occupation and parity information. The qubits store partial sums of occupation numbers, according to the BK matrix, β_{pq},

$$|o_1 \ldots o_M\rangle \to |q_M \ldots q_1\rangle, \qquad q_{p'} = \left[\sum_{q=1}^{p} \beta_{pq} o_q \right] (\mathrm{mod}\ 2),$$

$$(82)$$

which is defined recursively

$$\beta_1 = \quad [1],$$
$$\beta_{2^{i+1}} = \begin{pmatrix} \beta_{2^i} & \mathbf{0} \\ \mathbf{A} & \beta_{2^i} \end{pmatrix},$$

$$(83)$$

where $\mathbf{A}$ is a $2^i \times 2^i$ matrix filled with zeros except the bottom row, which is filled with ones. For example for $M = 4$, the BK matrix reads

$$\beta_4 = \begin{pmatrix} 1 & 0 & 0 & 0 \\ 1 & 1 & 0 & 0 \\ 0 & 0 & 1 & 0 \\ 1 & 1 & 1 & 1 \end{pmatrix}. \tag{84}$$

The construction of second-quantized operators in the BK mapping is much more involved than in the JW mapping and we will not discuss it here, but rather refer readers to the work of Seeley *et al.* [28]. The ingenious BK mapping, which combines the occupation and parity as can be clearly seen from the structure of the BK matrix, Eq. (84), in fact leads to the $\mathcal{O}(\log_2 M)$ scaling. Recently, also more sophisticated mappings with certain advantages have been presented, e.g., generalizations of the BK mapping, which reduce the number of qubits due to symmetries (particle number, spin, or point group symmetries) [5].

5   Quantum algorithms for quantum chemistry

In this section, we will discuss the two main approaches which are cornerstones of most of the quantum algorithms for chemistry. In particular, the phase estimation which is an ultimate algorithm for error-corrected quantum devices with a potential to simulate very accurately the most complex molecular systems in future, and the variational quantum eigensolver, which combines the power of both quantum and classical computers and is suitable for NISQ devices.

5.1   Phase estimation

5.1.1   Phase estimation algorithm

The phase estimation algorithm (PEA) [9] is a quantum algorithm for obtaining an eigenvalue of a unitary operator U, based on a given initial guess of the corresponding eigenvector. Since a unitary U can be written as $U = e^{iH}$, with H Hermitian, the PEA can be viewed as a quantum substitute of the classical diagonalization.
Suppose that $|u\rangle$ is an eigenvector of U and that it holds

$$U|u\rangle = e^{2\pi i\varphi}|u\rangle, \qquad \varphi \in [0, 1), \tag{85}$$

where φ is the phase which is estimated by the algorithm. The quantum register is divided into two parts. The first one, called the read-out part, is composed of m qubits on which the binary representation of φ is measured at the end and which is initialized to the state $|0\rangle^{\otimes m}$. The second part contains the corresponding eigenvector $|u\rangle$.
The PEA quantum circuit is shown in Fig. 6. The application of Hadamard gates on all qubits in the first part of the register gives

$$|\text{reg}\rangle = \frac{1}{\sqrt{2^m}}\Big(|0\rangle + |1\rangle\Big)\dots\Big(|0\rangle + |1\rangle\Big)|u\rangle = \frac{1}{\sqrt{2^m}}\sum_{j=0}^{2^m-1}|j\rangle|u\rangle. \tag{86}$$
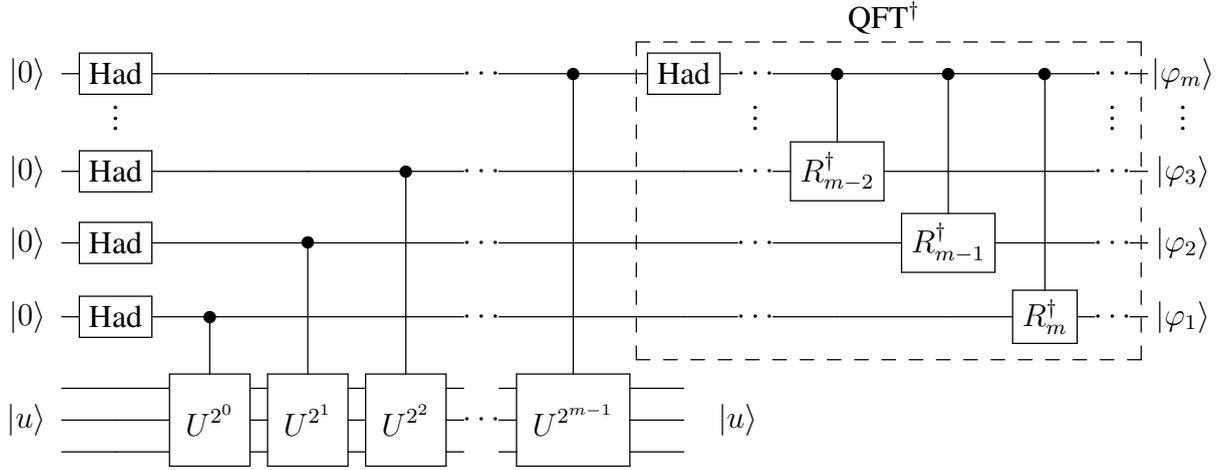
Fig. 6: *The PEA circuit with the highlighted part corresponding to the inverse quantum Fourier transform [9].*

Next, after the application of a sequence of controlled powers of U, the register is transformed into

$$|\text{reg}\rangle = \frac{1}{\sqrt{2^m}}\left(|0\rangle + e^{2\pi i 2^{m-1}\varphi}|1\rangle\right)\left(|0\rangle + e^{2\pi i 2^{m-2}\varphi}|1\rangle\right)\dots\left(|0\rangle + e^{2\pi i 2^0 \varphi}|1\rangle\right)|u\rangle$$

$$= \frac{1}{\sqrt{2^m}}\sum_{j=0}^{2^m-1} e^{2\pi i j \varphi}|j\rangle|u\rangle. \tag{87}$$

The crucial part of the PEA is the *efficient* inverse quantum Fourier transform (QFT†, highlighted in Fig. 6) performed on the read-out part of the register. The R_j operator is defined as [9]

$$R_j = \begin{pmatrix} 1 & 0 \\ 0 & e^{2\pi i/2^j} \end{pmatrix}. \tag{88}$$

If the phase can be expressed exactly with m bits

$$\varphi = 0.\varphi_1\varphi_2\dots\varphi_m = \frac{\varphi_1}{2} + \frac{\varphi_2}{2^2} + \dots + \frac{\varphi_m}{2^m}, \qquad \varphi_i \in \{0,1\}, \tag{89}$$

it (and consequently the eigenvalue) is recovered with unit probability by a measurement on the first part of the quantum register, which is by QFT† transformed into $|2^m\varphi\rangle$.

When the phase cannot be expressed exactly with m bits, in order to obtain this precision with the success probability of at least $1-\varepsilon$, one has to use n qubits [9]

$$n = m + \lceil \log_2(2 + 1/2\varepsilon) \rceil. \tag{90}$$

If the desired eigenvector is not known explicitly (as is typically the case in quantum chemistry), we can start the algorithm with an arbitrary initial guess vector $|\psi\rangle$, which can be expanded in terms of eigenvectors of U

$$|\psi_{\text{init}}\rangle = \sum_i c_i |u_i\rangle. \tag{91}$$

When using the number of ancillary qubits according to the Eq. (90), the success probability is decreased to $|c_i|^2(1-\varepsilon)$ (due to the linearity of quantum mechanics). It is therefore crucial for the success of the algorithm to be initialized with a wave function, which has a non-zero overlap with the exact targeted state. We will discuss some of the techniques of the initial state preparation in the following subsection.

We would like to note that the original phase estimation algorithm briefly sketched above has been improved in many aspects over the years. For example only one ancillary qubit can be used for sequential measurement of the phase. Also modifications for better efficiency, including parallelization or resistance to noise, have been proposed [6, 5].

5.1.2 Initial state preparation

Initial states with a large-enough overlap with the exact targeted state are key for the success of the phase estimation algorithm. In fact, a randomly chosen state from an exponentially large Hilbert space would have an exponentially decreasing overlap with the exact state, as the system size increases. This is indeed in agreement with the fact that solving the ground state problem of a completely general local Hamiltonian is a QMA-complete (quantum Merlin-Arthur complete, the quantum analogue of NP-complete) problem, i.e., considered difficult even for a quantum computer [29]. Nevertheless, the electronic structure problem of physically relevant systems, is believed to be *efficiently* solvable by means of quantum computers. In this case, the initial state preparation methods outlined below may be used.

Aspuru-Guzik *et al.* in their seminal work [8] proposed the adiabatic state preparation (ASP) algorithm inspired by the adiabatic model of quantum computing. In this approach, one slowly varies the Hamiltonian of the quantum register, starting with a trivial one and the register in its (exactly known) ground state, e.g. the Hartree-Fock state, and ending with the final exact one in the following simple way

$$H = (1 - t/T)H_{\text{init}} + (t/T)H_{\text{exact}} \qquad t : 0 \longrightarrow T, \tag{92}$$

where t is time and T the maximum annealing time. The efficiency of ASP depends on the minimum energy gap between the ground- and the first excited state along the adiabatic path, $g_{\min}$

$$g_{\min} = \min_{0 \leq s \leq 1} \big(E_1(s) - E_0(s) \big), \qquad s = t/T. \tag{93}$$

In particular, the maximum annealing time scales as

$$T \approx \mathcal{O}\left(\frac{M^4}{g_{\min}^2}\right). \tag{94}$$

Similarly to the phase estimation also ASP has been improved in several aspects. For example, non-linear adiabatic paths, more efficient for chemical problems, have been proposed and numerically tested [30].

Alternative options for the initial state preparation can be variational methods discussed in Sec. 5.2, or employing reference states obtained by some polynomially scaling computational methods. Several such methods including CI, CASSCF, selected CI, or tensor networks have already been used in numerical simulations [6].

5.1.3 Hamiltonian time evolution

If we take U in Eq. (85) in the form

$$U = e^{-iH\tau}, \tag{95}$$

where τ is a suitable parameter (equivalent to time in a time evolution) assuring φ being in the interval $[0, 1)$ and H the electronic Hamiltonian, then the phase estimation algorithm reveals its energy spectrum. The whole procedure can be simply viewed as a time propagation of a trial wave function followed by the QFT switching from the time to energy domain and a measurement projecting out a certain eigenstate. Looking at the circuit in Fig. 6 and observing that the unitary U is applied up to the power 2^{n-1} and that the number of ancillary qubits is related to the precision according to Eq. (90), the total evolution time (the number of e^{-iH} calls) is proportional to $\mathcal{O}(1/\varepsilon)$. This number of calls governs the cost of a simulation. For the case of molecular Hamiltonians (Eq. (51)), Reiher *et al.* showed numerically that a number of calls scales as $\pi/2\varepsilon$ [23].

There are multiple ways how to implement the time evolution operator of the form e^{-iHt}. In Sec. 2.2, we have already mentioned the first-order Trotter approximation, Eq. (18). In order to achieve accuracy ε, the number of Trotter steps $N = \mathcal{O}(t^2/\varepsilon)$. This can be improved by using higher order product formulae. It was also shown that the accuracy can be further improved by, e.g., randomly ordering the terms in the Trotter sequence [5]. The gate counts of all Trotter-based approaches scale as $\mathcal{O}(\text{poly}(1/\varepsilon))$.

Several more advanced methods for time evolution, which are more efficient than Trotterization have been proposed [6]. Description of these approaches is, however, beyond the scope of this chapter. We will only briefly mention the Taylor series method, in which the Hamiltonian evolution, Eq. (95), is divided into shorter segments and each of the segment exponentials is approximated by a truncated Taylor series, which can be expanded as a linear combination of unitaries (LCU). These unitaries are then applied in a superposition employing oracle circuits. For a detailed summary of different Hamiltonian simulation techniques and references to original papers, we refer readers to the review [6].

In order to study the asymptotic scaling of the phase estimation based algorithms, one typically employs the fixed chemical accuracy. The scaling properties largely depend on the basis set employed, i.e., number of terms in the Hamiltonian (as discussed in Sec.3.1) as well as the actual algorithm used for implementation of the Hamiltonian time evolution (Eq. (95)). In the Gaussian basis, the second quantized Hamiltonian contains $\mathcal{O}(M^4)$ terms and the Taylor series method, which is more sophisticated than the Trotter based approaches, scales as $\mathcal{O}(M^5)$ [5]. On the other hand, it is well known that rigorous bounds on the Trotter error are loose by several orders of magnitude. In the plane wave dual basis, the Hamiltonian contains $\mathcal{O}(M^2)$ terms and the Taylor series method was shown to scale as $\mathcal{O}(M^{2.67})$ [5]. We would like to note, however, that more advanced Hamiltonian simulation techniques, which were not discussed here, can lead to even lower scaling. For example in the plane wave basis, algorithms which achieve sublinear scaling in M have been developed.

In spite of the recent development of highly sophisticated algorithms for Hamiltonian simula-
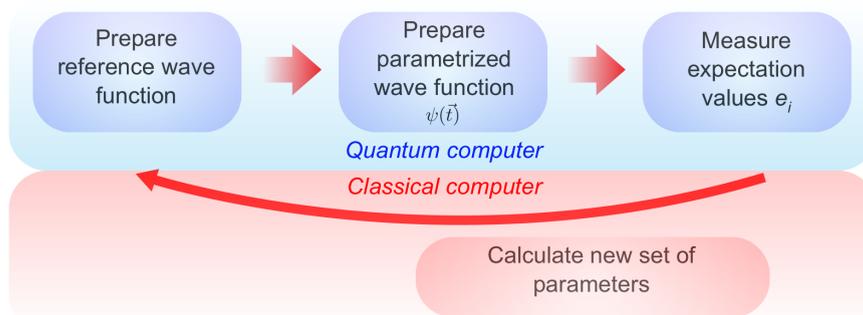
Fig. 7: *Flow chart of the variational quantum eigensolver.*

tions, the phase estimation based approaches require quantum circuits with a large number of gates, which are expected to require some form of a quantum error correction. Therefore they are not suitable for near term devices, which will not have enough qubits for this purpose.

5.2 Variational quantum-classical algorithms

A promising alternative to the phase estimation for near-term quantum devices is the variational quantum eigensolver (VQE) approach [31, 32], which combines classical variational energy minimization over normalized trial wave functions $\Psi(\vec{\vartheta})$

$$E = \min_{\vec{\vartheta}} \left\langle \Psi(\vec{\vartheta}) \middle| H \middle| \Psi(\vec{\vartheta}) \right\rangle \tag{96}$$

with a state preparation and a measurement of the Hamiltonian expectation value on a quantum computer. The VQE method in fact trades long coherent quantum circuits for short circuits and lots of measurements (though at the cost of asymptotically worse scaling in terms of precision). The scheme of VQE is depicted in Fig. 7.

The starting point of VQE is a preparation of the fixed reference state $|\Psi_{\text{ref}}\rangle$, which can be the Hartree-Fock determinant or also some multireference state. Then for an initial set of a polynomial number of parameters $\vec{\vartheta}$, a series of parametrized gates $U(\vec{\vartheta})$ (ansatz circuit) is applied on $|\Psi_{\text{ref}}\rangle$, producing the so called ansatz state $\left|\Psi(\vec{\vartheta})\right\rangle$. Here comes the advantage of quantum hardware, since ansatz states cannot be stored and manipulated on a classical computer for general $U(\vec{\vartheta})$ (due to the exponentially large Hilbert space). We will discuss different types of ansatz circuits below.

After preparing the ansatz state, the expectation value of the Hamiltonian is measured. We are working with the second-quantized representation and we have already shown in Sec. 4.2 that when employing the JW transformation (or the BK one), the Hamiltonian is mapped to a linear combination of products of Pauli operators, as shown in Eq. (74). The energy can be written as

$$E(\vec{\vartheta}) = \sum_j h_j \left\langle \Psi(\vec{\vartheta}) \middle| \prod_i \sigma_i^j \middle| \Psi(\vec{\vartheta}) \right\rangle, \tag{97}$$

where, as in Eq. (74), σ_i^j stands for one of the Pauli operators (X, Y, Z) or the identity acting on the ith qubit, the sum over j runs over all one and two-electron terms and h_j formally represent one and two-electron integrals. In the Hamiltonian averaging method [32], each term is

repeatedly measured (each time the ansatz state must be prepared) in order to get the desired precision. This approach requires $\mathcal{O}(1/\varepsilon^2)$ measurements to get the energy with precision ε.

The measured energy is then together with the actual values of $\vec{\vartheta}$ passed to a classical optimization routine. This can be a gradient-free optimization, such as Nelder-Mead simplex, or some gradient-descent, since strategies to directly measure the energy gradients with respect to one of the parameters were also developed [5]. The classical optimization produces a new set of parameters $\vec{\vartheta}$ and the whole procedure is repeated until energy convergence.

The advantage of VQE over classical computational methods certainly depends on the employed ansatz. Two types of ansätze have been used so far. The first category are so called hardware efficient ansätze and it comprises the limited parametrized gate set, which is easy to implement on a given quantum architecture. The aim is to produce as much flexible ansatz state as possible with a minimal number of gates. These approaches do not use any information about a system studied, however, have been successfully demonstrated on several small molecules [5].

The second category comprises chemically inspired ansätze. To the best of our knowledge, all VQE methods of this type are based on the unitary coupled cluster theory (Sec. 3.3.2) usually restricted up to double excitations and employ

$$U(\vec{\vartheta}) = e^{T-T^\dagger}. \tag{98}$$

The point is that the UCCSD method cannot be performed *efficiently* on a classical computer due to infinite commutator expansions, as discussed in Sec. 3.3.2, but it can be implemented on a quantum computer. The CC amplitudes are then the VQE variational parameters. Moreover, the fully variational UCCSD method is expected to outperform traditional CCSD in accuracy [32] and converge even for multireference problems.

Since T and $T^\dagger$ in Eq. (98) do not commute, some sort of numerical approximation similar to those used in the Hamiltonian time evolution (Sec. 5.1.3) has to be used in order to implement the circuit ansatz by means of single and two-qubit gates. If we assume that we have a reasonable $|\Psi_{\text{ref}}\rangle$, which is close enough to the exact state, the CC amplitudes are expected to be small numbers (much smaller than 1). In this case, much less Trotter steps are necessary than for the phase estimation based approaches. In fact, it was shown that even a single Trotter step can be used to implement the circuit ansatz from Eq. (98), which yields accurate results [5]. In this case, the number of quantum gates for the UCCSD circuit ansatz implementation scales as $\mathcal{O}(M^3 N^2)$ when the JW mapping is employed [$\mathcal{O}(M^2 N^2 \log_2 M)$ for the BK mapping].

Undoubtedly, the biggest bottleneck of VQE is the huge number of measurements (requiring repeated state preparation) in the Hamiltonian averaging method. It was shown [32] that the number of measurements N_m required to estimate the energy with precision ε is bounded by

$$N_m = \frac{\left(\sum_i |h_i|\right)^2}{\varepsilon^2}, \tag{99}$$

where h_i again represent one and two-electron integrals. The number of measurements thus scales as $\mathcal{O}(M^8/\varepsilon^2)$ in a Gaussian basis, which can be reduced by using local basis sets to $\mathcal{O}(M^6/\varepsilon^2)$, and $\mathcal{O}(M^4/\varepsilon^2)$ in a plane wave dual basis [6]. However, as in the case of the phase

estimation based approaches, advanced techniques, whose presentation is behind the scope of this chapter, have been developed, which reduce this scaling in certain cases by orders of magnitude [5].

The VQE method has also been extended for excited state calculations. One such approach is the quantum subspace expansion (QSE) of McClean *et al.* [33], in which a polynomial number of additional measurements allows the treatment of excited states. In this method, excited states are expanded in a subspace around the ground state $|\Psi_0\rangle$ spanned by single excitations $a_p^\dagger a_q |\Psi_0\rangle$ for all possible p, q. They can be found by solving the generalized eigenvalue problem

$$H^{\mathrm{QSE}}C = S^{\mathrm{QSE}}CE, \tag{100}$$

where C is a matrix of eigenvectors, E a diagonal matrix of energies and the Hamiltonian matrix H^{QSE} is given by

$$H_{pq,rs}^{\mathrm{QSE}} = \langle \Psi_0 | a_p a_q^\dagger H a_r^\dagger a_s | \Psi_0 \rangle. \tag{101}$$

Since the subspace states are not orthogonal, the overlap matrix has to be also obtained

$$S_{pq,rs}^{\mathrm{QSE}} = \langle \Psi_0 | a_p a_q^\dagger a_r^\dagger a_s | \Psi_0 \rangle. \tag{102}$$

One can see in Eq. (100) that this approach of excited state calculations requires, on top of measuring the one-particle and two-particle reduced density matrices (1-RDMs, 2RDMs), which are measured in standard VQE,[5] also measuring the 3-RDMs and 4-RDMs.

6 Summary

In this chapter, we have reviewed some of the basic concepts, which were developed for the simulation of chemical problems on quantum computers. In fact, quantum computational chemistry [5] has achieved enormous progress recently and it would be impossible to include all important developments in this field. On the small illustrative examples, we have rather shown the basic strategies, which may be used also in case of more advanced algorithms.

We have presented how to map the quantum chemistry problems onto a register of qubits both in the first and second quantization and most of the time restricted ourselves to the electronic structure problem. The two main approaches to this problem have been discussed: the phase estimation algorithm, which is an ultimate algorithm for error-corrected quantum devices as well as the variational quantum eigenvalue solver, which combines power of both quantum and classical computers and is due to short quantum circuits suitable for near-term devices.

---

[5]These are indeed the individual expectation values in Eq. (97)

References

[1] R.P. Feynman, Int. J. Theor. Phys. **21**, 467 (1982)

[2] F. Arute, K. Arya, R. Babbush, D. Bacon, J.C. Bardin, R. Barends, R. Biswas, S. Boixo, F.G.S.L. Brandao, D.A. Buell, B. Burkett, Y. Chen, Z. Chen, B. Chiaro, R. Collins, W. Courtney, A. Dunsworth, E. Farhi, B. Foxen, A. Fowler, C. Gidney, M. Giustina, R. Graff, K. Guerin, S. Habegger, M.P. Harrigan, M.J. Hartmann, A. Ho, M. Hoffmann, T. Huang, T.S. Humble, S.V. Isakov, E. Jeffrey, Z. Jiang, D. Kafri, K. Kechedzhi, J. Kelly, P.V. Klimov, S. Knysh, A. Korotkov, F. Kostritsa, D. Landhuis, M. Lindmark, E. Lucero, D. Lyakh, S. Mandrà, J.R. McClean, M. McEwen, A. Megrant, X. Mi, K. Michielsen, M. Mohseni, J. Mutus, O. Naaman, M. Neeley, C. Neill, M.Y. Niu, E. Ostby, A. Petukhov, J.C. Platt, C. Quintana, E.G. Rieffel, P. Roushan, N.C. Rubin, D. Sank, K.J. Satzinger, V. Smelyanskiy, K.J. Sung, M.D. Trevithick, A. Vainsencher, B. Villalonga, T. White, Z.J. Yao, P. Yeh, A. Zalcman, H. Neven, and J.M. Martinis, Nature **574**, 505 (2019)

[3] H.S. Zhong, H. Wang, Y.H. Deng, M.C. Chen, L.C. Peng, Y.H. Luo, J. Qin, D. Wu, X. Ding, Y. Hu, P. Hu, X.Y. Yang, W.J. Zhang, H. Li, Y. Li, X. Jiang, L. Gan, G. Yang, L. You, Z. Wang, L. Li, N.L. Liu, C.Y. Lu, and J.W. Pan, Science **370**, 1460 (2020)

[4] J. Preskill, Quantum **2**, 79 (2018)

[5] S. McArdle, S. Endo, A. Aspuru-Guzik, S.C. Benjamin, and X. Yuan, Rev. Mod. Phys. **92**, 015003 (2020)

[6] Y. Cao, J. Romero, J.P. Olson, M. Degroote, P.D. Johnson, M. Kieferová, I.D. Kivlichan, T. Menke, B. Peropadre, N.P.D. Sawaya, S. Sim, L. Veis, and A. Aspuru-Guzik, Chem. Rev. **119**, 10856 (2019)

[7] K. Head-Marsden, J. Flick, C.J. Ciccarino, and P. Narang, Chem. Rev. **121**, 3061 (2020)

[8] A. Aspuru-Guzik, A.D. Dutoi, P.J. Love, and M. Head-Gordon, Science **309**, 1704 (2005)

[9] M.A. Nielsen and I.L. Chuang: *Quantum Computation and Quantum Information* (Cambridge University Press, 2000)

[10] I. Buluta and F. Nori, Science **326**, 108 (2009)

[11] S. Lloyd, Science **273**, 1073 (1996)

[12] D.S. Abrams and S. Lloyd, Phys. Rev. Lett. **79**, 2586 (1997)

[13] N. Hatano and M. Suzuki: *Finding Exponential Product Formulas of Higher Orders*, in *Lecture Notes in Physics* (Springer, Heidelberg, 2005)

[14] Y. Li and S.C. Benjamin, Phys. Rev. X **7** (2017)

[15] D.S. Abrams and S. Lloyd, Phys. Rev. Lett. **83**, 5162 (1999)

[16] I. Kassal, S.P. Jordan, P.J. Love, M. Mohseni, and A. Aspuru-Guzik,
Proc. Natl. Acad. Sci. U.S.A **105**, 18681 (2008)

[17] L. Veis, J. Višňák, H. Nishizawa, H. Nakai, and J. Pittner,
Int. J. Quantum Chem. **116**, 1328 (2016)

[18] A. Szabo and N.S. Ostlund: *Modern quantum chemistry* (MacMillan, New York, 1982)

[19] B.P. Pritchard, D. Altarawy, B. Didier, T.D. Gibson, and T.L. Windus,
J. Chem. Inf. Modeling **59**, 4814 (2019)

[20] R. Babbush, N. Wiebe, J. McClean, J. McClain, H. Neven, and G.K.L. Chan,
Phys. Rev. X **8** (2018)

[21] J. Gauss: In P. v. R. Schleyer, N.L. Allinger, T. Clark, J. Gasteiger, P.A. Kollman,
H.F. Schaefer III, and P.R. Scheiner (eds.) *The Encyclopedia of Computational Chemistry*
(Wiley, Chichester, 1998), pp. 615–636

[22] D.I. Lyakh, M. Musiał, V.F. Lotrich, and R.J. Bartlett, Chem. Rev. **112**, 182 (2011)

[23] M. Reiher, N. Wiebe, K.M. Svore, D. Wecker, and M. Troyer,
Proc. Natl. Acad. Sci. U.S.A. **114**, 7555 (2017)

[24] A.G. Taube and R.J. Bartlett, Int. J. Quantum Chem. **106**, 3393 (2006)

[25] P. Jordan and E. Wigner, Z. Phys. A **47**, 631 (1928)

[26] J.D. Whitfield, J. Biamonte, and A. Aspuru-Guzik, Mol. Phys. **109**, 735 (2011)

[27] S.B. Bravyi and A.Y. Kitaev, Ann. Phys. **298**, 210 (2002)

[28] J.T. Seeley, M.J. Richard, and P.J. Love, J. Chem. Phys. **137**, 224109 (2012)

[29] J. Kempe, A. Kitaev, and O. Regev, SIAM J. Comput. **35**, 1070 (2006)

[30] L. Veis and J. Pittner, J. Chem. Phys. **140**, 214111 (2014)

[31] A. Peruzzo, J. McClean, P. Shadbolt, M.H. Yung, X.Q. Zhou, P.J. Love, A. Aspuru-Guzik,
and J.L. O'Brien, Nat. Commun. **5** (2014)

[32] J.R. McClean, J. Romero, R. Babbush, and A. Aspuru-Guzik,
New J. Phys. **18**, 023023 (2016)

[33] J.R. McClean, M.E. Kimchi-Schwartz, J. Carter, and W.A. de Jong, Phys. Rev. A **95** (2017)

13 Quantum Computing – Quo Vadis?

David DiVincenzo
Peter Grünberg Institut
Forschungszentrum Jülich GmbH

Contents

1   Quantum computing science is everywhere

In this small lecture, I will first comment on the generalities of quantum computing, and then plunge into some particulars.

Quantum computing continues to evolve as a science. It is now entering a phase where some concrete applications are seriously anticipated. Highly technological projects are underway in various companies and large organizations, and very ambitious efforts to assemble the unique and complex hardware required have borne some fruit. The 53-qubit device of the Google laboratory, and now the 56-qubit device of the Chinese Academy of Sciences, has executed a few algorithms that, to a very limited extent, were difficult for conventional computers. Tentative plans are drawn up for executing some additional algorithms, for example from quantum chemistry, for which these new machines may be capable of some modest successes.

We have, however, not reached the stage where truly society-changing computations are performable on any existing quantum computer. One issue is sheer size: estimates can be made of the size of quantum computer that would be transformative, and these estimates are generally in the millions of qubits. This is still far short of the bit-counts in even modest conventional computers of today, but it is a big, and expensive, leap from the unique Google and CAS processors. The optimistic timelines (I draw from IBM's projections here) for getting there involve many, many years of additional work.

Much of this work is a clearly engineering effort, required to make a unique, high precision piece of hardware at $10,000$ times the present scale. Work on quantum computers have reached such a highly technological stage.

But, looking at IBM and others, we see reasons for the field cannot be purely one involving systems engineering. No qubit in use today meets the precision requirements needed to make the $10,000$-fold leap. To tell the story for the superconducting qubits of the Google/CAS/IBM machines, they have in about 20 years improved in the quality of operation by about 6 orders of magnitude. However, the consensus is that about another 2 orders of magnitude are needed.

The improvements that I have just referred to require pure quantum physics insights. This is connected with a realization that we had 20 years ago, and that remains the focal point of our struggle: quantum physics has the property that it can, under the right circumstances, predict physical properties to fantastically high precision. But these circumstances are also fantastically difficult to bring into being.

One can see this as related to the struggle that we have had in crystal physics in the last 100 years. We have a wonderfully complete understanding of band theory, Fermi surfaces, van-Hove singularities, thermal conductivity, and a host of other properties. But the things we predict were quite hard to realize: materials are no perfect crystals, it takes a lot of work to make them so.

On the quantum computer side, the big stumbling block has been the many manifestations of decoherence. Quantum mechanics predicts in wonderful detail what happens to a two-level system when you apply forces to it, if it is isolated from everything else. We can tell less well what happens when you take account of the environment. But we know enough about this to

say that it creates a no-go condition for quantum computing.

So, quantum theorists have been forced to tell the growers (or better synthesizers, because it is both the materials and the devices that you make from them) to achieve conditions that are unquestionably very hard, and to not even be able to tell them what the exact target is. It is a fortunate thing that progress has been possible under these conditions. It has been iterative and slow, but at least it has been steady.

In the area of superconducting qubits, we might have been persuaded to say that 30 years ago there was already not really that much more to learn about the physics of superconductivity in Aluminium. The trouble was, this physics knowledge said that it would be possible to make ideal quantum two-level systems with Aluminium, with its superconductivity and with the Josephson effect made possible by tunnel junctions of AlO_x. All derivations could have been confidently done on the basis of material given in lectures at the time.

It initially didn't work at all. The things left out about the actual state of these devices made reality completely different from the model. It exposed our ignorance of the physics that really went on when you put an Aluminium junction into a circuit.

But over the last 20 years, we have gradually learned. Our models have been extended, experiments have become more sophisticated. Interestingly, this didn't require much new work from the crystal grower, the important sources of imperfections were not so much in her domain.

2 My main thesis

The thesis that I announce based on these observations is that progress on quantum computers, including from the pure engineering point of view, requires all the physics knowledge that we've got and that we know how to make. In short, quantum computing science is all of physics theory. Let me take as examples the other lectures of this school. In most cases, I can see an application for these efforts that have a chance to impact the efforts to build a quantum computer. Let me go through them:

- The Hubbard model. This is the fundamental model on which we base our thinking about spin qubits. It is also a good model to think about in working on algorithms for quantum simulation.

- Frustrated magnetism. This topic connects with ideas of topological order in eigenstates, and therefore with problems in quantum error correcting codes.

- Quantum chemistry. This is a topic for devising quantum algorithms and quantum simulations.

- Calculating with Green functions. This has been taken up in other work on quantum simulation, notably in the work of Jim Freericks, who has lectured in several of these schools in years past. See his article [1].

- Second quantization. The language used throughout quantum information science.

- Superconductivity. This is one of the most basic topological states of matter. Protection from dissipation and decoherence is very fundamental here.

- Entanglement. It goes without saying that this is the cornerstone of most thinking in quantum information science.

My premise for the rest of these lecture notes is that since quantum information science needs all of theoretical physics, I will just proceed to give a few living examples of how we need all details of our understanding to make progress on the problems of quantum computing, including those in the most engineering directions.
My examples will be in the area of semiconductor physics.

3 Electron theory for qubits

I will go through a small case study of a "correlation" effect in electronic qubits that has many consequences, some good and some bad, for the quality of the qubits. The qubit I have in mind is that defined by the electron spin of extra carriers in semiconductors. The "correlation" effect is that which arises from spin-orbit interaction.
One should immediately object that I have a strange definition of "correlation" here, since spin-orbit is a single-electron term in the Hamiltonian. This is a good objection: in the right basis, the electron problem with spin-orbit but without electron-electron interaction still has eigenstates that are single Slater determinants, so there is always a way in which the computational problem for this setting is "easy". On the other hand, there is an important new correlation: with spin-orbit interaction, the spin and orbital degrees of freedom are *entangled*, while they occur in an unentangled product state in the absence of spin-orbit coupling. This entanglement already occurs at the single-particle level: the single-particle states from which the single Slater determinant eigensolutions are constructed are already entangled between spin and orbit. This entanglement varies dramatically from one part of the single-particle spectrum to another, which is very consequential for electron-qubit physics.
Recall the general situation from relativistic quantum mechanics: Foldy and Wouthuijsen derived a series in $1/c$ for the effective Hamiltonian. The terms to be added to the Pauli-Schrödinger Hamiltonian are

$$-\frac{p^4}{8m^3c^2} \, , \text{ mass-velocity term} \tag{1}$$

$$-\frac{e\hbar}{8m^2c^2}\boldsymbol{\nabla}\cdot\mathbf{E} \, , \text{ Darwin term} \tag{2}$$

$$-\frac{e\hbar}{8m^2c^2}\boldsymbol{\sigma}\cdot\big(\mathbf{E}{\times}\mathbf{p} - \mathbf{p}{\times}\mathbf{E}\big), \textbf{ spin-orbit term}. \tag{3}$$

The first two terms are quantitatively important but do not change the entanglement structure of the electron state, while the last term does, so we will continue with this term in the following. First, we slightly rewrite the spin-orbit term in the conventional way

$$H_{so} = -\frac{\hbar}{4m^2c^2}\boldsymbol{\sigma}\cdot\boldsymbol{\nabla}V(\mathbf{r}){\times}\mathbf{p}. \tag{4}$$

Three things to note: 1) $V(\mathbf{r})$ is now a potential energy, not a voltage; 2) The form here given doesn't look hermitian, since in general p_i doesn't commute with $\partial_j V$, but the situation is saved because $\boldsymbol{\nabla} \times \boldsymbol{\nabla} V = 0$; 3) the replacement is not correct if $\mathbf{E}$ is time dependent, but the effect of this error is negligible at ordinary frequencies.

I always find it informative to analyze how big a term is for atomic matter. Given that the characteristic scale of p_i is $\hbar/a_0$ and the characteristic scale of $\boldsymbol{\nabla} V$ is E_h/a_0, we rewrite Eq. (4) as

$$H_{so} = \frac{E_h}{4} \left(\frac{1}{4\pi\epsilon_0} \frac{e^2}{\hbar c} \right)^2 \boldsymbol{\sigma} \cdot \frac{\boldsymbol{\nabla} V(\mathbf{r})}{E_h/a_0} \times \frac{\mathbf{p}}{\hbar/a_0} = \frac{E_h}{4} \alpha^2 \boldsymbol{\sigma} \cdot \frac{\boldsymbol{\nabla} V(\mathbf{r})}{E_h/a_0} \times \frac{\mathbf{p}}{\hbar/a_0}. \qquad (5)$$

Here the Rydberg constant $E_h = \hbar^2/ma_0^2$, the Bohr radius $a_0 = 4\pi\epsilon_0\hbar^2/me^2$, and the fine structure constant $\alpha = \frac{1}{4\pi\epsilon_0} \frac{e^2}{\hbar c} \approx 1/137$. The appearance of the square of the fine structure constant signals the smallness of the term for atomic matter. However, we will see that under some circumstances, this term is nevertheless fully entangling.

3.1   Other spin-orbit terms

I referred to Eq. (4) as *the* spin-orbit term. But there are in fact many others that could occur. In this generous way of looking at things, we will call any Hamiltonian term a spin-orbit term if it involves both the electron coordinate, or momentum, and its spin. An example would be

$$i\alpha^{18} E_h \, \sigma_x \, e^{y/y_0} \tanh\left(\frac{p_z}{p_0} \right) \left(\frac{x}{x_0} \right)^7 \sigma_z + h.c. \qquad (6)$$

Very few such expressions will pass muster as being physically interesting. There are two major exceptions, that is, two other spin-orbit terms are worth our attention:

1. First is the "micromagnet" term:

$$- g\mu_B \, \boldsymbol{\sigma} \cdot \mathbf{B}(\mathbf{r}) \qquad (7)$$

   There is nothing fundamental one can say about the size or importance of this term, since it requires engineering a spatial dependence to the applied magnetic field. With the use of micromagnets, its effect can indeed be significant in laboratory experiments on spin qubits.

2. Next is the magnetic dipole-dipole interaction:

$$\frac{\mu_0 g^2 \mu_B^2}{16\pi|\mathbf{r}|^3} \Big(3(\boldsymbol{\sigma}_1 \cdot \hat{\mathbf{r}}) (\boldsymbol{\sigma}_2 \cdot \hat{\mathbf{r}}) - \boldsymbol{\sigma}_1 \cdot \boldsymbol{\sigma}_2 \Big), \quad \mathbf{r} = \mathbf{r}_1 - \mathbf{r}_2 \qquad (8)$$

   This can indeed lead to spin-orbit entanglement – the barely-bound p states of $^{129}\mathrm{Xe}_2$ is the cleanest example that I know of. While we often use Eq. (8) in the case where one or the other of the spins are nuclear, it is also a perfectly good Hamiltonian for the pure electron problem. In this setting, it is not to be confused with the Heisenberg exchange Hamiltonian $J\boldsymbol{\sigma}_1 \cdot \boldsymbol{\sigma}_2$), which is merely an effective Hamiltonian that describes electrons

in particular orbital configurations. The dipole-dipole interaction Eq. (8), by contrast, is "fundamental" – at least as fundamental as the normal spin-orbit interaction. Like that, it has the status of a leading relativistic correction. To see this, we "de-dimsionalize" Eq. (8) using atomic units. The new replacement we must employ is Maxwell's relation $\mu_0 = \frac{1}{\epsilon_0 c^2}$. With this, the de-dimensionalized form of the overall factor in the electronic dipole-dipole interaction is

$$\frac{\mu_0 g^2 \mu_B^2}{16\pi |\mathbf{r}|^3} = \frac{g^2}{16}\frac{E_h}{(r/a_0)^3}\frac{4}{4\pi\epsilon_0 c^2}\frac{\mu_b^2}{E_h a_0^3} = \frac{g^2}{16}\frac{E_h}{(r/a_0)^3}\alpha^2. \tag{9}$$

Thus, just like the normal spin-orbit term, the dipolar term is second order in the fine structure constant.

Given that it is of the same order, why does it not emerge as a term in the Foldy-Wouthuijsen series? The answer is that is a *two-electron* spin-orbit term, which can never emerge from the one-particle Dirac equation. It is understood that it emerges from the same sort of analysis (as a series in α) applied to the two-particle relativistic wave equation, the Bethe-Salpeter equation. The dipolar term, along with another novel orbit-orbit term, emerges from this. The derivation via the Breit equation is also informative, but less rigorous.

Now let's turn to the consequences of spin-orbit coupling in a semiconductor that hosts a spin qubit. The relevant semiconductors, the various group-IV and III-V compound semiconductors like GaAs, have a rather universal structure near the Fermi energy. All these semiconductors have full cubic symmetry, so that the electron states at the center of the Brillouin zone have high symmetry. The relevant irreducible representations at the Gamma point are isomorphic to those for full spherical symmetry.

Thus, the states at the Gamma point, in the absence of spin-orbit, have a conserved orbital angular momentum L. It happens that the states near the Fermi energy always have $L = 1$, in $\hbar$ units, at the top of the valence band (which can host hole qubits), and the first state of the conduction band is always $L = 0$. Around an origin of high symmetry, we can rewrite the spin-orbit Hamiltonian as in atomic physics

$$V(\mathbf{r}) \approx V(|r|) \tag{10}$$

$$\boldsymbol{\nabla} V \approx \hat{r}\frac{\partial V}{\partial r} \tag{11}$$

$$H_{so} \propto \frac{1}{r}\frac{\partial V}{\partial r}\boldsymbol{\sigma} \cdot (\mathbf{r}\times\mathbf{p}) = \frac{1}{r}\frac{\partial V}{\partial r}\boldsymbol{\sigma} \cdot \mathbf{L}. \tag{12}$$

An aside: it is sometimes said that the atomic spin-orbit operator is $\boldsymbol{\sigma} \cdot \mathbf{L}$. This is misleading; $\frac{1}{r}\frac{\partial V}{\partial r}$ is an operator too, on the position Hilbert space! When this is replaced by a "spin-orbit constant", it should rather be understood as a matrix element between specific radial orbital pairs.

Thus, the situation with the top of the valence band is the same as with the p-state in an atom: the total angular momentum, $\mathbf{J} = \mathbf{S}+\mathbf{L} = \frac{1}{2}\boldsymbol{\sigma}+\mathbf{L}$ is conserved. The angular momentum addition

rules say that the angular momentum states are $J = 3/2$ and $J = 1/2$, due to the composition rule for irreducible representations $\frac{1}{2} \otimes 1 = \frac{1}{2} \oplus \frac{3}{2}$. This also means that the p-states, which would be 6-fold degenerate (3 orbital times 2 spin), split up into a 4-fold degenerate set of states $J = \frac{3}{2}$, and a two-fold pair $J = \frac{1}{2}$.

In semiconductors of interest the $J = \frac{3}{2}$ states are always the higher ones, and thus define the valence-band edge. The $J = \frac{1}{2}$ states are, rather prosaically, referred to as the "split-off band". the spin-orbit splitting between these multiplets, Δ, is one of the important band parameters in semiconductors. We will see below the crucial role that it plays in the behavior of electron [sic] spin qubits.

Note that this lifting of valence-band degeneracy comes along with there being strong spin-orbit entanglement in these states. For example, one of the eigenstates in the $J = \frac{3}{2}$ space, made non-degenerate by a magnetic field in the (100) crystal direction, is

$$\left| \frac{3}{2}, \frac{1}{2} \right\rangle = \frac{1}{\sqrt{3}} \left(\psi_{p_+}(\mathbf{r}) \chi_\downarrow + \sqrt{2}\, \psi_{p_z}(\mathbf{r}) \chi_\uparrow \right). \tag{13}$$

Here $\psi_{p_+}(\mathbf{r})$ is the $k = 0$ Bloch state constructed from the orbital $p_x + ip_y$, $\psi_{p_z}(\mathbf{r})$ is the different orbital Bloch state constructed from the p_z orbital, and $\chi_\downarrow$ and $\chi_\uparrow$ are the orthogonal spin wavefunctions that can also be denoted $\binom{0}{1}$ and $\binom{1}{0}$. Thus, the "weak" spin-orbit interaction can, in this circumstance, result in an almost maximally entangled wavefuction.

We will pursue this interesting topic much further, but note that the $J = \frac{3}{2}$ states come with two different effective masses, so that away from the Gamma point they disperse into two pairs of states. A remaining two-fold degeneracy is guaranteed by Kramers' theorem plus the inversion symmetry in the point group. Because of these two different masses, the top of the valence band is further split if the crystal is strained, as happens in the formation of heterostructures.

The bottom of the conduction band, the place where we normally put electrons in order to make spin qubits, is at first glance immune from the large effect of spin-orbit interaction. The state is essntially of the simple form

$$\left| \frac{1}{2}, \frac{1}{2} \right\rangle \approx \psi_s(\mathbf{r}) \chi_\downarrow, \tag{14}$$

with basically no spin-orbit entanglement. But I say "basically" because the spin-orbit Hamiltonian still couples this state perturbatively to other eigenstates.

This, in some cases, produces a significant physical effect. This is very evident in the effective g-factor of these states, in other words, the splitting between the $|1/2, 1/2\rangle$ and $|1/2, -1/2\rangle$ due to a magnetic field, Without spin-orbit interaction this splitting is $g\mu_B B$, with a g factor always equal to $g = 2 + \alpha/2\pi$ (that is, a fraction of a percent above 2, with additional, even smaller terms of higher order in α). The fine structure constant α appears here due to a distinct vacuum relativistic effect, the coupling of the electron to the quantized electromagnetic field.

But spin-orbit effects in crystalline matter modify this dependence dramatically. First, the Zeeman splitting in no longer rigorously linear in B, there are B^2, etc. terms. But more dramatic and significant is the departure of g far from 2. This can be analyzed by perturbation theory. The most significant contributors are couplings to the six valence band states. A beautiful formula

emerges from this, due to Laura Roth in 1959 [2]

$$g = 2 - \frac{2\Delta}{3E_g + 2\Delta}\left(\frac{m}{m_{\mathit{eff}}} - 1\right).$$ (15)

(This is ignoring the Schwinger correction $\alpha/2\pi$, which is almost always far smaller.) Here Δ is the valence band spin-orbit splitting discussed a above, E_g is the band gap of the semiconductor, and m_{eff} is the effective mass of the conduction band electrons. These latter two parameters are not primarily determined by spin-orbit interaction, while Δ is only non-zero when spin-orbit is included.

The parameters on the right-hand side of the Roth formula are all accurately known from experiment. For example, $\Delta = 44, 295, 341, 380, 930$ (in meV) for Si, Ge, GaAs, InAs, and ZnTe, respectively. Plugging these in gives for GaAs $g^R_{\mathrm{GaAs}} = 0.09$, and for InAs $g^R_{\mathrm{InAs}} = -14.9$. The Zeeman splittings are also readily measured, and the experimental values are $g_{\mathrm{GaAs}} = -0.44$, and for $g_{\mathrm{InAs}} = -15$. While not being precisely accurate, Roth's analysis correctly predicts the dramatic departures of the Zeeman splitting from its non-relativistic value, and the trend of increasing departure when going to heavier elements.

The important message of this formula is that the g factor depends, potentially strongly, on details of the orbital electronic structure. One can imagine, based on the kind of perturbation theory involved, that the result will depend on where we are in $\mathbf{k}$-space. To get ahead of our story somewhat, this tells us something of what will happen when we form a quantum dot: depending on the size of the dot, the resulting wavefunction will sample a greater or lesser part of this $\mathbf{k}$ space – thus, the g factor will depend on the degree of confinement. This variation, while not particularly large in, e.g., Si, has been observed recently and is definitely a source of concern for applications as qubits.

While the derivation of the Roth formula is a bit time consuming, I will give a flavor of this kind of band perturbation for the simpler problem of the band effective masses that appear in her formula. This formula has nothing to do with spin-orbit, so we revert to the regular Schrödinger equation.

When we substitute the Bloch function

$$\Phi_{nk}(\mathbf{r}) = e^{i\mathbf{k}\cdot\mathbf{r}}u_{nk}(\mathbf{r})$$ (16)

in the Schrödinger equation

$$\left(\frac{p^2}{2m} + V(\mathbf{r})\right)\Phi_{nk}(\mathbf{r}) = E_{nk}(r)\Phi_{nk}(\mathbf{r}),$$ (17)

we get the wave equation for the periodic part of the Bloch function,

$$\left(\frac{p^2}{2m} + \frac{\hbar^2 k^2}{2m} + \frac{\hbar}{m}\mathbf{k}\cdot\mathbf{p} + V(\mathbf{r})\right)u_{nk}(\mathbf{r}) = E_{nk}(r)u_{nk}(\mathbf{r}).$$ (18)

The new term here is referred to as the "cay-dot-pee" perturbation; although it is not really a perturbation, Eq. (18) is just an exact rewriting of Eq. (17).

The procedure is as follows: one obtains solutions for $\mathbf{k} = 0$, $u_{n0}(\mathbf{r})$ and E_{n0}. Then one treats the $\mathbf{k} \cdot \mathbf{p}$ term (together with the simple k^2 term) using perturbation theory to get the dispersion. Around $\mathbf{k} = 0$ the lowest order perturbation result is quadratic in $|k|$. The band curvature gives the effective mass. The simple formula for this is

$$\frac{1}{m_{eff}} = \frac{1}{m} + \frac{2}{m^2} \sum_{n' \neq n} \frac{\left| \hat{\mathbf{k}} \cdot \langle u_{n0} | \mathbf{p} | u_{n'0} \rangle \right|^2}{E_{n0} - E_{n'0}} . \tag{19}$$

In our high symmetry situation, m_{eff} is independent of the direction of the unit vector $\hat{\mathbf{k}}$.
We can note that, generically, large contributions to $1/m_{eff}$ will occur (so that m_{eff} will have a small magnitude) if the energy gap is small.
With spin-orbit interaction, our Schrödinger equation Eq. (17) becomes

$$\left(\frac{p^2}{2m} + V(\mathbf{r}) + \frac{\hbar}{4m^2c^2} \mathbf{p} \cdot (\boldsymbol{\sigma} \times \boldsymbol{\nabla} V) \right) e^{i\mathbf{k}\cdot\mathbf{r}} u_{nk\sigma}(\mathbf{r}) = E_{nk\sigma}(r) e^{i\mathbf{k}\cdot\mathbf{r}} u_{nk\sigma}(\mathbf{r}). \tag{20}$$

The band energies E and the periodic part of the Bloch wavefunction u have acquired spin labels σ. As above, one obtains a $\mathbf{k} \cdot \mathbf{p}$-style Schrödinger equation for the u function

$$\left(H_0 + \frac{\hbar^2 k^2}{2m} + \frac{\hbar}{m} \mathbf{k} \cdot \mathbf{p} + \frac{\hbar^2}{4m^2c^2} \mathbf{k} \cdot (\boldsymbol{\sigma} \times \boldsymbol{\nabla} V) \right) u_{nk\sigma}(\mathbf{r}) = E_{nk\sigma}(r) u_{nk\sigma}(\mathbf{r}). \tag{21}$$

Here H_0 is the whole Hamiltonian for the $\mathbf{k} = 0$ states, including the spin-orbit contributions; often this is left as a separate term to be treated, along with the $\mathbf{k}$-dependent terms, with perturbation theory. We will again look at what happens to the conduction band in, e.g., GaAs. The approach is as for the effective mass: take into account the effect of other bands perturbatively. Since the conduction band is two spin states, we get not a single corrected dispersion, but an effective 2×2 Hamiltonian

$$H_{eff} = \frac{\hbar^2 k^2}{2m_*} + \gamma \hbar^2 \left(\sigma_x k_x \left(k_y^2 - k_z^2 \right) + \text{cyclic permutation } x \to y \to z \to x \right). \tag{22}$$

The form here is universal for s-bands in crystals with a form of cubic symmetry, with only γ depending on details of the perturbation matrix elements; but for full cubic symmetry (i.e., including inversion symmetry, e.g., in Si and Ge) $\gamma = 0$. This set of terms is called "Dresselhaus spin-orbit coupling".
A few interesting notes about this term: 1) While it respects cubic symmetry, it does not have full rotational symmetry, so the band dispersion is not isotropic. 2) Except along high-symmetry directions, the energy splitting of the two spin states is nonzero with a quantization axis that is a function of $\mathbf{k}$. 3) There is a superficially similar term, called the Rashba spin-orbit coupling, that is *not* intrinsic to the crystal structure, but is activated by additional applied magnetic fields. This Rashba coupling produces a variety of interesting effects, but in the interests of space will not go into them here.
We are now going to see how this affects the electrons that are confined to quantum dots, for the purpose of making spin qubits. I will state without proof the use of effective Hamiltonians like

Eq. (22) when we consider the envelope function approximation. When we describe an electron as being confined to a quantum dot, we have in mind that the Bloch function is modulated by a slowly varying envelope wavefunction

$$\psi_{env,n\sigma}(\mathbf{r})e^{i\mathbf{k}_0 \cdot \mathbf{r}}u_{nk_0\sigma}(\mathbf{r}). \tag{23}$$

Here $\mathbf{k}_0$ is the extremum of the band, i.e., $\mathbf{k}_0 = 0$ for the examples we have been discussing. The envelope-function theory shows that to apply the effective Hamiltonian to ψ_{env} alone to get an eigenvalue equation, the prescription is to elevate $\mathbf{k}$ to operator status with the replacement $\mathbf{k} \to i\boldsymbol{\nabla}$. You are probably very familiar with this in the case of the simple effective mass term, where we say that the kinetic energy operator in the effective mass approximation is just

$$-\frac{\hbar^2 \nabla^2}{2m_{eff}}. \tag{24}$$

With spin-orbit interaction, we just make this replacement everywhere in Eq. (22).

We will now explore what consequences this has for the control of two spin-qubits. We will follow the derivation of Kavokin [3]. We will assume the Hamiltonian consists of Eq. (22), along with a spatial confining potential. This potential is assumed smooth on the scale of the lattice constant. Notationally we will write this double quantum dot Hamiltonian as

$$H(\mathbf{r}, \mathbf{k}) = H_{eff}(\mathbf{k}) + V_{conf}(\mathbf{r}). \tag{25}$$

This notation indicates, as suggested above, that the envelope coordinate $\mathbf{r}$ and the crystal momentum $\mathbf{k}$ will function as conjugate variables. "conf" refers to "confinement".

We will solve the two-electron problem. Importantly, we will proceed with first quantization, which flexibly deals with undetermined and non-orthogonal space orbitals. In first quantization the two electron Hamiltonian is

$$H_{tot} = \sum_{i=1}^{2} H(\mathbf{r}_i, \mathbf{k}_i) + C(\mathbf{r}_1 - \mathbf{r}_2). \tag{26}$$

C is some screened electron-electron interaction whose details will not be important here.

One can proceed with a Heitler-London (two-orbital) calculation which, in the absence of spin-orbit, gives the familiar Heisenberg exchange expression for the effective qubit-qubit interaction (calculated in [4])

$$H_{2qu} = J\,\mathbf{S}_A \cdot \mathbf{S}_B. \tag{27}$$

Here we specialize to a double-well confinement potential, with distinct wells A and B. We expect that with two electrons, electron one will occupy the A well, and electron two will occupy the B well, and vice versa. Note we are again using the first quantized language. In second quantization we should just say that the state is obtained from the vacuum (i.e., filled semiconductor bands) by applying a creation operator for spatial orbital A, and a creation operator for spatial orbital B, with the spin content of the orbital left for the present unspecified.

Kavokin begins by specializing the Dresselhaus contribution Eq. (22). We consider quantum dots that are strongly confined in one direction (z direction). This means that we will only

consider dynamics in the xy plane. It also means that, if we think in terms of expectation values, we expect that the strong confinement will mean that $\langle k_z^2 \rangle \gg \langle k_x^2 \rangle, \langle k_y^2 \rangle$. Thus, we approximate Eq. (22) by

$$
\begin{aligned}
H &= \frac{\hbar^2 k^2}{2m_*} + V_{conf}(\mathbf{r}) + \gamma \hbar^2 \left(-\sigma_x k_x \langle k_z^2 \rangle + \sigma_y k_y \langle k_z^2 \rangle \right) \\
&= -\frac{\hbar^2 \nabla^2}{2m_*} + V_{conf}(\mathbf{r}) + ia \left(-\sigma_x \nabla_x + \sigma_y \nabla_y \right),
\end{aligned} \tag{28}
$$

where $a = \gamma \hbar^2 \langle k_z^2 \rangle$.

I now proceed, following closely Sec. IV of [3]. Again with our mindset of first-quantization, we write a wavefunction basis states involving "electron 1" and "electron 2", providing for the possibility of antisymmetrization

$$
\Psi_A(1)\Psi_B(2)\chi_1^{\sigma_1}\chi_2^{\sigma_2} \quad \text{and} \quad \Psi_A(2)\Psi_B(1)\chi_1^{\sigma_1'}\chi_2^{\sigma_2'}. \tag{29}
$$

Note that unlike in second quantization, the spin functions χ are associated with electron number 1, 2 and not with spatial orbital A, B. Also, $(1, 2)$ is shorthand for $(\mathbf{r}_{1,2})$. The σ's are indices for the spin basis states $\uparrow$ and $\downarrow$, and are not to be confused with Pauli matrices. Observe that these are 8 basis functions overall, but we will come back to a 4D space due to antisymmetrization.

We now proceed with Heitler-London. The sleight of hand here involves recognizing that orbitals A and B are almost, but not quite, orthogonal, so that where their non-orthogonality is crucial for the leading-order term, it is accounted for; but other parts of the calculation are done as if the orbitals are orthogonal.

We will get matrix elements for the basis above. The two-electron Hamiltonian is split into two parts

$$
\begin{aligned}
H_{tot} &= H_0 + H_1 \tag{30} \\
H_0 &= \sum_{i=1}^{2} \left(-\frac{\hbar^2 \nabla^2(i)}{2m_*} + V_{conf}(\mathbf{r}_i) \right) + C(\mathbf{r}_1 - \mathbf{r}_2). \tag{31} \\
H_1 &= i\frac{2a}{\hbar} \sum_{i=1}^{2} \left(-S_x(i)\nabla_x(i) + S_y(i)\nabla_y(i) \right). \tag{32}
\end{aligned}
$$

In Heitler London the key matrix element is the off-diagonal one

$$
\langle \Psi_A(1)\Psi_B(2)\chi_1^{\sigma_1}\chi_2^{\sigma_2} | H_0 | \Psi_A(2)\Psi_B(1)\chi_1^{\sigma_1'}\chi_2^{\sigma_2'} \rangle = J\,\delta_{\sigma_1,\sigma_1'}\delta_{\sigma_2,\sigma_2'}. \tag{33}
$$

This gives the usual exchange constant J of the Heisenberg model Eq. (27). Note that it is only nonzero if orbitals A and B are *nonorthogonal*.

The interesting new spin-orbit contribution is

$$\langle \Psi_A(1)\Psi_B(2)\chi_1^{\sigma_1}\chi_2^{\sigma_2}|H_1|\Psi_A(2)\Psi_B(1)\chi_1^{\sigma_1'}\chi_2^{\sigma_2'}\rangle$$
$$= i\langle\Psi_A|\Psi_B\rangle\langle\sigma_2|\mathbf{b}\cdot\mathbf{S}_2|\sigma_2'\rangle\delta_{\sigma_1,\sigma_1'} - i\langle\Psi_B|\Psi_A\rangle\langle\sigma_1|\mathbf{b}\cdot\mathbf{S}_1|\sigma_1'\rangle\delta_{\sigma_2,\sigma_2'}, \quad (34)$$

$$\mathbf{b} \equiv \frac{2a}{\hbar}\begin{pmatrix} -\langle\Psi_A|\nabla_x|\Psi_B\rangle \\ \langle\Psi_A|\nabla_y|\Psi_B\rangle \\ 0 \end{pmatrix}. \quad (35)$$

The minus sign in Eq. (34) comes from the fact that the matrix elements comprising the vector $\mathbf{b}$ are real and antisymmetric (Anti-Hermitian) in A, B. We give a 3D version of the vector $\mathbf{b}$ because there are other spin-orbit terms, e.g., the 'Rashba' spin-orbit coupling, for which z-components of this vector are recovered.

One is now to infer the effective spin Hamiltonian that this leads to, and see how the effective interaction departs from the Heisenberg form. We simplify Eq. (35) further, by setting the coordinate system in spin space so that the z spin axis is parallel to the vector $\mathbf{b}$. Then we can write

$$\langle\Psi_A(1)\Psi_B(2)\chi_1^{\sigma_1}\chi_2^{\sigma_2}|H_{tot}|\Psi_A(2)\Psi_B(1)\chi_1^{\sigma_1'}\chi_2^{\sigma_2'}\rangle = \left(J + i\Omega\,|\mathbf{b}|\,(S_{2z}-S_{1z})\right)\delta_{\sigma_1,\sigma_1'}\delta_{\sigma_2,\sigma_2'}$$
$$\approx J'e^{i(\gamma/2)(S_{1z}-S_{2z})}\delta_{\sigma_1,\sigma_1'}\delta_{\sigma_2,\sigma_2'} \quad (36)$$

Here Ω is the real number $\langle\Psi_A|\Psi_B\rangle$, $J' = \sqrt{J^2 + (\Omega|\mathbf{b}|)^2}$ and $\gamma = \arctan\left(\Omega|\mathbf{b}|/J\right)$. Typically $J' \approx J$ and $\gamma \ll \pi$, but I will review Kavokin's estimates at the end, indicating that this will not be an entirely negligible effect.

Finding eigensolutions to the full Hamiltonian (all the interesting spin dependence comes from the "exchange integral" Eq. (36)), we can write these down by requiring antisymmetry. These are constructed in precise analogy to the case of no spin-orbit ($\gamma = 0$), with the change of sign characterizing the antisymmetry appearing in one of two factors, according to the quantum number I

$$\Phi_{IM} = \tfrac{1}{2}(\Psi_A(1)\Psi_B(2)e^{i(\gamma/2)(S_{1z}-S_{2z})} + (-1)^I\Psi_A(2)\Psi_B(1)e^{-i(\gamma/2)(S_{1z}-S_{2z})})\zeta_{IM} \quad (37)$$

Here ζ_{IM} are the usual spin eigenfunctions of the two-particle system, i.e., the triplets ($I = 1$, $M = -1, 0, 1$), and the singlet ($I = 0$, $M = 0$). Our last task is to understand what effective two-spin Hamiltonian will produce such states as eigenstates. To understand how this works, I show the singlet case of these states in a more explicit notation, in which the spin operators have been applied to the state

$$\Phi_{00} = \frac{1}{2}\Big(\Psi_A(1)\Psi_B(2)\big(e^{i\gamma/2}|\uparrow_1\downarrow_2\rangle - e^{-i\gamma/2}|\downarrow_1\uparrow_2\rangle\big) + \Psi_A(2)\Psi_B(1)\big(e^{-i\gamma/2}|\uparrow_1\downarrow_2\rangle - e^{i\gamma/2}|\downarrow_1\uparrow_2\rangle\big)\Big).$$
$$(38)$$

Note this does not factorize into a spin part and a space part, but the total is clearly antisymmetric with respect to $1 \leftrightarrow 2$.

We will take a next step that will give us an effective wavefunction for the spins alone. It is based on the following premise: we suppose that the A and B orbitals are disjoint in space (clearly

not exactly true in reality, since they have a finite inner product Ω), and that the wavefunction has no double-occupancy character. Then we see that the first term of wavefunction Eq. (38) is only nonzero if electron 1 is in the A quantum dot, and electron 2 is in the B quantum dot. Then, the spin state associated with this first term is

$$\Psi_{spin} = e^{i\gamma/2}|\uparrow_A\downarrow_B\rangle - e^{-i\gamma/2}|\downarrow_A\uparrow_B\rangle. \tag{39}$$

Note the crucial change of labeling $1, 2 \rightarrow A, B$ motivated by our argument. If we apply the same reasoning to the second term of Eq. (38), noting that it is only nonzero if electron 1 is in the B quantum dot, and electron 2 is in the A quantum dot (note the reversal from above). We then transcribe the spin wavefunction of this term as

$$e^{-i\gamma/2}|\uparrow_B\downarrow_A\rangle - e^{i\gamma/2}|\downarrow_B\uparrow_A\rangle, \tag{40}$$

which is in fact exactly the same (after rearranging) as Ψ_{spin}. The same observations go through for the triplet states. This encourages us to look for an effective Hamiltonian with only spin operators which has Eq. (39) as an eigenstate. The answer is

$$H_{spin} = \exp\left(i\tfrac{\gamma}{2}(S_{Az} - S_{Bz})\right)\mathbf{S}_A \cdot \mathbf{S}_B \exp\left(-i\tfrac{\gamma}{2}(S_{Az} - S_{Bz})\right) = \mathbf{S}'_A \cdot \mathbf{S}'_B. \tag{41}$$

So this is a kind of Heisenberg exchange, except that the coordinate system has been rotated, so there are two different frames of reference used at the A site and the B site. Let me comment that the line of argument just given is basically a switchover from first-quantized to second-quantized thinking, since it changed from "which electron is where?" to "where are the electrons?". It has the limitation that it is only proper if the A and B orbitals are orthogonal; I note that Eq. (41) is not even Hermitian if A and B are non-orthogonal.

Finally, I mention Kavokin's calculations for the size of this effect. He estimates:

1. quantum dots in GaAs, 10 nm heterostructure: $\gamma \approx 0.1$

2. shallow donors, bulk GaAs: $\gamma \approx 0.01$

3. donors near oxide interface in Si: $\gamma \approx 0.03$

This just serves to illustrate that this is not necessarily a very small effect.

4 A few thoughts about electron-electron interaction for spin qubits

I will here briefly discuss the electronic structure of the double quantum dot from another angle. We have taken into account electron-electron interaction in the calculation done above. More generally, how do interaction effects enter the electron problem for the quantum dot? Is there a basically one-electron picture that is close to the truth?

For this I explain some of the insights of [5]. In this work we retreat from the problem of spin-orbit interaction, considering only the electronic structure of few-electron dots in the non-relativistic limit.

Let me review some of the most basic facts about multi-electron eigenstates. I will state the facts in both first- and second-quantization.

If there are no e-e interactions, then eigenstates are single spin-orbital Slater determinants.

Not to be confused with the spin-orbit interaction, spin-orbital functions are single-electron functions of both space and spin. In the nonrelativistic case there will be functions like the kind we have seen above, single products like $\Psi_{A\sigma} = \Psi_A(1)\chi_1$. (If we were doing spin-orbit coupling, these would be entangled spin and space functions.) Then a single Slater determinant of two electrons would have the form

$$\begin{vmatrix} \Psi_A(1)\chi_1 & \Psi_B(1)\chi_1' \\ \Psi_A(2)\chi_2 & \Psi_B(2)\chi_2' \end{vmatrix} \tag{42}$$

Here I use the convention that in a Slater determinant, the rows are indexed by electron number, and the columns are indexed by the distinct spin-orbital (which may involve a repetition of the spatial orbital). This seems to immediately contradict the observation that two electron systems have triplet eigenstates of the form

$$\begin{vmatrix} \Psi_A(1) & \Psi_B(1) \\ \Psi_A(2) & \Psi_B(2) \end{vmatrix} \left(|\uparrow_A\downarrow_B\rangle + |\downarrow_A\uparrow_B\rangle \right), \tag{43}$$

split off from the other triplets in the presence of a magnetic field. This appears to be, and indeed is, a sum of two spin-orbital Slater determinants. But there is no contradiction here, as this state is degenerate with the singlet state (even in a magnetic field), so each determinant is separately an eigenstate. It is only if we also insist that we have eigenstates that are labelled by total spin that superpositions become necessary.

Note that the equivalent statement in second quantization is that an eigenstate can be formed by applying, to the vacuum, two spin-orbital creation operators

$$a_{A\chi}^\dagger a_{B\chi'}^\dagger |0\rangle. \tag{44}$$

We will be considering two and four electron systems. We will not get further than the story of a single quantum dot. For this, the "vacuum" will be the filled valence band, and all calculations will be done at the level of the envelope function ("effective mass theory"). But the gigantic complication of many-electron theory is that the eigenstates are *not* single Slater determinants. But the Slater determinants form a complete, orthonormal basis for the many-electron Hilbert space. This means that the general form for these eigenstates is, using the second-quantized notation,

$$\sum_{i,j}{}' c_{ij}\, a_i^\dagger a_j^\dagger |0\rangle. \tag{45}$$

Here the sums run over the orthogonal spin-orbitals i, j. The prime is a reminder that the $i = j$ term gives nothing, since $(a^\dagger)^2 = 0$.

In quantum chemistry the terms in Eq. (45) are called configurations, and using a set of basis functions like this is called the *configuration-interaction (CI) technique*. Convergence in this technique is difficult, the only useful calculations use a computer.

In [5] we have done a fairly large calculation for a harmonically confined quantum dot in a magnetic field, with two or four electrons. Here the number of single-particle eigenstates used is 50, meaning that the CI basis has $\binom{50}{2}$ or $\binom{50}{4}$ elements. Bases of these size were apparently necessary for good convergence.

We describe now a step which leads to a much more powerful starting basis. This is called the Natural Orbital (NO) method due to Löwdin.

Suppose we have chosen a spin sector to examine, e.g., the singlet; thus, we are left with just orbital determinants such as in Eq. (43). Löwdin's procedure involves first obtaining the first-order density matrix of the N-particle orbital wavefunction

$$\rho(\mathbf{r}', \mathbf{r}) = N \int d\mathbf{r}_2 ... d\mathbf{r}_N \, \psi^*(\mathbf{r}', \mathbf{r}_2, ... \mathbf{r}_N) \psi(\mathbf{r}, \mathbf{r}_2, ... \mathbf{r}_N). \tag{46}$$

He next notes that if there were no e-e interactions and the eigenstate was a single Slater determinant, the first-order density matrix would be given by a simple sum over the single-particle orbitals in that determinant

$$\rho(\mathbf{r}', \mathbf{r}) = \sum_\alpha \phi_\alpha^*(\mathbf{r}') \phi_\alpha(\mathbf{r}). \tag{47}$$

But very generally, as a symmetric, positive semi-definite function of $\mathbf{r}$ and $\mathbf{r}$', the first order density matrix has a spectral decomposition

$$\rho(\mathbf{r}', \mathbf{r}) = \sum_\alpha \rho_\alpha \, \phi_{(NO),\alpha}^*(\mathbf{r}') \phi_{(NO),\alpha}(\mathbf{r}). \tag{48}$$

This set of "natural orbitals" $\phi_{(NO)}$ is in general quite different from any approximate single particle orbital, and should provide a CI expansion that is more rapidly convergent. Note that the "NO occupation numbers" $\rho_\alpha \geq 0$, and obey the sum rule $\sum_\alpha \rho_\alpha = N$.

We find that a relatively small number of NOs (i.e., somewhat larger than N) capture most of the weight of Eq. (48). So, if we had been lucky enough to be given (say by some wizard Merlin) these NO functions, we could have done a very compact CI expansion with good convergence on the full many-body answer.

Our calculation in [5] is for a harmonically confined quantum dot for GaAs (in the sense of using the effective mass of the conduction band) in a heterostructure-confined structure, so it is a 2D calculation. A large CI basis is used for convergence. We do calculations for two electrons and for four electrons, fixing the spin state to be singlet and then triplet, as in Eq. (43). For the two electron case there is nothing more to be said about the spin state, but for four electrons there are several alternatives for making these spin states. We do it in shell-style, where the lowest two orbitals are "paired" (that is, in their own singlet), while the highest occupied orbitals have the freedom to be singlet or triplet.

Figure 1 just shows the Hartree-Fock one-particle spectrum for this dot, indicating the range of magnetic field of interest. The quantum numbers are those of the so-called "Fock-Darwin"
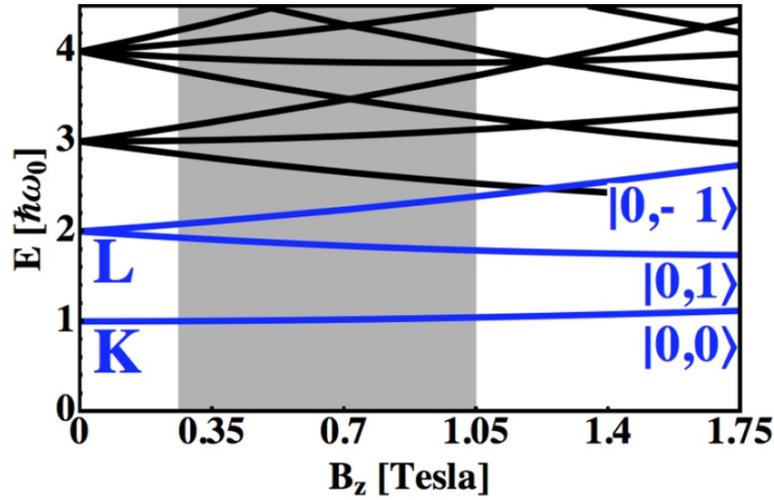
Fig. 1: *Single-particle energy levels of the quantum dot, in the Hartree-Fock approximation.*
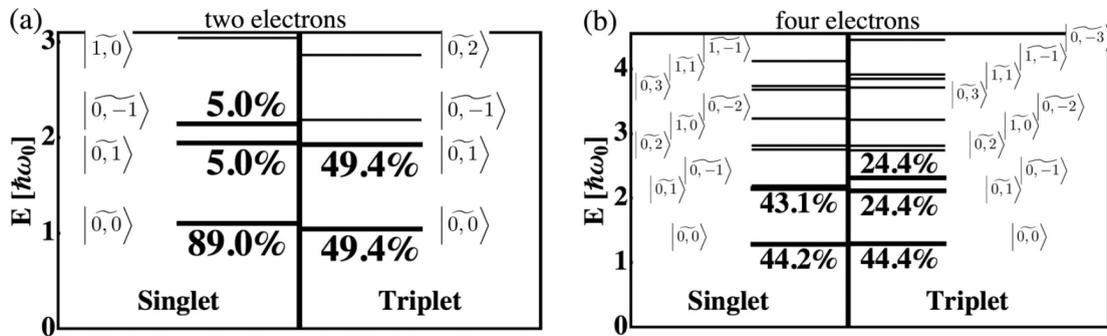
Fig. 2: *Weights of natural orbitals for the four settings considered here.*

states. In all four cases, the full CI calculation is done, and then the natural orbitals are extracted from the first-order density matrix as above. These give new orbitals which are indicated by a tilde; they can still be put in one-to-one correspondence with the Hartree-Fock orbitals. Figure 2 shows the results for these four cases. It shows percentages, we can multiply by the electron number N to talk about the number of electrons in different orbitals. The $N = 2$ singlet case shows that $2 \times 0.89 = 1.98$ of the electron weight is in the lowest orbital, doubled since both spin states can be occupied. In the $N = 2$ triplet case, 0.988 electrons are in each of the two first orbitals, as expected from the Pauli exclusion principle. The quality of the $N = 4$ case is only a bit less ideal: in the singlet case $4 \times 0.442 = 1.768$ electrons are a singlet in the first "shell", with the second shell with 1.762 occupancy. This leaves 0.47 of an electron "unaccounted for", in the sense that multiple Slater determinants are necessary to capture the effect of this much of the weight in the many-electron wavefunction. Finally, the story is similar for the $N = 4$ triplet: 1.776 electrons are in the core singlet, and 0.97 electrons each in the two next orbitals. 0.284 is "unaccounted for". It is understandable that the single Slater determinant is a little better for the triplet cases, since the antisymmetric orbital wavefunction does a better job of keeping the electrons out of each other's way and avoiding effects due to the Coulomb interaction.
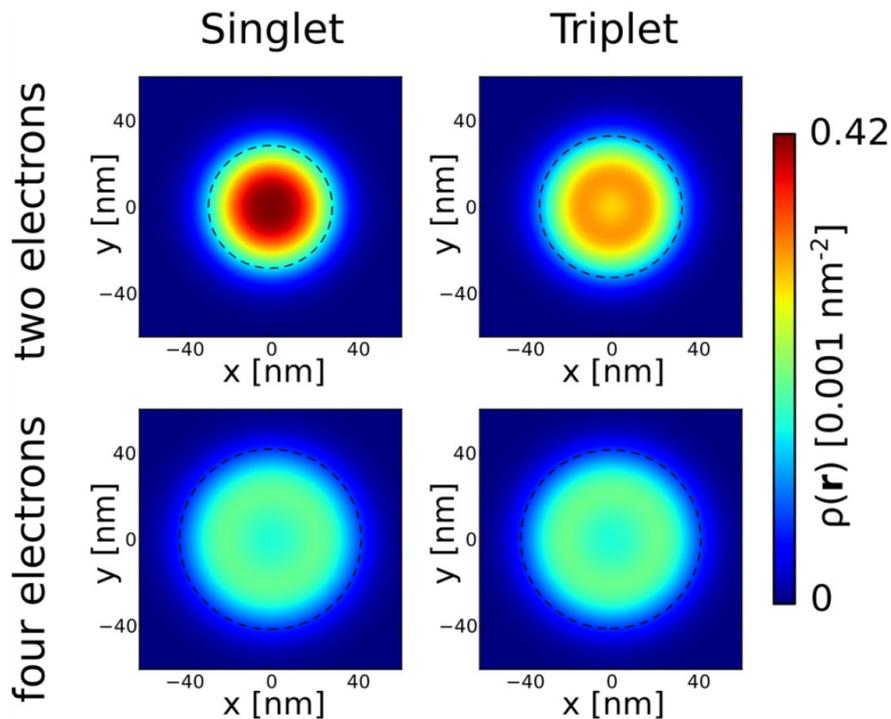
Fig. 3: *Charge density of the four quantum-doty settings considered here, with full interaction effects.*

Finally, this numerical study uncovered an important fact about the natural orbitals: to very good approximation, they are just the non-interacting Fock-Darwin orbitals with a simple rescaling of the radial coordinate. The natural orbital is in almost all cases blown-up compared with the Hartree-Fock orbitals – interactions push the electrons away from the center. This expansion is about 40% for the lowest-energy orbital, and is about half that for the next orbitals that participate in the $N = 2, 4$ states discussed above.

A concluding word about this study is that interaction effects are not so overwhelming, causing a definite renormalization of the Hartree-Fock picture but leaving it qualitatively intact. This is somewhat at odds with the general experience that very low-density electron systems have the largest departures from single electron physics (think of the Wigner crystal). But fortunately for our quantum-dot qubits, the mental picture of single-electron physics is shown to work quite well.

References

[1] J. Cohn, F. Yang, K. Najafi, B. Jones, and J.K. Freericks, Phys. Rev. A **102**, 022622 (2020)

[2] L.M. Roth, B. Lax, and S. Zwerdling, Phys. Rev. **114**, 90 (1959)

[3] K.V. Kavokin, Phys. Rev. B **64**, 075305 (2001)

[4] G. Burkard, D. Loss, and D.P. DiVincenzo, Phys. Rev. B **59**, 2070 (1999)

[5] M.A. Bakker, S. Mehl, T. Hiltunen, A. Harju, and D.P. DiVincenzo,
    Phys. Rev. B **91**, 155425 (2015)

Index

Schriften des Forschungszentrums Jülich
Modeling and Simulation

1. **The LDA+DMFT approach to strongly correlated materials**
   Lecture Notes of the Autumn School 2011 Hands-on LDA+DMFT
   edited by E. Pavarini, E. Koch, D. Vollhardt, A. Lichtenstein (2011), 420 pages
   ISBN 978-3-89336-734-4

2. **Correlated Electrons: From Models to Materials**
   Lecture Notes of the Autumn School on Correlated Electrons 2012
   edited by E. Pavarini, E. Koch, F. Anders, and M. Jarrell (2012), 450 pages
   ISBN 978-3-89336-796-2

3. **Emergent Phenomena in Correlated Matter**
   Lecture Notes of the Autumn School on Correlated Electrons 2013
   edited by E. Pavarini, E. Koch, and U. Schollwöck (2013), 520 pages
   ISBN 978-3-89336-884-6

4. **DMFT at 25: Infinite Dimensions**
   Lecture Notes of the Autumn School on Correlated Electrons 2014
   edited by E. Pavarini, E. Koch, D. Vollhardt, A. Lichtenstein (2014), 450 pages
   ISBN 978-3-89336-953-9

5. **Many-Body Physics: From Kondo to Hubbard**
   Lecture Notes of the Autumn School on Correlated Electrons 2015
   edited by E. Pavarini, E. Koch, and P. Coleman (2015), 500 pages
   ISBN 978-3-95806-074-6

6. **Quantum Materials: Experiments and Theory**
   Lecture Notes of the Autumn School on Correlated Electrons 2016
   edited by E. Pavarini, E. Koch, J. van den Brink, G. Sawatzky (2016), 420 pages
   ISBN 978-3-95806-159-0

7. **The Physics of Correlated Insulators, Metals, and Superconductors**
   Lecture Notes of the Autumn School on Correlated Electrons 2017
   edited by E. Pavarini, E. Koch, R. Scalettar, and R. Martin (2017), 450 pages
   ISBN 978-3-95806-224-5

8. **DMFT: From Infinite Dimensions to Real Materials**
   Lecture Notes of the Autumn School on Correlated Electrons 2018
   edited by E. Pavarini, E. Koch, A. Lichtenstein, D. Vollhardt (2018), 480 pages
   ISBN 978-3-95806-313-6

9. **Many-Body Methods for Real Materials**
   Lecture Notes of the Autumn School on Correlated Electrons 2019
   edited by E. Pavarini, E. Koch, and S. Zhang (2019), 520 pages
   ISBN 978-3-95806-400-3